

The Origin of Compositional and Textural Zoning of Shallow-level Granitoid Plutons

Charles University in Prague, Faculty of Science
Institute of Petrology and Structural Geology

Jakub Trubač



Charles University in Prague

Faculty of Science

Institute of Petrology and Structural Geology

Study program: Geology (P1201)

Field of study: 4XGEOL (1201V000)



Jakub Trubač

The Origin of Compositional and Textural Zoning of Shallow-Level Granitoid Plutons

Ph.D. Thesis

Supervisor: Doc. Mgr. Vojtěch Janoušek, Ph.D.

Consultant: Prof. RNDr. Jiří Žák, Ph.D.

Prague, 2015

Univerzita Karlova v Praze

Přírodovědecká fakulta

Ústav petrologie a strukturní geologie

Studijní program: Geologie (P1201)

Studijní obor: 4XGEOL (1201V000)



Jakub Trubač

Vznik kompoziční a texturní zonálnosti mělce uložených granitoidních těles

Disertační práce

Vedoucí závěrečné práce: Doc. Mgr. Vojtěch Janoušek, Ph.D.

Konzultant: Prof. RNDr. Jiří Žák, Ph.D.

Praha, 2015



"So do the stones speak, when all else is silent."

Linnaeus

DECLARATION

I, Jakub Trubač, declare that this thesis, presented for the Ph.D. degree at Charles University in Prague, is a result of my own original research and has not been previously submitted to Charles University in Prague or any other institution.

I have clearly indicated, when appropriate, the contributions of colleagues and have made every effort to acknowledge all collaborative work. The copyright to the material within this thesis belongs to the author and any information or quotation taken from it should be acknowledged and published only if prior consent has been given.

Jakub Trubač

Prague, 29th May, 2015

PROHLÁŠENÍ

Prohlašuji, že jsem závěrečnou práci zpracoval samostatně a že jsem uvedl všechny použité informační zdroje a literaturu. Tato práce ani její podstatná část nebyla předložena k získání jiného nebo stejného akademického titulu.

Jakub Trubač

V Praze, 29. května 2015

ABSTRACT

The principal goal of this Ph.D. Thesis is to contribute to the research on formation of compositional and textural zoning in shallow-level plutons. Processes responsible for emplacement of individual plutons/pulses and the origin of compositional zoning in are addressed in a great detail, from the pluton-scale down to the micro-scale.

The main emphasis in the more focused part of this text is on a combination of various quantitative data sets from two well-selected plutons (the Říčany Pluton in the Central Bohemian Plutonic Complex and the Melechov Pluton in the Moldanubian Batholith). These detailed studies are supported by further research on the Štěnovice, Čistá and Ševětín plutons. In this way we cover the evolution of Variscan magmatism in the heart of Bohemian Massif in its entirety, from Late Devonian till Permian.

The thesis is based on combining field and structural studies (including the anisotropy of magnetic susceptibility, AMS), textural analysis, petrological, geochronological and geochemical methods with geophysical investigations. Mathematical approaches have been designed and applied to the interpretation of geochemical data, with potential applications to other igneous systems.

I strongly believe that only such comprehensive studies on well-selected case examples have a potential to provide a generally applicable, in-depth understanding of zoning origin, mechanisms of pluton construction, and melt sources/evolution in the composite magmatic systems.

The most important conclusions of the thesis are as follow:

1. Using the case study of the Říčany Pluton, a new model for the origin of reverse zoning is proposed invoking a thermally-driven overturn of a deeper stratified magma chamber. Information about sources and geochemical evolution of highly fractionated nested granite pulses is reported and the behaviour of many trace elements in differentiation of the felsic granitic system is described. Lastly, a new mechanism of helicoidal magma flow is formulated on example of the Říčany Pluton.
2. Quantitatively characterized variations in magnetic fabric throughout the Melechov Pluton and the AMS-to-strain inversion method (SUSIE) are used to infer the strain distribution in the proposed Melechov diapir head. Data are compared with theoretical models for diapiric structures; the applicability of the SUSIE method for strain analysis in granite plutons is also discussed.

3. Much of the research effort was concerned with the regional tectonic setting and large-scale fabric patterns in granitoid plutons in the Bohemian Massif, from Late Devonian subduction, through Early Carboniferous collision till Permian orogenic collapse. Particular problems were addressed using case studies of subduction-related Štěnovice and Čistá plutons as well as the post-orogenic collapse-related Ševětín Pluton.
-

Taken together, the integration of field and quantitative data sets obtained by range of methods on several selected plutons has provided new insights into emplacement mechanisms of granitoid magma in the upper crust and the origin of modal/compositional zoning. Moreover, the study brings broader implications for timing, sources and development of Variscan plutonism in Bohemian Massif and as such to the magmatic and tectonic evolution of the Variscan orogen as a whole.

ABSTRAKT

Základním cílem této Ph.D. práce je přispět k výzkumu formování kompoziční a texturní zonálnosti mělce uložených plutonů. Procesy vedoucí ke vzniku kompoziční zonálnosti v těchto tělesech jsou zde popisovány jak na úrovni měřítka celého magmatického tělesa (plutonu), tak z hlediska mikroměřítka.

Hlavní důraz v podrobnějších částech této práce je kladen na kombinaci různých kvantitativních souborů dat ze dvou dobře vybraných plutonů (říčanský pluton ve středočeském plutonickém komplexu a melechovský pluton v moldanubickém batolitu). Detailní studie jsou podpořeny dalším výzkumem plutonů štěnovického a ševětínského a plutonu Čistá. Uvedené příklady shrnují vývoj variského magmatismu přímo v srdci Českého masivu, od pozdního devonu do období permu.

Ph.D. práce je založena na kombinaci terénních a strukturních studií (včetně metody anizotropie magnetické susceptibility, AMS), texturní analýzy, petrologických, geochronologických a geochemických metod a geofyzikálních výzkumů. Dále byly navrženy a aplikovány matematické přístupy k interpretaci geochemických dat, s potenciálním využitím v ostatních magmatických systémech.

Pevně věřím, že tyto souhrnné studie na pečlivě vybraných příkladech mají potenciál poskytnout všeobecně užitečné a důkladné porozumění vzniku zonálnosti včetně mechanismů stavby plutonu a zdrojů/vývoje tavenin v kompozitních magmatických systémech.

Nejdůležitější závěry této práce:

1. Na příkladu říčanského plutonu je navržen nový model vzniku reverzní zonálnosti vyvoláním termálně řízené změny v hlubokém stratifikovaném magmatickém krbu. Jsou zde zaznamenány informace o zdrojích a geochemickém vývoji vysoce frakcionovaných granitových pulsů a popsána distribuce mnoha stopových prvků během diferenciací felsického granitového systému. Dále je zde formulován nový mechanismus tzv. helikálního magmatického toku opět na příkladu říčanského plutonu.
2. Kvantitativně charakterizované variace v magnetické stavbě v melechovském plutonu a inverzní metoda AMS-to-strain (SUSIE) jsou použity k určení přírůstku napětí ve svrchních partiích granitového diapiru při finálním umístění do podmínek střední kůry. Data jsou porovnána s teoretickými modely pro diapirické struktury; též je prodiskutována použitelnost metody SUSIE pro analýzu napětí v granitových plutonech.

3. Mnoho úsilí bylo věnováno výzkumu tektonického vývoje a strukturní analýze vnitřních staveb v granitoidních plutonech v Českém masivu. Tektonický vývoj je zaznamenán ve strukturách vzniklých během subdukce v pozdním devonu na příkladové studii štěnovického a čisteckého plutonu, v kolizní události v raném karbonu i v kolapsu orogénu v období permu (ševětínský pluton).

Souhrnně řečeno, spojení terénních a kvantitativních datových souborů získaných škálou metod na několika vybraných plutonech poskytlo nové pohledy na mechanismy vmístění granitoidního magmatu do podmínek svrchní kůry a na vznik modální/kompoziční zonálnosti. Dále Ph.D. teze přináší širší implikace pro vývoj variského plutonismu v Českém masivu a také pohled na magmatismus a tektonický vývoj variského orogénu jako celku.

TABLE OF CONTENTS

Preface.....	15
Aims.....	18
Methodology.....	20
Introduction.....	24
References.....	44
Results.....	55
Chapter I: Magma Differentiation and Pluton Zoning.....	55
Article I-1.....	56
Article I-2.....	144
Chapter II: Internal Structure of Zoned Plutons.....	193
Article II-1.....	194
Article II-2.....	252
Chapter III: Zoned Plutons in various tectonic settings.....	263
Article III-1.....	264
Article III-2.....	310
Article III-3.....	342
Summary of the main conclusions.....	399
Appendices.....	406

ACKNOWLEDGEMENTS

The past six years have had their ups and downs and without the following people, completion of this thesis would never have been possible.

I would like to thank my supervisor, Vojtěch Janoušek. He provided me not only with scientific support during the whole course of my Ph.D. study, but also created amazingly familiar and friendly environment for my research.

I am greatly indebted to my consultant Jiří Žák for his unbelievably kind approach, never ending discussions, patience and expanding my horizons.

My Ph.D. Thesis was supported by other scientists with experience in mutually complementary fields closely related to the topic of this thesis (structural geology, petrology, igneous geochemistry and isotope geochemistry/dating). Namely I would like to thank David Dolejš (Charles University, Prague); Wolfgang Dörr; Vojtěch Erban (Czech Geological Survey, Prague); Fritz Finger (University of Salzburg, Salzburg); Axel Gerdes (Goethe Universität, Frankfurt am Main); František V. Holub (Charles University, Prague); Marta Chlupáčová (Charles University, Prague); Petr Kabele (Czech Technical University, Prague); Václav Kachlík (Charles University, Prague); František Laufek (Czech Geological Survey, Prague); Luděk Minařík (Institute of Geology AS CR, v. v. i., Prague); Jan Mrlina (Institute of Geophysics, ASČR, v.v.i., Prague); Tomáš Návrátil (Institute of Geology, AS ČR, v. v. i., Prague); Martin Racek (Charles University, Prague); Miloš René (Institute of Rock Structure and Mechanics, ASČR, v.v.i., Prague); Jiří Sedlák (Miligal, s.r.o., Brno); Jiří Sláma (University of Bergen, Bergen); Michael Somr (Czech Technical University, Prague); Ladislav Strnad (Charles University, Prague); Jan Švancara (Masaryk University, Brno); Kryštof Verner (Czech Geological Survey, Prague); Jiří Zachariáš (Charles University, Prague) and all editors and reviewers who helped me with revisions of published manuscripts.

Of course, there are many others; I would like to thank especially Carlos Villaseca for his invitation to Dept. of Petrology and Geochemistry, Universidad Complutense de Madrid, where I spent marvellous months learning the essentials of lab work and writing up the thesis. Also important was collaboration with the Spanish colleagues, making possible to see outcrops of

granitoids of the Spanish Central Massif and discuss their nature and petrogenesis with leading experts.

The penultimate thanks go to my parents, my sister and Lenka Ekeke, providing me with support during all my life.

Last – but not least – this work was financed by project No. P210/11/1168 of Czech Science Foundation (GAČR), by the Special Studies, Research Methodology, Doctoral and Diploma Thesis (No. 323000; Czech Geological Survey), the Training Agreement of the Erasmus Programme (Charles University in Prague) and the Hlávka Foundation.

PREFACE



The leading theme of this Ph.D. thesis, which I started to work on at the Institute of Petrology and Structural Geology, Charles University, in autumn 2010, is the compositional and textural zoning in shallow-level granitoid plutons.

In any serious attempt to explain the nature and genesis of a complex zonation pattern in a granitic pluton, a multidisciplinary approach has to be used, combining structural, petrological, geochronological and geochemical methods with geochemical modelling and geophysical investigations. An excellent setting where such a multidisciplinary approach could be developed and tested is the Bohemian Massif, the easternmost fragment of the Variscan collisional orogen in Europe. Among the numerous shallow-level granitoid plutons that intruded this complex unit in Late Devonian to Early Carboniferous times, we have found the following two particularly suitable for the thesis:

1. The **Říčany Pluton**, which crops out at the north-eastern extremity of the Central Bohemian Plutonic Complex. It has a roughly elliptical outline and consists of three (muscovite)–biotite granite facies that define a sub-concentric compositional and textural zoning. Within the analytical uncertainties, the emplacement ages of the two main facies are the same (~337 Ma). As the degree of fractionation decreases inwards, the pluton shows reverse zoning. But it is “cryptic”, being reflected nearly exclusively in the trace-element compositions (see Results, **Article I.-1**, **Article I.-2**, **Article II.-2**).
2. The **Melechov Pluton** is the northernmost intrusion of the composite Moldanubian Batholith, which is the largest plutonic body in the Variscan Internides. The pluton consists of four concentric units of peraluminous, S-type granites. The TIMS-ID Concordia ages for Mnz populations of the three outer facies dated (Lipnice, Světlá, and Kouty) range between 332 ± 1 and 323 ± 0.4 Ma (mostly 327–325 Ma). This compares well with LA ICP-MS dating of the Lipnice Mnz (324.8 ± 2.4 Ma) and previous conventional U–Pb dating of Zrn and Mnz from the ‘Eisgarn’ granites (see Results, **Article II.-1**).

Even though most of our attention was directed to the two zoned plutons listed above, the results of other studies of Bohemian granitic bodies (e.g., **Ševětín**, **Štěnovice** and **Čistá plutons**) are discussed in separate **Articles III.-1**, **III.-2** and **III.-3**.

This **Ph.D. thesis** consists of several parts. The main scientific questions and goals are listed in the **Aims**. The analytical methods used to study the selected plutons are briefly summarized in **Methodology**. The state-of-the-art knowledge is outlined in the **Introduction** subdivided into three Chapters. The main part of the thesis consisting of seven journal articles and one book chapter is organized into **Results**. The most significant outcomes of the thesis are finally highlighted in the **Summary**.



AIMS

The principal goal of the **Ph.D. thesis** is to modestly contribute to understanding of shallow-level felsic systems. In particular, we ask what can be learned from the granitoid pluton/host-rock structures and geochemical variation about physico-chemical processes in magma chambers.

In brief, the main aims of this Ph.D. thesis are to:

- describe the nature of zoning in individual plutons, as well as the external and internal contacts, in terms of petrology, textures, internal fabrics, and chemical composition;
- investigate the structural evolution, textures, fabrics (including anisotropy of magnetic susceptibility, AMS) in granites, as well as thermal and structural evolution of the individual plutons with their contact aureoles;
- compare field and laboratory data pertaining to thermal and crystallization history with the numerical simulation of conductive cooling of the individual plutons;
- using the major- and trace-element data and radiogenic isotope methods to provide information on sources of individual pulses, their mutual relationship and development in space and time, and to constrain the processes that may have modified the magma composition (e.g., fractional crystallization, magma mixing, crustal assimilation);
- combining the above datasets with viscosity simulations to constrain the viable ascent and emplacement mechanisms of granitic magma in shallow-level plutons; in particular to assess the importance of granitoid diapirism and incremental growth models.

METHODOLOGY



The principal approach adopted in this work is to use careful observations and detailed structural mapping in the field as a firm basis for further quantitative analysis in the laboratory. Field data are complemented by a wide range of other analytical methods:

- **Anisotropy of magnetic susceptibility (AMS) and inverse strain estimation.** The AMS method was used to quantify cryptic (magnetic) characteristics of compositional zones in the plutons, including bulk susceptibility (related to the rock composition and magnetic minerals content), shape of the fabric ellipsoid, and fabric intensity and orientation. This method was hopeful to reveal magmatic strain patterns related to the origin of zoning, for example, resulting from magma inflow, melt relocation, or melt escape. The AMS was measured on KLY3-S Kappabridge and processed using ANISOFT 4 software in the Laboratory of Rock Magnetism at Faculty of Science, Charles University. For determining strain in igneous body of the Melechov Pluton was used the program Inverse strain estimation from magnetic susceptibility (SUSIE; Ježek and Hroudá 2002, 2007).
- **Gravimetric studies** on two plutons (the Říčany granite and Štěnovice Pluton) was carried out to estimate the shape (and thus initial emplacement geometry) at depth. The gravity anomalies caused by the granite plutons were separated from the Bouguer gravity field using 2D Fourier domain filtering. Along selected profiles, the gravity modeling was performed applying 2 3/4 dimensional approaches. It used interactive GM-SYS software of Northwest Geophysical Associates (USA) and was carried out by Jan Švancara (the Říčany Pluton) and Jan Mrlina (the Štěnovice Pluton).
- **Quantitative textural analysis** was important component of the **Article I.-1** in the **Říčany Pluton**. The textural analysis studies can reveal much about how and under what conditions magmatic rocks solidify, including their rates of solidification, and is also capable of identifying interactions between magma pulses (mixing). Sampling was completed along several transects across the Říčany Pluton. Laboratory work included preparation of the polished rock slabs. In addition, after creating photos of these slabs were obtained textural parameters (size, modulus, perimeter, aggregation index R) with use special software (QGIS and ImageJ).

- **Petrology, mineral chemistry (EMPA).** For newly acquired samples, petrological study included microscopy (\pm optical cathodoluminescence, CL at Charles University, Prague), determination of mineral assemblages and rock classification. Extensive electron microprobe work aimed at identification of unknown phases, imaging (CL + BSE) and studying internal zoning in selected minerals. In all cases was employed the electron microprobe Cameca SX 100 housed at laboratory at Institute of Geological Sciences, Masaryk University (Brno), Institute of Geology AS CR, v. v. i., Prague and Department of Petrology and Geochemistry, Universidad Complutense de Madrid. The mineral chemistry served also as a basis to assess the relationships between, and development within, each of the magmatic units and as an input to the subsequent geochemical modelling.
- **Whole-rock and radiogenic isotope geochemistry, geochemical modelling.** The major- and trace-element chemistry was used, in conjunction with Sr–Nd isotope data (provided by thermal ionization mass spectrometer Finnigan MAT 262 and multi-collector ICP MS on the Czech Geological Survey in Prague), to determine the compositions of individual magmatic units, their spatial variation, mutual relationships, and likely genesis. Additional goal was to assess the relative role and mechanism of the possible petrogenetic process (e.g., partial melting, fractional crystallization/accumulation, hybridization, assimilation). The whole-rock major- and trace-element analyses were carried out in the Acme Analytical Laboratories (Vancouver) Ltd., Canada. Selected major-element analyses were obtained by wet chemistry in the laboratories of the Czech Geological Survey, Prague–Barrandov. The numeric modelling of the major- and trace-element geochemical data (fractional crystallization) was done using the *GCDkit* package (Janoušek *et al.* 2006a, 2011) and developed by techniques described in Janoušek *et al.* (2015).
- **U–Th–Pb radiometric dating** (LA-ICP-MS and conventional by TIMS) of zircon and monazite. For understanding of development in each of the studied plutons, a precise and reliable dating of individual pulses was essential. The problems with low-T Pb loss and large proportion of inherited zircon in low-T, peraluminous anatectic granites (e.g. Janoušek 2006b; Miller *et al.* 2003) was overcome by *in situ* methods, namely LA ICP-MS dating of zircon and monazite, as well as by conventional monazite dating (provided by Axel Gerdes and Wolfgang Dörr, respectively, at Goethe University in Frankfurt). In addition, the U–Pb ages from inherited cores of zircon crystals provided invaluable information on nature of prospective magma source(s) to individual dated units.

- ***Thermal modelling and magma viscosity simulations.*** For the Říčany Pluton, conductive thermal model using the finite element method and was developed by Petr Kabele and Michael Somr from Czech Technical University. The model involved specific parameters obtained through other methods as detailed above, such as pluton shape and size (taken from geologic maps and inferred from gravimetric modelling), thermal properties and initial temperatures of magmas estimated from geochemical composition and zircon saturation temperature, respectively. The modelling provided information on how long the plutons could have remained magmatically active and what was the distribution of melt in space and time during their cooling histories. Following the thermal calculations, major-element compositions were used to simulate evolution of magma viscosities within the main facies of the Říčany Pluton.

INTRODUCTION



Chapter I: Magma Differentiation and Pluton Zoning

Chapter I provides a summary of key physico-chemical processes involved in formation of compositional and textural zoning in plutons (Fig. 1).

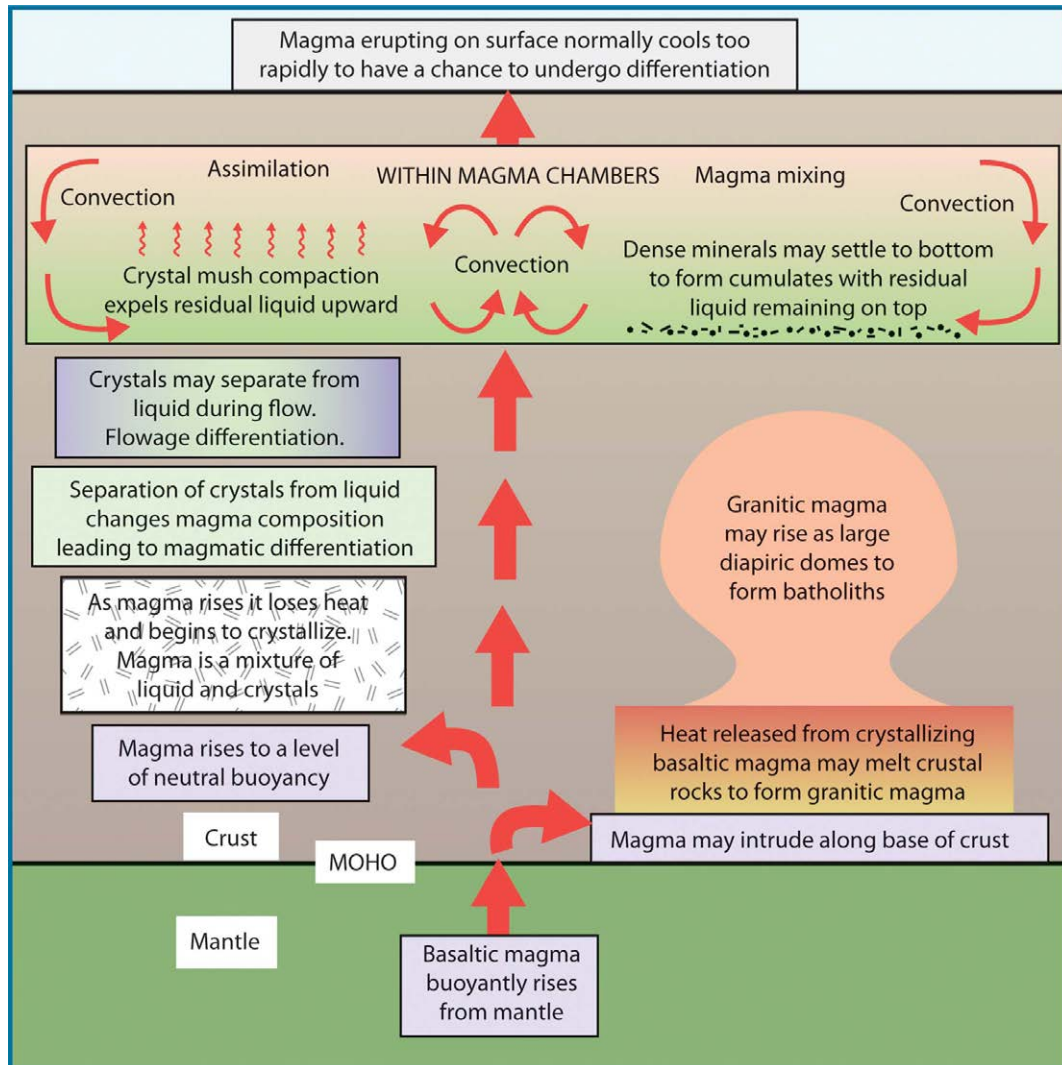


Fig. 1 Figure summarizing the main processes that may lead to diversification of magma (adapted after Klein 2012).

Igneous rocks, formed by crystallization of magma that has risen from the planet's interior, are the most abundant rock types in the Earth's crust. As the magma ascends and begins to cool, it becomes a mixture of liquid and crystals that can, to a various extent, separate from one another and produce the compositionally variable differentiated magmas. Eventually, the magma solidifies to form an igneous rock. The processes leading to formation of igneous rocks are of great importance because they have controlled, and still do, the distribution of elements between Earth's mantle and variable levels of the crust.

FROM MAGMA SOURCE TO IGNEOUS ROCK

Magma compositions are determined in the **source region** by the nature of rock that undergoes **partial melting** as well as its mechanism and conditions (e.g., Vigneresse *et al.* 1996), but they can also be modified during **ascent, emplacement** and **solidification** (e.g., Brown 1994; Clemens 1998; Petford 2003), especially in large **magma chambers** (e.g., Blake 1981; Miller and Mittlefehldt 1984; Hill *et al.* 1985; Jellinek *et al.* 2003). Collectively, the changes in bulk chemistry of magmas during the partial melting, ascent, emplacement, or eruption are known as the magmatic differentiation (e.g., Ruprecht *et al.* 2012).

Most granitic magmas are generated near the base of the continental crust, where the suitable protoliths are heated by deep burial, decompression melting during exhumation of subducted continental crust (e.g., Auzanneau *et al.* 2006), influx of water and/or volatiles (e.g. Litvinovsky and Podladchikov 1993; Weinberg and Hasalová 2015), lithosphere thinning, delamination and mantle upwelling (e.g. Henk *et al.* 2000), in situ accumulation of radiogenic heat (Gerdes *et al.* 2000) and/or by the intrusion of the mantle-derived mafic magma (Huppert and Sparks 1988). Other magmas have their source in the upper mantle. All magmas are less dense than the solid rock from which they form, and consequently they tend to rise toward the surface due to the buoyancy forces, known as the **Rayleigh-Taylor instability** (e.g., Sharp 1984). Whether the melt actually leaves the source depends mainly on the melt percentage, connectivity and degree of deformation.

First, the partial melt dispersed throughout the source rock must segregate from the unmelted residue, collect and form larger bodies before it can rise at geologically significant rates. The **critical melt fraction**, or **rheological critical melt percentage (RCMP)** (Wickham 1987; Fernandez and Gasquet 1994), describes the percentage of melt at which a crystal-dominated, more rigid granular framework gives way to a melt-dominated, fluid suspension – crystal mush. Next, in the plastic mantle and lower crust, these segregated melt batches may assume lens or inverted drop shapes, but upon reaching the brittle crust, sheet-like bodies become common. In these thin sheets, magma solidification may occur rapidly (depending on the magma ascent rate in the dyke, its width and temperature of surroundings; Petford 2003), but in large **magma chambers** (e.g., Turner and Campbell 1986; Karlstrom *et al.* 2010), it may take thousands or millions of years. When magma solidifies slowly, crystals can separate from the liquid, which can produce igneous rocks that are either richer in early crystallizing minerals or enriched in the residual liquid. This process of **fractional crystallization** (e.g., Arth 1976; Bohron and Spera 2002) plays an important role in creating the diversity of igneous rocks.

Magma diversity produced by partial melting

The great variety of magmas is initially produced by partial melting (anatexis; e.g., Clemens and Vielzeuf 1987; Sawyer 1994, 2008; Brown 2013), which produces (1) a liquid melt fraction, and (2) a residual rock component enriched in refractory elements (restite). The type of magma produced by partial melting depends upon several factors such as (i) the chemical and modal composition of the source rock, temperature and depth of melting, (ii) the exact mechanism (e.g., equilibrium vs. fractional) and degree of partial melting, (iii) presence/lack of fluid phase and its composition, (iv) the source rock's previous melting history, and (v) processes that change the composition of the magma before/while it leaves the source region (restite unmixing, peritectic phases entrainment, back-reactions between melt and melanosome, crystal accumulation...).

Magma differentiation during ascent and emplacement

(compiled after Wilson 1993; Pitcher 1997; Winter 2009; Klein 2012)

The post-anatectic differentiation involves changes in the bulk magma chemistry after its initial generation. Besides closed-system processes it involves open-system processes related to magma-country rock interaction or hybridization with contrasting magmas.

1. Closed-system processes

In course of closed-system differentiation processes, the parental melt evolves into one or more magmas with a different composition, without material exchange with an external reservoir. Closed-system differentiation processes include several mechanisms whereby early-formed crystals are segregated from the remaining melt, or vice versa.

- (a) **Fractional crystallization** involves the mutual separation of crystals (cumulate) and liquid from an originally homogeneous magma. Models for fractional crystallization involve **marginal accretion** (sidewall accretion), **gravitational separation** (crystal settling and flotation – due to the density contrast between the crystals and the melt), **convective flow segregation** (thermally-induced movement of magma in the magma chamber), **filter pressing** or **compaction** (melt is expelled from the residual crystal mush mechanically), and **flowage differentiation** (driven by the melt movement, typically in a narrow conduit or a dyke).

- (b) Recent studies of magma chambers have shown that many are diversified in ways not adequately explained by the classical crystal settling (e.g., Martin and Nokes 1988). This has led several researchers to re-evaluate ideas of magmatic differentiation and to propose alternative methods in which diversification takes place by **in situ crystallization** (e.g., Langmuir 1989) and compositionally induced convective processes within an initially stationary liquid or liquid–solid boundary layer. The **boundary-layer crystallization**, in which the crystals remain in situ, can produce gravitational instabilities where highly evolved interstitial liquids near the walls are less dense than the crystals and the liquid in the interior of chamber. As a result, the marginal liquids rise toward the top and are replaced by liquid moving toward the boundary layer from the interior. This process is called **thermogravitational diffusion**, whereby the low-density material rises not because it is hot and expanded but because it has lost the heavy elements, such as Fe, Ca, and Mg, to the crystals as it has been solidifying (e.g., Hildreth 1979; Walker *et al.* 1981).
- (c) **In liquid fractionation**, one parental magma fractionates to produce two or more chemically distinct daughter magmas. Liquid fractionation processes include thermal (Soret) diffusion (e.g. Walker and DeLong 1982), liquid immiscibility and liquation.

2. Open-system processes

Open-system processes such as assimilation, magma mixing and mingling involve compositional changes due to interaction of magma with the surrounding country rock or with contrasting magmas entering the system. The most effective tools for recognition of open-system processes represent radiogenic isotopes (e.g. Sr, Nd, Os, Hf).

- (a) In final stages of its ascent, magma commonly fractures the wall rock by a process called **stoping**. Wall-rock fragments entrained in the magma are called **xenoliths**. Many xenoliths display reaction rims, strongly suggesting that chemical reactions occurred with the host magma. **Assimilation** takes place where the wall rock chemically reacts with the intruding magma. Magma composition evolves when minerals (xenocrysts/antecrysts) or elements from the wall rock are incorporated into the magma and/or when elements from the magma are transferred into the wall rocks (e.g., during contact metamorphism). Fracturing and fragmentation of country rock increases the potential for the material exchange between the wall rocks and advancing magma by increasing the contact surface area. Next important factors represent the time, the thermal contrast between the magma and wall rock and

a composition of the assimilant, especially how refractory it is (e.g. Koyaguchi and Kaneko 1999; Davidson *et al.* 2001).

(b) **Magma mingling and mixing** (e.g., Barbarin and Didier 1992; Hibbard 1995; Baxter and Feely 2002). In plutonic environments, magma intrusion is unlikely to be a single event. Rather, intermittent pulses of magma are injected into the magma chamber from either the same or different sources over periods of time. Such a magma replenishment produces complex relationships and constitutes an important diversification mechanism. **Magma mingling** occurs when two or more dissimilar magmas coexist, still displaying contact relations but retaining their distinctive characteristics. Magma mingling implies that the magmas were interjected but did not mix well. **Magma mixing** (e.g., Anderson 1976; Kistler *et al.* 1986; Frost and Mahood 1987) implies thorough homogenization so that the original individual magma components are no longer recognizable, producing an intermediate hybrid magma of intermediate chemistry.

(c) Chemical differentiation can also be accomplished when a separate vapour phase coexists with magma and **liquid–vapour fractionation** takes place. A vapour phase may be introduced in any of three principal ways. First, a fluid may be released by heating of hydrated or carbonated wall rocks. Second, as a volatile-bearing but vapour-undersaturated magma rises and pressure is reduced, the magma may eventually become saturated, and a free vapour phase is released. The light vapour phase rises, diffuses through the magma, and is concentrated near the top of the magma chamber or even escapes to the country rock. A third mechanism for generating a separate fluid phase is a result of progressive, and often protracted, fractional crystallization.

3. Combination of processes

Because many of the petrogenetic processes cause similar effects, it may be difficult to distinguish the relative contributions of each of them with confidence. One approach to the problem is to devise mathematical model for the behaviour of certain trace elements and isotopic ratios based on a combination of processes. This has been done for the assimilation + fractional crystallization (AFC: DePaolo 1981), fractional crystallization + recharge of more primitive magmas (e.g., O'Hara and Matthews 1981), and all three combined (e.g., Aitchison and Forrest 1994), using iterative techniques to model the ratio of contaminant to original magma.

Indeed, the most significant petrogenetic processes in most plutons include magma recharge (with possible enclave formation and magma mixing), assimilation of anatectic melt derived from wall-rock and fractional crystallization/crystal accumulation. The main drawback of the classical AFC formulation, namely that it does not take into account the energy conservation, has been removed by the Energetically Constrained Assimilation and Fractional Crystallization (EC-AFC) model of Spera and Bohrsen (2001) and Bohrsen and Spera (2001). Its subsequent modification, Energy-Constrained Recharge, Assimilation, and Fractional Crystallization (EC-RAFC) model tracks the trace element and isotopic composition of melt, cumulates and enclaves during simultaneous recharge, assimilation and fractional crystallization.

Overview on the origin of zoning in magmatic bodies

In the map view, many circular or elliptical shallow plutons display remarkable concentric compositional zoning on length scales of $\sim 10^2$ – 10^4 m. Generally, the zoning is defined by more mafic rocks (e.g., gabbro, diorite) occurring along pluton margins and felsic rocks (e.g., granite, tonalite) in the centres or vice versa (normal and reverse zoning, respectively).

In the field the zoning can be recognized based on regular variation in the modal contents of rock-forming minerals (e.g., plagioclase, biotite, hornblende, and/or pyroxene), abundance/size of K-feldspar phenocrysts, intrusive contacts between pulses, or the nature and volumetric proportion of mafic microgranular enclaves (MME).

Moreover, normal or reverse zoning is revealed by systematic spatial variations in whole-rock and mineral compositions (e.g., Ayuso *et al.* 1984; Gastil *et al.* 1991; Mikoshiba *et al.* 2004; Antunes 2008; Seaman *et al.* 2011).

In rare cases, the zoning may be cryptic, i.e. being defined by chemical variations in (some of) trace-elements or in contents of accessory minerals (e.g., Fridrich and Mahood 1984; Nabelek *et al.* 1986; Janoušek *et al.* 1997).

Formation of concentric zoning in granitoid plutons has been commonly interpreted as a result of several physico-chemical processes, such as:

- In situ crystal–melt separation via flow sorting, gravitational settling, filter pressing or side-wall crystallization within a single magma pulse/batch (e.g., Bateman and Chappell 1979; Tindle and Pearce 1981; Bateman 1984);
- Nested emplacement (“telescoping”) of multiple magma pulses sharing a single conduit (e.g., Allen 1992; Paterson and Vernon 1995; Molyneux and Hutton 2000), with or without

mixing between separate outer and inner batches (Stephens and Halliday 1980; Vigneresse and Bouchez 1997; Lux *et al.* 2007; Coint *et al.* 2013);

- Intrusion of an essentially single pulse of magma preserving a vertical compositional gradient from a deeper level magma chamber (e.g., Bourne and Danis 1987, Wada *et al.* 2004; Pupier *et al.* 2008);
- Continuous cyclic thermal evolution of an incrementally constructed magma chamber (e.g., Parada *et al.* 2002; Lipman 2007; Gray *et al.* 2008; Coleman *et al.* 2012; Glazner and Johnson 2013).

Apparently, the textural and compositional zonation in plutons records complex evolution that may have taken place not only at the final emplacement level and solidification stage. In many cases, important role is played by petrogenetic processes operating deeper and reflecting vertical and/or horizontal heterogeneity in the whole magma-plumbing system.

The problem has been tackled using an integrated approach combining structural, petrological, geochronological and geochemical methods with geochemical modelling and geophysical investigations. The first paper of the thesis [**Article I.-1; Origin of reverse compositional and textural zoning in granite plutons by localized thermal overturn of stratified magma chambers**] examines an example of zoning in the Říčany Pluton, Bohemian Massif. Within analytical uncertainties (2σ), the emplacement ages of the two main facies are the same: the weakly-porphyrific granite (zircon): 337.3 ± 3.0 Ma and strongly porphyritic granite (monazite): 337.4 ± 2.4 Ma. All data sets (petrology, textural analysis and whole-rock geochemistry, including Sr–Nd isotopes) serve as a background for a general discussion about origin of compositional and textural zoning in granitic plutons. This article provides a comprehensive review of processes which take place deeper in the magma chamber and could be important to explanation of differentiation of magma in upper continental crust. Finally, a new model for the origin of zoning is proposed invoking a thermally-driven overturn of a deeper stratified magma chamber.

The second **Article I.-2 [Distribution of elements among minerals of a single (muscovite-) biotite granite sample, the Říčany Pluton – an optimal approach and general implications]**, focuses on methodological issues connected with obtaining a modal analysis representative of a large, coarse-grained granite sample. The various methods are compared and the most trustworthy approach/modal dataset chosen. Then, using a combination of EMPA with (LA) ICP-MS data, an

attempt is made to identify the principal mineral hosts for individual elements, evaluating the relative contributions of each of them to the whole-rock budget. This information is used to assess the distribution of individual elements among the main-rock forming minerals and accessories, with general consequences for petrogenesis of the Říčany granite and availability of selected geochemical species during weathering. Finally, general implications are discussed for obtaining modal analyses of coarse-grained rocks, modelling igneous processes, obtaining reliable whole-rock trace-element analyses and saturation thermometry. The research confirms the notion that the accessory phases play a key role in controlling the behaviour of many trace elements during the differentiation of felsic granitic systems by processes such as partial melting or fractional crystallization.

Chapter II: Internal Structure of Zoned Plutons

Chapter II describes the importance of internal fabrics in zoned plutons. Unravelling the geometrical patterns and the likely physical causes of magma flow in granitic magma chambers is one of the central aspects of understanding magma dynamics. In many (or most?) cases, however, direct field evidence for magma flow is completely erased from the rock record. Magmatic fabrics in plutons (i.e., foliations and lineations formed in the presence of a melt; Paterson *et al.* 1989; Arzi 1978; Fernandez and Gasquet 1994) commonly fail to provide unambiguous evidence for chamber-wide magma flow or convection. Instead, the preserved pluton fabrics are acquired late in magma chamber history along migrating crystallization fronts and are also easily reset by regional tectonic deformation, making inferences on large-scale convection or flow patterns problematic (e.g., Paterson *et al.* 1998; Borradaile and Henry 1997; Petford 2003). From a structural record it is possible, under certain assumptions, to interpret the magma ascent, magma emplacement and deformation events of regional importance.

Modern studies commonly address the formation of magmatic fabrics on three different scales, namely: (i) the *pluton-scale* by the mapping of foliation and lineation patterns in order to evaluate chamber-wide processes and the degree of coupling between pluton and host-rock structures, (ii) the *outcrop-scale* by determining fabric characteristics and their temporal and geometrical relationships to other structures; and (iii) the *grain-scale* using microstructural observations in order to constrain likely fabric-forming mechanisms and magma rheology. The formation and significance of magmatic fabrics in plutons remains, however, a matter of lively debate and vigorous scientific discussion resulting in contrasting interpretations of magmatic fabrics, of fabric-forming processes, and of the relationships of fabrics to strain and magma flow (see e.g., Paterson *et al.* 1998; Martín-Hernández 2004 for review).

Internal fabrics in igneous rocks

According to Paterson *et al.* (1998), Borradaile and Henry (1997), Benn *et al.* (2001) and others, fabrics in magmatic rocks are defined by the shape-preferred orientation of rock-forming minerals on the macro- and microscale. These structures may reflect in particular: (i) physical processes in magma chambers (e.g., Abbott (1989), (ii) the processes during magma ascent (e.g., Murray 1979), and (iii) regional stress during emplacement and crystallization (e.g., Paterson *et al.* 1998; Petford 2003).

On the basis of two main factors which play a role in origin of fabrics, (i) the proportion of the melt

vs. crystals and (ii) P–T conditions, are fabrics in magmatic rocks assigned to one of the following three stages (Paterson *et al.* 1998):

a) Igneous stage

Magmatic fabrics are defined as textural anisotropy of rocks without internal deformation of crystals formed at relatively high content of the melt. Criteria for identification of magmatic structures include according to Vernon (2000): (i) the shape-preferred orientation of euhedral phenocrysts of major rock-forming minerals (feldspar, biotite and amphibole); (ii) imbrication of rotated phenocrysts (“tiling”); (iii) preferred orientation of mafic microgranular enclaves (MME); (iv) a deflection of fabrics around rigid particles (xenoliths and enclaves); (v) schlieren layering; (vi) gravitational (way-up) structures and (vii) magmatic folds.

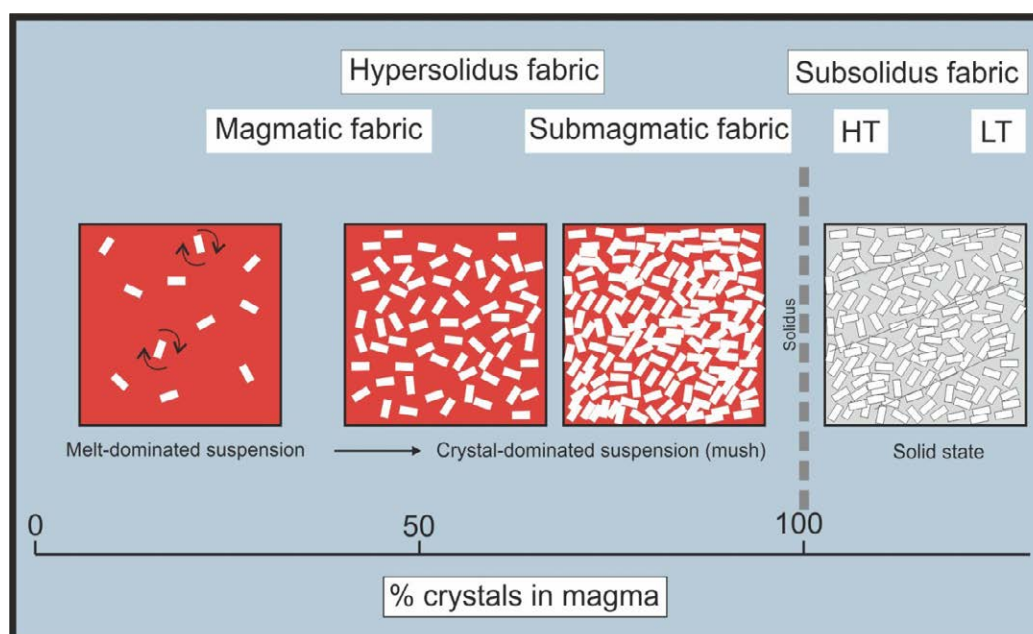


Fig. 2 Sketch of internal fabrics and rheology in igneous rocks depending on the amount of crystals in magma (drawn by J. Žák).

b) Sub-magmatic stage

Sub-magmatic fabrics form in crystallizing magma with a very low content of melt (on the order of a few percent). To identify submagmatic stage Blumenfeld and Bouchez (1988) and Vernon (2000) provided the following criteria: (i) recrystallized imbrication aggregates of feldspar; (ii) albite exsolution lamellae; (iii) migration of grain boundaries; (iv) rotation and dynamic recrystallization (reduction) of mineral grains (e.g., amphibole); (v) formation of S–C structures; (v) crystallization of mineral grains in pressure shadows and (vi) c-slip in quartz aggregates.

c) High- and low-temperature sub-solidus stage

Sub-solidus fabrics reflect deformation without the presence of residual melt. The basic criterion for the identification of these structures is demonstrable presence of internal deformation of crystals. On the microscale, Vernon (2000) summarized the following criteria: (i) the presence of internal deformation and recrystallization of mineral aggregates; (ii) formation of recrystallized grains in deformed tails and quartz ribbons; (iii) the presence of elongated recrystallized aggregates; (iv) grain-size reduction; (v) formation of myrmekite and perthite, (vi) boudinage of rigid minerals (e.g., amphiboles), (vii) anastomosing planar structures; (viii) the presence of local deformation zones and (ix) fracture formation and mica recrystallization.

Paterson *et al.* (1998) suggested the following guidelines for interpretation of the magmatic, sub-magmatic and sub-solidus fabrics: (i) the observed structures form late, in the magma chamber and rarely reflect the earlier process during ascent and emplacement of magma; (ii) fabrics are often slightly reprinted and present only the most recent increase in strain during crystallization; (iii) in plutons with discordant orientation of fabrics against those of regional structures is often the formation of internal fabrics controlled by the internal processes in magma and (iv) with increasing depth of magma emplacement is formation of fabrics controlled by regional deformation.

A vast majority of studies has documented a single magmatic fabric in a single pluton and, logically, has inferred a single fabric-forming process. The fabric formation thus has been traditionally thought to result either from internal magmatic processes or regional tectonics, depending on the temporal evolution of mechanical coupling of the pluton/host rock system (Paterson *et al.* 1998; Barros *et al.* 2001). This approach has also been adopted in numerous anisotropy of magnetic susceptibility (AMS) studies of granitoid plutons, as the AMS provides a fast and efficient method for analysis and quantification of magnetic fabric controlled by the orientation of ferromagnetic and paramagnetic minerals.

In regards to the interpretation of chamber-wide fabric patterns, some studies have downplayed the importance of foliations overprinting internal intrusive boundaries and attributed fabric formation to magma flow, ascent or emplacement. In contrast to the still popular kinematic interpretation that magmatic foliations and lineations represent flow planes and flow lines in a magma body, respectively. Paterson and Vernon (1995); Paterson *et al.* (1998); Paterson and Miller (1998) have published several examples of both nested and sheeted plutonic complexes where magmatic foliations cross-cut internal contacts between juxtaposed magma pulses. They have used this

observation to suggest that fabrics reflect post-emplacement strain before final crystallization of a magma chamber and have no direct relationship to flow during ascent or emplacement.

Theoretical and analogue models of salt, shale, and igneous diapirs (Vendeville *et al.* 2000) have shown that their internal dynamics and strain patterns are largely governed by viscosity contrasts between the ascending diapir and its host, and by the travel distance from the source region. These models have led to an idealized image of diapirs with predictions about their internal circulation, strain variations, and compositional zoning. A characteristic feature of the model diapirs is strain and associated fabric distribution whereby peripheral flattening in the diapir head passes inward to strongly constrictional diapir centres and tails.

Natural examples, however, may depart significantly from the theoretical models owing to rheological and temperature variations in the diapir and its host, multiple pulses of the ascending magma (Žák *et al.* 2005, 2007) passing through a single conduit and variable imprint of tectonic deformation. One of the key issues for understanding the dynamics of diapiric intrusions in the Earth's crust is thus a quantitative comparison of theoretical models with the observed strain patterns. Unfortunately, natural diapirs lack reliable strain markers (Benn *et al.* 2001), as best exemplified by the rather problematic microgranular enclaves, and exhibit mineral fabric that is a poor recorder of total strain experienced by the ascending fluid. Instead, granular and mineral fabrics in both salt and granites, respectively, are interpreted to record only late strain increments that postdate diapiric ascent. Still, a promising means for evaluating strain patterns in natural diapirs is the AMS analysis, allowing quantification of fabric parameters even in macroscopically isotropic rocks without strain markers.

The **Article II.-1 [Magnetic fabric and modelled strain distribution in the head of a nested granite diapir, the Melechov pluton, Bohemian Massif]** explores the potential of the AMS technique for inferring strain patterns in granite diapirs (and in other types of intrusions as well) on the basis of data from the mid- to late-Carboniferous (Pennsylvanian) Melechov Pluton, which is interpreted as a composite diapiric intrusion into hot mid-crustal migmatites. Quantitatively characterized variations in magnetic fabric throughout the pluton and the AMS-to-strain inversion method (SUSIE) of Ježek and Hrouda (2002, 2007) are used to infer the strain distribution in the proposed diapir head. Finally, these data are compared with theoretical models for diapiric structures and discuss applicability of this method for strain analysis in granite plutons.

In **Article II.-2 [Magnetic fabric of the Říčany granite, Bohemian Massif: a record of helicoidal magmatic flow]** is investigated an example of the post-tectonic Říčany Pluton, where the magmatic fabrics have not been overprinted by regional deformation and thus likely preserve a record of internal processes and magma flow. The article presents integrated structural, microstructural, and AMS data, which revealed an unusual pattern of magmatic fabrics in the pluton. The observed fabrics and AMS are interpreted to record a helicoidal flow, a rarely documented flow mechanism in granitoid plutons.

Chapter III: Zoned plutons in various tectonic settings

Firstly, Chapter III deals with the significance of magmatic fabrics in plutons, especially with the question how they record regional tectonic deformation superimposed onto granitoid bodies prior the final solidification. These aspects are described on examples of the Štěnovice and Čistá plutons, Ševětín Pluton and selected other (pre- and syn-tectonic) Variscan granitic intrusions in the Bohemian Massif. Secondly, in the Chapter III shows that granitoids with well-defined petrographic, mineralogical, chemical features and ages may provide information on the spatial/temporal changes in tectonic settings. This approach is used in a different petrogenetic classifications of granitoid rocks and they are listed below in the text.

Significance of magmatic fabrics in plutons in regional tectonic scale

Since the pioneering work of German geologists, most importantly Cloos (1925), magmatic fabrics in plutons have been used to track the changing strain and inferred stress fields in arcs and orogens through time as well as to examine the links between magmatism and regional tectonic processes in orogenic belts.

Granitic batholiths, plutons and stocks play an important role in the evolution of mountain belts (Miller and Paterson 1991). Granitic magmas can be emplaced throughout the history of these belts, starting with subduction, through collision to the post-collisional orogenic collapse. Fabrics within plutons and in country rocks reflect the timing of granitic magma emplacement with respect to tectonic activity. Based on the relative timing we can distinguish three types of emplacement:

- (a) **Pre-tectonic** plutons that are emplaced prior to the orogenic episode. Plutons record the deformational and metamorphic processes associated with the orogeny. Alternatively, the regional foliation may curve around a non-foliated pluton because of ductility contrast.
- (b) **Syn-tectonic** plutons are intruded during the orogen-related deformation. Regional foliation will be continuous with emplacement-related foliations in the pluton.
- (c) **Post-tectonic** plutons follow the orogenic/metamorphic event, and the igneous rocks thus lack any deformation features such as foliations other than those related to intrusion. The regional deformational fabrics and structures of the country rocks will be cut discordantly by the pluton.

In addition to timing, the depth of emplacement affects structural and textural features of plutons. Many of these characteristics were summarized by Buddington (1959) who distinguished three depth levels of emplacement (epizone, mesozone and catazone).

Petrogenetic classifications of granitoid rocks

Especially, classification of the granitic rocks has remained one of the fundamental and inseparable aspects of the granitic study from the beginning.

Over the years, there have been proposed many classification schemes which have resulted in chaos rather than putting things in order. The reason for such large number of classification schemes is that many different sources and processes converge to give rise to essentially the same end-product granite mineralogy.

The commonly used classification schemes include:

- 1) Modal mineralogy/IUGS classification (Le Maitre 2002) – This scheme employs modal proportions of quartz, alkali feldspar and plagioclase. However, it has the major disadvantage of not taking into account the mafic minerals and other minor phases like muscovite, which may have great petrogenetic implications. Moreover, obtaining a truly representative modal analysis of a coarse-grained, or even porphyritic granitoid is not straightforward (**Article I.-2**).
- 2) 'Alphabet soup' classification – This scheme is based on measured-to-inferred parameters. Chappell and White (1974); White and Chappell (1977, 1983) initially introduced just two letters, I and S, to denote two distinct types of granitoids. I-type granitoids are metaluminous to weakly peraluminous, relatively sodic and have a wide range of silica content. It is inferred that I-type granitoids have formed from a metagneous source. S-type granitoids are strongly peraluminous and relatively potassic with restricted but higher silica contents. They are presumed to have formed from metasedimentary rocks. The classification was expanded by adopting one more type (A). This denotes anorogenic granitoids with alkaline and anhydrous characteristics (Loiselle and Wones 1979). Two more letters, M (White 1979) and C (Kilpatrick and Ellis 1992) soon followed. M-type refers to granitoids that are thought to have formed from mantle or by melting of a juvenile crust, presumably in an island-arc setting. C-type stands for charnockitic granitoids. Castro *et al.* (1991) proposed the various H-types to encompass the granitoids showing hybrid characteristics of both the mantle and the crust. Altogether, alphabet

classification, being a genetic classification, is not objective and fails in more complex geotectonic settings.

- 3) **Normative mineralogy classification** – One simple way to substitute the rigorous point counting for modal analysis is to opt for normative mineralogy, calculated from the major-element composition of the rock. Using the CIPW normative abundance of albite, anorthite and orthoclase, O'Connor (1965) and Barker (1979) proposed analogous ternary classification schemes to classify the granitoids into tonalite, trondhjemite, granodiorite, granite and quartz monzonite.
- 4) **Alumina saturation** – This system uses the concept of alumina saturation. A simple parameter A/CNK , defined as $\text{molecular Al}_2\text{O}_3 / (\text{CaO} + \text{Na}_2\text{O} + \text{K}_2\text{O})$, is used to classify the rocks into metaluminous ($A/CNK < 1$), or peraluminous ($A/CNK > 1$) or peralkaline $A < NK$, Shand (1943).
- 5) **Magnetite-ilmenite series** – Ishihara (1977) observed that granitoid rocks of magmatic arcs can be conveniently divided into two groups: magnetite series and ilmenite series. Magnetite series is relatively oxidized, whereas ilmenite series is more reduced. It has been found that although such distinction between magnetite series and ilmenite series may be possible in arc environments, the scheme may fail in other tectonic environments.
- 6) **Mineralogical classification** – Barbarin (1999) identified six types of granitoids based on mineralogy and its relationship with alumina saturation of the granitoids. The scheme is further supported by whole-rock geochemistry and isotope geochemistry, and then correlated them with distinct tectonic environments.
- 7) **Multi-cationic functions** – De la Roche *et al.* (1980) proposed two multicationic functions, $R_1 [= 4\text{Si} - 11(\text{Na} + \text{K}) - 2(\text{Fe} + \text{Ti})]$ and $R_2 [= \text{Al} + 2\text{Mg} + 6\text{Ca}]$, which is a two-dimensional projection of the basalt tetrahedron of Yoder and Tilley (1962). The two functions are particularly suitable for the basaltic rocks, but less so for the granitoids as K-feldspar and plagioclase plot at the same point on this diagram. As a consequence, most granitic rocks are encompassed within a very small area on this diagram. Debon and Le Fort (1983) also proposed a number of multi-cationic parameters, of which several are useful for classification purposes. The parameters $P = \text{K} - (\text{Na} + \text{Ca})$, and $Q = \text{Si}/3 - (\text{K} + \text{Na} + 2 \times \text{Ca}/3)$ denote the proportion of K-feldspars to plagioclase and quartz, respectively.

Parameters A and B, defined as $A = Al - (K + Na + 2Ca)$ and $B = Fe + Mg + Ti$. They have identified three major granitoid suites, aluminous, calcic and aluminous-calcic. **T**

- 8) **Tectonic discriminant diagrams** – Many authors have attempted to establish the links between chemical composition of the granitoids and the tectonic setting of their emplacement. Batchelor and Bowden (1985) proposed a tectonic discriminant scheme based on R_1 and R_2 parameters of De la Roche *et al.* (1980). A similar attempt was made by Maniar and Piccoli (1989). They classified the granitoids on the basis of major elements into seven tectonic settings: (1) island-arc granitoids (IAG), (2) continental-arc granitoids (CAG), (3) continental-collision granitoids (CCG), (4) post-orogenic granitoids (POG), (5) rift-related granitoids (RRG), (6) continental epeirogenic uplift granitoids (CEUG), and (7) oceanic plagiogranites (OP). Similarly Rogers and Greenberg (1990) discriminated the granitoids into four groups based on major-elements and trace-elements chemistry to late orogenic, post-orogenic, anorthosite–rapakivi domain, and ring complexes. The tectonic classification scheme that has found wide application is the one by Pearce *et al.* (1984). The scheme, solely based on trace elements, discriminates granitoids into four major tectonic environments: volcanic arc, ocean ridge, within plate and syn-collision. The major drawback of the tectonic discriminant diagrams is that the elemental composition of the granitoids is a direct manifestation of the sources and the magmatic processes, and thus not necessarily the tectonic environment in which they are emplaced.
- 9) **Three-tier chemical scheme** – Frost *et al.* (2001) proposed a classification scheme based on three geochemical parameters: Fe-number, modified alkali-lime index (MALI) and alumina saturation index (ASI). Based on $Fe\# (= FeO / (FeO + MgO))$, the granitoids have been divided into two groups: ferroan and magnesian. On the basis of $MALI (= Na_2O + K_2O - CaO)$, the granitoids have been divided into four groups: calcic, calc-alkalic, alkali-calcic and alkalic. Based on $ASI (= molecular\ Al / (Ca - 1.67P + Na + K))$, granitoids have been grouped as peraluminous ($ASI > 1.0$), metaluminous ($ASI < 1.0$, but $Na + K < Al$) and peralkaline ($ASI < 1.0$, but $Na + K > Al$). A total of sixteen compositional groups has been proposed for the whole compositional range of the granitoids. All compositional groups are not equally represented in geological history and some are not reported at all, e.g. ferroan calcic granitoids.

The articles addressed below contribute to the overall geotectonic picture based on structural, geochemical and geotectonic datasets.

Consequently, the goal of **Article III.-1 [Structure, emplacement, and tectonic setting of Late Devonian granitoid plutons in the Teplá–Barrandian unit, Bohemian Massif]** is to provide an integrated overview of the principal field, geophysical, and geochemical characteristics of the two Late Devonian granodiorite plutons (Štěnovice and Čistá) in western Bohemia. New data are presented for the former pluton, including field observations, host-rock and magmatic microstructures, AMS, gravimetry, zircon geochronology and whole-rock geochemistry. The intrusion of the Štěnovice Pluton was constrained by at 375 ± 2 Ma using the laser ablation ICP-MS technique. Based on structural data, it is argued for an upper-crustal diapir-like emplacement of these two plutons. Critically assessed is their tectonic significance for reconstructing and constraining the ages of initial deformation during the Variscan cycle. Lastly, timing, geometry and polarity of Late Devonian to Early Carboniferous subduction in the Bohemian Massif are discussed.

On the other hand, youngest phases of the Variscan orogeny in the Bohemian Massif is examined in **Article III.-2 [Intrusive and deformation history of the Ševětín Pluton, Moldanubian Batholith: record of polyphase tectonic evolution of the Blanice Graben, Bohemian Massif]**. The studied Ševětín Pluton is a small, isolated, petrologically and structurally complex intrusive body that is genetically related to the youngest intrusions of the Moldanubian Batholith. The pluton's overall shape, internal magmatic fabric as well as brittle structures (dikes, veins, joints, and faults) are related to the formation and polyphase tectonic evolution of the NNE–SSW-trending Blanice–Kaplice–Rödl fault zone/graben (further abbreviated as Blanice graben), an about 200 km long and 5–15 km wide, deep-seated fault zone that cuts across the Moldanubian Unit (e.g. Fiala 1995). The faults of the Blanice graben have been repeatedly reactivated; the oldest identified tectonic activity was of Permo–Carboniferous age (inferred from the presence of Pennsylvanian (Gzhelian) to Cisuralian (Asselian) coal-bearing sediments: Holub 2001).

The Variscan magmatic evolution of the Bohemian Massif is finally reviewed and discussed in **Article III.-3 [A plate-kinematic model for the assembly of the Bohemian Massif constrained by structural relationships around granitoid plutons]**. Summary starts with the growth of a Late Devonian to Early Carboniferous Andean-type magmatic arc (**Article III.-1**). It was associated with orogeny-perpendicular shortening due to the c. 354–346 Ma subduction and continental underthrusting of the Saxothuringian domain. This was followed by a collapse of the Teplá–Barrandian

upper crust and exhumation of the high-grade (Moldanubian) orogenic root at c. 346–337 Ma. At the end of this event intruded the Říčany Pluton (see **Articles I.-1, I.-2 and II.-2**). Subsequently, the late readjustments within the amalgamated Bohemian Massif included crustal exhumation and c. 330–327 Ma mainly S-type granite plutonism along the edge of the easterly (Brunian; Kalvoda et al. 2008) continental indentor and peripheral tectono-thermal activity driven by strike-slip faulting and possibly mantle delamination until late Carboniferous–earliest Permian times. With this geotectonic setting were connected intrusions of the Melechov Pluton (**Article II.-1**). With tectonic activity of Permo–Carboniferous age in the Blanice graben also related intrusion of the Ševětín Pluton (see **Article III.-2**). The surrounding a microgranodiorite dyke around the Ševětín Pluton presumably related to the maximum tectonic activity (270 ± 2 Ma; hornblende, $^{40}\text{Ar}/^{39}\text{Ar}$, Košler et al. 2001).

REFERENCES

- Abbott, R. N. (1989). Internal structures in part of the South Mountain batholith, Nova Scotia, Canada. *Geological Society of America Bulletin*, 101(11), 1493–1506.
- Aitchison, S. J., & Forrest, A. H. (1994). Quantification of crustal contamination in open magmatic systems. *Journal of Petrology*, 35(2), 461–488.
- Allen, C. M. (1992). A nested diapir model for the reversely zoned Turtle Pluton, southeastern California. *Transactions of the Royal Society of Edinburgh, Earth Sciences* 83, 179–190.
- Anderson, A. T. (1976). Magma mixing: petrological process and volcanological tool. *Journal of Volcanology and Geothermal Research*, 1(1), 3–33.
- Antunes, I. M. H. R., Neiva, A. M. R., Silva, M. M. V. G. & Corfu, F. (2008). Geochemistry of S-type granitic rocks from the reversely zoned Castelo Branco Pluton (central Portugal). *Lithos* 103, 445–465.
- Arth, J. G. (1976). Behavior of trace elements during magmatic processes: a summary of theoretical models and their applications. *J. Res. US Geol. Surv. (United States)*, 4(1).
- Arzi, A. A. (1978). Critical phenomena in the rheology of partially melted rocks. *Tectonophysics*, 44(1), 173–184.
- Auzanneau, E., Vielzeuf, D., & Schmidt, M. W. (2006). Experimental evidence of decompression melting during exhumation of subducted continental crust. *Contributions to Mineralogy and Petrology*, 152(2), 125–148.
- Ayuso, R. A. (1984). Field relations, crystallization, and petrology of reversely zoned granitic plutons in the Bottle Lake complex, Maine. *U.S. Geological Survey Professional Paper* 1320, 1–58.
- Barbarin, B. (1999). A review of the relationships between granitoid types, their origins and their geodynamic environments. *Lithos*, 46(3), 605–626.
- Barbarin, B., & Didier, J. (1992). Genesis and evolution of mafic microgranular enclaves through various types of interaction between coexisting felsic and mafic magmas. *Transactions of the Royal Society of Edinburgh: earth sciences*, 83(1-2), 145–153.
- Barker, F. (1979). Trondhjemite: definition, environment and hypotheses of origin. *Trondhjemites, dacites and related rocks*, 6, 1–12.
- Barros, C. E. M., Barbey, P., & Boullier, A. M. (2001). Role of magma pressure, tectonic stress and crystallization progress in the emplacement of syntectonic granites. The A-type Estrela Granite Complex (Carajás Mineral Province, Brazil). *Tectonophysics*, 343(1), 93–109.

- Batchelor, R. A., & Bowden, P. (1985). Petrogenetic interpretation of granitoid rock series using multicationic parameters. *Chemical geology*, 48(1), 43–55.
- Bateman, P. C. & Chappell, B. W. (1979). Crystallization, fractionation, and solidification of the Tuolumne Intrusive Series, Yosemite National Park, California. *Geological Society of America Bulletin* 90, 465–482.
- Bateman, R. (1984). On the role of diapirism in the, segregation, ascent and final emplacement of granitoid magmas. *Tectonophysics*, 110(3), 211–231.
- Batchelor, R. A., & Bowden, P. (1985). Petrogenetic interpretation of granitoid rock series using multicationic parameters. *Chemical geology*, 48(1), 43–55.
- Baxter, S., & Feely, M. (2002). Magma mixing and mingling textures in granitoids: examples from the Galway Granite, Connemara, Ireland. *Mineralogy and Petrology*, 76(1-2), 63–74.
- Benn, K., Paterson, S. R., Lund, S. P., Pignotta, G. S., & Kruse, S. (2001). Magmatic fabrics in batholiths as markers of regional strains and plate kinematics: example of the Cretaceous Mt. Stuart batholith. *Physics and Chemistry of the Earth, Part A: Solid Earth and Geodesy*, 26(4), 343–354.
- Blake, S. (1981). Eruptions from zoned magma chambers. *Journal of the Geological Society*, 138(3), 281–287.
- Blumenfeld, P., & Bouchez, J. L. (1988). Shear criteria in granite and migmatite deformed in the magmatic and solid states. *Journal of Structural Geology*, 10(4), 361–372.
- Bohrson, W. A., & Spera, F. J. (2001). Energy-constrained open-system magmatic processes II: application of energy-constrained assimilation – fractional crystallization (EC-AFC) model to magmatic systems. *Journal of Petrology*, 42(5), 1019–1041.
- Bohrson, W. A., & Spera, F. J. (2002). Insights into magmatic differentiation; energy constrained open-system processes. *Geochimica et Cosmochimica Acta*, 66, 88.
- Borradaile, G. J., & Henry, B. (1997). Tectonic applications of magnetic susceptibility and its anisotropy. *Earth-Science Reviews*, 42(1), 49–93.
- Bourne, J., & Danis, D. (1987). A proposed model for the formation of reversely zoned plutons based on a study of the Lacorne Complex, Superior Province, Quebec. *Canadian Journal of Earth Sciences*, 24(12), 2506–2520.
- Brown, M. (1994). The generation, segregation, ascent and emplacement of granite magma: the migmatite-to-crustally-derived granite connection in thickened orogens. *Earth-Science Reviews*, 36(1), 83–130.

-
- Brown, M. (2013). Granite: From genesis to emplacement. *Geological Society of America Bulletin*, 125(7-8), 1079–1113.
- Buddington, A. F. (1959). Granite emplacement with special reference to North America. *Geological Society of America Bulletin*, 70, 671.
- Castro, A., Moreno-Ventas, I., & De la Rosa, J. D. (1991). H-type (hybrid) granitoids: a proposed revision of the granite-type classification and nomenclature. *Earth-Science Reviews*, 31(3), 237–253.
- Clemens, J. D., & Vielzeuf, D. (1987). Constraints on melting and magma production in the crust. *Earth and Planetary Science Letters*, 86(2), 287–306.
- Clemens, J. D. (1998). Observations on the origins and ascent mechanisms of granitic magmas. *Journal of the Geological Society*, 155(5), 843–851.
- Cloos, H. (1925). Einfuhrung in die tectonische Behandlung magmatischer Erscheinungen: pt 1: Das Riesengebirge in Shlesien. *Gebr., Borntraeger, Berlin*, 194.
- Coint, N., Barnes, C. G., Yoshinobu, A. S., Chamberlain, K. R., & Barnes, M. A. (2013). Batch-wise assembly and zoning of a tilted calc-alkaline batholith: Field relations, timing, and compositional variation. *Geosphere*, 9(6), 1729–1746.
- Coleman, D. S., Bartley, J. M., Glazner, A. F., & Pardue, M. J. (2012). Is chemical zonation in plutonic rocks driven by changes in source magma composition or shallow-crustal differentiation?. *Geosphere*, 8(6), 1568–1587.
- Davidson, J., Tepley, F., Palacz, Z., & Meffan-Main, S. (2001). Magma recharge, contamination and residence times revealed by in situ laser ablation isotopic analysis of feldspar in volcanic rocks. *Earth and Planetary Science Letters*, 184(2), 427–442.
- Debon, F., & Le Fort, P. (1983). A chemical–mineralogical classification of common plutonic rocks and associations. *Transactions of the Royal Society of Edinburgh: Earth Sciences*, 73(03), 135–149.
- De La Roche, H., Leterrier, J., Grandclaude, P., & Marchal, M. (1980). A classification of volcanic and plutonic rocks using R1-R2 diagram and major-element analyses - its relationships with current nomenclature. *Chemical geology*, 29(1), 183–210.
- DePaolo, D. J. (1981). Trace element and isotopic effects of combined wallrock assimilation and fractional crystallization. *Earth and planetary science letters*, 53(2), 189–202.
- Fernandez, A. N., & Gasquet, D. R. (1994). Relative rheological evolution of chemically contrasted coeval magmas: example of the Tichka plutonic complex (Morocco). *Contributions to Mineralogy and Petrology*, 116(3), 316–326.

- Fiala J., Fuchs, G., Wendt, J. I. (1995). VII. C. 1 Stratigraphy. In: Dallmeyer, R. D., Franke, W., Weber, K. (eds.) Pre-Permian Geology of Central and Eastern Europe. Springer-Verlag, Berlin, pp 417–428.
- Fridrich, C. J., & Mahood, G. A. (1984). Reverse zoning in the resurgent intrusions of the Grizzly Peak cauldron, Sawatch Range, Colorado. *Geological Society of America Bulletin*, 95(7), 779–787.
- Frost, T. P., & Mahood, G. A. (1987). Field, chemical, and physical constraints on mafic-felsic magma interaction in the Lamarck Granodiorite, Sierra Nevada, California. *Geological Society of America Bulletin*, 99(2), 272–291.
- Frost, B. R., Barnes, C. G., Collins, W. J., Arculus, R. J., Ellis, D. J., & Frost, C. D. (2001). A geochemical classification for granitic rocks. *Journal of petrology*, 42(11), 2033–2048.
- Gastil, R. G., Kimbrough, J., Tainosho, Y., Shimizu, M., & Gunn, S. (1991). Plutons of the eastern peninsular ranges, southern California, USA and Baja California, Mexico. In *Geological Excursions in Southern California and México: San Diego, California, Geological Society of America Annual Meeting Guidebook*, pp. 319–331.
- Gerdes, A., Wörner, G., & Henk, A. (2000). Post-collisional granite generation and HT–LP metamorphism by radiogenic heating: the Variscan South Bohemian Batholith. *Journal of the Geological Society*, 157(3), 577–587.
- Glazner, A. F., & Johnson, B. R. (2013). Late crystallization of K-feldspar and the paradox of megacrystic granites. *Contributions to Mineralogy and Petrology*, 166(3), 777–799.
- Gray, W., Glazner, A. F., Coleman, D. S., & Bartley, J. M. (2008). Long-term geochemical variability of the Late Cretaceous Tuolumne intrusive suite, central Sierra Nevada, California. *Geological Society, London, Special Publications*, 304(1), 183–201.
- Henk, A., Von Blanckenburg, F., Finger, F., Schaltegger, U., & Zulauf, G. (2000). Syn-convergent high-temperature metamorphism and magmatism in the Variscides: a discussion of potential heat sources. *Geological Society, London, Special Publications*, 179(1), 387–399.
- Hibbard, M. J. 1995, Petrography to Petrogenesis. *Prentice Hall*, pp. 1–587.
- Hildreth, W. (1979). The Bishop Tuff: evidence for the origin of compositional zonation in silicic magma chambers. *Geological Society of America Special Papers*, 180, 43–76.
- Hill, D. P., Bailey, R. A., & Ryall, A. S. (1985). Active tectonic and magmatic processes beneath Long Valley caldera, eastern California: an overview. *Journal of Geophysical Research: Solid Earth (1978–2012)*, 90(B13), 11111–11120.

- Holub V (2001) The occurrences of the Permo–Carboniferous sequences in the Blanice Graben. In: Pešek, J., Holub, V., Jaroš, J., Malý, L., Martínek, K., Prouza, V., Spudil, J. & Tásler R (eds.) *Geology and Deposits of Upper Paleozoic Limnic Basins of the Czech Republic*. Czech Geological Survey, Prague, pp. 197–207 (in Czech).
- Huppert, H. E., & Sparks, R. S. J. (1988). The generation of granitic magmas by intrusion of basalt into continental crust. *Journal of Petrology*, 29(3), 599–624.
- Chappell, B., & White, A. (1974). Two contrasting granite types. *Pacific geology*, 8(2), 173–174.
- Ishihara, S. (1977) The magnetite-series and ilmenite-series granitic rocks. *Mining Geology*, 27, 293–305.
- Janoušek, V., Rogers, G., Bowes, D. R., & Vaňková, V. (1997). Cryptic trace-element variation as an indicator of reverse zoning in a granitic pluton: the Ricany granite, Czech Republic. *Journal of the Geological Society*, 154(5), 807–815.
- Janoušek, V., Farrow, C. M., & Erban, V. (2006a). Interpretation of whole-rock geochemical data in igneous geochemistry: introducing Geochemical Data Toolkit (GCDkit). *Journal of Petrology*, 47(6), 1255–1259.
- Janoušek, Vojtěch (2006b). Saturnin, R language script for application of accessory-mineral saturation models in igneous geochemistry. *Geologica Carpathica*, 57, 131–142.
- Janoušek, V., Farrow, C. M., Erban, V., & Trubač, J. (2011). Brand new geochemical data toolkit (GCDkit 3.0) – Is it worth upgrading and browsing documentation? (YES!). *Geol. Výzk. Mor. Slez*, 18, 26–30.
- Janoušek, V., Moyen, J. F., Martin, H., Erban, V. & Farrow, C. M. (2015). *Geochemical Modelling of Igneous Processes – Principles and Recipes in R Language*. Springer, ISBN 978-3-662-46791-6.
- Jellinek, A. M., & DePaolo, D. J. (2003). A model for the origin of large silicic magma chambers: precursors of caldera-forming eruptions. *Bulletin of Volcanology*, 65(5), 363–381.
- Ježek, J., & Hrouda, F. (2002). Software for modeling the magnetic anisotropy of strained rocks. *Computers & geosciences*, 28(9), 1061–1068.
- Ježek, J., & Hrouda, F. (2007). SUSIE: A program for inverse strain estimation from magnetic susceptibility. *Computers & geosciences*, 33(6), 749–759.
- Kalvoda, J., Bábek, O., Fatka, O., Leichmann, J., Melichar, R., Nehyba, S., & Spacek, P. (2008). Brunovistulian terrane (Bohemian Massif, Central Europe) from late Proterozoic to late Paleozoic: a review. *International Journal of Earth Sciences*, 97(3), 497–518.

- Karlstrom, L., Dufek, J., & Manga, M. (2010). Magma chamber stability in arc and continental crust. *Journal of Volcanology and Geothermal Research*, 190(3), 249–270.
- Kilpatrick, J. A., & Ellis, D. J. (1992). C-type magmas: igneous charnockites and their extrusive equivalents. *Geological Society of America Special Papers*, 272, 155–164.
- Kistler, R. W., Chappell, B. W., Peck, D. L., & Bateman, P. C. (1986). Isotopic variation in the Tuolumne intrusive suite, central Sierra Nevada, California. *Contributions to Mineralogy and Petrology*, 94(2), 205–220.
- Klein, C., & Philpotts, A. (2012). *Earth materials: introduction to mineralogy and petrology*. Cambridge University Press, pp. 1–552.
- Košler, J., Kelley, S., & Vrána, S. (2001). $^{40}\text{Ar}/^{39}\text{Ar}$ hornblende dating of a microgranodiorite dyke: implications for early Permian extension in the Moldanubian Zone of the Bohemian Massif. *International Journal of Earth Sciences*, 90(2), 379–385.
- Koyaguchi, T., & Kaneko, K. (1999). A two-stage thermal evolution model of magmas in continental crust. *Journal of Petrology*, 40(2), 241–254.
- Langmuir, C. H. (1989). Geochemical consequences of in situ crystallization. *Nature*, 340(6230), 199–205.
- Le Maitre, R. W., Streckeisen, A., Zanettin, B., Le Bas, M. J., Bonin, B., & Bateman, P. (Eds.). (2002). *Igneous rocks: a classification and glossary of terms: recommendations of the International Union of Geological Sciences Subcommission on the Systematics of Igneous Rocks*. Cambridge University Press, pp.1–236.
- Lipman, P. W. (2007). Incremental assembly and prolonged consolidation of Cordilleran magma chambers: Evidence from the Southern Rocky Mountain volcanic field. *Geosphere*, 3(1), 42–70.
- Litvinovsky, B. A., & Podladchikov, Y. Y. (1993). Crustal anatexis during the influx of mantle volatiles. *Lithos*, 30(2), 93–107.
- Loiselle, M. C., & Wones, D. R. (1979, November). Characteristics and origin of anorogenic granites. In *Geological Society of America Abstracts with Programs*, 11(7), pp. 1–468.
- Lux, D. R., Hooks, B., Gibson, D., & Hogan, J. P. (2007). Magma interactions in the Deer Isle granite complex, Maine: field and textural evidence. *The Canadian Mineralogist*, 45(1), 131–146.
- Maniar, P. D., & Piccoli, P. M. (1989). Tectonic discrimination of granitoids. *Geological society of America bulletin*, 101(5), 635–643.
- Martin, D., & Nokes, R. (1988). Crystal settling in a vigorously converting magma chamber 332, 534–536.

-
- Martín-Hernández, F., Lüneburg, C. M., Aubourg, C., & Jackson, M. (2004). Magnetic fabric: methods and applications – an introduction. *Geological Society, London, Special Publications*, 238(1), 1-7.
- Mikoshiya, M. U., Kanisawa, S., Matsuhisa, Y., & Togashi, S. (2004). Geochemical and isotopic characteristics of the Cretaceous Orikabe Plutonic Complex, Kitakami Mountains, Japan: magmatic evolution in a zoned pluton and significance of a subduction-related mafic parental magma. *Contributions to Mineralogy and Petrology*, 146(4), 433–449.
- Miller, C. F., McDowell, S. M., & Mapes, R. W. (2003). Hot and cold granites? Implications of zircon saturation temperatures and preservation of inheritance. *Geology*, 31(6), 529–532.
- Miller, C. F., & Mittlefehldt, D. W. (1984). Extreme fractionation in felsic magma chambers: a product of liquid-state diffusion or fractional crystallization?. *Earth and Planetary Science Letters*, 68(1), 151–158.
- Miller, R. B., & Paterson, S. R. (1991). Geology and tectonic evolution of the Bear Mountains Fault Zone, Foothills Terrane, central Sierra Nevada, California. *Tectonics*, 10(5), 995–1006.
- Molyneux, S. J., & Hutton, D. H. W. (2000). Evidence for significant granite space creation by the ballooning mechanism: the example of the Ardara pluton, Ireland. *Geological Society of America Bulletin*, 112(10), 1543–1558.
- Murray, J. D. (1979). Outlines of the structure and emplacement history of a tonalite pluton in the Peninsular Ranges batholith, Baja California, México. *Mesozoic Crystalline Rocks*, 163–176.
- Nabelek, P. I., Papike, J. J., & Laul, J. C. (1986). The Notch Peak granitic stock, Utah: Origin of reverse zoning and petrogenesis. *Journal of petrology*, 27(5), 1035–1069.
- O'Hara, M. J., & Mathews, R. E. (1981). Geochemical evolution in an advancing, periodically replenished, periodically tapped, continuously fractionated magma chamber. *Journal of the Geological Society*, 138(3), 237–277.
- O'Connor, J. T. (1965). A classification for quartz-rich igneous rocks based on feldspar ratios. *US Geological Survey Professional Paper B*, 525, 79–84.
- Parada, M. A., Larrondo, P., Guisresse, C., & Roperch, P. (2002). Magmatic gradients in the Cretaceous Caleu pluton (central Chile): injections of pulses from a stratified magma reservoir. *Gondwana Research*, 5(2), 307–324.
- Paterson, S. R., & Vernon, R. H. (1995). Bursting the bubble of ballooning plutons: a return to nested diapirs emplaced by multiple processes. *Geological Society of America Bulletin*, 107(11), 1356–1380.

- Paterson, S. R., & Miller, R. B. (1998). Mid-crustal magmatic sheets in the Cascades Mountains, Washington: implications for magma ascent. *Journal of Structural Geology*, 20(9), 1345–1363.
- Paterson, S. R., Vernon, R. H., & Tobisch, O. T. (1989). A review of criteria for the identification of magmatic and tectonic foliations in granitoids. *Journal of structural geology*, 11(3), 349–363.
- Paterson, S. R., Fowler, T. K., Schmidt, K. L., Yoshinobu, A. S., Yuan, E. S., & Miller, R. B. (1998). Interpreting magmatic fabric patterns in plutons. *Lithos*, 44(1), 53–82.
- Pearce, J. A., Harris, N. B., & Tindle, A. G. (1984). Trace element discrimination diagrams for the tectonic interpretation of granitic rocks. *Journal of petrology*, 25(4), 956–983.
- Petford, N. (2003). Rheology of granitic magmas during ascent and emplacement. *Annual Review of Earth and Planetary Sciences*, 31(1), 399–427.
- Pitcher, W. S. (1997). *The nature and origin of granite*. Springer Science & Business Media.
- Pupier, E., Barbey, P., Toplis, M. J., & Bussy, F. (2008). Igneous layering, fractional crystallization and growth of granitic plutons: the Dolbel Batholith in SW Niger. *Journal of Petrology*, 49(6), 1043–1068.
- Rogers, J. J. W. & Greenberg, J. K. (1990): Late-orogenic, post-orogenic and anorogenic granites: distinction by major-element and trace-element chemistry and possible origins. *The Journal of Geology*, 98, 291–309.
- Ruprecht, P., Bergantz, G. W., Cooper, K. M., & Hildreth, W. (2012). The crustal magma storage system of Volcán Quizapu, Chile, and the effects of magma mixing on magma diversity. *Journal of Petrology*, 53(4), 801–840.
- Sawyer, E. W. (1994). Melt segregation in the continental crust. *Geology*, 22(11), 1019–1022.
- Sawyer, E. W. (2008). *Atlas of migmatites* (Vol. 9). NRC Research Press, pp 1–371.
- Seaman, S. J., Gylling, H., Hogan, J. P., Karner, F., & Koteas, G. C. (2011). Concentric zoning in the Tunk Lake pluton, coastal Maine. *Contributions to Mineralogy and Petrology*, 162(6), 1291–1314.
- Shand, S. J. (1943). *Eruptive Rocks. Their Genesis, Composition, Classification, and Their Relation to Ore-Deposits with a chapter on Meteorite*. New York: John Wiley & Sons.
- Sharp, D. H. (1984). An overview of Rayleigh-Taylor instability. *Physica D: Nonlinear Phenomena*, 12(1), 3–18.
- Spera, F. J., & Bohrsen, W. A. (2001). Energy-constrained open-system magmatic processes I: general model and energy-constrained assimilation and fractional crystallization (EC-AFC) formulation. *Journal of Petrology*, 42(5), 999–1018.

-
- Stephens, W. E., & Halliday, A. N. (1980). Discontinuities in the composition surface of a zoned pluton, Criffell, Scotland. *Geological Society of America Bulletin*, 91(3), 165–170.
- Tindle, A. G., & Pearce, J. A. (1981). Petrogenetic modelling of in situ fractional crystallization in the zoned Loch Doon pluton, Scotland. *Contributions to Mineralogy and Petrology*, 78(2), 196–207.
- Turner, J. S., & Campbell, I. H. (1986). Convection and mixing in magma chambers. *Earth-Science Reviews*, 23(4), 255–352.
- Vendeville, B. C., Mart, Y., & Vigneresse, J. L. (Eds.). (2000). Salt, shale, and Igneous Diapirs in and around Europe. Geological Society of London.
- Vernon, R. H. (2000). Review of microstructural evidence of magmatic and solid-state flow. *Visual Geosciences*, 5(2), 1–23.
- Vigneresse, J. L., Barbey, P., & Cuney, M. (1996). Rheological transitions during partial melting and crystallization with application to felsic magma segregation and transfer. *Journal of Petrology*, 37(6), 1579–1600.
- Vigneresse, J. L., & Bouchez, J. L. (1997). Successive granitic magma batches during pluton emplacement: the case of Cabeza de Araya (Spain). *Journal of Petrology*, 38(12), 1767–1776.
- Wada, H., Harayama, S., & Yamaguchi, Y. (2004). Mafic enclaves densely concentrated in the upper part of a vertically zoned felsic magma chamber: the Kurobegawa granitic pluton, Hida Mountain Range, central Japan. *Geological Society of America Bulletin*, 116(7-8), 788–801.
- Walker, D., & DeLong, S. E. (1982). Soret separation of mid-ocean ridge basalt magma. *Contributions to Mineralogy and Petrology*, 79(3), 231–240.
- Walker, J. L. (1981). The diffusion of knowledge, policy communities, and agenda setting: the relationship of knowledge and power. *New strategic perspectives on social policy*, 75–96.
- Weinberg, R. F., & Hasalová, P. (2015). Water-fluxed melting of the continental crust: A review. *Lithos*, 212, 158–188.
- White, A. J. R. (1979). Sources of granite magmas. In *Geological Society of America, Abstracts with Programs* (Vol. 11), pp. 1–539.
- White, A. J., & Chappell, B. W. (1977). Ultrametamorphism and granitoid genesis. *Tectonophysics*, 43(1), 7–22.
- White, A. J. R., & Chappell, B. W. (1983). Granitoid types and their distribution in the Lachlan Fold Belt, southeastern Australia. *Geological Society of America Memoirs*, 159, 21–34.
- Wickham, S. M. (1987). The segregation and emplacement of granitic magmas. *Journal of the Geological Society*, 144(2), 281–297.

Wilson, M. (1993). Magmatic differentiation. *Journal of the Geological Society*, 150(4), 611–624.

Winter, J. D. (2009). *Principles of igneous and metamorphic petrology* (Vol. 2). New York: Prentice Hall, pp. 1–720.

Yoder, H. S., & Tilley, C. E. (1962). Origin of basalt magmas: an experimental study of natural and synthetic rock systems. *Journal of Petrology*, 3(3), 342–532.

Žák, J., & Paterson, S. R. (2005). Characteristics of internal contacts in the Tuolumne Batholith, central Sierra Nevada, California (USA): implications for episodic emplacement and physical processes in a continental arc magma chamber. *Geological Society of America Bulletin*, 117(9-10), 1242–1255.

Žák, J., Paterson, S. R., & Memeti, V. (2007). Four magmatic fabrics in the Tuolumne batholith, central Sierra Nevada, California (USA): implications for interpreting fabric patterns in plutons and evolution of magma chambers in the upper crust. *Geological Society of America Bulletin*, 119(1-2), 184–201.



RESULTS

CHAPTER I:

MAGMA DIFFERENTIATION

AND PLUTON ZONING

Chapter I:

Magma Differentiation and Pluton Zoning

Article I.-1:

Origin of reverse compositional and textural zoning in granite plutons by localized thermal overturn of stratified magma chambers

Trubač J., Janoušek V., Žák J., Somr M., Kabele P., Švancara J., Gerdes A., Žáčková E.

Status: Re-submitted to *Journal of Petrology*

Origin of reverse compositional and textural zoning in granite plutons by localized thermal overturn of stratified magma chambers

[Running title: Thermal overturn of stratified magma chambers]

Jakub Trubač^{1,2*}, Vojtěch Janoušek^{1,2}, Jiří Žák³, Michael Somr⁴, Petr Kabele⁴, Jan Švancara⁵, Axel Gerdes^{6,7}, Eliška Žáčková¹

¹ Czech Geological Survey, Klárov 3, 118 21 Prague, Czech Republic

² Institute of Petrology and Structural Geology, Faculty of Science, Charles University, Albertov 6, 128 43 Prague, Czech Republic

³ Institute of Geology and Palaeontology, Faculty of Science, Charles University, Albertov 6, 128 43 Prague, Czech Republic

⁴ Department of Mechanics, Faculty of Civil Engineering, Czech Technical University in Prague, Thákurova 7, 166 29, Prague, Czech Republic

⁵ Institute of Physics of the Earth, Faculty of Science, Masaryk University, Tvrdeho 12, 602 00 Brno, Czech Republic

⁶ Institut für Geowissenschaften, Goethe Universität, Altenhöferallee 1, D-60438, Frankfurt am Main, Germany

⁷ Department of Earth Sciences, Stellenbosch University, Private Bag X1, Matieland, 7602, South Africa

Keywords: granite pluton; magma chamber; gravity modelling; geochemistry; reactivated crystal mushes

ABSTRACT

Using the early Carboniferous (*ca.* 337 Ma) Říčany Pluton, Bohemian Massif, as an example, this study integrates gravimetry and thermal modelling with petrology, U–Th–Pb monazite and zircon geochronology and geochemistry to discuss the origin of compositional and textural zoning in granitic plutons and complex histories of horizontally stratified, multiply replenished magma chambers. The Říčany Pluton consists of two coeval, nested biotite (–muscovite) granite facies: outer, strongly porphyritic granite (SPm) and inner, weakly porphyritic granite (WPc). Their contact is concealed but is likely gradational over several hundreds of metres. Furthermore, the gravimetric data show that the nested pluton is only a small outcrop of a large anvil-like body at depth with an at least 14 km deep feeder channel.

The two main granite facies share nearly identical modal composition, are subaluminous to slightly peraluminous and geochemically evolved. Mafic microgranular enclaves, commonly associated with K-feldspar phenocryst patches, are abundant in the pluton centre and indicate repeated basic magma input and its multistage interactions with the granitic magma and nearly solidified cumulates.

The pluton is interesting in that it is *doubly* reversely zoned. On the pluton scale, the outer SRG is geochemically more evolved than the inner WPc. On the scale of individual units, whole-rock geochemical variations within each facies (SPm, WPc) are compatible with fractional crystallization dominated by K-feldspar. Both types of zoning are cryptic, manifested by variations in the trace-element compositions rather than in major elements or gross petrography.

The proposed genetic model invokes vertical overturn of a deeper, horizontally stratified anvil-shaped magma chamber driven by reactivation of resident felsic magma mush by injection of hot basic magmas. The energy for melt remobilization and extraction from the K-feldspar-rich crystal mush and for its subsequent ascent is thought to have been provided by a long-lived thermal anomaly above the pluton feeding zone, enhanced by multiple injections of hot basic magmas.

In general, it is concluded that the three-dimensional shape of the granitic bodies exerts a first-order control on their cooling histories and thus also on their physico-chemical evolution. Thicker and longer lived portions of magma chambers are sites for extensive fractionation and potentially vigorous interaction with basic magmas. These hot domains are then particularly prone to rejuvenation and subsequent extraction of highly mobile magma leading potentially to volcanic eruptions.

INTRODUCTION

Many circular to elliptical granitic plutons in the middle and upper crust exhibit remarkable concentric compositional and textural zoning. Compositionally zoned plutons also may provide a geological snapshot of the density stratification in a magma chamber before eruption. The zoning can be recognized in the field, for instance, by regular variation in the modal contents of rock-forming minerals, abundance/size of K-feldspar phenocrysts, the nature and volumetric proportion of enclaves, or by hydrothermal alteration and mineralization (Candela, 1997). This is commonly supported by analytical studies which reveal systematic spatial variations in chemical composition as well, with more mafic/less evolved rocks occurring along pluton margins and felsic/more evolved rocks in the centres, or vice versa (normal and reverse zoning, respectively; e.g., Ayuso *et al.* 1984; Nabelek *et al.*, 1986; Gastil *et al.* 1991; Allen, 1992; Hecht *et al.* 1997; Bachl *et al.* 2001; Barbey *et al.* 2001; Miller and Miller 2002; Mikoshiba *et al.* 2004; Hildreth and Wilson, 2007; Antunes, 2008; Miller *et al.*, 2011; Seaman *et al.*, 2011; Imaoka *et al.*, 2014; Putirka *et al.* 2014). In addition, the pluton zoning can be cryptic, defined only, for example, by the trace-element variation (e.g., Janoušek *et al.*, 1997).

Formation of concentric zoning has been commonly explained as a result of several physico-chemical processes, operating alone or in combination: (1) in situ crystal–melt separation via flow sorting, gravitational settling, filter pressing or sidewall crystallization within a single magma pulse (Bateman & Chappell, 1979; Tindle and Pearce, 1981; Bateman 1984); (2) nested emplacement of multiple magma pulses sharing a single conduit (e.g., Allen, 1992; Stephens, 1992; Paterson & Vernon, 1995; Weinberg, 1997, Molyneux and Hutton, 2000), with or without mixing between separate outer and inner batches (Stephens and Halliday, 1980; Huppert *et al.*, 1982; Vigneresse and Bouchez, 1997; Lux *et al.*, 2007, Coint *et al.* 2013); (3) intrusion of an essentially single pulse of magma preserving a vertical compositional gradient from a deeper level magma chamber (Fridrich & Mahood, 1984; Bourne & Danis, 1987, Wada *et al.*, 2004; Pupier *et al.*, 2008); and (4) continuous cyclic thermal evolution of an incrementally constructed magma chamber (Parada *et al.*, 2002; Pichavant *et al.*, 2002; Johnson *et al.*, 2002; Walker *et al.*, 2007; Lipman, 2007; Gray *et al.*, 2008; Johnson & Glazner, 2010; Coleman *et al.*, 2012; Glazner & Johnson, 2013).

Taken together, the observed zonation in plutons records complex processes that may have taken place not only at the final emplacement level, but also deep in the magma plumbing system, reflecting its vertical and/or horizontal heterogeneity. An indispensable tool to constrain the

vertical extent of magma plumbing systems and their shapes at depth is gravimetry (Miller and Tuach 1989; Vigneresse 1995a, b). But any serious attempts to understand the nature and genesis of a complex zonation pattern in a granitic pluton have to be multidisciplinary, combining structural, petrological, geochronological and geochemical methods with geochemical modelling and geophysical investigations.

Using such an integrated approach, this contribution addresses formation of concentric zoning on the example of the Říčany Pluton, Bohemian Massif (Fig. 1a–b). This granitic body is unique in that it exhibits a normal concentric textural zoning, defined by an inward decrease in modal content of K-feldspar phenocrysts, but also reveals an inverse cryptic zoning expressed by the trace-element abundances. Field observations combined with a gravimetric survey and with geobarometric data provide input parameters for three-dimensional modelling of thermal evolution of the pluton. This, together with additional data sets (petrology, textural analysis, geochronology and whole-rock geochemistry, including Sr–Nd isotopes), serves as a background for a general discussion on the nature of magma source as well as on the origin of compositional and textural zoning in granitic plutons. Finally, a new model for the origin of zoning is proposed invoking a thermally-driven overturn of a deeper stratified magma chamber.

GEOLOGICAL SETTING

The Central Bohemian Plutonic Complex (CBPC; ~3200 km²; Fig. 1a–b) intruded a broad zone along a NE–SW-trending boundary between the Teplá–Barrandian Unit in the NW and the Moldanubian Zone in the SE (Janoušek *et al.*, 1995; Holub *et al.*, 1997; Janoušek *et al.*, 2000b). While the early (c. 355 Ma) plutons were related to a magmatic arc and overall transpressional setting, the younger ones (c. 346 Ma) intruded during collapse of the Teplá–Barrandian upper crust and exhumation of the high-grade orogenic root (Moldanubian Zone) (see Žák *et al.* 2014 for review of tectonic setting). After this event, the Říčany Pluton was emplaced post-tectonically in the north-eastern part of the CBPC.

In the map, this shallow-level pluton is roughly elliptical with dimensions of about 13 × 9 km (~85 km²; Fig. 1c) and consists of two main granite facies which define a concentric zoning (Katzer, 1888; Kašpar, 1936). In an approximately 0.8 to 2.5 km wide zone, the outer pluton margin is delineated by the strongly porphyritic, (muscovite–) biotite Říčany granite (SPm) with abundant K-feldspar phenocrysts. The contact between the outer SPm and the inner weakly porphyritic, (muscovite–) biotite granite (WPC) is concealed in a zone of several hundred metres wide. Otherwise both granite

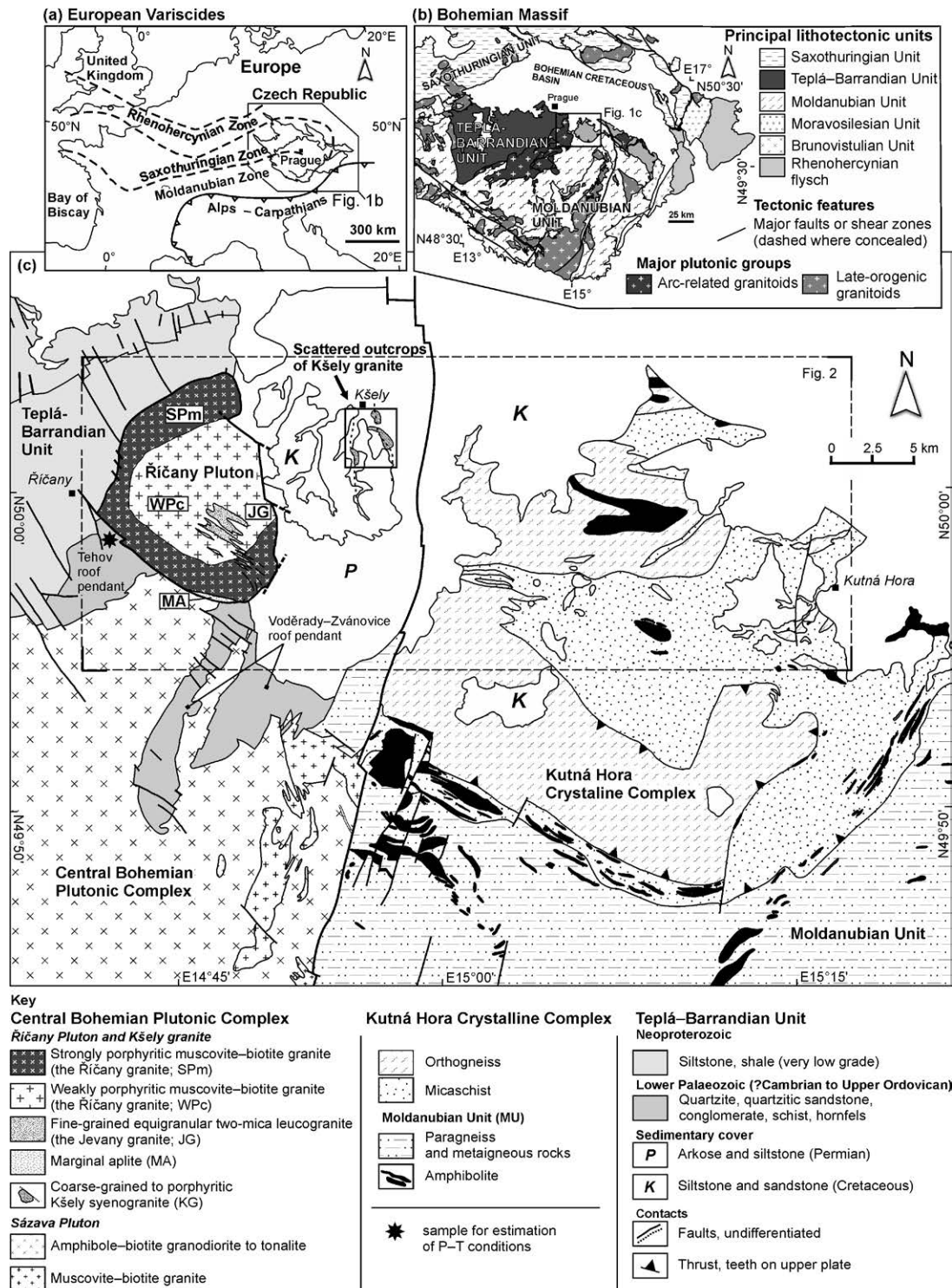


Fig. 1. (a) Map showing basement outcrop areas and principal lithotectonic zones of the Variscan orogenic belt in Europe. Bohemian Massif is the easternmost inlier of the orogen. (b) Simplified geologic map of the interior Bohemian Massif emphasizing principal lithotectonic units and plutonic groups. Based on 1:500,000 Geologic map of the Czech Republic (Cháb *et al.*, 2007). (c) Simplified geologic map of the Říčany Pluton and its host rocks (based on the Czech Geological Survey 1:200,000 map, sheet Praha).

facies appear superficially homogeneous on outcrops and devoid of any internal contacts or sheets. Both main facies of the Říčany granite are weakly peraluminous, geochemically evolved, and strongly fractionated (Holečková & Šmejkalová, 1958; Vejnar, 1973). The relatively evolved Sr–Nd isotopic signatures of the granite, together with other geochemical data, were explained as a result of partial melting of a metasedimentary source, similar to the Moldanubian paragneisses, followed by fractional crystallization (Janoušek *et al.*, 1995; 1997). The mafic microgranular enclaves (MME) are fine-grained and have textures of rapidly quenched hybrid mafic melts (acicular apatites, numerous small plagioclase laths, blade-shaped biotite etc. – Hibbard, 1991, 1995). Thus their abundance, especially in the pluton centre, is taken to indicate an interaction with coeval basic magmas. Felsic microgranular enclaves (FEL) are rare but may show similar field relations indicative of injection into a colder granitic crystal–melt ‘mush’. The enclaves have commonly a composition similar to the host granite magma.

The central to south-eastern part of the pluton has been intruded by a small, poorly exposed body of the fine-grained, equigranular, two-mica Jevany leucogranite (JG) (Šmejkalová, 1960; Němec, 1978). The southern margin of the pluton is rimmed by a ~1 km wide zone (in plan view) of numerous late-stage boron-rich pegmatite, microgranite and aplite dikes, collectively referred to as the ‘marginal aplite’ (MA; Němec, 1978).

There is a dearth of geochronological information from the Říčany Pluton. Apart from older and imprecise K–Ar data, the granite cooling was constrained to 336 ± 3.5 Ma (unpublished ^{40}Ar – ^{39}Ar biotite age of H. Maluski, cited in Janoušek *et al.*, 1997).

The existing gravity data indicate that the Říčany granite, or its correlatives, may extend farther east and that its present-day outcrop may represent only an apical part of a much larger granitoid body at depth (Orel, 1975). This interpretation is supported by several outcrops of compositionally and texturally similar Kšely granite (KG) which emerges from beneath a Lower Permian cover some 6–8 km northeast of the main pluton (Fig. 1c). This granite is coarse-grained and commonly porphyritic. Except for several modal and whole-rock analyses (Kodym, 1963; Pivec & Pivec Jr., 1996), modern geochemical data are lacking.

The exposed part of the Říčany Pluton is in intrusive contact with very low-grade Neoproterozoic siliciclastic rocks of the Teplá–Barrandian Unit to the northwest (Fig. 1c). The contact is steep and is delineated by a c. 0.5 km wide thermal aureole (Kodym, 1925; Kettner, 1930; Orlov, 1933; Kachlík, 1992). The southwestern contact with the Lower Paleozoic roof pendants and with the 354.1 ± 3.5 Ma Sázava Pluton (Janoušek *et al.*, 2004a) has been modified by late post-emplacement faults.

The eastern margin of the pluton is overlain by Upper Carboniferous to Lower Permian continental siliciclastic successions (Pešek *et al.*, 2001; Zachariáš & Hübst, 2012), whose basal conglomerates contain pebbles of the Říčany granite (e.g., Steinocher, 1969); this contact has also been reactivated by brittle faults.

ANALYTICAL TECHNIQUES

Gravimetry

The area around the Říčany Pluton is covered by gravimetric map on the scale of 1:200,000 with an average spacing of gravity stations of 2.5 km (Ibrmajer, 1963; Švancara, 2004) and in part also by detailed (1:25,000) gravity map with station spacing about 0.5 km. The Bouguer gravity anomalies were calculated from this data set for reduction density of $2670 \text{ kg}\cdot\text{m}^{-3}$, the gravity station network was tied to a local gravity system S-Gr95 (Švancara, 2004). The topographic corrections were calculated up to a distance of 167 km from the gravity station. The Bouguer anomaly map was then constructed from these gravity data and interpolated to a regular grid $0.25 \times 0.25 \text{ km}$. Furthermore, the residual gravity map for wavelengths shorter than 110 km was constructed from the regular grid using Butterworth filter to emphasize gravity effects of the upper part of the crust (approximately to depth of 18 km) and to eliminate the lower crustal and upper mantle contribution to the total gravity field. Fourier domain filtering was accomplished by the MAGMAP extension (Whitehead & Musselman, 2010) of the geophysical mapping and processing system Oasis Montaj (Whitehead, 2010). In order to estimate the pluton shape at depth more quantitatively, a 2.75D model was constructed along a NW–SE profile across the negative gravity anomaly. This model allows for approximation of three-dimensional irregular geologic bodies using multiple tabular prisms of finite length oriented perpendicular to the profile axis, the two ends of the prisms may be independently specified. Gravity modelling was performed by GM-SYS (Northwest Geophysical Associates, USA) software. For modelling we used residual gravity profile as the observed gravity, because we modelled geological bodies only in the upper part of the crust. Rock densities are shown in the Electronic Appendix 1 and were complemented by our new density measurements. For gravity modelling the wet bulk densities of rocks were used. The wet bulk density is defined as the mass of the water saturated rock per unit volume. We assumed that the micro cracks and pores close-off depth was approximately 7.5 km, below which the wet bulk density approaches the grain density.

Textural analysis

Eight oriented samples (blocks) were taken from both the outer and inner parts of the Říčany Pluton (Electronic Appendix 2). About 2–3 cm thick slabs were cut out of each block by a diamond saw, photographed, and processed by Adobe Photoshop CS5. In addition, six outcrops (mostly smooth joint planes) were photographed in field and also subjected to the image analysis. The same area (305 × 175 mm²) was analysed in each photograph for the sake of scale consistency. Next step involved an inversion of colour channels in the images. This procedure enabled distinguishing K-feldspar from plagioclase. Subsequently only phenocrysts with a perimeter of more than 1 cm were selected for analysis; K-feldspars in the matrix were omitted. The phenocrysts were manually outlined, then scanned and automatically traced, coloured, and saved in a separate layer. The result was a picture containing black polygons of various sizes. Such modified images were saved with a high resolution (400 dpi) and processed using the ImageJ programme (<http://imagej.nih.gov/ij>). A statistical analysis of the acquired images yielded phenocryst size ('perimeter'), their mode expressed as percentage of the analysed area, and x, y coordinates of phenocrysts' centroids. These centroids were used to obtain values for the aggregation index (R) of Clark and Evans (1954) (also known as the ordering index) with the help of the statistical nearest neighbour method. The aggregation index (R) shows that packings of spherical particles have more cluster than packings of rods and it is a measure of particle clustering (particles are represented by points in a plane) and is expressed as:

$$(1) \quad R = \frac{r_A}{r_E} ,$$

where r_A is the mean of the distances separating points from their nearest neighbours, r_E

$$(2) \quad r_E = \frac{1}{2\sqrt{\lambda}} ,$$

is the expected value of r_A for complete spatial randomness, λ is the number of points per unit area. If $R = 1$, the points are distributed randomly, for $R < 1$ they are clustered (the distance to the respective nearest neighbours is shorter than that expected for complete spatial randomness), whereas for $R > 1$ the points are ordered (see Higgins, 2006; Rudge *et al.*, 2008 for details).

Electron microprobe analyses (EPMA) and BSE imaging

Analyses of the major rock-forming and selected accessory minerals were carried out by fully automated CAMECA SX-100 electron microprobe at Czech Academy of Sciences (Z. Korbelová) and JEOL

SuperProbe JXA-8900M at Universidad Complutense de Madrid (A. Fernández Larios), in both cases employing correction procedure (Pouchou and Pichoir, 1985). All were performed at an acceleration voltage of 15 kV. Currents of 20–40 nA and a spot sizes of 5–10 μm were employed for apatite, titanite, rutile, monazite, magnetite, ilmenite and zircon–thorite solid solution. For feldspars, micas and quartz, the beam current was 10–15 nA and spot size 2 μm . Minor-element interferences have been checked routinely and corrected by measuring the corresponding standards. All the mineral abbreviations are after Whitney and Evans (2010).

Minerals in marginal aplite were analyzed using the Vega TESCAN electron microscope equipped with the X-Max 50 EDS detector (INCA Oxford Instruments), hosted at the Institute of Petrology and Structural Geology, Charles University in Prague (IPSG; M. Racek). Accelerating voltage of 15 kV, probe current of 1.5 nA and counting time 100 s were used. Beam diameter was 3 μm for all minerals but plagioclase, where the signal was recorded during scanning of an area $5 \times 5 \mu\text{m}$ in order to minimize sodium loss.

U–Pb LA ICP-MS dating

Zircons and monazites were concentrated from the 60–125 μm fraction by combined Wilfley shaking table, magnetic and heavy liquid (tetrabromomethane) separation. The zircons and monazites were finally handpicked, mounted in epoxy resin and polished. Prior to laser analyses all grains were characterized by cathodoluminescence (CL) imaging at IPSG (zircons) and Goethe Universität, Frankfurt (GUF) (monazites).

Uranium, thorium and lead isotope analyses were carried out by laser ablation – inductively coupled plasma – mass spectrometry (LA-ICP-MS) at GUF, using a slightly modified method of Gerdes & Zeh (2006), Gerdes & Zeh (2009) and Zeh & Gerdes (2012). A ThermoScientific Element 2 sector field ICP-MS was coupled to a Resolution M-50 (Resonetics) 193 nm ArF Excimer laser (CompexPro 102, Coherent) equipped with two-volume ablation cell (Laurin Technic, Australia). The laser was fired with 5.5 Hz at a fluence of c. 5 J cm^{-2} . The above configuration led to a spot size of 26 μm , a depth penetration of 0.6 $\mu\text{m s}^{-1}$ and a sensitivity of 10000–13000 cps/ $\mu\text{g g}^{-1}$ for ^{238}U . Raw data were corrected offline for background signal, common Pb, laser-induced elemental fractionation, instrumental mass discrimination, and time-dependent elemental fractionation of Pb/U using an in-house MS Excel® spreadsheet program (Gerdes & Zeh, 2006, 2009). Laser-induced elemental fractionation and instrumental mass discrimination were corrected by normalization to the reference zircon GJ-1 (0.0984 ± 0.0003 ; ID-TIMS GUF value). Repeated analyses of the reference zircon Plešovice, Felix and

91500 (Wiedenbeck *et al.*, 1995; Sláma *et al.*, 2008; Millonig *et al.*, 2012) during the same analytical session yielded an accuracy better than 1% and a reproducibility of < 2% (2σ). All uncertainties are reported at the 2 sigma level. The data were plotted using ISOPLOT (Ludwig, 2003).

Whole-rock geochemical analyses

In total, large (c.15–30 kg) and fresh samples were taken in active or abandoned quarries for whole-rock geochemical studies in order to account for the presence of phenocrysts as well as to yield precise data on trace elements that are hosted mostly by accessories (Janoušek *et al.*, 2014). Samples were crushed by steel jaw crusher in the laboratories of the Czech Geological Survey (CGS) to grain fraction 2–4 cm, homogenized and split to 500–1500 g. Finally, aliquots of c. 300 g were ground in an agate mill.

Whole-rock major- and trace-element analyses were carried out in the Acme Analytical Laboratories (Vancouver) Ltd., Canada. Newly re-analysed by modern techniques were also rock powders of 22 samples that were originally studied by Janoušek *et al.* (1997) using less precise methods (XRF). Total abundances of the major oxides and several minor elements were analysed by ICP-OES following a lithium metaborate or tetraborate fusion and dilute nitric digestion of a 0.2 g sample (method 4A). Loss on ignition (LOI) was obtained by weight difference after heating at 1000 °C. In addition, total carbon and sulphur contents were analysed by Thermogravimetric Analyser – LECO. The REE and refractory metals were determined by ICP-MS following a lithium metaborate or tetraborate fusion and nitric acid digestion of a 0.2 g sample (method 4B). In addition, separate 0.5 g splits were dissolved in aqua regia and analysed by ICP-MS to report the precious and base metals (method 1DX). For further analytical details, see <http://acmelab.com>.

Selected major-element analyses were carried out by wet chemistry in the laboratories of the Czech Geological Survey, Prague–Barrandov. The relative 2σ uncertainties were better than 1 % (SiO_2), 2 % (FeO), 5 % (Al_2O_3 , K_2O , Na_2O), 7 % (TiO_2 , MnO, CaO), 6 % (MgO) and 10 % (Fe_2O_3 , P_2O_5).

Interpretation and plotting of the whole-rock geochemical data was facilitated by the freeware R-language package GCDkit, version 3.0 (Janoušek *et al.*, 2006; 2011).

Radiogenic isotopes

For the radiogenic isotope determinations, samples were dissolved using a combined HF–HCl– HNO_3 digestion. Strontium and REE were isolated from the bulk matrix by the chromatography techniques using PP columns filled with Sr.spec and TRU.spec Eichrom resins, respectively (Pin *et*

al., 1994). The Nd was further separated from the REE fraction on PP columns with Ln.spec Eichrom resin (Pin & Zalduegui, 1997). Further analytical details were reported by Míková & Denková (2007). Isotopic analyses of Sr and Nd were performed on a Finnigan MAT 262 thermal ionization mass spectrometer housed at CGS in dynamic mode using a single Ta filament for Sr and double Re filament assembly for Nd. The $^{143}\text{Nd}/^{144}\text{Nd}$ ratios were corrected for mass fractionation to $^{146}\text{Nd}/^{144}\text{Nd} = 0.7219$ (Wasserburg *et al.*, 1981), $^{87}\text{Sr}/^{86}\text{Sr}$ ratios assuming $^{86}\text{Sr}/^{88}\text{Sr} = 0.1194$. External reproducibility is estimated from repeat analyses of the JNdi1 (Tanaka *et al.*, 2000) ($^{143}\text{Nd}/^{144}\text{Nd} = 0.512101 \pm 14$ (2σ , $n = 10$)) and NBS 987 ($^{87}\text{Sr}/^{86}\text{Sr} = 0.710247 \pm 26$ (2σ , $n = 22$)) isotopic standards. The decay constants applied to age-correct the isotopic ratios are from Steiger & Jäger (1977 – Sr) and Lugmair & Marti (1978 – Nd). The e_{Nd} values were obtained using Bulk Earth parameters of Jacobsen & Wasserburg (1980), the two-stage Depleted Mantle Nd model ages ($T_{\text{DM}}^{\text{Nd}}$) were calculated after Liew & Hofmann (1988).

Thermodynamic modelling

The P–T sections were modelled with the Perple_X thermodynamic software (Connolly, 2005: 2012 upgrade) using the internally consistent thermodynamic dataset of Holland & Powell (1998: 2004 upgrade). Mixing properties of phases used in the calculations were taken from Newton & Haselton (1981) for plagioclase, Holland *et al.* (1998) for chlorite, Powell & Holland (1999) for biotite, white mica, staurolite, epidote, garnet and chloritoid, and Waldbaum & Thompson Jr. (1968) for K-feldspar.

THE THREE-DIMENSIONAL PLUTON SHAPE AT DEPTH INFERRED FROM GRAVIMETRY

New gravimetric modelling was used to constrain the subsurface shape and minimum vertical extent of the granite body (Electronic Appendix 1). The Bouguer gravity anomaly map shows a pronounced, approximately rectangular negative anomaly that underlies an area of about 23 × 38 km to the southeast of the present-day outcrop of the Říčany Pluton (see also Mottlová, 1970; Orel, 1975) and contains a well-defined gravity minimum in its western half outlined by the –40 mGal contour line (Fig. 2a; cross section in Fig. 2b). Based on the gravity data, the three-dimensional shape of the granite body at depth was approximated by set of prisms as an eastward-tapered wedge with a flat top at a depth less than 1 km below the present-day surface (Fig. 2c). In cross-section, the wedge thickens to the northwest, forming at least 14 km deep root zone below the Říčany Pluton (Fig. 2d).

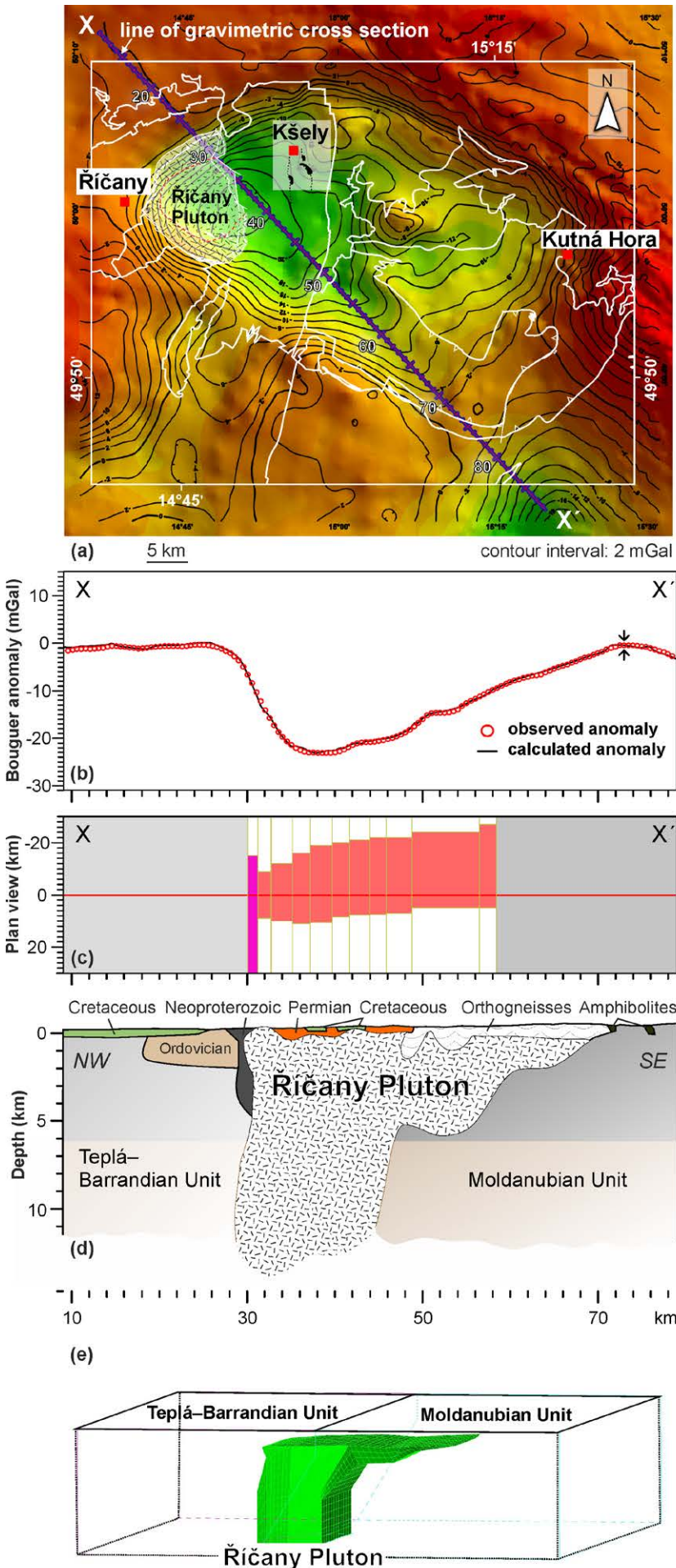


Fig. 2. (a) Bouguer anomaly map with marked gravity profile showing the gravity effect around the Říčany body and contour lines at 2 mGal intervals. (b) Residual gravity profile (circles) and calculated gravity (solid line) of the Říčany Pluton. (c) The plan view displays a horizontal slice through the model at 4 km depth. (d) Geological cross-section through the Říčany Pluton and its host rocks based on gravity modelling, vertical exaggeration 2x.

MODELING THE THERMAL EVOLUTION OF THE PLUTON

Rationale of the model

A transient thermal finite-element analysis was carried out in order to estimate a possible thermal evolution (Annen, 2009, Gelman *et al.*, 2013) of the Říčany Pluton. It should be emphasized that, in general, any attempt to model thermal evolution of granitoid plutons is always arbitrary and includes a number of underlying assumptions that can never be fully constrained. In all cases, the unknown parameters include the three-dimensional shape (in most models vaguely assumed as sill-like), dimensions, and composition of the pluton at depth, its emplacement history (numerous small magma pulses vs. a few large batches), and the role of intra-chamber convection and hydro-thermal fluid flow. Given that the shape of the Říčany Pluton is well established from gravimetry (while the other model parameters are unknown), our main goal in the thermal modelling was to examine a relative temperature distribution within such an asymmetric, anvil-shaped pluton and to constrain a maximum time span for pluton cooling. Another goal was to simulate how vertical temperature variations in a pluton feeder (e.g., due to the presence of hotter basic magmas or higher magma temperatures at depth) will affect the pluton's thermal history at shallower levels.

Model description and results

The three-dimensional shape and dimensions of the modelled pluton body (Fig. 2e) were taken from the gravimetric interpretation (Fig. 2d) but the root was arbitrarily extended down to a depth of 28 km to simulate pluton feeder from the lower crust (Fig. 3). The exact root depth below the gravimetric model cannot be established but, on the other hand, its vertical dimension has little effect on the relative temperature distribution in upper parts of the pluton. The pluton intersected the inclined boundary between the Teplá–Barrandian and Moldanubian units, its top was placed to a depth of 7 km, and the surrounding lithologies were taken from both geological map and gravimetric interpretation. The whole modelled domain (outside the pluton) had a prismatic shape with horizontal dimensions of 97 × 100 km and depth of 35 km. The outer boundaries were placed far enough to minimize the effects of boundary conditions on the simulated thermal evolution of the pluton.

Due to unknown thermal state of the crust during magma emplacement, the host rocks were assigned two different geothermal gradients of 30 and 25 °C/km to cover a range of possible scenarios in a collisional orogen. This means that the temperature at the lower horizontal boundary

(a) Geothermal gradient 30°/km, temperature at the base 895 °C

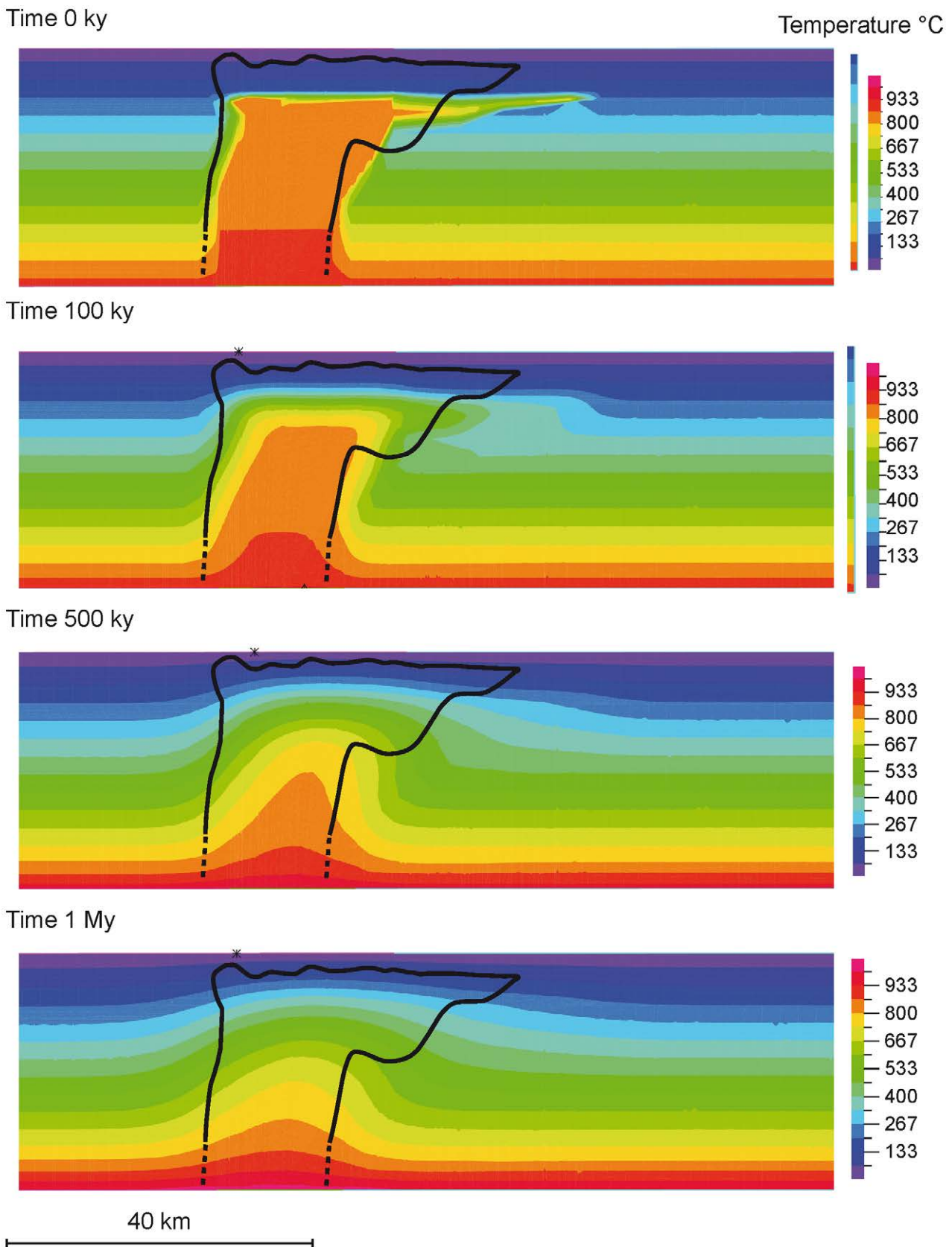


Fig. 3a Isotherms calculated for times 0, 100, 500 and 1000 ky (from the top) after emplacement and geothermal gradients 25 °C/km. The front face of the depicted body corresponds to a longitudinal vertical section passing through the pluton.

(b) Geothermal gradient $25^{\circ}/\text{km}$, temperature at the base 1070°C

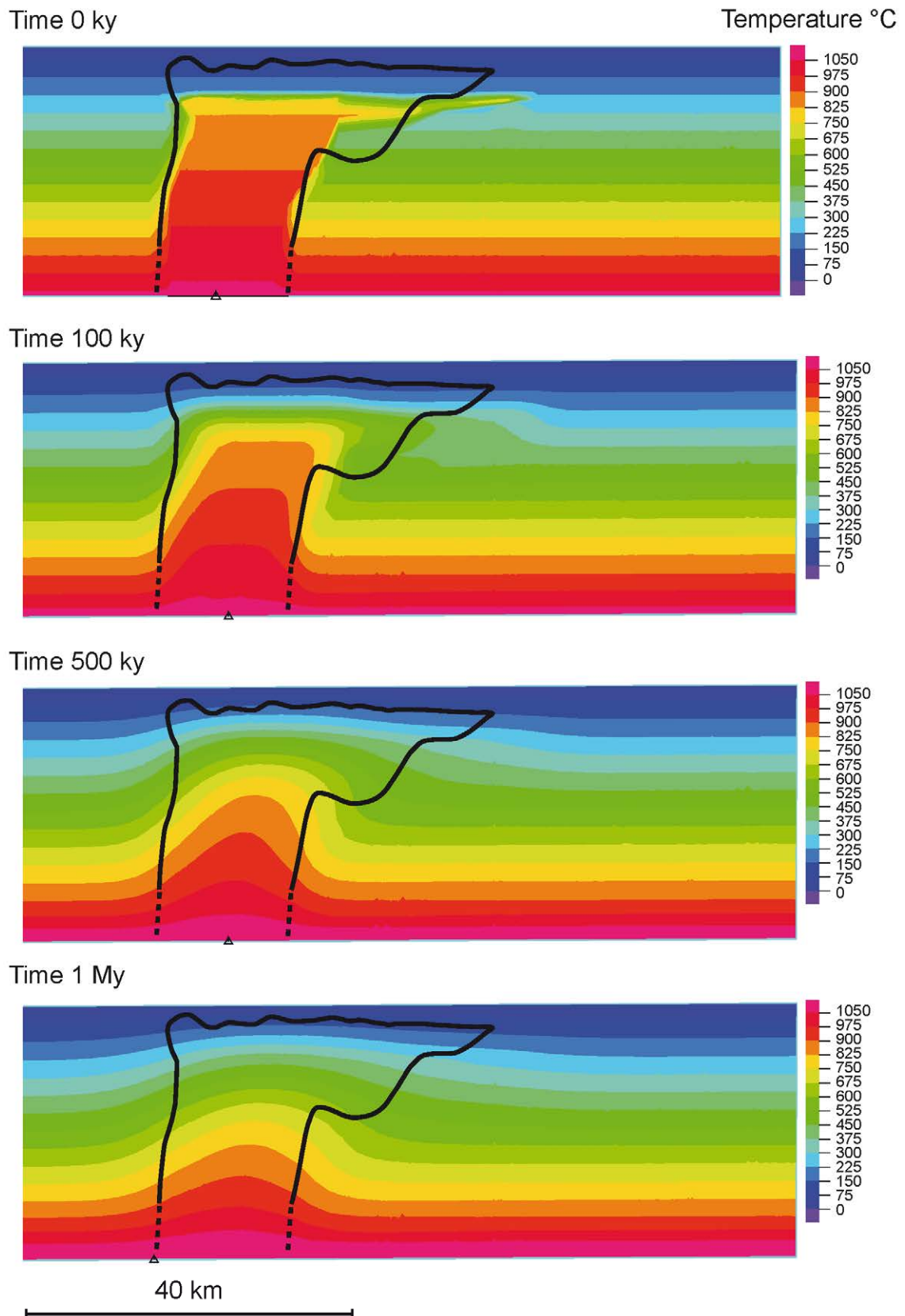


Fig. 3b Isotherms calculated for times 0, 100, 500 and 1000 ky (from the top) after emplacement and geothermal gradients $30^{\circ}\text{C}/\text{km}$. The front face of the depicted body corresponds to a longitudinal vertical section passing through the pluton.

reached 1070 °C and 895 °C, respectively. The initial temperature of the granitic magma at the top of the intrusion was 800 °C, in agreement with the zircon saturation temperatures estimated using the method of Harrison and Watson (1983) (Table 1). Vertical geothermal gradients were also prescribed to the intrusion in such a way that the magma at the lower boundary had the same temperature as the host rocks (i.e. 1070 °C and 895 °C).

The following boundary conditions were applied to the model. Geothermal heat flux of 0.06 W/m²

Table 1 Overview of calculated zircon (Watson & Harrison, 1983) and monazite (Montel, 1993) saturation temperatures for the Říčany Pluton

Intrusion	T zircons	T monazites	Number of samples
SPm	792 ± 10 °C	776 ± 4 °C	N = 22
WPc	807 ± 11 °C	774 ± 13 °C	N = 04
Jevany granite	775 ± 3 °C	748 ± 4 °C	N = 02
Marginal aplite	664 °C	665 °C	N = 01
MME	843 ± 19 °C	797 ± 21 °C	N = 09

was assigned to the lower horizontal boundary. Zero heat flux was prescribed at the vertical boundaries to simulate the continuity of the body beyond the modelled boundaries. Temperature of 20 °C was assigned directly to the ground surface at the upper horizontal boundary of the entire body. It would be more realistic to consider ground to air convection, but both approaches yield almost the same results (Žák et al., 2009).

Conduction was the only heat transfer mechanism taken into account in the present thermal analysis and the other phenomena were neglected. Thermal conductivity k and heat capacity ρc were considered to be temperature-dependent. The dependence was expressed using curves from Vosteen & Schellschmidt (2003). The curves were then calibrated to the particular type of the rock to match the values of the conductivity and capacity at the reference temperatures (Table 2; Čermák et al., 1982).

Table 2: Thermal properties at reference temperature and density of the studied rocks.

Rock	Density ρ [kg m ⁻³]	Reference temperature [°C]	Specific heat capacity c [J kg ⁻¹ K ⁻¹]	Thermal conductivity k [W m ⁻¹ K ⁻¹]
Granite	2630	50	860	3.09
Barrandian	2700	50	910	2.63
Moldanubian	2700	20	1130	2.44
Orthogneiss	2610	20	1350	2.08

The result of the analyses was a time-dependent evolution of the temperature field in the whole three-dimensional domain. For both geothermal gradients, the field is shown in four time steps, at the beginning, after 100 ky, 500 ky, and 1 My (Fig. 3). Regardless of the prescribed geothermal gradient, the modelling clearly shows virtually the same cooling pattern in the pluton. The upper-crustal eastward-tapered tip of the pluton 'wedge' cooled relatively fast and after about 6 ky (for 30 °C/km gradient; Fig. 3a) or 5.6 ky (for 25 °C/km gradient; Fig. 3b) passed into solidus conditions (Johannes & Holtz, 1996). In contrast, the domain above the inferred pluton root, i.e. beneath the present-day exposure of the pluton, stayed above solidus even after 20 ky (for 25 °C/km gradient; Fig. 3b). This effect and the development of a thermal anomaly was even accentuated for 30 °C/km gradient, wherein the hot domain was long-lived and the magma maintained temperature above solidus for more than 30 ky (Fig. 3b).

FIELD OBSERVATIONS

The bulk of the pluton consists of (Mu-) Bt granites (Janoušek *et al.* 2014) of a uniform modal composition. Both facies (SPm and WPc, Figs 4, 5a–b) are relatively fresh, with plagioclase showing the initiation of argillitization and biotite only incipient chloritization. The K-feldspar phenocrysts tend to be whitish and with a glassy lustre, only some are cloudy. The average grain size of the groundmass is 1–5 mm.

Both facies of the Říčany granite provide abundant field evidence for magmatic origin of the K-feldspar phenocrysts (Vernon, 1986; Vernon & Paterson, 2008), including: (1) euhedral shapes (Fig. 4a), (2) simple twinning and oscillatory zoning, (3) the presence of crystallographically oriented inclusion trails, forming a macroscopically obvious hour-glass sector zoning (Fig. 4b; Pivec, 1969), (4) lack of fracturing and plastic deformation implying that the K-feldspar megacrysts were suspended in liquid, (5) magmatic fabric defined by the shape-preferred orientation of the K-feldspar megacrysts and biotite schlieren, also enclosing oriented K-feldspar phenocrysts, observed especially in the outer part of the Říčany granite (Trubač *et al.*, 2009), (6) modal concentrations of K-feldspar megacrysts (patches) in some portions of the granite and their association with MME, whereby both represented clearly rigid objects in the magma (Fig. 4c–f) and (7) the presence of partially resorbed K-feldspar xenocrysts in MME, apparently captured from the surrounding crystal-bearing magma mush (Fig. 4a, b, e).

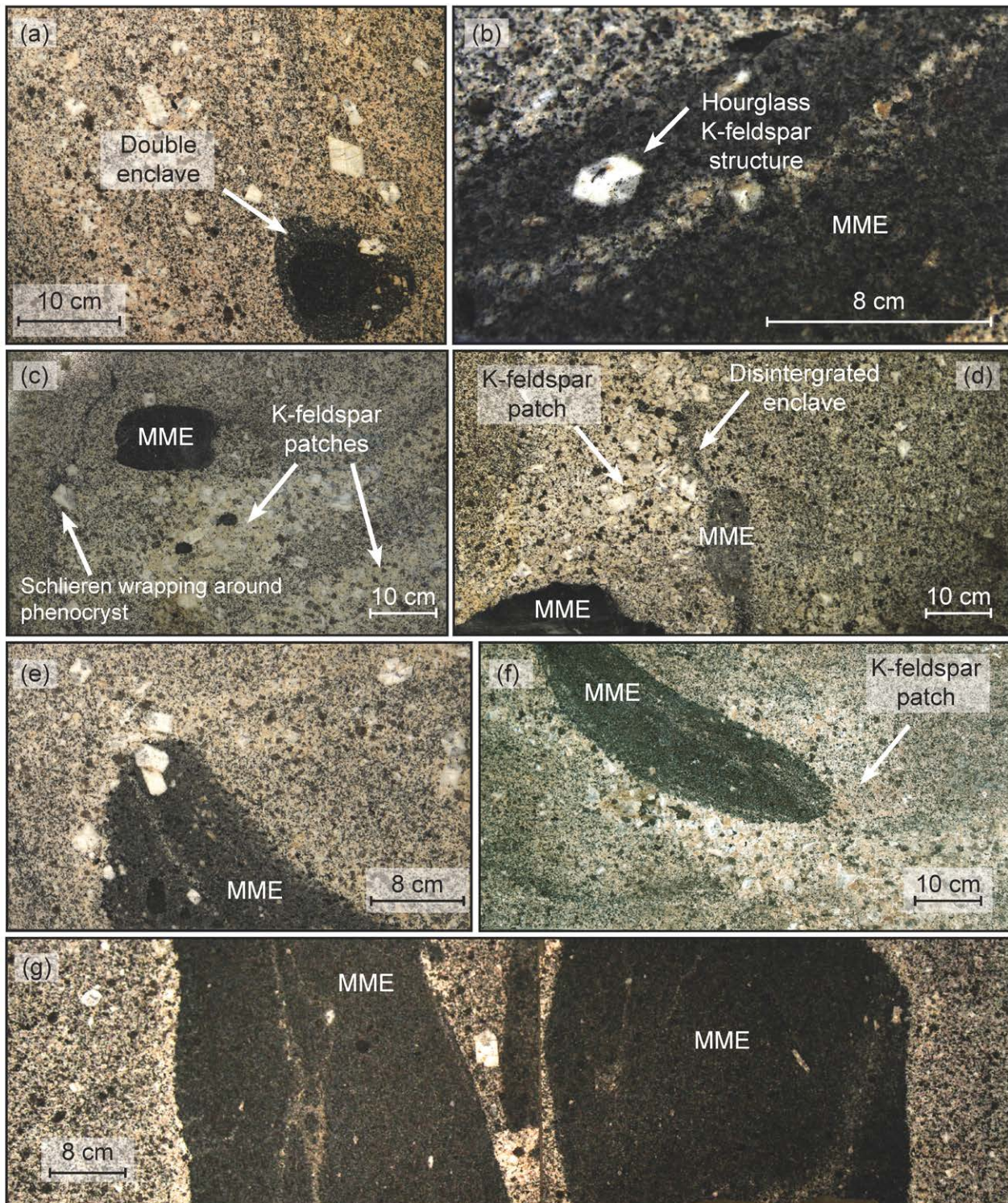


Fig. 4. Examples of mafic–felsic magma interactions in the central part of the Řičany Pluton. (a) Double mafic microgranular enclave (MME) in the weakly porphyritic granite. K-feldspar phenocrysts in the granite exhibit euhedral shapes, simple twinning and sector zoning and lack any evidence of solid-state deformation. (b) Detail of an elongated MME cross-cut by a veinlet of the host granite. The enclave encloses K-feldspar xenocrysts with crystallographically oriented inclusion trails, forming a macroscopically obvious sector zoning ('hourglass structure'). (c) Modal layering in a strongly inhomogeneous portion of the granite. The granite encloses a MME in close association with modal concentrations (patches) of K-feldspar phenocrysts. Thin biotite schlieren (left) wrap around the euhedral K-feldspar phenocrysts. (d) Compositionally

and texturally variable MME in inhomogeneous granite. Note a MME attached to an irregular K-feldspar phenocryst patch. Hybrid portion of the granite shows arrested stages of a MME decomposition and modification to biotite-rich schlieren (centre). (e) Partially resorbed K-feldspar xenocrysts enclosed by a large hybrid MME. (f) K-feldspar phenocryst patch wrapped around an elongated MME. (g) Mafic enclaves disintegrated by the host granite; enclave margins are sharp and lack reaction rims. All photographs were taken on un-oriented polished slabs of the weakly porphyritic granite (WPc) from the Žernovka quarry (WGS84 coordinates are 50°0'22.439"N, 14°44'55.049"E). The slabs also decorate the Palmovka Prague Underground Station.

Strongly porphyritic (muscovite–) biotite granite

This rock is light grey, in places commonly pinkish, and encloses relatively rare, dm-sized felsic enclaves with average size c. 15–20 cm, with irregular shapes and occasionally net veined by pegmatite. The K-feldspar phenocrysts, 3–10 cm long, contain abundant small biotite flakes. Plagioclase grains, 3–6 mm across, occur in the groundmass or form clusters with biotite. Another macroscopically recognizable mineral is quartz, which forms conspicuous dark drop-like, nearly anhedral grains 1–10 mm across. Biotite flakes have an average size of 1–5 mm. The muscovite (2–4 mm) is only subordinate, being associated with biotite, or, above all, pegmatitic nests.

Weakly porphyritic (muscovite–) biotite granite

In contrast, this facies shows a significantly lower modal percentage of the K-feldspar as phenocrysts; also their average size becomes smaller (3–5 cm). The matrix K-feldspars are light ochre, which is probably caused by the presence of limonite. Plagioclase occurs as whitish grains up to 5 mm across. The size and appearance of the remaining matrix minerals is identical with the strongly porphyritic facies, i.e. the biotite 1–5 mm, quartz up to 1 cm and muscovite 2–4 mm.

Various types of enclaves, especially biotite-bearing MME (Didier & Barbarin, 1991b) are abundant in the pluton centre; surmicaceous enclaves are rarer. The MME show a great variability: the more mafic ones are small, usually ellipsoidal, whereas the others tend to be larger (up to several meters) and angular. Double enclaves were also observed, with hybrid rims surrounding more mafic and homogeneous cores (Fig. 4a). Although many enclaves are partially resorbed and disintegrated by the host granite (Fig. 4d, f), forming biotite schlieren, margins of coherent enclaves are mainly sharp and lack reaction rims (Fig. 4g); chilled margins are rare. The K-feldspar phenocrysts show a marked tendency to form patches with pegmatoid matrix and frequently occur close to, or wrap around, the MME (Fig. 4c, d, f). The pegmatoid matrix also contains subordinate quartz,

plagioclase, and, rarely, needle-like tourmaline. In some cases were observed polygenic enclave swarms (Barbarin & Didier, 1991), i.e. sub-vertical parallel zones up to 5 m wide, in which numerous MME were enclosed in a matrix of a coarse-grained granite of pegmatoid appearance (Cimbáliková *et al.*, 1977; Palivcová *et al.*, 1992).

Fine-grained two-mica Jevany leucogranite and marginal aplite

The Jevany leucogranite is usually white to pinkish rock. Compared with the Říčany granite, its grain is finer (0.5–1 mm) and muscovite always prevails over biotite. In contrast to the marginal aplites it is tourmaline free.

The highly evolved 'marginal' aplite of the Říčany Pluton (Fig. 1c) is modally and texturally variable, massive or layered, and contains tourmaline-rich or locally garnet-rich bands, pegmatite pockets/layers, stockscheiders and comb layers. Rocks are classified as granites to alkali feldspar granites.

Coarse-grained to weakly porphyritic Kšely granite

The modal composition resembles that of the Říčany granite. However, the Kšely granite shows variable solid-state mylonitic to cataclastic fabric (Fig. 5c), in particular along shear zones, with the fractures stained by Fe oxides or hydroxides. The granite also hosts aplite veins and MME. The most conspicuous minerals are quartz (up to 1 cm), biotite (1–3 mm) and muscovite (1–2 mm), in places converted to sericite. Plagioclase occurs as white grains up to 6 mm in diameter. If present, the K-feldspar phenocrysts are up to 2–3 cm long and light ochre in colour.

QUANTITATIVE TEXTURAL ANALYSIS

The textural analysis was used to quantify the abundance and size distribution of K-feldspar phenocrysts in both facies of the Říčany granite. Methodology, location of samples and results of the analysis are summarized in Fig. 6 and in Electronic Appendix 2.

From the pluton margin inwards, the phenocrysts mode decreases significantly from 27 % (maximum value in the outer SPm) to 4 % (minimum value in the WPC; Fig. 6b). Similarly, the phenocrysts size, represented by their perimeter, decreases from 5.6 cm (maximum average value in the SPm) to 2.1 cm (minimum average value in the WPC; Fig. 6c). Furthermore, the aggregation index R was used to distinguish between random, clustered, and ordered patterns in the spatial distribution of K-feldspar phenocryst in the Říčany granite (Fig. 6d). Most of the samples exhibit $R < 1$ (phenocryst ordering), only three are characterized by $R > 1$ (clustering). Importantly, the textural analysis reveals a transition in the proportion and size of K-feldspar phenocrysts (Fig. 6b–c) and

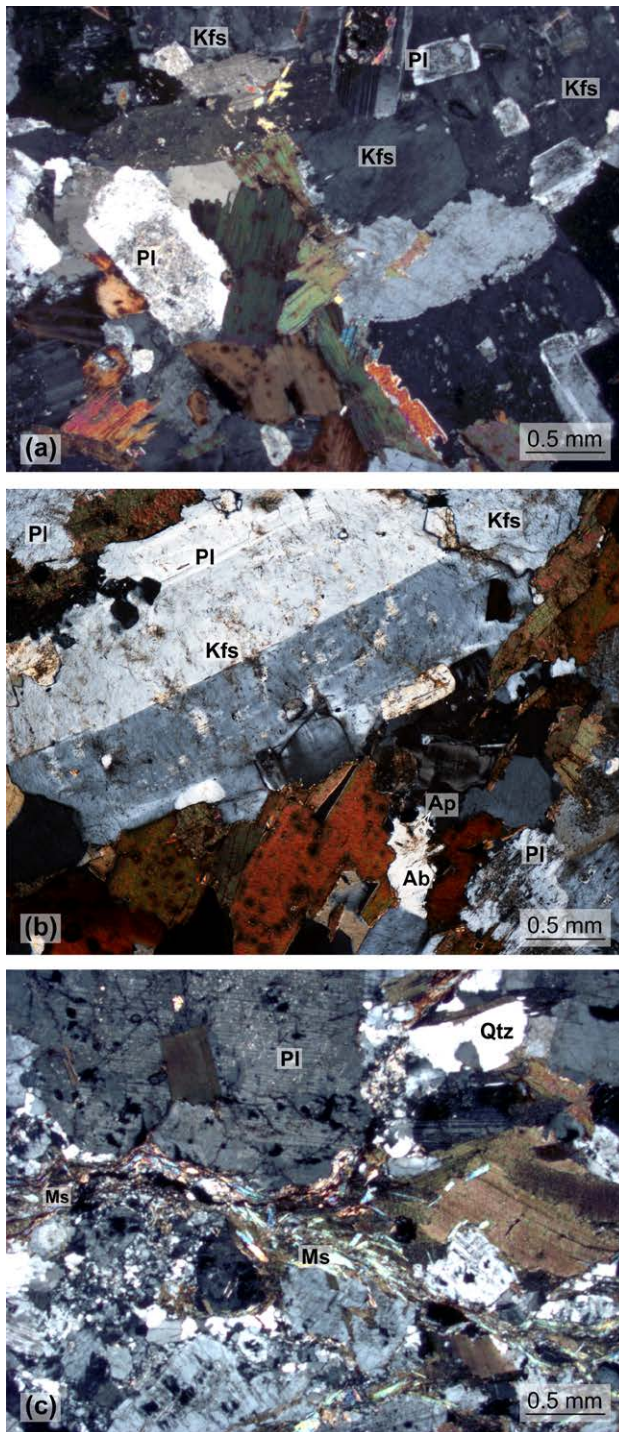


Fig. 5. (a) Magmatic texture of the SPM (sample JT41 – Plachta [50°1'55.369"N, 14°43'37.657"E]), showing no evidence of solid-state deformation. Small plagioclase grains are enclosed by K-feldspar. Crossed polars. (b) Euhedral K-feldspar crystal in contact with biotite aggregates with pleochroic haloes in the weakly porphyritic granite (WPC – sample JT68 – Srbín [49°58'46.506"N, 14°44'13.346"E]). Crossed polars. (c) Mortar texture of the Kšely granite (KG – sample TR10 [50°1'53.756"N, 14°54'31.316"E]) in which large porphyroclasts of quartz are surrounded by recrystallized and locally cataclastic matrix. Crossed polars. Abbreviations of mineral names are after Whitney and Evans (2010)..

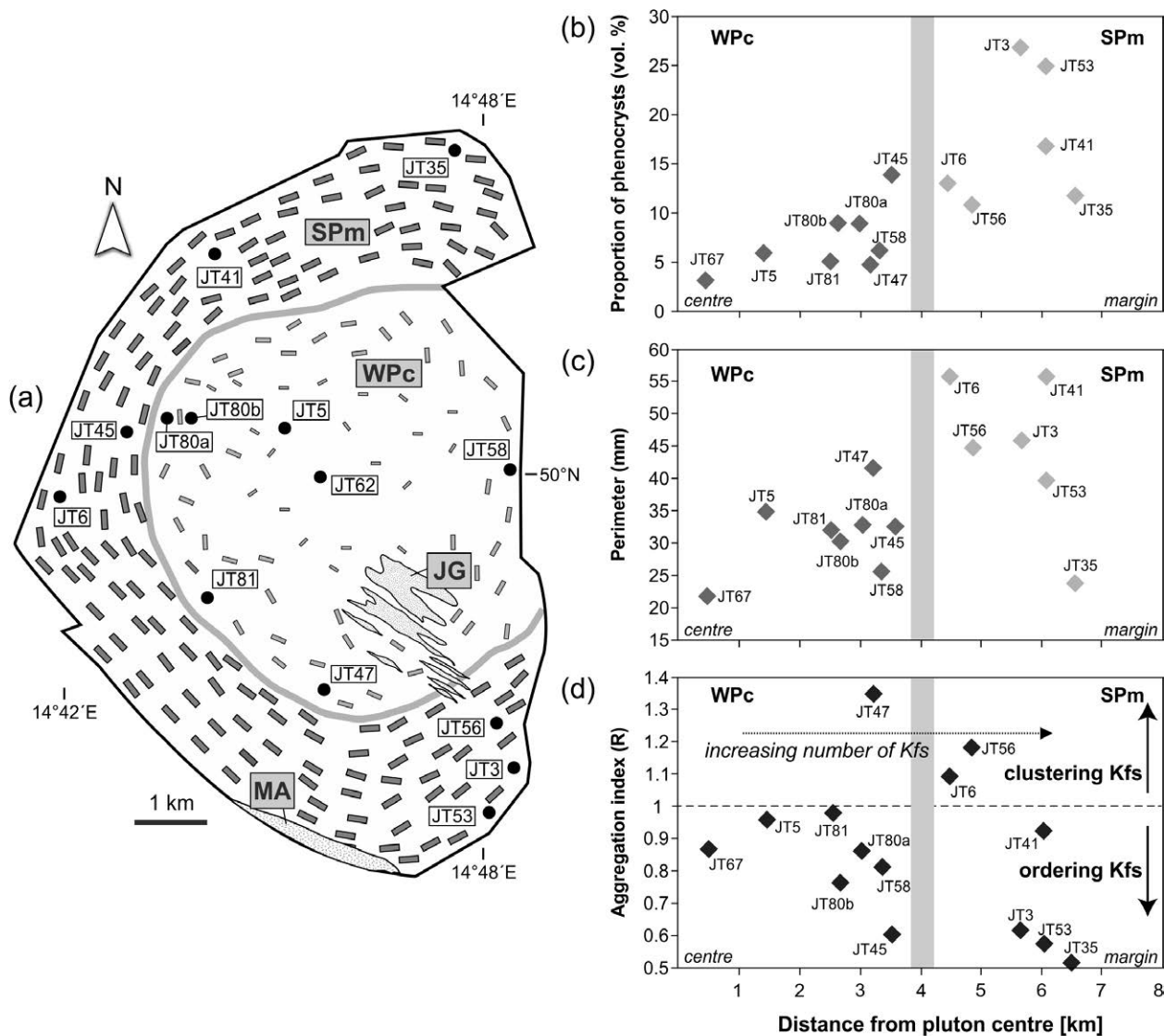


Fig. 6. Results of textural analysis of the Říčany granite. (a) Map of the whole pluton with marked localization of the contact between the strongly (SPm) and weakly (WPC) porphyritic facies. (b) Diagram portraying volumetric proportion of K-feldspar phenocrysts decreasing from the margin towards the centre of the pluton. (c) Diagram showing spatial variation in size of K-feldspar phenocrysts (expressed as the perimeter values). The phenocrysts size increases from the centre towards margin of the pluton. (d) Diagram showing spatial variations in the aggregation index (R) in the pluton; note that the K-feldspars in two granite facies overall do not tend to be clustered between margin and core of the Říčany Pluton. Standard deviation for aggregation index (R) is 0.2.

their tendency to cluster between the outer SPm and inner WPC as expressed by the aggregation index (Fig. 6d). In the map, this interface is located at around 4 km from the pluton margin and overlaps with the inferred contact between the two granite units.

PETROLOGY AND MINERAL CHEMISTRY

Říčany granite

Quartz occurs in light grey anhedral grains, up to 2 mm across, often forming aggregates with sharp boundaries. The perthitic K-feldspar shows commonly cross-hatched or Carlsbad twinning. Euhedral, early K-feldspar phenocrysts (3–5 mm) are sharply separated from the matrix. In contrast, the K-feldspars in the matrix are much smaller (0.5–1 mm) and anhedral. The K-feldspar phenocrysts contain small (< 0.5 mm) subhedral laths of sodic plagioclase, overgrown by thin albite rims. Minute inclusions of biotite and accessories (e.g., apatite and zircon) are abundant and usually arranged parallel to the cross-sections of the K-feldspar phenocrysts. Myrmekitic textures are locally developed along grain boundaries between K-feldspar and plagioclase. The K-feldspars are compositionally uniform throughout the pluton (Or_{87-90}); the sole exception represents BaO (SPm; 0.008–0.293 wt. %, WPC; 0.190–0.539 wt. %). The P_2O_5 concentrations are often close to, or slightly above, the detection limit (0.01–0.07 wt. %). Plagioclase forms mostly subhedral grains, on average 1.2–2.0 mm across, with common albite law twin lamellae. The crystals were markedly affected by sericitization or kaolinization. Except those enclosed within the K-feldspar, they are of uniform oligoclase composition throughout the pluton (An_{11-20}) (see Electronic Appendix 3 for a full analytical set). Cores are slightly normally zoned and some characteristically mantled by a sodic plagioclase (SPm: An_{4-9} and WPC: An_{2-8}).

Biotite occurs as subhedral to euhedral flakes 0.5–1.5 mm, rarely up to 1.8 mm across. It is mostly fresh, but in places chloritization commences along the cleavage planes. Pleochroism is strong, X: straw yellow, Y = Z: dark honey-brown. Biotite encloses often zircon, apatite and magnetite. It is phlogopite with 13.7–17.2 wt. % total Al_2O_3 and 11.6–13.4 wt. % MgO. The biotite from the WPC is characterized by mg# (molar $Mg/[Mg + Fe_{tot}]$) of 0.45–0.41, i.e. higher than in the SPm (0.41–0.38). While the MnO contents are uniformly low (0.2–0.3 wt. %), the K_2O abundance decreases outwards in the pluton (from 9.47–10.24 to 9.61–9.97 wt. %). Biotites in the central WPC contain on average more TiO_2 (2.86–3.51 wt. %) than those in the marginal facies (2.49–3.43 wt. %). There is a trend of decreasing F in biotite from the pluton center (1.76 wt. %) to the margin (1.22 wt. %). The biotite may also be overgrown by the scarce muscovite (up to 0.2 mm). Also the plagioclase encloses some small (0.1–0.2 mm) flakes of muscovite, oriented along the (100) and (010) planes. Some of them occur in almost fresh plagioclase, implying a primary magmatic origin. The muscovites in the WPC have lower mg# values (0.32) as compared to those in the SPm (0.65–0.76) and exhibit low MnO

contents comparable in both facies (0.01–0.1 wt. %). The total FeO contents in muscovite decrease from the centre (3.7 wt. %) toward the pluton margin (1.4–2.4 wt. %) whereas the K₂O abundance (WPC: 9.79 wt. %; SPm: 10.61–11.28 wt. %) and the F contents show an opposite trend (from 0.13 to 0.44 wt. %).

Fluorapatite in prisms or needles 0.1–0.2 mm long (WPC: 0.8–0.9, SPm: 1.8–1.9 apfu F) is a particular abundant accessory. The proportion of elements that are incorporated into the PO₄-tetrahedra (Si, Al) is low. Apatites from the SPm are rich in Ca, Th and U as well as comparably poor in Mn.

Relatively common are euhedral rutile grains (0.1 mm), which are chemically unzoned except for rare clear patches that are enriched by Fe. Otherwise the range of substitutions is small and sum of analyses near 100 %. Rutiles from the SPm contain more admixtures, especially Fe, Mn and Y.

Monazite usually occurs in aggregates of small spherical grains (0.2 mm), only a few of which show well-developed crystal faces. The single grains are fresh and compositionally sector zoned. The monazites always have high ThO₂ (9–13 wt. %) and moderate UO₂ concentrations (0.3–0.6 wt. %).

Titanite is a less common accessory, observed solely in the SPm. It forms euhedral crystals (0.1 mm), brown to reddish in colour. The grains show sector zoning in the BSE. They contain on average 0.08 wt. % F and are rich in the REE. The sums of analyses are always significantly lower than 100 % and the deficit may be explained by unanalyzed elements such as Na, Mg, Sr or some of the REE.

Euhedral zircon (0.2 mm) forms pink to pale brown, short-prismatic (dipyramidal) crystals. Zircons from the SPm (0.90–1.02 apfu) are corroded and characterized by higher Al, Fe, Ca, Hf, U, REE and Y contents. Moreover, the SPm zircons are characterized by lower Th if compared with the WPC (0.80–0.97 apfu). The P contents are negligible throughout.

Ilmenite and magnetite grains were seen in the WPC only. Ilmenite forms black opaque grains (0.1 mm) of non-metallic lustre, sometimes lamellated. The most significant substitution is the Fe–Mn replacement. On average, the ilmenite is relatively poor in Th, U and Y. Also black magnetite occurs mostly in anhedral fragments, only rarely forming octahedra, up to 0.5 mm across. Effects of weak martitization can be observed along the edges of the grains. Contents of TiO₂ are very low (0.01 wt. %) but MnO is elevated (1.17 wt. %). The contents of Th, U and Y are below their respective detection limits; Mg, Cr and Ni were not determined.

Newly described subangular zircon-like ABO₄-type phase (up to 0.1 mm across), which is Th–U and HREE-rich, is a rare accessory (Janoušek *et al.*, 2014). It occurs in plagioclase, often together with monazite. Due to relatively high Th contents, crystals are metamict and altered.

The phase is a member of the zircon–thorite solid solution series (0.26–0.33 apfu Th, 0.37–0.55 apfu Zr) with high amounts of FeOt (0.73–23.56 wt. %) and CaO (3.45–4.88 wt. %).

Allanite-(Ce) was found only in one of the SPM thin sections as compositionally zoned euhedral grains (c. 1.5 mm across) intergrown with biotite. The CaO content ranges between 10.9 and 13.7 wt. % and the sum of $\text{REE}_2\text{O}_3 + \text{Y}_2\text{O}_3$ between 18.52 and 26.64 wt. % (9.65–12.65 wt. % Ce_2O_3). Rare tourmaline is present as subhedral grains (up to 1 mm) with optical zoning (ochre rim–green core) and was not analysed.

Jevany leucogranite and marginal aplite

The Jevany leucogranite contains subhedral to anhedral oscillatory-zoned plagioclase (0.5–1 mm; An_{6-8}) with effects of sericitization and kaolinization. Subhedral K-feldspar (up to 1 mm across) is perthitic. It shows rare cross-hatched twinning and weak sericitization. Muscovite flakes (~0.6 mm) are common. Biotite (0.5–1.5 mm) forms subhedral–euhedral flakes enclosing inclusions of zircon and apatite surrounded by conspicuous pleochroic haloes.

Marginal aplite represents a very modally heterogeneous part of the Říčany Pluton. All aplites and pegmatites usually contain mutually comparable proportions of quartz, albite-rich plagioclase (An_{8-11}), K-feldspar, as well as various amounts of tourmaline (up to ~15 vol. %), muscovite, garnet, and accessory biotite, cassiterite, rutile, zircon, fluorapatite, columbite–tantalite, ilmenite–pyrophanite, xenotime-(Y), monazite-(Ce), beryl and/or topaz. All K-feldspar grains are rather pure (up to Or_{88}). Biotite can be classified as phlogopite to siderophyllite with 16.4–21.4 wt. % Al_2O_3 and 2.0–10.7 wt. % MgO. Muscovite is mainly ferroaluminoceladonite. Garnet corresponds to a spessartine–almandine solid solution, mainly a hydrous spessartine. Zoned tourmaline can be classified as dravite, schorl or elbaite.

Kšely granite

The groundmass contains euhedral crystals of perthitic microcline (1–2 mm) (Or_{87-95}), often showing cross-hatched twinning. The weakly discontinuously zoned and polysynthetically twinned plagioclase (0.2–0.5 mm) is mostly subhedral oligoclase (An_{10-15}). The grey anhedral, recrystallized and granulated quartz grains, up to 1–2 mm across, show undulatory extinction.

Biotite (0.5–1 mm) occurs as subhedral to euhedral rusty red flakes and contains pleochroic haloes around inclusions of zircon or apatite. It can be classified as annite with 15.8–17.2 wt. % Al_2O_3 and 5.9–7.5 wt. % MgO. In the Kšely biotite, the FeOt contents are higher (19.5 wt. %), the mg# lower

(0.3–0.4), the MnO very similar (0.15–0.43 wt. %) and F significantly lower (0.10–0.37 wt. %), than in the Říčany granite. Muscovite flakes (~0.6 mm) are much more common. It is characterized by mg# of 0.49–0.56, relatively low Fe (1.2–1.7 wt. %) and F (0.08–0.2 wt. %).

Small fluorapatite prisms (4.17 wt. % F), up to 0.2 mm in length, are enclosed by biotite and muscovite. The F contents are higher, and the MnO lower (0.08 wt. %), than in the Říčany granite. The concentrations of Y, U and Th are below the detection limits. Zircon is rare, but several euhedral crystals (< 0.05 mm across), were seen in biotite flakes. If compared with analyses from the Říčany granite, the Kšely zircon has lower concentrations of HfO₂ (1.18–1.42 wt. %). Primary anhedral zoned monazite-(Ce) (< 1.1 mm; Ce₂O₃ = 21.7–26.9 wt. %) contains significant amounts of all the LREE and ThO₂ (5.9–15.6 wt. %). There is little CaO (1.1–2.4 wt. %), and minor amounts of Y + HREE. Few altered euhedral xenotime-(Y) grains (< 0.05 mm) were found enclosed by monazite. Their composition is characterized by variably elevated ThO₂ (0.4–4.6 wt. %) and UO₂ (1.8–2.6 wt. %), as well as HREE (e.g., 4.2–5.0 wt. % Dy₂O₃ and 3.3–4.0 wt. % Yb₂O₃). Zirconium component is low (1.2–4.1 wt. % ZrO₂). Anhedral rutile (< 0.2 mm) is associated with biotite and muscovite and contains 1.7 wt. % FeO, and more ZrO₂ (0.114 wt. %) than in the Říčany granite.

WHOLE-ROCK GEOCHEMISTRY

Major and trace elements

Our dataset contains 26 samples of both facies of the Říčany Pluton (SPm: Ri21, 22; TR6, 7; WPC: Ri1–11, Ri13–19, TR4, TR14–16), two Jevany granites (Je-2, 4), one Marginal aplite (OAP1), 9 MME (RiE-1–4; TR12, 13, 17, 18) with one felsic microgranular enclave (FEL;TR11) and one Kšely granite (TR10). The samples marked as Ri, Je and RiE are re-analysed powders from Janoušek *et al.* (1997) and OAP, TR were newly obtained (see Table 3 for representative analyses and Electronic Appendix 4 for complete whole-rock geochemical data set, including sample locations).

The two main Říčany granite facies are silicic (SiO₂ = 69.8–71.9 wt. %) as is the Kšely granite (SiO₂ = 65.2 wt. %). The Jevany leucogranite and marginal aplite contain even more silica (71.8–75.8 wt. %). The MME are more basic (SiO₂ = 61.2–70.1 wt. %). This is indicated also by the Q'–ANOR classification diagram (Streckeisen, 1974; Fig. 7a). All the rock types are subaluminous to moderately peraluminous, as shown by A/CNK values (molar A/CNK = Al₂O₃/(CaO + Na₂O + K₂O); Shand, 1943) of 0.98–1.06 (MME) and 1.01–1.13 (all the remaining rock types). This is also confirmed by the B–A diagram of (Villaseca *et al.*, 1998; Fig. 7b).

Magma Differentiation and Pluton Zoning

Table 3: Representative whole-rock major- and trace-element compositions of the individual rock types in the Říčany Pluton.

Sample	TR10	TR11	TR18	RIE-2	RI7	RI1	TR4	RI12	TR14	TR7	RI22	JE-2	OAP1
Locality	Kšely	Žernovka	Žernovka	Žernovka	Žernovka	Žernovka	Kamenka	Srbín	Žernovka	Lom na Plachtě	Břeží	Vyžlovka	Zvánovice
Intrusion	KG	FEL	MME	MME	WPc	WPc	WPc	WPc	Kfs cumulate	SPm	SPm	JG	MA
SiO ₂	65.24	70.85	61.22	70.13	69.77	71.43	71.40	71.99	70.70	71.45	71.94	71.80	75.80
TiO ₂	0.49	0.33	1.13	0.48	0.35	0.30	0.33	0.31	0.14	0.34	0.22	0.16	0.09
Al ₂ O ₃	16.37	15.12	14.06	13.62	15.05	14.58	14.47	14.56	16.10	14.44	14.44	14.87	13.45
FeOt	3.12	1.30	6.42	2.47	1.51	1.22	1.59	1.50	0.78	1.91	1.38	0.95	0.44
MnO	0.04	0.03	0.10	0.05	0.028	0.010	0.03	0.040	0.01	0.04	0.030	0.02	0.02
MgO	2.19	0.70	5.19	2.49	1.23	1.12	1.00	0.78	0.37	1.27	1.04	0.28	0.11
CaO	1.30	1.23	2.29	1.60	1.41	1.27	1.04	1.19	1.20	1.20	1.09	1.08	0.58
Na ₂ O	3.54	3.85	2.88	3.33	3.64	3.32	3.72	2.83	3.95	3.64	3.65	4.12	4.11
K ₂ O	5.96	5.79	4.02	4.75	5.78	5.29	5.52	5.11	6.17	4.79	4.53	5.34	3.97
P ₂ O ₅	0.343	0.121	0.690	0.278	0.200	0.170	0.159	0.140	0.078	0.173	0.13	0.049	0.060
CO ₂	–	–	0.03	0.03	0.06	0.03	–	0.18	–	–	0.02	–	–
H ₂ O ⁺	–	–	–	–	0.43	0.51	–	0.51	–	–	0.64	–	–
H ₂ O ⁻	–	–	–	–	0.10	0.04	–	0.05	–	–	0.03	–	–
LOI	1.1	0.4	1.6	0.5	–	–	0.5	–	0.3	0.6	–	1.1	1.5
Total	99.69	99.72	99.63	99.73	99.56	99.29	99.76	99.21	99.8	99.85	99.14	99.77	100.10
A/CNK	1.12	1.02	1.06	1.01	1.02	1.08	1.03	1.18	1.05	1.08	1.12	1.02	1.11

Analyses were performed by standard wet chemistry techniques in the laboratories of the Czech Geological Survey, Prague except those shown in italics, which were carried out in the ACME Laboratories, Canada by sample fusion/ICP-OES. See Appendix 1 for analytical details. "–" not analysed; LOI – Loss on ignition

Intrusion	KG	FEL	MME	MME	WPc	WPc	WPc	WPc	Kfs cumulate	SPm	SPm	JG	MA
Ba	1054	1111	727	807	1316	1043	865	908	1025	524	489	934	20
Rb	278.5	319.1	487	331.2	311.3	338.5	337.9	337.4	274.4	346	388.8	266.2	373.0
Sr	359.1	360.8	211.3	340.8	471.6	418.9	328.3	329	414.7	243.2	222.1	540.6	24.0
Be	6	13	16	12	10	15	12	13	15	11	16	11	17
Cs	15.7	51.0	86.2	24.0	23.1	59.7	17.7	43.4	21.4	38.6	55.1	10.2	73.3
Ga	24.5	20.7	27	23.3	21.9	23.2	23.4	23	20.7	23.9	24	24.6	25
Nb	15.8	21.6	48.0	20.3	18.7	19.4	23.3	20.5	11.5	18.8	17.3	18.1	15.2
Th	28.2	44.2	76.9	42.2	39.1	36.1	35.9	31	20.3	28.6	28.1	42.1	8.08
U	4.2	12.4	9.3	8.8	15.6	14.9	15.3	17.4	4.6	8.4	3.6	17.6	4.24
Zr	316.5	254.4	529.0	254.6	272.5	242.5	217.2	189.5	146.4	185.7	142.1	150.7	29
Hf	10.2	8.4	16.9	8.2	8.8	7.5	7.7	6.2	4.9	6.4	5.0	5.6	1.6
Mo	0.1	<5	<5	0.3	<5	<5	<5	0.3	<5	<5	<5	0.2	<5
Cu	1.9	0.7	4.1	4.6	2.1	1.2	0.7	8.9	1.8	0.6	3.3	1.0	< 10
Pb	8.2	11	13.6	6.8	20.4	9.7	18.9	17.2	13.1	14.4	13.9	23.7	50
Zn	78	29	163	50	47	40	45	34	15	45	45	<0.1	<30
Ni	38.1	7.5	128.3	55.2	16.5	14.0	13.2	13.0	4.9	16.1	12.2	4.2	<20
Co	8.3	2.8	18.9	8.8	4.3	3.7	3.6	3.3	1.3	5.0	3.2	1.3	<1
As	0.5	5.8	5.2	6.4	15.7	9.3	11.1	25.0	5.0	17.7	2.8	6.6	<5
Au	0.5	2.3	3.5	0.8	4.1	21.8	1.0	1.7	2	3	<5	1.1	<5
Sb	0.1	0.5	0.2	0.2	0.4	0.8	<5	0.6	0.4	0.1	0.2	0.1	0.3
Bi	0.1	1.2	0.4	0.5	0.9	1.4	2.5	1.3	0.7	1.6	0.9	0.1	2.4
V	46	14	90	32	21	18	17	13	6	21	17	5	<5
Cr	99	13	251	165	41	40	34	28	14	37	30	15	<20
Sn	3	11	41	14	9	16	9	20	6	19	31	3	37
W	0.2	0.2	0.1	0.4	0.1	0.1	<5	0.1	<5	0.2	0.2	0.25	<5
Sc	4.5	2.7	11.2	4.7	3.1	3.2	4.0	2.5	1.2	4.3	3.2	<0.01	4
Tl	1.1	0.6	4.4	1.6	0.8	0.8	1.0	0.7	0.4	1.2	1.3	1.1	2.19
Rb/Sr	0.78	0.88	2.3	0.97	0.66	0.83	1.03	1.03	0.66	1.42	1.75	0.49	15.54
Rb/Ba	0.26	0.29	0.67	0.41	0.24	0.32	0.39	0.37	0.27	0.66	0.80	0.28	18.65

Table 3 continued

Sample	TR10	TR11	TR18	RIE-2	RI7	RI1	TR4	RI12	TR14	TR7	RI22	JE-2	OAP1
Locality	Kšely	Žernovka	Žernovka	Žernovka	Žernovka	Žernovka	Kamenka	Srbín	Žernovka	Lom na Plachtě	Březí	Vyžlovka	Zvánovice
Intrusion	KG	FEL	MME	MME	WpC	WpC	WpC	WpC	Kfs cumulate	SPm	SPm	JG	MA
Y	11.1	11.3	30.0	10.9	10.5	10.6	12.0	10.5	6.2	13.2	11.2	5.8	12.7
La	28.7	45.6	57.7	41.4	37.9	33.2	31.5	30.9	17.3	29.1	25.9	26.6	4.4
Ce	60.7	93.6	134.9	84.7	75.2	66.9	63.5	60.0	37.0	57.0	49.4	50.1	9.1
Pr	7.15	11.03	18.87	10.73	8.53	7.61	7.67	6.98	3.95	6.60	5.66	5.58	1.07
Nd	26.5	40.0	80.0	41.1	30.7	27.6	28.4	24.8	14.2	23.0	19.6	18.6	3.6
Sm	4.63	5.96	14.05	6.72	4.94	4.18	4.76	3.96	2.28	4.15	3.43	2.75	1.20
Eu	1.14	0.90	0.88	0.91	0.91	0.82	0.65	0.68	0.82	0.52	0.47	0.52	0.03
Gd	3.36	3.58	9.74	3.82	3.15	2.87	3.05	2.48	1.47	3.04	2.45	1.75	1.23
Tb	0.49	0.50	1.24	0.50	0.42	0.39	0.43	0.37	0.23	0.46	0.39	0.22	0.27
Dy	2.14	2.42	5.87	2.17	2.08	1.83	2.29	1.89	1.19	2.38	2.00	1.08	1.80
Ho	0.37	0.40	0.94	0.35	0.33	0.33	0.39	0.31	0.22	0.45	0.38	0.18	0.35
Er	0.99	1.04	2.44	0.93	0.90	0.90	1.04	0.89	0.59	1.25	1.01	0.51	1.12
Tm	0.15	0.16	0.38	0.15	0.14	0.15	0.16	0.14	0.10	0.20	0.17	0.08	0.19
Yb	0.80	0.90	2.13	0.83	0.82	0.87	0.92	0.84	0.60	1.10	1.01	0.46	1.36
Lu	0.12	0.13	0.28	0.13	0.11	0.13	0.14	0.11	0.10	0.18	0.15	0.07	0.20
ΣREE	137.24	206.22	329.42	194.44	166.13	147.78	144.9	134.35	80.05	129.43	112.02	108.50	25.97
La _N /Yb _N	24.19	34.16	18.26	33.63	31.16	25.73	23.08	24.8	19.44	17.84	17.29	38.99	2.19
Eu/Eu*	0.88	0.60	0.23	0.55	0.71	0.72	0.52	0.66	1.37	0.45	0.50	0.72	0.07

Analyses of trace elements were carried out in the ACME Laboratories, Canada by sample fusion/ICP-MS. Numbers following the "lower than" sign indicate determinations that were below detection limit. See Appendix 1 for analytical details.

Samples can be characterized as mostly shoshonitic rocks, overlapping into the adjacent high-K calc-alkaline field of the SiO₂-K₂O diagram (Peccerillo & Taylor, 1976; Fig. 7c).

Compared with the average upper crustal composition (Taylor & McLennan, 1995; Fig. 8a), the two main facies (SPm, WpC) are enriched in Large-Ion Lithophile Elements (LILE; Cs, Rb, Th, U, K) and depleted in some High Field Strength Elements (HFSE; Nb, Ti, HREE). The central, weakly porphyritic facies shows markedly lower Cs, Rb and HREE contents at elevated Ba, U, Sr, Hf, Zr and MREE if compared with the outer, strongly porphyritic facies. The feldspar-rich samples are also characterized by depletion in Nb and HREE but show higher contents of U and Sr.

The Jevany granite is significantly enriched in Cs, Rb, Ba, Th, U, Sr and depleted in Nd, P and HREE (Fig. 8b). Marginal aplite is rich in Cs and Rb, and poor in Ba, Sr, P, Zr, Hf, Ti and REE. The Kšely granite is richer in LILE (Cs, Rb, Ba, U, K) and poorer in some HFSE (Nb, HREE + Y) if compared with average upper crustal composition. The group of MME samples is highly enriched in LILE (Cs, Rb, Th, U), LREE + MREE and P, Hf, Zr and depleted in Ba, Sr and in HREE + Y.

The REE contents in the Říčany granites do not vary greatly (ΣREE = 111–143 ppm for SPm and 124–166 ppm for WpC and Kfs cumulates; Electronic Appendix 4). The chondrite-normalized patterns (Boynnton, 1984) are steep (La_N/Yb_N = 15.7–19.2 for SPm and 22.1–31.2 for WpC). Negative Eu anomalies are present, the magnitude of which increases from the pluton's centre (WpC; Eu/Eu* = 0.7–0.5) outwards, reaching its maximum in the SPm facies (Eu/Eu* = 0.5–0.4; Fig. 8c). Feldspar-rich samples have more variable total REE contents (80–148 ppm) with a high degree of LREE/HREE enrichment

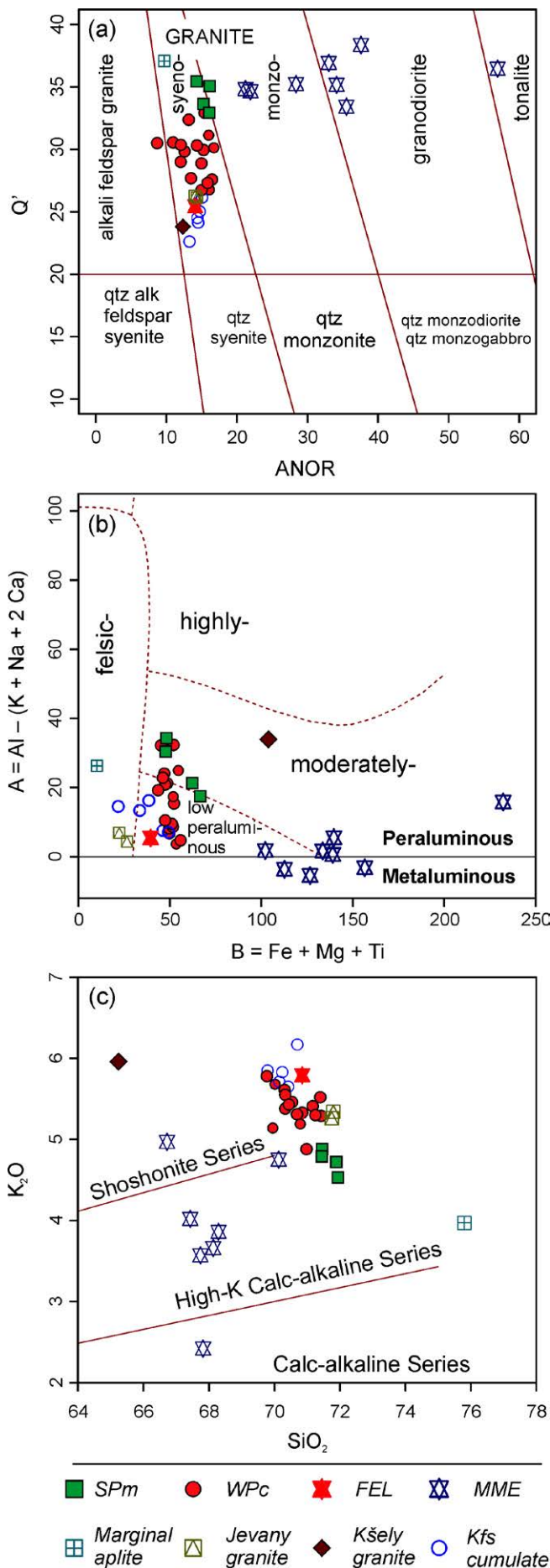


Fig. 7. Major-element based classifications. (a) Diagram of the normative compositions Q' -ANOR (Streckeisen & Le Maitre, 1979) calculated using Improved Granite Mesonorm (Mielke & Winkler, 1979). (b) P-Q multicationic plot after Debon & Le Fort (1983, 1988) (c) B-A multicationic plot of the same authors modified by Villaseca *et al.* (1998). (d) SiO_2 - K_2O diagram of Peccerillo & Taylor (1976).

($La_N/Yb_N = 19.4-27.4$). Their Eu anomaly varies from negative ($Eu/Eu^* = 0.7-0.9$) to positive ($Eu/Eu^* = 1.4$ in sample TR14).

The Jevany granite is characterized by low total REE contents (101–109 ppm), high La_N/Yb_N ratios (36.1–38.9) and negative Eu anomalies ($Eu/Eu^* = 0.7$). The marginal aplite is REE-poor ($\Sigma REE = 26$ ppm) and its chondrite-normalized pattern flat ($La_N/Yb_N = 2.2$) with low LREE contents ($La_N = 14.3$) and deep negative Eu anomaly ($Eu/Eu^* = 0.07$). The REE patterns for the MME and FEL are also steep ($La_N/Yb_N = 13.0-33.6$) and feature negative Eu anomalies ($Eu/Eu^* = 0.2-0.6$; Fig. 8b). The Kšely granite is characterized by fairly high total REE contents ($\Sigma REE = 137$), high degree of LREE/HREE fractionation ($La_N/Yb_N = 24.2$) and negligible negative Eu anomaly ($Eu/Eu^* = 0.9$).

The decrease in Zr with increasing silica and the common occurrence of inheritance in zircon crystals indicates that the

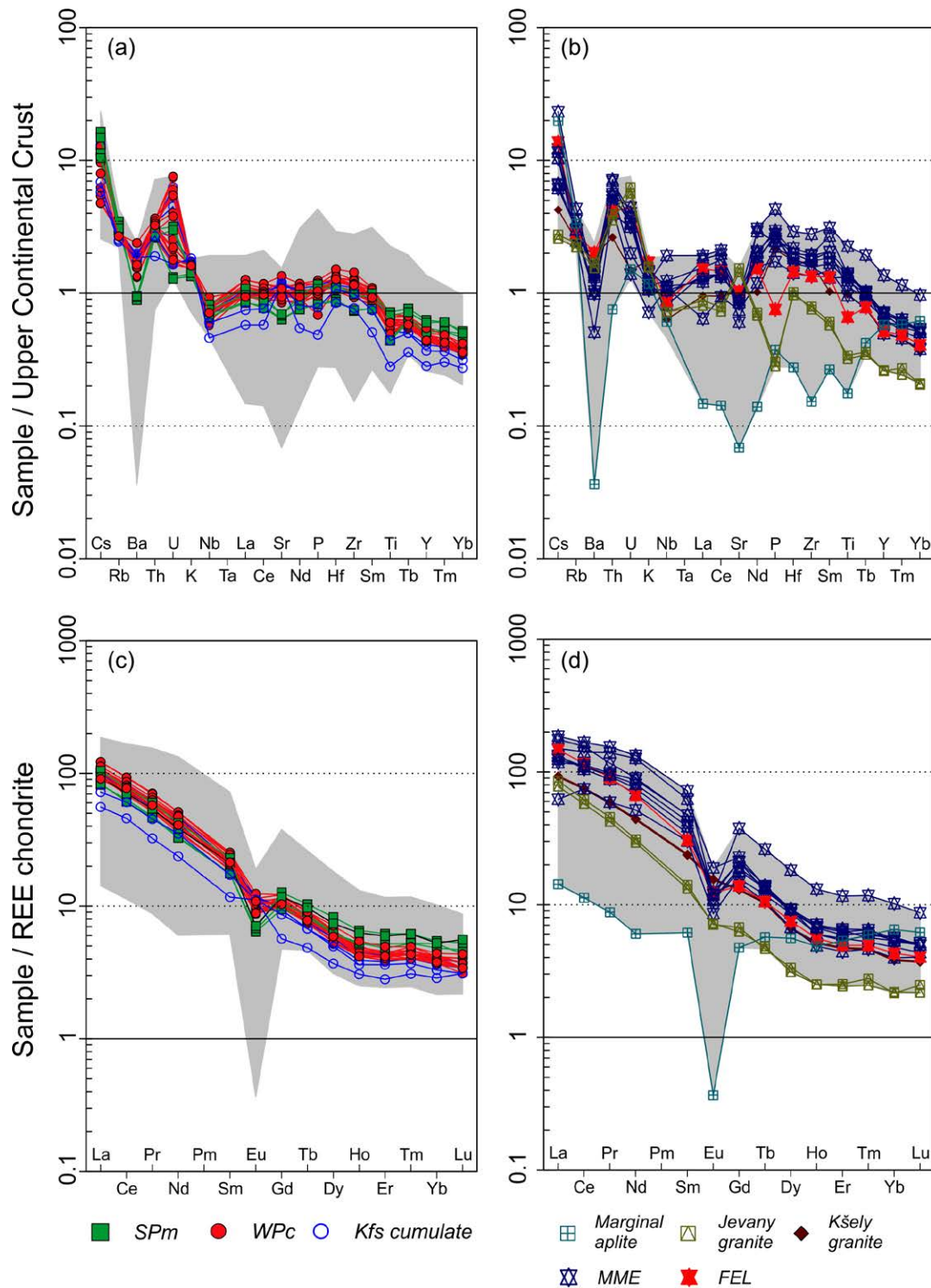


Fig. 8. Spider plots of (a–b) trace-element contents normalized by the average composition of the Upper Continental Crust (Taylor & McLennan, 1995) and (c–d) REE contents normalized by the chondritic abundances (Boynton, 1984).

magma was saturated (Lee & Bachmann, 2014) during the whole history and that the zircon thermometry (Watson & Harrison, 1983) is applicable (Hoskin *et al.*, 2000; Miller *et al.*, 2003; Janoušek, 2006). The average zircon saturation temperatures for the main facies of the Říčany Pluton (SPm, WPC, JG) are ~ 800 °C (Table 1). Even though somewhat overestimated due to the presence of inheritance, they seem to indicate a rather high liquidus T of the magma. Also the average monazite saturation temperatures (Montel, 1993) are consistent with zircon saturation data for SPm, WPC and JG (~ 750–780 °C) (Table 1).

Radiogenic isotopes

In order to further constrain geochemical variations in the pluton, 13 samples were analyzed for their Sr–Nd isotopic composition (see Table 4). The additional 7 isotopic analyses were taken from the literature (Janoušek *et al.*, 1995) (see Table 4).. The two main facies of the Říčany granite are characterized by evolved crust-like Sr–Nd isotopic signatures, with the margin showing more radiogenic Sr and less radiogenic Nd than the centre (SPm: $^{87}\text{Sr}/^{86}\text{Sr}_{337} \sim 0.7110\text{--}0.7117$; $\epsilon\text{Nd}_{337} \sim -6.7$; WPC: $^{87}\text{Sr}/^{86}\text{Sr}_{337} = 0.7093\text{--}0.7105$; $\epsilon\text{Nd}_{337} = -6.8$ to -7.8) (Fig. 9). The Nd isotopic signature of the Kšely granite is undistinguishable from the two main facies of the Říčany Pluton

Table 4: Sr–Nd isotopic data for the main rock types within the Říčany Pluton.

Sample	Locality	Intrusion	Rb (ppm)	Sr (ppm)	$^{87}\text{Rb}/^{86}\text{Sr}$	$^{87}\text{Sr}/^{86}\text{Sr}$	2 SE	$(^{87}\text{Sr}/^{86}\text{Sr})_{337}$	Sm (ppm)	Nd (ppm)	$^{147}\text{Sm}/^{144}\text{Nd}$	$^{143}\text{Nd}/^{144}\text{Nd}$	2 SE	$(^{143}\text{Nd}/^{144}\text{Nd})_{337}$	$\epsilon_{\text{Nd}}^{337}$	T_{DM}^{Nd} (Ga)
Ri-1†	Žernovka	WPC	311	347	2.4058	0.721540	3	0.71000	4.1	24.1	0.1020	0.512053	6	0.51183	-7.4	1.63
Ri-2†	Žernovka	WPC	327	360	2.6299	0.722668	3	0.71005	5.0	29.0	0.1005	0.512035	6	0.51181	-7.8	1.66
Ri-4†	Žernovka	WPC	319	378	2.4483	0.722162	4	0.71042	4.6	27.9	0.0995	0.512062	11	0.51184	-7.1	1.60
Ri-5†	Žernovka	WPC	310	400	2.2510	0.721341	4	0.71054	3.8	23.6	0.0980	0.512074	14	0.51186	-6.8	1.58
Ri-6†	Žernovka	WPC	317	387	2.3776	0.721858	3	0.71045	4.6	28.1	0.0980	0.512068	7	0.51185	-6.9	1.59
Ri-10†	Srbín	WPC	322	322	2.9034	0.724306	3	0.71038	4.4	26.5	0.1005	0.512075	9	0.51185	-6.9	1.59
RI15	Kozojedy	WPC	344.7	297.4	3.3593	0.725374	8	0.70926	4.5	29.0	0.0938	0.512053	7	0.51185	-7.0	1.40
TR16	Žernovka	WPC	301	379	2.3035	0.721314	10	0.71026	4.2	24.5	0.1029	0.512061	14	0.51183	-7.2	1.62
RI22	Břeží	SPm	388.8	222.1	5.0787	0.735323	6	0.71096	3.4	19.6						
TR6	Plachta	SPm	362	238	4.4154	0.732888	9	0.71171	4.5	25.3	0.1070	0.512098	9	0.51186	-6.7	1.57
TR7	Plachta	SPm	346	243	4.1259	0.731479	16	0.71169	4.2	23.0	0.1091	0.512101	6	0.51186	-6.7	1.58
TR10	Vitice	KG	–	–	–	–	–	–	4.6	26.5	0.1049	0.512082	8	0.51185	-6.9	1.59
TR17	Žernovka	MME	277	261	3.0840	0.725206	10	0.71041	5.9	31.0	0.1147	0.512097	14	0.51184	-7.0	1.60
RIE-1†	Žernovka	MME	330	298	3.2146	0.725713	4	0.71029	12.6	71.0	0.1071	0.511989	6	0.51175	-8.8	1.74
RIE-2	Žernovka	MME	331	341	2.8164	0.724252	9	0.71074	6.7	41.1	0.0988	0.512046	9	0.51183	-7.4	1.63
RIE-3*	Žernovka	MME	314	310	2.9403	0.724970	16	0.71103	7.5	45.0	0.1013	0.512090	9	0.51187	-6.6	1.57
RIE-4*	Žernovka	MME	332	331	2.8461	0.723233	6	0.70913	9.2	54.0	0.1030	0.512059	5	0.51183	-7.3	1.62
JE-2	Vyžlovka	JG	266.2	540.6	1.4257	0.714933	9	0.70809	2.8	18.6	0.0894	0.512116	6	0.51192	-5.6	1.49
JE-4	Vyžlovka	JG	247.7	503.7	1.4238	0.714789	8	0.70796	2.6	17.6	0.0883	0.512123	5	0.51193	-5.4	1.47
OAP1	Zvánovice	MA	–	–	–	–	–	–	1.2	3.6	0.2004	0.512243	15	0.51180	-7.9	1.67

Isotopic ratios with subscript '337' were age-corrected to 337 Ma; decay constants are from Steiger & Jäger (1977 – Sr) and Lugmair and Marti (1978 – Nd). The T_{DM}^{Nd} values were obtained using Bulk Earth parameters of Jacobsen & Wasserburg (1980). The two-stage Nd model ages (T_{DM}^{Nd}) were calculated after Liew & Hofmann (1988). "–" not analysed

*Isotopic ratios of $^{143}\text{Nd}/^{144}\text{Nd}$ for samples RIE-3 and RIE-4 were obtained by MC-ICP MS. Previously published analyses: † – Janoušek *et al.* (1995)

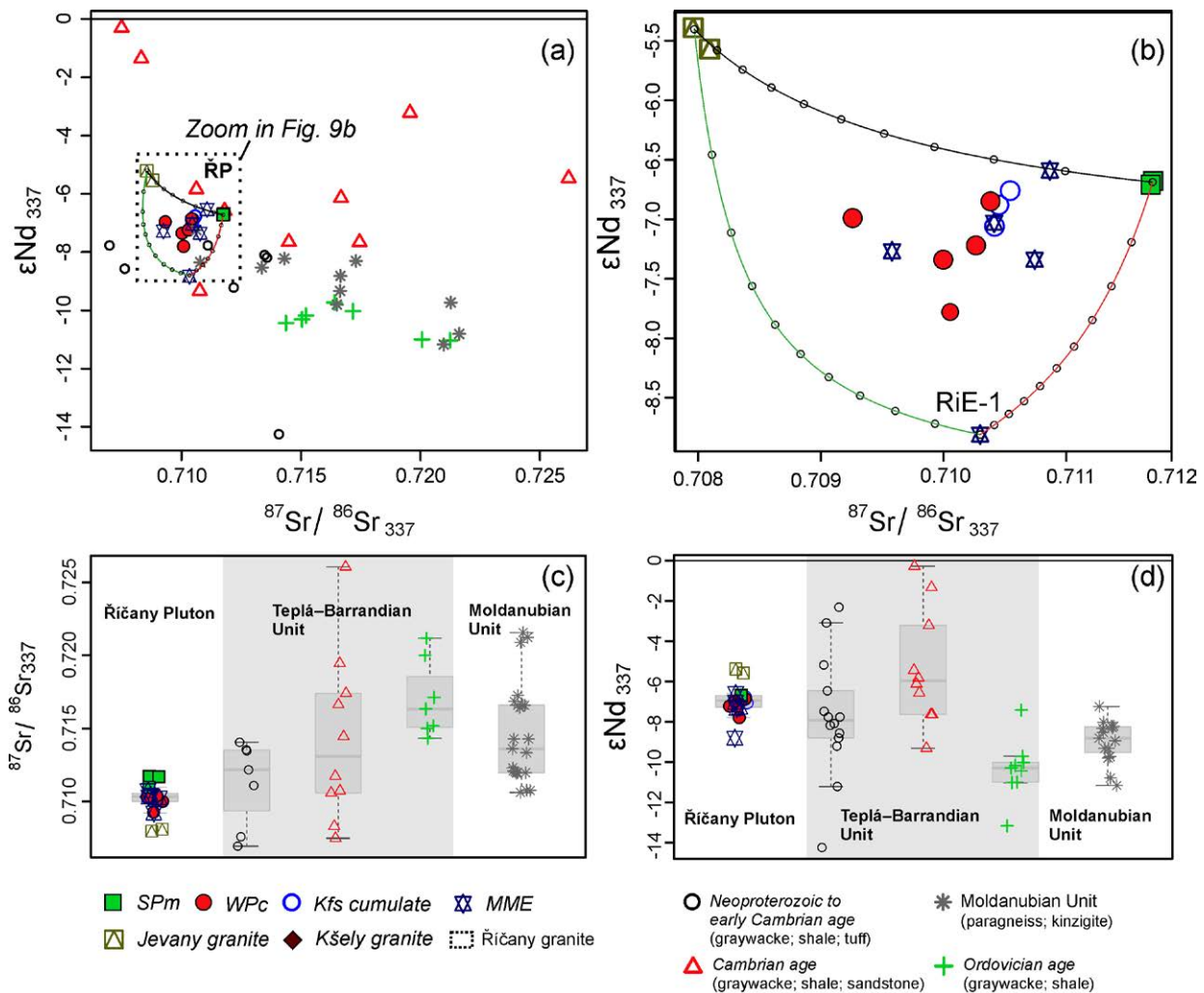


Fig. 9. (a) Binary plot $^{87}\text{Sr}/^{86}\text{Sr}_{337}$ – ϵNd_{337} for the Říčany intrusion and its host rocks: Teplá-Barrandian (meta-) sedimentary rocks of Neoproterozoic to Ordovician age (Drost *et al.* 2007; Pin & Waldhausová 2007; Janoušek *et al.*, 1995, unpublished data) and Moldanubian (meta-) sedimentary rocks (Janoušek *et al.*, 1995, unpublished data). (b) Zoomed portion of the same plot as (a) with superimposed binary mixing curves between Jevany leucogranite (Je-4), sample of the SPm facies (TR6) and a mafic microgranular enclave (RiE-1). (c–d) Stripplots of $^{87}\text{Sr}/^{86}\text{Sr}_{337}$ and ϵNd_{337} values for the Říčany intrusion and its country rocks.

($\epsilon\text{Nd}_{337} = -6.9$); its Sr was not examined as the samples were too altered. The MME show a broad range of Sr–Nd isotopic compositions ($^{87}\text{Sr}/^{86}\text{Sr}_{337}$ 0.7096–0.7109, ϵNd_{337} –6.6 to –8.8). The depleted-mantle Nd model ages (calculated using the two-stage model of Liew & Hofmann 1988) are uniform at ~ 1.6 Ga.

The two samples of Jevany leucogranite contain a somewhat less radiogenic Sr and significantly more radiogenic Nd ($^{87}\text{Sr}/^{86}\text{Sr}_{337} \sim 0.7080$, ϵNd_{337} –5.4 to –5.6). The aplite yields ϵNd_{337} of –7.9 but its initial Sr isotopic composition was not possible to determine precisely due to the extremely high Rb/Sr ratio used for age-correction.

U–Th–Pb ZIRCON AND MONAZITE GEOCHRONOLOGY

In order to constrain the intrusive age for both main pulses within the Říčany Pluton, we have analysed zircons of the sample Ri-1 (WpC) and monazites of the sample TR7 (SPm) by the LA ICP-MS method (see Electronic Appendix 5 for complete data set). Cathodoluminescence (CL) imaging (Electronic Appendix 6) of the zircons revealed typically magmatic oscillatory zoning in many grains, which is however often blurred and recrystallized. The inherited cores in zircons are common. Other grains tend to be uniformly dark or patchily zoned. Regarding zircon, there does not seem to be

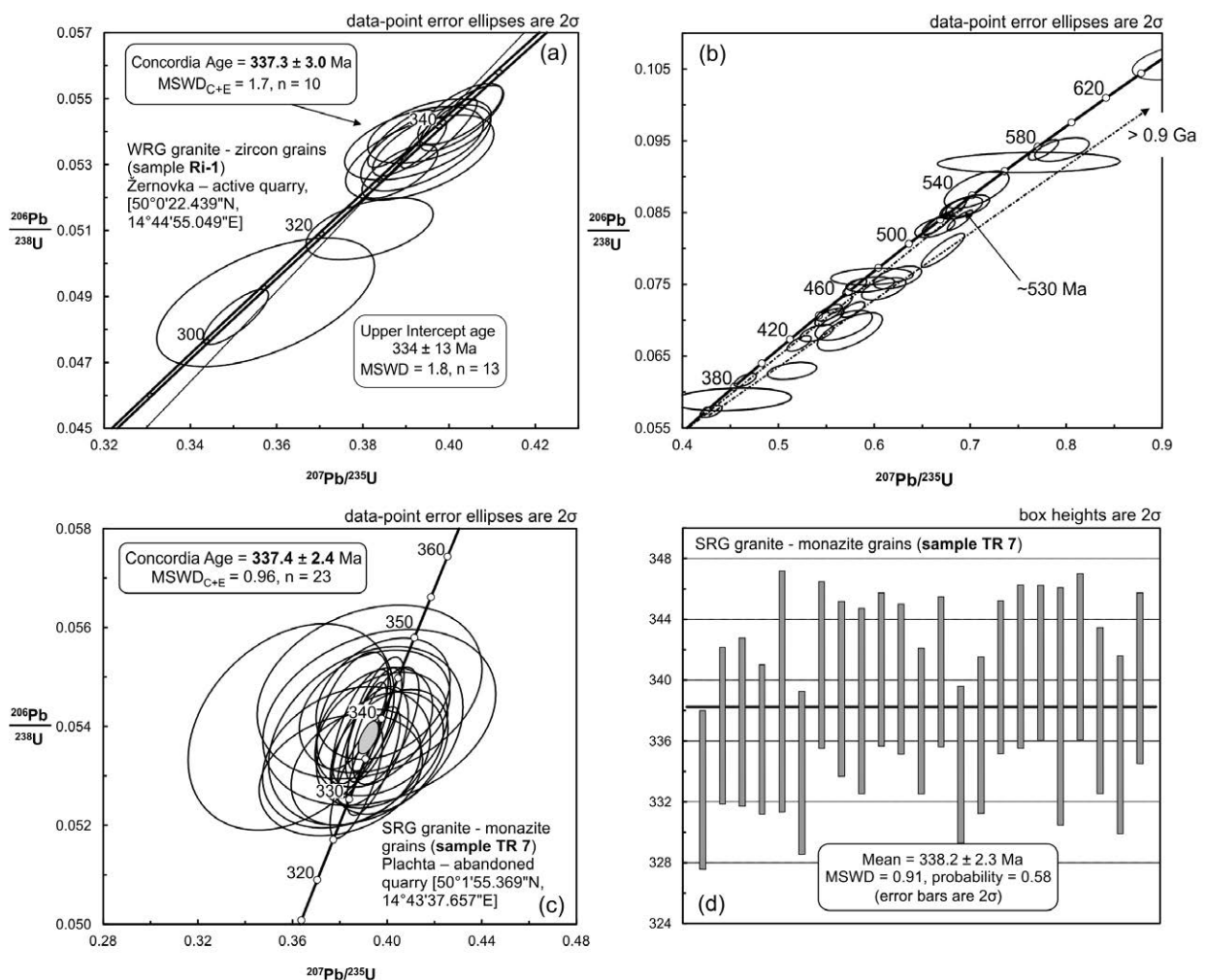


Fig. 10. (a–b) Zircon and (c) monazite concordia plots for the LA ICP-MS U–Th–Pb data from the WpC and SPm pulses. All the isotope data including the older inherited zircon ages are listed in the Electronic Appendix 5. (d) Weight average plot for the same SPm monazite. All diagrams were plotted using the ISOPLOT software (Ludwig, 2003).

a simple relationship between U contents or Th/U ratios. However, the featureless nearly uniformly dark grains gave solely Variscan ages. The Variscan zircon and monazite ages for each granite sample are summarized in Fig. 10a, c.

These data are interpreted as timing the magma emplacement and, within analytical uncertainties (2σ), these ages are the same for Ri-1 (zircon): 337.3 ± 3.0 Ma and TR7 (monazite): 337.4 ± 2.4 Ma (Fig. 10a, c). The weighted age for the same monazite analyses is only slightly higher (338.2 ± 2.3 Ma; Fig. 10d).

Moreover, the sample Ri-1 shows a complex pattern of inherited ages in zircon, coming often from (variously overprinted) oscillatory zoned crystals or their domains. The inheritance seems to be dominated by a Late Neoproterozoic to Early Cambrian component (~ 530 Ma), with some concordant Ordovician ages also present (~ 470 Ma); much fewer are Palaeoproterozoic ages (Fig. 10b). Significance of the inherited ages that are younger than Cambrian is not clear and may just reflect variable Pb loss.

THERMODYNAMIC MODELLING OF THE P–T CONDITIONS OF THE CONTACT METAMORPHISM

Thermodynamic modelling is used here to estimate the P–T conditions and approximate depth of emplacement of the Říčany Pluton. The modelling is based on the observed mineral assemblages, microstructural relationships of the individual phases and a P–T pseudosection calculated for slates, spotted schists and hornfelses from the pluton's thermal aureole.

A P–T section representative of slates from the Tehov roof pendant (Fig. 1c; sample MZ-6 taken from Kachlík, 1992) was constructed in the system $\text{MnO}-\text{Na}_2\text{O}-\text{CaO}-\text{K}_2\text{O}-\text{FeO}-\text{MgO}-\text{Al}_2\text{O}_3-\text{SiO}_2-\text{H}_2\text{O}$ (MnNCKFMASH) with excess quartz and water (Fig. 11). The sample is characterized by mineral assemblage Bt–Crd–And–Plg–Qtz with accessory relics of staurolite and new muscovite formed at the expense of cordierite. Modelling of this sample was based on the following molar bulk-rock composition: $\text{MnO} = 0.15$, $\text{Na}_2\text{O} = 0.71$, $\text{CaO} = 0.75$, $\text{K}_2\text{O} = 1.72$, $\text{FeO} = 10.87$, $\text{MgO} = 4.36$, $\text{Al}_2\text{O}_3 = 14.89$ and $\text{SiO}_2 = 66.56$. The calculated P–T section indicates that the stability of the present mineral assemblage is restricted to maximum pressures of 2.3 kbar and temperatures in the range of 500–630 °C.

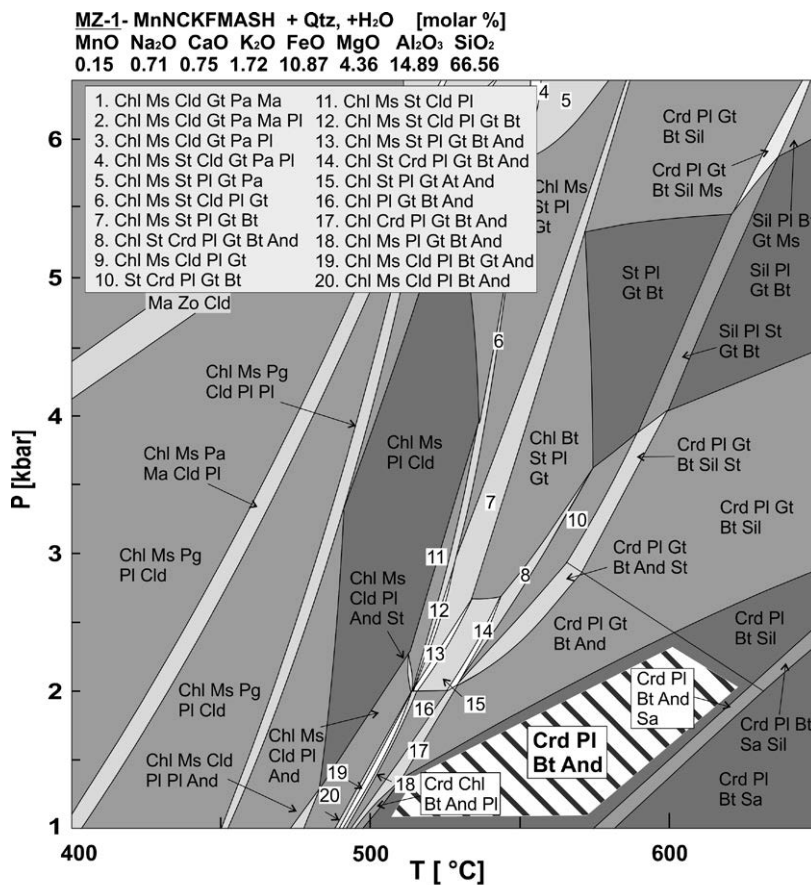


Fig. 11. Pseudosection (MnNCK-FMASH system) constrained for the contact metamorphism shale from the Tehov roof pendant (the Světice quarry, Fig. 1). All fields contain quartz and H₂O. Mineral abbreviations: And – andalusite, Bt – biotite, Chl – chlorite, Cld – chloritoid, Crd – cordierite, Gt – goethite, Ma – margarite, Ms – muscovite, Pg – paragonite, Pl – plagioclase, Sa – sanidine, St – staurolite, Zo – zoisite.

DISCUSSION

Integration of the multiple data sets described above provides an insight into the complex physico-chemical evolution of the Řičany magma plumbing system. This particular case will then be discussed as a general example of complex petrogenetic evolution of a vertically extensive, horizontally stratified and multiply replenished silicic magma chamber.

Two-scale compositional zoning in the pluton at the present-day erosion level

Pluton-scale zoning

All the petrographic facies in the Řičany Pluton are fairly fractionated (Fig. 12) and the SiO₂ contents do not vary greatly because the composition of cumulus in course of fractional crystallization was not too different from that of the evolving melt (Chappell *et al.*, 1987). Harker plots are thus of little use for genetic interpretation. Instead, Eu in feldspars can be employed as a fractionation index because the two feldspars likely represent key phases in the near-eutectic crystallization and binary plots are characterized by reasonably smooth trends and a broad variation (Fig. 12).

Regarding major elements, they change only slightly from the pluton margin to the centre. While the contents of SiO₂ broadly decrease (Fig. 12), TiO₂, K₂O and P₂O₅ show an opposite trend. More

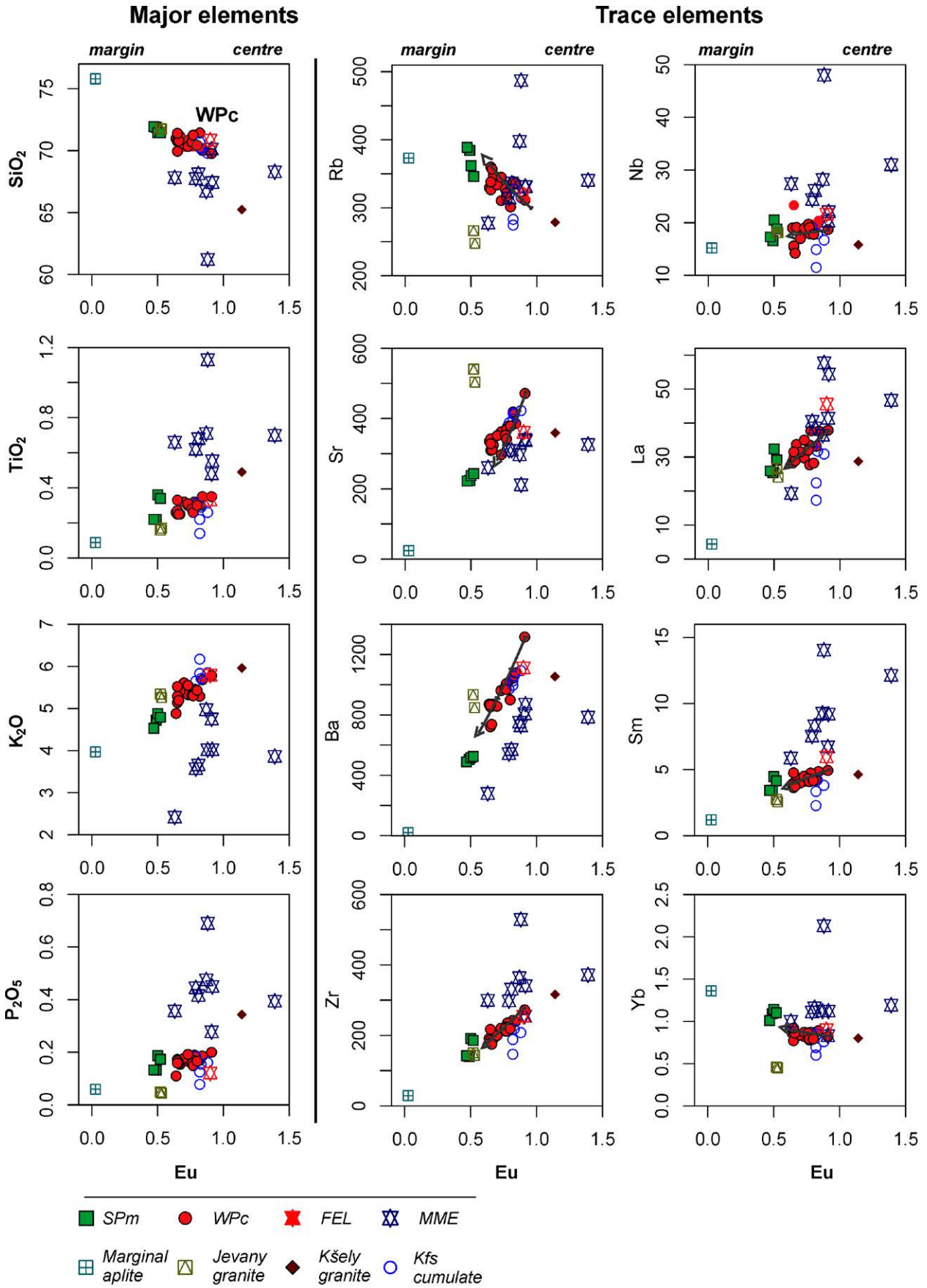


Fig. 12. Binary plots Eu vs. selected major- and trace-elements (wt. % and ppm, respectively). The modelled fractional crystallization trend (step 5%) is marked by a green curve. The symbols correspond with legend in the classifications diagrams (e.g., Fig. 8). The variations within each WPC and SPm indicate pulse-scale reverse zoning, while the overall picture documents a pluton-scale reverse zoning.

significant differences are revealed by trace elements. For the whole pluton, there are inward trends of Ba, Sr, Zr, La and Sm increase (Fig. 12), and Yb with Rb decrease, albeit the plot involving the latter element is somewhat scattered. These trends underline an important role of feldspars-dominated fractionation, accompanied by biotite and some Ti, P, Zr and LREE-rich accessories, such as Rt, Ap, Zrn and Mnz. Taken together, the degree of fractionation (expressed by decreasing Eu contents) seems to decrease from the outer SPm to the central WPC facies. This is opposite from what is typically seen in granitic plutons (apart from apical parts potentially overprinted by the late migration and accumulation of residual melt) and documents the reverse zoning of the Říčany Pluton (Janoušek *et al.*, 1997).

One of the possible mechanisms to explain the pluton-scale reverse zoning could be continuous fractionation of a single magma batch. However, the two facies show largely independent trends in some of the binary plots of both major- and trace elements (Fig. 12). The notion that the two facies represent discrete magma pulses is further supported by their distinct initial Sr–Nd isotope compositions, and by results of the textural analysis. Although the phenocrysts' abundance shows a transition between the SPm and WPC, the phenocryst size distribution and aggregation index clearly do not do so (Fig. 6b–d).

Another scenario that could potentially lead to reversely zoned plutons is a successive emplacement of several magma pulses within a single conduit (e.g., Ayuso, 1984; Nabelek *et al.*, 1986; Allen, 1992; Paterson & Vernon, 1995; Antunes *et al.*, 2008). The differences between the nested pulses would then be interpreted in terms of variable sources and/or of distinct degree of fractionation at depth. There were never observed any angular blocks of the SPm in the WPC or vice versa, so neither of the facies was likely fully solidified and the time interval between emplacement of both facies was short. For this reason, both the SPm and WPC magma pulses are interpreted as nearly coeval, with their contact representing a rheological boundary. This inference is not at odds with our new U–Th–Pb ages of the WPC and SPm, which are identical within errors. Unfortunately, our LA ICP-MS dating is not capable of resolving age differences smaller than several Myr. Were the still largely molten SPm invaded by the magma parental to the WPC, the Říčany granites would

represent variable mixtures of melt (solidified to groundmass), recycled antecrysts, and true phenocrysts formed during emplacement (e.g., Davidson, 2007; Larrea, 2013).

The evidence gathered here argues for the existence of two genetically related, broadly coeval, but discrete magma pulses parental to the WPC and SPm. Moreover, re-examination of the across-pluton geochemical variation shows that in fact each of the two main pulses is itself reversely zoned (Fig. 12). This double reverse zoning, i.e. on the pluton- and pulse-scale, has to be explained either by some processes near the site of final emplacement, or deeper.

Pulse-scale zoning

(Near-) in situ models. In theory, several mechanisms can produce a reversely zoned magma pulse essentially in situ, e.g., at the emplacement level: flow differentiation, crystal accumulation, filter pressing, country-rock contamination and magma mixing (e.g., Gastil *et al.*, 1991; Allen, 1992; Pitcher, 1993).

The higher modal proportion and size of K-feldspar phenocrysts in the SPm (Fig. 6b–c) apparently support the crystal accumulation model. However, the SPm is also richer in SiO₂, poorer in K₂O and shows significantly deeper negative Eu anomalies in the chondrite-normalized REE patterns (Fig. 8b). Thus the chemistry does not reflect any significant K-feldspar accumulation. Moreover, as suggested by the aggregation index, the texture of most of the SPm samples does not record mechanical phenocryst accumulation (Fig. 6d).

Alternatively, the abundance of larger K-feldspar phenocrysts may reflect the observation that the nucleation density of K-feldspar decreases with increasing water contents in the magma, eventually leading to formation of larger crystals (Vernon 1986 and references therein). This reinforces the argument that the SPm and WPC represent discrete magma pulses of distinct chemistry and volatile contents.

The SPm contains rare metasedimentary xenoliths many of which are partially molten and/or resorbed, suggesting a potential role for some country-rock contamination. However, the country rocks are fairly variable in lithology and thus also in composition. Any significant contamination by such a heterogeneous material would have inevitably disrupted the generally regular geochemical variations observed in both granite facies. Moreover, extensive assimilation of cold upper crustal lithologies by granitic magmas is also considered unlikely on thermal grounds, for it would lead to extensive crystallization and freezing of the system (Thompson *et al.*, 2002).

Models invoking an existence of a deeper magma chamber. Alternatively, the compositional

differences can reflect processes in a stratified magma chamber at depth, the presence of which is, in the Říčany case, in agreement with gravimetric modelling (Fig. 2). The geochemical variation and stratification in such a deep magma reservoir may have been a result of progressive melting, filter pressing or continuous fractional crystallization, accompanied by convection and/or gravitational differentiation, and, or may have resulted from open-system processes such as Assimilation and Fractional Crystallization (AFC) or magma mixing. The pulse-scale reverse zoning would then be generated during a sudden extraction of the melt from such a compositionally stratified magma and its ascent to higher crustal levels (e.g., Ayuso 1984; Fridrich & Mahood, 1984; Bourne & Danis, 1987; Couch *et al.*, 2001; Kaneko & Koyaguchi, 2004). Such a scenario seems the most appropriate for the Říčany Pluton.

From source to magma chamber: origin and evolution of the parental magma

Magma source

Given the inferred tectonic setting in the heart of the Bohemian Massif at ~337 Ma, the studied granites most likely originated by partial melting of crustal material after continental thickening, manifested by granulite-facies metamorphic event at ~340 Ma (see Schulmann *et al.*, 2009; Žák *et al.*, 2014 for details). Given the whole-rock geochemical characteristics (selected major elements and trace-element ratios), the granites were probably derived by melting of subaluminous to weakly peraluminous sources with high biotite contents.

Specifically, the diagram $\text{Al}_2\text{O}_3 + \text{FeOt} + \text{MgO} + \text{TiO}_2$ vs. $\text{Al}_2\text{O}_3/(\text{FeOt} + \text{MgO} + \text{TiO}_2)$ (Jung *et al.*, 2009 based on experiments of Patiño Douce, 1999) is capable of distinguishing anatectic melts from metapelitic, metapsammitic and metabasic protoliths. The most plausible source for the Říčany granite magma is psammitic (Fig. 13a), such as greywacke/paragneiss. Similarly, the values of Rb/Sr (0.5–16) vs. Rb/Ba (0.2–19) indicate a metapsammitic parentage. Moreover, the CaO/Na₂O ratios ranging from 0.23 to 0.54 imply that the granites were most likely generated from clay-poor, plagioclase-rich (~ 25 wt. %) psammitic rocks (Sylvester, 1998). Both diagrams point in the same direction, i.e. to a (meta-) psammitic parentage. Similar result would, however, produce also anatexis of a metaigneous source (orthogneiss) as its modal composition could have been nearly identical. Sylvester (1998) suggested that the $\text{Al}_2\text{O}_3/\text{TiO}_2$ ratio in granitic magmas decreases with a rising temperature of crustal anatexis. The Říčany and Kšely granites are characterized by low $\text{Al}_2\text{O}_3/\text{TiO}_2$ (39.1–65.7) and thus seem to be products of apparently high-T melting (Fig. 13c). This is in accord

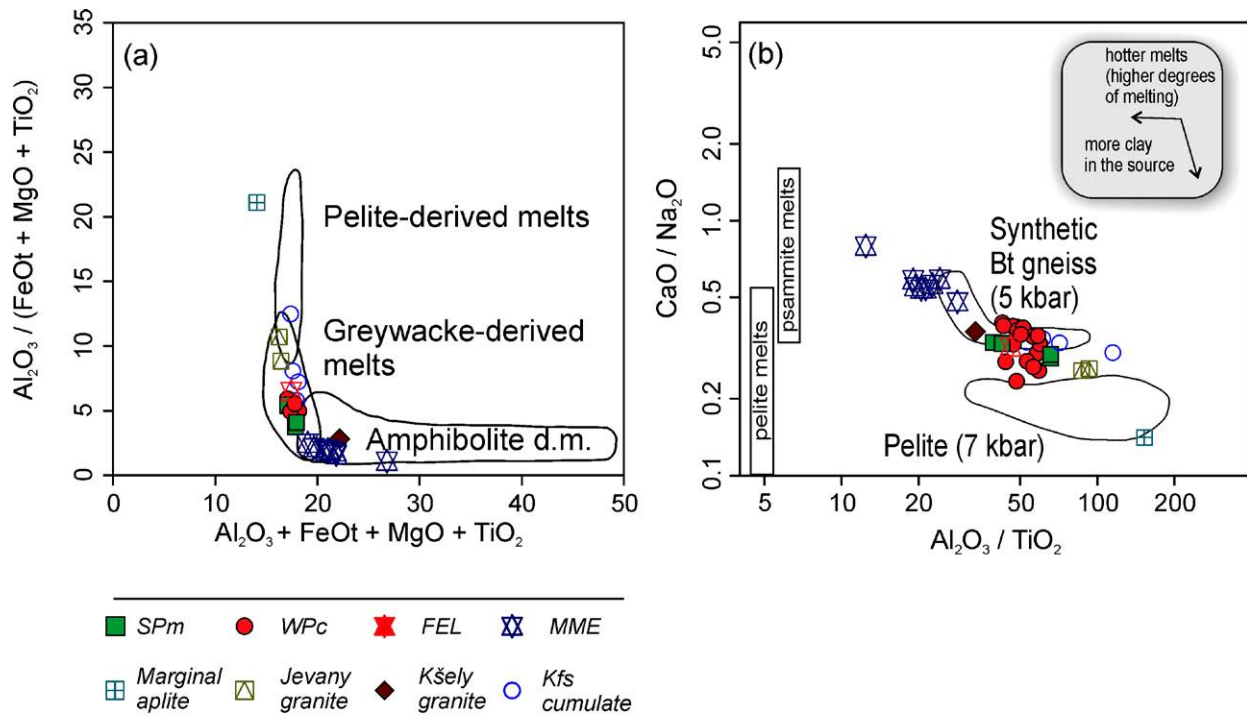


Fig. 13. (a) Binary plot of $\text{Al}_2\text{O}_3 + \text{FeOt} + \text{MgO} + \text{TiO}_2$ vs. $\text{Al}_2\text{O}_3 / (\text{FeOt} + \text{MgO} + \text{TiO}_2)$; outlined are domains occupied by experimental granitic melts obtained by partial melting of metapelites, metagreywackes and amphibolites (previous experimental works as summarised by Jung *et al.*, 2009 and references therein). (b) Diagram of $\log \text{Rb}/\text{Sr}$ vs. $\log \text{Rb}/\text{Ba}$ after Sylvester (1998) to distinguish between the granites derived by anatexis of clay-rich (metapelitic) sources and metagreywackes. (c) Binary plot $\text{Al}_2\text{O}_3 / \text{TiO}_2$ vs. $\text{CaO} / \text{Na}_2\text{O}$ with superimposed fields of experimental melts of several typical metasedimentary protoliths (after Sylvester, 1998; Janoušek *et al.*, 2010a and references therein). The ranges of $\text{CaO} / \text{Na}_2\text{O}$ ratios in the melts of pelitic and psammitic sources, shown as grey bars next to the ordinate, are after Jung & Pfänder (2007).

with average zircon and monazite saturation temperatures, which range, for WPC and SPm, from 775 to 810 °C.

Zircon inheritance of the WPC and SPm facies of the Říčany Pluton indicates a (predominantly?) early Cambrian source (~530 Ma; Figure 10b). Given the geological setting of the pluton, the possible sources were metasedimentary and metavolcanic rocks either of Teplá–Barrandian or Moldanubian affinity (Košler *et al.*, 2014). The Sr–Nd isotopic compositions for the Neoproterozoic or Cambrian material are extremely variable and thus do not contradict such an idea ($^{87}\text{Sr}/^{86}\text{Sr}_{337} = 0.7070\text{--}0.7262$; $\epsilon\text{Nd}_{337} = -14.3$ to -0.3 ; Janoušek *et al.*, 1995; Drost *et al.*, 2007; Pin & Waldhausrová, 2007; Drost, 2008 and our unpublished data). On the other hand, the Ordovician sedimentary rocks have too radiogenic Sr ($^{87}\text{Sr}/^{86}\text{Sr}_{337} = 0.7144\text{--}0.7212$) and Moldanubian metasedimentary rocks also tend to have too radiogenic Sr and less radiogenic Nd ($^{87}\text{Sr}/^{86}\text{Sr}_{337} = 0.7106\text{--}0.7216$; $\epsilon\text{Nd}_{337} = -11.2$ to -7.3 ; Scharbert

& Veselá, 1990; Janoušek *et al.*, 1995 and unpublished data) (Fig. 9). Of course, the protolith could have been also metapsammites or (rather felsic) orthogneisses unexposed, or at least unsampled, at the current erosional level.

The occurrence of MME, particularly abundant in the pluton centre, points to a possible role for interaction with hot mafic melts (Fig. 4). The MME show particularly high K_2O and MgO contents (Fig. 7d), and crustal-like Sr–Nd isotopic compositions (Fig. 9), with Nd in the most basic sample RiE-1 significantly less radiogenic than the metasedimentary host rocks and the Říčany granite itself. This points to a strongly enriched lithospheric mantle source, similar to that of near-contemporaneous ultrapotassic magmas of the Moldanubian Zone in the Bohemian Massif (Holub, 1997; Janoušek *et al.*, 2010), as well as further west within the European Variscan Belt (von Raumer *et al.*, 2014; Tabaud *et al.*, 2015). The anomalous mantle source was most likely strongly contaminated by deeply subducted and relaminated felsic metaigneous crust (Janoušek *et al.*, 2004b; Janoušek & Holub, 2007; Schulmann *et al.*, 2014).

Subsequent magma evolution

As argued above, fractional crystallization of the K-feldspar-dominated assemblage was presumably an important process in the pluton. Further constrains on the process (exact fractionating assemblage and degree of fractional crystallization for each of the two pulses) were obtained by numerical modelling using the whole-rock and mineral compositions, as follows.

First, major-element based reverse modelling was undertaken using the constrained least-squares method (Albarède, 1995; Janoušek & Moyen, 2014). The input data were the compositions of the most primitive sample (parental magma), the presumed most fractionated melt and typical chemistries of the likely crystallizing mineral phases. The calculations were carried out for each of the facies (WPC and SPM) separately, using our unpublished R-language plugin for the GCDkit software. The model for the weakly porphyritic facies (WPC, Table 5) assumes the sample Ri7 ($SiO_2 = 69.77$ wt. %) as the parent and Ri12 or TR4 ($SiO_2 = 71.99$ and 71.40 wt. %, respectively) as the evolved magmas. The variation can be modelled by ~15–21% fractional crystallization of K-feldspar, plagioclase \gg biotite. The $\sum R^2$ (sum of squared residuals) for both trends is much less than unity and thus reasonable (Table 5).

Modelling of selected key trace elements was pursued using the direct method. For granitic compositions are particularly useful LILE (e.g., Rb, Ba, Sr) hosted by the main rock-forming minerals, feldspars and micas (Hanson, 1978). Added were elements concentrated in accessory

Table 5: Model of fractional crystallization for the weakly porphyritic facies (WPC).**Table 5** Results of the fractional crystallization modelling of WPC granite, Řičany PlutonTrend Ri7–Ri12 (degree of fractional crystallization 21.1 %) $R^2 = 0.59$

	Parent (Ri7)	Kfs (39.0 %)	Pl (47.2 %)	Bt (13.8 %)	Daughter (Ri12)	Calculated	Difference	Cumulate
SiO ₂	69.77	65.03	65.72	37.50	71.99	71.97	0.02	61.55
Al ₂ O ₃	15.05	17.34	20.54	14.80	14.56	14.13	0.43	18.50
FeOt	1.51	0.14	0.00	16.95	1.50	1.27	0.23	2.40
MgO	1.23	0.00	0.00	13.35	0.78	1.07	-0.29	1.84
CaO	1.41	0.00	2.62	0.04	1.19	1.46	-0.27	1.24
Na ₂ O	3.64	1.07	10.07	0.14	2.83	3.23	-0.40	5.18
K ₂ O	5.78	15.78	0.26	9.47	5.11	5.30	-0.19	7.59

Trend Ri7–TR4 (degree of fractional crystallization 15.3 %) $R^2 = 0.38$

	Parent (Ri7)	Kfs (40.2 %)	Pl (44.7 %)	Bt (15.0 %)	Daughter (TR4)	Calculated	Difference	Cumulate
SiO ₂	69.77	65.03	65.72	37.50	71.40	71.31	0.09	61.20
Al ₂ O ₃	15.05	17.34	20.54	14.80	14.47	14.45	0.02	18.39
FeOt	1.51	0.14	0.00	16.95	1.59	1.31	0.28	2.61
MgO	1.23	0.00	0.00	13.35	1.00	1.09	-0.09	2.01
CaO	1.41	0.00	2.62	0.04	1.04	1.45	-0.41	1.18
Na ₂ O	3.64	1.07	10.07	0.14	3.72	3.40	0.32	4.95
K ₂ O	5.78	15.78	0.26	9.47	5.52	5.40	0.12	7.89

Proportions of accessory minerals: Ap (0.9 %), Rt (0.04 %), Mnz (0.03 %), Zrn (0.01 %) $\Sigma = 0.98$

phases (e.g., Zr, U, Th, REE) (Bea, 1996a, b). The distribution coefficients (Kd) selected from the literature are given in Electronic Appendix 7.

Using the proportions of main rock-forming minerals and degree of fractionation derived from the major-element mass-balance, and adding minor amounts of accessory phases (0.9 % apatite, 0.04 % rutile, 0.03 % monazite, 0.01 % zircon), Rayleigh-type fractional crystallization reproduces well the Ba, Rb, Sr, Zr, Nb, and REE (e.g., La, Sm, Eu, Yb) variation in the WPC (Fig. 12).

Second trend for strongly porphyritic granite (SPm) is short and poorly constrained. It can be nevertheless reproduced in major elements by ~ only 3% fractionation of Kfs >> Pl + Bt > Ap. Apart from likely low degree of fractionation, the limited variation may be due to the fact that the silica contents in the SPm samples are also close to granite minimum.

Origin of the Sr–Nd isotopic heterogeneity

The prevalence of felsic over mafic to intermediate rocks at the present-day exposure level seems to point to only a limited role of mantle-derived magmas in the genesis of the granites. Moreover, it should be noted that there is no evidence to indicate the presence of a large body of basic material at upper to mid-crustal depth (at least down to 14 km) as the residual gravity anomaly is compatible

with a large low-density (granitic) pluton (Fig. 2).

This observation, together with lack of mafic cumulate enclaves in the Říčany granite, rules out a model in which the granitic magma originated by extensive closed-system crystal fractionation of the basic, mantle-derived magma, as it would inevitably produce large amounts of mafic cumulates at deeper crustal levels. This is also in line with the Sr–Nd isotopic data, which show considerable variation among the granites and various types of MME (Fig. 9). Both the main facies show their own identity in the whole-rock chemical compositions (including the Sr–Nd isotopes) and little microstructural evidence for magma mixing (rarely observed antirapakivi texture – Janoušek, 1994).

In contrast, the MME enclose rather abundant biotite-mantled quartz ocelli to ovoids 0.5–1 cm across and resorbed K-feldspar megacrysts (Fig. 4; Palivcová *et al.*, 1992). Moreover, some MME contain micropegmatitic patches. This points to a hybrid origin of the MME and suggests that the quartz ocelli and resorbed K-feldspar crystals are in fact xenocrysts, derived from the granitic system and captured by the invading more basic melt (e.g., Hibbard, 1991, 1995). Moreover, abundance of blade-shaped biotite and acicular apatite in the MME support their quick cooling presumably as the hotter basic melt came into contact with cooler granitic magma (e.g., Didier & Barbarin, 1991a; Wiebe *et al.*, 1997; Janoušek *et al.*, 2000a, 2004a; Barbarin, 2005).

In this context, it is also important to note that our gravimetry data do not rule out the presence of mafic material in lower crust, where it could have formed for instance a basic underplate, triggering/contributing to the crustal melting (e.g., Huppert & Sparks, 1988; Dufek & Bergantz, 2005; Annen *et al.*, 2006).

Given its fairly homogeneous, radiogenic Sr and Nd isotopic composition, and relative rarity of MME, the SPm pulse may be close to composition to the pristine anatectic melt (Fig. 9). The same may hold true also for the late Jevany leucogranite, albeit its source had to be significantly more primitive in its Sr–Nd isotopic composition. However, the Sr–Nd isotopic signatures of the WPc and (most) MME require a three-component mixing.

A plausible model thus seems a partial melting of a thickened, heterogeneous metapsammitic source containing variable proportions of material resembling, in their Sr–Nd signature, the marginal SPm facies and Jevany leucogranite. Such an anatectic melt could have then interacted with minor mafic magmas, perhaps compositionally similar to the sample RiE-1. Given the microstructural evidence with whole-rock major and trace element composition, the Sr–Nd isotopic variation in the MME can be viewed as a consequence of binary mixing with prevalent granitic magma or, more likely, the complex, AFC-style contamination of a mafic magma by country-rock metasediments (Knesel &

Davidson, 1996; Knesel *et al.*, 1999; Wolff *et al.*, 1999) that would be further complicated as the felsic system was partly crystallized (Beard 2008).

The most basic MME (RiE-1; Fig. 9) should provide some idea about the isotopic signature of the mafic end-member, even though its interpretation is not straightforward. First, the proportion of felsic end-member possibly present in the sample RiE-1 remains unconstrained. Second, especially the strontium isotopic ratios in MME are likely not to reflect the original composition of the basic magma, as this element is prone to reequilibration, shifting the Sr isotopic ratios towards the more radiogenic signature of the host granites. This may be the case for many major- and trace-elements but neodymium ratios tend to be more resistant (Pin *et al.*, 1990; Pin, 1991; Elburg, 1996).

Taken together, the SPm forms a group of rather restricted Sr–Nd isotopic signatures (Fig. 9), so the amount of mafic-system derived Sr and Nd was probably close to nil and/or degree of homogenization within the magma chamber (at that point) high. The K-feldspar crystals forming the cumulates are likely to have crystallized relatively early, but already after an interaction of the SPm-like magma with some mafic component. It is assumed that another pulse of mafic magma then intruded the K-feldspar crystal-rich mush, disrupting it and contaminating the magma chamber even further. In such a way could have been generated the WPC magma rich in mafic schlieren and MME often surrounded by, or associated with, patches of K-feldspar phenocrysts (Fig. 4). The process was multistage, as shown by the presence of double enclaves with more hybrid rims (Fig. 4a). The interplay between fractionation and multistage interaction would also lift the rheological barriers between the two contrasting magmas with very different SiO₂ and volatile contents, solidi and thus viscosities (e.g., Fernandez & Gasquet, 1994; Sparks & Marshall, 1986; Bateman, 1995; Dingwell *et al.*, 1996; Mader *et al.*, 2013). The last batches of the very felsic residual magma rich in enclaves and K-feldspar crystals have intruded the nearly-solidified granite, forming the polygenic enclave swarms. At the waning stages of the magmatic activity, the centre of the already solidified Říčany Pluton was intruded by a minor body of the Jevany leucogranite, a nearly pristine crustally derived melt without any significant imprint of the enriched-mantle derived potassic magmas.

Summary: a model for evolution of the Říčany magma plumbing system

Based on the above inferences, the physico–chemical evolution of the Říčany magma plumbing system is interpreted as having involved three main stages:

During the **first stage** (Fig. 14a) vertical stratification in an upper-crustal magma chamber was established. Sidewall-cooling led to the solidification of the thinner tabular part of the pluton (Fig.

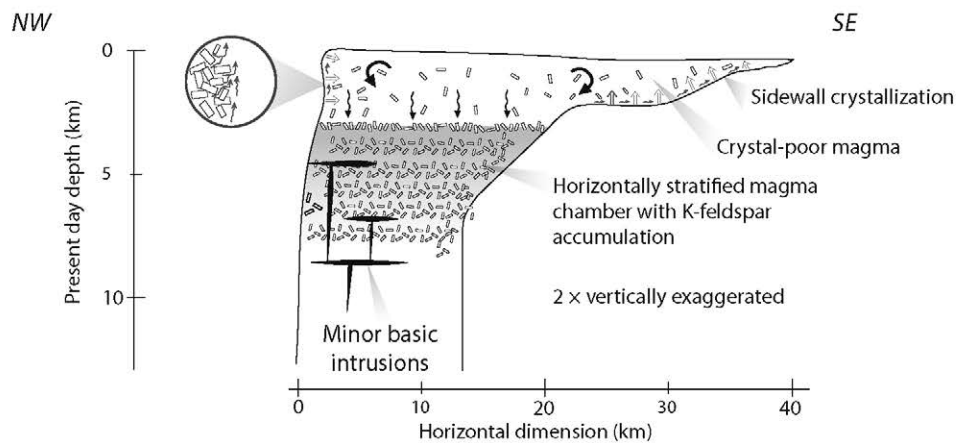
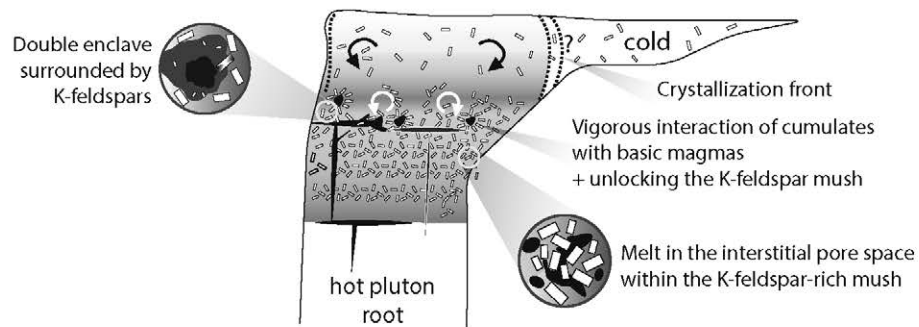
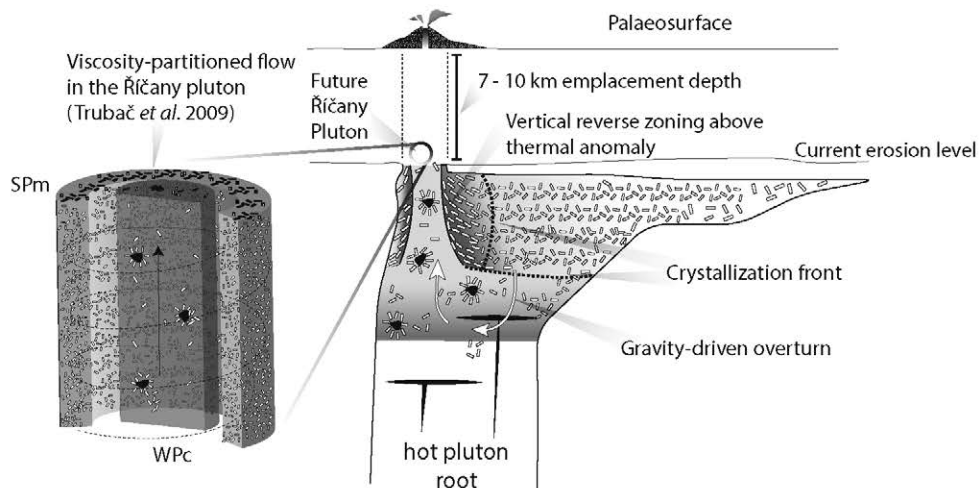
Stage I: Formation of a stratified magma chamber**Stage II: Vigorous interaction with basic magmas and unlocking of the K-feldspar mush****Stage III: Gravity-driven overturn and final emplacement of the Říčany Pluton**

Fig. 14. A three-stage model for the development of the Říčany magma plumbing system. The shape is based on gravimetry; distribution of hot and cold regions within the magma chamber is taken from thermal modelling. See text for discussion.

3) while the active magma chamber was localized to a hot domain above the pluton root (Fig. 3). Whole-rock geochemical modelling indicates that the crustally-derived SPm magma evolved by K-feldspar-dominated fractional crystallization. We assume that the K-feldspar megacrysts gradually sunk in the magma, forming cumulates deeper in the magma chamber, and were overlain by a layer of residual, phenocryst-poor magma (Lee & Morton, 2015). Further, in thermochemical convection, the effect of decreasing temperature at the wall is counteracted by water enrichment in residual melts produced by sidewall crystallization, which creates a less dense, positively buoyant boundary layer that can float upward. In addition, minor amounts of basic mantle-derived melts likely interacted with the K-feldspar cumulate layers. On the other hand, the overlying granitic liquid was to a large effect shielded from this interaction as shown by its preserved Sr–Nd isotopic signature as well as by the lack of MME.

Second stage (Fig. 14b) invokes a more voluminous intrusion of basic, enriched-mantle derived melt, underplating the K-feldspar-rich crystal mush. During this process, the magma parental to the fractionated WPc occupied the interstitial pore space within the K-feldspar-rich mush. The magma was mobilized by the heat and fluids from the basic melt, and then extracted from the phenocryst framework by porous flow. Parts of this phenocryst framework, with or without MME, have been broken off and carried up with the ascending magma (e.g.,; Bachmann *et al.*, 2007; Bachmann & Bergantz, 2008; Huber *et al.*, 2011; Pistone *et al.*, 2013).

During the **third stage** (Fig. 14c), this hotter and likely more buoyant portion of the magma chamber evolved into a gravitational instability, leading to disruption of the originally horizontal stratification. The diapir-like ascent of the coeval SPm and WPc magmas to shallow crustal levels (less than c. 8 km) produced the inverse vertical zoning in the exposed part of the pluton and could have been accompanied by a volcanic eruption on the surface (Bachmann *et al.*, 2007). Magnetic fabrics suggest complex magma flow whereby the outer magma pulse (SPm) may have ascended helically (Trubač *et al.*, 2009).

Thus, the Jevany leucogranite (JG) may represent a melt lens in the pluton that formed through gas filter-pressing (Sisson & Bacon, 1999), whereas the marginal aplite (MA) is a residue of various melt/crystal ratios (Imaoka *et al.*, 2014).

CONCLUSIONS

- The Říčany Pluton represents a subaluminous to moderately peraluminous, geochemically evolved, high-level, porphyritic (muscovite-) biotite granite intrusion. It consists of two concentrically arranged broadly coeval granite pulses, the outer strongly porphyritic granite (SPm) and the inner weakly porphyritic granite (WPc). Their modal composition and petrology are nearly identical.
- Texturally and modally variable biotite-bearing MME are abundant in the central part of the intrusion, indicating repeated basic magma input and multistage interactions with granitic magma in the magma chamber.
- U–Th–Pb geochronological data are interpreted as representing within-error identical magma emplacement ages of 337.3 ± 3.0 Ma for the WPc (zircon) and 337.4 ± 2.4 Ma for the SPm (monazite).
- Whole-rock major- and trace-element concentrations and the phenocryst size distribution and aggregation index suggest that the SPm and WPc represent two coeval magma pulses from a mutually comparable source.
- The pluton exhibits double reverse zoning. On the pluton scale, the outer SPm is geochemically more evolved than the inner WPc. On the pulse scale, whole-rock geochemical variations within each unit (SPm, WPc) are compatible with outward fractional crystallization. Both types of zoning are cryptic, manifested by variations in the trace-element compositions rather than in major elements or gross petrography.
- Petrological study and geochemical modelling of fractional crystallization of the WPc indicate limited (up to ~20 %) fractional crystallization of $Pl + Kfs \gg Bt$ with minor Ap, Mnz, Rt and Zrn . Second trend for the SPm can be reproduced by ~ only 3% fractionation of $Kfs \gg Pl + Bt > Ap$. Apart from likely low degree of fractionation, the limited variation may be due to the fact that the silica contents in the SPm samples are also close to granite minimum. The K-feldspar dominated fractional crystallization with crystal accumulation took place probably in a deep magma chamber, producing the trace-element variability observed.

- The proposed model for the origin of zoning in the Říčany Pluton is as follows. The **first stage** was an establishment of vertical stratification in the magma chamber. The wedge-like shape of the pluton (as inferred from gravimetry) resulted in its asymmetric cooling with a longer lived 'hot' domain above the pluton root. As a consequence of deep fractional crystallization, the K-feldspar megacrysts formed cumulate layers overlain by residual, but still phenocryst-bearing magma. The **second stage** invokes intrusion of basic, enriched-mantle derived melts, underplating the K-feldspar-rich crystal mush. In turn, the fractionated WPC was mobilized and extracted by a porous flow and parts of the phenocryst framework have been broken off and carried up by the ascending magma. At the **third stage**, the thermal anomaly located above the deep-seated root was further enhanced by intrusion of hot basic magmas into otherwise largely solidified magma chamber. This led to the development of a localized gravitational instability, overturn of the originally horizontal stratification, and magma intrusion to shallow crustal levels (<8 km). The vertical reverse zoning in the pluton is thus interpreted as reflecting the original layering of the underlying magma chamber, steepened during magma ascent.
- The main general implication of the current study is that the three-dimensional shape of plutonic bodies largely determines their cooling histories and thus also the physico-chemical evolution. Thicker and longer lived portions of magma chambers are sites of extensive fractionation and vigorous interaction with basic magmas. These hot domains are then particularly prone to rejuvenation and extraction of eruptible magma, leading potentially to volcanic eruptions.

FUNDING

This work was supported by the Grant Agency of the Czech Republic [Grant No. P210/11/1168 to Jiří Žák] and [ECOP 2.3. – CZ 1.07/2.3.00/20.0052 to Jan Švancara]. From the Charles University projects PRVOUK P44, [SVV261203], and Operational Programmes [OPPK CZ.2.16/3.1.00/21516].

ACKNOWLEDGEMENTS

We gratefully acknowledge Pavel Ondra for measurement of density values for the Říčany granite and Václav Kachlík for help with estimation of P–T conditions. This study is part of Ph.D. research of Jakub Trubač.

SUPPLEMENTARY DATA

Supplementary data for this paper are available at Journal of Petrology online.

REFERENCES

- Albarède, F. (1995). *Introduction to Geochemical Modeling*. Cambridge: Cambridge University Press.
- Allen, C. M. (1992). A nested diapir model for the reversely zoned Turtle Pluton, southeastern California. *Transactions of the Royal Society of Edinburgh, Earth Sciences* **83**, 179–190.
- Annen, C., Blundy, J. D. & Sparks, R. S. J. (2006b): The genesis of intermediate and silicic magmas in deep crustal hot zones. *Journal of Petrology* **47**, 505–539.
- Annen, C. (2009). From plutons to magma chambers: thermal constraints on the accumulation of eruptible silicic magma in the upper crust. *Earth and Planetary Science Letters* **284**, 409–416.
- Antunes, I. M. H. R., Neiva, A. M. R., Silva, M. M. V. G. & Corfu, F. (2008). Geochemistry of S-type granitic rocks from the reversely zoned Castelo Branco Pluton (central Portugal). *Lithos* **103**, 445–465.
- Ayuso, R. A. (1984). Field relations, crystallization, and petrology of reversely zoned granitic plutons in the Bottle Lake complex, Maine. U.S. Geological Survey Professional Paper **1320**, 1–58.
- Bachl, C. A., Miller, C. F., Miller, J. S. & Faulds, J. E. (2001). Construction of a pluton: evidence from an exposed cross section of the Searchlight Pluton, Eldorado Mountains, Nevada. *Geological Society of America Bulletin* **113**, 1213–1228.
- Bachmann, O., Miller, C. F. & de Silva, S. L. (2007). The volcanic-plutonic connection as a stage for understanding crustal magmatism. *Journal of Volcanology and Geothermal Research* **167**, 1–23.
- Bachmann, O. & Bergantz, G. W. (2008). Rhyolites and their source mushes across tectonic settings. *Journal of Petrology* **49**, 2277–2285.
- Bachmann, O., Deering, C. D., Lipman, P. W. & Plummer, C. (2014). Building zoned ignimbrites by recycling silicic cumulates: insight from the 1,000T km³ Carpenter Ridge Tuff, CO. *Contributions to Mineralogy and Petrology* **167**: 1025, 1–13.
- Barbarin, B. (2005). Mafic magmatic enclaves and mafic rocks associated with some granitoids of the central Sierra Nevada batholith, California: nature, origin, and relations with the hosts. *Lithos* **80**, 155–177.
- Barbarin, B. & Didier, J. (1991). Macroscopic features of mafic microgranular enclaves. In: Didier, J. & Barbarin, B. (eds) *Enclaves and Granite Petrology*. Amsterdam: Elsevier, 253–262.
- Barbey, P., Nachit, H. & Pons, J. (2001). Magma–host interactions during differentiation and emplacement of a shallow-level, zoned granitic pluton (Tarçouate Pluton, Morocco): implications for magma emplacement. *Lithos* **58** 125–143

- Batchelor, R. A. & Bowden, P. (1985). Petrogenetic interpretation of granitoid rock series using multicationic parameters. *Chemical Geology* **48**, 43–55.
- Bateman, R. (1984). On the role of diapirism in the, segregation, ascent and final emplacement of granitoid magmas. *Tectonophysics* **110** 211–231.
- Bateman, R. (1995). The interplay between crystallization, replenishment and hybridization in large felsic magma chambers. *Earth-Science Reviews* **39**, 91–106.
- Bateman, P. C. & Chappell, B. W. (1979). Crystallization, fractionation, and solidification of the Tuolumne Intrusive Series, Yosemite National Park, California. *Geological Society of America Bulletin* **90**, 465–482.
- Bea, F. (1996a). Controls on the trace element composition of crustal melts. *Transactions of the Royal Society of Edinburgh, Earth Sciences* **87**, 33–41.
- Bea, F. (1996b). Residence of REE, Y, Th and U in granites and crustal protoliths; implications for the chemistry of crustal melts. *Journal of Petrology* **37**, 521–552.
- Beard, J. S. (2008). Crystal–melt separation and the development of isotopic heterogeneities in hybrid magmas. *Journal of Petrology* **49**, 1027–1041.
- Bourne, J. & Danis, D. (1987). A proposed model for the formation of reversely zoned plutons based on study of the Lacorne Complex, Superior Province, Quebec. *Canadian Journal of Earth Sciences* **24**, 2506–2520.
- Boynnton, W. V. (1984). Cosmochemistry of the rare earth elements: meteorite studies. In: Henderson, P. (ed.) *Rare Earth Element Geochemistry*. Amsterdam: Elsevier, 63–114.
- Coint, N., Barnes, C. G., Yoshinobu, A. S., Chamberlain, K. R. & Barnes, M. A. (2013). Batch-wise assembly and zoning of a tilted calc-alkaline batholith: field relations, timing, and compositional variation. *Geosphere* **9**, 1729–1746.
- Cháb, J., Straník, Z. & Eliáš, M. (2007). *Geological map of the Czech Republic 1 : 500 000*. Prague: Czech Geological Survey.
- Chappell, B. W., White, A. J. R. & Wyborn, D. (1987). The importance of residual source material (restite) in granite petrogenesis. *Journal of Petrology* **28**, 571–604.
- Candela, P. A. (1997). A review of shallow, ore-related granites: textures, volatiles, and ore metals. *Journal of Petrology* **38**, 1619–1633.

- Cimbáľníková, A., Palivcová, M., Hejl, V. & Arakeljanc, M. M. (1977). Biotit iz ržičanskoga granita i ego bogatych biotitom xenolitov (ČSSR, Sredněčeskij pluton). In: Afanasjev, G. D. (ed.) Opyt Korreljacji Magmatičeskich i Metamorfičeskich Porod Čechoslovakiji i Někotorych Rajonov SSSR. Moskva: Nauka, 178–187.
- Clark, P. J. & Evans F. C. (1954) Distance to nearest neighbour as a measure of spatial relationships in populations. *Ecology* **35**, 445–453.
- Coleman, D. S., Bartley, J. M., Glazner, A. F. & Pardue, M. J. (2012). Is chemical zonation in plutonic rocks driven by changes in source magma composition or shallow-crustal differentiation? *Geosphere* **8**, 1568–1587.
- Connolly, J. A. D. (2005). Computation of phase equilibria by linear programming: A tool for geodynamic modeling and its application to subduction zone decarbonation. *Earth and Planetary Science Letters* **236**, 524–541.
- Couch, S., Sparks, R. S. J. & Carroll, M. R. (2001). Mineral disequilibrium in lavas explained by convective self-mixing in open magma chambers. *Nature* **411**, 1037–1039.
- Čermák, V., Huckenholz, H.G., Rybach, L., Schmid, R. Schopper, J.R., Schuch, M., Stoeffler, D. & Wohlenberg, J. (1982). Physical properties of rocks. In: Angenheiser, M. (ed.) Landolt-Börnstein, Numerical Data and Functional Relationships in Science and Technology, Group V: Geophysics and Space Research. Berlin: Springer, 315–371.
- Davidson, J. P., Morgan, D. J., Charlier, B. L. A., Harlou, R. & Hora, J. M. (2007). Microsampling and isotopic analysis of igneous rocks: implications for the study of magmatic systems. *Annual Review of Earth and Planetary Sciences* **35**, 273–311.
- De La Roche, H., Leterrier, J., Grandclaude, P. & Marchal, M. (1980). A classification of volcanic and plutonic rocks using R_1R_2 -diagram and major element analyses – its relationships with current nomenclature. *Chemical Geology* **29**, 183–210.
- Debon, F. & Le Fort, P. (1983). A chemical-mineralogical classification of common plutonic rocks and associations. *Transactions of the Royal Society of Edinburgh, Earth Sciences* **73**, 135–149.
- Debon, F. & Le Fort, P. (1988). A cationic classification of common plutonic rocks and their magmatic associations: principles, method, applications. *Bulletin de Minéralogie* **111**, 493–510.
- Didier, J. & Barbarin, B. eds. (1991a). *Enclaves and Granite Petrology*. Amsterdam: Elsevier.
- Didier, J. & Barbarin, B. (1991b). The different types of enclaves in granites – nomenclature. In: Didier, J. & Barbarin, B. (eds) *Enclaves and Granite Petrology*. Amsterdam: Elsevier, 19–24.

- Dingwell, D. B., Hess, K. U. & Knoche, R. (1996). Granite and granitic pegmatite melts: volumes and viscosities. *Transactions of the Royal Society of Edinburgh, Earth Sciences* **87**, 65–72.
- Drost, K. (2008). Sources and geotectonic setting of Late Neoproterozoic–Early Palaeozoic volcano-sedimentary successions of the Teplá–Barrandian Unit (Bohemian Massif): evidence from petrographical, geochemical, and isotope analyses. *Geologica Saxonica* **54**, 1–168.
- Drost, K., Romer, R. L., Linnemann, U., Fatka, O., Kraft, P. & Marek, J. (2007). Nd–Sr–Pb isotopic signatures of Neoproterozoic–Early Paleozoic siliciclastic rocks in response to changing geotectonic regimes: a case study from the Barrandian area (Bohemian Massif, Czech Republic). In: Linnemann, U., Nance, R. D., Kraft, P. & Zulauf, G. (eds) *The Evolution of the Rheic Ocean: From Avalonian–Cadomian Active Margin to Alleghenian–Variscan Collision*. Geological Society of America Special Papers **423**, 191–208.
- Dufek, J. & Bergantz, G. W. (2005). Lower crustal magma genesis and preservation: a stochastic framework for the evaluation of basalt–crust interaction. *Journal of Petrology* **46**, 2167–2195.
- Elburg, M. A. (1996). Evidence of isotopic equilibration between microgranitoid enclaves and host granodiorite, Warburton Granodiorite, Lachlan Fold Belt, Australia. *Lithos* **38**, 1–22.
- Fernandez, A. & Gasquet, D. R. (1994). Relative rheological evolution of chemically contrasted coeval magmas: example of the Tichka Plutonic Complex (Morocco). *Contributions to Mineralogy and Petrology* **116**, 316–326.
- Fridrich, C. J. & Mahood, G. A. (1984). Reverse zoning in the resurgent intrusions of the Grizzly Peak cauldron, Sawatch Range, Colorado. *Geological Society of America Bulletin* **95**, 779–787.
- Gastil, G., Nozawa, T. & Tainosho, Y. (1991). The tectonic implications of asymmetrically zoned plutons. *Earth and Planetary Science Letters* **102**, 302–309.
- Gelman S. E., Gutierrez F. J. & Bachmann O. (2013). The longevity of large upper crustal silicic magma reservoirs. *Geology* **41**, 759–762.
- Gerdes, A. & Zeh, A. (2006). Combined U–Pb and Hf isotope LA-(MC-)ICP-MS analyses of detrital zircons: Comparison with SHRIMP and new constraints for the provenance and age of an Armorican metasediment in Central Germany. *Earth and Planetary Science Letters* **249**, 47–61.
- Gerdes, A. & Zeh, A. (2009). Zircon formation versus zircon alteration – New insights from combined U–Pb and Lu–Hf in-situ LA-ICP-MS analyses, and consequences for the interpretation of Archean zircon from the Central Zone of the Limpopo Belt. *Chemical Geology* **261**, 230–243.
- Glazner, A. F. & Johnson, B. R. (2013). Late crystallization of K-feldspar and the paradox of megacrystic granites. *Contributions to Mineralogy and Petrology* **166**, 777–799.

- Gray, W., Glazner, A. F., Coleman, D. S. & Bartley, J. M. (2008). Long-term geochemical variability of the Late Cretaceous Tuolumne Intrusive Suite, central Sierra Nevada, California. In: Annen, C. & Zellmer, G. F. (eds) *Dynamics of Crustal Magma Transfer, Storage and Differentiation*. Geological Society London Special Publications **304**, 183–201.
- Hanson, G. N. (1978). The application of trace elements to the petrogenesis of igneous rocks of granitic composition. *Earth and Planetary Science Letters* **38**, 26–43.
- Hayden, L. A. & Watson, E. B. (2007). Rutile saturation in hydrous siliceous melts and its bearing on Ti-thermometry of quartz and zircon. *Earth and Planetary Science Letters* **258**, 561–568.
- Hecht, L., Vigneresse, J. & Morteani, G. (1997). Constraints on the origin of zonation of the granite complexes in the Fichtelgebirge (Germany and Czech Republic): evidence from a gravity and geochemical study. *Geologische Rundschau* **86**, 93–109.
- Hibbard, M. J. (1991). Textural anatomy of twelve magma-mixed granitoid systems. In: Didier, J. & Barbarin, B. (eds) *Enclaves and Granite Petrology*. Amsterdam: Elsevier, 431–444.
- Hibbard, M. J. (1995). Mixed Magma Rocks. In: *Petrography to Petrogenesis*. New Jersey: Prentice Hall, 242–260.
- Higgins, M. D. (2006). *Quantitative Textural Measurements in Igneous and Metamorphic Petrology*. Cambridge: Cambridge University Press.
- Hildreth, W. & Wilson, C. J. N. (2007). Compositional zoning of the Bishop Tuff. *Journal of Petrology* **48**, 951–999.
- Holland, T. J. B., Baker, J. & Powell, R. (1998). Mixing properties and activity-composition and relationships of chlorites in the system $\text{MgO-FeO-Al}_2\text{O}_3\text{-SiO}_2\text{-H}_2\text{O}$. *European Journal of Mineralogy* **10**, 395–406.
- Holland, T. J. B. & Powell, R. (1998). An internally consistent thermodynamic data set for phases of petrological interest. *Journal of Metamorphic Geology* **16**, 309–343.
- Holečková, H. & Šmejkalová, H. (1958). Petrochemie říčanské žuly. *Sborník Vysoké školy chemicko-technologické v Praze, oddělení fakult anorganické a organické technologie* **2**, 302–321.
- Holub, F. V. (1997). Ultrapotassic plutonic rocks of the durbachite series in the Bohemian Massif: petrology, geochemistry and petrogenetic interpretation. *Sborník geologických věd, Ložisková geologie–mineralogie* **31**, 5–26.
- Holub, F. V., Machart, J. & Manová, M. (1997). The Central Bohemian Plutonic Complex: geology, chemical composition and genetic interpretation. *Sborník geologických věd, Ložisková geologie–mineralogie* **31**, 27–50.

- Hoskin, P. W. O., Kinny, P. D., Wyborn, D. & Chappell, B. W. (2000). Identifying accessory mineral saturation during differentiation in granitoid magmas: an integral approach. *Journal of Petrology* **41**, 1365–1396.
- Huber, C., Bachmann, O. & Dufek, J. (2011). Thermo-mechanical reactivation of locked crystal mushes: Melting-induced internal fracturing and assimilation processes in magmas. *Earth and Planetary Science Letters* **304**, 443–454.
- Huppert, H. & Sparks, R. (1982). Effects of volatiles on mixing in calc-alkaline magma systems. *Nature* **297**, 554.
- Huppert, H. E. & Sparks, R. S. J. (1988): The generation of granitic magmas by intrusion of basalt into continental crust. *Journal of Petrology* **29**, 599–624.
- Ibrmajer, J. (1963). Gravimetrická mapa ČSSR 1 : 200,000. *Věstník Ústředního ústavu geologického*, **38**, 217–226.
- Imaoka, T., Nakashima, K., Kamei, A., Hayasaka, Y., Ogita, Y., Ikawa, T., Itaya, T., Takahashi, Y. & Kagami, H. (2014). Anatomy of the Cretaceous Hobenzan Pluton, SW Japan: internal structure of a small zoned pluton, and its genesis. *Lithos* **208-209**, 81–103.
- Jacobsen, S. B. & Wasserburg, G. J. (1980). Sm–Nd isotopic evolution of chondrites. *Earth and Planetary Science Letters* **50**, 139–155.
- Janoušek, V. (1994). Geochemistry and Petrogenesis of the Central Bohemian Pluton, Czech Republic. Unpublished PhD. thesis, University of Glasgow.
- Janoušek, V. (2006). Saturnin, R language script for application of accessory-mineral saturation models in igneous geochemistry. *Geologica Carpathica* **57**, 131–142.
- Janoušek, V. & Holub, F. V. (2007). The causal link between HP-HT metamorphism and ultrapotassic magmatism in collisional orogens: case study from the Moldanubian Zone of the Bohemian Massif. *Proceedings of the Geologists' Association* **118**, 75–86.
- Janoušek, V. & Moyen, J. F. (2014). Mass Balance Modelling of Magmatic Processes in GCDkit. In: Kumar, S. & Singh, R. N. (eds) *Modelling of Magmatic and Allied Processes*. Society of Earth Scientists Series **83**, Berlin: Springer, 225–238.
- Janoušek, V., Rogers, G. & Bowes, D. R. (1995). Sr–Nd isotopic constraints on the petrogenesis of the Central Bohemian Pluton, Czech Republic. *Geologische Rundschau* **84**, 520–534.
- Janoušek, V., Rogers, G., Bowes, D. R. & Vaňková, V. (1997). Cryptic trace-element variation as an indicator of reverse zoning in a granitic pluton: the Říčany granite, Czech Republic. *Journal of the Geological Society (London)* **154**, 807–815.

- Janoušek, V., Bowes, D. R., Braithwaite, C. J. R. & Rogers, G. (2000a). Microstructural and mineralogical evidence for limited involvement of magma mixing in the petrogenesis of a Hercynian high-K calc-alkaline intrusion: the Kozárovec granodiorite, Central Bohemian Pluton, Czech Republic. *Transactions of the Royal Society of Edinburgh, Earth Sciences* **91**, 15–26.
- Janoušek, V., Bowes, D. R., Rogers, G., Farrow, C. M. & Jelínek, E. (2000b). Modelling diverse processes in the petrogenesis of a composite batholith: the Central Bohemian Pluton, Central European Hercynides. *Journal of Petrology* **41**, 511–543.
- Janoušek, V., Braithwaite, C. J. R., Bowes, D. R. & Gerdes, A. (2004a). Magma-mixing in the genesis of Hercynian calc-alkaline granitoids: an integrated petrographic and geochemical study of the Sázava intrusion, Central Bohemian Pluton, Czech Republic. *Lithos* **78**, 67–99.
- Janoušek, V., Finger, F., Roberts, M. P., Frýda, J., Pin, C. & Dolejš, D. (2004b). Deciphering the petrogenesis of deeply buried granites: whole-rock geochemical constraints on the origin of largely undepleted felsic granulites from the Moldanubian Zone of the Bohemian Massif. *Transactions of the Royal Society of Edinburgh, Earth Sciences* **95**, 141–159.
- Janoušek, V., Farrow, C. M. & Erban, V. (2006). Interpretation of whole-rock geochemical data in igneous geochemistry: introducing Geochemical Data Toolkit (GCDkit). *Journal of Petrology* **47**, 1255–1259.
- Janoušek, V., Holub, F. V., Magna, T. & Erban, V. (2010). Isotopic constraints on the petrogenesis of the Variscan ultrapotassic magmas from the Moldanubian Zone of the Bohemian Massif. *Mineralogia - Special Papers* **37**, 32–36.
- Janoušek, V., Konopásek, J., Ulrich, S., Erban, V., Tajčmanová, L. & Jeřábek, P. (2010a). Geochemical character and petrogenesis of Pan-African Amspoort suite of the Boundary Igneous Complex in the Kaoko Belt (NW Namibia). *Gondwana Research* **18**, 688–707.
- Janoušek, V., Wiegand, B. & Žák, J. (2010b). Dating the onset of Variscan crustal exhumation in the core of the Bohemian Massif: new U–Pb single zircon ages from the high-K calc-alkaline granodiorites of the Blatná suite, Central Bohemian Plutonic Complex. *Journal of the Geological Society (London)* **167**, 347–360.
- Janoušek, V., Farrow, C. M., Erban, V. & Trubač, J. (2011). Brand new Geochemical Data Toolkit (GCDkit 3.0) - is it worth upgrading and browsing documentation? (Yes!). *Geologické výzkumy na Moravě a ve Slezsku* **18**, 26–30.

- Janoušek, V., Navrátil, T., Trubač, J., Strnad, L., Laufek, F. & Minařík, L. (2014). Distribution of elements among minerals of a single muscovite-biotite granite sample - the best approach and general implications. *Geologica Carpathica* **65**, 257—271.
- Johannes, W. & Holtz, F. (1996). *Petrogenesis and Experimental Petrology of Granitic Rocks*. Berlin: Springer, 1–331.
- Johnson, B. R. & Glazner, A. F. (2010). Formation of K-feldspar megacrysts in granodioritic plutons by thermal cycling and late-stage textural coarsening. *Contributions to Mineralogy and Petrology* **159**, 599–619.
- Johnson, S. E., Schmidt, K. L. & Tate, M. C. (2002). Ring complexes in the Peninsular Ranges Batholith, Mexico and the USA: magma plumbing systems in the middle and upper crust. *Lithos* **61**, 187–208.
- Jung, S. & Pfänder, J. A. (2007). Source composition and melting temperatures of orogenic granitoids: constraints from CaO/Na₂O, Al₂O₃/TiO₂ and accessory mineral saturation thermometry. *European Journal of Mineralogy* **19**, 859–870.
- Jung, S., Masberg, P., Mihm, D. & Hoernes, S. (2009). Partial melting of diverse crustal sources – constraints from Sr–Nd–O isotope compositions of quartz diorite–granodiorite–leucogranite associations (Kaoko Belt, Namibia). *Lithos* **111**, 236–251.
- Kachlík, V. (1992). Litostratigrafie, paleogeografický vývoj a metamorfnní postižení hornin pláště v severovýchodní části ostrovní zóny střeđočeského plutonu. Prague: Unpublished Habilitation Thesis, Charles University.
- Kaneko, K. & Koyaguchi, T. (2004). Experimental study on the effects of crustal temperature and composition on assimilation with fractional crystallization at the floor of magma chambers. *Journal of Volcanology and Geothermal Research* **129**, 155–172.
- Kašpar, J. V. (1936). Stručný nástin mineralogie a geochemie říčanské žuly. *Věda přírodní* **17**, 168–171.
- Katzer, F. (1888). Geologische Beschreibung der Umgebung von Říčan. *Jahrbuch der Geologischen Reichanstalt* **38**, 355–417.
- Kettner, R. (1930). Geologie střeđočeského žulového masívu. *Příroda* **23**, 431–437.
- Knesel, K. M., Davidson, J. P. (1996). Isotopic disequilibrium during melting of granite and implications for crustal contamination of magmas. *Geology* **24**, 243–246.
- Knesel, K. M., Davidson J. P., Duffield W. A. (1999). Evolution of silicic magma through assimilation and subsequent recharge: Evidence from Sr isotopes in sanidine phenocrysts, Taylor Creek Rhyolite, NM. *Journal of Petrology* **40**, 773–786.

- Kodym, O. (1925). Poznámka ke geologii říčanské žuly. Věstník Státního geologického ústavu Československé republiky **1**, 77–83.
- Kodym, O. (1963). Vysvětlivky k přehledné geologické mapě ČSSR 1:200 000 M-33-XXI Tábor. Prague: ÚÚG.
- Košler, J., Konopásek, J., Sláma, J. & Vrána, S. (2014). U–Pb zircon provenance of Moldanubian metasediments in the Bohemian Massif. *Journal of the Geological Society, London* **171**, 83–95.
- Larrea, P., França, Z., Lago, M., Widom, E., Galé, C. & Ubide, T. (2013). Magmatic processes and the role of antecrysts in the genesis of Corvo Island (Azores Archipelago, Portugal). *Journal of Petrology* **54**, 769–793.
- Le Maitre, R. W. (1982). *Numerical Petrology*. Amsterdam: Elsevier.
- Lee, C.T. A. & Bachmann, O. (2014). How important is the role of crystal fractionation in making intermediate magmas? Insights from Zr and P systematics. *Earth and Planetary Science Letters* **393**, 266–274.
- Lee, C.T. A. & Morton, D. M. (2015). High silica granites: terminal porosity and crystal settling. *Earth and Planetary Science Letters* **409**, 23–31.
- Liew, T. C. & Hofmann, A. W. (1988). Precambrian crustal components, plutonic associations, plate environment of the Hercynian Fold Belt of Central Europe: indications from a Nd and Sr isotopic study. *Contributions to Mineralogy and Petrology* **98**, 129–138.
- Lipman, P. W. (2007). Incremental assembly and prolonged consolidation of Cordilleran magma chambers: evidence from the Southern Rocky Mountain volcanic field. *Geosphere* **3**, 42.
- Ludwig, K. R. (2003). *Isoplot/Ex version 3.00. A geochronological toolkit for Microsoft Excel, User's Manual*. Berkeley Geochronology Center Special Publications No. 4.
- Lugmair, G. W. & Marti, K. (1978). Lunar initial $^{143}\text{Nd}/^{144}\text{Nd}$: differential evolution line of the lunar crust and mantle. *Earth and Planetary Science Letters* **39**, 349–357.
- Lux, D. R., Hooks, B., Gibson, D. & Hogan, J. P. (2007). Magma interactions in the Deer Isle Granite Complex, Maine: field and textural evidence. *Canadian Mineralogist* **45**, 131–146.
- Mader, H. M., Llewellyn, E. W. & Mueller, S. P. (2013). The rheology of two-phase magmas: a review and analysis. *Journal of Volcanology and Geothermal Research* **257**, 135–158.
- Mielke, P. & Winkler, H. G. F. (1979). Eine bessere Berechnung der Mesonorm für granitische Gesteine. *Neues Jahrbuch für Mineralogie, Monatshefte* 471–480.

- Mikoshiba, M. U., Kanisawa, S., Matsuhisa, Y. & Togashi, S. (2004). Geochemical and isotopic characteristics of the Cretaceous Orikabe Plutonic Complex, Kitakami Mountains, Japan: magmatic evolution in a zoned pluton and significance of a subduction-related mafic parental magma. *Contributions to Mineralogy and Petrology* **146**, 433–449.
- Míková, J. & Denková, P. (2007). Modified chromatographic separation scheme for Sr and Nd isotope analysis in geological silicate samples. *Journal of Geosciences* **52**, 221–226.
- Miller, C. F. & Miller, J. S. (2002). Contrasting stratified plutons exposed in tilt blocks, Eldorado Mountains, Colorado River Rift, NV, USA. *Lithos* **61**, 209–224.
- Miller, C. F., McDowell, S. M. & Mapes, R. W. (2003). Hot and cold granites? Implications of zircon saturation temperatures and preservation of inheritance. *Geology* **31**, 529–532.
- Miller, C. F., Furbish, D. J., Walker, B. A., Claiborne, L. L., Koteas, G. C., Bleick, H. A. & Miller, J. S. (2011). Growth of plutons by incremental emplacement of sheets in crystal-rich host: evidence from Miocene intrusions of the Colorado River region, Nevada, USA. *Tectonophysics* **500**, 65–77.
- Millonig, L. J., Gerdes, A. & Groat, L. A. (2012). U–Th–Pb geochronology of meta-carbonatites and meta-alkaline rocks in the southern Canadian Cordillera: a geodynamic perspective. *Lithos* **152**, 202–217.
- Molyneux, S. J. & Hutton, D. H. W. (2000). Evidence for significant granite space creation by the ballooning mechanism: the example of the Ardara Pluton, Ireland. *Geological Society of America Bulletin* **112**, 1543–1558.
- Montel, J. M. (1993). A model for monazite/melt equilibrium and application to the generation of granitic magmas. *Chemical Geology* **110**, 127–146.
- Mottlová, L. & Suk, M. (1970). K rozšíření granitických hornin v hlubší stavbě moldanubika. *Časopis pro mineralogii a geologii* **15**, 383–392.
- Nabelek, P. I., Papike, J. J. & Laul, J. C. (1986). The Notch Peak granitic stock, Utah: origin of reverse zoning and petrogenesis. *Journal of Petrology* **27**, 1035–1069.
- Newton, R. C. & Haselton, H. T. (1981). Thermodynamics of the garnet-plagioclase- Al_2SiO_5 -quartz geobarometer. In: Newton, R. C. (ed.) *Thermodynamics of Minerals and Melts*. New York: Springer, 131–147.
- Němec, D. (1978). Genesis of aplite in the Říčany massif, central Bohemia. *Neues Jahrbuch für Mineralogie, Abhandlungen* **132**, 322–339.

- Orel, P. (1975). Metalogenetické a prognózní důsledky vymezení říčansko-kutnohorského batolitu. In: Sborník Nerostné surovinové zdroje, vědecká konference-sekce 2 –geologie. Ostrava: Mining University, 1–118.
- Orlov, A. (1933). Příspěvek k petrografii středočeského žulového masívu (Říčansko–Benešovsko–Milevsko–Písecko). Věstník Státního geologického ústavu Československé republiky **9**, 135–144.
- Palivcová, M., Waldhausrová, J., Ledvinková, V. & Fatková, J. (1992). Říčany granite (Central Bohemian Pluton) and its ocelli- and ovoids- bearing mafic enclaves. *Krystalinikum* **21**, 33–66.
- Parada, M. A., Larrondol, P., Guiressel, C. & Roperch, P. (2002). Magmatic gradients in the Cretaceous Caleu Pluton (Central Chile): injections of pulses from a stratified magma reservoir. *Gondwana Research* **5**, 307–324.
- Paterson, S. R. & Vernon, R. H. (1995). Bursting the bubble of ballooning plutons: a return to nested diapirs emplaced by multiple processes. *Geological Society of America Bulletin* **107**, 1356–1380.
- Patiño Douce, A. E. (1999). What do experiments tell us about relative contributions of crust and mantle to the origin of granitic magmas? In: Castro, A., Fernández, C. & Vigneresse, J. L. (eds) *Understanding Granites: Integrating New and Classical Techniques*. Geological Society of London Special Publications **168**, 55–75.
- Peccerillo, A. & Taylor, S. R. (1976). Geochemistry of Eocene calc-alkaline volcanic rocks from the Kastamonu area, Northern Turkey. *Contributions to Mineralogy and Petrology* **58**, 63–81.
- Pešek, J., Holub, V., Jaroš, J., Malý, L., Martínek, K., Prouza, V., Spudil, J. & Tásler, R. (2001). *Geologie a ložiska svrchnopaleozoických limnických pánví České republiky*. Prague: Czech Geological Survey.
- Pichavant, M., Martel, C., Bourdier, J. & Scaillet, B. (2002). Physical conditions, structure, and dynamics of a zoned magma chamber: Mount Pelée (Martinique, Lesser Antilles Arc). *Journal of Geophysical Research* **107**, 1978–2012.
- Pin, C. (1991). Sr–Nd isotopic study of igneous and metasedimentary enclaves in some Hercynian granitoids from the Massif Central, France. In: Didier, J. & Barbarin, B. (eds) *Enclaves and Granite Petrology*. Amsterdam: Elsevier, 333–344.

- Pin, C. & Waldhausrová, J. (2007). Sm–Nd isotope and trace element study of Late Proterozoic metabasalts (“spilites”) from the Central Barrandian domain (Bohemian Massif, Czech Republic). In: Linnemann, U., Nance, R. D., Kraft, P. & Zulauf, G. (eds) *The Evolution of the Rheic Ocean: From Avalonian–Cadomian Active Margin to Alleghenian–Variscan Collision*. Geological Society of America Special Papers **423**, 231–247.
- Pin, C. & Zalduegui, J. F. S. (1997). Sequential separation of light rare-earth elements, thorium and uranium by miniaturized extraction chromatography: application to isotopic analyses of silicate rocks. *Analytica Chimica Acta* **339**, 79–89.
- Pin, C., Binon, M., Belin, J. M., Barbarin, B. & Clemens, J. D. (1990). Origin of microgranular enclaves in granitoids – equivocal Sr–Nd evidence from Hercynian rocks in the Massif Central (France). *Journal of Geophysical Research* **95**, 17821–17828.
- Pin, C., Briot, D., Bassin, C. & Poitrasson, F. (1994). Concomitant separation of strontium and samarium-neodymium for isotopic analysis in silicate samples, based on specific extraction chromatography. *Analytica Chimica Acta* **298**, 209–217.
- Pistone, M., Caricchi, L., Ulmer, P., Reusser, E. & Ardia, P. (2013). Rheology of volatile-bearing crystal mushes: mobilization vs. viscous death. *Chemical Geology* **345**, 16–39.
- Pitcher, W. S. (1993). *The Nature and Origin of Granite*. London: Chapman & Hall.
- Pivec, E. (1969). Potassium feldspars with hourglass structure in biotite adamellite and their genetic interpretation. *Acta Universitatis Carolinae, Geologica* **1**, 20–30.
- Pivec, E. & Pivec E., Jr. (1996). The Kšely Granite, lesser known granite type of the Bohemian Massif. *Acta Universitatis Carolinae, Geologica* **40**, 23–32.
- Pouchou, J.L. & Pichoir, F. (1985). “PAP” (– ρ -Z) procedure for improved quantitative microanalysis. In: Armstrong JT (ed) *Microbeam Analysis*. San Francisco Press, pp 104–106.
- Powell, R. & Holland, T. J. B. (1999). Relating formulations of the thermodynamics of mineral solid solutions; activity modeling of pyroxenes, amphiboles, and micas. *American Mineralogist* **84**, 1–14.
- Pupier, E., Barbey, P., Toplis, M. J. & Bussy, F. (2008). Igneous layering, fractional crystallization and growth of granitic plutons: the Dolbel Batholith in SW Niger. *Journal of Petrology* **49**, 1043–1068.
- Putirka, K. D., Canchola, J., Rash, J., Smith, O, Torrez, G., Paterson, S. R. & Ducea, M. N. (2014). Pluton assembly and the genesis of granitic magmas: insights from the GIC pluton in cross section, Sierra Nevada Batholith, California. *American Mineralogist* **99**, 1284–1303

- Rudge, J. F., Holness, M. B. & Smith, G. C. (2008). Quantitative textural analysis of packings of elongate crystals. *Contributions to Mineralogy and Petrology* **156**, 413–429.
- Seaman, S. J., Gylling, H., Hogan, J. P., Karner, F. & Koteas, G. C. (2011). Concentric zoning in the Tunk Lake Pluton, coastal Maine. *Contributions to Mineralogy and Petrology* **162**, 1291–1314.
- Sisson, T. W., & Bacon, C. R. (1999). Gas-driven filter pressing in magmas. *Geology*, **27**, 613–616.
- Scharbert, S. & Veselá, M. (1990). Rb–Sr systematics of intrusive rocks from the Moldanubicum around Jihlava. In: Minaříková, D. & Lobitzer, H. (eds) *Thirty years of geological cooperation between Austria and Czechoslovakia*. Prague: Czech Geological Survey, 262–271.
- Schulmann, K., Konopásek, J., Janoušek, V., Lexa, O., Lardeaux, J. M., Edel, J. B., Štípská, P. & Ulrich, S. (2009). An Andean type Palaeozoic convergence in the Bohemian Massif. *Comptes Rendus Geoscience* **341**, 266–286.
- Schulmann, K., Lexa, O., Janoušek, V., Lardeaux, J. M. & Edel, J. B. (2014). Anatomy of a diffuse cryptic suture zone: an example from the Bohemian Massif, European Variscides. *Geology* **42**, 275–278.
- Shand, S. J. (1943). *Eruptive Rocks. Their Genesis, Composition, Classification, and Their Relation to Ore-Deposits with a Chapter on Meteorite*. New York: John Wiley & Sons.
- Sláma, J., Košler, J., Condon, D. J., Crowley, J. L., Gerdes, A., Hanchar, J. M., Horstwood, M. S. A., Morris, G. A., Nasdala, L., Norberg, N., Schaltegger, U., Schoene, B., Tubrett, M. N. & Whitehouse, M. J. (2008). Plešovice zircon – a new natural reference material for U-Pb and Hf isotopic microanalysis. *Chemical Geology* **249**, 1–35.
- Sparks, R. S. J. & Marshall, L. A. (1986). Thermal and mechanical constraints on mixing between mafic and silicic magmas. *Journal of Volcanology and Geothermal Research* **29**, 99–124.
- Steiger, R. H. & Jäger, E. (1977). Subcommittee on Geochronology; convention on the use of decay constants in geo- and cosmochronology. *Earth and Planetary Science Letters* **36**, 359–362.
- Steinöcher, V. (1969). Látkové složení, provinciální charakter a petrogenese středočeského plutonu. *Rozpravy ČSAV* **79**, 1–98.
- Stephens, W. E. (1992). Spatial, compositional and rheological constraints on origin of zoning in the Criffell Pluton, Scotland. *Transactions of the Royal Society of Edinburgh, Earth Sciences* **83**, 191–199.
- Stephens, W. E. & Halliday, A. N. (1980). Discontinuities in the composition surface of a zoned pluton, Criffell, Scotland. *Geological Society of America Bulletin* **91**, 165–170.
- Streckeisen, A. (1976). To each plutonic rock its proper name. *Earth-Science Reviews* **12**, 1–33.

- Streckeisen, A. & Le Maitre, R. W. (1979). A chemical approximation to the modal QAPF classification of the igneous rocks. *Neues Jahrbuch für Mineralogie, Abhandlungen* **136**, 169–206.
- Sylvester, P. J. (1998). Post-collisional strongly peraluminous granites. *Lithos* **45**, 29–44.
- Švancara, J. (2004). Gravimetrická mapa České republiky. *Československý časopis pro fyziku*, **54**, 217–220.
- Tabaud, A. S., Janoušek, V., Skrzypek, E., Schulmann, K., Rossi, P., Whitechurch, H., Guerrot, C. & Paquette, J. L. (2015). Chronology, petrogenesis and heat sources for successive Carboniferous magmatic events in the southern-central Variscan Vosges Mts. (NE France). *Journal of the Geological Society (London)* **172**, 87–102.
- Tanaka, T., Togashi, S., Kamioka, H., Amakawa, H., Kagami, H., Hamamoto, T., Yuhara, M., Orihashi, Y., Yoneda, S., Shimizu, H., Kunimaru, T., Takahashi, K., Yanagi, T., Nakano, T., Fujimaki, H., Shinjo, R., Asahara, Y., Tanimizu, M. & Dragusanu, C. (2000). JNdi-1: a neodymium isotopic reference in consistency with LaJolla neodymium. *Chemical Geology* **168**, 279–281.
- Taylor, S. R. & McLennan, S. M. (1995). The geochemical evolution of the continental crust. *Reviews in Geophysics* **33**, 241–265.
- Tindle, A. G. & Pearce, J. A. (1981). Petrogenetic modelling of in situ fractional crystallization in the zoned Loch Doon pluton, Scotland. *Contributions to Mineralogy and Petrology* **78**, 196–207.
- Thompson, A. B., Matile, L. & Ulmer, P. (2002). Some thermal constraints on crustal assimilation during fractionation of hydrous, mantle-derived magmas with examples from Central Alpine Batholiths. *Journal of Petrology* **43**, 403–422.
- Trubač, J., Žák, J., Chlupáčová, M. & Janoušek, V. (2009). Magnetic fabric of the Říčany granite, Bohemian Massif: a record of helical magma flow? *Journal of Volcanology and Geothermal Research* **181**, 25–34.
- Vejnar, Z. (1973). Petrochemistry of the Central Bohemian Pluton. *Geochemical methods and data* **2**, 1–115.
- Vernon, R. H. (1986). K-feldspar megacrysts in granites – phenocrysts, not porphyroblasts. *Earth-Science Reviews* **23**, 1–63.
- Vernon, R. H. & Paterson, S. R. (2008). How late are K-feldspar megacrysts in granites? *Lithos* **104**, 327–336.
- Vignerresse, J. L. (1995a). Control of granite emplacement by regional deformation. *Tectonophysics* **249**, 173–186.

- Vigneresse, J. L. (1995b). Crustal regime of deformation and ascent of granitic magma. *Tectonophysics* **249**, 187–202.
- Vigneresse, J. L. & Bouchez, J. L. (1997). Successive granitic magma batches during pluton emplacement: the Case of Cabeza de Araya (Spain). *Journal of Petrology* **38**, 1767–1776.
- Villaseca, C., Barbero, L. & Herreros, V. (1998). A re-examination of the typology of peraluminous granite types in intracontinental orogenic belts. *Transactions of the Royal Society of Edinburgh, Earth Sciences* **89**, 113–119.
- von Raumer, J. F., Finger, F., Veselá, P. & Stampfli, G. M. (2014). Durbachites-Vaugnerites – a geodynamic marker in the central European Variscan orogen. *Terra Nova* **26**, 85–95.
- Vosteen, H. D. & Schellschmidt, R. (2003). Influence of temperature on thermal conductivity, thermal capacity and thermal diffusivity for different types of rock. *Physics and Chemistry of the Earth* **28**, 499–509.
- Wada, H., Harayama, S. & Yamaguchi, Y. (2004). Mafic enclaves densely concentrated in the upper part of a vertically zoned felsic magma chamber: the Kurobegawa granitic pluton, Hida Mountain Range, central Japan. *Geological Society of America Bulletin* **116**, 788–801.
- Waldbaum, D. R. & Thompson Jr, J. B. (1968). Mixing properties of sanidine crystalline solutions: II. Calculations based on volume data. *American Mineralogist* **53**, 2000–2017.
- Walker, B. a., Miller, C. F., Lowery Claiborne, L., Wooden, J. L. & Miller, J. S. (2007). Geology and geochronology of the Spirit Mountain Batholith, southern Nevada: implications for timescales and physical processes of batholith construction. *Journal of Volcanology and Geothermal Research* **167**, 239–262.
- Wasserburg, G. J., Jacobsen, S. B., DePaolo, D. J., McCulloch, M. T. & Wen, T. (1981). Precise determination of Sm/Nd ratios, Sm and Nd isotopic abundances in standard solutions. *Geochimica et Cosmochimica Acta* **45**, 2311–2324.
- Watson, E. B. & Harrison, T. M. (1983). Zircon saturation revisited: temperature and composition effects in a variety of crustal magma types. *Earth and Planetary Science Letters* **64**, 295–304.
- Weinberg, R. F. (1997). Diapir-driven crustal convection: decompression melting, renewal of the magma source and the origin of nested plutons. *Tectonophysics* **271**, 217–229.
- Whitehead N. (2010) Oasis montaj 7.2 Mapping and Processing System, www.geosoft.com
- Whitehead N., Musselman Ch. (2010) Montaj MAGMAP Filtering, www.geosoft.com
- Whitney, D. L., & Evans, B. W. (2010). Abbreviations for names of rock-forming minerals. *American Mineralogist*, **95**, 185–187.

- Wiebe, R. A., Smith, D., Sturm, M., King, E. M. & Seckler, M. S. (1997). Enclaves in the Cadillac Mountain granite (Coastal Maine): samples of hybrid magma from the base of the chamber. *Journal of Petrology* **38**, 393–423.
- Wiedenbeck, M., Allé, P., Corfu, F., Griffin, W. L., Meier, M., Oberli, F., von Quadt, A., Roddick, J. C. & Spiegel, W. (1995). Three natural zircon standards for U-Th-Pb, Lu-Hf, trace element and REE analyses. *Geostandards Newsletter* **19**, 1–23.
- Wolff, J. A., Ramos, F. C. & Davidson, J. P. (1999). Sr isotope disequilibrium during differentiation of the Bandelier Tuff: constraints on the crystallization of a large rhyolitic magma chamber. *Geology* **27**, 495–498.
- Zachariáš, J. & Hübst, Z. (2012). Structural evolution of the Roudný gold deposit, Bohemian Massif: a combination of paleostress analysis and review of historical documents. *Journal of Geosciences* **57**, 87–103.
- Zeh, A. & Gerdes, A. (2012). U-Pb and Hf isotope record of detrital zircons from gold-bearing sediments of the Pietersburg Greenstone Belt (South Africa) - Is there a common provenance with the Witwatersrand Basin? *Precambrian Research* **204-205**, 46–56.
- Žák, J., Paterson, S. R., Janoušek, V. & Kabele, P. (2009). The Mammoth Peak sheeted complex, Tuolumne batholith, Sierra Nevada, California: a record of initial growth or late thermal contraction in a magma chamber? *Contributions to Mineralogy and Petrology* **158**, 447–470.
- Žák, J., Verner, K., Janoušek, V., Holub, F. V., Kachlík, V., Finger, F., Hajná, J., Tomek, F., Vondrovic, L. & Trubač, J. (2014). A plate-kinematic model for the assembly of the Bohemian Massif constrained by structural relationships around granitoid plutons. In: Schulmann, K., Martínez Catalán, J. R., Lardeaux, J. M., Janoušek, V. & Oggiano, G. (eds) *The Variscan Orogeny: Extent, Timescale and the Formation of the European Crust*. Geological Society London Special Publications **405**, 169–196.

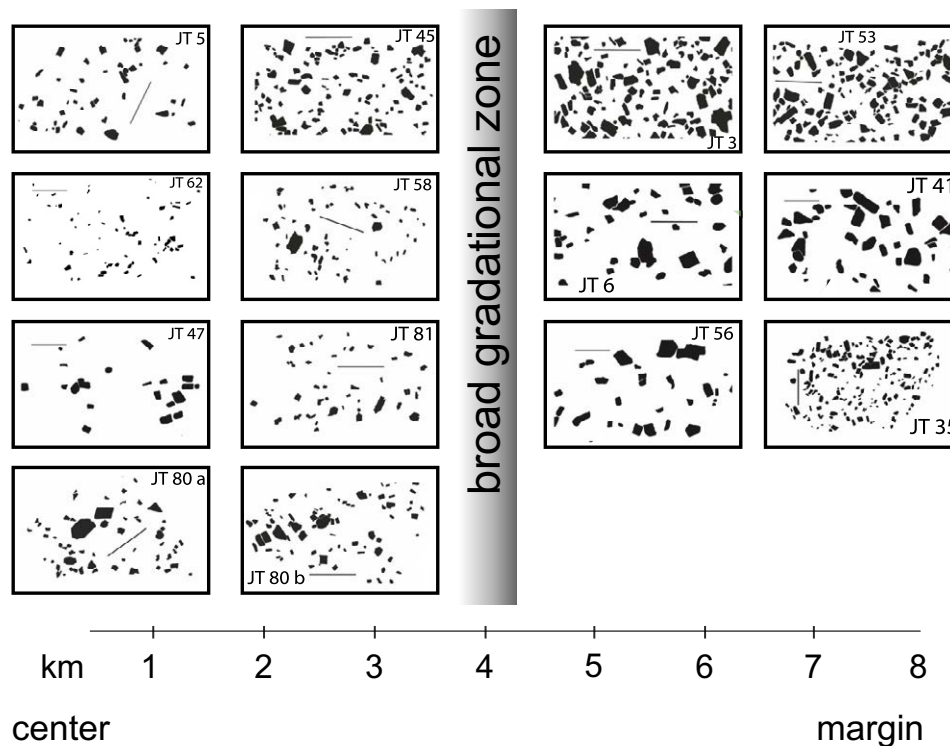
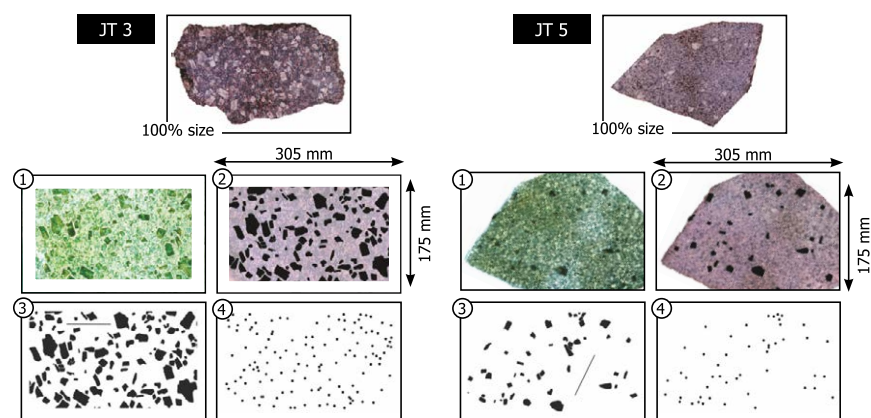
ELECTRONIC APPENDICES

Appendix 1: Values of density for both facies of the Říčany granite.

N = 15	volume density (g.cm^{-3})	mineral density (g.cm^{-3})	porosity (%)
SRG	2.601 ± 0.015	2.659 ± 0.010	2.162 ± 0.379
WRG	2.593 ± 0.022	2.644 ± 0.007	1.928 ± 0.920

* 1σ , excluding the calibration and analytical errors

Appendix 2: Methods of image analysis of the porphyritic sample of the Říčany granite



Appendix 3: Selected typical mineral analyses from the Řičany and Kšely granite

Sample	feldspars													
	SRG_Kfs6	SRG_Kfs9	WRG_Kfs8	WRG_Kfs9	Ks5	Ks6	Pl6	Pl7	Pl17T	Pl14T	PIKSG1	PIKSG10	ZV2A	ZV2A
Type	rim	core	rim	core	rim	core	rim	core	rim	core	rim	core	rim	core
Group	SPm	SPm	WPc	WPc	KG	KG	SPm	SPm	WPc	WPc	KG	KG	MA	MA
Mineral	Kfs	Kfs	Kfs	Kfs	Kfs	Kfs	Pl	Pl	Pl	Pl	Pl	Pl	Kfs	Pl
SiO ₂	65.10	64.80	64.98	64.51	64.82	64.03	65.30	67.21	68.51	64.05	65.77	64.78	64.70	66.30
TiO ₂	0.01	n.d.	n.d.	0.02	n.d.	0.05	0.01	0.02	n.d.	n.d.	n.d.	0.00	-	-
Al ₂ O ₃	18.33	18.05	17.64	17.93	18.36	18.63	21.75	20.27	19.30	21.76	20.85	22.10	18.74	20.45
FeOt	0.06	n.d.	n.d.	0.02	0.06	0.02	0.00	n.d.	0.14	0.04	0.56	0.05	-	-
MnO	n.d.	n.d.	n.d.	n.d.	n.d.	0.01	0.00	0.01	0.00	0.05	n.d.	0.00	-	-
MgO	n.d.	0.03	n.d.	n.d.	0.01	0.02	0.03	0.01	n.d.	0.00	0.02	0.01	-	-
CaO	0.02	0.03	n.d.	0.07	0.06	0.07	2.92	1.25	0.41	3.87	1.01	3.46	n.d.	1.13
Na ₂ O	1.16	0.69	0.75	1.35	1.36	1.44	9.80	11.04	11.79	9.42	10.59	9.53	0.86	10.95
K ₂ O	15.31	15.96	15.97	15.25	15.14	14.67	0.09	0.15	0.12	0.40	0.20	0.11	15.29	0.12
P ₂ O ₅	0.05	0.03	n.d.	n.d.	0.03	0.04	n.d.	0.06	n.d.	0.06	0.02	0.01	0.12	n.d.
BaO	0.29	0.24	0.38	0.54	0.31	0.47	0.06	0.11	n.d.	0.09	0.05	0.05	-	-
Total	99.99	99.56	99.33	99.15	99.80	98.93	99.97	100.12	100.27	99.72	99.06	100.11	99.79	99.01
Si apfu	3.00	3.01	3.02	3.00	2.99	2.98	2.87	2.94	2.99	2.84	2.92	2.85	2.98	2.93
Ti	0.00	0.00	0.00	0.00	0.00	0.00	0.00	0.00	0.00	0.00	0.00	0.00	-	-
Al	1.00	0.99	0.97	0.98	1.00	1.02	1.13	1.05	0.99	1.14	1.09	1.15	1.02	1.07
Fe	0.00	0.00	0.00	0.00	0.00	0.00	0.00	0.00	0.01	0.00	0.02	0.00	-	-
Mn	0.00	0.00	0.00	0.00	0.00	0.00	0.00	0.00	0.00	0.00	0.00	0.00	-	-
Mg	0.00	0.00	0.00	0.00	0.00	0.00	0.00	0.00	0.00	0.00	0.00	0.00	-	-
Ca	0.00	0.00	0.00	0.00	0.00	0.00	0.14	0.06	0.02	0.18	0.05	0.16	-	0.05
Na	0.10	0.06	0.07	0.12	0.12	0.13	0.84	0.94	1.00	0.81	0.91	0.81	0.08	0.94
K	0.90	0.94	0.95	0.91	0.89	0.87	0.00	0.01	0.01	0.02	0.01	0.01	0.90	0.01
P	0.00	0.00	0.00	0.00	0.00	0.00	0.00	0.00	0.00	0.00	0.00	0.00	0.01	-
Ba	0.01	0.00	0.01	0.01	0.01	0.01	0.00	0.00	0.00	0.00	0.00	0.00	-	-
An mol. %	0.07	0.15	0.00	0.35	0.27	0.36	14.06	5.82	1.86	18.08	4.94	16.62	0.00	5.34
Ab	10.32	6.16	6.64	11.82	11.95	12.91	85.43	93.34	97.47	79.71	93.92	82.73	7.87	93.97
Or	89.61	93.70	93.36	87.82	87.78	86.72	0.51	0.84	0.67	2.22	1.14	0.65	92.13	0.69
Cin	0.004	0.004	0.005	0.009	0.005	0.008	0.001	0.002	0.000	0.000	0.001	0.001	-	-

Calculated on the basis of 8 oxygen per formula unit.

n.d. - not detected

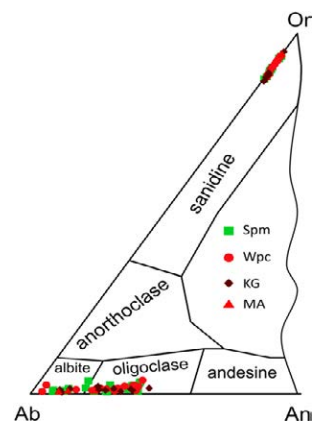
hom. - homogenous

SPm - strongly porphyritic granite

WPc - weakly porphyritic granite

KG - Kšely granite

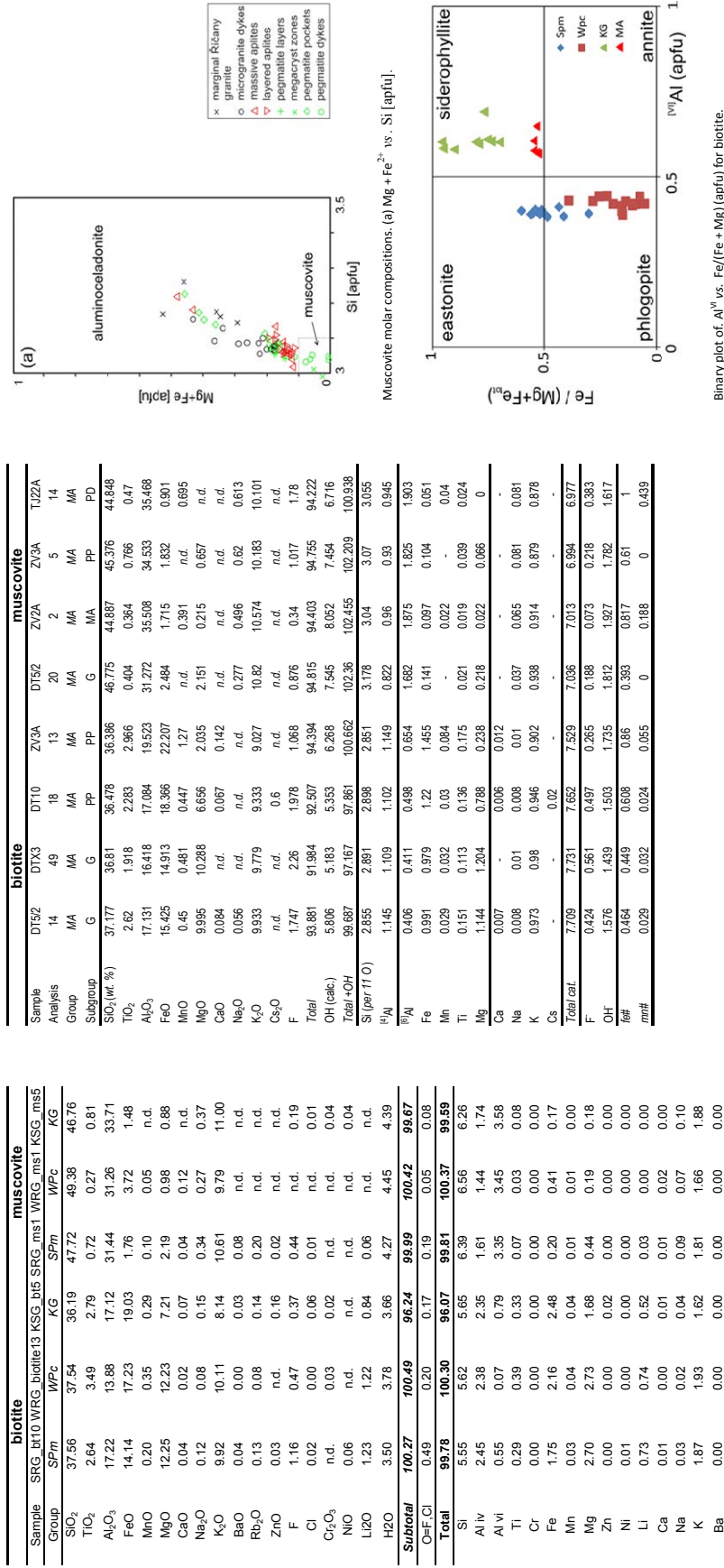
MA - marginal aplite



Ternary plot of Ab-Or-An (mol. %) for feldspars.

Magma Differentiation and Pluton Zoning

Appendix 3: Representative chemical composition of minerals of the Řičany and Kšely granite - MICAS



		biotite			muscovite				
Sample		SRG_bt10	WRG_biotite13	KG_bts	SRG_mst1	WRG_mst1	KG_mst1	KG_mst5	KG_mst5
Group		SPm	WPC	SPm	SPm	WPC	WPC	WPC	KG
SiO ₂		37.56	37.54	36.19	47.72	49.38	46.76	46.76	
TiO ₂		2.64	3.49	2.79	0.72	0.27	0.81	0.81	
Al ₂ O ₃		17.22	13.88	17.12	31.44	31.26	33.71	33.71	
FeO		14.14	17.23	19.03	1.76	3.72	1.48	1.48	
MnO		0.20	0.35	0.29	0.10	0.05	n.d.	n.d.	
MgO		12.25	12.23	7.21	2.19	0.98	0.88	0.88	
CaO		0.04	0.02	0.07	0.04	0.12	n.d.	n.d.	
Na ₂ O		0.12	0.08	0.15	0.34	0.27	0.37	0.37	
K ₂ O		9.92	10.11	8.14	10.61	9.79	11.00	11.00	
BaO		0.04	0.00	0.03	0.08	n.d.	n.d.	n.d.	
Rb ₂ O		0.13	0.08	0.14	0.20	n.d.	n.d.	n.d.	
ZnO		0.03	n.d.	0.16	0.02	n.d.	n.d.	n.d.	
F		1.16	0.47	0.37	0.44	n.d.	0.19	0.19	
Cl		0.02	0.00	0.06	0.01	n.d.	0.01	0.01	
Cl ₂ O ₃		n.d.	0.03	0.02	n.d.	n.d.	0.04	0.04	
NiO		0.06	n.d.	n.d.	n.d.	n.d.	0.04	0.04	
Li ₂ O		1.23	1.22	0.84	0.06	n.d.	n.d.	n.d.	
H ₂ O		3.50	3.78	3.66	4.27	4.45	4.39	4.39	
Subtotal		100.27	100.49	96.24	99.99	100.42	99.67	99.67	
OH/F		0.49	0.20	0.17	0.19	0.05	0.08	0.08	
Total		99.78	100.30	96.07	99.81	100.37	99.59	99.59	
Si		5.55	5.62	5.65	6.39	6.56	6.26	6.26	
Al iv		2.45	2.38	2.35	1.61	1.44	1.74	1.74	
Al vi		0.55	0.07	0.79	3.35	3.45	3.58	3.58	
Ti		0.29	0.39	0.33	0.07	0.03	0.08	0.08	
Cr		0.00	0.00	0.00	0.00	0.00	0.00	0.00	
Fe		1.75	2.16	2.48	0.20	0.41	0.17	0.17	
Mn		0.03	0.04	0.04	0.01	0.01	0.00	0.00	
Mg		2.70	2.73	1.68	0.44	0.19	0.18	0.18	
Zn		0.00	0.00	0.02	0.00	0.00	0.00	0.00	
Ni		0.01	0.00	0.00	0.00	0.00	0.00	0.00	
Li		0.73	0.74	0.52	0.03	0.00	0.00	0.00	
Ca		0.01	0.00	0.01	0.01	0.01	0.02	0.00	
Na		0.03	0.02	0.04	0.09	0.07	0.10	0.10	
K		1.87	1.93	1.62	1.81	1.66	1.88	1.88	
Ba		0.00	0.00	0.00	0.00	0.00	0.00	0.00	
Rb		0.01	0.01	0.01	0.02	0.00	0.00	0.00	
OH		3.45	3.78	3.80	3.81	3.95	3.92	3.92	
F		0.54	0.22	0.18	0.19	0.05	0.08	0.08	
Cl		0.01	0.00	0.02	0.00	0.00	0.00	0.00	
Total		19.98	20.11	19.55	18.03	17.83	17.98	17.98	
Y total		6.05	6.14	5.86	4.10	4.09	4.01	4.01	
X total		1.93	1.96	1.69	1.93	1.74	1.97	1.97	
Al total		3.00	2.45	3.15	4.96	4.89	5.32	5.32	
Fe/Fe+Mg		0.39	0.44	0.60	0.31	0.68	0.48	0.48	
Mg/(Mg+Fe)		0.61	0.56	0.40	0.69	0.32	0.52	0.52	

Calculated on the basis of 22 oxygen atoms, tetrahedral positions have full occupancy.

n.d. - not detected

SPm - strongly porphyritic granite
WPC - weakly porphyritic granite
KG - Kšely granite
MA - marginal a plite

Appendix 3: Representative chemical composition of minerals of the Říčany and Kšely granite - ZIRCONS

zircon			
Sample	SRG_zr2	Zrn4	Zrn10
Group	SRG	WRG	KSG
SiO ₂	31.23	32.35	31.33
TiO ₂	0.00	0.00	0.04
Al ₂ O ₃	0.00	0.05	0.06
P ₂ O ₅	0.14	0.00	0.29
FeO	0.03	0.17	0.49
MnO	0.00	0.00	0.01
CaO	0.01	0.02	0.00
Y ₂ O ₃	0.11	0.00	0.27
ZrO ₂	67.40	63.69	65.43
HfO ₂	1.13	1.77	1.35
Ce ₂ O ₃	0.00	0.00	n.d.
La ₂ O ₃	n.d.	0.03	n.d.
Nd ₂ O ₃	0.01	0.00	n.d.
Pr ₂ O ₃	0.01	0.06	n.d.
Sm ₂ O ₃	0.01	0.00	0.03
Eu ₂ O ₃	n.d.	0.00	n.d.
Gd ₂ O ₃	n.d.	0.00	n.d.
Tb ₂ O ₃	n.d.	0.00	n.d.
Dy ₂ O ₃	0.03	0.01	0.05
Ho ₂ O ₃	n.d.	0.05	n.d.
Er ₂ O ₃	n.d.	0.00	n.d.
Tm ₂ O ₃	0.01	0.04	0.04
Yb ₂ O ₃	0.07	0.01	0.11
Lu ₂ O ₃	n.d.	0.00	0.02
ThO ₂	0.02	0.02	0.02
U ₂ O ₃	0.16	0.09	0.02
Total	100.37	98.37	99.55
Si apfu	0.965	1.009	0.973
Ti	0.000	0.000	0.000
Al	0.000	0.002	0.002
P	0.004	0.000	0.008
Fe ²⁺	0.001	0.004	0.013
Mn	0.000	0.000	0.000
Ca	0.000	0.001	0.000
Y	0.002	0.000	0.004
Zr	1.016	0.969	0.991
Hf	0.010	0.016	0.012
Ce	0.000	0.000	0.000
La	0.000	0.000	0.000
Nd	0.000	0.000	0.000
Pr	0.000	0.001	0.000
Sm	0.000	0.000	0.000
Eu	0.000	0.000	0.000
Gd	0.000	0.000	0.000
Tb	0.000	0.000	0.000
Dy	0.000	0.000	0.000
Ho	0.000	0.001	0.000
Er	0.000	0.000	0.000
Tm	0.000	0.000	0.000
Yb	0.001	0.000	0.001
Lu	0.000	0.000	0.000
Th	0.000	0.000	0.000
U	0.002	0.001	0.000
A	1.033	0.993	1.024
B	0.969	1.011	0.983
sum cat.	2.001	2.004	2.007

Calculated on basis of 4 oxygens.

n.d. - not detected

SPm - strongly porphyritic granite
 WPc - weakly porphyritic granite
 KG - Kšely granite

Appendix 3: Representative chemical composition of minerals of the Říčany and Kšely granite - MONAZITES

monazite			
Sample	SRG_mnz3	Mnz8	KSG_mnz4
Group	SPm	WPc	KG
SiO ₂	1.43	1.89	0.94
Al ₂ O ₃	n.d.	0.01	n.d.
MgO	n.d.	n.d.	n.d.
K ₂ O	26.44	26.61	28.41
CaO	n.d.	0.00	n.d.
P ₂ O ₅	n.d.	0.12	n.d.
SO ₂	1.24	0.41	1.49
Sc ₂ O ₃	0.81	0.55	1.54
FeO	27.20	32.74	25.31
As ₂ O ₃	14.28	15.07	12.88
Y ₂ O ₃	9.40	9.35	10.65
ZrO ₂	2.66	2.87	2.75
SnO	1.11	1.07	1.83
Ce ₂ O ₃	n.d.	n.d.	n.d.
PbO	1.63	0.48	1.98
ThO ₂	n.d.	0.08	n.d.
UO ₂	0.23	0.04	0.50
HfO ₂	n.d.	0.01	0.01
SmO	0.09	0.05	0.27
Gd ₂ O ₃	0.05	0.08	0.09
Dy ₂ O ₃	0.09	n.d.	0.08
Er ₂ O ₃	0.00	n.d.	0.02
Yb ₂ O ₃	12.36	8.18	11.47
Nb ₂ O ₅	1.01	0.50	0.66
Total	100.02	100.11	100.88
Si	0.058	0.077	0.037
Al	0.000	0.000	0.000
Mg	0.000	0.000	0.000
K	0.000	0.912	0.000
Ca	0.000	0.000	0.000
P	0.000	0.004	0.000
S	0.054	0.018	0.063
Sc	0.018	0.012	0.032
Fe	0.407	0.485	0.367
As	0.215	0.225	0.188
Y	0.137	0.135	0.151
Zr	0.040	0.042	0.040
Sn	0.016	0.015	0.025
Ce	0.000	0.000	0.000
Pb	0.022	0.006	0.026
Th	0.000	0.001	0.000
U	0.003	0.000	0.006
Hf	0.000	0.000	0.000
Sm	0.001	0.001	0.003
Gd	0.001	0.001	0.001
Dy	0.001	0.000	0.001
Er	0.000	0.000	0.000
Yb	0.115	0.075	0.103
F	0.009	0.005	0.006
Nb	1.016	1.020	0.987
site A	0.974	0.988	0.990
site B	1.990	2.015	1.977

Calculated on basis of 4 oxygens

n.a. - not analyzed

n.d. - not detected

SPm - strongly porphyritic granite
 WPc - weakly porphyritic granite
 KG - Kšely granite

Appendix 3: Representative chemical composition of minerals of the Říčany and Kšely granite - APO₄

APO ₄	
Sample	Th 6
Group	WPc
SiO ₂	13.25
Al ₂ O ₃	0.84
MgO	0.21
K ₂ O	0.09
CaO	4.29
P ₂ O ₅	6.10
SO ₂	0.16
Sc ₂ O ₃	0.00
TiO ₂	0.04
MnO	0.50
FeO	10.60
As ₂ O ₃	0.29
Y ₂ O ₃	0.19
ZrO ₂	24.51
SnO	0.03
Ce ₂ O ₃	1.88
PbO	0.21
ThO ₂	31.07
UO ₂	1.19
HfO ₂	0.53
SmO	0.39
Gd ₂ O ₃	0.05
Dy ₂ O ₃	0.18
Er ₂ O ₃	0.01
Yb ₂ O ₃	0.15
Nb ₂ O ₅	0.05
Total	96.81
Si	0.550
Al	0.041
Mg	0.013
K	0.005
Ca	0.191
P	0.214
S	0.006
Sc	0.000
Ti	0.001
Mn	0.018
Fe	0.368
As	0.007
Y	0.004
Zr	0.496
Sn	0.001
Ce	0.029
Pb	0.002
Th	0.294
U	0.011
Hf	0.006
Sm	0.006
Gd	0.001
Dy	0.002
Er	0.000
Yb	0.002
F	0.000
Nb	0.001
site A	0.820
site B	1.451

Calculated on the basis of four oxygen atoms per
Site B includes Si, Al, P, As and S, the site A .

Appendix 3: Representative chemical composition of minerals of the Kšely granite - XENOTIME

xenotime	
Sample	17
Group	KG
SiO ₂	0.48
TiO ₂	0.01
FeO	0.20
CaO	0.25
UO ₂	2.61
ThO ₂	0.41
PbO	0.40
P ₂ O ₅	34.65
Y ₂ O ₃	40.56
La ₂ O ₃	0.03
Ce ₂ O ₃	0.19
Pr ₂ O ₃	0.04
Nd ₂ O ₃	0.52
Sm ₂ O ₃	0.23
Gd ₂ O ₃	1.84
Tb ₂ O ₃	0.55
Dy ₂ O ₃	5.03
Ho ₂ O ₃	1.09
Er ₂ O ₃	4.80
Tm ₂ O ₃	0.69
Yb ₂ O ₃	4.04
Lu ₂ O ₃	1.22
Total	99.84
Si	0.016
Ti	0.000
Fe	0.006
Zn	0.000
Ca	0.009
U	0.020
Th	0.003
Pb	0.004
P	0.992
Y	0.730
La	0.000
Ce	0.002
Pr	0.000
Nd	0.006
Sm	0.003
Gd	0.021
Tb	0.006
Dy	0.055
Ho	0.012
Er	0.051
Tm	0.007
Yb	0.042
Lu	0.012
sum cat.	2.00

Calculated on basis of 4 oxygens.

KG - Kšely granite

Appendix 3: Representative chemical composition of minerals of the Říčany granite - ALLANITE

allanite	
Sample	12
Group	<i>SPm</i>
SiO ₂	31.17
TiO ₂	0.18
Al ₂ O ₃	19.04
FeO	9.75
MnO	0.30
CaO	12.85
ZrO ₂	0.01
Y ₂ O ₃	0.08
La ₂ O ₃	5.41
Ce ₂ O ₃	11.01
Pr ₂ O ₃	1.15
Nd ₂ O ₃	3.92
Sm ₂ O ₃	0.42
Gd ₂ O ₃	0.68
Dy ₂ O ₃	0.05
Er ₂ O ₃	0.07
Tm ₂ O ₃	0.03
Yb ₂ O ₃	0.00
Total	96.13
Si	2.96
Al(IV)	0.04
ΣT	3.00
Al(VI)	2.09
Ti	0.01
Fe	0.77
Mn	0.02
ΣM	2.90
Ca	1.31
Zr	0.00
Hf	0.00
Y	0.00
La	0.19
Ce	0.38
Pr	0.04
Nd	0.13
Pm	0.00
Sm	0.01
Gd	0.02
Tb	0.00
Dy	0.00
Ho	0.00
Er	0.00
Tm	0.00
Yb	0.00
ΣA	2.10

Calculated on the basis of 8 cations.
Al(IV) calculated as 3-Si apfu

SPm - strongly porphyritic granite

Appendix 3: Representative chemical composition of minerals of the Říčany and Kšely granite - APATITES

apatite			
Sample	SRG_ap3	WRG_apatite1	KSG_ap1
Group	<i>SPm</i>	<i>WPc</i>	<i>KG</i>
P ₂ O ₅	42.78	42.75	42.53
SiO ₂	n.d.	0.05	n.d.
Al ₂ O ₃	0.02	0.00	n.d.
FeO	n.d.	0.04	0.20
MnO	n.d.	0.04	0.08
MgO	0.01	n.d.	n.d.
CaO	54.77	55.60	54.66
Na ₂ O	0.09	n.d.	0.06
K ₂ O	0.08	n.d.	n.d.
SrO	0.09	n.d.	0.10
BaO	0.10	n.d.	n.d.
ZnO	0.01	n.d.	n.d.
F	3.36	3.15	4.17
Cl	0.01	0.01	0.03
F corr.	3.36	3.15	4.17
H ₂ O*	0.20	0.31	0.00
Subtotal	101.50	101.94	101.83
O=F,Cl	1.42	1.33	1.76
Total	100.09	100.62	100.07
P	6.06	6.02	6.04
Si	0.00	0.01	0.00
Al	0.00	0.00	0.00
Fe	0.00	0.01	0.03
Mn	0.00	0.01	0.01
Mg	0.00	0.00	0.00
Zn	0.00	0.00	0.00
Ca	9.81	9.91	9.83
Na	0.03	0.00	0.02
K	0.02	0.00	0.00
Sr	0.01	0.00	0.01
Ba	0.01	0.00	0.00
OH*	0.22	0.34	0.00
F	1.78	1.66	2.21
Cl	0.00	0.00	0.01
Total	17.93	17.96	18.16
A sum	6.06	6.02	6.04
B sum	9.88	9.92	9.90
C sum	2.00	2.00	2.22

Calculated based on 25 oxygens.
H₂O calculated on the basis of filling the C site.
n.d. - not detected

SPm - strongly porphyritic granite
WPc - weakly porphyritic granite
KG - Kšely granite

Appendix 3: Representative chemical composition of minerals of the Marginal aplite (MA) and pegmatite - GARNET

Sample	TJ10A	TJ16	TJ16	TJ6A	TD2	TD2	TJ22A	TJ22A
Analysis	39	26	27	33	1	2	1	3
Group	MA	MA	MA	MA	MA	MA	MA	MA
Subgroup	LA	LA	LA	PL-band	PL	PL	PD	PD
position	rim	center	rim	center	center	rim	center	rim
SiO ₂ (wt. %)	34.838	34.826	35.343	33.896	33.449	35	34.709	35.012
TiO ₂	0.095	0.241	<i>n.d.</i>	0.363	0.326	0.15	0.277	0.131
Al ₂ O ₃	19.996	19.965	20.151	19.806	19.597	19.563	19.999	20.186
FeO	23.133	17.924	20.151	16.672	11.366	14.499	7.519	4.651
MnO	19.507	25.49	23.343	26.426	31.891	28.898	36.101	38.518
MgO	0.134	<i>n.d.</i>	0.118	0.084	<i>n.d.</i>	<i>n.d.</i>	<i>n.d.</i>	<i>n.d.</i>
CaO	0.376	0.254	0.351	0.213	0.37	0.393	0.386	0.351
P ₂ O ₅	<i>n.d.</i>	<i>n.d.</i>	<i>n.d.</i>	<i>n.d.</i>	0.192	0.087	0.13	<i>n.d.</i>
Total	98.127	98.767	99.554	97.641	97.19	98.59	99.121	98.939
OH (calc.)	1.389	1.711	1.371	2.52	2.932	1.204	2.093	1.649
Total + OH	99.517	100.478	100.925	100.161	100.167	99.8	101.214	100.588
P (per 5 cat.)	-	-	-	-	0.013	0.006	0.009	-
Si	2.898	2.875	2.901	2.809	2.772	2.906	2.84	2.88
Al	1.961	1.943	1.949	1.935	1.914	1.914	1.929	1.957
Fe ³⁺	0.033	0.042	0.051	0.043	0.065	0.076	0.054	0.035
Ti	0.006	0.015	-	0.023	0.02	0.009	0.017	0.008
Mg	0.017	-	0.014	0.01	-	-	-	-
Fe ²⁺	1.576	1.195	1.332	1.113	0.722	0.93	0.46	0.285
Mn	1.374	1.782	1.623	1.855	2.238	2.032	2.502	2.684
Ca	0.034	0.022	0.031	0.019	0.033	0.035	0.034	0.031
Total cat.	7.898	7.875	7.901	7.812	7.779	7.909	7.844	7.88
Total O	11.782	11.737	11.776	11.621	11.548	11.79	11.679	11.747
OH	0.408	0.499	0.398	0.738	0.859	0.353	0.605	0.479
<i>mn#</i>	0.466	0.599	0.549	0.625	0.756	0.686	0.845	0.904

n.d. – below detection limit, LA – layered aplites, PL – pegmatite layers, PD – pegmatite dykes

MA - marginal aplite

Appendix 3: Representative chemical composition of minerals of the Marginal aplite (MA) and pegmatite - TOURMALINES

Sample	TDX2	TDX2	TJ10A	TJ10A	TJ10A	TJ6A	DT20/1	DT10	TJ22A	TJ22A
Analysis	26	25	16	15	24	5	14	12	23	21
Group	MA	MA	MA	MA	MA	MA	MA	MA	MA	MA
Subgroup	AD	AD	LA	LA	LA	PL	MZ	PP	PD	PD
zone in grain	dark	light	dark	light	unzonal	dark	dark	light	light	dark
SiO ₂ (wt. %)	35.022	34.367	34.324	33.745	33.646	35.243	35.113	34.137	33.577	35.072
TiO ₂	1.191	0.786	0.859	0.891	0.383	0.35	0.4	0.486	0.881	0.429
Al ₂ O ₃	32.007	33.053	32.105	32.857	33.022	35.074	35.195	32.55	33.393	36.747
FeO	7.993	11.76	11.231	13.507	13.879	14.001	9.002	11.425	12.807	4.155
MnO	0.098	0.268	0.151	0.364	0.552	0.541	<i>n.d.</i>	<i>n.d.</i>	1.388	3.922
MgO	5.614	2.627	3.673	1.555	1.057	0.672	3.533	3.053	0.518	0.384
CaO	0.397	0.129	0.29	0.153	0.147	<i>n.d.</i>	0.13	0.21	0.145	0.332
Na ₂ O	2.319	1.999	2.115	2.006	1.99	1.498	1.676	1.977	1.968	2.514
K ₂ O	0.078	0.04	0.049	0.063	0.071	<i>n.d.</i>	<i>n.d.</i>	<i>n.d.</i>	0.087	<i>n.d.</i>
F	0.445	<i>n.d.</i>	0.281	<i>n.d.</i>	<i>n.d.</i>	<i>n.d.</i>	<i>n.d.</i>	0.513	0.449	1.383
Total	84.976	85.11	84.965	85.193	84.746	87.444	85.169	84.302	85.024	84.36
B ₂ O ₃ (calc.)	10.288	10.185	10.175	10.089	10.024	10.431	10.394	10.079	10.096	10.353
Total + B ₂ O ₃	95.264	95.295	95.141	95.282	94.771	97.875	95.563	94.381	95.12	94.713
(per T+Z+Y=15)									(per 24.5 O)	
Si	5.917	5.865	5.864	5.814	5.834	5.873	5.872	5.888	5.781	5.888
^T Al	0.083	0.135	0.136	0.186	0.166	0.127	0.128	0.112	0.219	0.112
^Z Al	6	6	6	6	6	6	6	6	6	6
^Y Al	0.292	0.514	0.328	0.486	0.584	0.762	0.81	0.505	0.558	1.161
Ti	0.151	0.101	0.11	0.115	0.05	0.044	0.05	0.063	0.114	0.054
Fe	1.129	1.678	1.604	1.946	2.012	1.951	1.259	1.648	1.844	0.583
Mn	0.014	0.039	0.022	0.053	0.081	0.076	-	-	0.202	0.558
Mg	1.414	0.668	0.935	0.399	0.273	0.167	0.881	0.785	0.133	0.096
Li	-	-	-	-	-	-	-	-	0.044	0.491
Ca	0.072	0.024	0.053	0.028	0.027	-	0.023	0.039	0.027	0.06
Na	0.759	0.661	0.7	0.67	0.669	0.484	0.543	0.661	0.657	0.818
K	0.017	0.009	0.011	0.014	0.016	-	-	-	0.019	-
Total cat.	15.848	15.694	15.764	15.712	15.712	15.484	15.566	15.7	15.554	15.331
Total O	24.716	24.649	24.615	24.636	24.628	24.603	24.686	24.628	24.5	24.5
F ⁻	0.238	-	0.152	-	-	-	-	0.28	0.244	0.734
mg#	0.556	0.285	0.368	0.17	0.12	0.079	0.412	0.323	0.067	0.141
mn#	0.012	0.023	0.013	0.027	0.039	0.038	0	0	0.099	0.489

n.d. – below detection limit, AD – aplite dykes, LA – layered aplites, PL – pegmatite layers, MZ – megacryst zones, PP – pegmatite pockets, PD – pegmatite dykes, MA – marginal aplite

Appendix 3: Representative chemical composition of minerals of the Řičany and Kšely granite - RUTILES

rutile			
Sample	SRG_rt5	WRG_rutile1	KsG
Group	SPm	WPc	KG
SiO ₂	0.03	0.51	0.12
TiO ₂	89.96	98.82	97.44
Al ₂ O ₃	0.24	0.01	0.03
FeO	2.25	0.46	1.67
MnO	0.03	n.d.	0.01
MgO	0.01	n.d.	0.02
CaO	0.00	0.10	n.d.
Cr ₂ O ₃	0.23	n.d.	0.01
NiO	n.d.	n.d.	0.01
Sc ₂ O ₃	0.02	n.d.	n.d.
Nb ₂ O ₅	5.33	n.d.	0.24
Ta ₂ O ₅	2.05	n.d.	0.11
UO ₂	n.d.	0.03	n.d.
ThO ₂	n.d.	0.02	n.d.
ZrO ₂	0.09	n.d.	0.11
HfO ₂	n.d.	n.d.	0.32
P ₂ O ₅	0.02	n.d.	n.d.
Y ₂ O ₃	0.01	0.06	0.02
Ce ₂ O ₃	n.d.	0.14	n.d.
Pr ₂ O ₃	n.d.	0.04	n.d.
Eu ₂ O ₃	n.d.	0.05	n.d.
Dy ₂ O ₃	n.d.	0.01	n.d.
Ho ₂ O ₃	n.d.	0.04	n.d.
Er ₂ O ₃	n.d.	0.00	n.d.
Tm ₂ O ₃	n.d.	0.02	n.d.
Yb ₂ O ₃	n.d.	0.02	n.d.
Lu ₂ O ₃	n.d.	0.00	n.d.
Total	100.27	100.32	100.12
Si	0.000	0.007	0.002
Al	0.004	0.000	0.000
Ti	0.930	0.988	0.984
Fe	0.026	0.005	0.019
Mn	0.000	0.000	0.000
Mg	0.000	0.000	0.000
Ca	0.000	0.001	0.000
Cr	0.002	0.000	0.000
Ni	0.000	0.000	0.000
Sc	0.000	0.000	0.000
Nb	0.033	0.000	0.001
Ta	0.008	0.000	0.000
U	0.000	0.000	0.000
Th	0.000	0.000	0.000
Zr	0.001	0.000	0.001
Hf	0.000	0.000	0.001
P	0.000	0.000	0.000
Y	0.000	0.000	0.000
Ce	0.000	0.001	0.000
Pr	0.000	0.000	0.000
Eu	0.000	0.000	0.000
Dy	0.000	0.000	0.000
Ho	0.000	0.000	0.000
Er	0.000	0.000	0.000
Tm	0.000	0.000	0.000
Yb	0.000	0.000	0.000
Lu	0.000	0.000	0.000
sum cat.	1.005	1.004	1.009

Calculated on basis of 2 oxygens.
n.d. - not detected

SPm - strongly porphyritic granite
WPc - weakly porphyritic granite
KG - Kšely granite

Appendix 3: Representative chemical composition of minerals of the Řičany and Kšely granite - TITANITES

titanite	
Sample	Ttn4
Group	WPc
SiO ₂	30.3
TiO ₂	36.32
Al ₂ O ₃	2.44
P ₂ O ₅	0.02
Fe ₂ O ₃	1.08
MnO	0.11
CaO	27.23
Y ₂ O ₃	0.36
Ce ₂ O ₃	0.5
La ₂ O ₃	0.07
Nd ₂ O ₃	0.6
Pr ₂ O ₃	0.23
Sm ₂ O ₃	0.02
Gd ₂ O ₃	0.15
Tb ₂ O ₃	0.08
Dy ₂ O ₃	0.08
Ho ₂ O ₃	0.02
Er ₂ O ₃	0.03
Tm ₂ O ₃	0.02
Yb ₂ O ₃	0.01
ThO ₂	0.02
U ₂ O ₃	0.01
Total	99.66
Si apfu	1.001
Ti	0.903
Al	0.095
P	0.001
Fe ³⁺	0.027
Mn	0.003
Ca	0.964
Y	0.006
Ce	0.006
La	0.001
Nd	0.007
Pr	0.003
Sm	0.000
Gd	0.002
Tb	0.001
Dy	0.001
Ho	0.000
Tm	0.000
Yb	0.000
Th	0.000
U	0.000
sum cat.	3.021

Calculated on the basis of 5 oxygen atoms per formula
All iron expressed as Fe₂O₃.

WPc - weakly porphyritic granite

Appendix 3: Representative chemical composition of minerals of the Řičany granite
- MAGNETITE

magnetite	
Sample	Mgt1
Group	WPc
SiO ₂	0.03
TiO ₂	0.01
Al ₂ O ₃	0.04
FeOt	95.55
MnO	1.17
CaO	0.01
Total	96.81
Si apfu	0.004
Ti	0.001
Al	0.005
Fe ²⁺	0.964
Fe ³⁺	1.995
Mn	0.037
Ca	0

Calculated on the basis of 2 cations per formula unit.

Fe³⁺ and Fe²⁺ calculated by charge balance based on three oxygen atoms.

WPc - weakly porphyritic granite

Appendix 3: Representative chemical composition of minerals of the Řičany granite - ILMENITE

ilmenite	
Sample	357 (15)
Group	WPc
SiO ₂	0.01
TiO ₂	51.06
Al ₂ O ₃	0.00
P ₂ O ₅	0.01
FeO	42.71
MnO	4.34
CaO	0.01
Y ₂ O ₃	0.01
U ₂ O ₃	0.01
Total	98.15
Fe	0.92
Si apfu	0.00
Ti	0.99
Al	0.00
P	0.00
Fe ³⁺	0.03
Fe ²⁺	0.89
Mn	0.09
Ca	0.00
Y	0.00
U	0.00

Calculated on the basis of 2 cations per formula unit.

Fe³⁺ and Fe²⁺ calculated by charge balance based on three oxygen atoms.

WPc - weakly porphyritic granite

Appendix 4: Major- and trace-element whole-rock geochemical analyses from the Řičany and Kšely granite (wt. % and ppm, respectively)

Sample	TR10	TR18	TR13	RiE-4	RiE-3	TR17
Intrusion	KSG	MME	MME	MME	MME	MME
Ba	1054	727	752	871	543	279
Rb	278.5	487.0	397.7	331.0	314.2	277.3
Sr	359.1	211.3	297.3	337.0	309.7	260.6
Be	6	16	12	14	15	17
Cs	15.7	86.2	42.8	24.6	45.1	38.2
Ga	24.5	27.0	22.9	25.0	25.1	25.0
Nb	15.8	48.0	28.2	22.1	24.4	27.4
Th	28.2	76.9	57.8	60.0	53.9	46.8
U	4.2	9.3	12.4	5.6	10.6	3.9
Zr	316.5	529.0	363.9	341.0	298.1	299.4
Hf	10.2	16.9	11.6	9.3	9.7	10.6
Mo	0.1	<5	<5	<5	0.1	<5
Cu	1.9	4.1	4.2	30.0	10.2	2.4
Pb	8.2	13.6	10.0	54.0	9.4	8.2
Zn	78	163	93	70	86	104
Ni	38.1	128.3	72.5	40.0	41.4	60.2
Co	8.3	18.9	13.3	10.0	11.2	11.7
As	0.5	5.2	8.1	9.0	7.2	3.3
Au	0.5	3.5	2.0	<5	0.9	1.2
Sb	0.1	0.2	0.2	0.9	1.4	0.3
Bi	0.1	0.4	0.5	0.5	0.9	0.4
V	46	90	50	53	49	56
Cr	99	251	242	160	151	195
Sn	3	41	17	13	16	19
W	0.2	0.1	0.1	<5	0.2	0.1
Sc	4.5	11.2	7.6	9.0	6.7	7.7
Tl	1.1	4.4	2.5	2.8	2.1	2.5
Rb/Sr	0.78	2.30	1.34	1.01	1.00	1.06
Rb/Ba	0.26	0.67	0.53	0.38	0.58	0.99
Y	11.1	30.0	15.6	15.4	15.2	14.2
La	28.7	57.7	36.4	54.4	40.5	19.3
Ce	60.7	134.9	91.5	126.0	88.6	60.3
Pr	7.15	18.87	11.94	14.20	11.35	7.22
Nd	26.5	80.0	52.4	54.0	45.0	31.0
Sm	4.63	14.05	9.27	9.20	7.54	5.88
Eu	1.14	0.88	0.87	0.92	0.79	0.63
Gd	3.36	9.74	5.50	5.45	4.65	4.08
Tb	0.49	1.24	0.66	0.60	0.63	0.56
Dy	2.14	5.87	2.97	2.99	2.82	2.77
Ho	0.37	0.94	0.48	0.51	0.49	0.43
Er	0.99	2.44	1.24	1.34	1.31	1.17
Tm	0.15	0.38	0.2	0.18	0.21	0.17
Yb	0.80	2.13	1.12	1.12	1.11	1.00
Lu	0.12	0.28	0.16	0.17	0.16	0.14
ΣREE	137.2	329.4	214.7	271.1	205.2	134.7
La_N/Yb_N	24.19	18.26	21.91	32.75	24.6	13.01
Eu/Eu*	0.88	0.23	0.37	0.40	0.41	0.39

Appendix 4: continued

Sample	TR12	RiE-1	RiE-2	TR11	Ri7	Ri18
Intrusion	MME	MME	MME	FEL	WRG	WRG
Ba	570	785	807	1111	1316	721
Rb	336.2	340.3	331.2	319.1	311.3	359.9
Sr	309.7	326.2	340.8	360.8	471.6	309.5
Be	16	17	12	13	10	14
Cs	38.5	22.7	24.0	51.0	23.1	60.0
Ga	25.9	23.4	23.3	20.7	21.9	24.2
Nb	26.1	31.0	20.3	21.6	18.7	15.6
Th	57.5	74.5	42.2	44.2	39.1	30.6
U	9.5	11.3	8.8	12.4	15.6	4.8
Zr	331.5	371.8	254.6	254.4	272.5	178.6
Hf	11.5	12.7	8.2	8.4	8.8	6.4
Mo	<5	0.4	0.3	<5	<5	0.2
Cu	5.4	13.7	4.6	0.7	2.1	5.1
Pb	10.5	6.8	6.8	11.0	20.4	7.0
Zn	88	53	50	29	47	48
Ni	39.7	63.0	55.2	7.5	16.5	13.9
Co	11.0	13.5	8.8	2.8	4.3	3.8
As	5.7	6.8	6.4	5.8	15.7	2.3
Au	2.0	1.0	0.8	2.3	4.1	0.9
Sb	0.8	0.2	0.2	0.5	0.4	0.3
Bi	0.7	0.9	0.5	1.2	0.9	0.9
V	50	53	32	14	21	19
Cr	221	283	165	13	41	34
Sn	19	14	14	11	9	23
W	0.1	0.2	0.4	0.2	0.1	0.3
Sc	7.1	7.4	4.7	2.7	3.1	3.5
Ti	2.1	2.2	1.6	0.6	0.8	1.2
Rb/Sr	1.09	1.11	0.97	0.88	0.66	1.16
Rb/Ba	0.59	0.43	0.41	0.29	0.24	0.50
Y	15.9	13.3	10.9	11.3	10.5	10.6
La	38.6	46.7	41.4	45.6	37.9	29.6
Ce	88.4	114.2	84.7	93.6	75.2	57.7
Pr	11.59	17.08	10.73	11.03	8.53	6.44
Nd	48.5	75.9	41.1	40.0	30.7	22.4
Sm	8.31	12.14	6.72	5.96	4.94	3.64
Eu	0.81	1.39	0.91	0.9	0.91	0.65
Gd	4.89	5.92	3.82	3.58	3.15	2.73
Tb	0.64	0.65	0.50	0.50	0.42	0.40
Dy	2.95	2.94	2.17	2.42	2.08	2.00
Ho	0.49	0.43	0.35	0.40	0.33	0.36
Er	1.38	1.13	0.93	1.04	0.9	0.9
Tm	0.21	0.19	0.15	0.16	0.14	0.14
Yb	1.16	1.19	0.83	0.9	0.82	0.88
Lu	0.16	0.16	0.13	0.13	0.11	0.12
ΣREE	208.1	280.0	194.4	206.2	166.1	128.0
La_N/Yb_N	22.43	26.46	33.63	34.16	31.16	22.68
Eu/Eu*	0.39	0.50	0.55	0.60	0.71	0.63

Appendix 4: continued

Sample	Ri2	Ri14	Ri9	Ri15	TR16	Ri3
Intrusion	WRG	WRG	WRG	WRG	WRG	WRG
Ba	1078	857	1006	961	899	1011
Rb	336.4	333.5	316.3	344.7	301.1	326.3
Sr	385.7	351.6	368.7	297.4	378.7	378.4
Be	12	13	13	12	13	11
Cs	42.1	41.7	42.5	35.7	29.5	40.8
Ga	22.2	22.7	21.9	21.5	22.1	22.7
Nb	20.4	17.0	17.9	19.0	17.8	19.7
Th	37.7	33.1	35.4	37.3	34.7	38.0
U	20.7	6.0	11.3	5.0	5.0	21.1
Zr	239.4	199.6	223.7	220.4	218.9	235.6
Hf	8.2	6.5	7.4	7.4	7.4	7.5
Mo	0.4	0.2	0.2	0.1	<5	0.3
Cu	1.7	4.3	6.6	5.3	1.5	1.7
Pb	8.9	7.4	11.1	11.9	11.1	8.6
Zn	42	40	39	44	40	38
Ni	17.9	12.4	15.4	13.2	14.0	16.8
Co	3.9	3.9	4.1	3.6	3.4	3.8
As	10.8	4.9	10.3	1.9	5.4	12.9
Au	12.3	0.6	3.0	1.8	1.7	9.3
Sb	0.9	0.4	0.8	0.7	0.4	0.9
Bi	1.2	0.8	1.2	1.1	1.0	1.2
V	19	17	18	18	17	18
Cr	47	30	37	34	34	44
Sn	17	18	17	15	11	16
W	0.3	<5	0.2	0.3	0.2	0.2
Sc	3.3	2.9	3.1	2.9	3.5	3.1
Tl	0.9	0.8	0.8	0.9	0.9	0.8
Rb/Sr	0.91	0.95	0.86	1.16	0.80	0.86
Rb/Ba	0.31	0.39	0.31	0.36	0.33	0.32
Y	10.9	10.0	9.8	11.0	9.7	10.7
La	37.6	31.5	33.5	35.0	28.2	37.7
Ce	75.9	61.4	66.9	69.8	62.5	75.3
Pr	8.66	6.82	7.63	8.04	7.04	8.62
Nd	30.7	24.5	27.3	29.0	24.5	30.6
Sm	4.86	3.99	4.22	4.50	4.17	4.74
Eu	0.84	0.70	0.77	0.73	0.80	0.78
Gd	3.15	2.59	2.67	2.95	2.68	2.99
Tb	0.43	0.37	0.35	0.4	0.37	0.4
Dy	2.12	1.92	1.74	2.06	1.90	1.90
Ho	0.35	0.31	0.30	0.34	0.30	0.33
Er	0.95	0.85	0.86	0.92	0.88	0.90
Tm	0.14	0.13	0.14	0.16	0.14	0.13
Yb	0.89	0.84	0.78	0.87	0.79	0.87
Lu	0.12	0.11	0.10	0.12	0.11	0.11
ΣREE	166.7	136.0	147.3	154.9	134.4	165.4
La_N/Yb_N	28.48	25.28	28.96	27.12	24.07	29.22
Eu/Eu*	0.66	0.67	0.70	0.61	0.73	0.63

Appendix 4: continued

Sample	Ri16	Ri13	Ri19	Ri8	Ri10	Ri11
Intrusion	WRG	WRG	WRG	WRG	WRG	WRG
Ba	974	853	737	962	871	871
Rb	327.8	326.4	356.7	310.5	329.3	347.1
Sr	352.7	342.4	310.5	362.3	335.4	324.7
Be	14	11	16	13	16	14
Cs	20.1	40.5	57.1	44.5	45.8	47.2
Ga	22.8	22.1	24.1	20.9	22.2	22.7
Nb	19.7	15.4	14.2	18.1	19.0	19.1
Th	34.2	31.0	27.6	32.6	31.8	33.0
U	7.1	10.6	4.6	16.9	21.2	5.2
Zr	219.6	186.4	174.9	211.8	190.9	189.4
Hf	7.5	6.3	6	7.1	6.3	6.1
Mo	<5	<5	<5	0.2	0.6	0.1
Cu	4.3	3.8	3.3	5.5	2.2	6.0
Pb	21.5	12.0	7.6	12.9	18.1	12.7
Zn	41	38	45	40	38	39
Ni	14.2	11.5	12.6	14.9	14.9	11.4
Co	4.2	3.5	3.4	3.7	3.5	3.6
As	4.6	6.0	3.4	17.8	20.8	5.8
Au	1.7	1.5	1.0	3.3	2.6	2.0
Sb	0.3	0.4	0.3	0.6	0.5	0.3
Bi	1.2	0.8	1.1	1.5	1.6	1.0
V	16	16	18	18	16	15
Cr	36	27	31	40	37	31
Sn	9	20	22	16	22	21
W	<5	0.1	0.1	0.2	0.3	0.1
Sc	3	2.8	3.3	3.2	2.9	2.7
Tl	0.7	0.8	1.1	0.9	0.8	0.9
Rb/Sr	0.93	0.95	1.15	0.86	1.00	1.07
Rb/Ba	0.34	0.38	0.48	0.32	0.38	0.4
Y	10.0	9.5	10.3	9.7	10.4	10.7
La	32.0	31.5	28.9	29.7	28.2	33.7
Ce	65.5	60.5	55.7	60.0	57.3	64.7
Pr	7.46	6.84	6.26	7.04	6.54	7.39
Nd	25.9	24.3	21.5	26.2	23.7	26.6
Sm	4.32	3.87	3.73	4.12	3.90	4.31
Eu	0.76	0.65	0.66	0.73	0.64	0.67
Gd	2.79	2.48	2.59	2.57	2.59	2.74
Tb	0.39	0.36	0.38	0.35	0.37	0.37
Dy	1.97	1.70	2.02	1.76	1.88	1.99
Ho	0.32	0.30	0.33	0.30	0.32	0.35
Er	0.87	0.82	0.94	0.82	0.87	0.95
Tm	0.14	0.13	0.14	0.13	0.15	0.15
Yb	0.86	0.77	0.86	0.82	0.86	0.82
Lu	0.13	0.11	0.12	0.11	0.11	0.11
ΣREE	143.4	134.3	124.1	134.7	127.4	144.9
La_N/Yb_N	25.09	27.58	22.66	24.42	22.11	27.71
Eu/Eu*	0.67	0.64	0.65	0.69	0.62	0.60

Appendix 4: continued

Sample	Ri17	TR4	Ri1	Ri12	Ri5	Ri6
Intrusion	WRG	WRG	WRG	WRG	Kfs cumulate	Kfs cumulate
Ba	968	865	1043	908	1093	1058
Rb	321.6	337.9	338.5	337.4	314.8	327.5
Sr	342.1	328.3	418.9	329.0	422.9	413.0
Be	13	12	15	13	14	13
Cs	17.6	17.7	59.7	43.4	45.9	46.5
Ga	22.5	23.4	23.2	23.0	23.1	22.9
Nb	19.1	23.3	19.4	20.5	16.7	17.9
Th	33.7	35.9	36.1	31.0	31.4	34.5
U	6.2	15.3	14.9	17.4	7.4	17.6
Zr	212.0	217.2	242.5	189.5	207.9	217.8
Hf	7.3	7.7	7.5	6.2	6.7	7.2
Mo	0.1	<5	<5	0.3	0.5	0.4
Cu	5.2	0.7	1.2	8.9	2.0	1.4
Pb	16.7	18.9	9.7	17.2	16.2	9.9
Zn	36	45	40	34	34	35
Ni	13.5	13.2	14.0	13.0	14.8	15.5
Co	3.8	3.6	3.7	3.3	3.3	3.6
As	4.5	11.1	9.3	25.0	6.7	9.0
Au	1.8	1.0	21.8	1.7	5.2	3.4
Sb	0.2	<5	0.8	0.6	0.4	0.6
Bi	1.1	2.5	1.4	1.3	1.1	1.4
V	15	17	18	13	14	16
Cr	32	34	40	28	38	40
Sn	8	9	16	20	15	17
W	<5	<5	0.1	0.1	0.2	0.3
Sc	2.6	4	3.2	2.5	2.6	2.9
Tl	0.7	1	0.8	0.7	0.7	0.8
Rb/Sr	0.94	1.03	0.83	1.03	0.78	0.82
Rb/Ba	0.33	0.39	0.32	0.37	0.29	0.31
Y	9.5	12.0	10.6	10.5	9.0	9.9
La	27.7	31.5	33.2	30.9	30.9	31.7
Ce	59.4	63.5	66.9	60.0	59.8	63.3
Pr	6.40	7.67	7.61	6.98	6.75	7.32
Nd	23.2	28.4	27.6	24.8	25.2	26.7
Sm	4.09	4.76	4.18	3.96	3.81	4.22
Eu	0.77	0.65	0.82	0.68	0.88	0.83
Gd	2.69	3.05	2.87	2.48	2.42	2.67
Tb	0.38	0.43	0.39	0.37	0.32	0.36
Dy	1.95	2.29	1.83	1.89	1.67	1.84
Ho	0.31	0.39	0.33	0.31	0.28	0.3
Er	0.85	1.04	0.90	0.89	0.80	0.87
Tm	0.13	0.16	0.15	0.14	0.13	0.14
Yb	0.79	0.92	0.87	0.84	0.76	0.85
Lu	0.11	0.14	0.13	0.11	0.11	0.11
ΣREE	128.8	144.9	147.8	134.4	133.8	141.2
La_N/Yb_N	23.64	23.08	25.73	24.8	27.41	25.14
Eu/Eu*	0.71	0.52	0.72	0.66	0.89	0.76

Appendix 4: continued

Sample	TR15	Ri4	TR14	TR7	TR6	Ri21
Intrusion	Kfs cumulate	Kfs cumulate	Kfs cumulate	SRG	SRG	SRG
Ba	996	969	1025	524	516	504
Rb	282.9	320.2	274.4	346.0	361.7	384.4
Sr	398.5	387.9	414.7	243.2	237.6	224.1
Be	13	12	15	11	12	14
Cs	25.5	48.6	21.4	38.6	41.9	60.7
Ga	21.7	22.8	20.7	23.9	24.1	23.4
Nb	14.9	19.1	11.5	18.8	20.5	16.6
Th	28.9	36.1	20.3	28.6	32.2	28
U	4.8	12.6	4.6	8.4	8.9	3.7
Zr	188.2	219.7	146.4	185.7	191.4	139.8
Hf	6.2	7.4	4.9	6.4	6.6	5.2
Mo	<5	0.6	<5	<5	<5	0.1
Cu	1.1	1.8	1.8	0.6	0.5	4.2
Pb	10.8	13.1	13.1	14.4	14.6	10.4
Zn	27	37	15	45	47	43
Ni	7.7	18.6	4.9	16.1	16.3	11.3
Co	2.2	3.7	1.3	5.0	5.2	3.0
As	4.6	10.4	5.0	17.7	17.1	5.3
Au	2.2	6.6	2.0	3.0	1.8	0.5
Sb	0.4	0.6	0.4	0.1	0.1	0.3
Bi	0.6	1.4	0.7	1.6	1.6	1.3
V	11	17	6	21	24	17
Cr	23	45	14	37	39	30
Sn	9	17	6	19	20	27
W	<5	0.3	<5	0.2	0.2	0.2
Sc	2.2	3.1	1.2	4.3	4.4	3.1
Tl	0.6	0.8	0.4	1.2	1.3	1.2
Rb/Sr	0.71	0.85	0.66	1.42	1.52	1.72
Rb/Ba	0.28	0.33	0.27	0.66	0.7	0.76
Y	8.1	9.7	6.2	13.2	13.8	12.0
La	22.4	33.1	17.3	29.1	32.4	25.4
Ce	49.0	67.2	37.0	57.0	62.9	51.4
Pr	5.52	7.65	3.95	6.60	7.35	5.78
Nd	21.1	28.2	14.2	23.0	25.3	20.0
Sm	3.35	4.26	2.28	4.15	4.48	3.45
Eu	0.82	0.79	0.82	0.52	0.50	0.49
Gd	2.24	2.75	1.47	3.04	3.28	2.71
Tb	0.32	0.35	0.23	0.46	0.49	0.41
Dy	1.60	1.87	1.19	2.38	2.66	2.01
Ho	0.26	0.32	0.22	0.45	0.47	0.37
Er	0.76	0.89	0.59	1.25	1.30	1.09
Tm	0.12	0.14	0.10	0.20	0.20	0.17
Yb	0.69	0.85	0.60	1.10	1.14	1.09
Lu	0.10	0.12	0.10	0.18	0.17	0.14
ΣREE	108.3	148.5	80.1	129.4	142.6	114.5
La_N/Yb_N	21.89	26.25	19.44	17.84	19.16	15.71
Eu/Eu*	0.92	0.71	1.37	0.45	0.40	0.49

Appendix 4: continued

Sample	Ri22	Je-2	Je-4	OAP1
Intrusion	SRG	Vyžlovka	Vyžlovka	Zvánovice
Ba	489	934	848	20
Rb	388.8	266.2	247.7	373.0
Sr	222.1	540.6	503.7	24
Be	16	11	10	17
Cs	55.1	10.2	9.5	73.3
Ga	24.0	24.6	22.6	25.0
Nb	17.3	18.1	18.1	15.2
Th	28.1	42.1	37.9	8.08
U	3.6	17.6	15.8	4.24
Zr	142.1	150.7	143.1	29
Hf	5.0	5.6	5.9	1.6
Mo	<5	0.2	0.2	<5
Cu	3.3	1	4.2	< 10
Pb	13.9	23.7	23	50
Zn	45	<0.1	0.1	<30
Ni	12.2	4.2	4.4	<20
Co	3.2	1.3	1.6	<1
As	2.8	6.6	6.7	<5
Au	<5	1.1	1.2	<5
Sb	0.2	0.1	0.2	0.3
Bi	0.9	0.1	0.4	2.4
V	17	5	6	<5
Cr	30	15	8	<20
Sn	31	3	3	37
W	0.2	0.25	0.24	<5
Sc	3.2	<0.01	0.01	4
Tl	1.3	1.1	1.2	2.19
Rb/Sr	1.75	0.49	0.49	15.54
Rb/Ba	0.8	0.28	0.29	18.65
Y	11.2	5.8	5.7	12.7
La	25.9	26.6	24.1	4.4
Ce	49.4	50.1	46.5	9.1
Pr	5.66	5.58	5.14	1.07
Nd	19.6	18.6	17.6	3.6
Sm	3.43	2.75	2.57	1.2
Eu	0.47	0.52	0.53	0.03
Gd	2.45	1.75	1.62	1.23
Tb	0.39	0.22	0.23	0.27
Dy	2.00	1.08	1.00	1.80
Ho	0.38	0.18	0.18	0.35
Er	1.01	0.51	0.53	1.12
Tm	0.17	0.08	0.09	0.19
Yb	1.01	0.46	0.45	1.36
Lu	0.15	0.07	0.08	0.20
ΣREE	112.0	108.5	100.6	26.0
La_N/Yb_N	17.29	38.99	36.11	2.19
Eu/Eu*	0.50	0.72	0.79	0.07

" < " below detection limit

Sample locations

Ri1, Ri2, Ri3, Ri4, Ri5, Ri6, Ri7, Ri8, Ri9, TR14, TR15, TR16 (WPC) – samples of the Říčany granites

RiE-1, RiE-2, RiE-3, RiE-4, TR12, TR13, TR18 (MME) – samples of microgranular mafic enclaves

TR11 (FEL) – sample of felsic enclave

Žernovka – Quarry, 1 km NW of bus stop, forest 'Horka' [50°0'22.439"N, 14°44'55.049"E]

Ri10, Ri11, Ri12 (WPC): Srbín – Disused quarry, 400 m SSW of bus stop; flooded quarry at Srbín-Svojetice road [49°58'46.506"N, 14°44'13.346"E]

Ri13, Ri14 (WPC): Babice – Disused quarry, 600 m SE of the bus stop Babice [50°0'28.457"N, 14°42'55.602"E]

Ri15 (WPC): Kozojedy – Abandoned quarry near the road [49°59'48.488"N, 14°48'55.446"E]

Ri16, Ri17 (WPC): Doubravčice – Abandoned quarry near the road [50°1'22.430"N, 14°47'17.539"E]

Ri18, Ri19 (WPC): Škvorec – Abandoned quarry near the road [50°2'47.718"N, 14°43'48.799"E]

Ri20, Ri21 (SPm): Březí – Abandoned quarry near the road [50°1'1.200"N, 14°41'47.162"E]

TR 4 (WPC): Kamenka – Disused quarry in the sanctuary Voděradské Bučiny [49°57'22.243"N, 14°48'31.037"E]

TR6, TR7 (SPm): Plachta – Flooded disused quarry [50°1'55.369"N, 14°43'37.657"E]

TR10 (KG): Vitice – Disused quarry, 300 m W of chapel in Vitice [50°1'53.756"N, 14°54'31.316"E]

Je-2, Je-4 (JG): Vyžlovka – Abandoned quarry in the middle of village Vyžlovka [49°59'10"N, E14°46'57"E]

OAP1 (MA): Zvánovice - Abandoned quarry near the road [49°56'37"N, 14°46'46"E]

"–" not analysed; LOI – Loss on ignition

Magma Differentiation and Pluton Zoning

Appendix 5: U–Th–Pb isotopic data for zircons from the Řičany granite

grain/spot	$^{207}\text{Pb}^a$	U^b	Pb^b	Th^b	$^{206}\text{Pb}^c$	$^{206}\text{Pb}^d$	$\pm 2\sigma$	$^{207}\text{Pb}^d$	$\pm 2\sigma$	$^{207}\text{Pb}^d$	$\pm 2\sigma$	rho^e	^{206}Pb	$\pm 2\sigma$	^{207}Pb	$\pm 2\sigma$	^{207}Pb	$\pm 2\sigma$	conc.
	(cps)	(ppm)	(ppm)	U	(%)	^{238}U	(%)	^{235}U	(%)	^{206}Pb	(%)		^{238}U	(Ma)	^{235}U	(Ma)	^{206}Pb	(Ma)	(%)
sample Ri-1	Žarnovka – Quarry, 1 km NW of bus stop, forest 'Horka' [50°0'22.439"N, 14°44'55.049"E] WRG - weakly porphyritic granite																		
A246	11075	337	25	0.26	0.1	0.07608	1.3	0.597	5.9	0.05691	5.7	0.21	473	6	475	23	488	127	97
A247	14714	439	31	0.08	0.0	0.07498	1.2	0.5952	3.5	0.05757	3.3	0.33	466	5	474	13	514	72	91
A248	18340	229	21	0.36	0.3	0.07595	1.7	0.6235	3.3	0.05955	2.8	0.52	472	8	492	13	587	61	80
A249	14075	670	35	0.22	0.1	0.05378	1.3	0.3885	1.6	0.05239	1.0	0.81	338	4	333	5	302	22	112
A250	11652	358	24	0.07	0.1	0.07220	1.4	0.5636	1.9	0.05661	1.2	0.76	449	6	454	7	476	27	94
A251	7711	248	16	0.07	0.1	0.07104	1.3	0.5526	2.0	0.05642	1.5	0.67	442	6	447	7	469	33	94
A252	13644	462	38	0.73	0.1	0.07461	1.3	0.5791	1.7	0.05629	1.2	0.74	464	6	464	7	464	26	100
A253	22340	289	35	0.46	0.2	0.11360	1.7	1.492	2.6	0.09523	2.0	0.63	694	11	927	16	1533	39	45
A254	15310	301	21	0.28	6.6	0.06295	1.6	0.5137	4.1	0.05919	3.8	0.38	394	6	421	14	574	82	69
A255	7913	189	16	0.44	0.8	0.07974	2.4	0.6708	2.7	0.06101	1.3	0.87	495	11	521	11	640	29	77
A256	71892	579	174	0.28	0.4	0.29410	1.5	4.240	1.9	0.1046	1.2	0.79	1662	22	1682	16	1706	22	97
A257	11418	359	20	0.49	2.9	0.05105	1.5	0.3811	3.2	0.05415	2.8	0.48	321	5	328	9	377	62	85
A258	18673	649	34	0.07	1.4	0.05350	2.0	0.3941	3.1	0.05343	2.4	0.64	336	7	337	9	347	54	97
A259	10335	306	29	0.36	1.2	0.09196	1.2	0.7602	10.2	0.05996	10.1	0.12	567	7	574	46	602	219	94
A260	2088	79	5	0.78	0.5	0.05364	1.7	0.3914	3.4	0.05292	2.9	0.51	337	6	335	10	326	66	103
A261	120903	265	121	0.77	0.3	0.38500	1.3	8.422	1.9	0.1586	1.3	0.70	2100	24	2278	17	2441	23	86
A262	8702	83	14	0.12	0.4	0.16560	1.3	2.223	2.1	0.09740	1.6	0.63	988	12	1188	15	1575	30	63
A263	17609	540	45	0.32	0.0	0.08349	1.6	0.6659	1.9	0.05785	1.0	0.86	517	8	518	8	524	21	99
A264	17105	554	45	0.15	0.1	0.08569	1.1	0.6826	1.5	0.05777	1.0	0.75	530	6	528	6	521	22	102
A265	9913	259	18	0.30	3.1	0.06820	1.4	0.5393	2.6	0.05735	2.2	0.54	425	6	438	9	505	49	84
A266	4620	207	11	0.35	0.5	0.05453	1.4	0.4021	2.0	0.05349	1.4	0.69	342	5	343	6	349	32	98
A267	7917	61	9	0.76	0.1	0.12300	1.6	1.963	2.1	0.1157	1.4	0.74	748	11	1103	14	1891	26	40
A268	8857	61	15	0.60	0.2	0.22690	1.4	3.620	2.0	0.1157	1.5	0.68	1318	17	1554	16	1891	27	70
A269	30141	1338	72	0.29	0.3	0.05394	1.6	0.3972	1.8	0.05341	0.9	0.88	339	5	340	5	346	20	98
A270	17675	694	41	0.39	0.7	0.05440	1.5	0.4025	2.0	0.05366	1.3	0.76	341	5	343	6	357	29	96
A271	16598	309	30	0.32	2.4	0.09377	1.4	0.7947	2.9	0.06147	2.5	0.49	578	8	594	13	656	54	88
A272	13274	428	28	0.21	0.0	0.06675	1.3	0.5211	2.0	0.05662	1.5	0.67	417	5	426	7	477	32	87
A274	16383	570	22	0.39	2.1	0.03456	2.4	0.2488	6.2	0.05222	5.8	0.38	219	5	226	13	295	131	74
A275	13185	284	21	0.10	2.3	0.07437	1.7	0.6092	3.1	0.05941	2.6	0.55	462	8	483	12	582	56	79
A276	38388	528	38	0.10	6.6	0.05897	2.2	0.4504	11.3	0.05539	11.1	0.19	369	8	378	36	428	247	86
A277	11032	326	23	0.17	0.1	0.07149	1.2	0.5770	1.8	0.05854	1.3	0.69	445	5	463	7	550	28	81
A278	6127	257	16	0.45	0.1	0.06167	1.2	0.4650	2.0	0.05469	1.6	0.62	386	5	388	6	400	35	97
A279	5739	245	14	0.39	0.0	0.05731	1.2	0.4295	2.2	0.05436	1.8	0.56	359	4	363	7	386	41	93
A280	8102	187	19	0.53	0.1	0.09375	1.2	0.7755	1.6	0.05999	1.1	0.76	578	7	583	7	603	23	96
A281	10524	230	19	0.08	1.9	0.08593	1.4	0.6966	2.7	0.05879	2.2	0.54	531	7	537	11	559	49	95
A282	10492	480	26	0.32	0.1	0.05353	1.3	0.3900	1.8	0.05289	1.2	0.75	336	4	335	5	324	27	104
A288	11088	304	24	0.09	0.1	0.08335	1.4	0.6635	1.8	0.05774	1.1	0.77	516	7	517	7	520	24	99
A289	18577	486	39	0.13	0.1	0.08391	1.3	0.6888	1.6	0.05953	0.8	0.85	519	7	532	7	587	18	89
A290	21685	155	25	0.66	5.4	0.13650	3.2	1.329	4.4	0.07058	3.0	0.73	825	25	858	26	945	62	87
A291	19223	152	26	0.81	4.9	0.15400	1.7	1.516	3.1	0.0714	2.6	0.54	923	14	937	19	969	53	95
A292	15895	619	35	0.58	0.8	0.05279	1.3	0.3881	1.8	0.05333	1.3	0.68	332	4	333	5	343	30	97
A293	4968	156	11	0.28	0.1	0.07040	1.5	0.5527	2.2	0.05694	1.7	0.66	439	6	447	8	489	37	90
A294	1161	22	3	0.90	0.4	0.10600	2.0	0.9164	4.2	0.06269	3.7	0.46	650	12	660	21	698	79	93
A295	423	19	1	0.05	0.7	0.05321	2.0	0.3927	3.6	0.05353	3.0	0.55	334	6	336	10	351	67	95
A296	148	6	0	0.13	1.7	0.04882	3.3	0.3570	5.8	0.05304	4.8	0.57	307	10	310	16	331	108	93
A297	2026	91	5	0.02	0.2	0.05401	1.5	0.3950	3.0	0.05304	2.6	0.50	339	5	338	9	331	58	103
A298	32419	433	37	0.31	7.1	0.06928	2.4	0.5675	4.3	0.05941	3.5	0.57	432	10	456	16	582	76	74
A299	13396	125	9	0.14	8.5	0.06838	3.2	0.5739	4.8	0.06087	3.6	0.66	426	13	461	18	635	78	67
A300	10136	478	22	0.05	0.6	0.04838	1.4	0.3502	1.8	0.05249	1.1	0.80	305	4	305	5	307	24	99
A301	15066	409	32	0.11	0.6	0.08292	1.4	0.6624	2.6	0.05794	2.2	0.53	514	7	516	10	528	48	97
A302	14574	413	34	0.13	0.8	0.08561	1.5	0.6900	2.6	0.05845	2.2	0.57	530	8	533	11	547	47	97
A303	9886	222	19	0.13	1.1	0.08817	2.4	0.7059	3.9	0.05807	3.1	0.62	545	13	542	17	532	67	102
A304	110899	126	85	0.51	0.2	0.58230	1.4	17.22	1.6	0.2145	0.6	0.92	2958	34	2947	15	2940	10	101
A305	18560	52	21	0.49	b.d.	0.36330	1.3	6.496	2.8	0.1297	2.4	0.49	1998	23	2045	25	2094	42	95
Pleso ^g	9540	433	22	0.12	0.12	0.05383	1.4	0.3942	2.3	0.05312	1.4	0.52	338	5	337	7	334	31	101
91500 ^g	5777	56	11	0.41	0.24	0.18121	2.0	1.8752	2.7	0.07505	1.1	0.62	1074	20	1072	18	1070	23	100

Spot size = 33 μm ; depth of crater $\sim 15\mu\text{m}$. $^{206}\text{Pb}/^{238}\text{U}$ error is the quadratic additions of the within run precision (2 SE) and the external reproducibility (2 SD) of the reference zircon. $^{207}\text{Pb}/^{206}\text{Pb}$ error propagation (^{207}Pb signal dependent) following Gerdes & Zeh (2009). $^{207}\text{Pb}/^{235}\text{U}$ error is the quadratic addition of the $^{207}\text{Pb}/^{206}\text{Pb}$ and $^{206}\text{Pb}/^{238}\text{U}$ uncertainty.

- Within run background-corrected mean ^{207}Pb signal in cps (counts per second).
- U and Pb content and Th/U ratio were calculated relative to GJ-1 reference zircon.
- percentage of the common Pb on the ^{206}Pb . b.d. = below detection limit.
- corrected for background, within-run Pb/U fractionation (in case of $^{206}\text{Pb}/^{238}\text{U}$) and common Pb using Stacy and Kramers (1975) model Pb composition and subsequently normalised to GJ-1 (ID-TIMS value/measured value); $^{207}\text{Pb}/^{235}\text{U}$ calculated using $^{207}\text{Pb}/^{206}\text{Pb}/(^{238}\text{U}/^{206}\text{Pb}*1/137.88)$
- rho is the $^{206}\text{Pb}/^{238}\text{U}/^{207}\text{Pb}/^{235}\text{U}$ error correlation coefficient.
- degree of concordance = $^{206}\text{Pb}/^{238}\text{U}$ age / $^{207}\text{Pb}/^{206}\text{Pb}$ age x 100
- Accuracy and reproducibility was checked by repeated analyses (n = 11) of reference zircon Plesovice and 91500; data given as mean with 2 standard deviation uncertainties

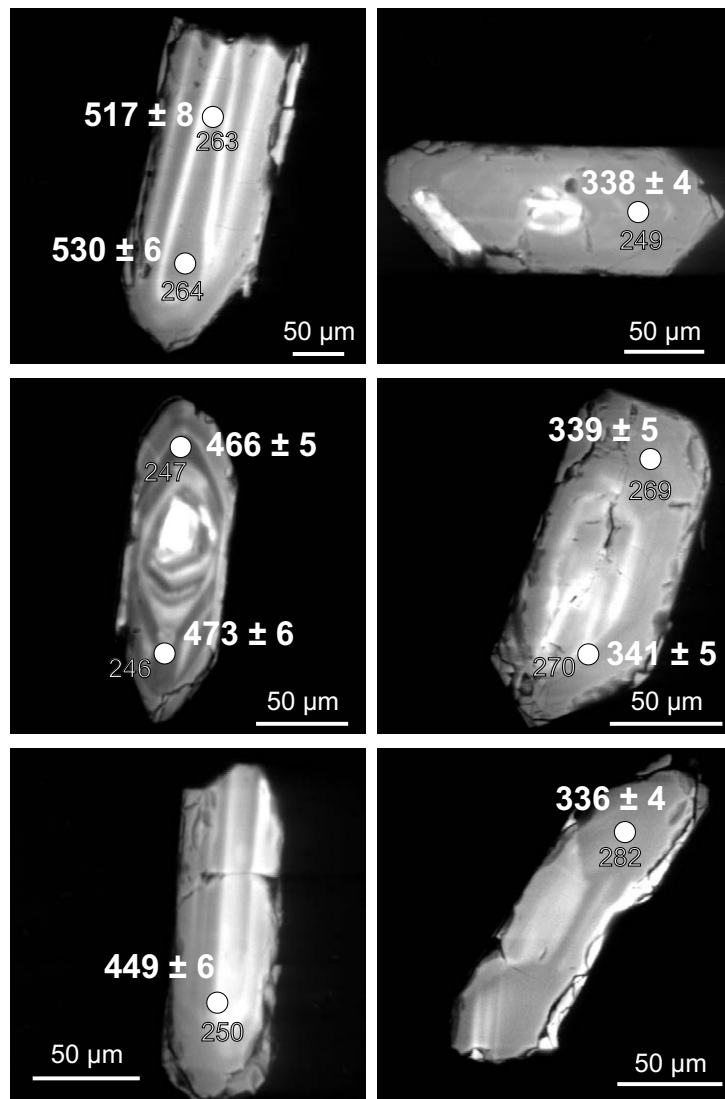
Appendix 5: U-Th-Pb isotopic data for monazites from the Říčany granite

grain/spot	$^{207}\text{Pb}^a$	U^b	Pb^c	Th^d	$^{206}\text{Pb}^c$	$^{206}\text{Pb}^a$	$\pm 2\sigma$	$^{207}\text{Pb}^a$	$\pm 2\sigma$	$^{206}\text{Pb}^a$	$\pm 2\sigma$	$^{207}\text{Pb}^a$	$\pm 2\sigma$	rho ^e	^{206}Pb	$\pm 2\sigma$	^{207}Pb	$\pm 2\sigma$	^{206}Pb	$\pm 2\sigma$	conc.		
sample TR 7	(cps)	(ppm)	(ppm)	U	(%)	^{238}U	(%)	^{235}U	(%)	^{232}Th	(%)	^{206}Pb	(%)		^{238}U	(Ma)	^{235}U	(Ma)	^{232}Th	(Ma)	^{206}Pb	(Ma)	(%)
SRG - strongly porphyritic granite																							
A06	34745	543	224	28.62	0.4	0.05330	1.7	0.3942	2.3	0.01660	1.8	0.0536	1.6	0.72	335	5	337	7	333	6	356	37	94
A07	41403	473	204	29.50	3.0	0.05398	1.8	0.3945	5.1	0.01681	1.7	0.053	4.8	0.36	339	6	338	15	337	6	329	108	103
A08	69769	505	220	29.75	6.8	0.05302	1.9	0.3804	7.4	0.01682	1.8	0.052	7.2	0.26	333	6	327	21	337	6	287	164	116
A09	34145	575	239	28.48	0.1	0.05287	1.7	0.3871	2.4	0.01677	1.7	0.0531	1.6	0.74	332	6	332	7	336	6	333	36	100
A11	50684	525	207	25.99	4.5	0.05456	1.8	0.3983	5.8	0.01666	1.8	0.053	5.5	0.32	342	6	340	17	334	6	327	125	105
A12	37526	578	242	28.80	1.1	0.05360	1.8	0.3928	3.4	0.01701	1.8	0.0532	2.8	0.55	337	6	336	10	341	6	335	64	100
A13	197118	534	232	28.17	7.7	0.05349	1.9	0.4009	5.1	0.01693	1.9	0.0544	4.7	0.38	336	6	342	15	339	6	386	105	87
A14	114704	585	238	26.38	16.6	0.05418	2.7	0.3967	10.1	0.01689	2.0	0.0531	9.8	0.26	340	9	339	30	339	7	333	222	102
A15	29856	514	225	30.24	0.1	0.05425	1.7	0.3952	2.5	0.01700	1.7	0.0528	1.7	0.71	341	6	338	7	341	6	322	40	106
A16	49845	399	169	28.17	6.4	0.05430	1.9	0.3947	6.6	0.01697	1.7	0.0527	6.3	0.28	341	6	338	19	340	6	317	144	108
B06	58295	553	213	26.01	5.0	0.05384	1.9	0.3976	5.8	0.01683	1.6	0.0536	5.4	0.33	338	6	340	17	337	6	352	123	96
B07	25438	395	160	26.38	0.8	0.05403	1.7	0.3943	2.5	0.01699	1.7	0.0529	1.7	0.71	339	6	338	7	341	6	326	40	104
B08	87885	512	228	30.44	10.3	0.05337	2.2	0.3828	7.6	0.01668	1.8	0.052	7.3	0.29	335	7	329	22	334	6	286	166	117
B09	33236	558	233	29.14	0.2	0.05372	1.8	0.3894	2.2	0.01678	1.7	0.0526	1.3	0.81	337	6	334	6	336	6	310	29	109
B10	38237	517	227	30.59	3.7	0.05317	1.8	0.3869	5.8	0.01697	1.7	0.0528	5.5	0.31	334	6	332	17	340	6	319	125	105
B11	34890	549	230	28.92	1.1	0.05401	1.8	0.3994	2.9	0.01701	1.8	0.0536	2.2	0.62	339	6	341	8	341	6	355	51	95
B12	57270	520	220	28.52	4.5	0.05352	1.8	0.3970	5.5	0.01702	1.7	0.0538	5.2	0.32	336	6	339	16	341	6	363	118	93
B13	144242	518	243	30.73	15.8	0.05381	2.7	0.3910	8.6	0.01688	2.5	0.0527	8.1	0.32	338	9	335	25	338	8	316	185	107
B14	36647	587	249	29.36	1.0	0.05432	1.8	0.3854	3.2	0.01704	1.8	0.0515	2.7	0.55	341	6	331	9	342	6	261	61	130
B15	30620	509	224	30.09	0.6	0.05400	1.7	0.3892	2.6	0.01686	1.8	0.0523	1.9	0.68	339	6	334	7	338	6	298	43	114
B16	214641	586	256	28.11	23.8	0.05399	3.2	0.3594	9.9	0.01675	1.9	0.0483	9.4	0.32	339	10	312	27	336	6	113	221	300
B17	129840	557	240	28.35	17.6	0.05470	2.6	0.3926	9.9	0.01697	1.9	0.0521	9.5	0.27	343	9	336	29	340	6	288	218	119
Moacyr ^g	56938	426	310	33.88	3.34	0.08232	0.9	0.6507	1.9	0.0	1.5	0.05733	1.8	0.59	510	4	509	7	509	8	504	40	101

Spot size = 25 μm ; depth of crater $\sim 12\mu\text{m}$. $^{206}\text{Pb}/^{238}\text{U}$ error is the quadratic additions of the within run precision (2 SE) and the external reproducibility (2 SD) of the reference zircon. $^{207}\text{Pb}/^{206}\text{Pb}$ error propagation (^{207}Pb signal dependent) following Gerdes & Zeh (2009). $^{207}\text{Pb}/^{235}\text{U}$ error is the quadratic addition of the $^{207}\text{Pb}/^{206}\text{Pb}$ and $^{206}\text{Pb}/^{238}\text{U}$ uncertainty

- Within run background-corrected mean ^{207}Pb signal in cps (counts per second).
- U and Pb content and Th/U ratio were calculated relative to GJ-1 reference zircon.
- percentage of the common Pb on the ^{206}Pb . b.d. = below detection limit.
- corrected for background, within-run Pb/U fractionation (in case of $^{206}\text{Pb}/^{238}\text{U}$) and common Pb using Stacy and Kramers (1975) model Pb composition and subsequently normalised to GJ-1 (ID-TIMS value/measured value); $^{207}\text{Pb}/^{235}\text{U}$ calculated using $^{207}\text{Pb}/^{206}\text{Pb}/(^{238}\text{U}/^{206}\text{Pb}*1/137.88)$
- rho is the $^{206}\text{Pb}/^{238}\text{U}/^{207}\text{Pb}/^{235}\text{U}$ error correlation coefficient.
- degree of concordance = $^{206}\text{Pb}/^{238}\text{U}$ age / $^{207}\text{Pb}/^{206}\text{Pb}$ age x 100
- Accuracy and reproducibility was checked by repeated analyses (n = 12) of reference monazite Moacyr; data given as mean with 2 standard deviation uncertainties

Appendix 6: Representative CL images of zircon grains from the analyzed granite samples.



Appendix 7: Selected partition coefficients used for modelling of fractional crystallization

	Rb	Sr	Ba	Nb	Zr	La	Sm	Eu	Yb
Pl	0.041 (a)	13 (h)	0.308 (ch)	0.06 (ch)	0.09b (h)	0.45 (h)	0.13 (a)	2.15 (a)	0.077 (ch)
Bt	2.24 (a)	0.12 (ch)	9.7 (ch)	9.5 (f)	1.8 (h)	3.55 (f)	0.26 (a)	0.24 (a)	0.179 (ch)
Kfs	0.34 (a)	3.87 (ch)	6.12 (ch)	0.032 (d)	0.36 (e)	0.020 (d)	0.018 (a)	1.13 (a)	0.012 (ch)
Ap	0.002 (d)	0.396 (d)	0.001 (d)	0.009 (d)	0.030 (d)	4.3 (b)	62.8 (a)	30.4 (a)	25 (ch)
Zrn	0.102 (d)	0.122 (d)	0.203 (d)	217 (d)	256 (d)	7.2 (f)	3.14 (a)	3.14 (a)	250 (ch)
Mnz	0.015 (d)	0.273 (d)	0.014 (d)	2.3 (d)	2.9 (d)	260 (g)	460 (g)	2859 (d)	200 (ch)
Rt	0.0076 (c)	0.06 (c)	0.0137 (d)	540 (c)	4.24 (ch)	262 (d)	102 (d)	81 (d)	59 (d)

References:

- (a) Arth, J. G. (1976). Behavior of trace elements during magmatic processes: a summary of theoretical models and their applications. *Journal of Research of the U. S. Geological Survey* 4.
- (b) Demaiffe, D. & Hertogen, J. (1981). Rare earth element geochemistry and strontium isotopic composition of a massif-type anorthositic-charnockitic body: the Hidra Massif (Rogaland, SW Norway). *Geochim. Geochimica et Cosmochimica Acta* 45, 1545–1561.
- (c) Foley, S. F., Barth, M. G. & Jenner, G. A. (2000). Rutile/melt partition coefficients for trace elements and an assessment of the influence of rutile on the trace element characteristics of subduction zone magmas. *Geochimica et Cosmochimica Acta* 64, 933–938.
- (d) Langmuir, C. H., & Hanson, G. N. (1981). Calculating Mineral—Melt Equilibria with Stoichiometry, Mass Balance, and Single-Component Distribution Coefficients. In: Newton, R.C.; Navrotsky, A. and Wood, B.J., (eds.) *Thermodynamics of Minerals and Melts*. New York: Springer, 247–271
- (e) Leeman, W. P. & Phelps, D. W. (1981). Partitioning of rare Earths and other trace elements between sanidine and coexisting volcanic glass. *Journal of Geophysical Research* 86, 10193–10199.
- (f) Mahood, G. & Hildreth, W. (1983). Large partition coefficients for trace elements in high-silica rhyolites. *Geochimica et Cosmochimica Acta* 47, 11–30.
- (g) Montel, J.-M. (1993). A model for monazite/melt equilibrium and application to the generation of granitic magmas. *Chemical Geology* 110, 127–146.
- (h) Nash, W. P. & Crecraft, H. R. (1985). Partition coefficients for trace elements in silicic magmas. *Geochim. Geochimica et Cosmochimica Acta* 49, 2309–2322.
- (ch) Tindle, A. G. & Pearce, J. A. (1981). Petrogenetic modelling of in situ fractional crystallization in the zoned Loch Doon pluton, Scotland. *Contributions to Mineralogy and Petrology* 78, 196–207.

Chapter I:

Magma Differentiation and Pluton Zoning

Article I.-2:

Distribution of elements among minerals of a single (muscovite-) biotite granite sample – an optimal approach and general implications (2014)

Janoušek V., Navrátil T., **Trubač J.**, Strnad L., Laufek F., Minařík L.

Geologica Carpathica **65**: 257–271

Status: Published

Distribution of elements among minerals of a single (muscovite–) biotite granite sample – the best approach and general implications

Vojtěch Janoušek^{1,2*}, Tomáš Navrátil³, Jakub Trubač^{1,2}, Ladislav Strnad⁴, František Laufek¹ and Luděk Minařík³

¹Czech Geological Survey, Klárov 3/131, 118 21 Prague 1, Czech Republic;

²Institute of Petrology and Structural Geology, Charles University in Prague, Albertov 6, 128 43 Prague 2, Czech Republic

³Institute of Geology, Academy of Science, Rozvojová 269, 165 00 Prague 6, Czech Republic;

⁴Laboratories of the Geological Institutes, Charles University in Prague, Albertov 6, 128 43 Prague 2, Czech Republic;

(Manuscript received January 17 2014; accepted in revised form June 5, 2014)

ABSTRACT

The Petrography and mineral chemistry of coarse-grained, weakly porphyritic (muscovite–) biotite Říčany granite (Variscan Central Bohemian Plutonic Complex, Bohemian Massif) were studied in order to assess the distribution of major and trace elements among its minerals, with consequences for granite petrogenesis and availability of geochemical species during supergene processes.

It is demonstrated that best suited for modal analyses of granites are chemistry-based approaches, especially methods taking into account compositions of a whole-rock sample as well as of its mineral constituents, such as constrained least-squares algorithm. They smooth out any local variations (mineral zoning, presence of phenocrysts, schlieren...) and are robust in respect to the presence of phenocrysts or fabrics.

The study confirms the notion that the accessory phases play a key role in incorporation of many elements during crystallization of granitic magmas. Especially the REE seem of little value in petrogenetic modelling, unless the role of accessories is properly assessed and saturation models for apatite, zircon, monazite ± rutile carefully considered. At the same time, the presence of several P-, Zr- and LREE-bearing phases may have some important consequences for saturation thermometry of apatite, zircon and monazite.

Key words: modal analyses, trace-element residence, ICP-MS, Central Bohemian Plutonic Complex, Říčany granite

INTRODUCTION

Distribution of chemical elements among minerals in a single granite specimen represents a fundamental and intriguing problem, which however has attracted surprisingly little attention in the current literature (e.g., Gromet & Silver 1983; Sawka 1988; Evans & Hanson 1993; Wark & Miller 1993; Bea 1996). Still, good understanding of the net contributions of individual phases to the whole-rock chemical budget is a necessary prerequisite should any relevant petrogenetic modelling be undertaken. Moreover, particular host minerals show variable resistance to alteration and/or weathering, thus controlling the degree to which the given element could be mobilized into the environment. For such studies, crucial are reliable and precise concentration data in small sample volumes, capable of minimizing the effects of the analysed material inhomogeneity (for individual minerals it could be the presence of zoning, inclusions, alteration zones...). The required precision is often far beyond limits of the electron microprobe microanalysis (EMPA); the prohibitive cost effectively rules out the ion probe as well. Fortunately the ICP-MS technique enables a reliable determination of sub-ppm amounts of elements both in the solution (dissolved whole-rock powders or monomineralic separates) and *in situ*, using the laser-ablation (LA) apparatus.

In addition, an accurate estimate of the mineral modal proportions has to be made. Theoretically this should pose no problem, given that the modal analyses provide a basis for classification of holocrystalline igneous rocks for over eighty years (Niggli 1931; Johannsen 1932, 1937, 1938, 1939; Streckeisen 1974; Le Maitre 2002).

The classical technique relies on counting of individual mineral grains over a regular grid, either in a standard thin section or a polished rock slab. More sophisticated alternatives include computer-aided image analysis, powder X-ray diffraction (P-XRD) and chemistry-based mathematical approaches (normative recalculations or statistical methods employing the chemistry of the bulk rock and its mineral constituents).

The current paper initially focuses on methodological issues connected with obtaining a modal analysis representative of a large, coarse-grained granite sample. The various methods are compared and the most trustworthy approach/modal data chosen (Appendix 1). Then, using a combination of EMPA with (LA) ICP-MS data, an attempt is made to identify the principal mineral hosts for individual elements, evaluating relative contributions each of them to the whole-rock budget.

Finally we discuss general implications for obtaining modal analyses of coarse-grained rocks, modelling of igneous processes, obtaining reliable whole-rock trace-element analyses and saturation thermometry.

Our case study concentrates on the Early Carboniferous Říčany (muscovite-) biotite granite pluton from the Central Bohemian Plutonic Complex (CBPC), Czech Republic (Fig. 1a). This small body is relatively well known, as it has been, over the years, a subject of numerous studies concerned with its geology, composition and genesis (e.g., Katzer 1888; Orlov 1933; Němec 1978; Palivcová et al. 1992; Janoušek et al. 1997; Trubač et al. 2009). Moreover, even more extensive was the research on element mobility during the weathering, mass fluxes, cycling and balance of elements within the model forest ecosystem (Minařík & Houdková 1986; Minařík & Kvídová 1986; Minařík et al. 1998, 2003; Navrátil et al. 2002, 2004, 2007). For both types of studies, detailed assessment of the elemental distribution among individual mineral phases has been clearly long overdue.

GEOLOGICAL SETTING

The CBPC is one of the largest composite granitoid complexes in the Central European Variscides (Fig. 1a). The individual petrographic types can be grouped into several suites, based on petrography, age, whole-rock and mineral geochemistry (Holub et al. 1997; Janoušek et al. 2000b; Žák et al. 2014 and references therein) (Fig. 1b). The oldest among them is the normal calc-alkaline *Sázava suite* (~ 355 Ma) building much of the north-eastern CBPC. The most common in the central–southern CBPC are ~ 346 Ma old, K-rich calc-alkaline granodiorites to granites of the *Blatná suite* with minor basic bodies. The (ultra-) potassic *Čertovo břemeno suite* (~337 Ma) is formed by K–Mg-rich melagranites and melasyenites, the most basic types corresponding to the so-called durbachites. Strongly peraluminous Mu–Bt granodiorites (often Crd-bearing) of the *Maršovice suite* are regionally rather insignificant.

The Říčany Pluton (Fig. 1c), the main representant of the namesake suite, is a late (post-tectonic), shallow-level granitic body that has intruded the boundary between low-grade Upper Proterozoic to Lower Palaeozoic metasediments of the Teplá–Barrandian Unit and dominantly high-grade metasediments of the Moldanubian Unit. Its eastern margin is obscured by Permo–Carboniferous sediments. The only modern geochronological information available is the ^{40}Ar – ^{39}Ar biotite age of 336 ± 3.5 Ma (unpublished data of H. Maluski, cited in Janoušek et al. 1997).

The intrusion has a roughly elliptical outline (13×9 km) and is mainly made up of two distinct granite varieties. The outer, ‘strongly porphyritic’ one contains more abundant K-feldspar phenocrysts,

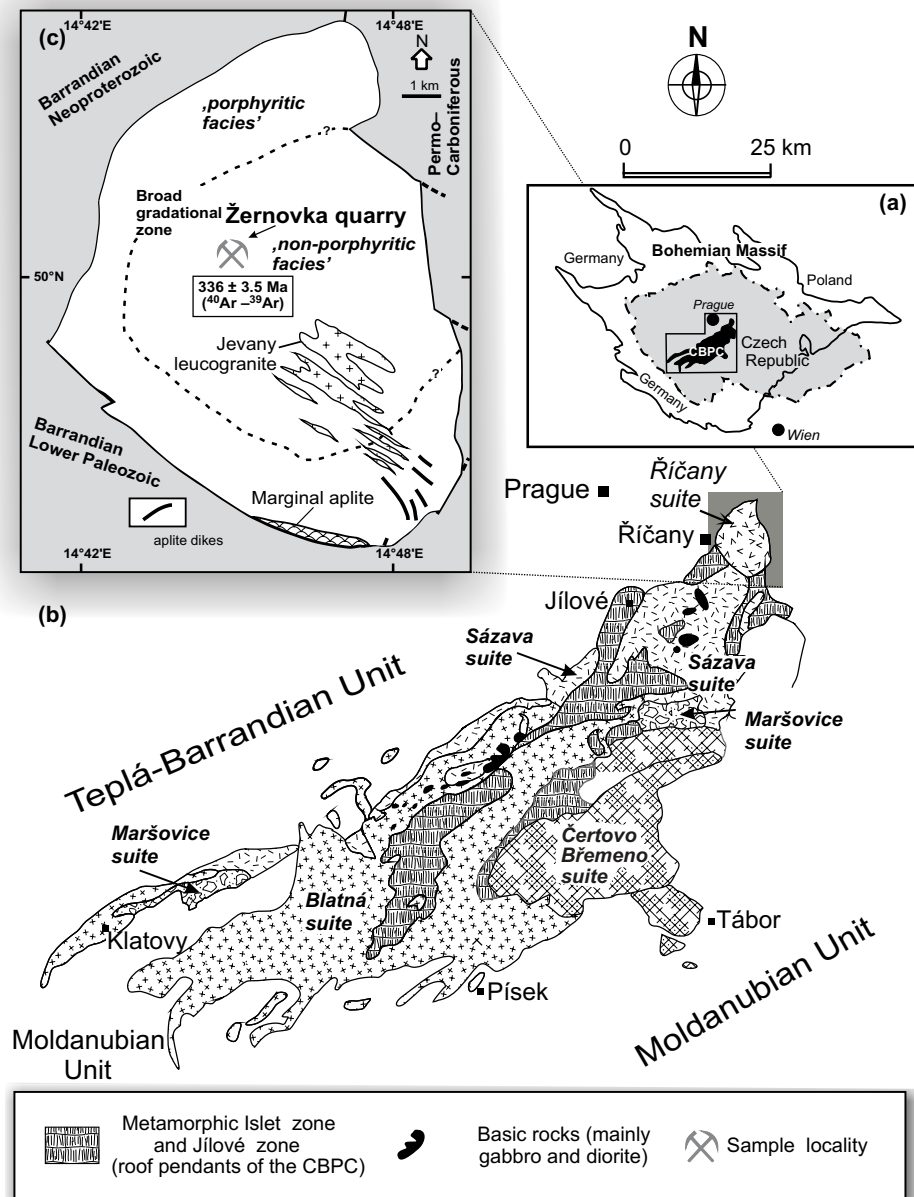


Fig.1 a - Location of the Variscan Central Bohemian Plutonic Complex (CBPC) within the Bohemian Massif. b – Sketch of the CBPC with the main granitoid suites after Janoušek et al. (2000b) (normal calc-alkaline Sázava, high-K calc-alkaline Blatná, peraluminous Maršovice and (ultra-) potassic Čertovo břemeno). vc – Geological outline of the Říčany Pluton and the surrounding units (after Janoušek et al. 1997). The position of the sampled locality, the working Žernovka quarry, is also indicated.

whereas in the central, 'weakly porphyritic' facies, the phenocrysts are scarce (Katzner 1888) (Fig. 1c). The granite encloses numerous large biotite-rich mafic enclaves and less common metasedimentary xenoliths. The Pluton is cut by many pegmatite and aplite dykes. The central part has been intruded by several small bodies of fine-grained, equigranular, two-mica Jevany leucogranite and the southern exocontact is rimmed by the so-called Marginal aplite (Němec 1978).

PETROLOGY AND MINERAL CHEMISTRY

The studied rock comes from the central, 'weakly porphyritic' facies. It is relatively fresh, with the plagioclase showing limited argillitization along the cleavage planes (Fig. 2a). The scarce small K-feldspar phenocrysts are however slightly kaolinized and the biotite suffered incipient chloritization. The average grain size of the groundmass is 1–5 mm and rare phenocrysts may attain up to 3–5 cm. Completely unweathered sample of the granite was not available due to nowadays only limited quarry activity and widespread surface kaolinization of the pluton (Pivec 1969).

The *K-feldspar* phenocrysts are strongly perthitic and many show pronounced cross-hatched twinning; Carlsbad twins are also common. They contain numerous inclusions of biotite, quartz and oligoclase (an 'hourglass' texture of Pivec 1970).

Plagioclase occurs as subhedral prismatic crystals with common albite law twin lamellae, on average 1.2–2.0 mm across. Apart from those enclosed within the K-feldspar, they are of uniform oligoclase composition (An_{11-19} ; Appendix 2) and are usually chemically unzoned.

Biotite forms subhedral flakes on average 0.5–0.75 mm (up to 1.2 mm) across, with a strong pleochroism: X: straw yellow, Y = Z: dark rusty-brown. Pleochroic haloes around submicroscopic inclusions are very distinct and common. Biotite is often associated with grains of magnetite (Fig. 2b).

Anhedral *quartz* grains with weak undulose extinction are up to 2 mm across.

The biotite may also be overgrown by scarce primary *muscovite* (up to 0.2 mm across). Also the plagioclase encloses some small (0.1–0.2 mm) flakes of muscovite, at least some of which appear to be of primary magmatic origin.

According to our microscopic and EPMA study and previous work of Kodymová & Vejnar (1974), the granite contains significant proportions of *rutile* (0.1 mm). Small *apatite* (0.1–0.2 mm) prisms or needles are often enclosed by biotite (Fig. 2c). Less common accessories represent euhedral crystals of *titanite* (0.1 mm), brown to reddish in colour, and euhedral dipyrmidal crystals of *zircon* (0.2 mm), pink to pale brown. *Monazite* (0.2 mm) usually forms aggregates of spherical grains. *Magnetite* (0.1 mm) occurs mostly in anhedral fragments, only rarely forming octahedra, up to 0.5 mm across. *Ilmenite* (0.1 mm) forms black opaque grains of non-metallic lustre, sometimes lamellated. Subhedral *zircon-like* ABO_4 -type phase (up to 0.1 mm across) represents a newly encountered, rather rare accessory mineral. It occurs in plagioclase, very often together with monazite (Fig. 2d).

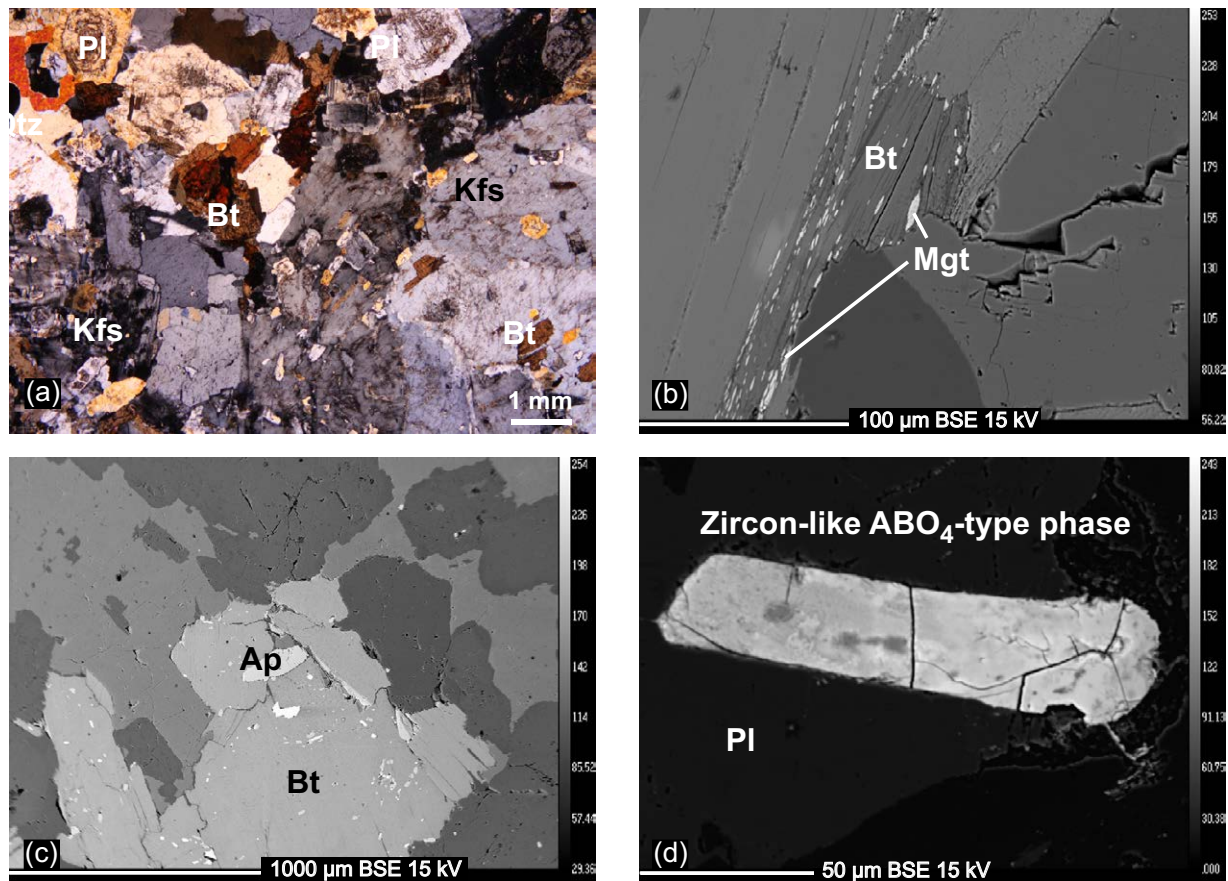


Fig. 2 Photomicrographs of the studied weakly porphyritic (muscovite–) biotite Říčany granite Žer-1. a – Photomicrograph of the typical magmatic texture at a rim of a small K-feldspar phenocryst with characteristic cross-hatched twinning. Crystals of the main rock-forming minerals exhibit no effects of solid-state deformation and are only slightly altered (plagioclase cores). Crossed polars. b – Back-scattered electron (BSE) image of microinclusions of magnetite in, and around, larger biotite flake. c – Typical BSE image of biotite, rich in apatite inclusions of variable shape and size. d – BSE image of the zircon-like ABO_4 -type phase enclosed in plagioclase.

MODAL PROPORTIONS

Petrographic approaches

In the present case, both the conventional point counting and image analysis of the stained slab (Fig. 3a–b; see Appendix 1 for full analytical details on all methods used) were taken to approximate well the mineral proportions in the studied sample's matrix, as no sizeable K-feldspar phenocrysts are present in the hand specimen. The results do not differ greatly (Table 1). The image analysis (Fig. 3c–e) indicates somewhat higher amounts of biotite (9.0 vs. 7.3 vol. %: image analysis vs. conventional point counting, plagioclase (31.2 vs. 27.1 vol. %) and quartz (38.1 vs. 32.8 vol. %), at expense of the K-feldspar (21.8 vs. 25.0 vol. %). Unfortunately the contents of kaolinite could not have been

determined by the image analysis. This mineral largely resisted staining and was thus counted, at least in part, as plagioclase.

Chemical methods

For sample Žer-1, the following mesonormative composition ('Improved Granite Mesonorm' of Mielke & Winkler (1979) is obtained (wt. %): Or 29.1, Pl (Ab + An) 36.8, Qtz 25.2, Bt 5.8, Ap 0.34, Mgt 0.9, Ilm 0.34, Cal 0.14 and Crn 0.54 (Table 1). The negligible proportion of normative corundum is in line with subaluminous nature of the sample ($A/CNK \sim 1.0$ – Table 2). Normative calcite and corundum were further not considered as they do not correspond to mineral phases present in the rock. The approximate proportions of the main rock-forming minerals (wt. %) were also obtained by the constrained least-squares (LSQ) method (Albarède 1995) implemented in the *GCDkit*. The whole-rock chemical composition and typical EMP analyses of the main rock-forming minerals served as an input (Table 3). Phosphorus, not present in appreciable amount in any of the main phases but representing an essential structural component in two common accessories, apatite and monazite, was disregarded. The low sum of squared residuals ($R^2 = 0.071$) indicates an excellent fit. The proportions of K-feldspar (29.4 wt. %) and plagioclase (36.6 wt. %) are closely comparable to the mesonorm; somewhat lower is the quartz percentage (24.7 wt. %) (Table 1). The amount of biotite, however, is nearly double (9.3 wt. %) but much closer to estimates by point counting and image analysis (if recast to wt. %).

Powder X-ray diffraction (P-XRD)

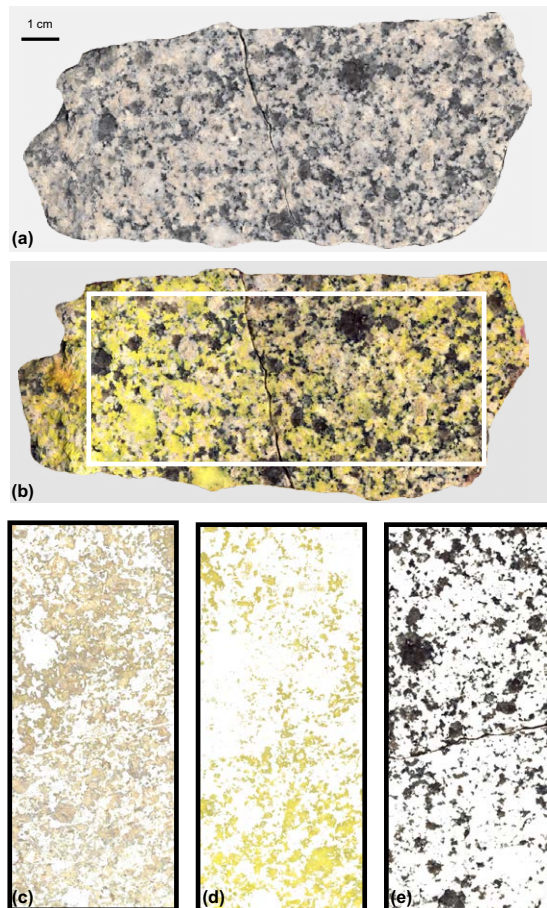
Results of Rietveld quantitative phase analysis (Appendix 1) are summarized in Table 1 and Fig. 4. Compared with other methods, the plagioclase content is somewhat significantly underestimated (25.1 wt. %). The reason may be the complex preferred orientation of plagioclase, which shows two cleavage plane systems, i.e. [001] and [010], while only one correction for preferred orientation (for [001] direction) was applied in the Rietveld fit. The amount of K-feldspar (30.4 wt. %) is in agreement with the results of constrained LSQ (29.4 wt. %) and mesonorm (29.1 wt. %); slightly higher is the quartz content (33.8 wt. %). The estimate of biotite (9.5 wt. %) is in line with other methods, except for the mesonorm. Clearly, the correction for preferred orientation in the [001] works sufficiently in this case. The content of kaolinite (1.2 wt. %) is significantly lower than that obtained by point counting (7.4 wt. %).

Tab. 1 Estimates of modal percentages (vol. % and wt. %, original data in bold) of the individual minerals in the Řičany granite Žer-1

Mineral phase	Ideal formula	Density ¹ [g·cm ⁻³]	Point counting ² (4890 points)	Image analysis	Granite mesonorm ³	Constrained least-squares	X-ray diffraction (P-XRD)
			[vol. %] [wt. %]	[vol. %] [wt. %]	[vol. %] [wt. %]	[vol. %] [wt. %]	[vol. %] [wt. %]
Main rock-forming minerals							
orthoclase	KAlSi ₃ O ₈	2.570	25	21.8	29.1	28.7	29.6
plagioclase (albite)	NaAlSi ₃ O ₈	2.620	27.1	31.2	36.8	36.3	25.1
kaolinite	Al ₂ Si ₂ O ₅ (OH) ₄	2.594	7.5	7.4			1.2
biotite (F-phlogopite)	KMg ₃ [AlSi ₃ O ₁₀]F ₂	2.878	7.3	9	5.8	10.2	9.5
quartz	SiO ₂	2.648	32.8	38	25.2	24.8	33.8
muscovite	KAl ₂ [AlSi ₃ O ₁₀](OH) ₂	2.831	0.2				
whole-rock		2.630					
Accessories							
ilmenite	FeTiO ₃	4.788	0.1		0.2		
apatite	Ca ₅ (PO ₄) ₃ F	3.200			0.3		
magnetite	Fe ₃ O ₄	5.200			0.9		
sum			100	100	98.7	99.8	100

¹Data on mineral densities used in recalculation of wt. % to vol. % (or vice versa) are from Robie et al. (1967), whole-rock density of the Řičany granite from Hejtman (1948). Original data are in bold. ² For explanation of the individual methods (point-counting, image analysis, least-squares calculation and XRD), see text. For more detailed outcome of the constrained least-squares method, see Table 3

³ 'Improved Granite Mesonorm' of Mielke and Winkler (1979)



Tab. 2 Whole-rock major- and minor-element analysis of the studied sample (wt. %)

SiO ₂	70.34
TiO ₂	0.36
Al ₂ O ₃	14.64
Fe ₂ O ₃	0.62
FeO	0.94
MgO	1.14
MnO	0.024
CaO	1.36
SrO	0.046
BaO	0.126
Li ₂ O	0.015
Na ₂ O	3.71
K ₂ O	5.55
P ₂ O ₅	0.145
F	0.153
CO ₂	0.06
C	0.016
S tot	<0.005
H ₂ O ⁺	0.51
H ₂ O ⁻	<0.05
F(ekv)	-0.064
S(ekv)	-0.001
Total	99.69
A/CNK	1.00
K ₂ O/Na ₂ O	1.50

A/CNK = molar Al₂O₃/(CaO + Na₂O + K₂O) uncorrected for apatite.

K₂O/Na₂O ratio is given by weight.

For whole-rock trace-element composition, see Appendix 4.

Fig. 3 Photograph of the polished hand specimen of the sample Žer-1, of natural appearance (a) and stained (b). The remaining images are separated colour components corresponding to the plagioclase (c) K-feldspar (d) and quartz with biotite (e). Box in figure (b) indicates the area used for image analysis (c–e).

Tab. 3 Constrained least-squares approximation to the modal composition (wt. %)

	plagioclase ¹ Pl14	K-feldspar Kfs1	biotite Bt14	quartz	whole rock ²			
					real	estimated	residual	squared residual
SiO ₂	64.05	64.16	37.50	99.86	70.34	70.44	-0.10	0.010
TiO ₂	0.00	0.00	3.33	0.00	0.36	0.31	0.05	0.002
Al ₂ O ₃	21.76	18.47	14.80	0.02	14.64	14.78	-0.14	0.019
FeOt	0.04	0.03	17.26	0.00	1.50	1.64	-0.14	0.018
MnO	0.05	0.03	0.24	0.00	0.02	0.05	-0.02	0.001
MgO	0.00	0.00	13.35	0.00	1.14	1.25	-0.11	0.011
CaO	3.87	0.01	0.04	0.00	1.36	1.42	-0.06	0.004
Na ₂ O	9.42	0.96	0.14	0.00	3.71	3.75	-0.04	0.001
K ₂ O	0.40	15.61	9.47	0.00	5.55	5.61	-0.06	0.004
wt. %	36.6%	29.4%	9.3%	24.7%			R sq	0.071 ³

¹Shown are real electron microprobe analyses of the main rock-forming minerals (see Appendix 2)

²The observed whole-rock concentrations (Table 2) and the best estimate by the constrained least-squares method, with the corresponding differences (residuals)

³The sum of squared residuals indicating a goodness of fit

MINERAL CHEMISTRY

The compositions of individual minerals were analysed by combination of three methods (Appendix 1), EMPA (see averages and typical analyses in Appendix 2), *in situ* LA ICP-MS and ICP-MS analyses of dissolved monomineralic separates (Appendix 3, summarized in Appendix 4). Laser-ablation analyses were preferred for mineral separates in which the presence of minor admixture of phases/inclusions with contrasting chemistry was of particular concern (quartz, plagioclase and biotite). On the other hand, wet analysis was chosen for K-feldspar, minimizing the problem of the small-scale heterogeneity (abundance of perthite lamellae). In Fig. 5 are shown selected trace-element patterns normalized by the whole-rock (WR) contents and in Fig. 6 the chondrite-normalized REE patterns.

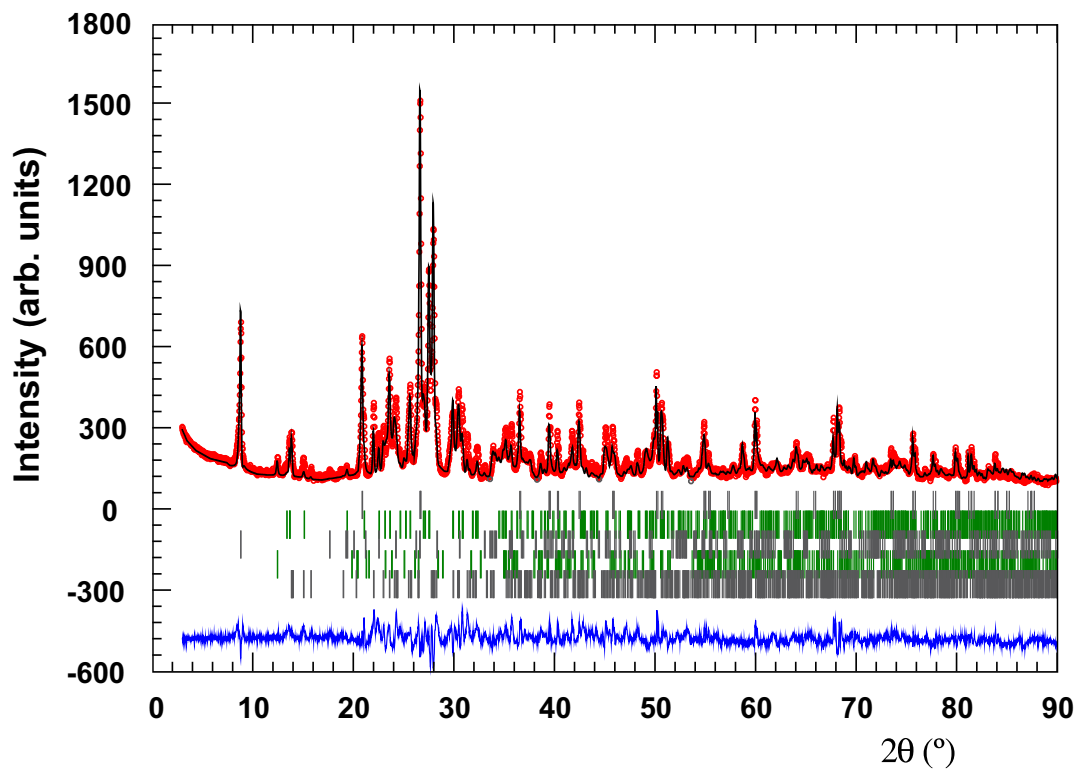


Fig. 4 Observed (circles), calculated (solid line) and difference Rietveld profiles for the studied sample. Markers of the peak positions (five rows of the vertical line segments) are for (from top to bottom) quartz, orthoclase, biotite, kaolinite and plagioclase.

Feldspars and kaolinite

K-feldspar is characterized by roughly double enrichment of Ba, Rb and Pb over the whole-rock abundances; also Sr is slightly elevated (Fig. 5a). The *plagioclase* contains rather high Sr and Be (see Navrátil et al. 2002; Navrátil 2003). On the other hand, concentrations of transition metals and high field strength elements (HFSE) in both feldspars are very low. The *kaolinite* is stripped of much of the original *K-feldspars*' large-ion lithophile (LILE) budget, and contains only Cd, Pb and Ta in amounts exceeding those in the whole rock.

The *plagioclase* contains more than double as much REE as the *K-feldspar* (81.3 vs. 26.6 ppm). Still the patterns are of similar shape, featuring high degree of LREE over HREE enrichment and sizeable positive Eu anomalies (Fig. 6a). The feldspars share normalized Eu contents nearly identical to the whole rock but the concentrations of the remaining REE are significantly lower. The limited REE mobility in course of feldspars' weathering resulted in significantly higher Ttn apparent concentrations in the residual *kaolinite* ($\Sigma\text{REE} \sim 191$ ppm). Only Eu contents approach those of the host rock and thus the Eu anomaly turns to a strongly negative one.

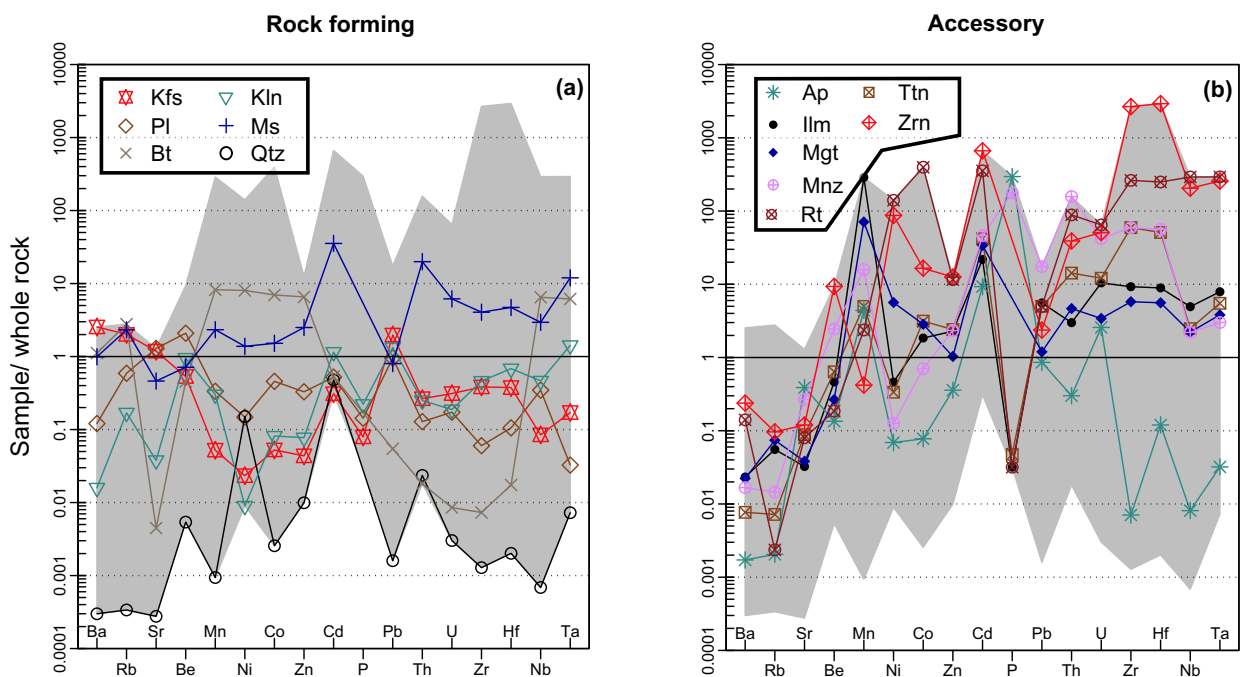


Fig. 5 Whole rock-normalized trace-element patterns for individual rock-forming (a) and accessory (b) minerals. Mineral abbreviations after Kretz (1983). Gray field denotes the total variation in the dataset.

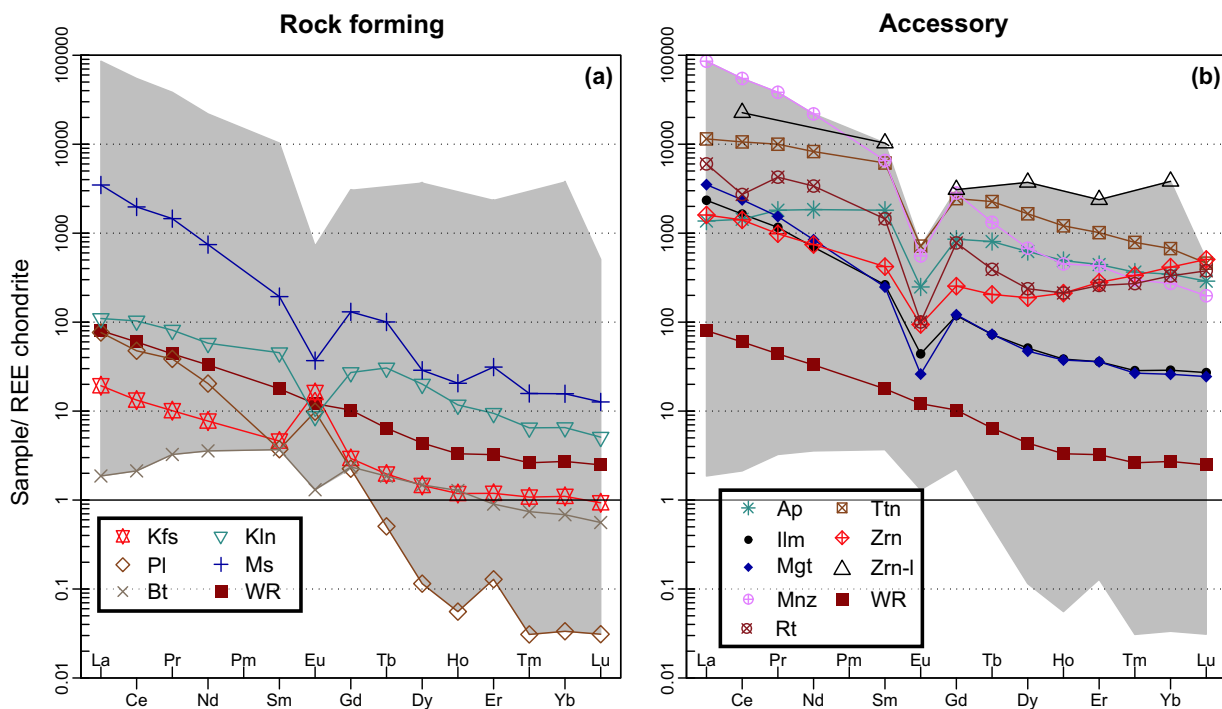


Fig. 6 Chondrite (Boynnton 1984)-normalized REE spiderplots for the individual minerals. Zrn-I = zircon-like ABO_4 -type phase. Gray field denotes the total variation in the dataset.

Biotite and muscovite

The biotite is classified as phlogopite with 13.7–17.2 wt. % total Al_2O_3 (Al^{IV} 1.10–1.18 and Al^{VI} 0.16–0.27 apfu) and is relatively Mg-rich ($Mg/(Fe^T + Mg) = 0.57–0.59$). The content of Al_2O_3 for muscovite is 31.3 wt. % total (Al^{IV} 1.44 and Al^{VI} 3.44 apfu). Both micas are slightly enriched in Rb, Mn (see Navrátil et al. 2007), Ni, Co, Zn, Nb and Ta. Characteristic of muscovite are also elevated contents of Cd, Th, U, Zr and Hf. The main differences consist in the total REE contents (7.3 ppm for biotite vs. 3396 ppm for muscovite). The muscovite REE pattern is steep, with much higher degree of LREE/HREE enrichment compared to biotite (Fig. 6a). The Eu anomaly is negative in both cases.

ACCESSORY MINERALS

Apatite

As shown by EMPA, the main minor constituents in apatite are Mn, Fe and Cl. It is further characterized by an enrichment of Mn, Cd and U (Fig. 5b). The Pb contents are close to those in the whole rock. Apatite is rich in REE, and the MREE in particular ($\Sigma REE = 3,962$ ppm; Fig. 6b); characteristic is a negative Eu anomaly.

Zircon

This mineral is rather Hf poor (0.01–0.02 apfu) but contains high concentrations of other HFSE, such as Nb and Ta. Zircon is a major Cd, Zn, Ni and Co bearing-phase. Typical are high concentrations of U with Th as well as high Σ REE (2,615 ppm) and parabolic, convex-up chondrite-normalized pattern with elevated HREE contents (Fig. 6b). While the Eu anomaly is negative, the Ce anomaly, typical of most igneous zircons (Hoskin & Schaltegger 2003), is absent. This, together with rather low degree of HREE enrichment, might reflect the presence of inclusions (see fig. 1 in Hoskin & Schaltegger op. cit.) or an admixture of the zircon-like (Zrn-I) phase.

Monazite

Monazite shows large concentrations of P, Zr and Hf. Characteristic is enrichment in radioactive elements, whereby Th prevails over U; also Pb contents are high. This mineral is enriched in REE, and especially LREE, with Ce being the most abundant (Σ REE = 91205 ppm; Fig. 6b); characteristic is a deep negative Eu anomaly.

Rutile

Rutile ($\text{TiO}_2 > 98$ wt. %) is a major transition metal-bearing phase (Ni, Co and Cd); it displays elevated U and Th contents. Typical are also high HFSE concentrations (Zr, Hf, Nb and Ta). It is a REE-rich mineral (Σ REE = 7,358 ppm) with a fair degree of LREE/HREE fractionation and a deep negative Eu anomaly.

Ilmenite and magnetite

Both minerals are characterized by high contents of metals (Mn and Cd, less enriched Pb, Zn, Co and Ni) as well as HFSE. The U and Th contents are also somewhat elevated (Fig. 5b). The minerals are enriched in REE (Σ REE for ilmenite is 2,735 ppm, for magnetite 3,818 ppm), and the LREE in particular (Fig. 6b). The Eu anomaly is deep negative in both cases.

Titanite

Titanite shows low Al (0.09–0.11 apfu) and Fe (0.03–0.03 apfu) contents. It is enriched in HFSE (Zr, Hf, Th and U, less so Nb and Ta); typical are also elevated Cd contents. On the other hand, the LILE (Ba, Rb and Sr) are depleted compared to the whole rock (Fig. 5b). The Σ REE is high (21,314 ppm) and the REE pattern relatively steep (Fig. 6b) with a pronounced negative Eu anomaly.

Zircon-like ABO_4 -type phase

The results of the EMPA of the zircon-like ABO_4 -type phase are summarized in Appendix 5. Because of the relatively high Th contents, crystals are metamict and altered, and yield low analytical totals. The analysed phase appears to be a member of the zircon–thorite solid solution series (0.27–0.33 apfu Th, 0.49–0.55 apfu Zr), with substitution of Si by P (0.22–0.24 apfu) in the tetrahedral position B. The phase is highly enriched in Fe (0.03–0.23 apfu) and Ca (0.20–0.22 apfu). The Fe and Ca atoms, which probably enter the crystal structure during self-amorphization and interactions with circulating fluids, could be positioned in channels running parallel to the c axis of the crystal structure (Geisler et al. 2002; 2003). Silica removal accompanied by a hydration by post-magmatic, low-T fluids is also very probable.

DISCUSSION

Modal analysis

Main rock-forming minerals

The choice of the most appropriate method for estimating modal abundances of the main rock-forming minerals was governed by comparison of the observed and calculated model whole-rock contents of the major- and minor-element oxides, as well as the most common among the LILE (Ba, Rb and Sr, which are in granites hosted mostly by feldspars and micas – Hanson 1978). Examining Fig. 7, it is clearly seen that the constrained LSQ method provides the most accurate estimate. As this approach does not assess well contents of minor phases, no muscovite was included in the calculation and 0.2 wt. % of this mineral was added on the basis of the point counting. The ‘best’ modal proportions of the main rock-forming minerals are thus estimated to be: 0.365 Pl, 0.293 Kfs, 0.247 Qtz, 0.093 Bt and 0.002 Ms.

As for the rock classification in the QAP triangle (Fig. 8) (here essentially the vol. % of Kfs, Pl and Qtz recast to 1), the modal estimates by all methods yield comparable results and the studied rock classifies consistently as monzogranite. Still, the image analysis and, to some extent, point counting tend to overestimate somewhat the Q proportion, whereas the P-XRD approach results in slightly lower $100 \cdot P / (A+P)$ ratio of 47 % (other methods giving 55–59 %).

Accessory phases

After subtracting the elements hosted by the main rock-forming minerals (not only incorporated in the lattice, but also contained in small inclusions, fluid inclusions or sorbed at grain boundaries, interfacial films etc.), the rest of the whole-rock chemical inventory has to be accounted for by the accessories. A crude estimate of a maximum modal abundance can be made using trace-element characteristics of the individual minerals. Assuming that such a phase accommodates the entire whole-rock inventory of the given element, these are as follows (Table 4, elements in brackets being the most restrictive ones): apatite < 0.314 wt. % (P), monazite < 0.046 wt. % (La), zircon < 0.032 wt. % (Zr), rutile < 0.081 wt. % (Nb), magnetite < 1.121 wt. % (La) and titanite < 0.255 wt. % (Y).

For some minerals, these constraints should approach the real modal abundances; the other contain no unique essential structural component, and instead share their trace-element load with other mineral phase(s). For instance, the maximal apatite content is likely to be overestimated, as

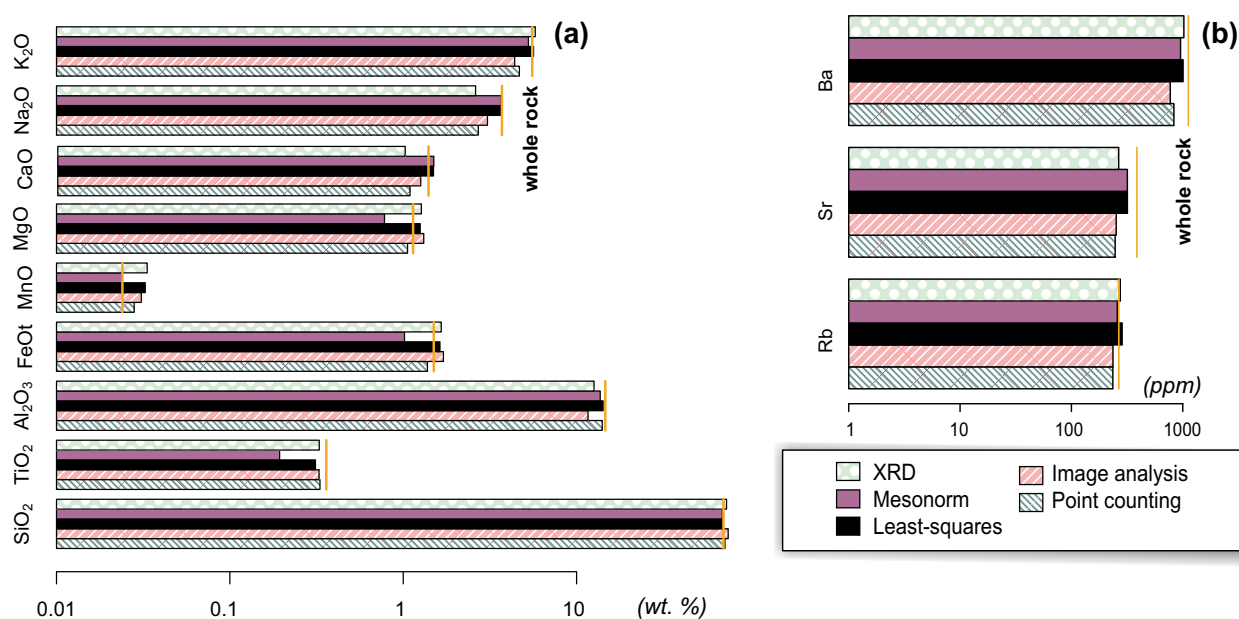


Fig. 7 Bar plots of calculated whole-rock contents of major- and minor-element oxides (a) and selected LILE (Rb, Sr and Ba) (b) calculated from representative mineral analyses (Appendices 2 and 4) and modal abundances estimated on the basis of the P-XRD, granite mesonorm, constrained least-squares (LSQ), image analysis of the stained thin slab and point counting of a standard thin section (Table 1). The best agreement with the whole-rock contents (vertical orange lines) is achieved by the LSQ method.

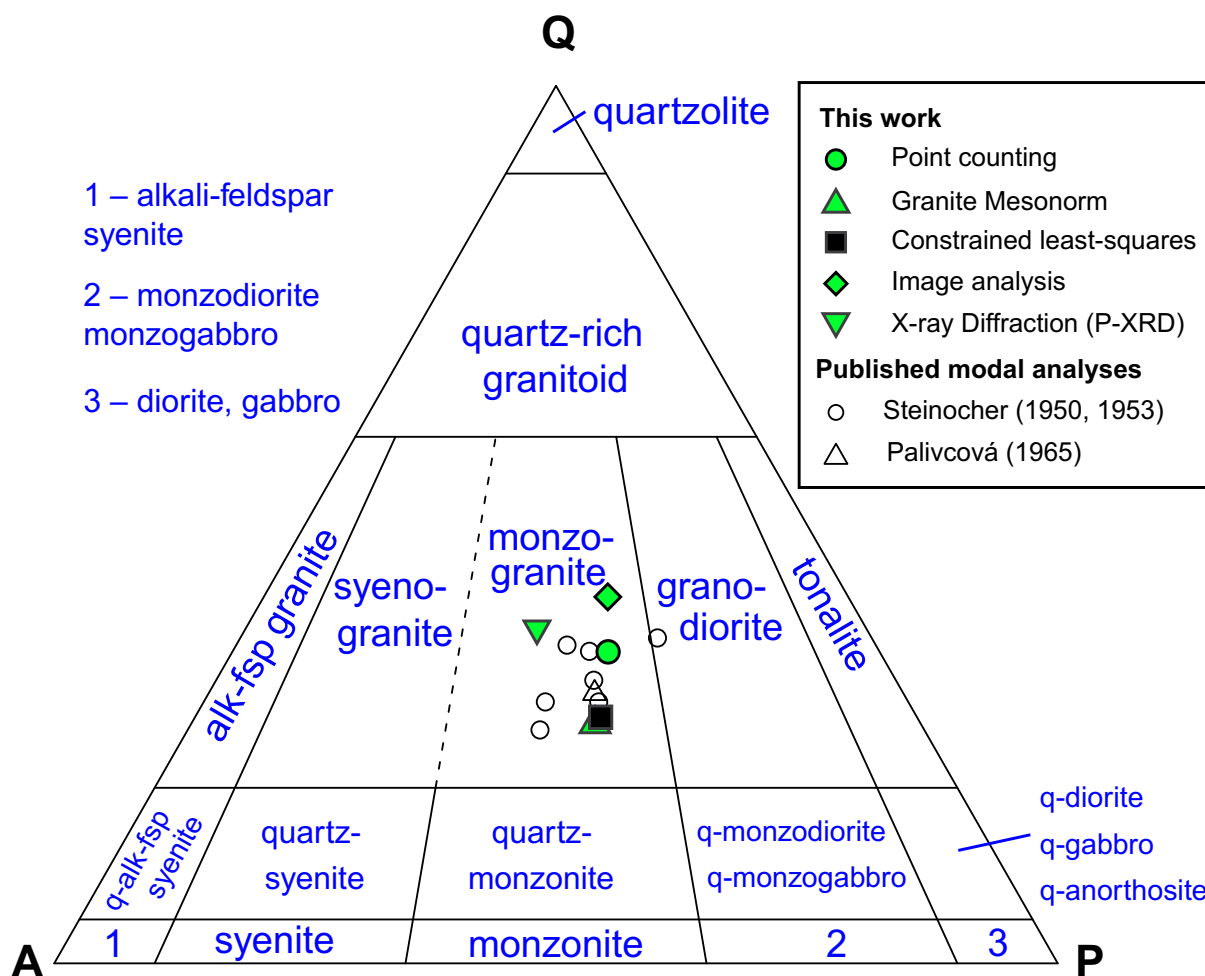


Fig. 8 QAP (quartz, K-feldspar, plagioclase) triangle of Streckeisen (1974) comparing previous modal analyses of the Říčany granite (Steinocher 1950, 1953; Palivcová 1965) with those obtained for sample Žer-1 in course of the present study by various methods. If necessary, the results were recast to vol. %.

part of P resides in monazite. Likewise, the LREE hosted in minerals other than monazite can hardly be neglected.

Regarding the opaque phases, ilmenite and magnetite are the possible carriers of ferromagnetic properties in the granite. It is worth stressing that the mean magnetic susceptibility of the Říčany granite is low ($13.13\text{--}105.3 \times 10^{-6}$ [SI]; Trubač et al. 2009) and thus the rock has to contain only very limited amount of ferromagnetic component. Moreover, in the constrained LSQ calculation, the whole-rock Fe budget is exhausted by biotite and residual TiO_2 is as low as 0.05 wt. % (Table 3). Based on petrographic investigation (Kodymová & Vejnar 1974), rutile seems to be the most important Ti-bearing accessory. Ilmenite, magnetite and titanite were therefore not taken into further consideration, in accord with the microscopic and electron-microprobe studies showing all three phases to be rather rare. The modal abundance of the zircon-like ABO_4 phase remains unknown as the complete trace-element data are not available.

Tab. 4 Constrained least-squares approximation to the modal composition (wt. %)

	Zr	Nb	La	Nd	Eu	Yb	Y	P	wt. %
Ap			2.875	1.166	1.431	0.661	0.473	0.314	0.314
Mnz	1.442	10.761	0.046	0.098	0.641	0.838	0.661	0.524	0.046
Zrn	0.032	0.116	2.459	2.882	3.780	0.550	1.240		0.032
Rt	0.327	0.081	0.655	0.634	3.543	0.691	1.391		0.081
Mgt	14.835	10.647	1.121	2.544	13.639	8.811	7.978		1.121
Ttn	1.443	9.563	0.343	0.260	0.498	0.340	0.255		0.255

Estimates are based on an assumption that the given mineral contains the full whole-rock inventory of the individual elements, after subtracting those hosted by the main phases (0.365 Pl, 0.293 Kfs, 0.247 Qz, 0.093 Bt and 0.02 Ms). Minima for each mineral are shown in bold; these represent maximum possible contents of each phase (last column)

In order to assess the abundances of the remaining accessory minerals (Ap, Mnz, Zrn and Rt), *unconstrained* LSQ method was employed to the outstanding trace-element inventory. Selected were trace elements which often represent their essential structural components (Zr, Nb, La, Nd, Eu, Yb, Y and P). In the solution (Table 5), Ap dominates (0.29 wt. %) over Rt (0.082 %), Mnz (0.04 %) and Zrn (0.023 %). The results are feasible as all obey the upper limits (Table 4) and the residuals for all modelled elements are satisfactory.

WHOLE-ROCK GEOCHEMICAL BUDGET

Total balance

The overall balance of individual elements in the studied sample is illustrated by means of the balloon plot (Jain & Warnes 2006). This diagram conveys important aspects of tabular data without obscuring the exact numeric values (Fig. 9, see caption for explanation of the principle). For the trace elements, the final balance is also presented as an upper continental crust (Taylor & McLennan 1995) normalized spiderplot (Fig. 10). In here, both the real concentrations and computed abundances match rather well. Only middle-heavy REE and, most notably, Th and U are strongly underestimated, suggesting the presence of an additional, U,Th,HREE-rich phase not accounted for in our model. The obvious candidate is the zircon-like ABO_4 mineral (Appendix 5; Fig. 6b), the role of which could not have been quantified as we do not have information on its modal percentage and most of the trace-element signature. Its mean concentrations of Th, U and Yb nevertheless correspond to $\sim 27,000$, $>3,500$ and $>350 \times$ of those found in the upper continental crust (Taylor & McLennan 1995).

wt. %	Or, 29.178	Pl, 36.379	Qtz, 24.527	Bt, 9.285	Ms, 0.199	Ap, 0.289	Mnz, 0.04	Zrn, 0.023	Rt 0.081 wt. %	
SiO ₂	16.72	22.91	24.49	3.48	0.1			0.01		69.71
TiO ₂				0.31					0.08	0.39
Al ₂ O ₃	5.39	7.3		1.37	0.06					14.12
FeOt	0.01			1.6	0.01					1.62
MnO	0.01			0.02						0.03
MgO				1.24						1.24
CaO		1.44				0.16				1.60
Na ₂ O	0.28	3.35		0.01						3.64
K ₂ O	4.55	0.16		0.88	0.02					5.61
P ₂ O ₅		0.01				0.12	0.01			0.14
ppm										
Rb	156.96	57.2	0.02	68.64	1.23			0.01		283.66
Sr	133.84	181.91	0.03	0.16	0.36	0.43	0.04	0.01	0.02	316.80
Ba	862.34	49.31	0.08	116.33	2.21	0.01	0.01	0.06	0.13	1000.48
Ni	0.1	0.77	0.53	10.72	0.04			0.29	1.63	14.08
Co	0.05	0.58		2.29	0.01			0.01	1.18	4.06
Zn	0.5	4.75	0.1	24.14	0.2	0.04	0.04	0.12	0.37	30.26
Cd	0.01	0.02	0.01	0.01	0.01			0.02	0.08	0.11
Be	1.61	7.89	0.01	0.44	0.02		0.01	0.02		9.99
Pb	36.39	21.95	0.02	0.32	0.1	0.16	0.44	0.04	0.26	59.68
Th	1.68	1.14	0.14	0.04	0.96	0.02	1.52	0.22	1.05	7.67
U	0.87	0.6	0.01	0.01	0.12	0.07	0.16	0.11	0.5	2.45
La	1.74	8.63		0.05	2.14	1.23	10.54	0.11	1.51	25.95
Ce	3.13	14		0.16	3.17	3.34	17.55	0.26	1.79	43.40
Pr	0.36	1.71		0.04	0.35	0.64	1.85	0.03	0.42	5.40
Nd	1.35	4.45		0.2	0.89	3.19	5.21	0.1	1.65	17.04
Sm	0.26	0.26		0.07	0.08	1.02	0.51	0.02	0.23	2.45
Eu	0.35	0.26		0.01		0.05	0.02		0.01	0.70
Gd	0.22	0.21		0.06	0.07	0.64	0.29	0.02	0.16	1.67
Tb	0.03	0.01		0.01	0.01	0.11	0.02		0.02	0.21
Dy	0.14	0.01		0.04	0.02	0.58	0.09	0.01	0.06	0.95
Ho	0.02			0.01		0.1	0.01		0.01	0.15
Er	0.07	0.01		0.02	0.01	0.27	0.04	0.01	0.04	0.47
Tm	0.01					0.05			0.01	0.05
Yb	0.07			0.01	0.01	0.21	0.02	0.02	0.06	0.40
Lu	0.01					0.03			0.01	0.05
Y	0.71	0.05		0.26	0.07	3.39	0.33	0.1	0.32	5.23
Nb	0.4	2.02		9.65	0.09		0.01	0.76	3.8	16.73
Ta	0.08	0.02		0.94	0.04			0.1	0.39	1.57
Zr	19.01	3.71	0.05	0.12	1.37		4	104.36	36.21	168.83
Hf	0.6	0.21		0.01	0.05		0.12	3.69	1.11	5.79

Fig. 9 Balloon plot (Jain & Warnes 2006) expressing the balance of individual elements in the studied granite sample. The relative contributions of individual minerals are expressed by the colour and size of circles plotted. Each number was obtained by multiplication of the particular element/oxide concentration within the given mineral and the best estimate of its modal abundance. The goodness of fit could be assessed comparing row totals with the real whole-rock analyses.

Tab. 5 Modal percentages of the most abundant accessories (wt. %) estimated by the unconstrained least-squares method

(ppm)	Ap ¹	Mnz	Zrn	Rt	Real ²	Calc. ⁴
Zr	1.2	10086.7	453122.0	44550.4	145.5	145.5
Nb	0.1	35.3	3288.9	4675.2	3.8	4.6
La	424.5	26574.3	496.4	1861.8	12.2	13.5
Nd	1105.0	13148.3	446.9	2031.7	12.9	10.2
Eu	18.3	40.8	6.9	7.4	0.3	0.1
Yb	72.2	57.0	86.9	69.1	0.5	0.3
Y	1173.8	839.3	447.3	398.7	5.5	4.2
P	186228.0	111734.2	0.0	17.5	585.4	585.4
estimated modal proportions (wt. %) ³	0.290%	0.040%	0.023%	0.082%		

¹ real mineral analyses are summarized in the Appendix 2

² the whole-rock composition not accounted for by the main rock-forming minerals. See text for discussion

³ estimated modal percentages obtained by the least-squares approach

⁴ composition of a mixture (ppm) calculated using these mineral proportions

Residence in individual minerals

Returning to the Fig. 9, one can examine the residence of particular elements in detail. Silica is hosted almost equally by quartz (35 wt. % of its whole-rock abundance), plagioclase (33 %), and somewhat less by K-feldspar (27 %). Bulk Ti, Fe and Mg are held by biotite, whereby rutile contains a fifth of the whole-rock TiO₂. Also much of the MnO is accounted for by biotite but almost a third is hosted by K-feldspar. As expected, the main reservoirs for Al₂O₃ are the feldspars (Pl: 52 %, Kfs: 38 %). Surprisingly little Al, however, resides in biotite (10 %), owing to its small modal abundance. Most of CaO and Na₂O are bound to plagioclase (~90 %); only 10 % of the former is stored in apatite and 8 % of the latter in K-feldspar. Part of the Na₂O contents in K-feldspar is to be ascribed to small plagioclase inclusions observed during petrographic studies. For K₂O, K-feldspar is clearly the key host (81 %), biotite accounting for mere 16 % of the whole-rock budget. The main reservoir for P represents apatite; monazite's contribution is small, close to 7 %.

Concerning the LILE, Rb is accumulated by K-feldspar (55 %), the second comes biotite (24 %) and third plagioclase (20 %). The two feldspars represent almost equally important Sr reservoirs (Pl: 57 %, Kfs: 42 %). The bulk of Ba is concentrated in K-feldspar (83 %); both biotite (12 %) and plagioclase (5 %) are rather unimportant. The overwhelming majority of Be (79 %) is located in plagioclase; K-feldspar and biotite share the rest. Lead is another element for which the feldspars are the main hosts (Kfs: 61 %, Pl: 37 %).

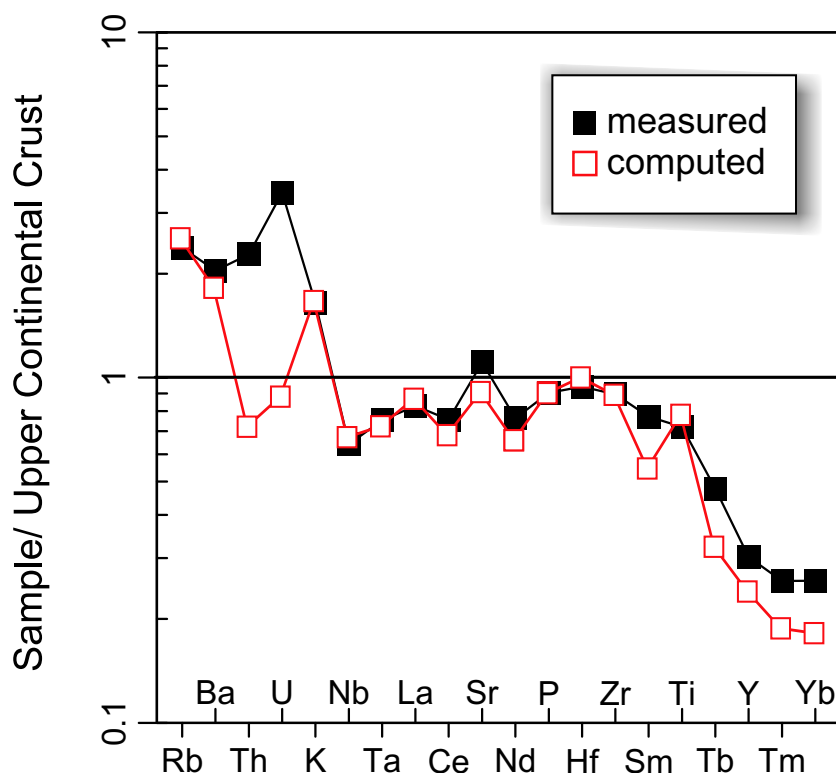


Fig. 10 Spiderplot of trace-element concentrations observed in the whole-rock sample Žer-1 (filled squares) and calculated (empty squares), normalized by abundances in the average upper continental crust (Taylor & McLennan 1995). The calculation was made for all minerals present in Fig. 9.

The most important LREE reservoirs are monazite (41 % La) and plagioclase (33 % La), much less significant seem muscovite, K-feldspar, rutile and apatite. The bulk of Eu is accounted for by the feldspars (Kfs 50 % and Pl 38 %); the apatite contribution represents mere 8 %. On the other hand, apatite is the most important host for the middle and heavy REE as well as Y. Less significant HREE-bearing phase is rutile. Surprisingly, zircon and monazite do not rank among important sinks for HREE, owing to their scarcity.

Regarding the radioactive elements, both feldspars seem to incorporate much U (Kfs: 35 and Pl: 25 %). Among accessories, rutile accounts for over 20 % of both Th and U. Almost equally significant for Th are K-feldspar, monazite and rutile, less so plagioclase (15 %) and muscovite (13 %). Minerals such as zircon and apatite play only marginal role in hosting the radioactive elements, unlike probably the newly recognized zircon-like ABO_4 phase, even though its role cannot be quantified.

Among the HFSE, the zircon contains only ~70 % of the total Zr and Hf; for rutile there remains the rest. About 60 % of the Nb and Ta budget are hosted by biotite. We can only speculate that this may be in a form of submicroscopic inclusions; for rutile remains approximately one fifth of the whole-rock inventory.

GENERAL IMPLICATIONS

Modal analysis

Petrographic techniques

In studies of granitic rocks, unstained thin sections are best suited for most textural observations, as well as description of optical properties and identification of mafic minerals. In many cases, however, it is difficult to determine some of the colourless phases, particularly if the feldspars are not twinned or their grains are small. One way out is to use cold-stage cathodoluminescence (CL), in which the (mostly) blue K-feldspars are easily distinguished from ochre–yellow plagioclases and almost non-luminescent quartz (Marshall 1988; Janoušek et al. 2000a, 2004). The CL also facilitates rapid determination and mapping of some accessory phases, such as of apatite, monazite and zircon. Nowadays largely neglected, staining turns K-feldspars yellow and plagioclase white, also facilitating point counting (Gabriel & Cox 1929; Hollocher 2013).

Obtaining a statistically valid modal analysis by point counting of a standard thin section can be troublesome, especially for coarse-grained or porphyritic rocks (Chayes & Fairbairn 1951; Chayes 1954; 1965; Hutchison 1974). In order to maximize the counted area in these cases, it was proposed to use rock slabs or point count directly on the outcrop (e.g., Hutchison 1974) – but such methods are cumbersome and seldom used. Clearly, the situation becomes even more complicated when the rock possesses a fabric, as one deals essentially with a 2D section of a three-dimensional anisotropic body.

In our case, the approach using the stained polished slab is superior, as it represents an area larger than the standard section (c. 119 vs. 6 cm²). The current work confirms that the tedious point-counting of the stained sample can be successfully replaced by computer-aided image analysis. However, this method also brings about some new problems, e.g. some degree of ambiguity caused by the feldspars alteration.

P-XRD

The Rietveld method has been widely used for quantitative phase analysis of various geological materials and industrial products (Madsen & Scarlett 2009 and references therein). This full-pattern profile fitting method has several advantages over other diffraction approaches to quantitative phase analysis using at most a few strongest reflections from each phase in the mixture (Bish & Post 1989). Nevertheless, the application of the Rietveld method to geological materials still poses significant problems. The most pronounced difficulties are microabsorption effects, complex preferred orientation, various chemical substitutions in minerals and also presence of structural defects.

Our estimate of modal composition obtained by P-XRD is probably biased by the defect structure of kaolinite, which is affected by planar disorder. Considering the complexity of the diffraction pattern, large number of reflections and presence of significant preferred orientation, the results from P-XRD are reasonable, i. e. comparable to other approaches. The advantage of the P-XRD method over standard petrographic techniques is that it represents, similar to the chemical approaches, the whole volume of the homogenized sample.

Chemical methods

For the sample Žer-1, the bulk-rock analysis represents ~30 kg, i.e. over 11,000 cm³ of the rock, and thus should be robust to the presence of fabrics, phenocrysts and local inhomogeneities such as schlieren. Major-element or norm-based schemes (Streckeisen & Le Maitre 1979; De La Roche et al. 1980; Debon & Le Fort 1988) have been preferred by many authors for classification purposes. However, some normative recalculations involve minerals not encountered in common felsic plutonites and thus their use is not straightforward (e.g., CIPW and Catanorm, Hutchison 1975). For this reason, Mielke & Winkler (1979) developed their 'Improved Mesonorm', designed specifically for granitic rocks.

With advancement of personal computers, mathematical methods became popular, that attempt to find the best estimate of modal proportions based on major- and minor-element analyses of the large whole-rock sample and its typical mineral constituents. As usual the number of chemical components exceeds that of the mineral phases, there is no unique solution and the algorithms rely on the least-squares or linear programming approaches (e.g., Wright & Doherty 1970; Le Maitre 1981; Laube et al. 1996; Paktunc 1998; Janoušek et al. 2006). Potential pitfalls could represent the choice of typical mineral compositions and/or the weathering/alteration effects.

The methods are also rather insensitive to the presence of minor or accessory phases, whose contents have to be assessed separately.

Here the results obtained by mesonormative and LSQ approaches are well comparable for felsic minerals (Fig. 8). The amount of biotite, however, is nearly half (5.8 vs. 9.3 wt. %, respectively), and much lower also than estimates by the remaining methods. The reason consists probably in the fact that the mesonorm also estimates the proportion of magnetite and ilmenite, whereby in the LSQ calculation the sole iron-bearing phase is biotite. The normative contents of the opaque phases seem overestimated by the mesonormative algorithm, especially that of magnetite (0.9 %).

Taken together, several of the methods employed here to estimate the modal proportions of the main rock-forming minerals have yielded comparable results. It needs to be stressed that the current case is a particularly favourable one, as in Říčany Pluton is not observed any significant zoning of mineral phases, not even of plagioclase. Moreover, K-feldspar phenocrysts in the studied sample are small and sparse. Still, the constrained LSQ method (Albarède 1995) was found superior to all other approaches. The obtained percentages of the main rock-forming minerals compare well with the modal analyses determined previously by conventional point counting (Steinöcher 1950; 1953; Palivcová 1965) (Fig. 8).

Petrogenetic modelling

Collectively, the four accessories, apatite, monazite, zircon and rutile host more than half of the total LREE and over three quarters of HREE + Y, Zr and Hf of the studied granite sample. Similar, albeit not so extreme, is the case of Th, U, Ti, Ni, Co, Nb and Ta. This confirms the notion that the accessories are often crucial in controlling the behaviour of many elements in granitic systems (e.g., Mittlefehldt & Miller 1983; Miller & Mittlefehldt 1984; Bea 1996). Particularly the REE are of little value in petrogenetic modelling of fractional crystallization of the main rock-forming minerals, unless the role of accessories is properly assessed.

Determination of the whole-rock trace-element abundances

Some 10–30 % of the whole-rock HREE, U, Th, Nb, Ta, Ti, Cd, Co and Ni, and even more of Zr and Hf, are contained in the resistant accessories, zircon and rutile. Thus the pressure bomb or sample fusion are absolutely essential in sample decomposition were these elements to be determined quantitatively (e.g., Potts 1987; García de Madinabeitia et al. 2008 and references therein).

Using a combined HF, HCl and HNO₃ attack is clearly inadequate and will induce low total REE contents and artificially increased degrees of LREE/HREE fractionation. Alas such cases are by no means rare – for instance, the acid decomposition casts serious doubts on some of the results by Minařík et al. (1998).

Saturation thermometry

Our study provides some interesting implications for the accessory phase saturation thermometry commonly used in the granite studies (see Janoušek 2006 and Anderson et al. 2008 for review). As in Říčany is phosphorus hosted nearly exclusively by apatite (86 % of the whole-rock contents), the saturation thermometry involving this mineral should be applicable. Indeed the temperature calculated for the uncorrected whole-rock P₂O₅ content and that based on apatite-hosted P₂O₅ are both mutually well comparable (946 vs. 931 °C according to the model of Harrison & Watson 1984). The fact that they are unrealistically high for a granitic magma can be related to the sensitivity of the algorithm to exact determinations of P₂O₅ contents, as the isotherms converge rapidly for increasingly acidic compositions (see fig. 3a in Janoušek 2006).

Zircon incorporates mere 62 % of the whole-rock Zr budget (Fig. 9), the rest being hosted by other phases, most importantly the early crystallizing rutile. The zircon saturation thermometry (Watson & Harrison 1983) thus yields a liquidus temperature estimate (784 °C) c. 40 °C higher than that calculated for the corrected Zr concentration.

The case of monazite is more complex, though. The model of Montel (1993) includes additional parameters apart from the temperature, major-element and LREE contents of the magma. One is the fraction of REE phosphates in the monazite but this can be directly measured (the average for Říčany monazite is 89.5 mol. %). More difficult to constrain are the water contents of the magma. Fortunately, the effect is not great (738 °C is obtained for 3 wt. % H₂O; 761–724 °C for 1–5 wt. % H₂O). Plagioclase represents an important sink for LREE, with monazite containing some 21–41 % of the whole-rock inventory. This brings problems for the LREE-based monazite thermometry. While the uncorrected LREE content yields 738 °C, corrected one gives barely 668 °C, i.e. some 70 °C less (for 3 wt. % H₂O in the melt). Such a corrected temperature seems to be too low for a granitic magma. However, one should take into account the petrological evidence indicating that the monazite saturation level was probably reached early, prior to onset of the plagioclase crystallization. Thus using the uncorrected temperature seems more justifiable here.

CONCLUSIONS

The study of petrography and mineral chemistry of a single large sample of coarse-grained, weakly porphyritic (muscovite–) biotite granite of the Říčany intrusion (Czech Republic) has yielded the following conclusions:

1. Particularly suitable for modal analyses of granitic rocks are the methods taking into account the whole-rock composition as well as the true mineral chemistries (linear programming or constrained least squares). The modes then represent a large volume of sample and thus (i) smooth out any local variations, e.g. small-scale crystal accumulation, (ii) account for the presence of phenocrysts, and (iii) are insensitive to shaped-preferred orientation/fabric.
2. Accessory phases control the behaviour of many trace elements in differentiation of felsic granitic systems. Clearly the REE are of little value in petrogenetic modelling of the main rock-forming minerals fractionation, unless the role of accessories is properly assessed and existing saturation models for apatite, zircon, monazite \pm rutile are carefully considered.
3. The fact that much of essential structural components (P, Zr, LREE) used in apatite, zircon and monazite saturation thermometry is incorporated into other minerals may lead to significant overestimation of the liquidus temperatures. In the present case, the saturation temperatures for zircon would be overestimated by c. 40 °C due to significant contents of Zr in the early crystallized rutile. However, the correction for monazite (–70 °C) probably should not be applied as most of the extra LREE are hosted by plagioclase, a relatively late mineral.
4. In the studied sample, over 80 % of the whole-rock Zr and Hf and c. 10–30 % of HREE, U, Th, Nb, Ta, Ti, Cd, Co and Ni are contained in resistant accessory phases Zrn and Rt. Thus the pressure vessel or sample fusion – and not merely a combined acid attack – are absolutely essential in sample decomposition were these elements to be determined quantitatively.

ACKNOWLEDGEMENTS

This manuscript benefited from insightful comments by I. Broska, an anonymous reviewer and handling editor I. Petřík, as well as from careful editing by E. Petříková. The authors are indebted to Z. Korblová for assistance at the electron microprobe and J. K. Novák (both Geological Institute, Czech Academy of Sciences, Prague – GLI) who carried out the point counting analysis. V. Sedláček (GLI) did the mineral separations, P. Hasalová (Czech Geological Survey) helped with staining of feldspars. Janoušek and Trubač acknowledge the support by the Grant Agency of the Czech Republic (GAČR, No. P210/11/1168) and Czech Ministry of Education, Youth and Sports (project LK 11202); Minařík and Navrátil were supported from institutional project No. RVO67985831. This study is

a part of Ph.D. research of Jakub Trubač.

REFERENCES

- Albarède F. 1995: Introduction to Geochemical Modeling. Cambridge University Press, Cambridge, 1-543.
- Anderson J.L., Barth A.P., Wooden J.L. & Mazdab F. 2008: Thermometers and Thermobarometers in Granitic Systems. In: Putirka K.D. & Tepley III F.J. (Eds.): Minerals, Inclusions And Volcanic Processes. Mineralogical Society of America and Geochemical Society Reviews in Mineralogy and Geochemistry 69, Washington, 121-142.
- Bea F. 1996: Residence of REE, Y, Th and U in granites and crustal protoliths; implications for the chemistry of crustal melts. *J. Petrol.* 37, 521-552.
- Bish D.L. & Post J.E. 1989: Modern Powder Diffraction. Mineralogical Society of America Reviews in Mineralogy 20, Washington, 1-369.
- Boynton W.V. 1984: Cosmochemistry of the rare earth elements: meteorite studies. In: Henderson P. (Ed.): Rare Earth Element Geochemistry. Elsevier, Amsterdam, 63-114.
- Chayes F. 1954: The theory of thin-section analysis. *J. Geol.* 62, 92-101.
- Chayes F. 1965: Reliability of point counting results. *Amer. J. Sci.* 263, 719-724.
- Chayes F. & Fairbairn H.W. 1951: A test of the precision of thin-section analysis by point counter. *Amer. Mineralogist* 36, 704-712.
- De La Roche H., Leterrier J., Grandclaude P. & Marchal M. 1980: A classification of volcanic and plutonic rocks using R1R2-diagram and major element analyses – its relationships with current nomenclature. *Chem. Geol.* 29, 183-210.
- Debon F. & Le Fort P. 1988: A cationic classification of common plutonic rocks and their magmatic associations: principles, method, applications. *Bull. Minéral.* 111, 493-510.
- Evans O.C. & Hanson G.N. 1993: Accessory-mineral fractionation of rare-earth element (REE) abundances in granitoid rocks. *Chem. Geol.* 110, 69-93.
- Gabriel A. & Cox E.P. 1929: A staining method for the quantitative determination of certain rock minerals. *Amer. Mineralogist* 14, 290-292.
- García de Madinabeitia S., Sánchez Lorda M.E. & Gil Ibarguchi J.I. 2008: Simultaneous determination of major to ultratrace elements in geological samples by fusion-dissolution and inductively coupled plasma mass spectrometry techniques. *Anal. Chim. Acta* 625, 117-130.
- Geisler T., Pidgeon R.T., van Bronswijk W. & Kurtz R. 2002: Transport of uranium, thorium, and lead in metamict zircon under low-temperature hydrothermal conditions. *Chem. Geol.* 191, 141-154.

- Geisler T., Pidgeon R.T., Kurtz R., van Bronswijk W. & Schleicher H. 2003: Experimental hydrothermal alteration of partially metamict zircon. *Amer. Mineralogist* 88, 1496-1513.
- Gromet L.P. & Silver L.T. 1983: Rare earth element distribution among minerals in a granodiorite and their petrogenetic implications. *Geochim. Cosmochim. Acta* 47, 925-939.
- Hanson G.N. 1978: The application of trace elements to the petrogenesis of igneous rocks of granitic composition. *Earth Planet. Sci. Lett.* 38, 26-43.
- Harrison T.M. & Watson E.B. 1984: The behavior of apatite during crustal anatexis: equilibrium and kinetic considerations. *Geochim. Cosmochim. Acta* 48, 1467-1477.
- Hejtman B. 1948: Directory of quarries in Czechoslovakia, No. 26, Český Brod. SGÚ ČSR, Praha, 1-71 (in Czech).
- Hollocher K 2013: Staining feldspars in thin section. Accessed on 23 December 2013 at http://minerva.union.edu/hollochk/c_petrology/staining_feldspars.htm.
- Holub F.V., Machart J. & Manová M. 1997: The Central Bohemian Plutonic Complex: geology, chemical composition and genetic interpretation. *Sbor. geol. Věd, ložisk. Geol. Mineral.* 31, 27-50.
- Hoskin P.W.O. & Schaltegger U. 2003: The composition of zircon and igneous and metamorphic petrogenesis. In: Hanchar J.M. & Hoskin P.W.O. (Eds.): *Zircon. Mineralogical Society of America and Geochemical Society Reviews in Mineralogy and Geochemistry* 53, Washington, 27-62.
- Hutchison C.S. 1974: *Laboratory Handbook of Petrographic Techniques*. John Wiley & Sons, New York, 1-527.
- Hutchison C.S. 1975: The norm, its variations, their calculation and relationships. *Schweiz. mineral. petrogr. Mitt.* 55, 243-256.
- Jain N. & Warnes G.R. 2006: Ballon plot. *R News* 6, 35-38.
- Janoušek V. 2006: Saturnin, R language script for application of accessory-mineral saturation models in igneous geochemistry. *Geol. Carpath.* 57, 131-142.
- Janoušek V., Rogers G., Bowes D.R. & Vaňková V. 1997: Cryptic trace-element variation as an indicator of reverse zoning in a granitic pluton: the Říčany granite, Czech Republic. *J. Geol. Soc. London* 154, 807-815.
- Janoušek V., Bowes D.R., Braithwaite C.J.R. & Rogers G. 2000a: Microstructural and mineralogical evidence for limited involvement of magma mixing in the petrogenesis of a Hercynian high-K calc-alkaline intrusion: the Kozárovec granodiorite, Central Bohemian Pluton, Czech Republic. *Trans. Roy. Soc. Edinb., Earth Sci.* 91, 15-26.
- Janoušek V., Bowes D.R., Rogers G., Farrow C.M. & Jelínek E. 2000b: Modelling diverse processes in

- the petrogenesis of a composite batholith: the Central Bohemian Pluton, Central European Hercynides. *J. Petrol.* 41, 511-543.
- Janoušek V., Braithwaite C.J.R., Bowes D.R. & Gerdes A. 2004: Magma-mixing in the genesis of Hercynian calc-alkaline granitoids: an integrated petrographic and geochemical study of the Sázava intrusion, Central Bohemian Pluton, Czech Republic. *Lithos* 78, 67-99.
- Janoušek V., Farrow C.M. & Erban V. 2006: Interpretation of whole-rock geochemical data in igneous geochemistry: introducing Geochemical Data Toolkit (GCDkit). *J. Petrol.* 47, 1255-1259.
- Johannsen A. 1932, 1937, 1938, 1939: A descriptive petrography of the igneous rocks. University of Chicago Press.
- Katzer F. 1888: Geologische Beschreibung der Umgebung von Říčán. *Jb. Geol. Reichsanst.* 38, 355-417.
- Kodymová A. & Vejnar Z. 1974: Accessoric heavy minerals in plutonic rocks of the Central Bohemian Pluton. *Sbor. geol. Věd, ložisk. Geol. Mineral.* 16, 89-128 (in Czech).
- Kretz R. 1983: Symbols for rock-forming minerals. *Amer. Mineralogist* 68, 277-279.
- Laube N., Hergarten S. & Neugebauer H.J. 1996: MODUSCALC - a computer program to calculate mode from a geochemical rock analysis. *Comput. and Geosci.* 22, 631-637.
- Le Maitre R.W. 1981: GENMIX - a generalized petrological mixing model program. *Comput. and Geosci.* 7, 229-247.
- Le Maitre R.W. 2002: Igneous rocks: a classification and glossary of terms: recommendations of the International Union of Geological Sciences, Subcommittee on the Systematics of Igneous Rocks. Cambridge University Press, 1-236.
- Madsen I.C. & Scarlett N.V.Y. 2009: Quantitative Phase Analysis. In: Dinnebier R.E. & Bilinge S.J.J. (Eds.): Powder Diffraction: Theory and Practise. RCS Publishing, Cambridge, 298-331.
- Marshall D.J. 1988: Cathodoluminescence of Geological Materials. Unwin Hyman, Boston, 1-145.
- Mielke P. & Winkler H.G.F. 1979: Eine bessere Berechnung der Mesonorm für granitische Gesteine. *Neu. Jb. Mineral., Mh.* 471-480.
- Miller C.F. & Mittlefehldt D.W. 1984: Extreme fractionation in felsic magma chambers; a product of liquid-state diffusion or fractional crystallization? *Earth Planet. Sci. Lett.* 68, 151-158.
- Minařík L. & Houdková Z. 1986: Element distribution during the weathering of granitic rocks and formation of soils in the area of the massif of Říčany. *Acta Montana* 74, 59-78 (in Czech with English summary).

- Minařík L. & Kvídová O. 1986: Fractionation of rare earth elements during weathering of rocks. *Acta Montana* 72, 63-74 (in Czech with English summary).
- Minařík L., Žigová A., Bendl J., Skřivan P. & Šťastný M. 1998: The behaviour of rare-earth elements and Y during the rock weathering and soil formation in the Říčany granite massif, Central Bohemia. *Sci. Total Environ.* 215, 101-111.
- Minařík L., Skřivan P., Novák J.K., Fottová D. & Navrátil T. 2003: Distribution, cycling and impact of selected inorganic contaminants in ecosystem of the Lesní potok catchment, the Czech Republic. *Ekologia (Bratislava)* 22, 305-322.
- Mittlefehldt D.W. & Miller C.F. 1983: Geochemistry of the Sweetwater Wash Pluton, California; implications for "anomalous" trace element behavior during differentiation of felsic magmas. *Geochim. Cosmochim. Acta* 47, 109-124.
- Montel J.M. 1993: A model for monazite/melt equilibrium and application to the generation of granitic magmas. *Chem. Geol.* 110, 127-146.
- Navrátil T. 2003: Biogeochemistry of the II.A group elements in a forested catchment. Unpublished Ph.D. thesis, Charles University in Prague, 1-113.
- Navrátil T., Skřivan P., Minařík L. & Žigová A. 2002: Beryllium geochemistry in the Lesní Potok Catchment (Czech Republic), 7 years of systematic study. *Aquat. Geochem.* 8, 121-133.
- Navrátil T., Vach M., Skřivan P., Mihaljevič M. & Dobešová I. 2004: Deposition and fate of lead in a forested catchment, Lesní potok, Central Czech Republic. *Water Air Soil Poll.: Focus* 4, 619-630.
- Navrátil T., Shanley J.B., Skřivan P., Krám P., Mihaljevič M. & Dražota P. 2007: Manganese biogeochemistry in a Central Czech Republic catchment. *Water Air Soil Poll.* 186, 149-165.
- Němec D. 1978: Genesis of aplite in the Říčany massif, central Bohemia. *Neu. Jb. Mineral., Abh.* 132, 322-339.
- Niggli P. 1931: Die quantitative mineralogische Klassifikation der Eruptivgesteine. *Schweiz. mineral. petrogr. Mitt.* 11, 296-364.
- Orlov A. 1933: Contribution to the petrography of the Central Bohemian Granite Massif (the Říčany—Benešov—Milevsko-Písek region). *Věst. St. geol. Úst. Čs. Republ.* 9, 135–144 (in Czech).
- Paktunc A.D. 1998: MODAN: an interactive computer program for estimating mineral quantities based on bulk composition. *Comput. and Geosci.* 24, 425-431.
- Palivcová M. 1965: The Central Bohemian Pluton – a petrographic review and an attempt at a new genetic interpretation. *Krystalinikum* 3, 99-131.

- Palivcová M., Waldhausrová J., Ledvinková V. & Fatková J. 1992: Říčany granite (Central Bohemian Pluton) and its ocelli- and ovoids-bearing mafic enclaves. *Krystalinikum* 21, 33-66.
- Pivec E. 1970: On the origin of phenocrysts of potassium feldspars in some granitic rocks of the Central Bohemian Pluton. *Acta Univ. Carol, Geol.* 1970, 11-25.
- Pivec E. 1969: Residues of surface kaolinization in granite of Říčany. *Čas. Mineral. Geol.* 14, 61-67 (in Czech with English summary).
- Potts P.J. 1987: *A Handbook of Silicate Rock Analysis*. Blackie & Son Ltd., Glasgow and London, 1-622.
- Robie R.A., Bethke P.M. & Beardsley K.M. 1967: Selected X-ray crystallographic data, molar volumes, and densities of minerals and related substances. *U. S. Geol. Surv. Bull.* 1248, Washington, 1-87.
- Sawka W.N. 1988: REE and trace element variations in accessory minerals and hornblende from the strongly zoned McMurry Meadows Pluton, California. *Trans. Roy. Soc. Edinb., Earth Sci.* 79, 157-168.
- Steinöcher V. 1950: The position of some plutonic and dike rocks of the plutonic mass of Central Bohemia in P. Niggli's quantitative mineralogical and chemical system. Part I. *Sbor. St. geol. Úst. Čs. Republ., Odd. geol.* 17, 721-764.
- Steinöcher V. 1953: The position of some plutonic and dyke rocks of the Pluton of Central Bohemia in P. Niggli's quantitative mineralogical and chemical system. Part II. *Sbor. Ústř. Úst. geol., Odd. geol.* 20, 241-288.
- Streckeisen A. 1974: Classification and nomenclature of plutonic rocks. *Geol. Rundsch.* 63, 773-786.
- Streckeisen A. & Le Maitre R.W. 1979: A chemical approximation to the modal QAPF classification of the igneous rocks. *Neu. Jb. Mineral., Abh.* 136, 169-206.
- Taylor S.R. & McLennan S.M. 1995: The geochemical evolution of the continental crust. *Rev. Geophys.* 33, 241-265.
- Trubač J., Žák J., Chlupáčová M. & Janoušek V. 2009: Magnetic fabric of the Říčany granite, Bohemian Massif: a record of helical magma flow? *J. Volcanol. Geotherm. Res.* 181, 25-34.
- Wark D.A. & Miller C.F. 1993: Accessory mineral behavior during differentiation of a granite suite: monazite, xenotime and zircon in the Sweetwater Wash pluton, southeastern California, U.S.A. *Chem. Geol.* 110, 49-67.
- Watson E.B. & Harrison T.M. 1983: Zircon saturation revisited: temperature and composition effects in a variety of crustal magma types. *Earth Planet. Sci. Lett.* 64, 295-304.

Wright T.L. & Doherty P.C. 1970: A linear programming and least squares computer method for solving petrologic mixing problems. *Geol. Soc. Amer. Bull.* 81, 1995-2008.

Žák J., Verner K., Janoušek V., Holub F.V., Kachlík V., Finger F., Hajná J., Tomek F., Vondrovič L. & Trubač J. 2014: A plate-kinematic model for the assembly of the Bohemian Massif constrained by structural relationships around granitoid plutons. In: Schulmann K., Martínez Catalán J.R., Lardeaux J.M., Janoušek V. & Oggiano G. (Eds.): *The Variscan Orogeny: Extent, Timescale and the Formation of the European Crust*. Geological Society, London, Special Publications 405, 169-196. doi: 10.1144/SP405.9

ELECTRONIC APPENDICES

Appendix 1: Analytical techniques

Sampling

The whole-rock sample Žer-1 (~ 30 kg) was collected in the Žernovka quarry, c. 850 m NNW of the namesake village off the pluton's centre (Fig. 1c, GPS 50°0'22.64"N; 14°44'56.13"E). Its bulk was crushed by steel jaw crusher, homogenized and ground in agate mill at the Laboratories of Institute of Geology, Czech Academy of Sciences, v. v. i. (CAS).

Mineral separation

Crushed material (<500 µm) was floated on Wilfley shaking table. Heavy fraction was filtered on glass frit, rinsed with ethanol and air dried. The light fraction was dried at 105 °C and was used for separation of the main rock-forming minerals. Fraction between 63 and 250 µm thereof served for magnetic separation of biotite. The biotite separate was finally cleaned in acetylene tetrabromide with density of 2.54 kg.m⁻³.

The quartz separate was obtained after biotite separation by flotation using ANP1 (amino nitro paraffin) agent. K-feldspar was separated in bromoform solution (2.59 kg.m⁻³). Material with density greater than 2.54 kg.m⁻³ was plagioclase. Following the separation of quartz and orthoclase, muscovite separation was achieved in bromoform with density 2.74–2.84 kg.m⁻³. Kaolinite was isolated by centrifugation of the fine fraction (< 25 µm) in bromoform.

Dried heavy fraction from the shaking table was sieved on 315 µm nylon sieve. Fine fraction was used for separation of heavy minerals – zircon and monazite. Apatite was recovered from the heavy fraction by centrifugation in methyleniodide with density 3.18–3.25 kg.m⁻³. Magnetite was obtained from the dark part of heavy fraction by magnetic separation with the intensity of magnetic field set to 0.2 A.

Electron microprobe and BSE imaging

The analyses of the major rock-forming and selected accessory minerals were done with fully automated CAMECA SX-100 electron microprobe, employing $\Phi(\rho z)$ correction procedure (Merlet 1992) at CAS. All analyses were performed at an acceleration voltage of 15 kV but with different beam currents and spot sizes chosen according to the mineral type. Thus 20–40 nA and a spot size of

10 µm were employed for analyses of apatite, titanite, rutile, monazite, magnetite, ilmenite and zircon–thorite solid solution. For feldspars, micas and quartz, the beam current was 10–15 nA and spot size 2 µm. Minor-element interferences have been checked routinely and corrected for by measuring the corresponding standards. All the mineral abbreviations are after Kretz (1983).

Whole-rock major- and minor-element analyses

The major-element whole-rock analysis of the whole-rock sample was undertaken by wet chemistry in the laboratories of the Czech Geological Survey, Prague–Barrandov. Further analytical details are given in Dempírová (2010); the relative 2σ uncertainties were better than 1 % (SiO_2), 2 % (FeO), 5 % (Al_2O_3 , K_2O and Na_2O), 7 % (TiO_2 , MnO, CaO), 6 % (MgO) and 10 % (Fe_2O_3 , P_2O_5). Interpretation and plotting of the whole-rock geochemical data was done by R-language package GCDkit (Janoušek et al. 2006).

Trace-element analyses

Solution ICP-MS analyses

The trace-element analyses of mineral separates and whole-rock samples were carried out after modified total digestion in mineral acids ($\text{HF} + \text{HClO}_4$) and borate fusion ($\text{Na}_2\text{CO}_3 + \text{Na}_2\text{B}_4\text{O}_7$) in Pt crucibles followed by solution nebulization ICP-MS PQ3 VG Elemental at Charles University in Prague. All the chemicals involved were reagent grade (Merck, Germany) and the acids were double distilled. Deionized water from a Millipore system (Milli-Q Academic, USA) was used for all dilutions. The measured data were processed on-line using VG PlasmaLab software, applying corrections for instrumental drift. The analytical precision for all the elements analyzed ranged from 0.5 to 5% relative. The accuracy of this analytical method was checked using the G-2 and BCR-2 reference materials (USGS, USA). Trace-element ICP-MS analyses followed the methods of Strnad et al. (2005).

In-situ laser ablation analyses

In-situ trace element analyses were performed on a quadrupole-based ICP-MS Thermo Fisher X-Series II (Charles University) coupled to a NewWave UP 213 laser microprobe (NewWave Research; USA) operating at output wavelength of 213 nm. All samples were prepared as a polished thin section. The data were acquired in the time-resolved and peak jumping mode with one point measured per mass peak and processed off-line by Thermo Fisher PlasmaLab software 2.5.11 321. The raster pattern was linear, approx. 80×400 μm. External calibration of the laser-ablation analyses was done using standards NIST 610 and 612 (Pearce et al. 1997). For internal standardization ²⁹Si concentrations based on electron microprobe measurements were applied. Data reduction included correction for the gas blank, the internal standard and a calibration check; the data were processed off-line in a MS Excel spreadsheet-based program. For details on analytical protocol and correction strategy see Strnad et al. (2005).

Modal analyses

Point counting

Point counting was done on a thin section 3×2 cm using a standard optical microscope. The total number of points counted was 4 890.

Image analysis of stained rock slab

Rock sample has been stained according to method of Gabriel & Cox (1929). The polished sample surface was exposed to fumes of HF for about 15 min., then treated with a concentrated solution of sodium cobaltinitrite for another 10 min., rinsed and dried. This reaction forms a yellow coating on K-feldspar and white on plagioclase; quartz remains unaffected.

The image analysis was performed on a scanned stained polished rock slab (c. 17×7 cm). The abundance of mineral phases was estimated on the basis of pixel colour analysis by Quick Photo Micro 2.2 software. Dark–black areas were attributed to biotite, grey and greyish glassy-like colour to quartz, white to plagioclase and yellow to K-feldspar.

Powder X-ray diffraction

Powder sample was prepared by grinding in agate mill and, subsequently, in agate mortar. The powder X-ray diffraction pattern was collected in a conventional Bragg–Brentano geometry on the Philips X'Pert diffractometer equipped with graphite secondary monochromator. The Cu K α

radiation was used. To minimize the background, the sample was placed on a flat low-background silicon wafer. Data were acquired in the angular range 3–90° 2 θ , with a step interval of 0.02° and a step-counting time of 9 s. A divergence slit of 0.5° and a receiving slit of 0.1 mm were used.

The quantitative phase analysis of the sample was performed using Rietveld method (Young 2000). Refinement was done by minimizing the sum of the weighted squared differences between observed and calculated intensities at every 2 θ step in a powder diffraction pattern (Bish & Post 1993). Quartz, orthoclase, plagioclase (albite), biotite and kaolinite were detected in the P-XRD pattern. The Rietveld refinement was performed using the FullProf program (Rodríguez-Carvajal 2006). The structure models used in the refinement were as follows: quartz (Le Page & Donnay 1976), orthoclase (Prince et al. 1973), albite (Ferguson et al. 1958), biotite (Brigatti & Davoli 1990) and kaolinite (Bish & Von Dreele 1989). The structural model of oligoclase instead of albite was also tested in Rietveld refinements, however the differences in the profile agreement factors between both Rietveld fits were insignificant. The differences in the estimated modal composition were below 0.1 wt. %. The background was determined by linear interpolation between consecutive breakpoints in the powder pattern. The pseudo-Voigt function was employed to generate the line shape of the diffraction peaks. The refinement involved the scale factor for each phase, unit-cell parameters for each phase except albite, peak-width parameters for each phase, two asymmetry parameters for biotite and 2 θ zero error. Atomic coordinates, overall isotropic displacement factors, and site occupancy parameters were fixed during the refinement for all phases. The unit-cell parameters of albite were also fixed, since their refinement caused divergence of the fit. The March–Dollase correction for preferred orientation was applied. The [001] direction was used for biotite, kaolinite, feldspar and plagioclase. The refinement converged to the values of the profile agreement factors $R_p = 8.9\%$ and $R_{wp} = 11.4\%$.

PRINCIPLES OF THE LEAST-SQUARES CALCULATIONS

The least-squares method is employed to solve an overdetermined set of linear algebraic equations, i.e. there are more independent equations than variables (Bryan et al. 1969). Given a matrix A and a vector y , we want to know the vector x that fulfils

$$y = Ax \quad (1)$$

Our estimate of the vector x should also be chosen so that the computed and real elements of the vector y differ as little as possible.

$$y' = Ax' \quad (2)$$

Commonly are minimized the squares of these differences (so-called least-squares method: Bryan et al. 1969; Albarède 1995):

$$R^2 = \sum |y' - y|^2 \quad (3)$$

$$R^2 = \min \quad (4)$$

and the sum of squared residuals is taken as the measure of the goodness of fit. Albarède (1995) discussed in a detail all the necessary mathematical apparatus that is behind the solution. Moreover, Janoušek & Moyen (in print) provide examples of various types of calculations (including normative calculations using real mineral compositions by the least-squares method) and their implementation into the freeware R language.

In geochemistry are very often examined some variables that sum up, for instance, to a unity or 100 %. The least-squares method generally does not produce normalized solutions, i.e. vectors whose components would sum up to a given number. We can define the Lagrange multiplier λ as (Albarède (1995):

$$\lambda = \frac{1 - J^T x}{J^T (A^T A)^{-1} J} \quad (5)$$

where x stands for an ordinary least-squares solution and J is a vector, all elements of which equal to 1. The constrained least-squares solution is then given by:

$$\hat{x} = x + \lambda (A^T A)^{-1} J \quad (6)$$

REFERENCES

- Albarède F. 1995: Introduction to Geochemical Modeling. *Cambridge University Press*, Cambridge, 1-543.
- Bish D.L. & Post J.E. 1993: Quantitative mineralogical analysis using the Rietveld full-pattern fitting method. *Amer. Mineralogist* 78, 932-940.
- Bish D.L. & Von Dreele R.B. 1989: Rietveld refinement of non-hydrogen atomic positions in kaolinite. *Clay Clay Miner.* 37, 289-296.
- Brigatti M.F. & Davoli P. 1990: Crystal-structure refinements of 1M plutonic biotites. *Amer. Mineralogist* 75, 305-313.
- Bryan W.B., Finger L.W. & Chayes F. 1969: Estimating proportions in petrographic mixing equations by least-squares approximation. *Science* 163, 926-927.
- Dempírová L. 2010: Zhodnocení stanovení SiO_2 , Na_2O , MgO a K_2O v silikátových vzorcích pomocí z-skóre získaných z devatenácti mezilaboratorních porovnávání. *Zpr. geol. Výzk. v Roce 2009* 323-326.
- Ferguson R.B., Traill R.J. & Taylor W.H. 1958: The crystal structures of low-temperature and high-temperature albites. *Acta Crystallogr.* 11, 331-348.
- Gabriel A. & Cox E.P. 1929: A staining method for the quantitative determination of certain rock minerals. *Amer. Mineralogist* 14, 290-292.
- Janoušek V. & Moyen J.F. in print: Mass balance modelling of magmatic processes in *GCDkit*. In: Kumar S. & Singh R.N. (Eds.): Modelling of Magmatic and Allied Processes. *Society of Earth Scientists Series 83, Springer*, Berlin, doi: 10.1007/978-3-319-06471-0_11
- Janoušek V., Farrow C.M. & Erban V. 2006: Interpretation of whole-rock geochemical data in igneous geochemistry: introducing Geochemical Data Toolkit (GCDkit). *J. Petrol.* 47, 1255-1259.
- Kretz R. 1983: Symbols for rock-forming minerals. *Amer. Mineralogist* 68, 277-279.
- Le Page Y. & Donnay G. 1976: Refinement of the crystal structure of low-quartz. *Acta Crystallogr., Sect. B* 32, 2456-2459.
- Merlet C. 1992: Accurate description of surface ionization in electron probe microanalysis: an improved formulation. *X-RAY Spectrom.* 21, 229-238.
- Pearce N.J.G., Perkins W.T., Westgate J.A., Gorton M.P., Jackson S.E., Neal C.R. & Chenery S.P. 1997: A compilation of new and published major and trace element data for NIST SRM 610 and NIST SRM 612 glass reference materials. *Geostand. Newsl.* 21, 115-144.

Prince E., Donnay G. & Martin R.F. 1973: Neutron diffraction refinement of an ordered orthoclase structure. *Amer. Mineralogist* 58, 500-507.

Rodríguez-Carvajal J. 2006: Full Prof .2k Rietveld profile matching & integrated intensities refinement of X-ray and/or neutron data (powder and/or single-crystal). *Laboratoire Léon Brillouin, Centre d' Etudes de Saclay, Gif-sur-Yvette Cedex, France,*

Strnad L., Mihaljevič M. & Šebek O. 2005: Laser ablation and solution ICP-MS determination of rare earth elements in USGS BIR-1G, BHVO-2G and BCR-2G glass reference materials. *Geost. Geoanal. Res.* 29, 303-314.

Young R.A. 2000: The Rietveld Method. *Oxford University Press*, Oxford, 1-312.

Appendix 2: Electron microprobe analyses**(a) Average electron-microprobe data used in mass-balance calculations (wt. %)**

	SiO ₂	TiO ₂	Al ₂ O ₃	FeOt	MnO	MgO	CaO	Na ₂ O	K ₂ O	P ₂ O ₅
WR	70.34	0.36	14.64	1.5	0.024	1.14	1.36	3.71	5.55	0.15
Qtz	99.86	n.d.	0.02	n.d.	n.d.	n.d.	n.d.	n.d.	n.d.	n.d.
Or	64.16	n.d.	18.47	0.03	0.034	n.d.	0.01	0.96	15.61	0.01
Pl	62.97	n.d.	20.07	n.d.	n.d.	0.01	3.95	9.2	0.44	0.02
Bt	37.5	3.33	14.8	17.26	0.24	13.35	0.04	0.14	9.47	n.d.
Ms	49.38	0.27	31.26	3.72	0.05	0.98	0.12	0.27	9.79	n.d.
Kln	45.59	0.91	39.84	0.02	0.01	n.d.	n.d.	n.d.	n.d.	0.03
Ilm	0.01	50.32	n.d.	42.71	3.091	n.d.	n.d.	n.d.	n.d.	0.01
Ttn	30.49	35.77	2.79	1.11	0.092	n.d.	27.58	n.d.	n.d.	0.01
Ap	0.04	0.01	n.d.	0.03	0.161	n.d.	55.98	n.d.	n.d.	42.68
Mgt	n.d.	n.d.	n.d.	n.d.	0.233	n.d.	n.d.	n.d.	n.d.	n.d.
Mnz	2.42	n.d.	n.d.	0.04	n.d.	n.d.	0.37	n.d.	n.d.	25.61
Zrn	31.1	n.d.	0.29	0.44	0.006	n.d.	0.14	n.d.	n.d.	n.d.
Rt	0.28	97.35	n.d.	1.59	0.031	n.d.	0.08	n.d.	n.d.	n.d.

n.d. – not detected

(b) Typical analyses for the main and accessory minerals (wt. % and apfu)

ID	feldspars			biotite		magnetite	
	Plg15T	Plg19T	16T	ID	Bt14	ID	Mgt1
SiO ₂	63.75	66.44	64.26	SiO ₂	37.50	SiO ₂	0.03
TiO ₂	n.d.	0.01	n.d.	TiO ₂	3.33	TiO ₂	0.01
Al ₂ O ₃	22.00	20.33	18.29	Al ₂ O ₃	14.80	Al ₂ O ₃	0.04
FeOt	n.d.	n.d.	0.02	FeOt	16.95	FeOt	95.55
MnO	0.02	n.d.	n.d.	MnO	0.24	MnO	1.17
MgO	0.009	n.d.	0.01	MgO	13.35	MgO	n.d.
CaO	3.59	1.72	0.03	CaO	0.04	CaO	0.01
Na ₂ O	9.72	10.84	1.30	Na ₂ O	0.14	Na ₂ O	n.d.
K ₂ O	0.38	0.21	15.48	K ₂ O	9.47	K ₂ O	n.d.
P ₂ O ₅	0.013	0.009	0.008	H ₂ O+	2.44	P ₂ O ₅	n.d.
Total	99.46	99.61	99.39	F	1.66	ThO ₂	n.d.
Si apfu	2.834	2.930	2.987	Total	99.92	U ₂ O ₃	n.d.
Ti	0.000	0.000	0.000	Si apfu	2.812	Y ₂ O ₃	n.d.
Al	1.153	1.057	1.002	Al(IV)	1.188	TR ₂ O ₃	n.d.
Fe	0.000	0.000	0.001	Σ	4.000	Total	96.81
Mn	0.001	0.000	0.000	Al(VI)	0.121	Si apfu	0.004
Mg	0.001	0.000	0.001	Ti	0.188	Ti	0.001
Ca	0.171	0.081	0.002	Fe	1.063	Al	0.005
Na	0.838	0.927	0.117	Mn	0.015	Fe ²⁺	0.964
K	0.021	0.012	0.918	Mg	1.492	Fe ³⁺	1.995
P	0.000	0.000	0.000	Σ	2.879	Mn	0.037
O	8.000	8.000	8.000	Ca	0.003	Mg	0.000
An mol. %	16.6	8.0	0.1	Na	0.020	Ca	0.000
Ab	81.3	90.9	8.5	K	0.906	Na	0.000
Or	2.1	1.2	91.4	Σ	0.930	K	0.000
				F	0.394	P	0.000
				OH*	1.606	Th	0.000
				XMg	0.58	U	0.000
				XFe	0.42	Y	0.000

n.d. – not detected, n.a. – not analysed

Magma Differentiation and Pluton Zoning

	zircon			monazite		rutile	titanite
ID	Zrn5	Zrn7	Zrn10	Mnz8	Mnz9	Rt1	Ttn4
SiO ₂	32.08	31.10	32.27	1.89	2.42	0.51	30.30
TiO ₂	0.02	n.d.	n.d.	0.01	0.00	98.82	36.32
Al ₂ O ₃	0.06	0.29	n.d.	n.d.	n.d.	0.01	2.44
P ₂ O ₅	n.d.	n.d.	n.d.	26.61	25.61	0.00	0.02
FeO	0.14	0.44	0.05	0.00	0.04	0.46	n.a.
Fe ₂ O ₃	n.a.	n.a.	n.a.	n.a.	n.a.	n.a.	1.08
MnO	n.d.	0.01	n.d.	0.12	n.d.	n.d.	0.11
CaO	0.02	0.14	n.d.	0.41	0.37	0.10	27.23
Y ₂ O ₃	n.d.	0.39	0.11	0.55	0.40	0.06	0.36
ZrO ₂	63.28	61.21	62.89	n.a.	n.a.	n.a.	n.a.
HfO ₂	1.87	1.89	1.30	n.a.	n.a.	n.a.	n.a.
Ce ₂ O ₃	n.d.	n.d.	0.04	32.74	32.78	0.14	0.50
La ₂ O ₃	0.13	0.07	n.d.	15.07	14.51	n.d.	0.07
Nd ₂ O ₃	n.d.	n.d.	0.08	9.35	8.66	n.d.	0.60
Pr ₂ O ₃	0.12	0.10	n.d.	2.87	2.86	0.04	0.23
Sm ₂ O ₃	0.00	0.09	0.04	1.07	1.18	0.00	0.02
Eu ₂ O ₃	0.01	0.02	0.01	n.d.	n.d.	0.05	n.d.
Gd ₂ O ₃	0.02	0.04	0.01	0.48	0.37	n.d.	0.15
Tb ₂ O ₃	n.d.	n.d.	n.d.	0.08	0.03	n.d.	0.08
Dy ₂ O ₃	0.01	0.01	0.04	0.04	n.d.	0.01	0.08
Ho ₂ O ₃	n.d.	0.01	0.03	0.01	0.01	0.04	0.02
Er ₂ O ₃	0.00	0.02	0.00	0.05	0.02	0.00	0.03
Tm ₂ O ₃	n.d.	n.d.	n.d.	0.08	0.09	0.02	0.02
Yb ₂ O ₃	n.d.	n.d.	0.04	n.d.	0.03	0.02	0.01
Lu ₂ O ₃	n.d.	n.d.	n.d.	n.d.	n.d.	0.00	n.d.
ThO ₂	0.13	0.17	0.03	8.18	10.42	0.02	0.02
U ₂ O ₃	0.18	0.20	0.60	0.50	0.37	0.03	0.01
Total	98.05	96.19	97.54	100.110	100.144	100.322	99.66
Si apfu	1.007	0.998	1.015	0.077	0.099	0.007	1.001
Ti	0.000	0.000	0.000	0.000	0.000	0.988	0.903
Al	0.002	0.011	0.000	0.000	0.000	0.000	0.095
P	0.000	0.000	0.000	0.912	0.887	0.000	0.001
Fe ²⁺	0.004	0.012	0.001	0.000	0.001	0.005	n.a.
Fe ³⁺	n.a.	n.a.	n.a.	n.a.	n.a.	n.a.	0.027
Mn	0.000	0.000	0.000	0.004	0.000	0.000	0.003
Ca	0.001	0.005	0.000	0.018	0.016	0.001	0.964
Y	0.000	0.007	0.002	0.012	0.009	0.000	0.006
Zr	0.968	0.958	0.965	n.a.	n.a.	n.a.	n.a.
Hf	0.017	0.017	0.012	n.a.	n.a.	n.a.	n.a.
Ce	0.000	0.000	0.000	0.485	0.491	0.001	0.006
La	0.001	0.001	0.000	0.225	0.219	0.000	0.001
Nd	0.000	0.000	0.001	0.135	0.127	0.000	0.007
Pr	0.001	0.001	0.000	0.042	0.043	0.000	0.003
Sm	0.000	0.001	0.000	0.015	0.017	0.000	0.000
Eu	0.000	0.000	0.000	0.000	0.000	0.000	0.000
Gd	0.000	0.000	0.000	0.006	0.005	0.000	0.002
Tb	0.000	0.000	0.000	0.001	0.000	0.000	0.001
Dy	0.000	0.000	0.000	0.000	0.000	0.000	0.001
Ho	0.000	0.000	0.000	0.000	0.000	0.000	0.000
Er	0.000	0.000	0.000	0.001	0.000	0.000	0.000
Tm	0.000	0.000	0.000	0.001	0.001	0.000	0.000
Yb	0.000	0.000	0.000	0.000	0.000	0.000	0.000
Lu	0.000	0.000	0.000	0.000	0.000	0.000	0.000
Th	0.001	0.001	0.000	0.075	0.097	0.000	0.000
U	0.001	0.001	0.004	0.005	0.003	0.000	0.000
A	0.995	1.005	0.988	1.020	1.024		
B	1.009	1.009	1.015	0.988	0.986		
sum cat.	2.004	2.014	2.003	2.015	2.016	1.004	3.021

Appendix 3: Laser-ablation ICP MS data for the main rock forming minerals (ppm)

LA ICPMS		Quartz										
DL (LA)	ppm	q1	q2	q3	q4	q1	q2	q3	q4	q1	Avg	SD
0.01	Be	0.08	0.11		0.17	0.03	0.00	0.05	0.00	0.00	0.06	0,06
0.35	Mn	0.12	0.12	0.16	0.10	0.09	0.21	0.22	0.20	0.20	0.16	0,05
0.095	Co	0.01	0.01	0.00	0.01	0.01	0.01	0.03	0.00	0.01	0.01	0,01
1.15	Ni	1.97	1.77	0.94	1.27	2.29	2.17	3.02	2.93	3.12	2.16	0,77
0.48	Zn	0.10	0.22	0.26	0.19	0.11	0.64	0.69	0.69	0.65	0.39	0,26
0.26	Rb	0.03	0.05	0.05	0.05	0.35	0.08	0.07	0.05	0.09	0.09	0,10
0.085	Sr	0.10	0.16	0.09	0.06	0.12	0.13	0.07	0.13	0.12	0.11	0,03
0.045	Y	0.00	0.00	0.01	0.05	0.00	0.00	0.00	0.00	0.00	0.01	0,02
0.25	Zr	0.05	0.03	1.31		0.09	0.14	0.06	0.04	0.03	0.22	0,44
0.05	Nb	0.01	0.00	0.00		0.00		0.04		0.01	0.01	0,01
0.23	Cd	0.16	0.08	0.02	0.01	0.11	0.05	0.01	0.01	0.03	0.05	0,05
0.085	Ba	0.19	0.28	0.12	0.13	0.80	0.39	0.36	0.38	0.38	0.34	0,20
0.020	La	0.001	0.009	0.003	0.007	0.001	0.01	0.00	0.00	0.00	0.004	0,00
0.028	Ce	0.008	0.013	0.007	0.021	0.011	0.03	0.00	0.01	0.00	0.012	0,01
0.008	Pr	0.000	0.000	0.000	0.003	0.000	0.00	0.00	0.00	0.00	0.001	0,00
0.083	Nd	0.000	0.000	0.007	0.004	0.003	0.01	0.00	0.00	0.00	0.003	0,00
0.097	Sm	0.000	0.000	0.000	0.000	0.000	0.00	0.00	0.00	0.00	0.000	0,00
0.008	Eu	0.000	0.000	0.000	0.000	0.000	0.00	0.00	0.00	0.00	0.000	0,00
0.032	Gd	0.000	0.000	0.000	0.000	0.000	0.00	0.00	0.00	0.00	0.000	0,00
0.009	Tb	0.000	0.000	0.000	0.000	0.000	0.00	0.00	0.00	0.00	0.000	0,00
0.030	Dy	0.000	0.000	0.000	0.001	0.000	0.00	0.00	0.00	0.00	0.000	0,00
0.004	Ho	0.000	0.000	0.001	0.001	0.000	0.00	0.00	0.00	0.00	0.000	0,00
0.012	Er	0.000	0.000	0.003	0.005	0.000	0.00	0.00	0.00	0.00	0.001	0,00
0.002	Tm	0.000	0.000	0.000	0.001	0.000	0.00	0.00	0.00	0.00	0.000	0,00
0.022	Yb	0.000	0.000	0.000	0.002	0.000	0.00	0.00	0.00	0.00	0.000	0,00
0.003	Lu	0.000	0.000	0.000	0.000	0.000	0.00	0.00	0.00	0.00	0.000	0,00
0.03	Hf	0.00	0.00	0.08		0.00	0.01	0.00	0.00	0.00	0.01	0,03
0.05	Ta	0.01	0.01	0.01		0.01		0.02	0.02	0.02	0.01	0,01
0.21	Pb	0.08	0.07	0.07	0.08	0.11	0.15	0.13	0.12	0.11	0.10	0,03
0.02	Th	0.66	1.01	0.11	0.04	0.35	0.97	0.31		1.13	0.57	0,43
0.011	U	0.01	0.01	0.04	0.11	0.01	0.02	0.02	0.02	0.02	0.03	0,03

DL = detection limit

Appendix 3: Laser-ablation ICP MS data for the main rock forming minerals (ppm)

	K-feldspar						
	k1	k2	k3	k4		Avg	SD
Be	0.58	0.85	2.15	1.77		1.34	0.74
Mn	2.15	2.44	1.33	1.72		1.91	0.49
Co	0.04	0.07	0.03	0.01		0.04	0.02
Ni	0.60	0.65	0.54	0.19		0.49	0.21
Zn	1.28	1.18	0.97	0.29		0.93	0.45
Rb	323.07	328.94	342.18	337.47		332.91	8.55
Sr	529.10	458.50	390.70	325.38		425.92	87.67
Y	0.07	0.56	0.14	0.10		0.21	0.23
Zr	2.05	5.52	5.23	1.16		3.49	2.21
Nb	0.10	0.13	0.04	0.05		0.08	0.04
Cd	0.06	0.04	0.02	0.04		0.04	0.02
Ba	4104.54	3186.51	1552.54	1134.56		2494.54	1391.38
La	1.76	1.77	1.58	1.49		1.65	0.14
Ce	1.41	2.07	2.61	1.26		1.84	0.62
Pr	0.07	0.17	0.12	0.12		0.12	0.04
Nd	0.14	0.72	0.46	0.44		0.44	0.24
Sm	0.02	0.17	0.08	0.06		0.08	0.06
Eu	1.21	1.07	0.93	0.75		0.99	0.19
Gd	0.02	0.14	0.05	0.04		0.06	0.05
Tb	0.00	0.02	0.00	0.00		0.01	0.01
Dy	0.01	0.09	0.02	0.02		0.03	0.04
Ho	0.00	0.01	0.00	0.00		0.00	0.01
Er	0.00	0.04	0.02	0.00		0.02	0.02
Tm	0.00	0.01	0.00	0.00		0.00	0.00
Yb	0.00	0.03	0.02	0.01		0.01	0.01
Lu	0.00	0.01	0.00	0.00		0.00	0.00
Hf	0.09	0.13	0.14	0.03		0.10	0.05
Ta	0.04	0.04	0.03	0.03		0.04	0.01
Pb	121.45	107.57	121.25	115.96		116.56	6.51
Th	0.14	0.16	0.23	0.07		0.15	0.07
U	0.10	0.28	0.25	0.83		0.36	0.32

DL = detection limit

Appendix 3: Laser-ablation ICP MS data for the main rock forming minerals (ppm)

	Plagioclase				Excluded from calculation			
	p1	p2	Avg	SD		p3	p4	p5
Be	19.66	23.66	21.66	2.83		17.25	18.36	22.67
Mn	77.23	33.80	55.52	30.71		47.62	40.88	56.09
Co	2.29	0.92	1.61	0.97		1.28	0.77	1.54
Ni	2.90	1.35	2.12	1.10		3.29	2.22	2.33
Zn	18.12	7.98	13.05	7.17		10.68	6.73	12.87
Rb	268.20	46.29	157.25	156.91		154.30	101.40	90.50
Sr	499.30	500.80	500.05	1.06		524.90	606.90	512.70
Y	0.13	0.16	0.15	0.02		0.66	0.57	5.25
Zr	16.53	3.90	10.21	8.93		14.43	6.36	293.40
Nb	9.51	1.60	5.55	5.59		0.24	1.77	1.47
Cd	0.07	0.04	0.06	0.02		0.10	0.03	0.11
Ba	213.10	57.97	135.54	109.69		104.40	111.10	72.53
La	20.43	27.00	23.72	4.65		213.50	326.80	54.60*
Ce	36.29	40.69	38.49	3.11		283.30	356.50	129.40
Pr	3.94	5.47	4.71	1.09		40.92	51.38	10.52
Nd	11.22	13.24	12.23	1.43		125.50	159.00	34.09
Sm	0.57	0.88	0.73	0.22		6.80	8.76	3.22
Eu	0.60	0.84	0.72	0.17		1.12	1.32	1.05
Gd	0.59	0.57	0.58	0.01		4.45	5.88	2.33
Tb	0.02	0.03	0.024	0.01		0.18	0.25	0.22
Dy	0.03	0.05	0.037	0.01		0.27	0.28	1.05
Ho	0.00	0.00	0.004	0.00		0.03	0.03	0.21
Er	0.03	0.03	0.027	0.00		0.17	0.25	0.61
Tm	0.00	0.00	0.001	0.00		0.01	0.01	0.10
Yb	0.01	0.00	0.007	0.01		0.03	0.03	0.80
Lu	0.00	0.00	0.001	0.00		0.00	0.00	0.12
Hf	0.95	0.20	0.58	0.53		0.63	0.19	7.68
Ta	0.09	0.02	0.05	0.05		0.02	0.18	0.03
Pb	62.66	58.04	60.35	3.27		78.75	78.32	76.86
Th	4.90	1.34	3.12	2.52		14.98	8.14	21.04
U	1.97	1.35	1.66	0.44		10.26	10.11	8.87

DL = detection limit

*inclusions of Mnz, Ap?

Appendix 3: Laser-ablation ICP MS data for the main rock forming minerals (ppm)

	Biotite					
	B1	B2	B3		Avg	SD
Be	4.481	5.162	4.468		4.70	0.40
Mn	1357.579	1380.579	1358.579		1365.58	13.00
Co	24.955	24.765	23.835		24.52	0.60
Ni	109.12	119.72	117.52		115.45	5.59
Zn	259.247	263.847	256.847		259.98	3.56
Rb	828.107	756.107	633.507		739.24	98.39
Sr	1.395	1.844	1.951		1.73	0.30
Y	0.053	4.416	4.036		2.84	2.42
Zr	0.915	2.243	0.567		1.24	0.88
Nb	91.419	95.239	124.999		103.89	18.38
Cd	0.079	0.096	0.005		0.06	0.05
Ba	1114.197	1186.197	1458.197		1252.86	181.43
La	0.031	0.801	0.901		0.58	0.48
Ce	0.03	2.372	2.756		1.72	1.48
Pr	0.001	0.623	0.568		0.40	0.34
Nd	0.003	3.189	3.232		2.14	1.85
Sm	0.001	1.139	1.017		0.72	0.62
Eu	0.054	0.103	0.132		0.10	0.04
Gd	0	0.915	0.918		0.61	0.53
Tb	0	0.139	0.124		0.09	0.08
Dy	0.002	0.733	0.695		0.48	0.41
Ho	0.001	0.134	0.141		0.09	0.08
Er	0.004	0.281	0.282		0.19	0.16
Tm	0	0.037	0.034		0.02	0.02
Yb	0.001	0.243	0.186		0.14	0.13
Lu	0.001	0.028	0.025		0.02	0.01
Hf	0.115	0.141	0.028		0.09	0.06
Ta	6.912	9.562	14.066		10.18	3.62
Pb	2.832	3.554	3.959		3.45	0.57
Th	0.076	0.709	0.534		0.44	0.33
U	0.027	0.133	0.086		0.08	0.05

DL = detection limit

Appendix 4: Trace-element composition of the whole-rock, individual rock-forming and accessory minerals determined by the ICP-MS technique (ppm)

ppm	WR wet ¹	Qtz LA ²	Qtz wet	Kfs wet	Kfs LA	Pl		Bt LA	Bt wet	Ms wet	Kln wet	Ilm wet	Ttn wet	Ap		Mgt wet	Mnz wet	Zrn wet	Rt wet
						LA	wet							wet	wet				
Rb	266.56	0.09	11.71	536.58	332.91	157.25	101.71	739.24	1179.96	617.99	45.16	14.78	1.92	0.55	19.75	3.88	25.72	0.63	
Sr	387.27	0.11	27.19	458.72	425.92	500.05	520.24	1.73	14.74	178.81	14.66	12.58	34.11	150.48	14.81	103.73	46.38	31.03	
Ba	1122.41	0.34	52.77	2852.66	2494.54	135.54	764.91	1252.86	1058.16	1114.74	17.83	26.17	8.63	1.93	25.01	18.74	267.48	157.93	
Be	10.38	0.06	1.08	5.53	1.34	21.66	21.35	4.70	5.50	7.40	9.90	4.81	6.61	1.40	2.76	25.40	97.00	1.92	
U	9.61	0.03	3.01	2.99	0.36	1.66	5.08	0.08	29.02	59.31	1.80	100.40	116.40	24.73	32.82	403.65	489.30	620.25	
Th	24.36	0.57	8.28	6.45	0.15	3.12	13.42	0.44	69.99	485.63	6.09	72.80	346.15	7.32	113.40	3836.40	950.53	2158.54	
Pb	63.28	0.10	5.59	124.73	116.56	60.35	56.10	3.45	23.41	50.69	84.00	352.15	315.93	54.30	75.60	1101.00	150.00	315.52	
Zr	169.91	0.22	56.83	65.16	3.49	10.21	96.48	1.24	647.91	687.74	78.37	1574.23	10081.73	1.20	980.73	10086.73	453122 ³	44550.43	
Hf	5.46	0.01	1.82	2.05	0.10	0.58	3.10	0.09	21.72	25.72	3.73	48.69	278.46	0.66	30.50	307.86	16010 ³	1361.33	
Nb	16.04	0.01	1.02	1.36	0.08	5.55	2.94	103.89	178.97	47.20	7.45	79.26	39.74	0.13	35.69	35.31	3288.90	4675.19	
Ta	1.66	0.01	0.10	0.28	0.04	0.05	0.61	10.18	18.18	19.83	2.36	13.08	9.09	0.05	6.32	4.97	425.15	484.02	
La	24.85	0.00	6.74	5.98	1.65	23.72	17.35	0.58	41.20	1078.53	34.07	726.72	3555.57	424.51	1088.71	26574.30	496.37	1861.82	
Ce	48.38	0.01	13.29	10.75	1.84	38.49	31.08	1.72	98.37	1593.25	83.38	1325.86	8572.95	1158.43	1918.03	44278.88	1138.86	2199.46	
Pr	5.37	0.00	1.47	1.23	0.12	4.71	3.20	0.40	12.36	177.72	9.92	141.69	1219.82	220.99	187.90	4676.15	120.19	519.95	
Nd	19.81	0.00	5.47	4.64	0.44	12.23	11.01	2.14	52.50	446.35	34.78	417.65	4961.41	1104.99	506.24	13148.31	446.92	2031.71	
Sm	3.47	0.00	0.98	0.90	0.08	0.73	1.67	0.72	12.06	37.75	8.84	51.27	1199.01	353.17	48.38	1278.54	82.09	282.37	
Eu	0.89	0.00	0.11	1.19	0.99	0.72	1.12	0.10	0.70	2.71	0.64	3.23	52.55	18.27	1.92	40.79	6.92	7.38	
Gd	2.66	0.00	0.79	0.76	0.06	0.58	1.46	0.61	9.37	33.80	7.03	30.68	633.40	221.64	31.35	732.12	65.78	201.21	
Tb	0.31	0.00	0.10	0.09	0.01	0.02	0.16	0.09	1.28	4.76	1.45	3.44	107.44	38.17	3.46	62.70	9.70	18.59	
Dy	1.41	0.00	0.50	0.47	0.03	0.04	0.73	0.48	6.63	9.27	6.48	16.46	531.87	200.26	15.20	217.73	60.58	76.40	
Ho	0.24	0.00	0.09	0.09	0.00	0.00	0.13	0.09	1.18	1.48	0.84	2.76	86.80	35.36	2.69	32.37	15.22	15.27	
Er	0.68	0.00	0.27	0.25	0.02	0.03	0.41	0.19	3.37	6.56	1.98	7.54	212.97	93.23	7.53	90.19	58.75	54.28	
Tm	0.09	0.00	0.04	0.04	0.00	0.00	0.05	0.02	0.46	0.51	0.21	0.92	25.52	11.83	0.87	9.66	10.83	8.78	
Yb	0.57	0.00	0.24	0.23	0.01	0.01	0.36	0.14	3.00	3.27	1.36	6.03	140.28	72.22	5.42	56.97	86.87	69.14	
Lu	0.08	0.00	0.04	0.03	0.00	0.00	0.05	0.02	0.41	0.41	0.16	0.87	14.81	9.30	0.79	6.37	16.32	12.16	
Y	6.65	0.01	2.46	2.43	0.21	0.15	3.76	2.84	33.98	33.32	16.61	78.31	2173.15	1173.80	69.54	839.34	447.34	398.70	
Ni	14.36	2.16	0.71	0.34	0.49	2.12	1.59	115.45	136.90	19.81	0.13	6.61	4.82	0.99	80.92	1.81	1252.13	2010.92	
Zn	39.69	0.39	0.53	1.73	0.93	13.05	6.19	259.98	471.14	99.10	3.08	90.73	95.48	14.21	40.96	92.83	497.63	458.62	
Co	3.52	0.01	0.13	0.19	0.04	1.61	0.50	24.52	32.95	5.34	0.29	6.49	11.05	0.27	10.01	2.47	58.26	1394.28	
Cd	0.11	0.05	0.05	0.04	0.04	0.06	0.08	0.06	0.57	4.00	0.13	2.47	4.73	1.05	3.83	5.21	75.11	40.01	

¹ Mineral separates dissolved and analyzed in solution by ICP-MS technique. See text for analytical details.² Averaged single-spot analyses as determined by the laser-ablation ICP-MS.³ Electron microprobe; too high to be determined by the ICP-MS.

In gray are shown analyses not taken into consideration. See text for discussion.

Appendix 5:

Typical electron-microprobe analyses of the zircon-like ABO_4 -type phase (wt. % and apfu)

	1	2	3	4	5	6
SiO ₂	16.055	14.810	14.704	15.398	14.739	16.300
TiO ₂	0.090	n.d.	0.087	n.d.	0.058	0.034
Al ₂ O ₃	0.667	0.733	0.650	0.642	0.878	0.704
FeO	1.220	2.241	4.426	0.732	6.781	1.002
MnO	0.026	0.132	0.186	0.057	0.439	0.058
MgO	0.101	0.202	0.174	0.186	0.236	0.128
CaO	4.765	4.875	4.612	4.795	4.574	4.641
K ₂ O	0.137	0.091	0.098	0.086	0.095	0.218
P ₂ O ₅	6.582	6.699	6.684	6.888	6.353	6.407
SO ₂	0.149	0.241	0.202	0.188	0.198	0.172
Sc ₂ O ₃	0.021	0.014	0.030	0.003	0.012	0.009
As ₂ O ₃	0.479	0.332	0.285	0.264	0.362	0.483
ZrO ₂	27.758	24.869	23.731	26.561	25.640	27.874
HfO ₂	0.570	0.569	0.596	0.617	0.571	0.692
Nb ₂ O ₅	n.d.	0.014	0.003	0.017	n.d.	n.d.
SnO	0.010	n.d.	0.029	n.d.	0.036	0.005
PbO	0.214	0.265	0.278	0.296	0.192	0.208
UO ₂	1.278	1.106	1.179	1.208	1.240	1.033
ThO ₂	31.947	32.353	31.751	35.250	29.028	31.265
Ce ₂ O ₃	3.236	2.377	2.104	2.238	2.058	3.378
SmO	0.122	0.172	0.011	0.061	0.213	0.206
Gd ₂ O ₃	n.d.	n.d.	0.169	0.210	n.d.	0.041
Dy ₂ O ₃	0.170	0.119	0.042	0.067	0.371	0.181
Er ₂ O ₃	n.d.	n.d.	n.d.	n.d.	n.d.	n.d.
Yb ₂ O ₃	0.077	0.099	n.d.	n.d.	n.d.	n.d.
Y ₂ O ₃	0.298	0.215	0.207	0.137	0.219	0.287
F	0.606	0.358	0.345	0.651	0.163	0.681
Total	96.578	92.886	92.583	96.552	94.456	96.007
Si	0.647	0.624	0.622	0.631	0.606	0.658
Ti	0.003	0.000	0.003	0.000	0.002	0.001
Al	0.032	0.036	0.032	0.031	0.043	0.034
Fe	0.041	0.079	0.156	0.025	0.233	0.034
Mn	0.001	0.005	0.007	0.002	0.015	0.002
Mg	0.006	0.013	0.011	0.011	0.014	0.008
Ca	0.206	0.220	0.209	0.210	0.201	0.201
K	0.007	0.005	0.005	0.004	0.005	0.011
P	0.225	0.239	0.239	0.239	0.221	0.219
S	0.006	0.010	0.008	0.007	0.008	0.007
Sc	0.001	0.001	0.001	0.000	0.000	0.000
As	0.012	0.008	0.007	0.007	0.009	0.012
Zr	0.546	0.511	0.489	0.530	0.514	0.549
Hf	0.007	0.007	0.007	0.007	0.007	0.008
Nb	0.000	0.000	0.000	0.000	0.000	0.000
Sn	0.000	0.000	0.001	0.000	0.001	0.000
Pb	0.002	0.003	0.003	0.003	0.002	0.002
U	0.011	0.010	0.011	0.011	0.011	0.009
Th	0.293	0.310	0.305	0.329	0.271	0.287
Ce	0.048	0.037	0.033	0.034	0.031	0.050
Sm	0.002	0.003	0.000	0.001	0.003	0.003
Gd	0.000	0.000	0.002	0.003	0.000	0.001
Dy	0.002	0.002	0.001	0.001	0.005	0.002
Er	0.000	0.000	0.000	0.000	0.000	0.000
Yb	0.001	0.001	0.000	0.000	0.000	0.000
Y	0.006	0.005	0.005	0.003	0.005	0.006
F	0.077	0.048	0.046	0.084	0.021	0.087
site A	0.921	0.917	0.909	0.914	0.886	0.929
site B	1.183	1.210	1.249	1.175	1.321	1.175

Site B includes Si, Al, P, As and S, the site A comprises all other elements (except F)

The EPMA results are recalculated on the basis of 4 O apfu. n.d.: not detected.



CHAPTER II:

INTERNAL STRUCTURE OF ZONED

PLUTONS

Chapter II:

Internal structure and formation mechanisms of zoned plutons at shallow crustal levels

Article II.-1:

Magnetic fabric and modeled strain distribution in the head of a nested granite diapir, the Melechov pluton, Bohemian Massif (2014)

Trubač, J., Žák, J., Chlupáčová, M., Janoušek, V.

Journal of Structural Geology, **66**: 271–283

Status: Published

Magnetic fabric and modeled strain distribution in the head of a nested granite diapir, the Melechov pluton, Bohemian Massif

Jakub Trubač^{1,2,3}, Jiří Žák⁴, Marta Chlupáčová⁵, Vojtěch Janoušek^{1,2}

¹ Czech Geological Survey, Klárov 3, Prague, 11821, Czech Republic

² Institute of Petrology and Structural Geology, Faculty of Science, Charles University, Albertov 6, Prague, 12843, Czech Republic

³ Institute of Geology, v.v.i., Academy of Sciences of the Czech Republic, Rozvojová 269, Prague, 16500, Czech Republic

⁴ Institute of Geology and Paleontology, Faculty of Science, Charles University, Albertov 6, Prague, 12843, Czech Republic

⁵ Boháčova 866, Prague, 14900, Czech Republic

ABSTRACT

The Melechov pluton, Bohemian Massif, is interpreted as a mid-crustal nested granitic diapir with an apical part exposed at the present-day erosion level. The diapir head exhibits a concentric structure defined by lithological zoning and by the anisotropy of magnetic susceptibility (AMS). In concert with theoretical models, outward-dipping margin-parallel magnetic foliations are associated with oblate shapes of the susceptibility ellipsoids and higher degree of anisotropy, passing inward into weaker triaxial to prolate fabric. By contrast, magnetic fabric in an inner granite unit is in places oriented at a high angle to internal contacts and is interpreted as recording an internal diapir circulation. We use inverse modeling to calculate strain variations across the diapir from the AMS data. The magnetic fabric parameters and calculated strains are in agreement with strain distribution in heads of model Newtonian diapirs travelling a distance of two body radii and suggest granitic magma ascent as a crystal-poor suspension followed by crystallization of fabric markers and their response to strain near the final emplacement level. The intrusive fabric thus formed late but, though generally weak, was still capable of recording incremental strain gradient in the granite diapir.

Keywords: Anisotropy of magnetic susceptibility (AMS); Diapir; Emplacement; Fabric; Granite; Strain

INTRODUCTION

Theoretical and analogue models of salt, shale, and igneous diapirs have shown that their internal dynamics and strain patterns are largely governed by viscosity contrasts between the ascending fluid and its host, and by the travel distance of the diapir from its source region (e.g., Berner et al., 1972; Dixon, 1975; Marsh, 1982; Talbot and Jackson, 1987; Schmeling et al., 1988; Cruden 1990; Weinberg and Podladchikov, 1994). These models have led to an idealized image of diapirs with predictions about their internal circulation, strain variations, and compositional zoning. A characteristic feature of the model diapirs is strain and associated fabric distribution where peripheral flattening in the diapir head passes inward to strongly constrictional diapir centers and tails (e.g., Bateman, 1984; Ramsay, 1989; England, 1990; Paterson and Fowler, 1993; Clemens, 1998; Kratinová et al., 2006). Natural examples, however, may depart significantly from the theoretical models owing to rheological and temperature variations in the diapir and its host, multiple pulses of the ascending fluid passing through a single conduit, and variable imprint of tectonic deformation (e.g., Paterson and Vernon, 1995; Miller and Paterson, 1999).

One of the key issues for understanding the dynamics of diapiric intrusions in the Earth's crust is thus a quantitative comparison of theoretical models with the observed strain patterns. Unfortunately, natural diapirs lack reliable strain markers, as best exemplified by the rather problematic microgranular enclaves (see Paterson et al., 2004 for discussion), and exhibit mineral fabric that is a poor recorder of total strain experienced by the ascending fluid. Instead, granular and mineral fabrics in both salt and granites, respectively, are interpreted to record only late strain increments that postdate diapiric ascent (e.g., Talbot and Jackson, 1987; Paterson and Miller, 1998; Paterson et al., 1998). Still, a promising means for evaluating strain patterns in natural diapirs is the analysis of the anisotropy of magnetic susceptibility (AMS), allowing quantification of fabric parameters even in macroscopically isotropic rocks without strain markers.

This paper explores the potential of the AMS technique for inferring strain patterns in granite diapirs (and in other types of intrusions as well) on the basis of data from the mid- to late-Carboniferous (Pennsylvanian) Melechov pluton, Bohemian Massif (Fig. 1), which is interpreted as a composite diapiric intrusion into hot mid-crustal migmatites. We first quantitatively characterize variations in magnetic fabric throughout the pluton and then use the AMS-to-strain inversion method of Ježek and Hrouda (2002, 2007) to infer the strain distribution in the proposed diapir head.

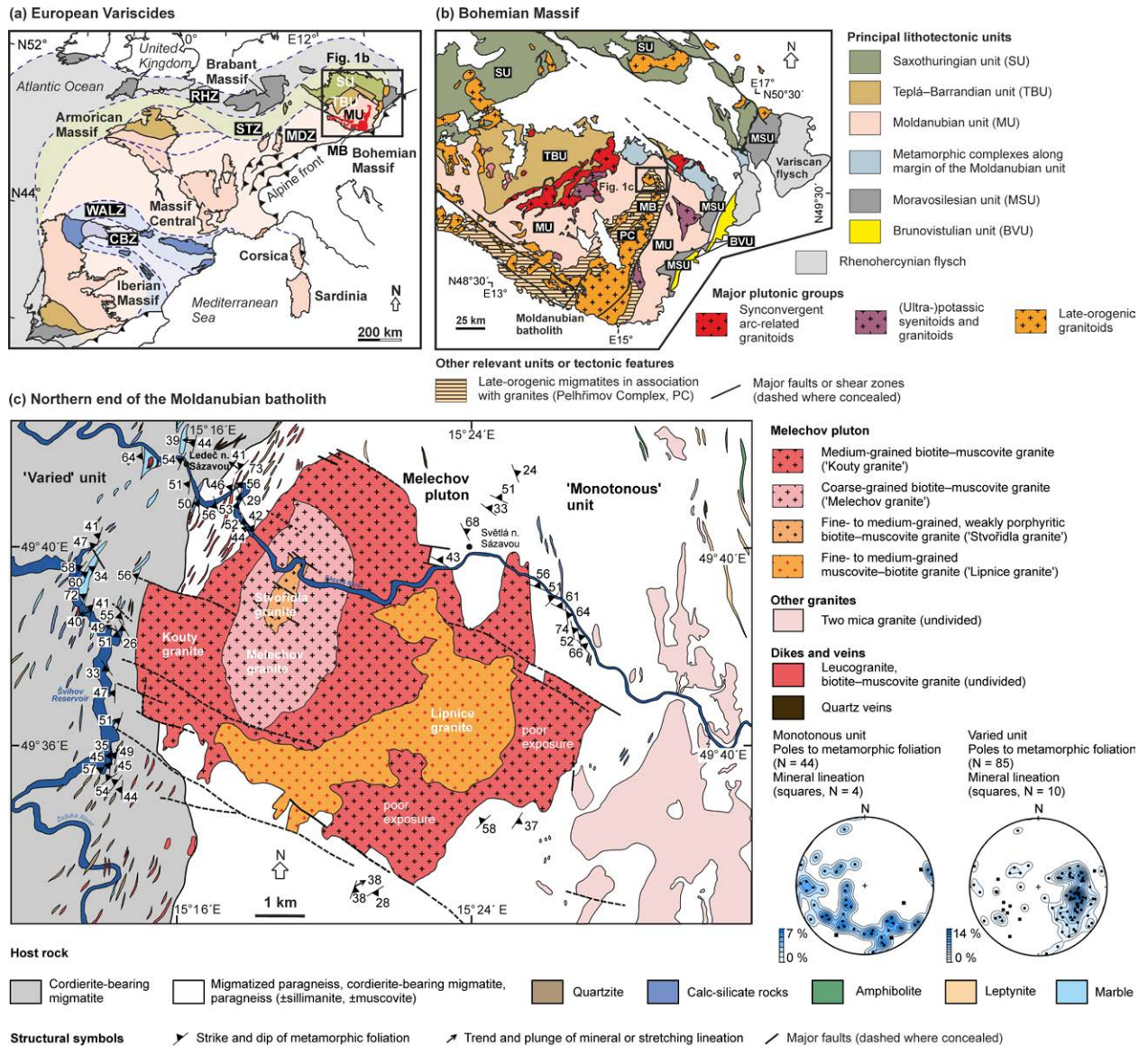


Fig. 1. (a) Geologic map showing basement outcrop areas and principal lithotectonic zones of the Variscan orogenic belt in Europe. Bohemian Massif is the easternmost inlier of the orogen, Moldanubian batholith (MB; highlighted in red) occupies its southern margin. Compiled from Winchester (2002), Asch (2003), and Martínez Catalán (2011). RHZ – Rhenohercynian Zone, STZ – Saxothuringian Zone, SU – Saxothuringian Unit, TBU – Teplá–Barrandian Unit, MDZ – Moldanubian Zone, MU – Moldanubian Unit, WALZ – West Asturian–Leonese Zone, CBZ – Cantabrian Zone. (b) Simplified geologic map of the interior Bohemian Massif emphasizing principal lithotectonic units and plutonic groups. The Pelhřimov core complex (PC) parallels the eastern edge of the underthrust Brunovistulian microplate. The Melechov pluton is the northernmost end of the complex. Compiled from Fusán et al. (1967) and Cháb et al. (2007). (c) Simplified geologic map of the Melechov pluton and its host rocks. Redrafted from Czech Geological Survey maps 1:50,000, sheets 23–12 Ledec nad Sázavou and 23–21 Havlíčkův Brod. Stereonets (equal area projection, lower hemisphere) show orientation of main structural elements.

Finally, we compare these data with theoretical models for diapiric structures and discuss applicability of this method for strain analysis in granite plutons.

2. GEOLOGIC SETTING

2.1. *Broader tectonic context*

The Melechov pluton (radiometric age is poorly constrained between 318 ± 7 Ma and 313 ± 14 Ma, electron-microprobe (CHIME) U–Th–Pb dating on monazite; Breiter and Sulovský, 2005) makes up the northernmost end of the Moldanubian batholith (Fig. 1b), one of the largest granite complexes in the Variscan orogenic belt. The bulk of the eastern portion of the batholith formed during a short time span between ~ 330 and ~ 327 Ma (e.g., Gerdes et al., 2003; Bankwitz et al., 2004; Žák et al., 2011) and was recently interpreted as a NNE–SSW-elongated crustal-scale dome (Verner et al., 2014) that straddles along a side edge of an underthrust continental microplate (Schulmann et al., 2008). The dome consists of crustally-derived two mica granites in close association with migmatites and was interpreted as resulting from diapiric upwelling of hot and partially molten metapelitic middle crust (Verner et al., 2014; Žák et al., in press and references therein). In several locations along its axis, the granite–migmatite dome was pierced by smaller late-stage stocks, including the Melechov pluton (Fig. 1c), that are circular to weakly elliptical in plan view and vertically extensive as compared to the host granites and migmatites.

2.2. *The three-dimensional shape of the Melechov pluton*

In the map, the pluton has an irregular, weakly NW–SE-elongated outline, 14×10 km, that to some extent is modified by later brittle faults (Fig. 1c). The three-dimensional shape of the pluton at depth is fairly well constrained by a large body of existing geologic and gravimetric data (e.g., Procházka and Mlčoch, 1997; Breiter, 2007). On the Bouguer anomaly map, the pluton is associated with a pronounced gravity minimum as low as -44 mGal (Fig. 2), which is one of the most striking negative gravity anomalies in the Bohemian Massif (Blížkovský and Novotný, 1982). On the interpretive gravimetric cross-sections (Fig. 2b), the upper portion of the pluton is shown to dip outward at moderate angles, which is in agreement with Linsser indications (see Linsser, 1967; Šefara, 1973; Lenhardt et al., 2007 for principles of the method) pointing towards denser rocks and portraying strike and dip of the density boundaries down to a depth of 6 km (Fig. 2a). Deeper portions of the pluton are inferred as dipping steeply inward.

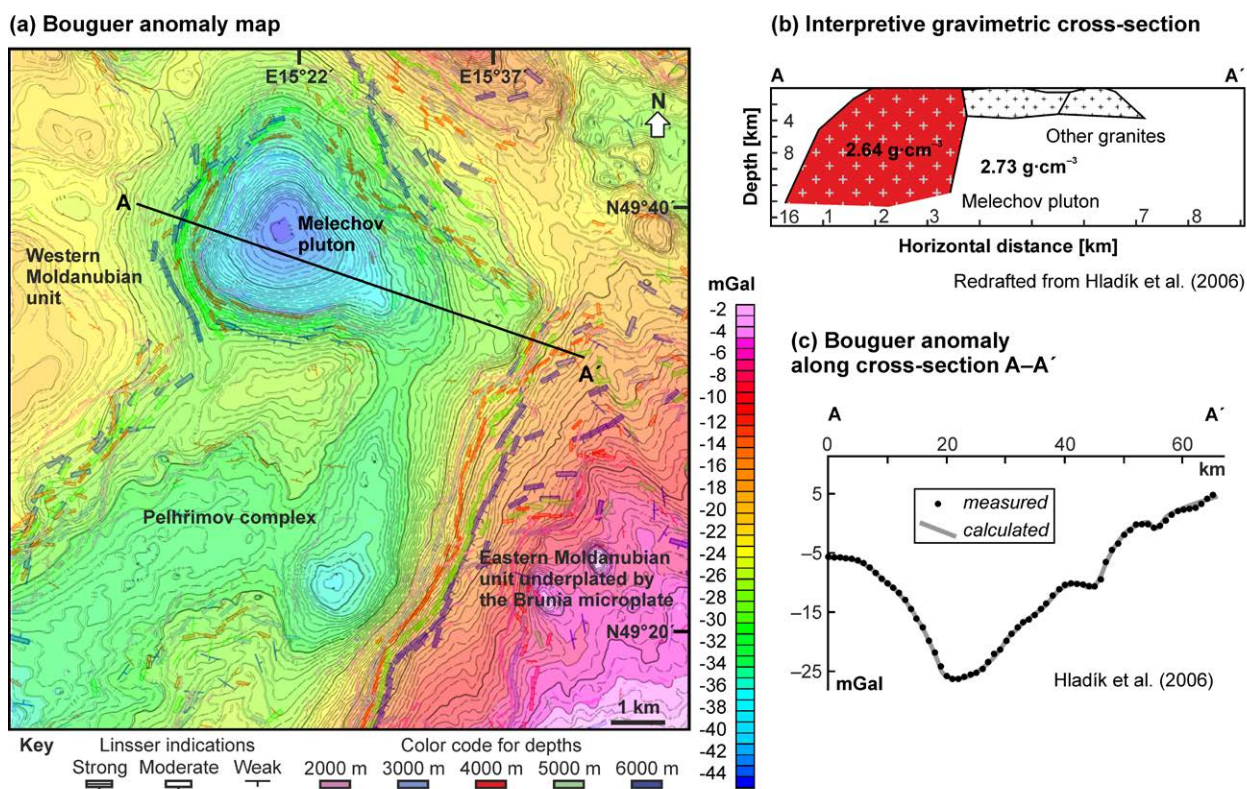


Fig. 2. (a) Bouguer gravity anomaly map of the Melechov pluton and its host rocks. Linsser indications portray principal density boundaries at different depths around the pluton and are consistent with its generally outward-dipping contacts. Map taken from Hladík et al. (2006), Linsser indications redrafted from Verner et al. (2014). (b) Gravimetric interpretation (cross-section) of the three-dimensional shape of the Melechov pluton at depth. (c) Measured and calculated Bouguer anomalies for each cross-section.

Based on the gravity data, the Melechov pluton can be traced to a depth of at least 14–16 km below the present-day erosion level (Mottlová, 1985; Hladík et al., 2006; Fig. 2b, c).

2.3. Internal zoning

Inside, the pluton consists of four granite units (Fig. 1c; Electronic Supplementary Material, Parts 1, 2), all peraluminous and derived from partial melting of a metasedimentary source with Sr–Nd isotopic signature similar to the Moldanubian paragneisses (Matějka and Janoušek, 1998; Harlov et al., 2008). The outer Kouty granite is medium-grained biotite–muscovite granite and is in contact with a southeasterly (off the pluton center) crescent-shaped body of the fine- to medium-grained muscovite–biotite Lipnice granite. In some places, the latter is foliated and rich in biotite schlieren and migmatite xenoliths (Staněk et al., 2013). The pluton center is occupied by an elliptical NE–SW-elongated body of the coarse-grained biotite–muscovite Melechov granite, which evolved separately from the remainder of the pluton (e.g., Mlčoch et al., 2000; Breiter and Sulovský, 2005)

and encloses the innermost fine- to medium-grained, slightly porphyritic biotite–muscovite Stvořidla granite. Geochemical data suggest that the latter was derived from the Melechov granite through fractional crystallization (Mlčoch et al., 2000). Internal contacts are not exposed, thus the exact cross-cutting relations between component units remain unclear. Nevertheless, the overall concentric architecture of the pluton was also corroborated by previous unpublished structural and magnetic fabric studies (Schulmann et al., 1998; Blažiček, 2002; Staněk, 2013; unfortunately, values of the primary AMS data are not provided in these reports, precluding comparison with our new measurements).

2.4. Host rock

The host rock is dominated by metasedimentary rocks of the Moldanubian unit, a high-grade core of the Variscan orogen. The main portion of the pluton intruded variously migmatized paragneisses (\pm sillimanite, \pm muscovite) and cordierite-bearing migmatites with minor intercalations and lenses of quartzite and calc-silicate rocks, traditionally termed the 'Monotonous' unit (Fig. 1c). To the west, the pluton intruded cordierite-bearing migmatites which contain more abundant lenses of marble, calc-silicate rocks, amphibolites, and quartzites, altogether referred to as the 'Varied' unit (Fig. 1c). The existing pressure–temperature estimations from contact-metamorphic assemblages indicate temperature of about 670–750 °C at the the pluton/host rock contact and pressure of about 0.5 GPa (Schulmann et al., 1998), which would correspond to mid-crustal emplacement at a depth of about 17–18 km.

The pluton/host rock contacts are generally poorly exposed, so their true attitude is difficult to determine. However, the dominant metamorphic foliation around the pluton (where exposed) exhibits a contact-parallel, outward-dipping pattern (Fig. 1c) which is in agreement with gravimetric data, and with Linsser indications in particular (Fig. 2a). In detail, the eastern and western portions of the pluton's structural aureole differ in intrusive geometries, fabric orientation and symmetry, structural style, and degree of partial melting and its temporal relation to deformation. To the east, the host rock is dominated by stromatic to nebulitic migmatites. Fabric is mostly oblate and defined by compositional banding in migmatites, suggesting deformation synchronous with anatexis. As the pluton is approached, the migmatites become intensely folded and commonly alternate with granite sheets (Fig. 3a) or even grade into larger bodies of anatectic granites. In contrast, the western portion of the aureole shows a lesser degree of partial melting and is characterized by presumably sharp, non-sheeted granite/host contact. Fabric is mostly solid-state, consists of equally developed

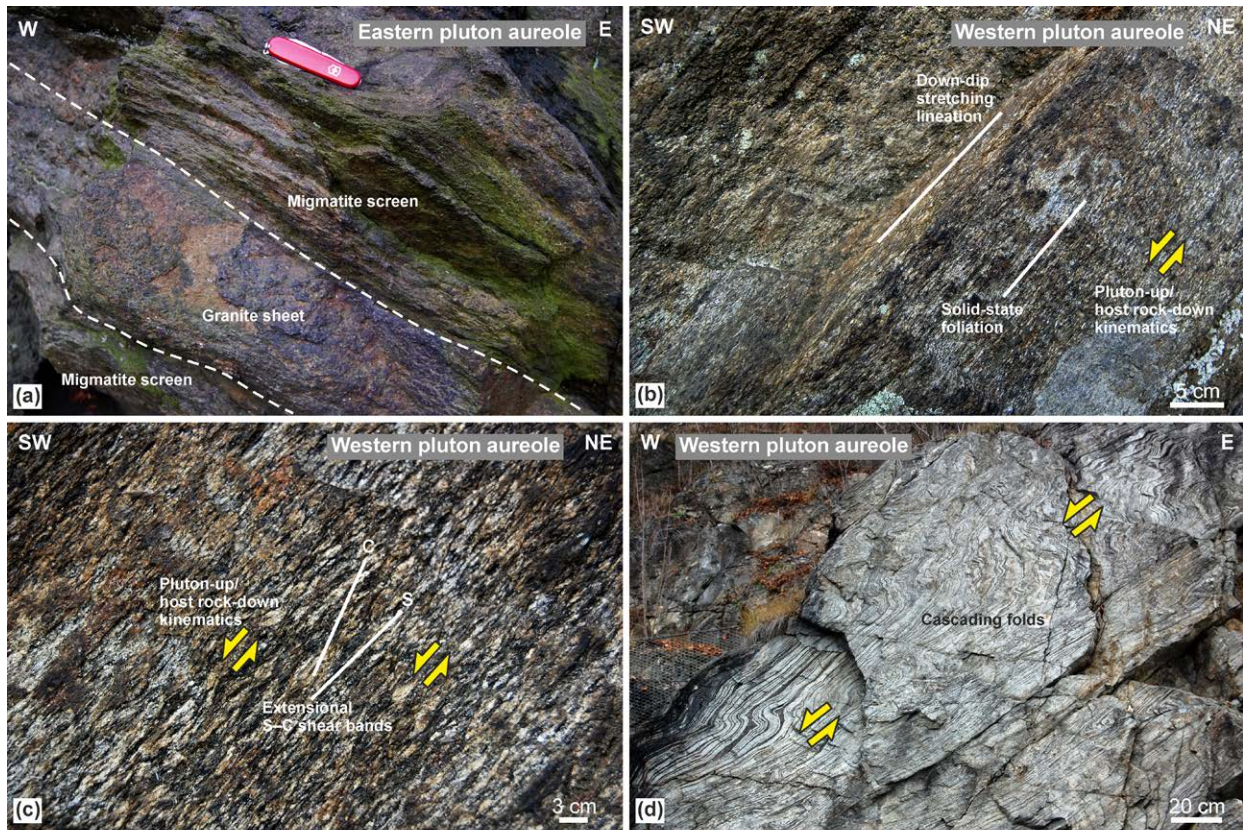


Fig. 3. Mesoscopic structures in the metamorphic host rocks around the Melechov pluton. (a) Close-up of an eastern contact of the pluton with outward-dipping granitic sheets intruding along banding in the host migmatites. Světlá nad Sázavou, GPS coordinates: N49°39.946', E15°23.510'. (b, c) Outward dipping solid-state fabric superposed on migmatized paragneiss and associated with pluton-up/host rock-down kinematics. South of Kožlí, GPS coordinates: N49°38.095', E15°14.947'. (d) Asymmetric minor folds in marbles, interpreted as flanking folds, consistent with pluton-up/host rock-down kinematics. Leděč nad Sázavou, GPS coordinates: N49°41.784', E15°16.868'.

foliation and lineation (Fig. 3b, c), and exhibits more homogeneous orientation (Fig. 1c). Mineral and stretching lineation is typically down-dip or slightly dip-oblique (Fig. 3b). This fabric is also associated with normal, west-side-down, pluton-up kinematics defined by asymmetric quartz–feldspar aggregates, quartz boudins, S–C mylonites (Fig. 3c), and asymmetric s-shaped flanking folds (Fig. 3d).

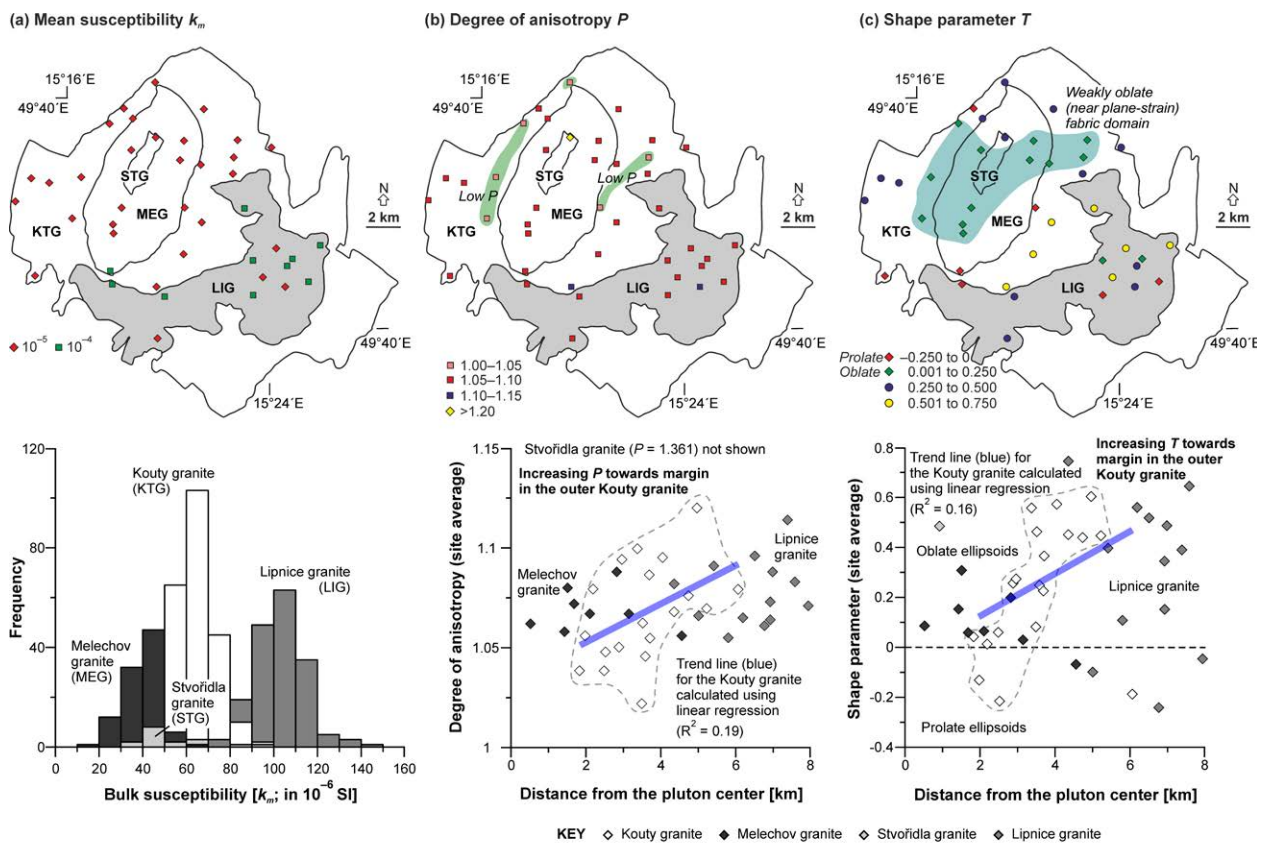


Fig. 4. Maps and graphs showing spatial distribution of the (a) mean susceptibility, (b) average degree of anisotropy, and (c) average shape parameter in the Melechov pluton. Gray lines (arrows) in the graphs show approximate spatial trends of magnetic fabric parameters in the outer Kouty granite. LIG – Lipnice granite, KTG – Kouty granite, MEG – Melechov granite, STG – Stvořidla granite.

MAGNETIC FABRIC OF THE PLUTON

3.1. Methodology

As mesoscopic fabric in the granites is mostly weak and difficult to discern with the exception of some portions of the Lipnice granite (see example fabrics in Electronic Supplementary Material, Parts 1, 2), the anisotropy of magnetic susceptibility (AMS) is used to quantitatively characterize the magnetic fabric and its gradients in the Melechov pluton. A total of 86 oriented cores were sampled using a hand-held drill at 41 stations across the four granites of the pluton (Fig. 4; Electronic Supplementary Material, Parts 3–5). After cutting, these samples yielded 553 standard specimens of 10 cm³ in volume. The AMS was measured in low field (450 Am⁻¹) with a MFK1-A Kappabridge in the Laboratory of Rock Magnetism, Institute of Geology and Paleontology, Charles University in Prague. A statistical treatment and analysis of the AMS data was conducted, using the ANISOFT 4.2 program package (www.agico).

com). The measured data and parameters are presented in Figs. 4–7 and Electronic Supplementary Material (Parts 3–5).

The AMS data are represented by the k_m , P , and T parameters defined as follows: (1) $k_m = (k_1 + k_2 + k_3)/3$; (2) $P = k_1/k_3$; and (3) $T = 2\ln(k_2/k_3)/\ln(k_1/k_3) - 1$, where $k_1 \geq k_2 \geq k_3$ are the principal susceptibilities (e.g., Fig. 4). The parameter k_m represents the mean bulk magnetic susceptibility, which reflects the proportion and type of magnetic minerals in the analyzed rock. The parameter P (Nagata, 1961), called the degree of AMS, reflects the eccentricity of the AMS ellipsoid and may relate to the intensity of preferred orientation of magnetic minerals. The parameter T (Jelínek, 1981) characterizes the symmetry of the AMS ellipsoid. It varies from -1 (perfectly prolate ellipsoid) through 0 (triaxial ellipsoid) to $+1$ (perfectly oblate ellipsoid). In magnetic fabric studies, the maximum principal susceptibility (k_1) is referred to as the magnetic lineation and the minimum principal susceptibility (k_3) defines a pole to the magnetic foliation. Their orientations are presented in stereonet in the geographic (in situ) coordinate system and as locality mean values on the map.

3.2. Magnetic mineralogy

The bulk magnetic susceptibility of the measured specimens is on the order of 10^{-5} to 10^{-4} (Fig. 4a; SI units are used throughout this paper), characteristic of paramagnetic granites (e.g., Hrouda and Kahan, 1991; Bouchez, 1997). A slight increase in the bulk susceptibility can be seen from the Melechov (19×10^{-6} to 67×10^{-6}) through Kouty (30×10^{-6} to 96×10^{-6}) to Lipnice granites (77×10^{-6} to 140×10^{-6} ; Fig. 4a). The bulk susceptibility of the Stvořidla granite is scattered and mostly overlaps with that of the other granites (39×10^{-6} to 97×10^{-6} ; Fig. 4a). These changes in bulk susceptibility for the different granites according to lithologic unit are also illustrated in the map of Fig. 4a.

To constrain the AMS carriers, we first calculated the maximum theoretical paramagnetic susceptibility (MTPS; Aydin et al., 2007; Hrouda, 2010) from representative analyses of Fe_2O_3 , FeO , and MnO (unpublished data of the authors) and then measured the variation of susceptibility with temperature (Fig. 5; Electronic Supplementary Material, Part 4). The calculated MTPS are 127×10^{-6} , 80×10^{-6} , and 74×10^{-6} for the Lipnice, Kouty, and Melechov granites, respectively. For the former two granites, the MTPS values correspond to the measured susceptibilities indicating that the AMS carriers are biotite and muscovite. For the Melechov granite, the MTPS is approximately two times higher than the measured susceptibility, indicating either the presence of a ferrimagnetic component (hematite–ilmenite) with greater Fe-content or greater proportion of diamagnetic quartz, decreasing the bulk susceptibility.

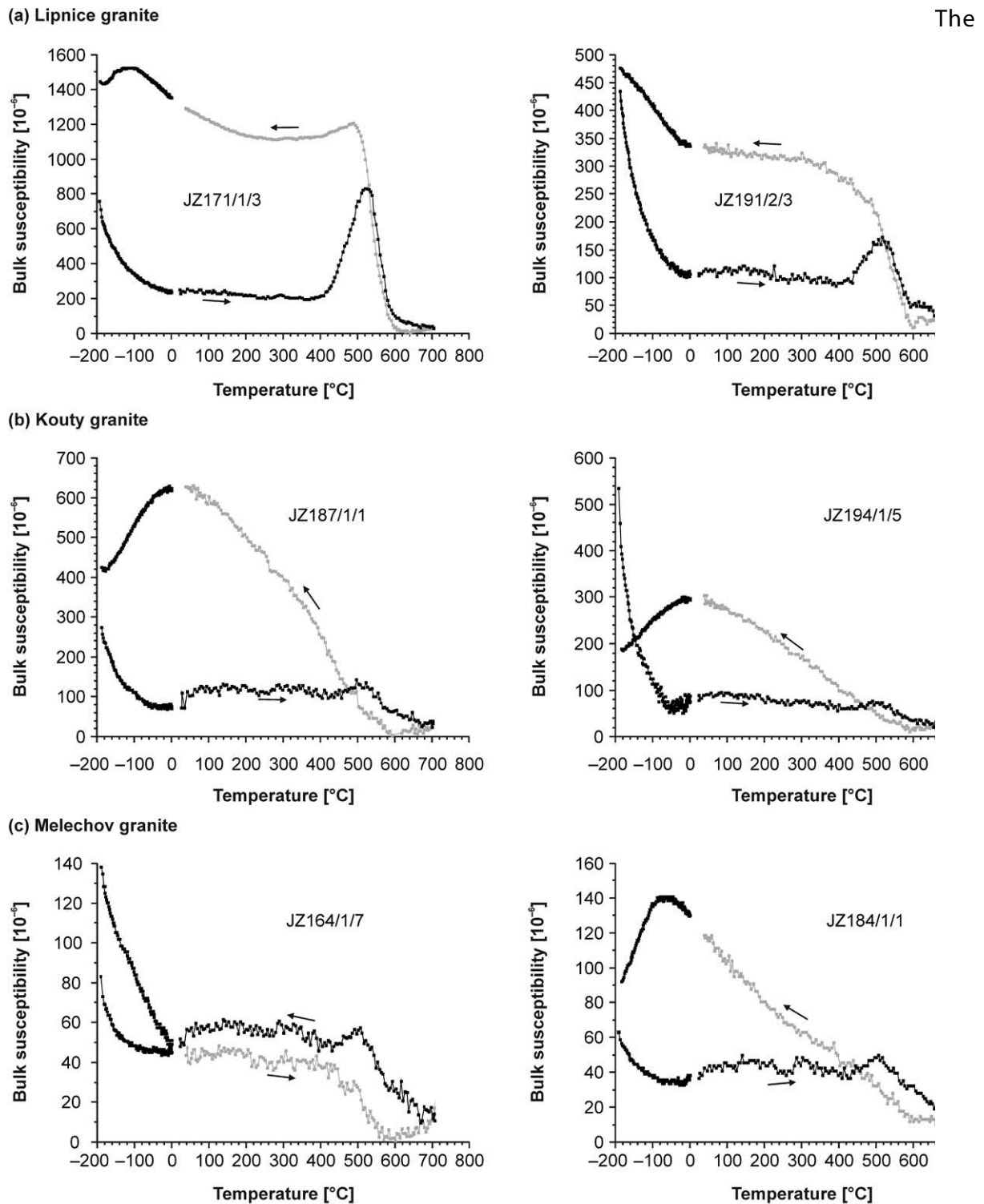


Fig. 5. Thermomagnetic curves for selected representative specimens from the Melechov pluton.

variation of magnetic susceptibility with temperature was measured on 6 representative coarsely powdered specimens using a CS-3 Furnace and CS-L Cryostat instruments in the laboratory of Agico, Inc., Brno, Czech Republic. The magnetic susceptibility variations with temperature were measured in the temperature range of $-196\text{ }^{\circ}\text{C}$ to $0\text{ }^{\circ}\text{C}$ and from room temperature to $700\text{ }^{\circ}\text{C}$ (Fig. 5). Argon atmosphere was applied to avoid oxidation during heating, the heating rate was $10\text{ }^{\circ}\text{C}$ per

minute. The measured data were processed using the program Cureval8 (AGICO, Inc.).

In the temperature interval between $-196\text{ }^{\circ}\text{C}$ and $0\text{ }^{\circ}\text{C}$, the thermomagnetic curves are hyperbolic, which is typical of paramagnetic mineralogy (Fig. 5). At temperatures of $0\text{ }^{\circ}\text{C}$ to $700\text{ }^{\circ}\text{C}$, however, the heating curves exhibit a susceptibility drop at around $550\text{ }^{\circ}\text{C}$ to $580\text{ }^{\circ}\text{C}$ and at $660\text{ }^{\circ}\text{C}$, indicating the presence of ferromagnetic admixtures. In detail, the shape of the heating curves also points to other complexities in magnetic mineralogy. The Lipnice granite (specimens JZ171/1/3, JZ191/2/2) differs from the other granites by a susceptibility increase above $400\text{ }^{\circ}\text{C}$, with a peak at around $500\text{ }^{\circ}\text{C}$ and the T_c between $560\text{ }^{\circ}\text{C}$ and $580\text{ }^{\circ}\text{C}$, suggesting growth of a ferromagnetic mineral during heating. The variability in composition of ferromagnetic components can also be demonstrated for specimens JZ164/1/7 and JZ184/1/1 (the Melechov granite; Fig. 5c), which thermomagnetic curves show a susceptibility drop near room temperature that is consistent with the Morin transition of hematite.

The low-temperature k vs. T curves were measured twice. The first measurement was made prior to heating and the second was made after heating and cooling procedure. The second low-temperature measurement then reflects in some way new minerals created during heating and cooling. Without additional mineralogical analyses, however, it is difficult to determine the newly formed mineral species. Nevertheless, the lack of Verwey transition suggests that pure magnetite, except for the specimen JZ171/1/3, is not among the newly formed magnetic minerals.

3.3. Magnetic fabric parameters and orientation

All four granites are characterized by low degree of anisotropy, not exceeding 1.2 (corresponding to 20% magnetic anisotropy) for most of the analyzed specimens (Fig. 6). The least anisotropic is the Kouty granite ($P = 1.015\text{--}1.249$, two data outliers up to 1.495) with 40 % of the data having $P < 1.05$ (5% anisotropy) and most data not exceeding $P = 1.1$ (Fig. 6). Slightly more anisotropic is the Lipnice granite ($P = 1.047\text{--}1.205$, 98 % of the data having $P > 1.05$; Fig. 6). The degree of anisotropy of the Melechov granite scatters more widely from 1.026 to 1.172 (Fig. 6). The greatest degree of anisotropy was measured in the Stvořidla granite ($P = 1.059\text{--}1.361$, one outlier with $P = 5.101$). In contrast to the slight differences in the P parameter, the granites are similar range for the shape parameter, ranging from highly prolate (T as low as -0.887) to highly oblate ($T = 0.955$ at most) and showing a distinct trend of increasing oblateness with increasing degree of anisotropy (Fig. 6).

Analysis of the map distribution of the P and T parameters in the pluton reveals that low-anisotropy, weakly oblate magnetic fabric occurs in domains along the internal contact between the Kouty

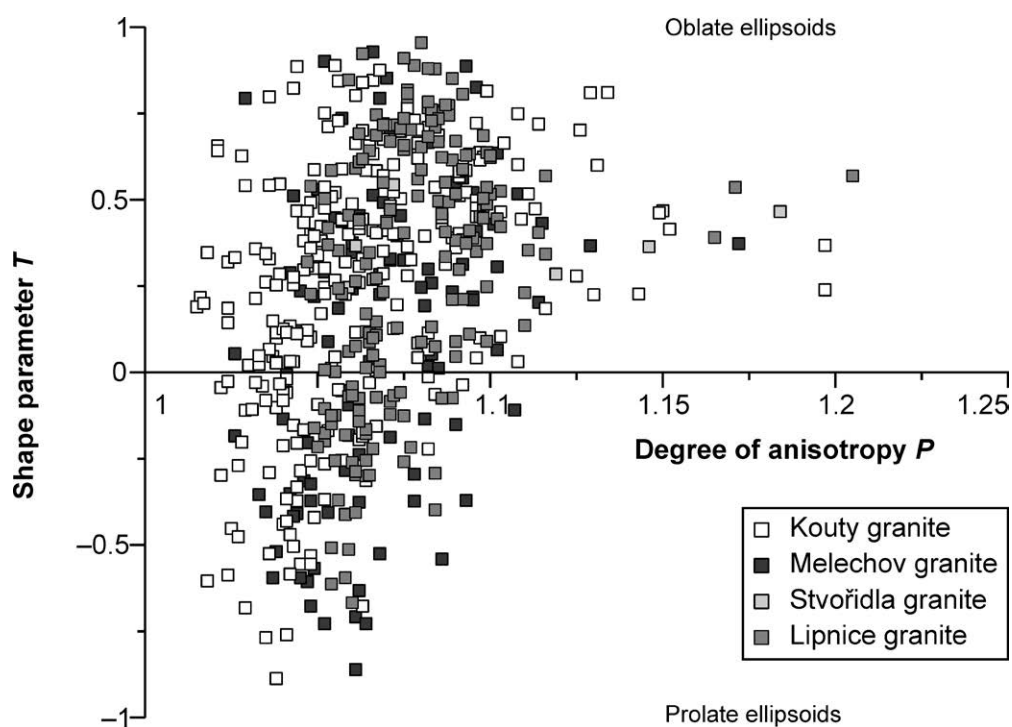


Fig. 6. Magnetic anisotropy P–T plot for all analyzed specimens from the Melechov pluton.

and Melechov granites, passing outward into domains with slightly more anisotropic and strongly oblate fabric (Fig. 4b, c). Prolate fabrics are mostly localized near the outer pluton margin or internal contacts (Fig. 4c). The Lipnice granite exhibits less systematic spatial variations in the two parameters, with one domain of highly oblate fabrics in the north-central part of the intrusion (Fig. 4c). In terms of orientation, the outer Kouty and Lipnice granites show margin-parallel magnetic foliations dipping outward at moderate to steep angles (Fig. 7a), well expressed on the stereonet as a broad circular band with several sub-maxima of foliation poles (k_3) about a vertical axis. On the map, both units display an ‘onion-skin’ foliation pattern (Fig. 7a). The exception to this overall trend are a few stations (JZ156, JZ173, JZ174, JZ177, JZ182, JZ187) with foliations at a high angle to the outer pluton margin or internal contacts (Fig. 7a). Magnetic lineations are mostly dip-oblique and follow a tangential pattern around the pluton (Fig. 7b). By contrast, only two stations (JZ164, JZ168) in the inner Melechov granite reveal margin-parallel, outward-dipping magnetic foliations, corresponding to the most prominent maximum of data points on the stereonet in Figure 7, which are associated with variably oriented lineations (Fig. 7b). In the remainder of this granite, foliations are at a high angle to the internal contact, and display scattered maxima along the periphery of the stereonet (Fig. 7) and are associated with lineations plunging moderately from the south to the north (Fig. 7b). On the stereonet, the lineations thus define a girdle over ca. 180° of an arc (Fig. 7).

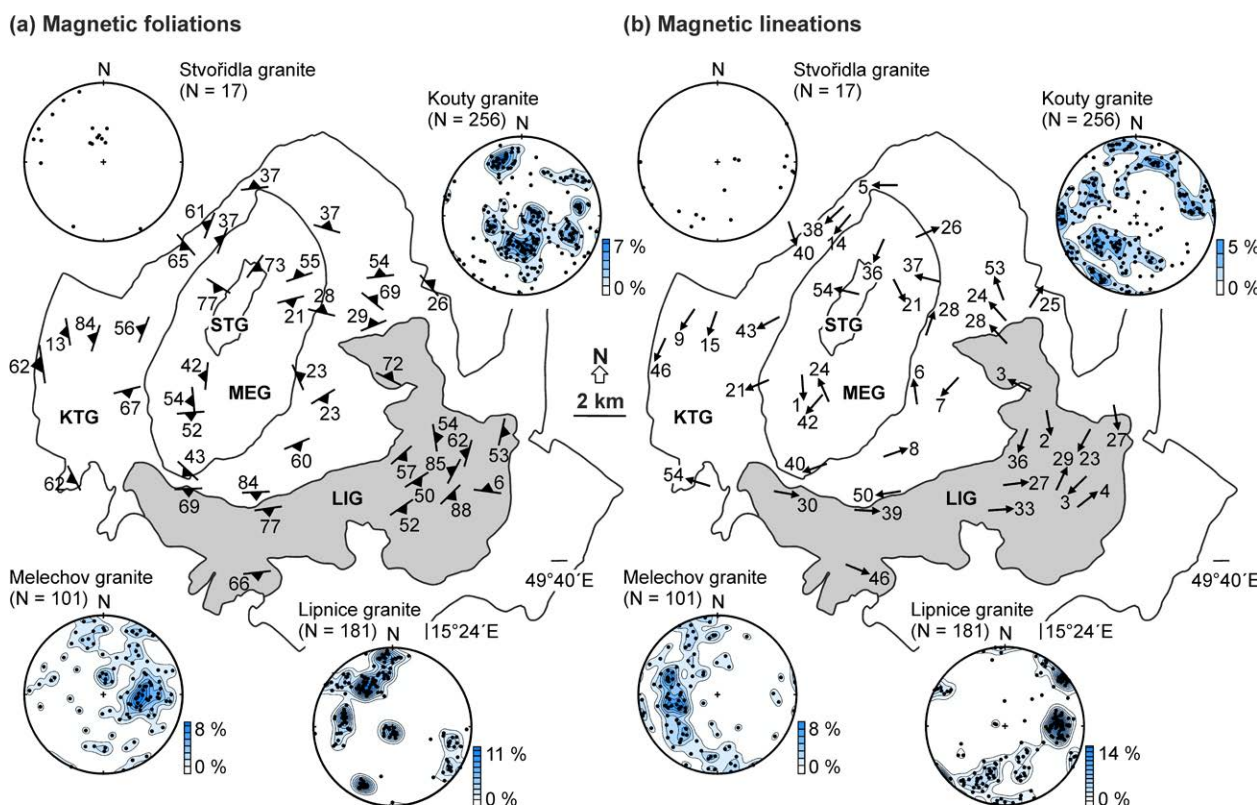


Fig. 7. Maps of (a) magnetic foliations and (b) magnetic lineations in the Melechov pluton. Stereonets (equal area, projection on lower hemisphere) show orientation of the minimum (k_3) and maximum (k_1) principal susceptibilities (i.e., poles to magnetic foliations and magnetic lineations, respectively). LIG – Lipnice granite, KTG – Kouty granite, MEG – Melechov granite, STG – Stvořidla granite.

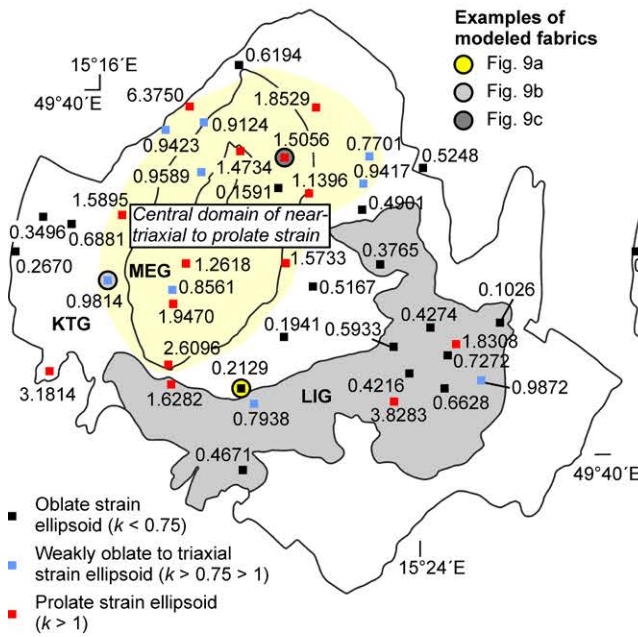
4. INVERSE STRAIN CALCULATION FROM MAGNETIC FABRIC

To estimate strain recorded by the granitic magma and hence, determine strain distribution across the Melechov pluton, we used a method supported by a freely available Matlab program SUSIE developed by Ježek and Hrouda (2002, 2007), allowing an inverse strain calculation from the AMS data. This procedure yields the k and D parameters (Ramsay and Huber, 1983) at each station in the pluton. The k parameter reflects strain symmetry and is defined as $k = \ln(X/Y)/\ln(Y/Z)$, where X , Y , and Z represent the long, intermediate, and short semiaxes of the strain ellipsoid, respectively. For $0 < k < 1$ the strain is oblate (flattening), for $k = 1$ is triaxial, and for $1 < k < \infty$ is prolate (constrictional). The D parameter relates to strain intensity and is expressed as $D = \{[\ln(X/Y)]^2 + [\ln(Y/Z)]^2\}^{1/2}$. The basic assumptions and input parameters for the modeling are: (1) The P and T parameters were taken as site-averaged values from the measured data (Electronic Supplementary Material, Part 3). (2) As the granites in question are paramagnetic and micas are the dominant carriers of the AMS, the modeled particle population consisted of biotite crystals with an axial ratio of 5, oblate

magnetocrystalline anisotropy, and the P parameter of 1.3 (Zapletal, 1990; Martín-Hernández and Hirt, 2003). (3) The magmatic strains recorded by the AMS are assumed to be coaxial, which is in agreement with the lack of synmagmatic asymmetric structures associated with the measured fabrics. In addition, it should be noted that the differences in the k and D parameters for pure and simple shears are negligible for small strains (Ježek and Hrouda, 2007). (4) For each station in the pluton, we calculated three different models of initial particle orientation (Ježek and Hrouda, 2007): random (200 crystals), Sanderson–Marchini (156 crystals), and Ježek–Hrouda (160 crystals in most cases). The range of calculated values for the k and D parameters were small for all three types of initial particle orientation populations (Fig. 8c, d; Electronic Supplementary Material, Part 6). Given the similarity of the results, the analysis was then simplified to consider only the case for the random orientation population which is most consistent with underformed rock fabric (Electronic Supplementary Material, Parts 1, 2).

Modeling the case with random orientations and considering the spatial distribution of the results across the granites of the pluton, the calculated k and D parameters (Electronic Supplementary Material, Part 6) reveal none or weak trends with respect to the distance from the pluton center (Fig. 8c, d, respectively), defined as the geometric center of the Stvořidla granite. However, a striking gradient in the k and D parameter emerges when only the outer and most voluminous Kouty granite, representing much of the pluton, is considered (Fig. 8e, f). In this granite, an outer zone near the pluton margin is characterized by stronger flattening strain ($k = 0.267–0.350$ for $D = 0.487–0.653$, respectively; Fig. 8), passing inward into a central domain of weak plane-strain to constriction ($k = 0.981–1.853$ for $D = 0.341–0.878$, respectively; Fig. 8). In the inner Melechov granite, the calculated strains are mostly constrictional, with the highest k (1.506–2.610) and D (0.483–0.623) parameters along the internal contact between the Melechov and Kouty granites and then decreasing inwards ($k = 0.959–1.262$ and $D = 0.448–0.560$; Fig. 8). The limited data set from the Stvořidla granite precludes a more rigorous assessment of the strain distribution. Nevertheless, the only analyzed station also corroborates overall constrictional strain in the pluton center ($k = 1.473$, $D = 3.010$; Fig. 8). In contrast, the Lipnice granite, forming a separate body off the pluton center, reveals more irregular variations in the calculated strains. This granite recorded predominantly oblate strains ($k = 0.103–0.727$) whereas plane-strain to constriction was calculated at several locations scattered across the granite ($k = 0.987–1.628$; Fig. 8). The associated strain intensity D varies with no apparent spatial pattern from 0.408–0.861 (Fig. 8).

(a) Calculated strain symmetry k



(b) Calculated strain intensity D

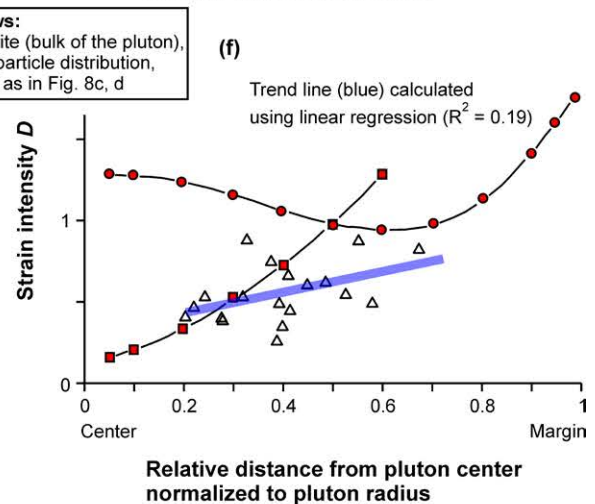
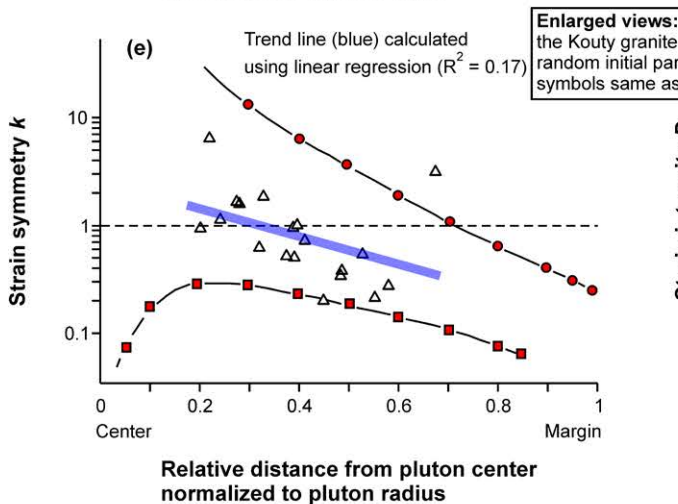
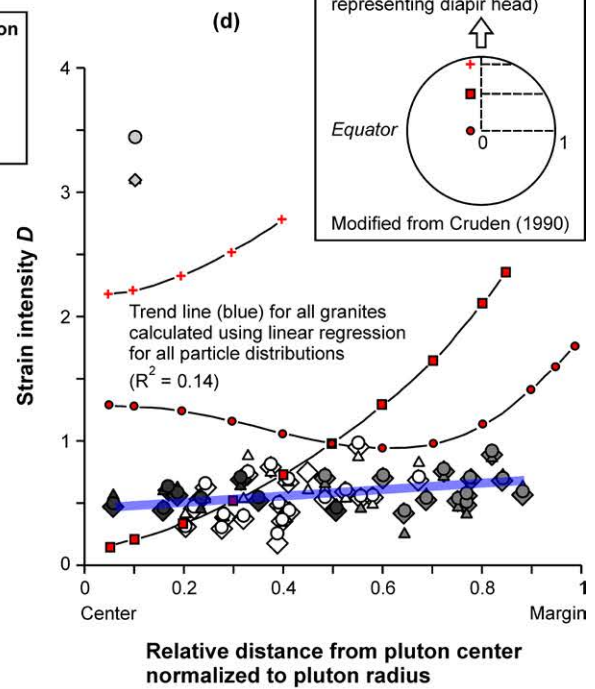
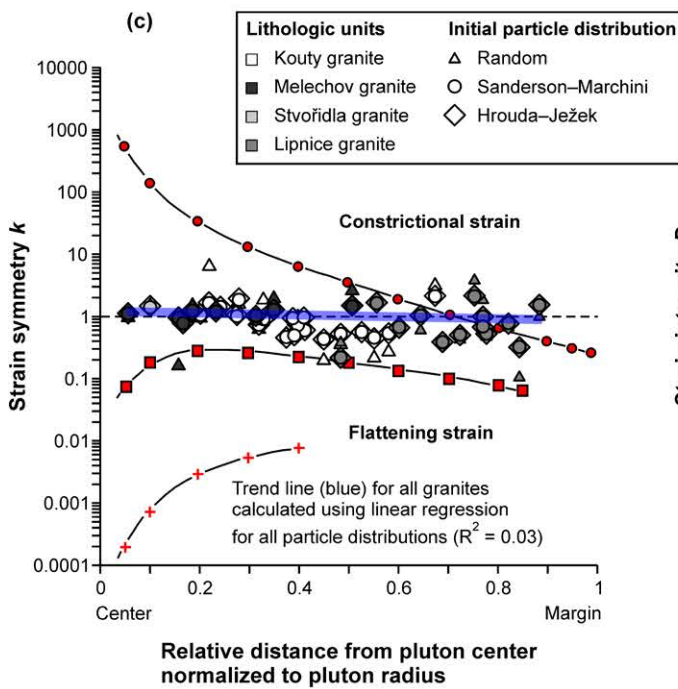
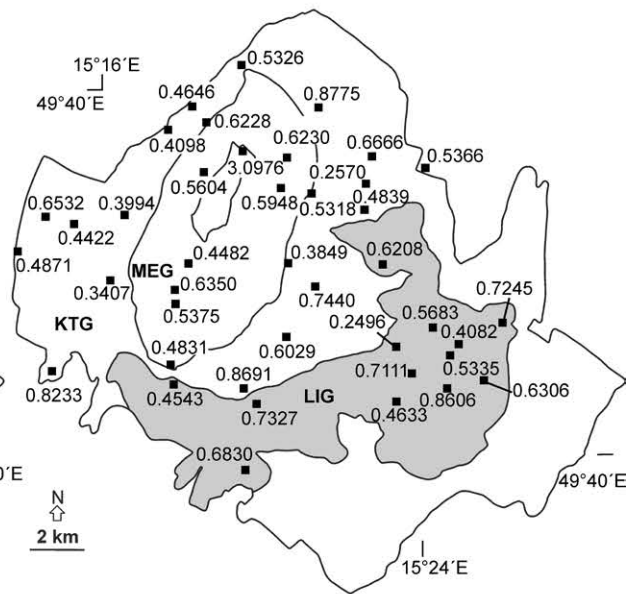


Fig. 8. Results of the inverse AMS-to-strain modeling using the Ježek–Hrouda method. Maps show spatial distribution of calculated (a) strain symmetry and (b) intensity at each station in the Melechov pluton (for random initial particle distribution). Graphs (c, d) show strain symmetry and intensity calculations from the Melechov pluton plotted against theoretically predicted values (red symbols) in an upper part of the model Newtonian diapir of Cruden (1990). Spatial trends in the calculated strain parameters in the outer Kouty granite highlighted by blue lines (arrows). Graphs (e, f) show highlighted symmetry and intensity calculations for random initial particle distribution (used in the interpretation).

5. DISCUSSION

5.1. Diapiric emplacement of the Melechov pluton

We favor diapiric emplacement of the Melechov pluton because: (1) An irregular, but more or less equant map outline in combination with the current gravimetric interpretation suggest a significant vertical extent and an overall inverted tear-drop shape of the pluton consisting of a cupola in the upper part, passing into a downward narrowing cone below ~5–6 km (Fig. 2b). (2) The crestal cupola is also defined by the generally outward-dipping pluton/host rock contacts and metamorphic foliation and compositional banding in the migmatites (Figs. 1c, 3). (3) The pluton reveals concentric compositional zoning (Fig. 1c), consistent with nested emplacement of at least three main magma batches, represented by the Kouty, Melechov, and Lipnice granites, completed by fractional crystallization of the innermost Stvořidla granite (Matějka and Janoušek, 1998; Mlčoch et al., 2000). (4) Widespread pluton-up/host rock-down kinematic indicators (Fig. 3c, d) are inferred to represent the structural result of downward return flow at the pluton aureole.

The measured AMS data are also inferred to lend a strong support to a model of diapiric emplacement. Below we first discuss the Kouty granite, which makes up the bulk of the pluton, and then the Lipnice and Melechov granites, which are smaller, 'second-order' intrusions inside the pluton (Fig. 1c). Foliations in the Kouty granite define a concentric, 'onion-skin' domal structure, suggesting that the present-day erosion surface intersects the head of the Melechov diapir. Assuming a simple AMS-to-strain relationship, the outward increasing degree of oblateness of the AMS ellipsoid in the Kouty granite (Fig. 4c) indicates syn-magmatic flattening of the pluton margin, passing into a broad central portion of the pluton that underwent near plane-strain (Fig. 4c). This transition in fabric symmetry is also linked to drop in the magnetic anisotropy from outer margin of the granite inward (Fig. 4b). Taken together, magnetic fabric orientation and spatial changes in fabric symmetry and intensity across the Kouty granite fit exceptionally well the theoretically predicted fabric

parameters in igneous diapirs (e.g., Cruden, 1990).

Assuming model-consistent internal circulation driven by drag forces along the diapir margin, the theoretical models also postulate a characteristic evolution of internal compositional contacts from originally horizontal through vertical to increasingly complex geometries as a function of the diapir travel distance (e.g., Schmeling et al., 1988). In the Melechov pluton, examining fabric and internal contacts reveals two different kinds of relationship. First, the crescent-like shape of the off-center Lipnice granite generally parallels the concentric internal structure of the pluton (Fig. 1c). The same applies for magnetic fabric, which is roughly concordant with both the margin of this granite and with fabric in the adjacent Kouty granite (Fig. 7; Electronic Supplementary Material, Part 5). We interpret this fabric/contact relationship and the lack of fabric refraction as recording a single strain field during growth of the granite dome (diapir head).

Second, the inner Melechov granite shows a more complex fabric/contact relationship. Assuming that the granite pierced the center of the dome built by the Kouty granite as a steep-sided cylindrical intrusion (Mlčoch et al., 2000), one would expect significant strain in the surrounding magma and thus margin-parallel foliations both inside and outside the Melechov granite. This behavior should be theoretically accompanied by increasing degree of anisotropy in the Kouty host granite as the internal contact is approached. Our AMS study reveals exactly the opposite, i.e., narrow zones of low-anisotropy (Fig. 4b) and fabrics oriented at a high angle to the internal contact in the Kouty granite (Fig. 7). An explanation for this disconnect between expectation and reality comes from understanding that fabrics oblique to or traversing internal boundaries are observed in many plutons and are interpreted to result from post-emplacment but still syn-magmatic tectonic overprint (e.g., Buddington, 1959; Cruden, 1990; Paterson and Vernon, 1995; Žák et al., 2007). However, for this explanation to apply, the fabric should be present in the pluton and the host rock, but for the Melechov granite, the fabric is confined to the granite, negating this explanation (Paterson et al., 1998). Another possible explanation for the fabric in the Melechov granite is provided from modeling by Cruden (1990) that showed that foliations may be discordant to internal contacts in central and lower parts of diapirs as a result of their internal fluid circulation.

5.2. Interpretation of strain gradients from the AMS

A striking feature of the granites in question is their weak magnetic anisotropy, mostly between 5 and 10 % and decreasing to even less than 5 % in two domains along the Kouty/Melechov internal contact (Figs. 4b, 6). Nevertheless, despite such small anisotropy magnitudes, the AMS mean

directions are well defined on most stations (Electronic Supplementary Material, Part 5) and fabric parameters vary systematically across the pluton, particularly for the outer Kouty granite (Fig. 4). Furthermore, the trend of anisotropy decreasing inward is consistent with an inward strain decrease as predicted in theoretical models of diapirs (e.g., Ramsay, 1989; Cruden, 1990). The question thus arises of how to explain the small calculated magmatic strains in the context of the required large magnitude of magma flow and hence, expected large strains during diapiric ascent. We address this issue quantitatively using fabric-to-strain modeling based on the method of Ježek and Hrouda (2002) and, for the first time in the literature, we also explore the applicability of this method to strain estimation in granite plutons.

Though the thermomagnetic measurements indicate an admixture of Ti-hematite and hemoilmenite in the analyzed specimens, perhaps formed due to hydrothermal alteration and weathering (see also Procházka and Matějka, 2006), the AMS signal is clearly dominated by paramagnetic micas (Fig. 5). In the following, we thus consider micas as the primary particles defining the measured fabric pattern in the pluton.

The low fabric intensity observed in the Melechov pluton can be explained in two ways. First, the larger fraction ($\Phi = 20\text{--}50\%$) of mica crystals (either restitic from the source or newly grown) was already present in the melt before emplacement but fabric development was oscillatory as predicted by the Jeffery's theory of rigid particle rotation in viscous flow (e.g., Ježek et al., 1994; Arbaret et al., 2000; and Jiang, 2007). In such a case, the flowing magma would go through transient periods of near-isotropic, low-intensity fabric periodically randomizing the earlier stronger fabric during ascent. However, we find this hypothesis unlikely because the magma would have to systematically freeze in the low-intensity fabric of the Jeffery's period across all the pluton without preserving any evidence for the high-intensity flow periods.

Alternatively, magma may have ascended a long distance as a crystal-poor, melt-dominated Newtonian suspension ($\Phi < 20\text{--}30\%$) and then crystallized near the final emplacement site, capturing only the latest strain increment at an inward-migrating crystallization front, and not the total strain. If the interpretation of the Newtonian crystal-poor magma is valid, the magmatic strains obtained from our fabric modeling can be directly compared with those modeled in the Newtonian diapirs, where strain is a function of position within the diapir and its travel distance. Cruden (1990) examined diapirs travelling a distance of two, five, and ten body radii for a diapir/host viscosity contrast of 10^{-3} . Given that the diameter of the Melechov pluton is ~ 7 km, our strain estimations can be compared only with the first case (hereinafter referred to as the 'model diapir'; see also fig. 4 in

Cruden, 1990), corresponding to a feasible ~14 km travel distance through the crust.

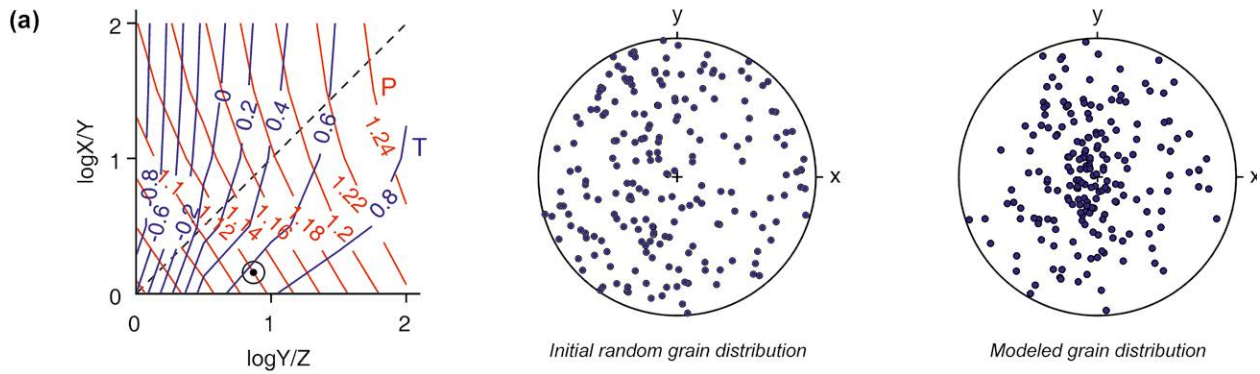
Our AMS-to-strain calculations are consistent with Cruden's model, especially when the outer Kouty granite is considered and the random initial particle orientation distribution is assumed (Fig. 8e, f). The calculated strain symmetries (k) fall between those expected near the equator ($z = 0$) and those at a half ($z = 0.5$) of the upper hemisphere of the model diapir (Fig. 8c, e; note that the entire Cruden's sphere in fact represents a head of a diapir whereas what corresponds to a diapir tail is the region below the sphere). The same applies also for strain intensities (D) which increase towards the pluton margin (Fig. 8d, f). The D values, however, exhibit only a weak, approximately linear gradient and significantly smaller strain magnitudes at a distance of 0.3 to 0.7 body radii as compared to exponential gradient in the model diapir (Fig. 8d, f). All in all, these findings support the notion that magmatic fabrics in granites generally record (very) low magnitudes of late incremental strain (e.g., Benn, 1994; Paterson et al., 1998; Benn et al., 2001) but still may capture even subtle gradients in strain intensities and especially symmetries from the ascent stage.

5.3. Some methodological notes on strain estimation from fabric in granite plutons

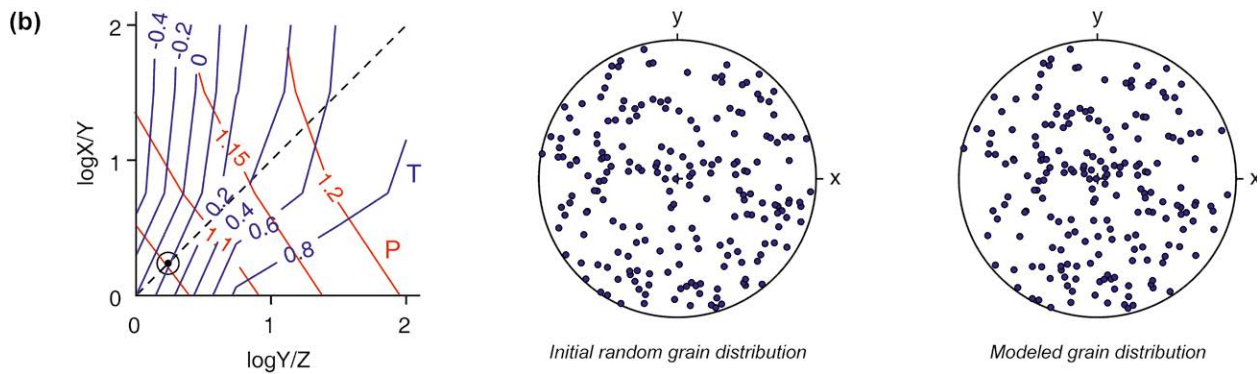
As discussed above, the Ježek–Hrouda method is capable of determining intrusive strain variations even for very low degree of magnetic anisotropy ($P < 1.1$), which is a common feature of many paramagnetic granite plutons (e.g., Bouchez, 1997; Pueyo et al., 2004). Despite the differences in strain magnitude between the model diapir and values calculated from our AMS data (Fig. 8d, f), the approach of Ježek and Hrouda (2002) reveals an unexplored potential for estimation of strain gradients in granite plutons, which normally lack reliable strain markers (see, e.g., Hutton, 1988; Archanjo et al., 1995; Paterson et al., 2004; Sen et al., 2005; Sen and Mamtani, 2006 for discussions). Consequently, the method could be used in the future to discriminate among various pluton emplacement models and to quantify the relative contribution of magmatic and tectonic strains during emplacement.

On a grain-scale, the modeling also allows indirect estimation and visualization of the orientation distribution of mica crystals for various degrees of anisotropy and symmetries of the AMS and inferred strain ellipsoids (Fig. 9). The statistical characterization of the modeled grain populations is then included in the model through the P and T parameters, calculated from the magnetic susceptibility tensor which is directly related to the orientation tensor (e.g., Ježek and Hrouda, 2000, 2004). Importantly, the (pseudo-)hexagonal single mica crystals

Flattening strain and modeled fabric near the pluton margin (Kouty granite, station JZ194)



Plane-strain and modeled fabric near the internal contact (Kouty granite, station JZ156)



Constrictional strain and modeled fabric in the pluton center (Melechov granite, station JZ186)

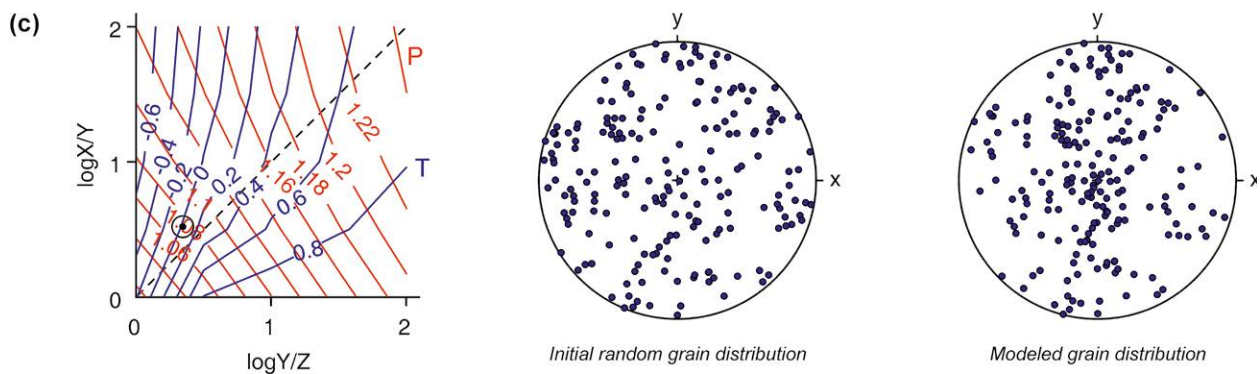


Fig. 9. Examples of three crystal orientations modeled using the Ježek–Hrouda method for flattening strain (a), plane-strain (a), and constrictional strain (c). The modeled crystal orientations are calculated for random initial grain distribution and plotted on equal area, lower hemisphere stereonet. The coordinate system for the stereonet is the strain axes. Logarithmic Flinn plots show finite strains (circles) calculated for each example; X, Y, Z are semiaxes of the finite strain ellipsoid. Red and blue contours represent the degree of anisotropy (P) and shape parameter (T).

possess a highly oblate magnetocrystalline anisotropy, raising the question of how to directly relate the single-crystal AMS ellipsoid to the overall rock fabrics with different symmetries and low anisotropy. We consider our strain calculations from three stations to address this matter (Fig. 9). The stations were selected to illustrate the main end-member strain types across an ideal diapir from a strongly flattened margin to a vertically stretched center (e.g., Ramsay, 1989; Paterson and Fowler, 1993; Clemens, 1998). For a highly oblate rock fabric and inferred flattening strain (Fig. 9a), the modeled population of mica crystals with an initially random orientation distribution exhibits a clustered orientation distribution with the minimum susceptibility (k_3) axes laying close to the Z axis of the strain ellipsoid. As the strain symmetry moves towards the plane-strain and constrictional field, the crystals' orientation distribution evolves from scattered (Fig. 9b) to a girdle about the X axis of the strain ellipsoid (Fig. 9c). In other words, our modeling confirms that in regions where stretching dominates the crystallizing magma, such as in diapir centers and tails, particles with oblate magnetocrystalline anisotropy will reorient to define the overall prolate AMS ellipsoid and magnetic lineation (k_1) as the zone axis (Henry, 1997).

CONCLUSIONS

- 1) The Melechov pluton is interpreted as a mid-crustal vertically extensive granitic diapir with an apical part (diapir head) exposed at the present-day erosion level. The diapir head exhibits an overall concentric structure defined both by compositional zoning and magnetic fabric, and especially the latter is consistent with an idealized picture of igneous diapirs.
- 2) Margin-parallel, outward-dipping magnetic foliations are associated with oblate shapes of the susceptibility ellipsoids and higher degree of anisotropy, passing inward into weaker triaxial to prolate fabric. Magnetic fabric of the inner Melechov granite, in places oriented at a high angle to the internal contacts and ductile host rock structures, is interpreted as recording the internal diapir circulation as predicted by theoretical models.

- 3) In terms of intensity and symmetry, the intrusive strain estimations from the AMS data using the Ježek–Hrouda method are in agreement with strain gradients in the heads of model Newtonian diapirs travelling a distance of two body radii, though magnitudes of the calculated strains are lower near the outer margin of the Melechov diapir. The low degree of anisotropy and calculated strain intensities across the diapir are consistent with granitic magma ascent as a dilute, crystal-poor suspension followed by crystallization of fabric markers and their response to strain near the final emplacement level. This mechanism explains why the generally weak intrusive fabrics may still be capable of recording the within-diapir strain gradient.
- 4) We conclude that the Ježek–Hrouda method has proven to be particularly useful for strain estimations from the AMS in granite plutons, which typically lack reliable strain markers. Future research could be directed towards comparing strain calculations against data obtained from microgranular enclaves or xenoliths, on comparing the modeled grain orientations with those of derived from some other independent method (e.g., image analysis, electron back-scatter diffraction), and examining strain variations for various pluton emplacement models.

ACKNOWLEDGEMENTS

We gratefully acknowledge two anonymous reviewers and Editor William M. Dunne for their detailed and constructive comments which helped to improve the original manuscript significantly. We also thank Josef Ježek, František Hrouda, Jan Švancara, Josef Šrámek, and Kryštof Verner for valuable discussions, and Jiří Sedlák for sharing gravimetric map of the pluton. Staff of the Hotel Stadion in Ledec nad Sázavou is thanked for hospitality during field work. This study is part of the Ph.D. research of Jakub Trubač. We acknowledge financial support from the Grant Agency of the Czech Republic through grants No. P210/11/1168 (to Jiří Žák) and from the Charles University in Prague Research Program PRVOUK P44.

REFERENCES

- Arbaret, L., Fernandez, A., Ježek, J., Ildefonse, B., Launeau, P., Diot, H., 2000. Analogue and numerical modelling of shape fabrics: application to strain and flow determination in magmas. *Transactions of the Royal Society of Edinburgh: Earth Sciences* 90, 97–109.
- Archanjo, C.J., Launeau, P., Bouchez, J.L., 1995. Magnetic fabric vs. magnetite and biotite shape fabrics of the magnetite-bearing granite pluton of Gameleiras (Northeast Brazil). *Physics of the Earth and Planetary Interiors* 89, 63–75.
- Asch, K., 2003. The 1:5 million international geological map of Europe and adjacent areas: development and implementation of a GIS-enabled concept. *Geologisches Jahrbuch, Sonderhefte*, A3. E. Schweizerbart'sche Verlagsbuchhandlung, Stuttgart.
- Aydin, A., Ferré, E.C., Aslan, Z., 2007. The magnetic susceptibility of granitic rocks as a proxy for geochemical differentiation: example from the Saruhan granitoids, NE Turkey. *Tectonophysics* 441, 85–95.
- Bankwitz, P., Bankwitz, E., Thomas, R., Wemmer, K., Kämpf, H., 2004. Age and depth evidence for pre-exhumation joints in granite plutons: fracturing during the early cooling stage of felsic rock. In: Cosgrove, J.W., Engelder, T. (Eds.), *The Initiation, Propagation, and Arrest of Joints and Other Fractures*. Geological Society, London, Special Publications, 231, pp. 25–47.
- Bateman, R., 1984. On the role of diapirism in the segregation, ascent and final emplacement of granitoid magmas. *Tectonophysics* 110, 211–231.
- Benn, K., 1994. Overprinting of magnetic fabrics in granites by small strains – numerical modeling. *Tectonophysics* 233, 153–162.
- Benn, K., Paterson, S.R., Lund, S.P., Pignotta, G.S., Kruse, S., 2001. Magmatic fabrics in batholiths as markers of regional strains and plate kinematics: example of the Cretaceous Mt. Stuart batholith. *Physics and Chemistry of the Earth* 26, 343–354.
- Berner, H., Ramberg, H., Stephansson, O., 1972. Diapirism in theory and experiment. *Tectonophysics* 15, 197–218.
- Blažiček, M., 2002. Analysis of fracture networks and their correlation with AMS fabrics in the Melechov massif. Diploma thesis, Charles University in Prague.
- Blížkovský, M., Novotný, A., 1982. Gravity map of the Bohemian Massif. *Geofyzika*, Brno.

- Bouchez, J.L., 1997. Granite is never isotropic: an introduction to AMS studies of granitic rocks. In: Bouchez, J.L., Hutton, D.H.W., Stephens, W.E. (Eds.), *Granite: From Segregation of Melt to Emplacement Fabrics*. Kluwer Academic Publishers, pp. 95–112.
- Breiter, K., 2007. New results from geological investigation of the Melechov pluton. *Geoscience Research Reports for 2006*, Czech Geological Survey, Prague, 202–205.
- Breiter, K., Sulovský, P., 2005. Geochronology of the Melechov granite massif. *Geoscience Research Reports for 2004*, Czech Geological Survey, Prague, 16–19.
- Buddington, A.F., 1959. Granite emplacement with special reference to North America. *Geological Society of America Bulletin* 70, 671–747.
- Cháb, J., Stráník, Z., Eliáš, M., 2007. Geological map of the Czech Republic 1:500,000. Czech Geological Survey, Prague.
- Clemens, J.D., 1998. Observations on the origins and ascent mechanisms of granitic magmas. *Journal of the Geological Society*, London 155, 843–851.
- Cruden, A.R., 1990. Flow and fabric development during the diapiric rise of magma. *Journal of Geology* 98, 681–698.
- Dixon, J.M., 1975. Finite strain and progressive deformation in models of diapiric structures. *Tectonophysics* 28, 89–124.
- England, R.W., 1990. The identification of granitic diapirs. *Journal of the Geological Society*, London 147, 931–933.
- Fusán, O., Kodým, O., Matějka, A., Urbánek, L. (1967). Geological map of Czechoslovakia 1:500,000. Central Geological Survey, Prague.
- Gerdes, A., Friedl, G., Parrish, R.R., Finger, F., 2003. High-resolution geochronology of Variscan granite emplacement – the South Bohemian Batholith. *Journal of the Czech Geological Society* 48, 53–54.
- Harlov, D.E., Procházka, V., Förster, H.J., Matějka, D., 2008. Origin of monazite–xenotime–zircon–fluorapatite assemblages in the peraluminous Melechov granite massif, Czech Republic. *Mineralogy and Petrology* 94, 9–26.
- Henry, B., 1997. The magnetic zone axis: a new element of magnetic fabric for the interpretation of the magnetic lineation. *Tectonophysics* 271, 325–331.
- Hladík, V., Sedlák, J., Šrámek, J., Zabadal, S., 2006. Gravity model of the Melechov massif. 2nd Workshop on International Gravity Field Research (abstracts), Smolenice, Slovakia, 40–44.

- Hrouda, F., 2010. Modelling relationship between bulk susceptibility and AMS in rocks consisting of two magnetic fractions represented by ferromagnetic and paramagnetic minerals – implications for understanding magnetic fabrics in deformed rocks. *Journal of the Geological Society of India* 75, 254–266.
- Hrouda, F., Kahan, Š., 1991. The magnetic fabric relationship between sedimentary and basement nappes in the High Tatra Mountains, N. Slovakia. *Journal of Structural Geology* 13, 431–442.
- Hutton, D.H.W., 1988. Granite emplacement mechanisms and tectonic controls: inferences from deformation studies. *Transactions of the Royal Society of Edinburgh: Earth Sciences* 79, 245–255.
- Jelínek, V., 1981. Characterization of the magnetic fabric of rocks. *Tectonophysics* 79, T63–T67.
- Ježek, J., Hrouda, F., 2000. The relationship between the Lisle orientation tensor and the susceptibility tensor. *Physics and Chemistry of Earth* 25, 469–474.
- Ježek, J., Hrouda, F., 2002. Software for modeling the magnetic anisotropy of strained rocks. *Computers and Geosciences* 28, 1061–1068.
- Ježek, J., Hrouda, F., 2004. Determination of the orientation of magnetic minerals from the anisotropy of magnetic susceptibility. In: Martín-Hernández, F., Lüneburg, C.M., Auborg, C., Jackson, M. (Eds.), *Magnetic Fabric: Methods and Application*. Geological Society, London, Special Publications 238, pp. 9–20.
- Ježek, J., Hrouda, F., 2007. SUSIE: a program for inverse strain estimation from magnetic susceptibility. *Computers and Geosciences* 33, 749–759.
- Ježek, J., Melka, R., Schulmann, K., Venera, Z., 1994. The behaviour of rigid triaxial ellipsoidal particles in viscous flows – modeling of fabric evolution in a multiparticle system. *Tectonophysics* 229, 165–180.
- Jiang, D., 2007. Numerical modeling of the motion of rigid ellipsoidal objects in slow viscous flows: a new approach. *Journal of Structural Geology* 29, 189–200.
- Kratinová, Z., Závada, P., Hrouda, F., Schulmann, K., 2006. Non-scaled analogue modelling of AMS development during viscous flow: a simulation on diapir-like structures. *Tectonophysics* 418, 51–61.
- Lenhardt, W.A., Švancara, J., Melichar, P., Pazdírková, J., Havíř, J., Sýkorová, Z., 2007. Seismic activity of the Alpine–Carpathian–Bohemian Massif region with regard to geological and potential field data. *Geologica Carpathica* 58, 397–412.

- Linsser, H., 1967. Investigation of tectonics by gravity detailing. *Geophysical Prospecting* 15, 480–515.
- Marsh, B.D., 1982. On the mechanics of diapirism, stoping, and zone melting. *American Journal of Science* 282, 808–855.
- Martínez Catalán, J.R., 2011. Are the oroclinal belts of the Variscan belt related to late Variscan strike-slip tectonics? *Terra Nova* 23, 241–247.
- Martín-Hernández, F., Hirt, A.M., 2003. The anisotropy of magnetic susceptibility in biotite, muscovite and chlorite single crystals. *Tectonophysics* 367, 13–28.
- Matějka, D., Janoušek, V., 1998. Whole-rock geochemistry and petrogenesis of granites from the northern part of the Moldanubian batholith (Czech Republic). *Acta Universitatis Carolinae, Geologica* 42, 73–79.
- Miller, R.B., Paterson, S.R., 1999. In defense of magmatic diapirs. *Journal of Structural Geology* 21, 1161–1173.
- Mlčoch, B., Breiter, K., Schulmannová, B., 2000. The Melechov granite massif. *Geoscience Research Reports for 1999, Czech Geological Survey, Prague*, 91–93.
- Mottlová, L., 1985. The deep structure of the central and Melechov massifs interpreted on the basis of alternative solutions of inverse gravity problems. *Bulletin of the Central Geological Survey* 57, 351–363.
- Nagata, T., 1961. *Rock Magnetism*. Maruzen, Tokyo.
- Paterson, S.R., Fowler, T.K., 1993. Re-examining pluton emplacement processes. *Journal of Structural Geology* 15, 191–206.
- Paterson, S.R., Vernon, R.H., 1995. Bursting the bubble of ballooning plutons: a return to nested diapirs emplaced by multiple processes. *Geological Society of America Bulletin* 107, 1356–1380.
- Paterson, S.R., Miller, R.B., 1998. Stopped blocks in plutons: paleo-plumb bobs, viscometers, or chronometers? *Journal of Structural Geology* 20, 1261–1272.
- Paterson, S.R., Fowler, T.K., Schmidt, K.L., Yoshinobu, A.S., Yuan, E.S., Miller, R.B., 1998. Interpreting magmatic fabric patterns in plutons. *Lithos* 44, 53–82.
- Paterson, S.R., Pignotta, G.S., Vernon, R.H., 2004. The significance of microgranitoid enclave shapes and orientations. *Journal of Structural Geology* 26, 1465–1481.
- Procházka, J., Mlčoch, B., 1998. Complex geological survey of Melechov massif (E-Bohemia). *Geoscience Research Reports for 1997, Czech Geological Survey, Prague*, 31–37.

- Procházka, V., Matějka, D., 2006. Rock-forming accessory minerals in the granites of the Melechov Massif (Moldanubian Batholith, Bohemian Massif). *Acta Universitatis Carolinae, Geologica* 48, 71–79.
- Pueyo, E.L., Román-Berdiel, T.M., Bouchez, J.L., Casas, A.M., Larrasoana, J.C., 2004. Statistical significance of magnetic fabric data in studies of paramagnetic granites. In: Martín-Hernández, F., Lüneburg, C.M., Auborg, C., Jackson, M. (Eds.), *Magnetic Fabric: Methods and Application*. Geological Society, London, Special Publications 238, pp. 395–420.
- Ramsay, J.G., 1989. Emplacement kinematics of a granite diapir: the Chindamora batholith, Zimbabwe. *Journal of Structural Geology* 11, 191–209.
- Ramsay, J.G., Huber, M.I., 1983. *The Techniques of Modern Structural Geology*. Volume 1: Strain Analysis. Academic Press, London.
- Schmeling, H., Cruden, A.R., Marquart, G., 1988. Finite deformation in and around a fluid sphere moving through a viscous medium: implications for diapiric ascent. *Tectonophysics* 149, 17–34.
- Schulmann, K., Venera, Z., Konopásek, J., Lexa, O., 1998. Structural and geological investigation of the Melechov massif. Unpublished report, Faculty of Science, Charles University in Prague.
- Schulmann, K., Lexa, O., Štípská, P., Racek, M., Tajčmanová, L., Konopásek, J., Edel, J.B., Peschler, A., Lehmann, J., 2008. Vertical extrusion and horizontal channel flow of orogenic lower crust: key exhumation mechanisms in large hot orogens? *Journal of Metamorphic Geology* 26, 273–297.
- Šefara, J., 1973. Interpretation of vertical density interfaces using a map of gravity anomalies by means of digital computer. *Journal of Geological Sciences, Applied Geophysics* 11, 19–29.
- Sen, K., Mamtani, M.A., 2006. Magnetic fabric, shape preferred orientation and regional strain in granitic rocks. *Journal of Structural Geology* 28, 1870–1882.
- Sen, K., Majumder, S., Mamtani, M.A., 2005. Degree of magnetic anisotropy as a strain intensity gauge in ferromagnetic granites. *Journal of the Geological Society, London* 162, 583–586.
- Staněk, M., 2013. Structural and petrophysical characterisation of granite intended for radioactive waste stocking. Ph.D. thesis, Charles University in Prague.
- Staněk, M., Géraud, Y., Lexa, O., Špaček, P., Ulrich, S., Diraison, M., 2013. Elastic anisotropy and pore space geometry of schlieren granite: direct 3-D measurements at high confining pressure combined with microfabric analysis. *Geophysical Journal International* 194, 383–394.
- Talbot, C.J., Jackson, M.P.A., 1987. Internal kinematics of salt diapirs. *American Association of Petroleum Geologists Bulletin* 71, 1068–1093.

- Verner, K., Žák, J., Šrámek, J., Paclíková, J., Zavřelová, J., Machek, M., Finger, F., Johnson, K., 2014. Formation of elongated granite–migmatite domes as isostatic accommodation structures in collisional orogens. *Journal of Geodynamics* 73, 100–117.
- Weinberg, R.F., Podladchikov, Y., 1994. Diapiric ascent of magmas through power law crust and mantle. *Journal of Geophysical Research* 99, 9543–9559.
- Winchester, J.A., 2002. Palaeozoic amalgamation of Central Europe: new results from recent geological and geophysical investigations. *Tectonophysics* 360, 5–21.
- Žák, J., Paterson, S.R., Memeti, V., 2007. Four magmatic fabrics in the Tuolumne batholith, central Sierra Nevada, California (USA): implications for interpreting fabric patterns in plutons and evolution of magma chambers in the upper crust. *Geological Society of America Bulletin* 119, 184–201.
- Žák, J., Verner, K., Finger, F., Faryad, S.W., Chlupáčová, M., Veselovský, F., 2011. The generation of voluminous S-type granites in the Moldanubian unit, Bohemian Massif, by rapid isothermal exhumation of the metapelitic middle crust. *Lithos* 121, 25–40.
- Žák, J., Verner, K., Janoušek, V., Holub, F.V., Kachlík, V., Finger, F., Hajná, J., Tomek, F., Vondrovic, L., Trubač, J., in press. A plate-kinematic model for the assembly of the Bohemian Massif constrained by structural relationships around granitoid plutons. In: Schulmann, K., Martínez Catalán, J.R., Lardeaux, J.M., Janoušek, V., Oggiano, G. (Eds.), *The Variscan Orogeny: Extent, Timescale and the Formation of the European Crust*. Geological Society, London, Special Publications 405, doi: 10.1144/SP405.9.
- Zapletal, K., 1990. Low-field susceptibility anisotropy of some biotite crystals. *Physics of the Earth and Planetary Interiors* 63, 85–97.

ELECTRONIC APPENDICES

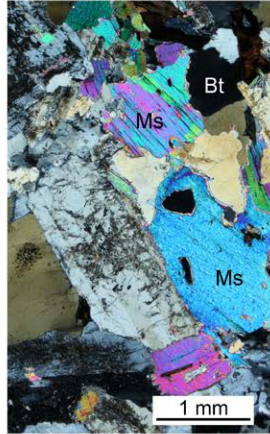
Representative textures and microstructures of the Melechov pluton granites Unoriented samples, AMS carriers (micas) emphasized, Ms muscovite, Bt biotite

Koutý granite

sample JZ155 (WGS84 coordinates N49.645868°; E15.279732°)



Scanned polished slab



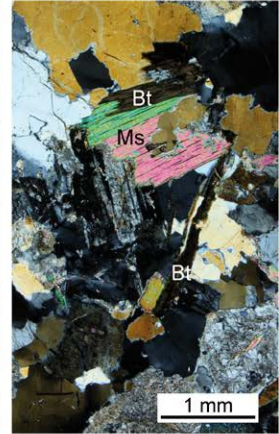
Micrograph, crossed polars

Melechov granite

sample JZ164 (WGS84 coordinates N49.640515°; E15.319368°)



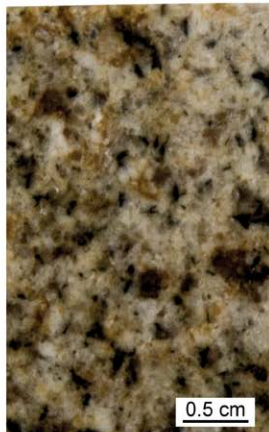
Scanned polished slab



Micrograph, crossed polars

Stvořidla granite

sample JZ163 (WGS84 coordinates N49.666143°; E15.332862°)



Scanned polished slab



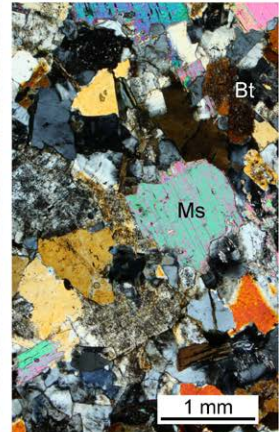
Micrograph, crossed polars

Lipnice granite

sample JZ158 (WGS84 coordinates N49.620500°; E15.410643°)



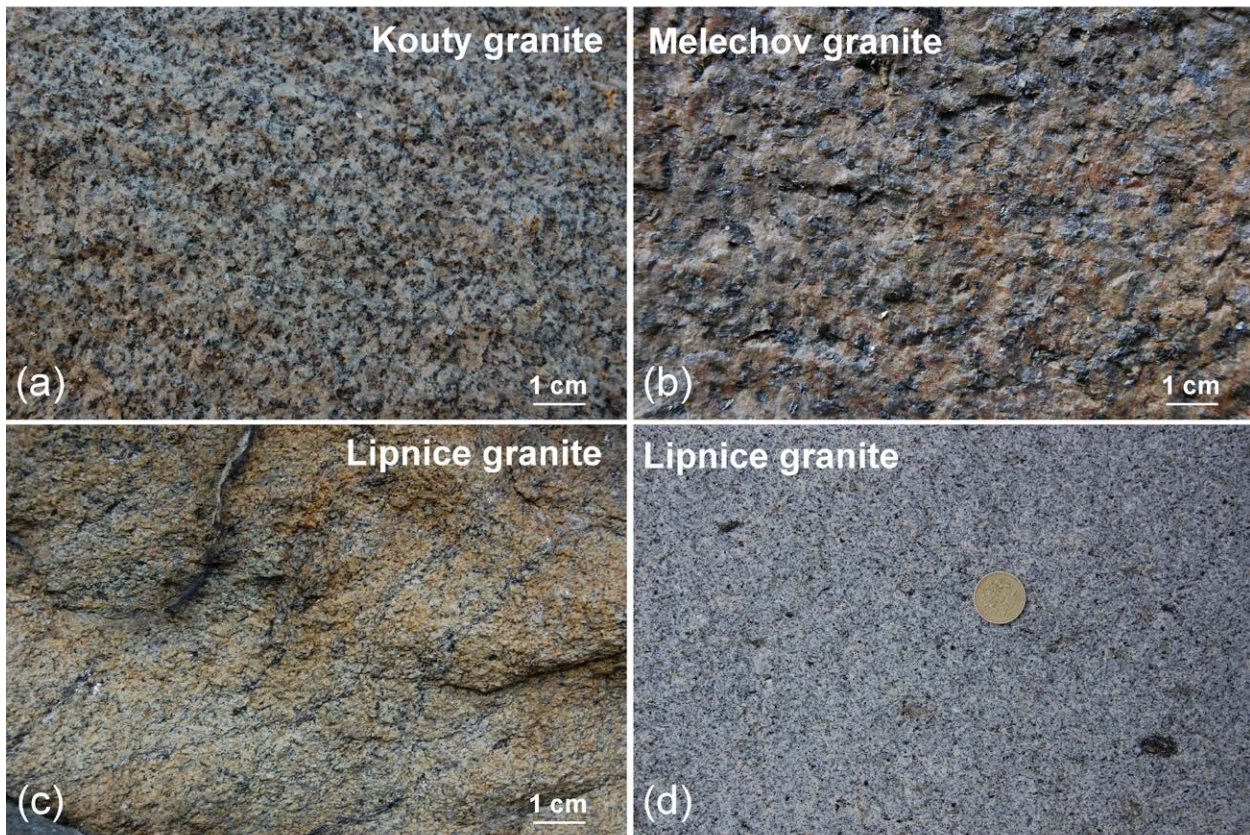
Scanned polished slab



Micrograph, crossed polars

Electronic Supplementary Material, Part 2

Field photographs of the main granite units in the Melechov pluton



- (a) Active quarry near Dolní Březinka (WGS84 coordinates: 49°40'6.589''N; 15°22'33.535''E)
(b) Road cut near Leštinka (WGS84 coordinates: 49°41'4.747''N; 15°19'43.493''E)
(c) Outcrop below castle, Lipnice (WGS84 coordinates: 49°36'51.862''N; 15°24'42.626''E)
(d) Active quarry in Dolní Město (WGS84 coordinates: 49°37'34.749''N; 15°23'42.871''E),
coin diameter is 2.2 cm

Electronic Supplementary Material. Part 3
List of the AMS data

Station	Latitude - WGS84. North (°)	Longitude - WGS84. East (°)	Lithologic unit	Specimen	Km	L	F	P	Pj	T	U	K1 trend	K1 plunge	K2 trend	K2 plunge	K3 trend	K3 plunge	
JZ155	49.646	15.280	Kouty granite	JZ155/1/1	0.000	1.01	1.01	1.02	1.02	1.02	-0.04	-0.05	33	5	129	54	309	36
				JZ155/1/2	0.000	1.06	1.13	1.20	1.20	1.20	0.37	0.33	171	82	297	5	117	85
				JZ155/1/3	0.000	1.01	1.03	1.05	1.05	1.05	0.43	0.42	7	14	100	13	280	77
				JZ155/1/4	0.000	1.02	1.02	1.03	1.03	1.03	0.02	0.01	18	6	121	62	301	28
				JZ155/1/5	0.000	1.01	1.02	1.03	1.03	1.03	0.54	0.54	263	21	99	68	279	22
				JZ155/1/6	0.000	1.00	1.02	1.02	1.02	1.02	0.66	0.65	191	6	81	74	261	16
				JZ155/1/7	0.000	1.02	1.04	1.06	1.06	1.06	0.33	0.32	265	8	126	79	306	11
				JZ155/1/8	0.000	1.01	1.00	1.02	1.02	1.02	-0.60	-0.61	211	13	112	33	292	57
				JZ155/2/1	0.000	1.01	1.05	1.07	1.07	1.07	0.63	0.62	196	47	102	4	282	86
				JZ155/2/2	0.000	1.01	1.07	1.08	1.09	1.09	0.76	0.75	194	61	284	0	104	90
				JZ155/2/3	0.000	1.02	1.05	1.07	1.07	1.07	0.48	0.47	193	26	286	5	106	85
				JZ155/2/4	0.000	1.01	1.09	1.11	1.12	1.12	0.75	0.74	190	27	282	4	102	86
				JZ155/2/5	0.000	1.01	1.02	1.03	1.03	1.03	0.63	0.62	176	2	80	71	260	19
				JZ155/2/6	0.000	1.01	1.02	1.02	1.02	1.02	0.32	0.32	204	17	84	60	264	30
				JZ155/2/7	0.000	1.01	1.01	1.02	1.02	1.02	0.22	0.21	213	26	97	41	277	49
JZ156	49.635	15.294	Kouty granite	JZ156/1/1	0.000	1.02	1.03	1.04	1.04	1.04	0.26	0.25	240	54	352	15	172	75
				JZ156/1/2	0.000	1.01	1.03	1.04	1.04	1.04	0.29	0.28	227	61	357	20	177	70
				JZ156/1/3	0.000	1.12	1.02	1.14	1.15	1.15	-0.70	-0.72	70	11	327	49	147	41
				JZ156/1/4	0.000	1.02	1.03	1.05	1.05	1.05	0.23	0.22	249	24	343	8	163	82
				JZ156/1/5	0.000	1.01	1.03	1.04	1.04	1.04	0.55	0.54	238	14	339	35	159	55
				JZ156/1/7	0.000	1.01	1.02	1.04	1.04	1.04	0.26	0.25	237	30	350	34	170	56
				JZ156/2/1	0.000	1.02	1.02	1.04	1.04	1.04	0.12	0.11	223	52	345	23	165	67
				JZ156/2/2	0.000	1.02	1.02	1.03	1.03	1.03	-0.04	-0.05	244	53	357	16	177	74
				JZ156/2/3	0.000	1.01	1.02	1.04	1.04	1.04	0.25	0.24	236	37	353	31	173	59
				JZ156/2/4	0.000	1.01	1.02	1.03	1.03	1.03	0.36	0.35	233	53	351	20	171	70

Station	Latitude - WGS84, North (°)	Longitude - WGS84, East (°)	Lithologic unit	Specimen	Km	L	F	P	Pj	T	U	K1 trend	K1 plunge	K2 trend	K2 plunge	K3 trend	K3 plunge
JZ157	49.639	15.362	Kouty granite	JZ156/2/5	0.000	1.00	1.03	1.04	1.04	0.80	0.79	209	56	344	26	164	64
				JZ156/2/6	0.000	1.01	1.02	1.04	1.04	0.33	0.32	232	64	357	16	177	74
				JZ156/2/7	0.000	1.01	1.03	1.04	1.04	0.54	0.54	232	38	352	33	172	57
				JZ157/1/1	0.000	1.05	1.07	1.12	1.12	0.19	0.16	79	3	347	38	167	52
				JZ157/1/2	0.000	1.03	1.08	1.11	1.11	0.44	0.42	248	8	344	38	164	52
				JZ157/1/3	0.000	1.02	1.11	1.13	1.14	0.70	0.69	136	17	17	57	197	33
				JZ157/1/4	0.000	1.02	1.09	1.11	1.12	0.60	0.59	169	6	269	61	89	29
				JZ157/1/5	0.000	1.01	1.06	1.08	1.08	0.63	0.62	185	4	286	69	106	21
				JZ157/1/6	0.000	1.01	1.07	1.08	1.08	0.66	0.65	207	6	325	78	145	12
				JZ157/1/7	0.000	1.01	1.07	1.09	1.09	0.69	0.68	187	3	288	72	108	18
				JZ157/2/1	0.000	1.03	1.04	1.07	1.07	0.20	0.18	241	0	331	40	151	50
				JZ157/2/2	0.000	1.01	1.07	1.08	1.09	0.70	0.69	187	11	305	68	125	22
				JZ157/2/3	0.000	1.01	1.07	1.08	1.08	0.77	0.76	197	10	306	63	126	27
				JZ157/2/4	0.000	1.07	1.12	1.20	1.20	0.24	0.20	219	14	118	37	298	53
				JZ157/2/5	0.000	1.00	1.06	1.07	1.08	0.88	0.87	176	24	328	63	148	27
JZ158	49.621	15.411	Lipnice granite	JZ158/1/1	0.000	1.02	1.09	1.12	1.12	0.57	0.55	281	81	127	8	307	82
				JZ158/1/2	0.000	1.05	1.11	1.17	1.17	0.39	0.36	226	5	136	6	316	84
				JZ158/1/3	0.000	1.03	1.08	1.11	1.12	0.41	0.38	219	12	125	15	305	75
				JZ158/1/4	0.000	1.04	1.06	1.10	1.10	0.25	0.23	215	10	122	18	302	72
				JZ158/1/5	0.000	1.03	1.06	1.09	1.10	0.37	0.35	216	13	121	21	301	69
				JZ158/1/6	0.000	1.03	1.05	1.09	1.09	0.21	0.19	218	15	125	12	305	78
				JZ158/2/1	0.000	1.01	1.06	1.07	1.08	0.71	0.70	51	22	313	19	133	71
				JZ158/2/2	0.000	1.04	1.16	1.21	1.22	0.57	0.54	75	69	340	2	160	88
				JZ158/2/3	0.000	1.04	1.07	1.11	1.11	0.35	0.33	50	4	318	16	138	74
				JZ158/2/4	0.000	1.04	1.07	1.11	1.11	0.23	0.21	49	7	317	15	137	75
				JZ158/2/5	0.000	1.05	1.06	1.11	1.11	0.14	0.11	52	8	320	14	140	76
				JZ158/2/6	0.000	1.03	1.07	1.10	1.10	0.37	0.35	50	11	317	15	137	75
				JZ158/2/7	0.000	1.02	1.07	1.10	1.10	0.50	0.49	49	12	317	10	137	80

Internal structure and formation mechanisms of zoned plutons at shallow crustal levels

Station	Latitude - WGS84, North (°)	Longitude - WGS84, East (°)	Lithologic unit	Specimen	Km	L	F	P	Pj	T	U	K1 trend	K1 plunge	K2 trend	K2 plunge	K3 trend	K3 plunge				
JZ159	49.668	15.376	Kouty granite	JZ159/1/1	0.000	1.05	1.37	1.43	1.48	0.74	0.70	6	37	201	52	21	38				
				JZ159/1/2	0.000	1.03	1.10	1.13	1.14	0.60	0.58	285	38	157	39	337	51				
				JZ159/1/3	0.000	1.02	1.04	1.06	1.06	0.26	0.25	83	41	235	45	55	45				
				JZ159/1/4	0.000	1.03	1.03	1.05	1.05	0.01	-0.00	274	20	14	25	194	65				
				JZ159/1/5	0.000	1.02	1.02	1.04	1.04	-0.03	-0.04	282	30	178	22	358	68				
				JZ159/1/6	0.000	1.03	1.01	1.04	1.04	-0.37	-0.38	268	35	172	8	352	82				
				JZ159/1/7	0.000	1.02	1.02	1.04	1.04	-0.08	-0.09	269	29	168	19	348	71				
				JZ159/1/8	0.000	1.01	1.05	1.05	1.06	0.75	0.75	272	24	166	32	346	58				
				JZ159/2/1	0.000	1.02	1.01	1.03	1.03	-0.48	-0.48	292	10	201	3	21	87				
				JZ159/2/2	0.000	1.02	1.03	1.04	1.04	0.28	0.27	9	76	142	10	322	80				
				JZ159/2/3	0.000	1.07	1.13	1.21	1.21	0.25	0.20	20	64	123	6	303	84				
				JZ159/2/4	0.000	1.03	1.03	1.06	1.06	0.05	0.03	281	34	177	20	357	71				
				JZ159/2/5	0.000	1.02	1.03	1.05	1.05	0.34	0.33	282	33	174	26	354	64				
				JZ159/2/6	0.000	1.01	1.04	1.05	1.06	0.54	0.53	301	41	174	35	354	55				
				JZ159/2/7	0.000	1.02	1.03	1.05	1.05	0.40	0.38	294	37	181	28	1	62				
				JZ159/2/8	0.000	1.02	1.03	1.05	1.05	0.36	0.35	295	43	169	33	349	57				
JZ160	49.628	15.410	Lipnice granite	JZ160/1/1	0.000	1.02	1.05	1.07	1.07	0.55	0.54	283	79	106	11	286	79				
				JZ160/1/2	0.000	1.01	1.07	1.08	1.09	0.71	0.70	183	9	92	7	272	83				
				JZ160/1/3	0.000	1.04	1.04	1.08	1.08	0.08	0.06	359	64	265	2	85	88				
				JZ160/1/4	0.000	1.04	1.05	1.09	1.09	0.09	0.07	45	50	193	36	13	54				
				JZ160/1/5	0.000	1.02	1.04	1.06	1.07	0.32	0.30	32	25	127	12	307	78				
				JZ160/2/1	0.000	1.01	1.06	1.07	1.07	0.69	0.68	40	6	132	16	312	75				
				JZ160/2/2	0.000	1.02	1.06	1.09	1.09	0.46	0.44	24	4	115	11	295	80				
				JZ160/2/4	0.000	1.02	1.04	1.07	1.07	0.27	0.26	31	9	121	0	301	90				
				JZ160/2/5	0.000	1.02	1.05	1.07	1.07	0.44	0.42	34	10	304	1	124	89				
				JZ160/2/6	0.000	1.03	1.03	1.07	1.07	0.02	0.01	32	2	301	12	121	78				
				JZ160/2/7	0.000	1.03	1.04	1.06	1.06	0.17	0.16	33	5	303	1	123	89				
				JZ160/2/8	0.000	1.02	1.04	1.07	1.07	0.35	0.33	32	3	302	0	122	90				
				JZ161	49.630	15.412	Lipnice granite	JZ161/1/1	0.000	1.03	1.04	1.07	1.07	0.23	0.22	201	23	100	24	280	66

Internal structure and formation mechanisms of zoned plutons at shallow crustal levels

Station	Latitude - WGS84, North (°)	Longitude - WGS84, East (°)	Lithologic unit	Specimen	Km	L	F	P	Pj	T	U	K1 trend	K1 plunge	K2 trend	K2 plunge	K3 trend	K3 plunge				
JZ162	49.614	15.320	Lipnice granite	JZ161/1/2	0.000	1.03	1.03	1.06	1.06	1.06	0.08	0.06	213	30	106	27	286	63			
				JZ161/1/3	0.000	1.02	1.04	1.06	1.06	1.06	0.24	0.23	207	26	97	35	277	55			
				JZ161/1/4	0.000	1.02	1.04	1.06	1.06	0.44	0.43	197	22	99	19	279	71				
				JZ161/1/5	0.000	1.03	1.04	1.07	1.07	0.11	0.10	203	17	104	26	284	64				
				JZ161/1/6	0.000	1.03	1.03	1.06	1.06	-0.04	-0.06	199	14	104	17	284	73				
				JZ161/2/1	0.000	1.02	1.04	1.05	1.05	0.37	0.36	207	23	100	35	280	55				
				JZ161/2/2	0.000	1.05	1.03	1.08	1.08	-0.26	-0.28	248	40	141	19	321	71				
				JZ161/2/3	0.000	1.03	1.04	1.07	1.07	0.13	0.11	206	8	108	48	288	42				
				JZ161/2/4	0.000	1.03	1.04	1.07	1.07	0.11	0.09	207	14	109	26	289	64				
				JZ161/2/5	0.000	1.02	1.04	1.06	1.06	0.26	0.25	208	26	108	19	288	71				
				JZ161/2/6	0.000	1.03	1.04	1.07	1.07	0.15	0.13	206	19	106	26	286	64				
				JZ163	49.666	15.333	Stvořidla granite	JZ162/1/1	0.000	1.02	1.05	1.07	1.07	0.47	0.46	95	31	353	19	173	71
								JZ162/1/2	0.000	1.02	1.06	1.09	1.09	0.50	0.48	103	38	352	25	172	65
								JZ162/1/3	0.000	1.03	1.03	1.06	1.06	0.01	-0.00	102	31	2	15	182	75
								JZ162/1/4	0.000	1.03	1.02	1.05	1.05	-0.20	-0.21	103	32	5	13	185	77
								JZ162/1/6	0.000	1.03	1.04	1.06	1.06	0.12	0.10	101	29	3	15	183	75
JZ162/1/7	0.000	1.04	1.03					1.06	1.06	-0.18	-0.19	103	24	7	13	187	77				
JZ162/2/1	0.000	1.04	1.05					1.10	1.10	0.09	0.07	102	40	351	24	171	66				
JZ162/2/2	0.000	1.05	1.01					1.06	1.06	-0.67	-0.68	99	21	358	27	178	63				
JZ162/2/3	0.000	1.04	1.01					1.05	1.06	-0.51	-0.52	102	28	0	20	180	70				
JZ162/2/4	0.000	1.05	1.01					1.06	1.06	-0.60	-0.61	99	28	360	16	180	74				
JZ162/2/5	0.000	1.03	1.02					1.06	1.06	-0.12	-0.14	102	26	350	38	170	52				
JZ163/1/1	0.000	1.15	1.05					1.21	1.22	-0.46	-0.50	85	68	269	22	89	68				
JZ163/1/2	0.000	1.02	1.06					1.07	1.08	0.54	0.53	94	16	342	54	162	37				
JZ163/1/3	0.000	1.03	1.26					1.29	1.32	0.78	0.76	166	60	289	18	109	72				
JZ163/1/4	0.000	1.05	1.21					1.27	1.29	0.60	0.57	237	1	327	8	147	82				
JZ163/1/5	0.000	1.02	1.04					1.06	1.06	0.25	0.23	270	3	6	70	186	20				
JZ163/2/1	0.000	1.04	1.08	1.12	1.12	0.29	0.26	251	1	341	7	161	83								
JZ163/2/2	0.000	1.08	4.74	5.10	6.30	0.91	0.83	202	29	297	9	117	81								

Internal structure and formation mechanisms of zoned plutons at shallow crustal levels

Station	Latitude - WGS84, North (°)	Longitude - WGS84, East (°)	Lithologic unit	Specimen	Km	L	F	P	Pj	T	U	K1 trend	K1 plunge	K2 trend	K2 plunge	K3 trend	K3 plunge
JZ164	49.641	15.319	Melechov granite	JZ163/2/3	0.000	1.07	1.15	1.22	1.23	0.35	0.30	61	0	151	4	331	86
				JZ163/2/4	0.000	1.02	1.04	1.06	1.06	0.37	0.35	112	15	351	62	171	28
				JZ163/2/5	0.000	1.01	1.06	1.07	1.08	0.70	0.69	98	2	6	55	186	35
				JZ163/3/1	0.000	1.05	1.13	1.18	1.19	0.47	0.43	80	72	205	11	25	79
				JZ163/3/2	0.000	1.03	1.32	1.36	1.41	0.81	0.78	194	27	288	8	108	82
				JZ163/3/3	0.000	1.04	1.10	1.15	1.15	0.36	0.33	218	22	313	13	133	77
				JZ163/3/4	0.000	1.02	1.04	1.07	1.07	0.27	0.26	97	5	356	66	176	24
				JZ163/3/5	0.000	1.01	1.07	1.08	1.08	0.84	0.83	85	13	325	66	145	24
				JZ163/3/6	0.000	1.01	1.07	1.09	1.09	0.73	0.72	167	26	346	64	166	26
				JZ163/3/7	0.000	1.02	1.06	1.09	1.09	0.45	0.43	202	13	328	69	148	22
				JZ164/1/1	0.000	1.03	1.01	1.04	1.04	-0.35	-0.36	358	26	96	16	276	74
				JZ164/1/2	0.000	1.06	1.00	1.06	1.07	-0.86	-0.87	330	29	70	17	250	73
				JZ164/1/3	0.000	1.03	1.01	1.04	1.04	-0.52	-0.53	339	25	96	44	276	46
				JZ164/1/4	0.000	1.01	1.07	1.07	1.08	0.85	0.85	264	39	107	49	287	41
JZ164/1/5	0.000	1.05	1.02	1.08	1.08	-0.37	-0.39	339	16	77	28	257	62				
JZ164/1/6	0.000	1.01	1.06	1.07	1.08	0.79	0.79	326	29	104	53	284	37				
JZ164/1/7	0.000	1.03	1.06	1.09	1.09	0.31	0.29	8	16	158	72	338	18				
JZ164/2/1	0.000	1.03	1.03	1.07	1.07	0.03	0.02	279	41	84	48	264	42				
JZ164/2/2	0.000	1.00	1.06	1.07	1.08	0.93	0.93	188	19	79	44	259	46				
JZ164/2/3	0.000	1.03	1.02	1.06	1.06	-0.18	-0.20	352	29	131	54	311	36				
JZ164/2/4	0.000	1.03	1.01	1.04	1.04	-0.60	-0.60	256	46	115	37	295	53				
JZ164/2/5	0.000	1.03	1.07	1.10	1.10	0.43	0.41	250	47	93	40	273	50				
JZ164/2/6	0.000	1.02	1.07	1.09	1.10	0.55	0.54	289	40	79	46	259	44				
JZ164/2/7	0.000	1.02	1.07	1.09	1.10	0.56	0.55	204	19	91	49	271	41				
JZ164/2/8	0.000	1.04	1.01	1.05	1.05	-0.61	-0.61	170	1	263	56	83	35				
JZ165	49.638	15.262	Kouty granite	JZ165/1/1	0.000	1.01	1.07	1.08	1.09	0.71	0.70	190	30	80	32	260	58
				JZ165/1/2	0.000	1.02	1.08	1.10	1.10	0.64	0.62	201	42	83	27	263	63
				JZ165/1/3	0.000	1.02	1.03	1.05	1.05	0.25	0.23	196	33	86	27	266	63
				JZ165/1/4	0.000	1.02	1.06	1.07	1.08	0.50	0.49	195	38	79	29	259	61

Internal structure and formation mechanisms of zoned plutons at shallow crustal levels

Station	Latitude - WGS84. North (°)	Longitude - WGS84. East (°)	Lithologic unit	Specimen	Km	L	F	P	Pj	T	U	K1 trend	K1 plunge	K2 trend	K2 plunge	K3 trend	K3 plunge
JZ166	49.647	15.270	Kouty granite	JZ166/1/5	0.000	1.02	1.03	1.05	1.05	0.30	0.29	201	42	82	28	262	62
				JZ166/2/1	0.000	1.02	1.05	1.07	1.07	0.41	0.40	214	51	79	30	259	60
				JZ166/2/2	0.000	1.02	1.06	1.09	1.09	0.45	0.43	214	50	87	27	267	63
				JZ166/2/3	0.000	1.02	1.05	1.07	1.07	0.41	0.40	215	55	79	26	259	64
				JZ166/2/4	0.000	1.03	1.05	1.08	1.08	0.33	0.31	207	51	81	26	261	64
				JZ166/2/5	0.000	1.02	1.04	1.06	1.06	0.40	0.39	208	47	82	29	262	61
				JZ166/2/7	0.000	1.01	1.04	1.06	1.06	0.52	0.51	210	51	81	27	261	63
				JZ166/1/1	0.000	1.02	1.03	1.05	1.05	0.30	0.29	206	9	76	76	256	14
				JZ166/1/2	0.000	1.02	1.04	1.06	1.06	0.32	0.31	209	10	75	76	255	14
				JZ166/1/3	0.000	1.01	1.06	1.07	1.08	0.60	0.59	219	12	86	73	266	17
				JZ166/1/4	0.000	1.02	1.04	1.07	1.07	0.29	0.27	208	5	94	78	274	12
				JZ166/1/5	0.000	1.03	1.06	1.09	1.09	0.31	0.29	221	12	92	72	272	18
				JZ166/1/6	0.000	1.01	1.04	1.05	1.06	0.51	0.50	217	12	66	77	246	13
				JZ166/2/1	0.000	1.01	1.05	1.06	1.06	0.59	0.58	218	10	55	79	235	11
JZ166/2/2	0.000	1.02	1.04	1.06	1.06	0.42	0.40	207	10	45	80	225	10				
JZ166/2/3	0.000	1.02	1.05	1.06	1.07	0.44	0.43	206	11	41	79	221	11				
JZ166/2/4	0.000	1.01	1.05	1.07	1.07	0.58	0.57	206	8	71	79	251	11				
JZ166/2/5	0.000	1.02	1.06	1.08	1.09	0.54	0.52	227	12	94	74	274	17				
JZ166/2/6	0.000	1.02	1.07	1.09	1.10	0.51	0.50	215	4	111	73	291	17				
JZ167	49.649	15.296	Kouty granite	JZ167/1/1	0.000	1.02	1.01	1.03	1.03	-0.11	-0.12	249	44	94	43	274	47
				JZ167/1/2	0.000	1.02	1.02	1.04	1.04	0.10	0.09	212	38	119	4	299	86
				JZ167/1/3	0.000	1.02	1.02	1.04	1.04	-0.10	-0.11	253	44	106	41	286	49
				JZ167/2/1	0.000	1.02	1.02	1.04	1.04	0.03	0.02	248	50	109	33	289	58
				JZ167/2/2	0.000	1.01	1.03	1.05	1.05	0.40	0.39	268	52	111	36	291	55
				JZ167/2/3	0.000	1.01	1.01	1.02	1.02	-0.03	-0.03	244	43	103	40	283	50
				JZ167/3/1	0.000	1.02	1.02	1.03	1.03	0.02	0.02	245	35	112	45	292	45
				JZ167/3/2	0.000	1.02	1.02	1.04	1.04	-0.04	-0.05	0	40	109	21	289	69
				JZ167/3/3	0.000	1.02	1.02	1.04	1.04	0.13	0.12	237	41	117	30	297	60
				JZ167/3/4	0.000	1.02	1.03	1.05	1.05	0.31	0.30	237	28	114	45	294	45

Internal structure and formation mechanisms of zoned plutons at shallow crustal levels

Station	Latitude - WGS84, North (°)	Longitude - WGS84, East (°)	Lithologic unit	Specimen	Km	L	F	P	Pj	T	U	K1 trend	K1 plunge	K2 trend	K2 plunge	K3 trend	K3 plunge	
JZ168	49.634	15.316	Melekov granite	JZ167/3/5	0.000	1.02	1.02	1.04	1.04	1.04	-0.06	-0.07	244	42	118	33	298	57
				JZ168/1/1	0.000	1.04	1.01	1.05	1.05	1.05	-0.68	-0.68	196	27	295	18	115	72
				JZ168/1/2	0.000	1.03	1.01	1.04	1.05	1.05	-0.41	-0.42	204	36	79	39	259	52
				JZ168/1/3	0.000	1.03	1.05	1.08	1.08	1.08	0.26	0.24	356	26	96	21	276	69
				JZ168/1/4	0.000	1.05	1.12	1.17	1.18	1.18	0.37	0.34	182	6	90	16	270	75
				JZ168/1/5	0.000	1.03	1.05	1.09	1.09	1.09	0.23	0.21	186	22	84	28	264	62
				JZ168/1/6	0.000	1.04	1.04	1.08	1.08	1.08	0.02	-0.00	339	7	75	39	255	51
				JZ168/2/1	0.000	1.01	1.09	1.10	1.11	1.11	0.83	0.82	331	1	62	41	242	49
				JZ168/2/2	0.000	1.03	1.05	1.08	1.08	1.08	0.19	0.17	351	2	85	65	265	25
				JZ168/2/3	0.000	1.00	1.05	1.05	1.06	1.06	0.90	0.90	319	51	94	30	274	60
JZ169	49.631	15.317	Melekov granite	JZ169/1/1	0.000	1.03	1.03	1.06	1.06	1.06	-0.05	-0.07	254	2	345	28	165	62
				JZ169/1/2	0.000	1.02	1.05	1.07	1.07	1.07	0.51	0.50	180	48	313	32	133	58
				JZ169/1/3	0.000	1.04	1.04	1.08	1.08	1.08	0.05	0.03	172	31	66	25	246	65
				JZ169/1/4	0.000	1.05	1.01	1.06	1.06	1.06	-0.71	-0.72	238	39	127	25	307	66
				JZ169/1/5	0.000	1.06	1.01	1.06	1.07	1.07	-0.73	-0.74	223	41	119	15	299	75
				JZ169/1/6	0.000	1.06	1.05	1.11	1.11	1.11	-0.10	-0.13	217	36	341	38	161	52
				JZ169/1/7	0.000	1.02	1.02	1.04	1.04	1.04	-0.14	-0.14	229	18	328	25	148	65
				JZ169/2/1	0.000	1.01	1.05	1.06	1.06	1.06	0.74	0.73	102	1	8	74	188	16
JZ170	49.618	15.318	Melekov granite	JZ170/1/1	0.000	1.04	1.02	1.05	1.05	1.05	-0.41	-0.42	257	34	1	20	181	70
				JZ170/1/2	0.000	1.07	1.02	1.09	1.09	1.09	-0.54	-0.56	239	26	336	15	156	75
				JZ170/1/3	0.000	1.05	1.02	1.07	1.07	1.07	-0.53	-0.54	273	52	53	31	233	59
				JZ169/2/2	0.000	1.03	1.05	1.08	1.08	1.08	0.25	0.23	286	34	25	13	205	77
				JZ169/2/3	0.000	1.01	1.06	1.07	1.08	1.08	0.71	0.70	191	59	339	27	159	63
JZ169/2/4	0.000	1.02	1.02	1.04	1.04	1.04	0.12	0.11	306	58	40	3	220	87				
JZ169/2/5	0.000	1.05	1.03	1.08	1.08	1.08	-0.30	-0.31	222	41	349	35	169	55				

Station	Latitude - WGS84, North (°)	Longitude - WGS84, East (°)	Lithologic unit	Specimen	Km	L	F	P	Pj	T	U	K1 trend	K1 plunge	K2 trend	K2 plunge	K3 trend	K3 plunge			
JZ171	49.612	15.348	Lipnice granite	JZ170/1/4	0.000	1.03	1.02	1.05	1.05	1.05	-0.32	256	40	165	1	345	89			
				JZ170/1/5	0.000	1.02	1.03	1.05	1.05	1.05	0.09	247	54	37	32	217	58			
				JZ170/1/6	0.000	1.03	1.01	1.04	1.04	-0.42	249	47	345	5	165	85				
				JZ170/2/1	0.000	1.01	1.03	1.04	1.04	0.51	231	26	22	61	202	29				
				JZ170/2/2	0.000	1.02	1.01	1.03	1.03	-0.35	243	7	9	78	189	12				
				JZ170/2/3	0.000	1.04	1.01	1.05	1.05	-0.60	221	34	359	48	179	42				
				JZ170/2/4	0.000	1.02	1.04	1.06	1.06	0.35	153	0	62	55	242	35				
				JZ170/3/1	0.000	1.02	1.03	1.05	1.05	0.29	285	36	35	25	215	65				
				JZ170/3/2	0.000	1.02	1.04	1.06	1.06	0.38	261	49	42	34	222	56				
				JZ170/3/3	0.000	1.01	1.07	1.08	1.09	0.67	271	38	77	51	257	39				
				JZ171	49.612	15.348	Lipnice granite	JZ171/1/1	0.000	1.04	1.05	1.09	1.09	0.11	89	31	356	5	176	85
								JZ171/1/2	0.000	1.03	1.06	1.09	1.09	0.39	95	43	353	13	173	77
								JZ171/1/3	0.000	1.01	1.05	1.06	1.07	0.69	159	50	355	39	175	51
				JZ171/1/4	0.000	1.04	1.06	1.09	1.09	0.21	92	36	353	12	173	78				
				JZ171/1/5	0.000	1.03	1.06	1.09	1.09	0.30	89	40	348	13	168	77				
				JZ171/1/6	0.000	1.03	1.06	1.09	1.09	0.38	91	35	352	13	172	78				
				JZ171/2/1	0.000	1.02	1.08	1.10	1.11	0.62	92	41	349	14	169	76				
				JZ171/2/2	0.000	1.03	1.07	1.10	1.11	0.45	90	42	352	9	172	81				
				JZ171/2/3	0.000	1.03	1.07	1.10	1.10	0.39	94	45	350	13	170	77				
				JZ171/2/4	0.000	1.03	1.07	1.10	1.10	0.47	97	43	354	14	174	76				
				JZ171/2/5	0.000	1.03	1.06	1.09	1.09	0.41	91	35	355	9	175	82				
				JZ171/2/6	0.000	1.03	1.06	1.09	1.09	0.34	89	41	356	4	176	86				
				JZ171/2/7	0.000	1.03	1.07	1.09	1.10	0.41	93	43	353	11	173	79				
JZ172	49.661	15.320	Melechov granite	JZ172/1/1	0.000	1.03	1.04	1.07	1.07	0.23	269	51	20	200	16	200	74			
				JZ172/1/2	0.000	1.02	1.05	1.06	1.06	0.45	294	7	204	0	24	90				
				JZ172/1/3	0.000	1.03	1.02	1.05	1.05	-0.31	238	73	353	8	173	83				
				JZ172/1/4	0.000	1.02	1.05	1.07	1.07	0.33	97	23	360	17	180	73				
				JZ172/1/5	0.000	1.03	1.02	1.05	1.05	-0.37	12	49	273	8	93	83				
				JZ172/1/6	0.000	1.02	1.02	1.04	1.04	-0.01	284	48	29	14	209	76				

Internal structure and formation mechanisms of zoned plutons at shallow crustal levels

Station	Latitude - WGS84, North (°)	Longitude - WGS84, East (°)	Lithologic unit	Specimen	Km	L	F	P	Pj	T	U	K1 trend	K1 plunge	K2 trend	K2 plunge	K3 trend	K3 plunge
JZ173	49.669	15.307	Kouty granite	JZ172/2/1	0.000	1.04	1.06	1.10	1.10	0.22	0.20	330	41	93	32	273	58
				JZ172/2/2	0.000	1.02	1.03	1.05	1.05	0.24	0.23	328	63	157	27	337	63
				JZ172/2/3	0.000	1.02	1.04	1.06	1.06	0.24	0.23	324	65	71	8	251	82
				JZ172/3/1	0.000	1.03	1.03	1.06	1.06	-0.09	-0.11	296	37	65	40	245	50
				JZ172/3/2	0.000	1.04	1.03	1.07	1.07	-0.19	-0.21	287	61	30	7	210	83
				JZ172/3/3	0.000	1.03	1.05	1.08	1.08	0.30	0.28	259	24	20	49	200	41
JZ174	49.643	15.353	Kouty granite	JZ173/1/1	0.000	1.02	1.01	1.03	1.03	-0.20	-0.21	159	42	61	9	241	81
				JZ173/1/2	0.000	1.02	1.06	1.08	1.08	0.40	0.38	144	23	36	37	216	53
				JZ173/1/3	0.000	1.02	1.02	1.04	1.04	0.05	0.04	163	39	50	26	230	64
				JZ173/1/4	0.000	1.02	1.02	1.04	1.04	0.07	0.06	162	38	49	27	229	63
				JZ173/1/5	0.000	1.03	1.02	1.05	1.05	-0.09	-0.11	152	35	31	36	211	54
				JZ173/1/6	0.000	1.01	1.03	1.04	1.05	0.47	0.46	175	55	51	21	231	69
				JZ173/1/7	0.000	1.02	1.02	1.04	1.04	-0.21	-0.22	150	35	49	15	229	75
				JZ173/1/8	0.000	1.02	1.02	1.03	1.03	0.05	0.04	163	40	56	19	236	71
				JZ173/2/1	0.000	1.01	1.01	1.02	1.02	-0.30	-0.30	174	51	68	13	248	77
				JZ173/2/2	0.000	1.01	1.01	1.02	1.02	0.35	0.34	218	80	58	10	238	80
				JZ173/2/3	0.000	1.04	1.02	1.06	1.06	-0.20	-0.21	181	41	44	40	224	50
				JZ173/2/4	0.000	1.02	1.01	1.03	1.03	-0.27	-0.28	158	30	61	13	241	77
				JZ173/2/5	0.000	1.02	1.02	1.04	1.04	0.13	0.12	181	47	50	31	230	59
				JZ173/2/6	0.000	1.02	1.01	1.03	1.03	-0.11	-0.12	166	45	58	18	238	72
JZ173/2/7	0.000	1.01	1.02	1.03	1.03	0.21	0.21	162	49	54	15	234	75				
JZ173/2/8	0.000	1.01	1.02	1.04	1.04	0.34	0.34	155	26	63	6	243	85				
JZ174	49.643	15.353	Kouty granite	JZ174/1/1	0.000	1.02	1.01	1.03	1.03	-0.68	-0.69	339	13	130	75	310	15
				JZ174/1/2	0.000	1.03	1.02	1.05	1.05	-0.26	-0.27	341	13	127	74	307	16
				JZ174/1/3	0.000	1.04	1.01	1.05	1.05	-0.53	-0.54	354	13	247	51	67	39
				JZ174/1/4	0.000	1.03	1.01	1.04	1.05	-0.50	-0.51	342	7	150	83	330	7
				JZ174/1/5	0.000	1.03	1.01	1.04	1.05	-0.37	-0.38	341	7	157	83	337	7
				JZ174/1/6	0.000	1.02	1.02	1.04	1.04	-0.02	-0.03	345	7	115	79	295	11
				JZ174/1/7	0.000	1.02	1.02	1.03	1.03	-0.03	-0.04	357	11	250	57	70	33

Internal structure and formation mechanisms of zoned plutons at shallow crustal levels

Station	Latitude - WGS84, North (°)	Longitude - WGS84, East (°)	Lithologic unit	Specimen	Km	L	F	P	Pj	T	U	K1 trend	K1 plunge	K2 trend	K2 plunge	K3 trend	K3 plunge
JZ175	49.627	15.355	Kouty granite	JZ174/1/8	0.000	1.02	1.02	1.04	1.04	0.11	0.10	339	5	160	85	340	5
				JZ174/2/1	0.000	1.01	1.12	1.13	1.14	0.81	0.80	165	22	285	51	105	39
				JZ174/2/2	0.000	1.03	1.02	1.04	1.04	-0.15	-0.16	5	14	250	59	70	31
				JZ174/2/3	0.000	1.03	1.02	1.04	1.04	-0.21	-0.22	355	14	245	53	65	38
				JZ174/2/4	0.000	1.03	1.01	1.04	1.04	-0.43	-0.44	352	16	220	67	40	23
				JZ174/2/5	0.000	1.03	1.01	1.04	1.04	-0.47	-0.48	347	8	238	67	58	23
				JZ174/2/6	0.000	1.03	1.02	1.05	1.05	-0.17	-0.18	351	4	251	71	71	19
				JZ174/2/7	0.000	1.03	1.02	1.04	1.05	-0.33	-0.34	356	10	249	57	69	33
				JZ175/1/1	0.000	1.01	1.08	1.10	1.10	0.72	0.71	233.9	8.2	328.5	29.3	149	61
				JZ175/1/2	0.000	1.01	1.09	1.10	1.11	0.82	0.81	244.4	8.5	338.3	24	158	66
JZ176	49.636	15.426	Lipnice granite	JZ175/1/3	0.000	1.03	1.07	1.10	1.11	0.47	0.45	236.1	2.8	328.7	43	149	47
				JZ175/1/4	0.000	1.02	1.07	1.09	1.10	0.57	0.55	63.6	1	333	31.4	153	59
				JZ175/1/5	0.000	1.02	1.08	1.10	1.11	0.62	0.61	239.9	6.5	333.9	31.4	154	59
				JZ175/1/6	0.000	1.01	1.07	1.08	1.09	0.73	0.72	69.7	5.4	336.8	28.7	157	61
				JZ175/1/7	0.000	1.03	1.06	1.09	1.09	0.39	0.37	73.6	14.7	334.1	32.2	154	58
				JZ175/1/8	0.000	1.02	1.07	1.09	1.10	0.58	0.57	76.7	27.3	330.6	28.3	151	62
				JZ175/2/1	0.000	1.02	1.07	1.09	1.10	0.52	0.51	241.5	2.8	333.3	32.6	153	57
				JZ175/2/2	0.000	1.01	1.07	1.09	1.09	0.76	0.75	67.4	5.8	334.7	25.1	155	65
				JZ175/2/3	0.000	1.03	1.06	1.09	1.09	0.36	0.34	83.3	22.7	341.1	26.8	161	63
				JZ175/2/4	0.000	1.02	1.09	1.10	1.11	0.66	0.65	88.2	30	345.9	20.3	166	70
JZ176	49.636	15.426	Lipnice granite	JZ175/2/5	0.000	1.02	1.07	1.09	1.10	0.59	0.57	87.2	27.7	345.5	21	166	69
				JZ175/2/6	0.000	1.02	1.07	1.10	1.10	0.50	0.48	83.9	20.3	344.5	23.7	165	66
				JZ175/2/7	0.000	1.04	1.08	1.13	1.13	0.28	0.25	243.4	10.5	346	49.5	166	41
				JZ175/2/8	0.000	1.02	1.07	1.09	1.10	0.60	0.58	77.9	13.1	340.5	29.3	161	61
				JZ176/1/1	0.000	1.02	1.08	1.09	1.10	0.63	0.62	155	42	285	35	105	55
JZ176/1/2	0.000	1.00	1.08	1.08	1.09	0.96	0.95	193	10	290	35	110	55				
JZ176/1/3	0.000	1.05	1.04	1.09	1.09	-0.08	-0.10	188	1	278	27	98	63				
JZ176/1/4	0.000	1.00	1.06	1.06	1.07	0.92	0.92	34	20	288	36	108	54				
JZ176/1/5	0.000	1.01	1.07	1.08	1.08	0.74	0.73	167	40	295	36	115	54				

Internal structure and formation mechanisms of zoned plutons at shallow crustal levels

Station	Latitude - WGS84, North (°)	Longitude - WGS84, East (°)	Lithologic unit	Specimen	Km	L	F	P	Pj	T	U	K1 trend	K1 plunge	K2 trend	K2 plunge	K3 trend	K3 plunge
JZ177	49.623	15.422	Lipnice granite	JZ176/1/6	0.000	1.02	1.06	1.08	1.08	0.51	0.50	164	29	282	40	102	50
				JZ176/1/7	0.000	1.02	1.07	1.09	1.09	0.62	0.61	163	34	286	38	106	52
				JZ176/2/1	0.000	1.02	1.08	1.09	1.10	0.63	0.62	150	39	281	39	101	51
				JZ176/2/2	0.000	1.01	1.07	1.09	1.09	0.75	0.74	186	2	277	39	97	51
				JZ176/2/3	0.000	1.00	1.05	1.06	1.07	0.85	0.84	50	39	280	38	100	52
				JZ176/2/4	0.000	1.02	1.05	1.07	1.07	0.43	0.42	126	48	274	37	94	53
				JZ176/2/5	0.000	1.01	1.08	1.08	1.09	0.88	0.88	166	33	283	36	103	54
				JZ176/2/6	0.000	1.02	1.07	1.09	1.09	0.52	0.50	186	6	280	37	100	53
				JZ176/2/7	0.000	1.02	1.08	1.10	1.11	0.69	0.67	158	33	281	40	101	50
				JZ176/2/8	0.000	1.02	1.08	1.10	1.11	0.63	0.61	158	36	280	36	100	54
				JZ177/1/1	0.000	1.04	1.03	1.07	1.07	-0.08	-0.10	48	9	195	79	15	11
				JZ177/1/2	0.000	1.03	1.02	1.05	1.05	-0.13	-0.14	52	11	235	80	55	11
				JZ177/1/3	0.000	1.03	1.02	1.06	1.06	-0.26	-0.27	55	5	189	82	9	8
				JZ177/1/4	0.000	1.03	1.03	1.07	1.07	0.05	0.03	51	4	230	86	50	4
				JZ177/1/5	0.000	1.04	1.05	1.08	1.08	0.13	0.11	51	1	148	84	328	7
				JZ177/1/6	0.000	1.04	1.05	1.09	1.09	0.05	0.03	241	1	114	88	294	2
JZ177/1/7	0.000	1.04	1.03	1.07	1.07	-0.12	-0.14	55	1	150	81	330	9				
JZ177/1/8	0.000	1.04	1.03	1.07	1.07	-0.07	-0.09	54	1	153	82	333	8				
JZ177/2/1	0.000	1.03	1.03	1.06	1.06	-0.07	-0.08	50	13	223	77	43	13				
JZ177/2/2	0.000	1.04	1.03	1.07	1.07	-0.07	-0.09	56	9	256	81	76	9				
JZ177/2/3	0.000	1.05	1.04	1.09	1.09	-0.07	-0.10	48	5	165	78	345	12				
JZ177/2/4	0.000	1.04	1.03	1.07	1.07	-0.06	-0.08	53	3	175	85	355	5				
JZ177/2/5	0.000	1.04	1.03	1.08	1.08	-0.13	-0.14	51	4	262	85	82	5				
JZ177/2/6	0.000	1.04	1.04	1.08	1.08	0.09	0.07	49	4	164	81	344	9				
JZ177/2/7	0.000	1.03	1.03	1.07	1.07	0.00	-0.02	50	2	166	85	346	5				
JZ177/2/8	0.000	1.03	1.04	1.07	1.07	0.10	0.08	48	3	165	84	345	6				
JZ177/2/9	0.000	1.04	1.03	1.06	1.06	-0.14	-0.16	48	5	278	83	98	7				
JZ178	49.616	15.394	Lipnice granite	JZ178/1/1	0.000	1.03	1.03	1.06	1.06	-0.11	-0.13	86	33	333	32	153	58
				JZ178/1/2	0.000	1.04	1.02	1.06	1.06	-0.37	-0.38	81	38	329	26	149	64

Internal structure and formation mechanisms of zoned plutons at shallow crustal levels

Station	Latitude - WGS84. North (°)	Longitude - WGS84. East (°)	Lithologic unit	Specimen	Km	L	F	P	Pj	T	U	K1 trend	K1 plunge	K2 trend	K2 plunge	K3 trend	K3 plunge
				JZ178/1/3	0.000	1.04	1.02	1.06	1.06	-0.41	-0.42	80	36	319	35	139	55
				JZ178/1/4	0.000	1.04	1.03	1.06	1.06	-0.17	-0.18	80	34	316	40	136	50
				JZ178/1/5	0.000	1.04	1.02	1.06	1.06	-0.30	-0.31	89	35	327	37	147	53
				JZ178/1/6	0.000	1.04	1.02	1.06	1.06	-0.26	-0.28	86	37	330	30	150	60
				JZ178/1/7	0.000	1.04	1.02	1.06	1.06	-0.41	-0.42	84	32	326	36	146	54
				JZ178/1/8	0.000	1.04	1.02	1.06	1.07	-0.30	-0.31	87	38	327	33	147	57
				JZ178/2/1	0.000	1.04	1.02	1.07	1.07	-0.30	-0.31	87	28	326	44	146	46
				JZ178/2/2	0.000	1.04	1.02	1.06	1.06	-0.26	-0.27	90	28	325	47	145	43
				JZ178/2/3	0.000	1.03	1.03	1.06	1.06	0.06	0.05	85	32	330	35	150	55
				JZ178/2/4	0.000	1.03	1.03	1.06	1.06	-0.08	-0.09	83	34	331	29	151	61
				JZ178/2/5	0.000	1.04	1.02	1.06	1.06	-0.29	-0.30	85	29	322	44	142	46
				JZ178/2/6	0.000	1.04	1.03	1.07	1.07	-0.22	-0.24	88	33	322	42	142	48
				JZ178/2/7	0.000	1.03	1.04	1.07	1.07	0.09	0.07	90	30	321	47	141	43
				JZ178/2/8	0.000	1.03	1.02	1.06	1.06	-0.18	-0.19	98	32	327	46	147	44
				JZ178/2/9	0.000	1.04	1.01	1.05	1.06	-0.61	-0.62	91	30	320	48	140	42
JZ179	49.623	15.398	Lipnice granite	JZ179/1/1	0.000	1.01	1.08	1.09	1.10	0.67	0.66	102	30	338	44	158	46
				JZ179/1/2	0.000	1.02	1.07	1.09	1.09	0.62	0.60	83	20	336	38	156	52
				JZ179/1/3	0.000	1.03	1.07	1.10	1.10	0.45	0.43	84	14	339	45	159	45
				JZ179/1/4	0.000	1.02	1.08	1.10	1.11	0.53	0.51	93	28	336	41	156	50
				JZ179/1/5	0.000	1.03	1.06	1.10	1.10	0.35	0.33	89	23	340	38	160	52
				JZ179/1/6	0.000	1.02	1.07	1.09	1.09	0.49	0.48	93	27	337	42	157	49
				JZ179/2/1	0.000	1.02	1.07	1.09	1.10	0.59	0.57	73	33	317	34	137	56
				JZ179/2/2	0.000	1.03	1.07	1.10	1.10	0.49	0.47	76	35	317	35	137	55
				JZ179/2/3	0.000	1.03	1.07	1.10	1.11	0.42	0.40	77	27	322	40	142	50
				JZ179/2/4	0.000	1.02	1.08	1.10	1.11	0.52	0.50	79	28	321	42	141	48
				JZ179/2/5	0.000	1.02	1.08	1.10	1.11	0.64	0.62	82	35	319	38	139	52
				JZ179/2/6	0.000	1.02	1.08	1.10	1.10	0.54	0.52	79	30	324	37	144	53
				JZ179/2/7	0.000	1.03	1.07	1.10	1.10	0.45	0.43	66	14	322	46	142	44
JZ180	49.628	15.392	Lipnice granite	JZ180/1/1	0.000	1.01	1.05	1.06	1.07	0.59	0.58	197	40	314	28	134	62

Internal structure and formation mechanisms of zoned plutons at shallow crustal levels

Station	Latitude - WGS84, North (°)	Longitude - WGS84, East (°)	Lithologic unit	Specimen	Km	L	F	P	Pj	T	U	K1 trend	K1 plunge	K2 trend	K2 plunge	K3 trend	K3 plunge
				JZ180/1/2	0.000	1.01	1.07	1.08	1.08	0.70	0.69	193	36	305	28	125	62
				JZ180/1/3	0.000	1.03	1.02	1.05	1.05	-0.22	-0.23	197	38	330	42	150	48
				JZ180/1/4	0.000	1.03	1.02	1.05	1.05	-0.11	-0.12	200	35	320	35	140	55
				JZ180/1/5	0.000	1.03	1.03	1.06	1.06	0.00	-0.01	206	41	307	13	127	77
				JZ180/1/6	0.000	1.03	1.02	1.05	1.05	-0.18	-0.19	211	47	306	5	126	85
				JZ180/1/7	0.000	1.03	1.02	1.05	1.05	-0.15	-0.16	200	42	306	17	126	74
				JZ180/1/8	0.000	1.02	1.04	1.06	1.06	0.23	0.22	195	50	315	23	135	67
				JZ180/1/9	0.000	1.04	1.01	1.06	1.06	-0.51	-0.52	214	20	321	39	141	51
				JZ180/2/2	0.000	1.03	1.03	1.05	1.05	0.01	-0.01	194	44	321	33	141	57
				JZ180/2/3	0.000	1.02	1.03	1.05	1.05	0.23	0.22	199	40	333	40	153	50
				JZ180/2/4	0.000	1.02	1.03	1.05	1.05	0.32	0.31	187	31	345	58	165	33
				JZ180/2/5	0.000	1.01	1.04	1.05	1.05	0.54	0.53	192	34	328	47	148	43
				JZ180/2/6	0.000	1.01	1.04	1.05	1.05	0.50	0.49	197	32	337	51	157	39
				JZ180/2/7	0.000	1.03	1.02	1.05	1.05	-0.16	-0.17	205	29	342	52	162	38
				JZ180/2/8	0.000	1.03	1.03	1.06	1.06	-0.07	-0.09	193	49	308	20	128	70
JZ181	49.633	15.403	Lipnice granite	JZ181/1/2	0.000	1.02	1.05	1.08	1.08	0.40	0.39	349	16	252	23	72	67
				JZ181/1/4	0.000	1.02	1.04	1.06	1.06	0.35	0.34	357	8	263	30	83	60
				JZ181/1/6	0.000	1.01	1.06	1.07	1.07	0.75	0.74	158	2	249	34	69	56
				JZ181/1/7	0.000	1.01	1.04	1.05	1.06	0.59	0.58	344	2	253	27	73	64
				JZ181/1/8	0.000	1.02	1.04	1.06	1.06	0.46	0.44	158	13	256	30	76	60
				JZ181/2/1	0.000	1.02	1.06	1.08	1.08	0.56	0.55	168	7	263	33	83	57
				JZ181/2/2	0.000	1.02	1.04	1.05	1.05	0.42	0.41	353	0	263	35	83	55
				JZ181/2/3	0.000	1.01	1.06	1.07	1.08	0.67	0.66	174	3	267	45	87	45
				JZ181/2/4	0.000	1.01	1.06	1.08	1.08	0.66	0.65	167	11	268	43	88	47
				JZ181/2/5	0.000	1.01	1.05	1.06	1.07	0.61	0.60	357	1	266	45	86	45
				JZ181/2/6	0.000	1.01	1.05	1.07	1.07	0.64	0.63	180	5	275	41	95	49
				JZ181/2/7	0.000	1.01	1.05	1.06	1.07	0.62	0.61	180	0	271	34	91	56
JZ182	49.657	15.376	Kouty granite	JZ182/1/1	0.000	1.02	1.03	1.05	1.05	0.30	0.29	350	45	174	45	354	45
				JZ182/1/2	0.000	1.02	1.03	1.05	1.05	0.17	0.16	335	39	175	50	355	40

Internal structure and formation mechanisms of zoned plutons at shallow crustal levels

Station	Latitude - WGS84, North (°)	Longitude - WGS84, East (°)	Lithologic unit	Specimen	Km	L	F	P	Pj	T	U	K1 trend	K1 plunge	K2 trend	K2 plunge	K3 trend	K3 plunge
				JZ182/1/3	0.000	1.02	1.04	1.05	1.05	0.38	0.37	4	38	178	52	358	38
				JZ182/1/4	0.000	1.01	1.04	1.05	1.05	0.49	0.48	350	37	181	53	1	37
				JZ182/1/5	0.000	1.02	1.04	1.06	1.06	0.23	0.21	311	32	162	54	342	36
				JZ182/1/6	0.000	1.02	1.04	1.06	1.06	0.31	0.29	330	25	152	65	332	25
				JZ182/1/7	0.000	1.00	1.04	1.04	1.05	0.82	0.82	293	14	175	62	355	28
				JZ182/1/8	0.000	1.00	1.04	1.04	1.05	0.89	0.88	350	17	171	73	351	17
				JZ182/2/1	0.000	1.02	1.05	1.07	1.07	0.35	0.34	331	26	153	64	333	26
				JZ182/2/2	0.000	1.02	1.06	1.07	1.08	0.52	0.51	310	28	147	61	327	29
				JZ182/2/3	0.000	1.02	1.04	1.06	1.06	0.43	0.42	307	33	160	53	340	38
				JZ182/2/4	0.000	1.03	1.07	1.10	1.10	0.45	0.43	304	24	131	66	311	24
				JZ182/2/5	0.000	1.01	1.06	1.07	1.07	0.68	0.67	292	24	156	59	336	31
				JZ182/2/6	0.000	1.02	1.05	1.07	1.07	0.40	0.39	305	28	145	60	325	30
				JZ182/2/7	0.000	1.03	1.06	1.09	1.09	0.40	0.38	303	22	131	68	311	22
				JZ182/2/8	0.000	1.01	1.05	1.06	1.07	0.59	0.58	318	21	153	69	333	21
JZ183	49.645	15.384	Lipnice granite	JZ183/1/1	0.000	1.01	1.07	1.08	1.09	0.77	0.76	121	0	211	24	31	66
				JZ183/1/2	0.000	1.01	1.08	1.09	1.10	0.77	0.77	301	6	208	23	28	67
				JZ183/1/3	0.000	1.01	1.08	1.09	1.10	0.75	0.74	302	19	204	20	24	70
				JZ183/1/4	0.000	1.02	1.06	1.08	1.08	0.59	0.58	301	16	204	21	24	69
				JZ183/1/5	0.000	1.01	1.07	1.08	1.09	0.76	0.75	298	1	208	13	28	77
				JZ183/1/6	0.000	1.01	1.08	1.09	1.10	0.85	0.85	299	9	206	17	26	74
				JZ183/1/7	0.000	1.01	1.07	1.09	1.09	0.74	0.73	112	11	206	18	26	72
				JZ183/1/8	0.000	1.01	1.08	1.09	1.10	0.78	0.77	114	5	206	20	26	70
				JZ183/2/1	0.000	1.01	1.07	1.08	1.08	0.80	0.79	108	32	210	19	30	71
				JZ183/2/2	0.000	1.01	1.06	1.07	1.08	0.72	0.71	117	8	209	13	29	77
				JZ183/2/3	0.000	1.01	1.07	1.08	1.08	0.81	0.80	299	3	208	14	28	76
				JZ183/2/4	0.000	1.01	1.07	1.08	1.09	0.78	0.78	304	19	208	17	28	73
				JZ183/2/5	0.000	1.01	1.07	1.09	1.09	0.67	0.66	113	3	204	17	24	73
				JZ183/2/6	0.000	1.01	1.07	1.08	1.09	0.68	0.67	298	14	203	18	23	72
				JZ183/2/7	0.000	1.01	1.07	1.08	1.09	0.73	0.72	297	0	207	21	27	69

Internal structure and formation mechanisms of zoned plutons at shallow crustal levels

Station	Latitude - WGS84, North (°)	Longitude - WGS84, East (°)	Lithologic unit	Specimen	Km	L	F	P	Pj	T	U	K1 trend	K1 plunge	K2 trend	K2 plunge	K3 trend	K3 plunge	
JZ184	49.659	15.347	Melechov granite	JZ184/1/1	0.000	1.02	1.03	1.05	1.05	0.22	0.21	81	1	351	20	171	70	
				JZ184/1/2	0.000	1.04	1.02	1.06	1.06	-0.28	-0.30	167	33	313	52	133	38	
				JZ184/1/3	0.000	1.01	1.05	1.07	1.07	0.64	0.63	266	5	8	69	188	21	
				JZ184/1/4	0.000	1.00	1.03	1.03	1.03	0.79	0.79	148	49	285	33	105	58	
				JZ184/1/5	0.000	1.02	1.05	1.07	1.08	0.40	0.38	163	19	349	71	169	19	
				JZ184/1/6	0.000	1.01	1.04	1.05	1.05	0.53	0.52	182	23	289	35	109	55	
				JZ184/2/1	0.000	1.04	1.04	1.09	1.09	0.01	-0.01	126	11	236	60	56	30	
				JZ184/2/2	0.000	1.02	1.01	1.04	1.04	-0.40	-0.41	89	30	199	31	19	59	
				JZ184/2/3	0.000	1.02	1.01	1.03	1.03	-0.18	-0.19	251	50	28	31	208	59	
				JZ184/2/4	0.000	1.03	1.07	1.10	1.10	0.31	0.28	169	12	34	74	214	16	
				JZ184/2/5	0.000	1.05	1.01	1.06	1.07	-0.63	-0.64	166	8	259	20	79	70	
				JZ184/2/6	0.000	1.02	1.04	1.06	1.06	0.44	0.43	267	36	43	45	223	45	
JZ185	49.685	15.329		Kouty granite	JZ185/1/2	0.000	1.02	1.02	1.04	1.04	0.15	0.14	265	11	155	61	335	29
					JZ185/1/3	0.000	1.03	1.03	1.06	1.06	0.12	0.10	272	4	176	55	356	35
			JZ185/1/4		0.000	1.02	1.04	1.06	1.06	0.49	0.48	88	1	178	44	358	46	
			JZ185/1/5		0.000	1.02	1.03	1.04	1.04	0.25	0.24	267	9	166	50	346	40	
			JZ185/1/6		0.000	1.01	1.04	1.05	1.05	0.59	0.58	277	10	177	42	357	48	
			JZ185/1/7		0.000	1.02	1.03	1.06	1.06	0.27	0.26	267	4	169	65	349	25	
			JZ185/1/8		0.000	1.02	1.02	1.04	1.04	0.03	0.02	274	8	173	54	353	36	
			JZ185/2/1		0.000	1.02	1.02	1.04	1.04	0.12	0.11	266	8	166	52	346	38	
			JZ185/2/2		0.000	1.02	1.04	1.05	1.05	0.42	0.41	272	8	170	55	350	36	
			JZ185/2/3		0.000	1.01	1.03	1.05	1.05	0.38	0.37	264	7	163	57	343	33	
			JZ185/2/4		0.000	1.01	1.04	1.05	1.05	0.48	0.47	279	6	180	54	0	36	
			JZ185/2/5		0.000	1.02	1.06	1.09	1.09	0.43	0.42	287	9	186	49	6	41	
			JZ185/2/6		0.000	1.02	1.03	1.05	1.05	0.10	0.09	86	2	179	58	359	32	
			JZ185/2/7		0.000	1.02	1.03	1.05	1.05	0.09	0.08	86	2	179	55	359	35	
			JZ185/2/8	0.000	1.02	1.02	1.04	1.04	-0.06	-0.07	79	0	170	59	350	31		
JZ186	49.666	15.348	Melechov granite	JZ186/1/1	0.000	1.04	1.02	1.06	1.06	-0.24	-0.25	279	20	168	46	348	44	
				JZ186/1/2	0.000	1.02	1.05	1.07	1.07	0.33	0.31	289	34	96	55	276	35	

Station	Latitude - WGS84. North (°)	Longitude - WGS84. East (°)	Lithologic unit	Specimen	Km	L	F	P	Pj	T	U	K1 trend	K1 plunge	K2 trend	K2 plunge	K3 trend	K3 plunge
				JZ186/1/3	0.000	1.04	1.02	1.06	1.06	-0.38	-0.39	290	25	147	59	327	31
				JZ186/1/4	0.000	1.02	1.05	1.07	1.07	0.49	0.48	23	59	179	29	359	61
				JZ186/1/5	0.000	1.04	1.09	1.13	1.13	0.37	0.34	75	18	178	33	358	57
				JZ186/1/6	0.000	1.03	1.08	1.11	1.11	0.52	0.50	260	55	156	10	336	80
				JZ186/1/7	0.000	1.02	1.08	1.10	1.11	0.64	0.62	242	52	145	5	325	85
				JZ186/2/1	0.000	1.04	1.01	1.05	1.05	-0.57	-0.58	255	36	32	45	212	45
				JZ186/2/2	0.000	1.02	1.03	1.04	1.04	0.29	0.28	258	33	97	56	277	34
				JZ186/2/3	0.000	1.05	1.04	1.09	1.09	-0.15	-0.17	319	43	190	34	10	56
				JZ186/2/4	0.000	1.02	1.05	1.07	1.08	0.45	0.44	359	57	147	29	327	61
				JZ186/2/5	0.000	1.06	1.03	1.09	1.10	-0.37	-0.39	304	38	36	2	216	88
				JZ186/2/6	0.000	1.05	1.01	1.05	1.06	-0.73	-0.73	187	6	279	19	99	71
				JZ186/2/7	0.000	1.01	1.01	1.03	1.03	0.05	0.05	256	5	358	68	178	22
				JZ186/2/8	0.000	1.02	1.03	1.06	1.06	0.19	0.17	314	15	206	49	26	42
JZ187	49.659	15.357	Kouty granite	JZ187/1/1	0.000	1.05	1.08	1.13	1.13	0.23	0.20	40	14	152	57	332	33
				JZ187/1/2	0.000	1.04	1.05	1.08	1.08	0.11	0.09	24	21	205	69	25	21
				JZ187/1/3	0.000	1.02	1.07	1.10	1.10	0.48	0.46	23	28	204	62	24	28
				JZ187/1/4	0.000	1.04	1.03	1.06	1.06	-0.18	-0.19	19	33	205	57	25	33
				JZ187/1/5	0.000	1.04	1.01	1.05	1.05	-0.56	-0.56	3	36	245	34	65	57
				JZ187/1/6	0.000	1.04	1.02	1.06	1.06	-0.26	-0.27	23	30	205	60	25	30
				JZ187/1/7	0.000	1.03	1.03	1.07	1.07	0.01	-0.01	17	32	203	58	23	32
				JZ187/1/8	0.000	1.05	1.04	1.09	1.09	-0.04	-0.06	23	28	183	61	3	29
				JZ187/2/1	0.000	1.04	1.04	1.08	1.08	0.09	0.07	11	27	192	63	12	27
				JZ187/2/2	0.000	1.04	1.04	1.08	1.08	0.07	0.05	1	22	206	66	26	24
				JZ187/2/3	0.000	1.04	1.04	1.08	1.08	0.04	0.02	20	29	204	61	24	29
				JZ187/2/4	0.000	1.03	1.03	1.07	1.07	-0.03	-0.05	24	32	196	58	16	32
				JZ187/2/5	0.000	1.04	1.04	1.08	1.08	-0.06	-0.08	18	31	187	58	7	32
				JZ187/2/6	0.000	1.02	1.05	1.08	1.08	0.36	0.35	34	28	208	62	28	28
				JZ187/2/7	0.000	1.05	1.06	1.10	1.10	0.10	0.08	10	28	208	61	28	29
				JZ187/2/8	0.000	1.04	1.03	1.07	1.07	-0.16	-0.17	14	28	188	62	8	28

Internal structure and formation mechanisms of zoned plutons at shallow crustal levels

Station	Latitude - WGS84, North (°)	Longitude - WGS84, East (°)	Lithologic unit	Specimen	Km	L	F	P	Pj	T	U	K1 trend	K1 plunge	K2 trend	K2 plunge	K3 trend	K3 plunge
JZ188	49.662	15.375	Kouty granite	JZ188/1/1	0.000	1.01	1.01	1.02	1.02	1.02	0.14	344	50	219	26	39	64
				JZ188/1/2	0.000	1.01	1.01	1.02	1.02	1.02	0.19	75	62	222	24	42	66
				JZ188/1/3	0.000	1.01	1.01	1.02	1.02	1.02	0.19	130	76	235	4	55	86
				JZ188/1/4	0.000	1.02	1.01	1.02	1.03	1.03	-0.59	324	10	230	21	50	69
				JZ188/2/1	0.000	1.00	1.02	1.02	1.02	1.02	0.64	85	38	194	23	14	67
				JZ188/2/2	0.000	1.01	1.02	1.03	1.03	1.03	0.33	320	2	230	5	50	85
				JZ188/2/3	0.000	1.01	1.01	1.02	1.02	1.02	0.20	275	2	163	86	343	4
				JZ188/2/4	0.000	1.02	1.01	1.03	1.03	1.03	-0.45	313	32	186	44	6	47
JZ189	49.674	15.314	Kouty granite	JZ189/1/1	0.000	1.04	1.03	1.06	1.06	1.06	-0.19	226	33	113	31	293	59
				JZ189/1/2	0.000	1.04	1.01	1.05	1.05	1.05	-0.56	223	36	119	20	299	71
				JZ189/1/3	0.000	1.04	1.04	1.08	1.08	1.08	-0.01	221	34	104	34	284	56
				JZ189/1/4	0.000	1.03	1.02	1.05	1.05	1.05	-0.27	228	41	106	31	286	59
				JZ189/2/1	0.000	1.02	1.02	1.04	1.04	1.04	0.03	229	40	118	23	298	67
				JZ189/2/2	0.000	1.03	1.05	1.08	1.08	1.08	0.28	230	45	107	29	287	62
				JZ189/2/3	0.000	1.03	1.03	1.06	1.06	1.06	-0.05	237	42	115	30	295	60
				JZ189/2/4	0.000	1.02	1.01	1.04	1.04	1.04	-0.29	230	34	132	11	312	79
JZ190	49.671	15.319	Melechov granite	JZ190/1/2	0.000	1.02	1.07	1.10	1.10	1.10	0.52	219	28	107	36	287	54
				JZ190/1/3	0.000	1.05	1.03	1.08	1.08	1.08	-0.14	218	24	112	31	292	59
				JZ190/1/4	0.000	1.03	1.02	1.05	1.05	1.05	-0.22	204	3	110	60	290	30
				JZ190/1/5	0.000	1.03	1.08	1.12	1.12	1.12	0.43	233	39	97	42	277	48
				JZ190/1/6	0.000	1.01	1.09	1.09	1.09	1.11	0.89	247	32	113	48	293	42
				JZ190/1/7	0.000	1.02	1.04	1.07	1.07	1.07	0.28	278	28	110	62	290	28
				JZ190/2/1	0.000	1.03	1.05	1.08	1.08	1.08	0.33	302	16	99	72	279	18
				JZ190/2/2	0.000	1.04	1.06	1.10	1.10	1.10	0.21	27	19	183	70	3	20
JZ190/2/3	0.000	1.02	1.04	1.06	1.06	1.06	0.45	296	31	130	58	310	32				
JZ191	49.597	15.347	Lipnice granite	JZ191/1/1	0.000	1.01	1.07	1.08	1.09	1.09	0.65	157	54	351	35	171	55
				JZ191/1/2	0.000	1.02	1.07	1.09	1.09	1.09	0.55	90	20	357	9	177	81
				JZ191/1/3	0.000	1.04	1.08	1.12	1.12	1.12	0.34	89	20	180	5	0	85

Station	Latitude - WGS84, North (°)	Longitude - WGS84, East (°)	Lithologic unit	Specimen	Km	L	F	P	Pj	T	U	K1 trend	K1 plunge	K2 trend	K2 plunge	K3 trend	K3 plunge
JZ192	49.678	15.356	Kouty granite	JZ191/1/4	0.000	1.05	1.03	1.08	1.09	-0.29	-0.31	138	57	280	27	100	63
				JZ191/1/6	0.000	1.01	1.07	1.08	1.08	0.82	0.81	235	36	350	31	170	59
				JZ191/1/7	0.000	1.01	1.08	1.09	1.10	0.81	0.80	238	31	355	37	175	53
				JZ191/1/8	0.000	1.01	1.08	1.08	1.09	0.88	0.87	157	55	353	34	173	56
				JZ191/2/1	0.000	1.02	1.05	1.07	1.07	0.47	0.46	135	66	343	21	163	69
				JZ191/2/2	0.000	1.04	1.13	1.17	1.18	0.54	0.51	91	47	203	20	23	70
				JZ191/2/3	0.000	1.06	1.02	1.08	1.09	-0.40	-0.42	113	46	13	9	193	81
				JZ191/2/4	0.000	1.05	1.03	1.08	1.08	-0.22	-0.23	140	54	338	35	158	55
				JZ191/2/5	0.000	1.01	1.06	1.08	1.08	0.65	0.63	187	55	344	33	164	57
				JZ191/2/6	0.000	1.01	1.06	1.07	1.08	0.72	0.71	138	55	346	31	166	59
				JZ191/2/7	0.000	1.00	1.07	1.08	1.09	0.89	0.89	149	53	353	35	173	56
				JZ191/2/8	0.000	1.00	1.07	1.08	1.09	0.91	0.91	178	58	357	33	177	58
				JZ192/1/1	0.000	1.03	1.08	1.11	1.12	0.52	0.50	40	29	188	57	8	33
				JZ192/1/2	0.000	1.02	1.10	1.11	1.12	0.72	0.71	306	35	113	54	293	36
				JZ192/1/3	0.000	1.04	1.02	1.06	1.07	-0.31	-0.33	68	34	212	50	32	40
				JZ192/1/4	0.000	1.03	1.08	1.11	1.12	0.47	0.45	87	20	203	49	23	41
JZ192/1/5	0.000	1.05	1.09	1.14	1.15	0.23	0.20	85	31	215	47	35	43				
JZ192/1/6	0.000	1.03	1.01	1.05	1.05	-0.42	-0.43	66	35	279	50	99	40				
JZ192/1/7	0.000	1.04	1.02	1.05	1.05	-0.37	-0.38	67	31	276	55	96	35				
JZ192/2/1	0.000	1.01	1.03	1.05	1.05	0.47	0.46	38	36	207	53	27	37				
JZ192/2/2	0.000	1.01	1.12	1.13	1.15	0.81	0.80	32	16	150	59	330	31				
JZ192/2/3	0.000	1.02	1.08	1.10	1.10	0.62	0.60	79	27	202	47	22	43				
JZ192/2/4	0.000	1.04	1.18	1.22	1.24	0.66	0.63	89	16	195	45	15	45				
JZ192/2/5	0.000	1.03	1.04	1.07	1.07	0.13	0.11	76	36	225	50	45	40				
JZ192/2/6	0.000	1.02	1.05	1.07	1.07	0.40	0.39	66	39	208	44	28	46				
JZ192/2/7	0.000	1.02	1.02	1.04	1.04	-0.08	-0.09	84	21	342	27	162	63				
JZ193	49.614	15.279	Kouty granite	JZ193/1/1	0.000	1.04	1.17	1.21	1.23	0.64	0.61	325.4	56.3	80.4	15.7	260	74
				JZ193/1/2	0.000	1.03	1.22	1.25	1.28	0.75	0.72	216.6	51.2	26	38.3	206	52
				JZ193/1/3	0.000	1.04	1.02	1.06	1.06	-0.41	-0.42	330.5	58	159.5	31.7	340	58

Internal structure and formation mechanisms of zoned plutons at shallow crustal levels

Station	Latitude - WGS84, North (°)	Longitude - WGS84, East (°)	Lithologic unit	Specimen	Km	L	F	P	Pj	T	U	K1 trend	K1 plunge	K2 trend	K2 plunge	K3 trend	K3 plunge
JZ194	49.615	15.343	Kouty granite	JZ193/1/4	0.000	1.03	1.02	1.05	1.05	1.05	-0.29	332.5	68.6	127.5	19.6	308	70
				JZ193/1/5	0.000	1.03	1.02	1.05	1.05	1.05	-0.17	338	65.7	121	19.8	301	70
				JZ193/1/6	0.000	1.04	1.00	1.04	1.04	1.04	-0.89	332.8	48.4	80.8	15.3	261	75
				JZ193/1/7	0.000	1.04	1.01	1.04	1.04	1.04	-0.76	318.9	60.5	163.5	27.2	344	63
				JZ193/1/8	0.000	1.03	1.00	1.04	1.04	1.04	-0.77	334.1	57.5	241.7	1.5	62	89
				JZ193/2/1	0.000	1.03	1.01	1.04	1.04	1.04	-0.53	312.9	42.7	219.1	4.1	39	86
				JZ193/2/2	0.000	1.03	1.01	1.04	1.04	1.04	-0.44	293.2	50.5	100	38.7	280	51
				JZ193/2/3	0.000	1.02	1.02	1.04	1.04	1.04	0.03	284.4	61	113.7	28.7	294	61
				JZ193/2/4	0.000	1.02	1.03	1.05	1.05	1.05	0.12	297.4	58.5	132.6	30.6	313	59
				JZ193/2/5	0.000	1.03	1.01	1.04	1.05	1.05	-0.58	296.4	47.3	115.7	42.7	296	47
				JZ193/2/6	0.000	1.05	1.05	1.10	1.10	1.10	0.04	293.8	31.4	45.8	31.6	226	58
				JZ193/2/7	0.000	1.04	1.11	1.15	1.16	1.16	0.47	270.1	30	27.6	38.6	208	51
				JZ193/2/8	0.000	1.05	1.03	1.08	1.08	1.08	-0.22	285.9	46.1	63.3	35.3	243	55
				JZ195	49.666	15.392	Kouty granite	JZ194/1/1	0.000	1.01	1.07	1.08	1.08	0.71	0.70	282.3	68.1
JZ194/1/2	0.000	1.10	1.11					1.23	1.23	0.03	-0.02	294.7	39	132.5	49.6	313	40
JZ194/1/3	0.000	1.04	1.11					1.15	1.16	1.16	0.42	246.4	34.2	119.9	41.2	300	49
JZ194/1/4	0.000	1.00	1.05					1.06	1.06	1.06	0.89	173	66.9	336.8	22.3	157	68
JZ194/1/5	0.000	1.06	1.41					1.50	1.55	1.55	0.72	119.3	26.5	212	5.4	32	85
JZ191/1/6	0.000	1.01	1.05					1.07	1.07	1.07	0.57	181.2	64.9	346.3	24.4	166	66
JZ194/1/7	0.000	1.01	1.05					1.06	1.07	1.07	0.66	212.7	59.2	345.1	21.9	165	68
JZ194/2/1	0.000	1.01	1.06					1.07	1.08	1.08	0.72	142.7	65	334.5	24.6	155	65
JZ194/2/2	0.000	1.01	1.05					1.06	1.07	1.07	0.69	115.9	60.5	336.8	23.1	157	67
JZ194/2/3	0.000	1.01	1.06					1.07	1.07	1.07	0.85	123.5	63.2	332.4	23.8	152	66
JZ194/2/4	0.000	1.01	1.05					1.05	1.06	1.06	0.71	206.4	62.6	332.5	17	153	73
JZ194/2/5	0.000	1.01	1.06					1.06	1.07	1.07	0.84	191	59.2	326.6	23.1	147	67
JZ194/2/6	0.000	1.05	1.05					1.11	1.11	1.11	0.03	243.8	26.2	129.8	39.6	310	50
JZ195	49.666	15.392	Kouty granite					JZ195/1/1	0.000	1.05	1.01	1.06	1.07	-0.68	-0.69	125.2	21.3
				JZ195/1/2	0.000	1.01	1.06	1.06	1.07	0.80	0.80	12.6	12.1	259.2	61.7	79	28
				JZ195/1/3	0.000	1.01	1.05	1.06	1.07	0.66	86.3	32.6	251.3	56.5	71	34	

Station	Latitude - WGS84, North (°)	Longitude - WGS84, East (°)	Lithologic unit	Specimen	Km	L	F	P	Pj	T	U	K1 trend	K1 plunge	K2 trend	K2 plunge	K3 trend	K3 plunge
				JZ195/1/4	0.000	1.00	1.05	1.06	1.06	0.84	0.84	41.9	31.8	248.4	55.3	68	35
				JZ195/1/5	0.000	1.01	1.06	1.08	1.08	0.62	0.61	41.4	25.7	162	46.6	342	43
				JZ195/2/1	0.000	1.01	1.05	1.06	1.06	0.73	0.72	32.4	25.5	248.2	59.6	68	30
				JZ195/2/2	0.000	1.01	1.05	1.07	1.07	0.66	0.65	65.5	35.5	253.6	54.2	74	36
				JZ195/2/3	0.000	1.01	1.06	1.07	1.08	0.72	0.71	52.7	33	260.3	53.8	80	36
				JZ195/2/4	0.000	1.02	1.04	1.06	1.06	0.44	0.43	55.3	33.6	239.8	56.3	60	34
				JZ195/2/5	0.000	1.05	1.04	1.10	1.10	-0.09	-0.12	63.4	38	199.7	42.8	20	47
				JZ195/2/6	0.000	1.04	1.05	1.10	1.10	0.10	0.08	32.5	12.2	172.1	74.2	352	16
				JZ195/2/7	0.000	1.04	1.11	1.15	1.16	0.46	0.44	337.7	23.8	106.2	54.7	286	35

Electronic Supplementary Material, Part 4

Curie temperature and other temperature changes

Lipnice			Kouty			Melechov		
granite			granite			granite		
JZ171/1/3	JZ191/2/3	Note	JZ187/1/1	JZ194/1/5	Note	JZ164/1/7	JZ184/1/1	Note
Heating								
(°C)								
10	0	MO?	-80	-80	ins.	-140	n.d.	ins.
230	220	ins.	30	0	MO?	20	20	MO?
360	380	ins.	230	220	ins.	220	240	
560	540	T _c	380	400	ins.	350	340	ins.
580	570	T _c	570	550	T _c	505	505	peak
660	660	ins.	510	505	peak	520	520	ins.
520	520	peak	660	640	T _c	580	570	T _c
						660	660	T _c
Cooling								
(°C)								
540	540	T _c	580	500	ins.	570	560	T _c
495	n.d.	peak	500	520	ins.	520	520	T _c
-20	-40	T _c	460	460	T _c and ins.	450	420	T _c
-150	n.d.	VW?	400	400	ins.	220	n.d.	
								ins. and
			260	260	ins.	-80	80	T _c ?
			20	20	peak	-140	n.d.	ins.
						n.d.	-70	peak

Explanations:

n.d. not determined

ins. insignificant

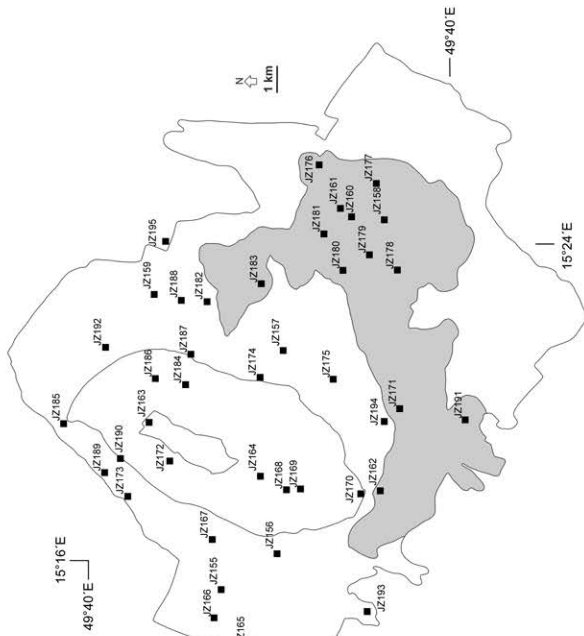
Verwey

VW transition

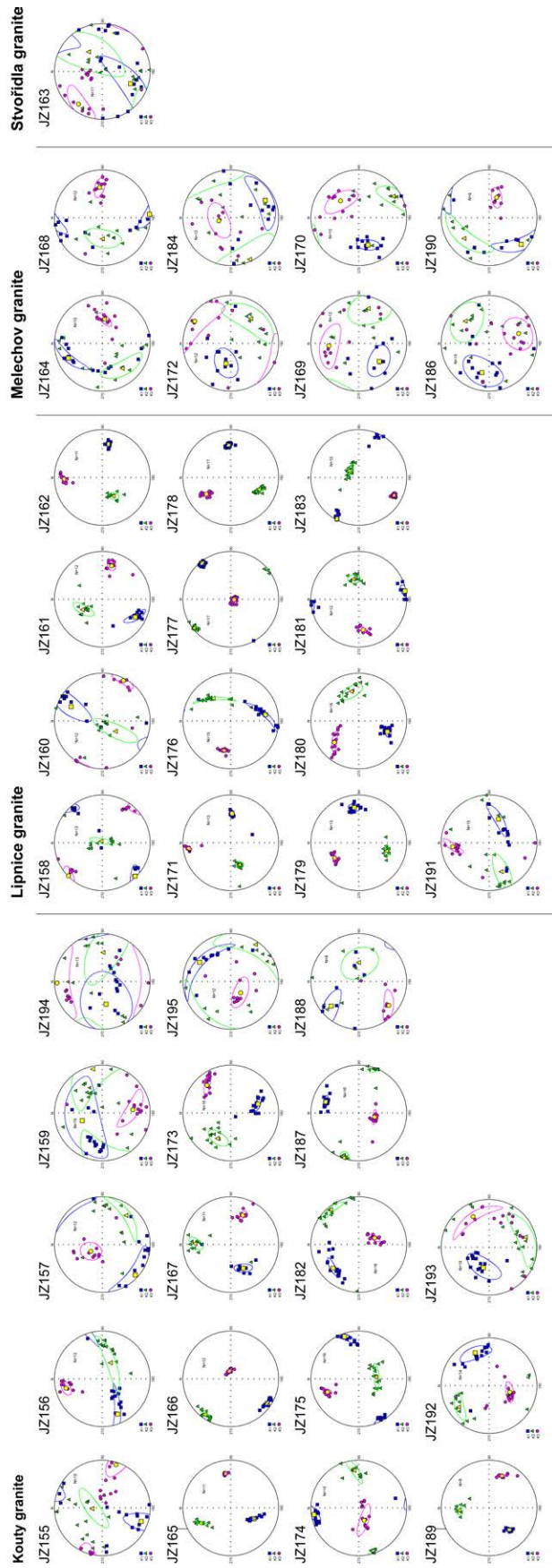
Morin

MO transition

Electronic Supplementary Material, Part 5
 Sampling sites (AMS)
 Stereographic projections (equal area, lower hemisphere) of the AMS axes at each sampling site



Key
 ■ Maximum principal susceptibility (magnetic lineation)
 ▲ Intermediate principal susceptibility
 ▼ Minimum principal susceptibility (pole to magnetic foliation)
 Yellow symbols represent mean directions of principal susceptibilities
 Colored lines represent respective 95% confidence ellipses



Electronic Supplementary Material. Part 6**Results of inverse AMS-to-strain modeling using SUSIE****Kouty granite**

Station	Distance (m)	random model			
		lnXY	lnZY	k	D
JZ165	5223	0.126	0.471	0.267	0.487
JZ166	4353	0.216	0.617	0.350	0.653
JZ155	3709	0.251	0.364	0.688	0.442
JZ167	2486	0.338	0.213	1.590	0.399
JZ156	3585	0.239	0.243	0.981	0.341
JZ173	1828	0.281	0.298	0.942	0.410
JZ189	1979	0.459	0.072	6.375	0.465
JZ185	2882	0.281	0.453	0.619	0.533
JZ193	6061	0.786	0.247	3.181	0.823
JZ194	4963	0.181	0.850	0.213	0.869
JZ175	4047	0.115	0.592	0.194	0.603
JZ157	3374	0.342	0.661	0.517	0.744
JZ174	2523	0.325	0.207	1.573	0.385
JZ187	2190	0.400	0.351	1.140	0.532
JZ182	3515	0.213	0.435	0.490	0.484
JZ188	3489	0.176	0.187	0.942	0.257
JZ159	3690	0.407	0.528	0.770	0.667
JZ192	2960	0.772	0.417	1.853	0.878
JZ195	4736	0.249	0.475	0.525	0.537

Station	Distance (m)	Ježek-Hrouda model			
		lnXY	lnZY	k	D
JZ165	5223	0.255	0.479	0.533	0.542
JZ166	4353	0.245	0.468	0.523	0.528
JZ155	3709	0.218	0.362	0.601	0.422
JZ167	2486	0.211	0.198	1.062	0.289
JZ156	3585	0.209	0.280	0.747	0.349
JZ173	1828	0.221	0.200	1.106	0.297
JZ189	1979	0.388	0.230	1.688	0.451
JZ185	2882	0.225	0.306	0.736	0.380
JZ193	6061	0.619	0.287	2.159	0.683
JZ194	4963	0.385	0.873	0.441	0.954
JZ175	4047	0.294	0.692	0.424	0.752
JZ157	3374	0.326	0.717	0.455	0.787
JZ174	2523	0.350	0.180	1.950	0.393
JZ187	2190	0.518	0.362	1.431	0.632
JZ182	3515	0.215	0.433	0.497	0.484
JZ188	3489	0.115	0.122	0.942	0.167

Station	Distance (m)	lnXY	lnZY	k	D
JZ159	3690	0.465	0.483	0.962	0.670
JZ192	2960	0.484	0.539	0.897	0.725
JZ195	4736	0.286	0.512	0.558	0.587

Sanderson-Marchini model

Station	Distance (m)	lnXY	lnZY	k	D
JZ165	5223	0.266	0.499	0.533	0.565
JZ166	4353	0.255	0.488	0.522	0.550
JZ155	3709	0.227	0.381	0.595	0.443
JZ167	2486	0.219	0.216	1.013	0.307
JZ156	3585	0.216	0.299	0.723	0.369
JZ173	1828	0.229	0.217	1.057	0.316
JZ189	1979	0.404	0.246	1.647	0.473
JZ185	2882	0.236	0.323	0.730	0.400
JZ193	6061	0.644	0.303	2.127	0.712
JZ194	4963	0.408	0.898	0.455	0.986
JZ175	4047	0.308	0.715	0.431	0.778
JZ157	3374	0.343	0.740	0.464	0.815
JZ174	2523	0.364	0.195	1.862	0.413
JZ187	2190	0.540	0.379	1.425	0.659
JZ182	3515	0.223	0.454	0.491	0.506
JZ188	3489	0.176	0.187	0.942	0.257
JZ159	3690	0.485	0.502	0.967	0.698
JZ192	2960	0.506	0.559	0.906	0.754
JZ195	4736	0.299	0.533	0.561	0.611

Melechov granite

random model

Station	Distance (m)	lnXY	lnZY	k	D
JZ172	520	0.388	0.405	0.959	0.560
JZ164	2104	0.351	0.278	1.262	0.448
JZ168	2822	0.413	0.482	0.856	0.635
JZ169	3147	0.478	0.246	1.947	0.538
JZ170	4559	0.451	0.173	2.610	0.483
JZ184	1428	0.094	0.588	0.159	0.595
JZ186	1684	0.519	0.345	1.506	0.623
JZ190	1511	0.420	0.460	0.912	0.623

Ježek-Hrouda model

Station	Distance (m)	lnXY	lnZY	k	D
JZ172	520	0.356	0.317	1.124	0.476
JZ164	2104	0.399	0.332	1.203	0.519
JZ168	2822	0.487	0.476	1.022	0.681
JZ169	3147	0.414	0.321	1.291	0.524

Station	Distance (m)	lnXY	lnZY	k	D
JZ170	4559	0.368	0.246	1.499	0.443
JZ184	1428	0.307	0.317	0.967	0.441
JZ186	1684	0.439	0.351	1.250	0.562
JZ190	1511	0.374	0.482	0.776	0.610

Sanderson-Marchini model

Station	Distance (m)	lnXY	lnZY	k	D
JZ172	520	0.371	0.334	1.114	0.499
JZ164	2104	0.417	0.349	1.195	0.543
JZ168	2822	0.509	0.495	1.028	0.710
JZ169	3147	0.432	0.337	1.280	0.548
JZ170	4559	0.383	0.263	1.455	0.464
JZ184	1428	0.319	0.335	0.952	0.463
JZ186	1684	0.458	0.368	1.244	0.588
JZ190	1511	0.391	0.502	0.779	0.636

Lipnice granite

random model

Station	Distance (m)	lnXY	lnZY	k	D
JZ162	5005	0.387	0.238	1.628	0.454
JZ171	5413	0.456	0.574	0.794	0.733
JZ191	6981	0.289	0.619	0.467	0.683
JZ180	5798	0.127	0.215	0.593	0.250
JZ179	6506	0.276	0.655	0.422	0.711
JZ178	6767	0.448	0.117	3.828	0.463
JZ181	6189	0.223	0.523	0.427	0.568
JZ161	6922	0.358	0.196	1.831	0.408
JZ160	6919	0.314	0.432	0.727	0.534
JZ158	7382	0.476	0.717	0.663	0.861
JZ177	7935	0.443	0.449	0.987	0.631
JZ176	7578	0.074	0.721	0.103	0.725
JZ183	4354	0.219	0.581	0.377	0.621

Ježek-Hrouda model

Station	Distance (m)	lnXY	lnZY	k	D
JZ162	5005	0.460	0.274	1.679	0.535
JZ171	5413	0.386	0.587	0.657	0.702
JZ191	6981	0.318	0.605	0.525	0.683
JZ180	5798	0.302	0.291	1.037	0.419
JZ179	6506	0.335	0.670	0.500	0.749
JZ178	6767	0.469	0.216	2.175	0.516
JZ181	6189	0.187	0.486	0.386	0.521
JZ161	6922	0.344	0.347	0.992	0.488

Station	Distance (m)	lnXY	lnZY	k	D
JZ160	6919	0.311	0.462	0.673	0.557
JZ158	7382	0.539	0.704	0.766	0.887
JZ177	7935	0.479	0.310	1.547	0.571
JZ176	7578	0.205	0.645	0.317	0.677
JZ183	4354	0.146	0.683	0.214	0.699

Sanderson-Marchini model

Station	Distance (m)	lnXY	lnZY	k	D
JZ162	5005	0.477	0.291	1.639	0.559
JZ171	5413	0.405	0.602	0.673	0.725
JZ191	6981	0.332	0.627	0.529	0.709
JZ180	5798	0.315	0.308	1.024	0.440
JZ179	6506	0.352	0.692	0.508	0.777
JZ178	6767	0.488	0.231	2.113	0.540
JZ181	6189	0.195	0.507	0.384	0.543
JZ161	6922	0.359	0.364	0.987	0.511
JZ160	6919	0.330	0.478	0.690	0.580
JZ158	7382	0.567	0.726	0.781	0.921
JZ177	7935	0.499	0.326	1.529	0.596
JZ176	7578	0.215	0.668	0.322	0.702
JZ183	4354	0.153	0.708	0.216	0.724

Stvořidla granite

random model

Station	Distance (m)	lnXY	lnZY	k	D
JZ163	920	2.563	1.740	1.473	3.098

Ježek-Hrouda model

Station	Distance (m)	lnXY	lnZY	k	D
JZ163	920	2.563	1.740	1.473	3.098

Sanderson-Marchini model

Station	Distance (m)	lnXY	lnZY	k	D
JZ163	920	2.807	1.995	1.407	3.444

Chapter II:

Internal structure and formation mechanisms of zoned plutons at shallow crustal levels

Article II.-2:

Magnetic fabric of the Říčany granite, Bohemian Massif (2010)

Trubač J., Žák J., Janoušek V.

Trabajos de Geología, **30**: 289–295

Status: Published

Magnetic fabric of the Říčany granite, Bohemian Massif

Jakub Trubač^{1,2,4}, Jiří Žák^{1,2}, Vojtěch Janoušek^{2,3}

¹ Institute of Geology and Paleontology, Faculty of Science, Charles University, Albertov 6, Prague, 128 43, Czech Republic

² Czech Geological Survey, Klárov 3, Prague, 118 21, Czech Republic

³ Institute of Petrology and Structural Geology, Faculty of Science, Charles University, Albertov 6, Prague, 128 43, Czech Republic

⁴ Institute of Geochemistry, Mineralogy and Mineral Resources, Faculty of Science, Charles University, Albertov 6, Prague, 128 43, Czech Republic

ABSTRACT

The Říčany pluton represents an elliptical shallow-level intrusion made up of outer, more fractionated, strongly porphyritic granite and inner, less evolved, weakly porphyritic granite. Mesoscopic foliation defines an onion-skin pattern and corresponds well with the magnetic (AMS) foliations. Magnetic lineation plunges shallowly (0–20°) and is sub-parallel to the contact in the outer part of the pluton, whereas in the pluton center lineation dips steeply (60–70°) with variable trends. We interpret the fabrics in the pluton as being a result of helical flow, whereby faster subvertical flow in low-viscosity pluton center generated subhorizontal flow in outer, higher-viscosity (phenocryst-rich) margin.

Keywords anisotropy of magnetic susceptibility (AMS), Bohemian Massif, granite, magma flow, pluton

INTRODUCTION

Unraveling the geometrical patterns and the likely physical causes of magma flow in granitic magma chambers is one of the central aspects of understanding magma chamber dynamics. In many (or most?) cases, however, direct field evidence for chamber-wide flow or convection is completely erased from the rock record. Magmatic fabrics in plutons (i.e., foliations and lineations formed during the presence of a melt; Paterson et al., 1989) commonly fail to provide unambiguous evidence for chamber-wide magma flow or convection. Instead, the preserved pluton fabrics are acquired late in magma chamber history along migrating crystallization fronts and are also easily reset by regional tectonic deformation, making inferences on large-scale convection or flow patterns difficult or rather problematic (e.g., Paterson et al., 1998).

In the present paper, we investigate an example of post-tectonic pluton (the Říčany pluton, Bohemian Massif; Fig. 1) where the magmatic fabrics have not been overprinted by regional deformation and thus likely preserve a record of internal processes and magma flow. Below we present integrated structural, microstructural, and anisotropy of magnetic susceptibility (AMS) data, which revealed an unusual pattern of magmatic fabrics in the pluton. Consequently, we discuss the significance of the observed fabrics and AMS and interpret these data to record a helical flow, a rarely documented flow mechanism in granitoid plutons.

GEOLOGICAL SETTING

The Říčany pluton of the Central Bohemian Plutonic Complex (Bohemian Massif; Fig. 1) represents a post-tectonic, shallow-level intrusion emplaced into low-grade Neoproterozoic and Lower Paleozoic siliciclastic rocks in early Carboniferous times (Fig 1; 336 ± 3.5 Ma, , unpublished ^{40}Ar - ^{39}Ar biotite data of H. Maluski, cited in Janoušek et al., 1997). In map-view, the pluton has a roughly elliptical outline (13×9 km) and is made up of three distinct granite varieties: (i) outer, strongly porphyritic, (muscovite-) biotite Říčany granite, (ii) inner, weakly porphyritic, (muscovite-) biotite Říčany granite, and (iii) a small, poorly exposed body of fine-grained, equigranular, two-mica Jevany leucogranite in the south-central part of the pluton. These granite varieties define a concentric pattern. The contact between the two porphyritic granites is gradational over several hundreds meters, the nature of outer contact of the Jevany leucogranite is unclear due to a poor exposure.

All varieties are fairly fractionated, peraluminous ($A/\text{CNK} = 1.01\text{--}1.13$), S-type granites enriched, if compared with average crustal composition (Taylor and McLennan 1995), in Large Ion Lithophile Elements (LILE: Cs, Rb, Th, U, Sr) and depleted in some High Field Strength Elements (HFSE: Nb, Ti, HREE) (Fig. 2a). In general, the major-element compositions are mutually comparable and do not vary greatly between the two facies of the Říčany granite. However, there are some conspicuous differences in the trace-element signatures. For instance, the central, weakly porphyritic facies shows markedly lower Rb, Sr, Ta and HREE contents at elevated Ba, U, Sr, Hf and Zr if compared with the outer, strongly porphyritic facies (Fig. 2b). All the rocks are characterized by fractionated REE patterns with high degree of LREE/HREE enrichment. Typical is also the presence of Eu anomalies, magnitude of which increases outwards, reaching its maximum in the strongly porphyritic Říčany granite (Fig. 2c). The degree of fractionation decreases from pluton margin inwards, the outer, strongly porphyritic granite being more evolved than the central, weakly porphyritic granite

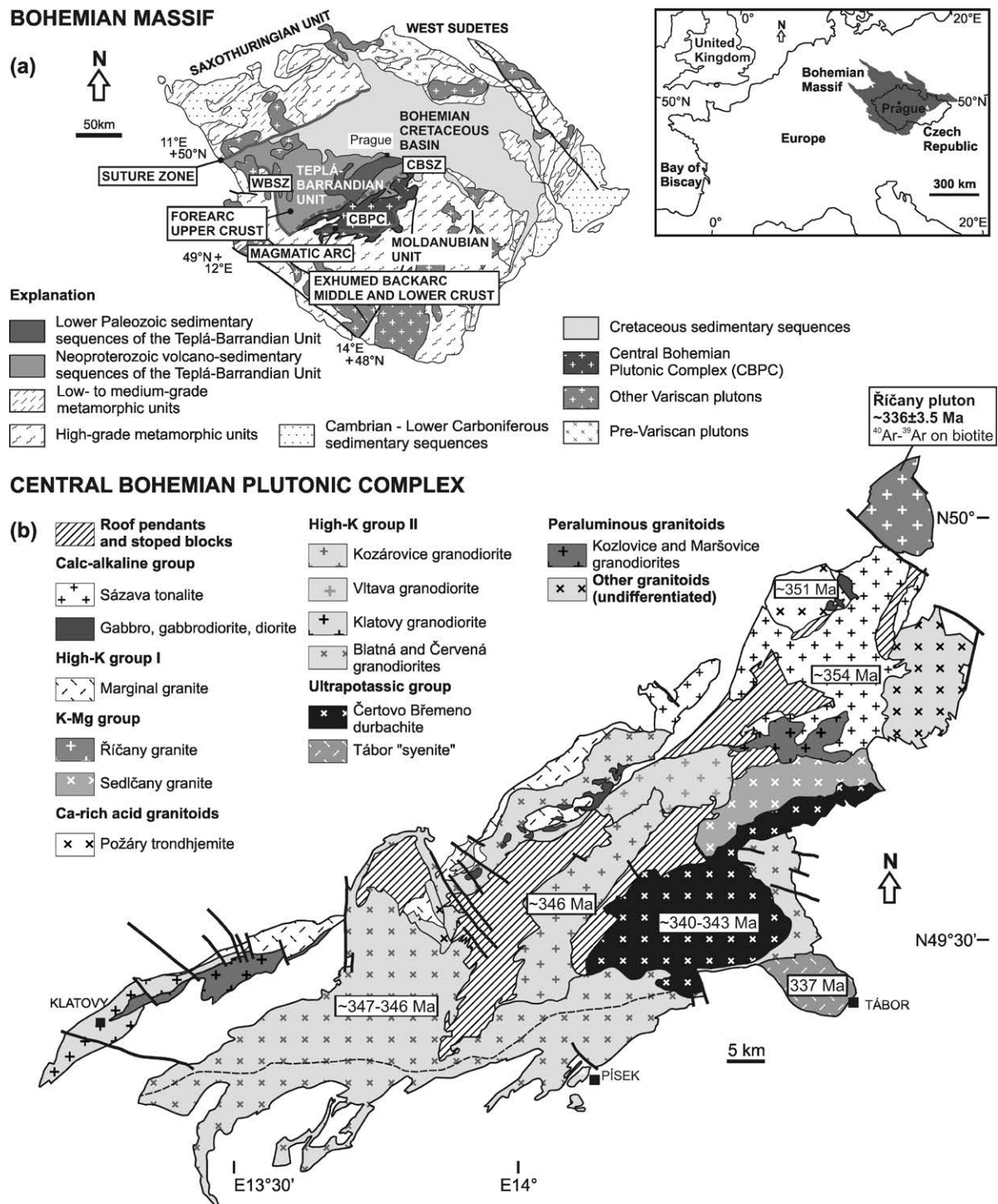


Fig. 1 Simplified geologic map of the Central Bohemian Plutonic Complex (b) and its position in the Bohemian Massif (a). The map is based on Czech Geological Survey 1:200 000 maps and Holub et al. (1997b). It shows the main intrusive units (or “types”) with some recently published radiometric ages (Holub et al. 1997a; Janoušek and Gerdes 2003).

(Janoušek et al. 1997). The position of the Jevany leucogranite is, to a large extent, independent and its genetic relation to the both Říčany granite varieties still poorly constrained (Němec 1978).

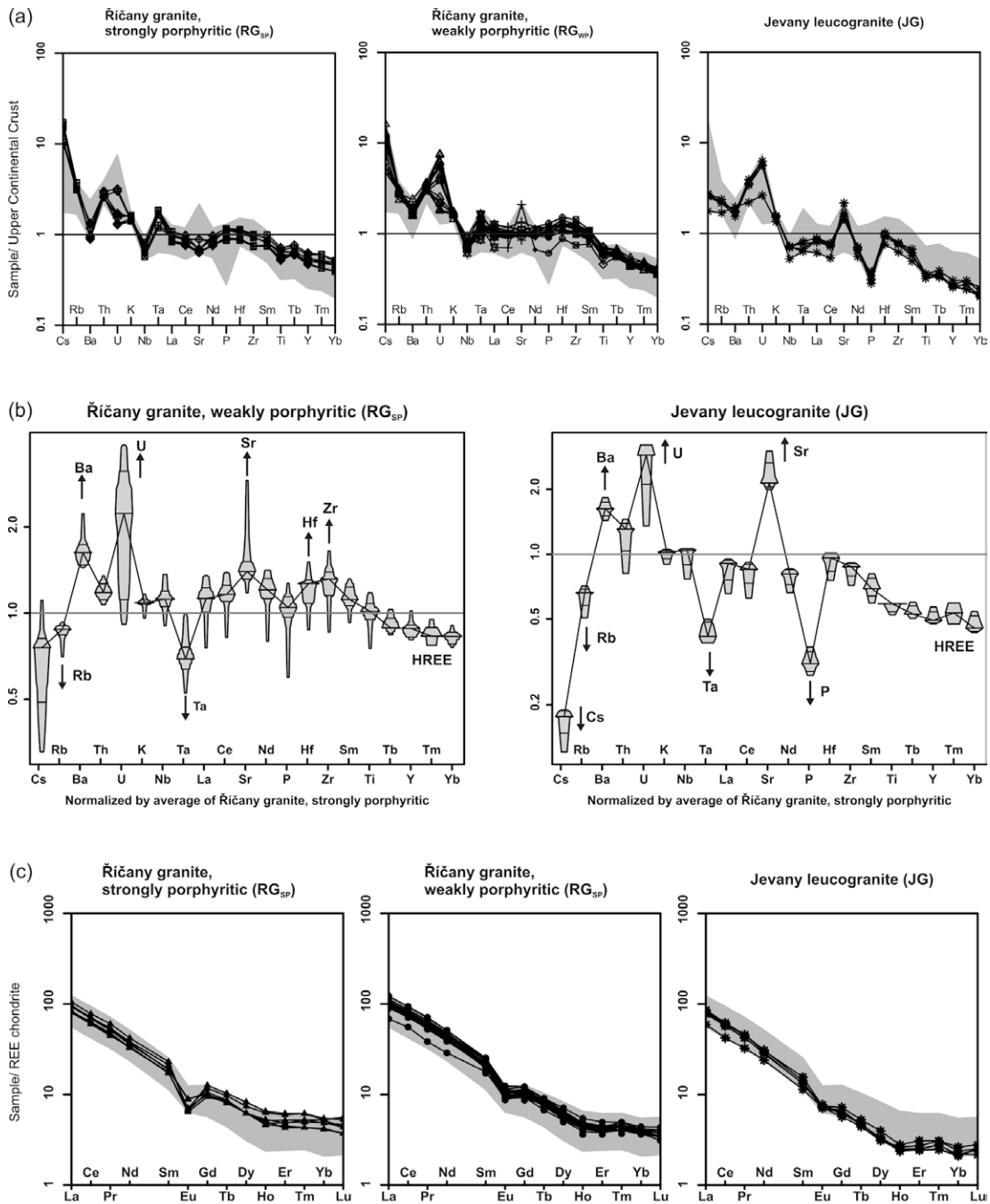


Fig. 2 (a) Spider plots normalized by average composition of the Upper Crust (Taylor and McLennan 1995) for the three main granite varieties of the Říčný pluton. (b) Spider box and percentile plots (Janoušek and Holub 2007) showing the statistical distribution of the trace-element abundances normalized by average contents in the outer, strongly porphyritic Říčný granite. (c) Chondrite normalized (Boynton 1984) REE patterns for the three main igneous pulses within the Říčný pluton.

MAGMATIC FABRIC AND ANISOTROPY OF MAGNETIC SUSCEPTIBILITY (AMS) OF THE GRANITE

Mesoscopic foliation in the porphyritic granites is defined by planar shape-preferred orientation of biotite and K-feldspar phenocrysts, lineation is mesoscopically not discernible (Fig. 3a, b). At the micro-scale, no evidence for sub-solidus deformation was observed throughout the pluton (Fig. 3c, d). The foliation dips steeply (70–80°), is subparallel to the outer contact of the pluton and is thus clearly discordant to the regional host rock structures (Fig. 4).

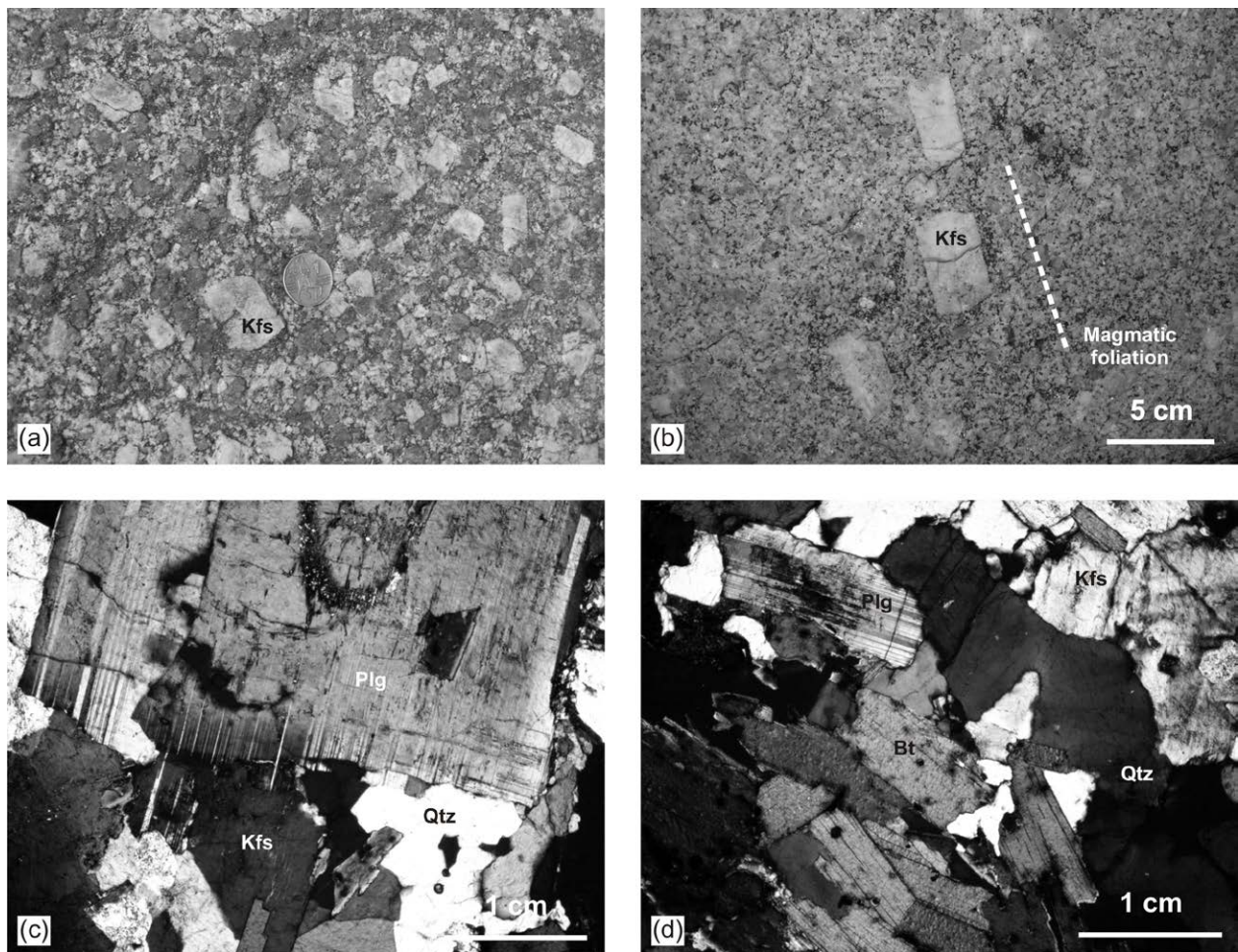


Fig. 3 (a) K-feldspar phenocrysts (up to 4 cm in size) in the strongly porphyritic Říčany granite; coin for scale. (b) Magmatic foliation defined by K-feldspar phenocrysts in the weakly porphyritic Říčany granite. (c) Photomicrograph of a magmatic texture of strongly porphyritic muscovite–biotite Říčany granite. (d) Photomicrograph of magmatic texture of weakly porphyritic muscovite–biotite Říčany granite. Crystals of main rock-forming minerals not exhibit internal solid-state deformation. The magmatic textures are typical of all granite varieties in the Říčany pluton.

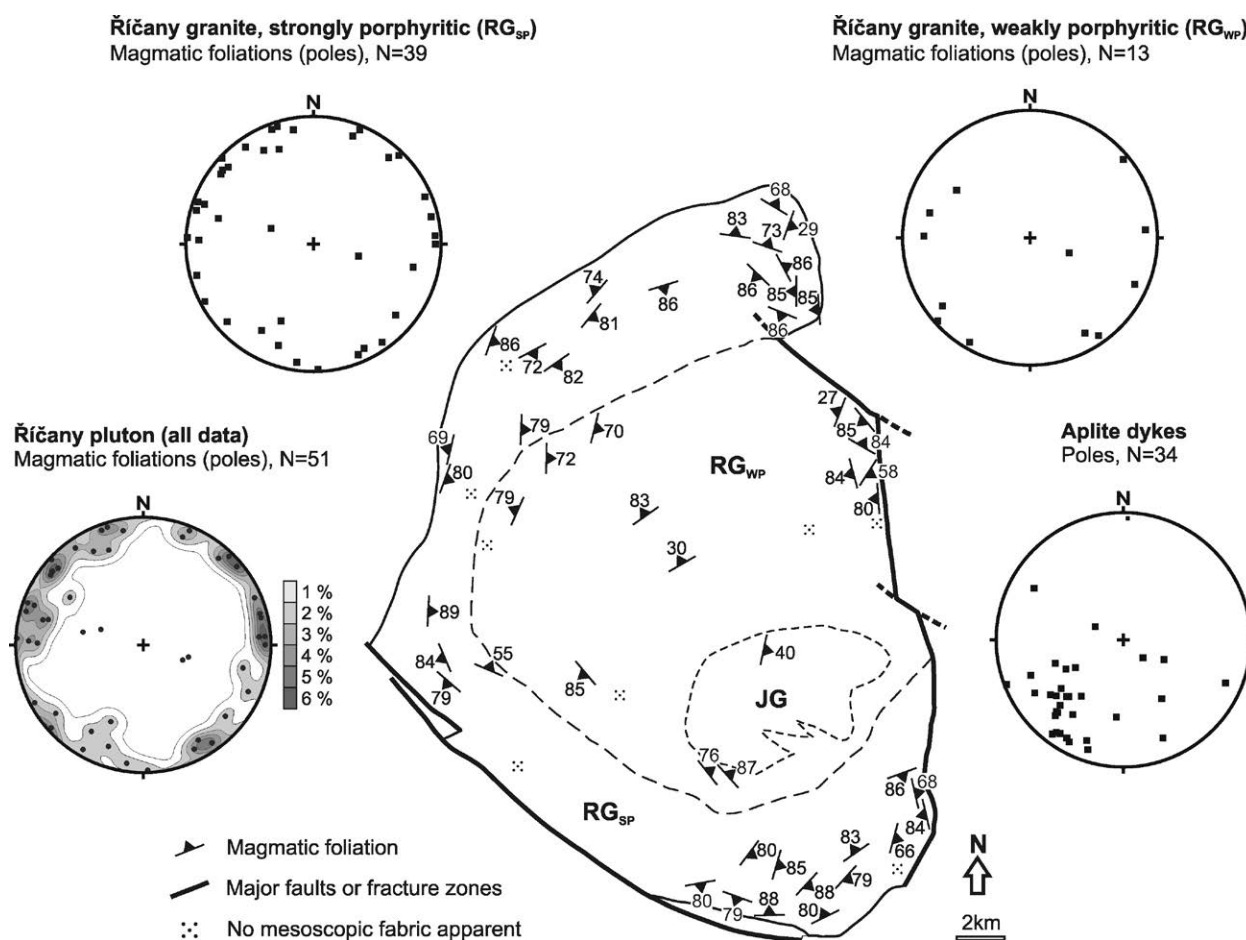


Fig. 4 Structural map to show mesoscopic magmatic foliation pattern. Stereonets (lower hemisphere, equal area projection) show orientation of magmatic foliations in each granite variety.

We used the anisotropy of magnetic susceptibility (AMS) method to investigate the magnetic fabric of the Říčany pluton in order to corroborate the structural data and to quantify the fabric parameters in the pluton. Seventy-one oriented samples were collected using a portable drill at 31 sampling sites. The AMS was measured with the KLY-4S Kappabridge apparatus and statistical analysis of AMS data was performed using the ANISOFT package of programs.

The AMS data are represented by the k_m , P , and T parameters defined as follows $k_m = (k_1 + k_2 + k_3)/3$; $P = k_1/k_3$; $T = 2 \ln(k_2/k_3) / \ln(k_1/k_3) - 1$. The k_m parameter represents the mean bulk magnetic susceptibility reflecting the qualitative and quantitative contents of magnetic minerals in the rock. The P parameter, called the degree of AMS, reflects the eccentricity of the AMS ellipsoid and thus indicates the intensity of the preferred orientation of the magnetic minerals in the rock. The higher the P parameter, the stronger is the preferred orientation. The T parameter indicates the symmetry of the AMS ellipsoid. It varies from -1 (perfectly linear magnetic fabric) through 0 (transition between linear and planar magnetic fabric) to $+1$ (perfectly planar magnetic fabric). The orientations of the

magnetic foliation poles and the magnetic lineations are presented either in contour diagram in the geographic (in situ) coordinate system or as locality means in a map.

The mean bulk magnetic susceptibility of the analyzed samples is low, ranging from 13.13×10^{-6} to 10.53×10^{-6} [SI]. Such a low susceptibility (in the order of 10^{-5}) is characteristic of paramagnetic granites (Bouchez, 1997), in which the main carriers of AMS are paramagnetic minerals. The degree of AMS (represented by parameter P) ranges from 1.009 to 1.149 in the strongly porphyritic granite and from 1.014 to 1.363 in the weakly porphyritic granite. The T parameter ranges from -0.754 to 0.904 in the strongly porphyritic granite and from -0.667 to 0.970 in the weakly porphyritic granite. No significant spatial variations in the degree of anisotropy or shape of the AMS ellipsoid were revealed in the pluton. In the Jevany leucogranite P parameter ranges from 1.07 to 1.27 and T parameter ranges from 0.1 to 0.9.

Magnetic fabric pattern (AMS) of the Říčany pluton is characterized by margin-parallel, moderately to steeply dipping magnetic foliation (Fig. 5); its geometry is consistent with the orientation of mesoscopic magmatic foliation. Foliation poles tend to concentrate along the periphery of the stereonet (Fig. 5). Magnetic lineation steepens significantly as a function of distance from the pluton margin. In the outer part of the pluton, the lineation plunges shallowly ($0-20^\circ$) and is sub-parallel to the contact whereas in the center lineation dips steeply ($60-70^\circ$) with variable trends (Fig. 5).

(a) Magnetic foliations

(b) Magnetic lineations

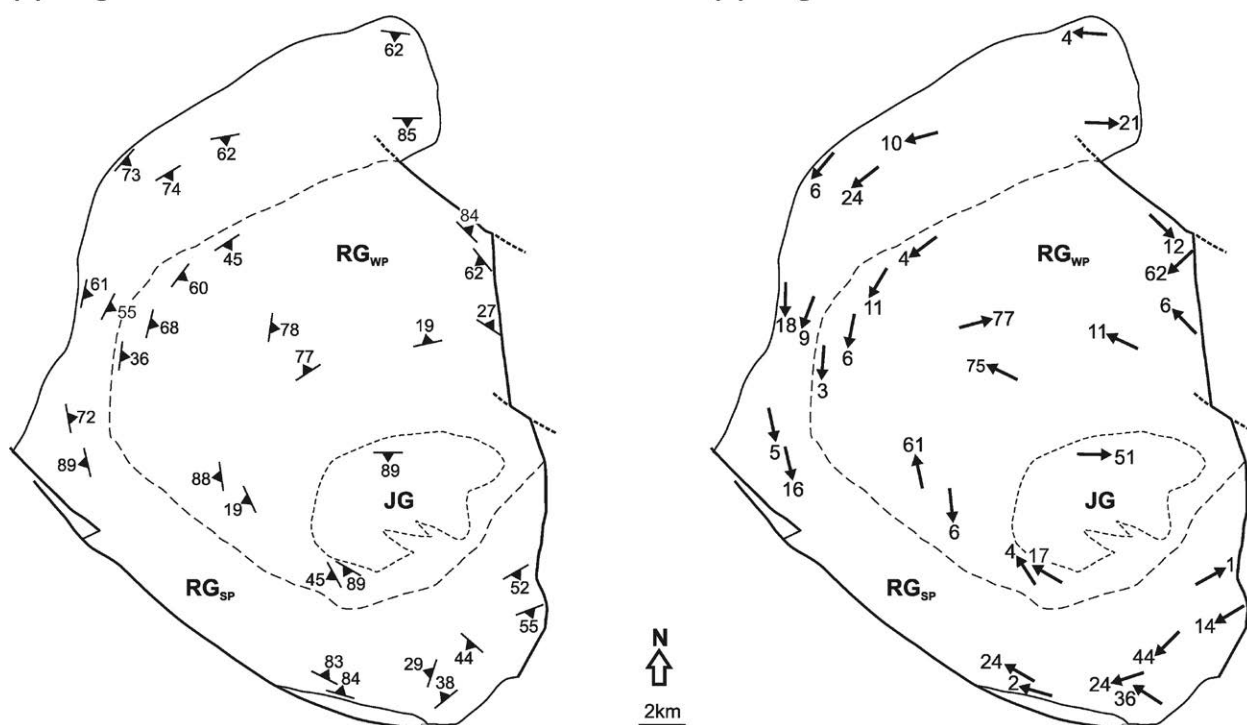


Fig. 5 Map of magnetic foliations and lineations in the Říčany pluton (AMS).

DISCUSSION AND CONCLUSIONS

Our structural and AMS data do not comply with existing models proposed for the emplacement of elliptical, onion-skin plutons (e.g., single-blob or nested diapirism, ballooning, laccolith-like emplacement). We interpret the mesoscopic and magnetic fabrics in the Říčany granite as a result of helical flow (as defined by Fowler 1996). In our model, we consider the strongly and weakly porphyritic granites as two nested magma batches having different viscosities during emplacement. We envisage that the difference in K-feldspar phenocryst content in the two granites caused significant difference in their viscosities: the outer, strongly porphyritic granite had presumably an orders of magnitude higher viscosity than the central, weakly porphyritic granite. This assumption is in agreement with an exponential increase in viscosity with crystal content as predicted by the Einstein-Roscoe equation for solid-liquid mixtures. Considering the Říčany pluton as a steep-sided cylindrical body, we can apply the Hagen-Poiseuille equation for fluid flow through pipe to infer the flow mechanism within the pluton. Contrasting viscosities of both magmas then would cause their different velocities during ascent. Consequently, faster subvertical flow of low-viscosity (phenocryst-poor) magma in the pluton center may have generated helical (subhorizontal) flow in the outer, high-viscosity and phenocryst-rich layer. This two-layer model explains well the finite fabric pattern with concentric, steep foliations and magnetic lineation being sub-horizontal along pluton margin and sub-vertical in the center. Taking into account the shallow emplacement level of the Říčany pluton, the pluton may be viewed as a conduit linking a deeper magma chamber with a volcanic system at the surface.

ACKNOWLEDGEMENTS

We would like to acknowledge comments by L.G. Corretgé which helped to improve the original version of the manuscript. This research is funded by grant of the Grant Agency of Charles University in Prague (GAUK) No. 131607 (to J. Trubač). This study is a part of Ph.D. research of Jakub Trubač.

REFERENCES

- Bouchez, J.L., 1997. Granite is never isotropic: an introduction to AMS studies of granitic rocks. In: J.L. Bouchez, D.H.W. Hutton and W.E. Stephens (Editors), *Granite: From Segregation of Melt to Emplacement Fabrics*. Kluwer Academic Publishers, Amsterdam, pp. 95–112.
- Boynton, W.V., 1984. Cosmochemistry of the rare earth elements: meteorite studies. In: P. Henderson (Editor), *Rare Earth Element Geochemistry*. Elsevier, Amsterdam, pp. 63–114.
- Fowler, T. J., 1996. The properties and geological environments of helicoids: axially symmetric surfaces in torsional and non-torsional deformations. *Journal of Structural Geology* 18, 505–517.
- Holub, F.V., Cocherie, A. and Rossi, P., 1997a. Radiometric dating of granitic rocks from the Central Bohemian Plutonic Complex: constraints on the chronology of thermal and tectonic events along the Barrandian-Moldanubian boundary. *Comptes Rendus de L' Academie des Sciences - Series IIA - Earth and Planetary Science*, 325: 19–26.
- Holub, F.V., Machart, J. and Manová, M., 1997b. The Central Bohemian Plutonic Complex: geology, chemical composition and genetic interpretation. *Journal of Geological Sciences, Economic Geology, Mineralogy*, 31: 27–50.
- Janoušek, V. and Gerdes, A., 2003. Timing the magmatic activity within the Central Bohemian Pluton, Czech Republic: conventional U-Pb ages for the Sázava and Tábora intrusions and their geotectonic significance. *Journal of the Czech Geological Society*, 48(1–2): 70–71.
- Janoušek, V. and Holub, F.V., 2007. The causal link between HP-HT metamorphism and ultrapotassic magmatism in collisional orogens: case study from the Moldanubian Zone of the Bohemian Massif. *Proceedings of the Geologists Association*, 118: 75–86.
- Janoušek, V., Rogers, G., Bowes, D.R. and Vaňková, V., 1997. Cryptic trace-element variation as an indicator of reverse zoning in a granitic pluton: the Říčany granite, Czech Republic. *Journal of the Geological Society, London*, 154: 807–815.
- Němec, D., 1978. Genesis of aplite in the Říčany massif, central Bohemia. *Neues Jahrbuch für Mineralogie, Abhandlungen*, 132: 322–339.
- Paterson, S.R. et al., 1998. Interpreting magmatic fabric patterns in plutons. *Lithos*, 44: 53–82.
- Paterson, S.R., Vernon, R.H. and Tobisch, O.T., 1989. A review of criteria for identification of magmatic and tectonic foliations in granitoids. *Journal of Structural Geology*, 11(3): 349–363.
- Taylor, S.R. and McLennan, S.M., 1995. The geochemical evolution of the continental crust. *Reviews in Geophysics*, 33: 241–265.

A photograph of a rocky outcrop with a blue geological hammer and a purple flower placed on it for scale. The hammer has a blue handle with a textured grip and a silver metal head. The flower is tall and slender with small purple blossoms. The rock surface is dark grey and shows signs of fracturing and weathering. The background is a lighter, more uniform rock surface.

**CHAPTER III:
ZONED PLUTONS IN VARIOUS TECTONIC
SETTINGS**

Chapter III:

Zoned plutons as markers of regional tectonic and geodynamic setting

Article III.-1:

Structure, emplacement, and tectonic setting of Late Devonian granitoid plutons in the Teplá–Barrandian unit, Bohemian Massif (2011)

Žák J., Kratinová Z., **Trubač J.**, Janoušek V., Sláma J., Mrlina J.

International Journal of Earth Sciences **100**: 1477–1495

Status: Published

Late Devonian granitoid plutonism in the Teplá–Barrandian unit, Bohemian Massif

Jiří Žák^{1,2}, Zuzana Kratinová^{3,4}, Jakub Trubač^{1,5}, Vojtěch Janoušek^{5,6}, Jiří Sláma^{7,8},

Jan Mrlina³

¹ Institute of Geology and Paleontology, Faculty of Science, Charles University, Albertov 6, Prague, 12843, Czech Republic

² Czech Geological Survey, Klárov 3, Prague, 11821, Czech Republic

³ Institute of Geophysics, Academy of Sciences of the Czech Republic, Boční II/1401, Prague, 14131, Czech Republic

⁴ Universidade Lisboa, CGUL/IDL, Edifício C8, 1749-016 Lisbon, Portugal

⁵ Czech Geological Survey, Geologická 6, Prague, 15200, Czech Republic

⁶ Institute of Petrology and Structural Geology, Charles University, Faculty of Science, Albertov 6, Prague, 12843, Czech Republic

⁷ Centre for Geobiology and Department of Earth Science, University of Bergen, Allegaten 41, N-5007 Bergen, Norway

⁸ Institute of Geology, Academy of Sciences of the Czech Republic, v.v.i., Rozvojová 135, Prague 6, 165 02, Czech Republic

ABSTRACT

The Štěnovice and Čistá granodiorite–tonalite plutons are small (~27 and ~38 km², respectively) intrusions that are largely discordant to regional ductile structures in the center of the upper-crustal Teplá–Barrandian unit, Bohemian Massif. Their whole-rock and trace-element compositions are consistent with medium-K calc-alkaline magma, generated above a subducted slab in a continental margin arc setting. The U–Pb zircon age of the Štěnovice pluton, newly determined at 375 ± 2 Ma using the laser ablation ICP-MS technique, is within the error of the previously published Pb–Pb age of 373 ± 1 Ma for the Čistá pluton. The two plutons also share other characteristics that are typical of concentrically expanded plutons (CEPs), such as elliptical cross-section in plan view, steep contacts, inferred downward-narrowing conical shape, faint normal zoning, and margin-parallel magmatic foliation decoupled from the regional host-rock structures. We interpret the Štěnovice and Čistá plutons as representing the initial Late Devonian stage of much more voluminous early Carboniferous arc-related plutonism (represented most typically by the Central Bohemian Plutonic Complex) in the upper crust of the central Bohemian Massif. These two plutons are important tectonic elements in that they indicate an overall shift of the arc-related plutonic activity from the ~NW to the ~SE, accompanied with a general compositional trend of the magmas from

medium-K calc-alkaline to shoshonitic/ultrapotassic. Such a pattern is compatible with SE-directed subduction of the Saxothuringian Ocean beneath the Teplá–Barrandian overriding plate as a cause of arc-related magmatism in this part of the Bohemian Massif.

Keywords: Bohemian Massif, Granite, Pluton, Subduction, Teplá–Barrandian unit, Variscan orogeny

INTRODUCTION

The Variscan orogeny in the Bohemian Massif was accompanied by episodic granitoid plutonism throughout the development of the orogen, with several peaks of plutonic activity during Carboniferous that are now well characterized by a large body of geochemical and geochronologic data (e.g., Janoušek *et al.* 1995, 2000, 2004a; Finger *et al.* 1997, 2009; Holub *et al.* 1997a, b; Siebel *et al.* 1997, 1999, 2003, 2008; Gerdes *et al.* 2000a, b, 2003; Gerdes 2001; Štemprok *et al.* 2003; Kovaříková *et al.* 2007, 2010; Slaby and Martin 2008; Kusiak *et al.* 2010; Timmerman 2008; Dörr and Zulauf 2010; Kotková *et al.* 2010). On the contrary, the initial Late Devonian (Frasnian to Famennian) calc-alkaline plutonism has been poorly documented despite its potential key role for interpreting the timing and polarity of Variscan subductions and constraining the ages and loci of early orogenic deformation. Compared to the voluminous Carboniferous plutonism, the Late Devonian granitoids and meta-granitoids are sparse, small intrusions localized in the upper-crustal Teplá–Barrandian unit (TBU) of the central Bohemian Massif (Fig. 1). The reported occurrences of the Late Devonian (meta-)granitoids include the ~380–365 Ma Staré Sedlo and Mirovice orthogneiss complexes (Fig. 1b; Košler *et al.* 1993, 1995), the ~359 Ma Teufelsberg diorite pluton (Fig. 1b; Bues *et al.* 2002; Dörr and Zulauf 2010) near the present-day Teplá–Barrandian/Moldanubian boundary, and the ~373 Ma Čistá granodiorite pluton in the north-central TBU (Fig. 1b; Klomínský 1963; Chlupáčová *et al.* 1975; Kopecký *et al.* 1997; Venera *et al.* 2000). Another pluton, the previously largely unexplored Štěnovice granodiorite–tonalite, intruded the Neoproterozoic basement of the south-central TBU (Fig. 1b; Klomínský 1965). The age of the Štěnovice intrusion has not been determined before by modern geochronologic methods; however, many similarities in the field relations and composition with the Čistá pluton were noted as early as in the 1960s (Klomínský 1965; Bartošek *et al.* 1969). The goal of this paper is to provide an integrated overview of the principal field, geophysical, and geochemical characteristics of the Štěnovice and Čistá plutons (Fig. 1b). We first describe our new data from the Štěnovice pluton, including field observations, host-rock and pluton microstructures, gravimetry, whole-rock geochemistry, zircon geochronology,

Zoned plutons as markers of regional tectonic and geodynamic setting

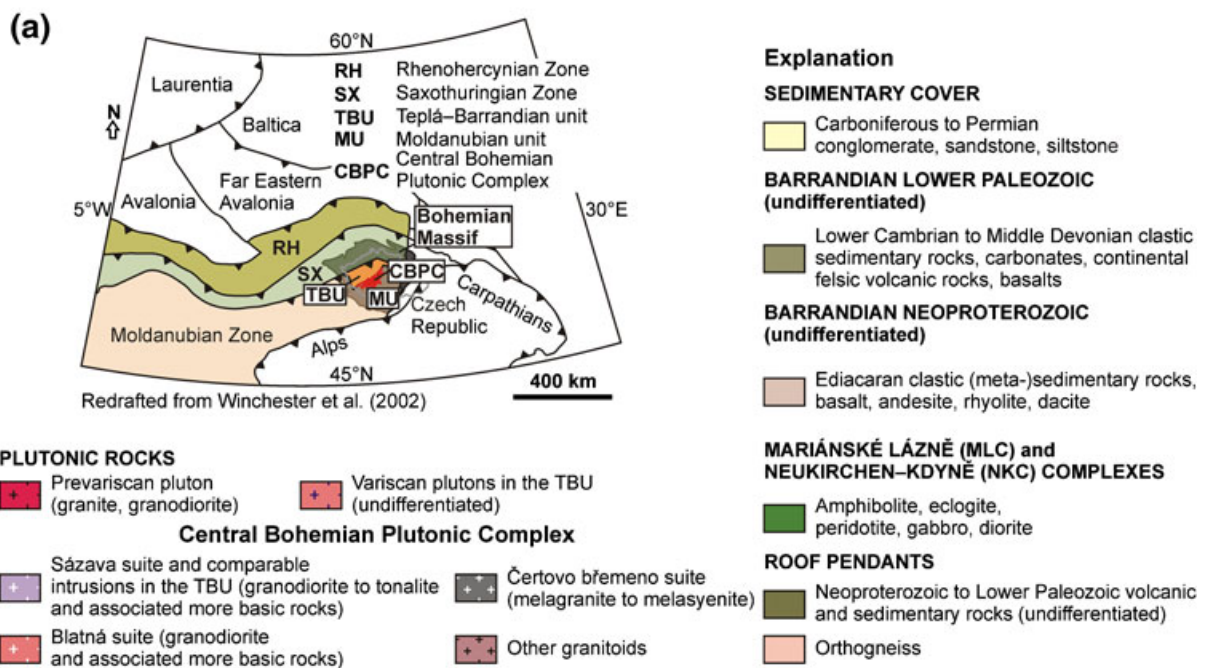
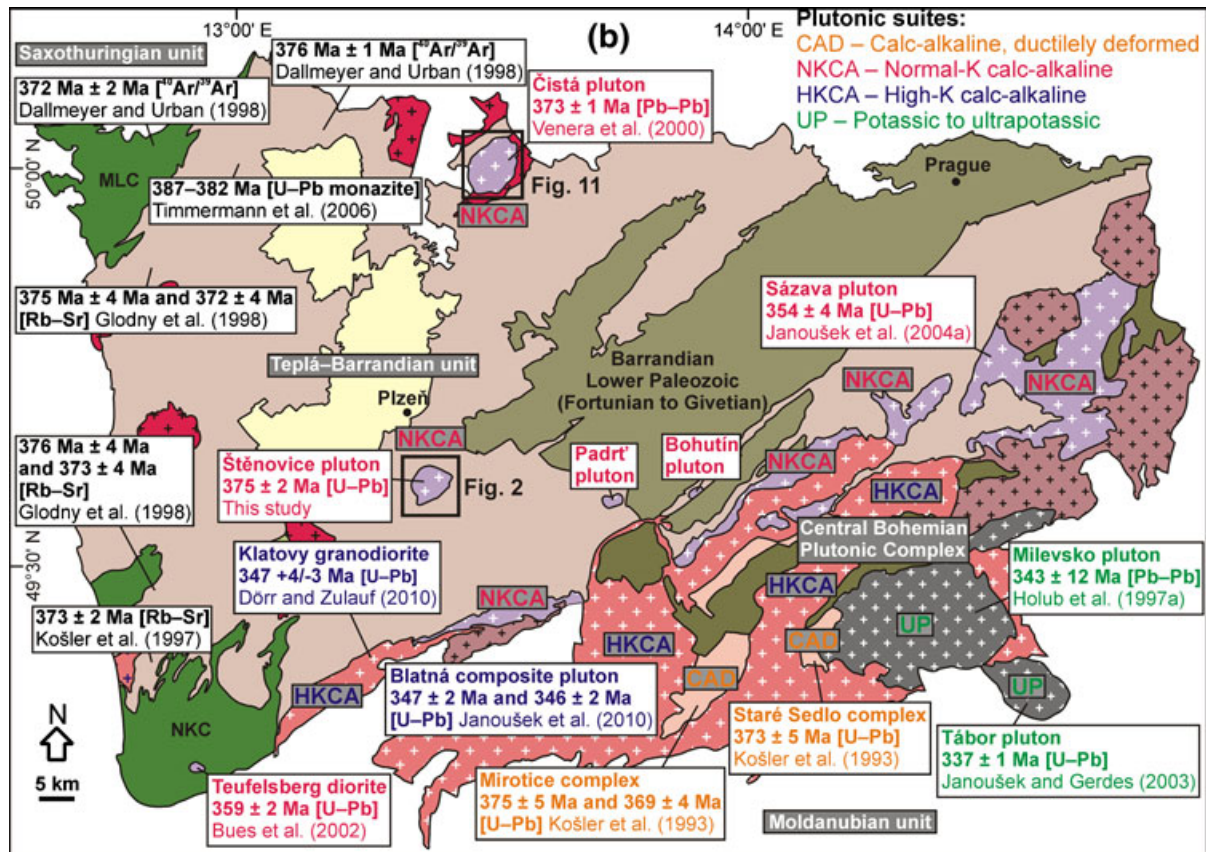


Fig. 1 (a) Greatly simplified map of basement structure and Variscan lithotectonic zonation of Europe showing main units and suture zones in the Bohemian Massif as discussed in the text; modified after Winchester (2002). **(b)** Simplified geologic map of the Teplá–Barrandian unit (TBU) showing the arc-related plutons including the two Late Devonian plutons examined in this study (bold rectangles). The Ar–Ar (Bt), Rb–Sr (Bt), and U–Pb (monazite) ages indicate the Late Devonian cooling after tectonothermal activity in the western part of the TBU, while the U–Pb and Pb–Pb zircon ages of plutonic suites illustrate the Late Devonian to early Carboniferous shift of plutonism from the ~NW to the ~SE accompanied by a general compositional trend of the magmas from medium-K calc-alkaline to shoshonitic/ultrapotassic. Geology based on 1:500,000 Geologic map of the Czech Republic published by the Czech Geological Survey in 2007.

and anisotropy of magnetic susceptibility (AMS). To provide readers with a complete picture, the Čistá pluton is then briefly described utilizing our field observations and large existing data sets acquired by others. Finally, we interpret the structure and emplacement mode of these two plutons and discuss their tectonic significance for reconstructing the initial stages of the Variscan orogeny and polarity of subductions in the Bohemian Massif.

THE ŠTĚNOVICE PLUTON—FIELD RELATIONSHIPS AND PETROGRAPHY

The Štěnovice pluton is weakly elliptical (5.5×5 km, ~ 27 km²) in plan view with its long axis oriented ~NE–SW (Fig. 2). The pluton intruded the low-grade Neoproterozoic (Ediacaran) basement rocks of the TBU, represented here by prehnite–pumpellyite to lower greenschist facies slates and (meta-) graywackes enclosing lenses of chert and elongated to irregular bodies of metabasalt. Away from the pluton, the regional trend of lithologic contacts, cleavage, and large-scale folds is ~NE–SW. The outer pluton/wall-rock contact, where not concealed by the Quaternary cover, is intrusive (sharp and non-sheeted), steep, or dips steeply to moderately (50–70°) outward along the northwestern pluton margin (Fig. 2).

The pluton has a well-developed thermal and structural aureole parallel to its outer margin. The thermal aureole, defined as a zone of detectable contact metamorphism around the pluton, is up to 600 m wide. The meta-graywackes in the contact aureole are characterized by spaced low-temperature pressure-solution cleavage, developed as short to continuous cleavage domains anastomosing around larger subangular detrital grains (Electronic Supplementary Material–ESM, Part 1a). During the contact metamorphism, irregular biotite aggregates grew preferentially along the cleavage domains but biotite also occurs as smaller grains in the fine-grained matrix (ESM, Part 1a).

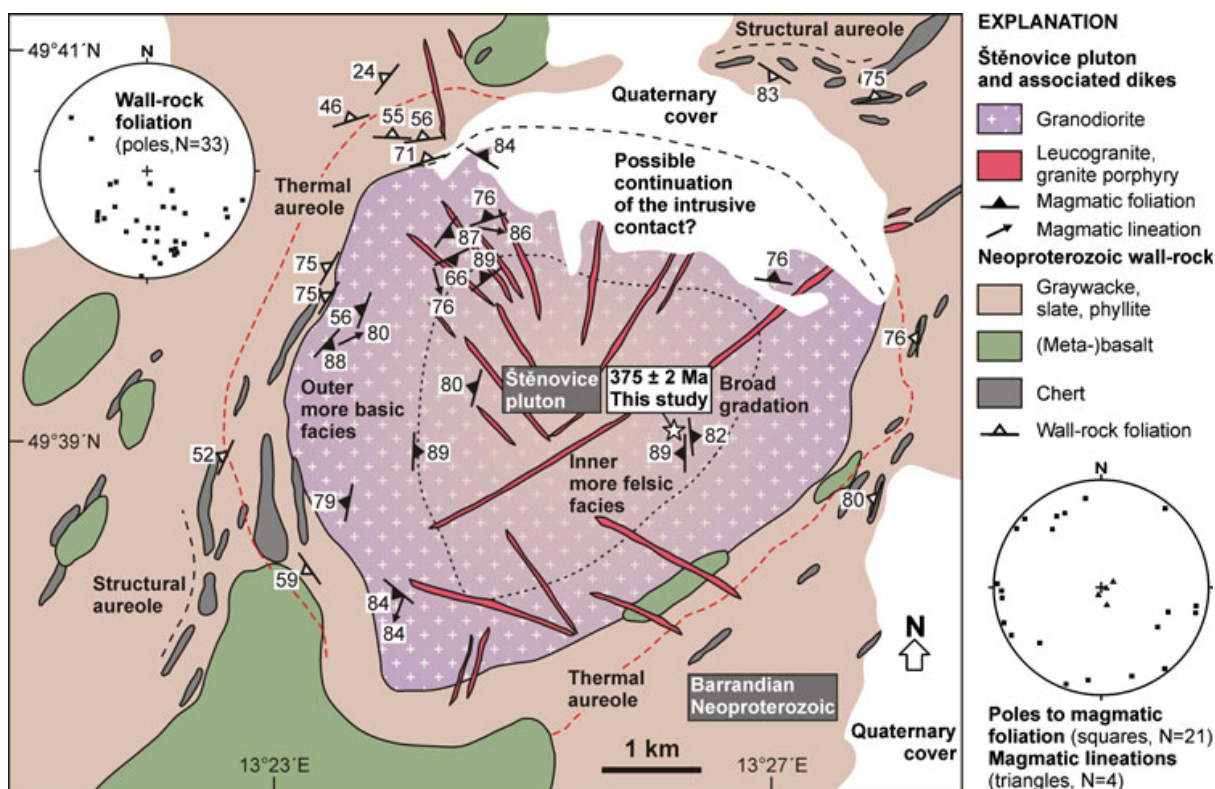


Fig. 2 Combined geologic and structural map of the Štěnovice pluton, associated dikes, and its Barrandian Neoproterozoic wall-rock. Stereonets (lower hemisphere, equal area projection) show orientations of wall-rock cleavage and of magmatic foliation and lineation in the pluton. Star indicates location of the geochronologic sample ZK-7. Geology based on Czech Geological Survey 1:50,000 map sheet 22-11 Přeštice.

The cherts in the thermal aureole have locally a well-developed foliation and host folded quartz veins (ESM, Part 1b).

The structural aureole, defined as a zone where the background (regional) host-rock structures have been overprinted by emplacement-related deformation, can be clearly delimited near the northern and southern ends of the pluton where the intrusive contact is at an angle to the regional host-rock markers (foliation, lithologic contacts). Crossing the aureole boundary, the host-rock markers are deflected from their regional orientation (~NE–SW) toward parallelism with the pluton margin (Fig. 2). The structural aureole is ~1 km wide, that is, approximately 1/3 of pluton radius and almost twice as wide as the thermal aureole.

The pluton is composed of medium-grained (~2–5 mm grain size) equigranular hornblende–biotite granodiorite to tonalite (ESM, Part 2a) and exhibits a faint normal compositional zoning defined by a more mafic outer facies grading into a more felsic center (Fig. 2; Klomínský 1965). The average modal composition of the granodiorite is 58% plagioclase (with normal oscillatory zoning), 20%

quartz, 11% K-feldspar, 5% biotite, and 4% amphibole (Klomínský 1965). The modal proportion of plagioclase relative to K-feldspar decreases inward within the pluton (Klomínský 1965). Common accessories are apatite, zircon, titanite, and opaque minerals (chiefly magnetite). Scattered decimeter-sized mafic microgranular enclaves composed mainly of diorite to quartz diorite (ESM, Part 2b–d), documenting multiple interactions between grano- dioritic and more mafic magmas (ESM, Part 2d; Vernon 1984; Didier and Barbarin 1991), occur throughout the pluton but are more common in the outer facies and sparse in the pluton center. Host-rock xenoliths (centimeter- to decimeter-sized) are rare. The pluton is cross-cut by more or less radially arranged leucogranite, aplite, and granite porphyry dikes (Fig. 2).

At the microscale, the textures are exclusively magmatic with no evidence for subsolidus deformation (defined using the criteria outlined in Paterson *et al.* 1989 and Vernon 2000); amphibole and feldspar grains have euhedral to subhedral shapes, and interstitial anhedral quartz is not recrystallized (ESM, Part 3a). Relatively abundant are microstructures indicative of material exchange/thermal disequilibrium due to the mixing between mafic and felsic magmas, such as mantled plagioclase, mixed acicular/ equant apatite grain populations, and resorbed biotite flakes enclosed in large euhedral to subhedral amphibole crystals (ESM, Part 3b–d; e.g., Hibbard 1991, 1995; Janoušek *et al.* 2004a and references therein)

GRAVIMETRIC CONSTRAINTS ON THE ŠTĚNOVICE PLUTON SHAPE

In this study, gravity data are used to constrain approximately the overall shape and the minimum vertical dimension of the Štěnovice pluton at depth. The gravity maps in Fig. 3a, b were constructed using the data owned by Geofond, Prague (Czech Republic), the gravity stations were positioned in a random grid and spaced 400–500 m apart (Fig. 3a, b).

The principal feature in the central part of the gravity map is a positive anomaly corresponding to the Neoproterozoic metabasalts and a negative anomaly reflecting the Carboniferous cover to the NW. The pronounced gravity minimum of an elliptical, ~NE–SW elongated shape (Fig. 3a) corresponds to the Štěnovice pluton. In order to better constrain the subsurface shape of the pluton, high-pass filtering was applied to construct the residual gravity map (Fig. 3b). This map also reveals an internal zoning within the pluton with the highest negative anomaly in the pluton center and along its southern margin (Fig. 3b). The rock densities (defined as a bulk density with all pore space filled by water) used in the modeling are granodiorite $\rho = 2.67\text{--}2.68\text{ g cm}^{-3}$, Neoproterozoic (meta-)sedimentary rocks $\rho = 2.70\text{--}2.75\text{ g cm}^{-3}$, and metabasalts $\rho = 2.85\text{--}2.95\text{ g cm}^{-3}$. On the

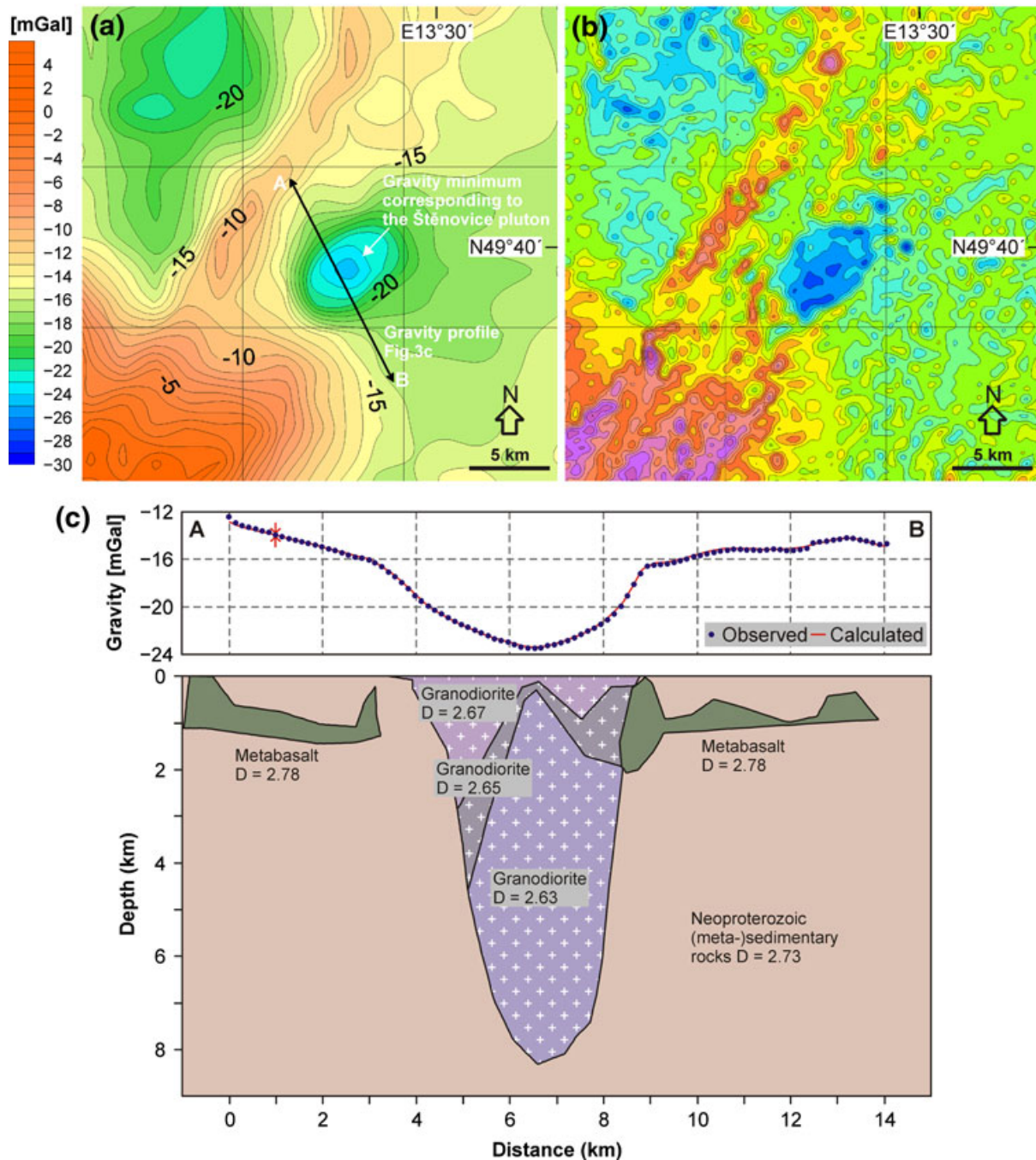


Fig. 3 (a) Gravity map showing a pronounced negative gravity anomaly corresponding to the Štěnovice pluton. (b) Residual gravity map (high-pass filter) highlights the Neoproterozoic metabasalts (~NE–SW-trending clusters of local positive gravity anomalies) and a negative gravity anomaly of the Štěnovice pluton. c Gravity/ density model of the Štěnovice pluton. D - density in g cm⁻³.

basis of simple modeling by Mrlina (1993) and our new 2.5D gravity modeling, the pluton seems to have a higher density in its upper part ($\rho = 2.65\text{--}2.67\text{ g cm}^{-3}$) and a lower density deeper section ($\rho = 2.63\text{--}2.65\text{ g cm}^{-3}$; Fig. 3c). The minimum vertical dimension of the pluton is estimated as $\sim 6\text{--}8$ km, and the pluton shape at depth is inferred as a steep-sided, downward-narrowing elliptical cone with its axis located close to the center of the gravity anomaly (Fig. 3c).

WHOLE-ROCK GEOCHEMISTRY

Six samples were taken in abandoned or active quarries to examine the whole-rock geochemical variations in the Štěnovice pluton (see Fig. 4 for sample locations, geo-graphic coordinates are given in ESM, Part 4). The samples were analyzed for major- and trace-element whole-rock composition in the Activation Laboratories Ltd., Ontario, Canada (<http://www.actlabs.com>; using the 4Litho-research and Ultratrace-2 analytical packages). The samples were dissolved following the lithium metaborate/tetraborate fusion, analyses were carried out using ICP-MS/OES except for precious and base metals determined by aqua regia digestion and analyzed on ICP-MS. In addition, the new whole-rock analyses (ESM, Part 4) were supplemented by major-element data from the literature (Klomínský 1965; Breiter and Sokol 1997; Kopecký *et al.* 1997) and, for comparison, by the available analyses of the Čistá granodiorite (Klomínský 1965; Čadková *et al.* 1985; Breiter and Sokol 1997). All the data were then recalculated and plotted using the GCDkit software (Janoušek *et al.* 2006a)

MAJOR ELEMENTS

Based on the newly obtained data, the granitoid rocks of the Štěnovice pluton are fairly acid ($\text{SiO}_2 = 66.6\text{--}69.7\text{ wt. \%}$), corresponding to granodiorite–tonalite in the multicationic P–Q diagram of Debon and Le Fort (1983; Fig. 4a); several analyses published in the literature indicate intermediate, quartz dioritic to dioritic composition (Fig. 4a–b). The samples reveal a tendency to somewhat more felsic compositions in the pluton center compared to the margin. The Štěnovice pluton is made up of exclusively subalkaline rocks, as demonstrated by the TAS diagram (Fig. 4b), that define a calc-alkaline trend in the AFM plot (Fig. 4c; Irvine and Baragar 1971). All but one felsic sample ($\text{SiO}_2 > 65\text{ wt. \%}$) can be characterized as medium-K rocks on the basis of the $\text{SiO}_2\text{--K}_2\text{O}$ diagram (Peccerillo and Taylor 1976; Fig. 4d). On the other hand, the more basic lithologies straddle the boundary with the adjacent low-K field. The Štěnovice granitoids are generally metaluminous, as shown by the Shand's index A/CNK (molar $\text{Al}_2\text{O}_3/(\text{CaO} + \text{Na}_2\text{O} + \text{K}_2\text{O})$) ranging from 0.95 to 0.98 (Fig. 4e; ESM, Part 4); only a few samples are subaluminous having A/CNK up to 1.03.

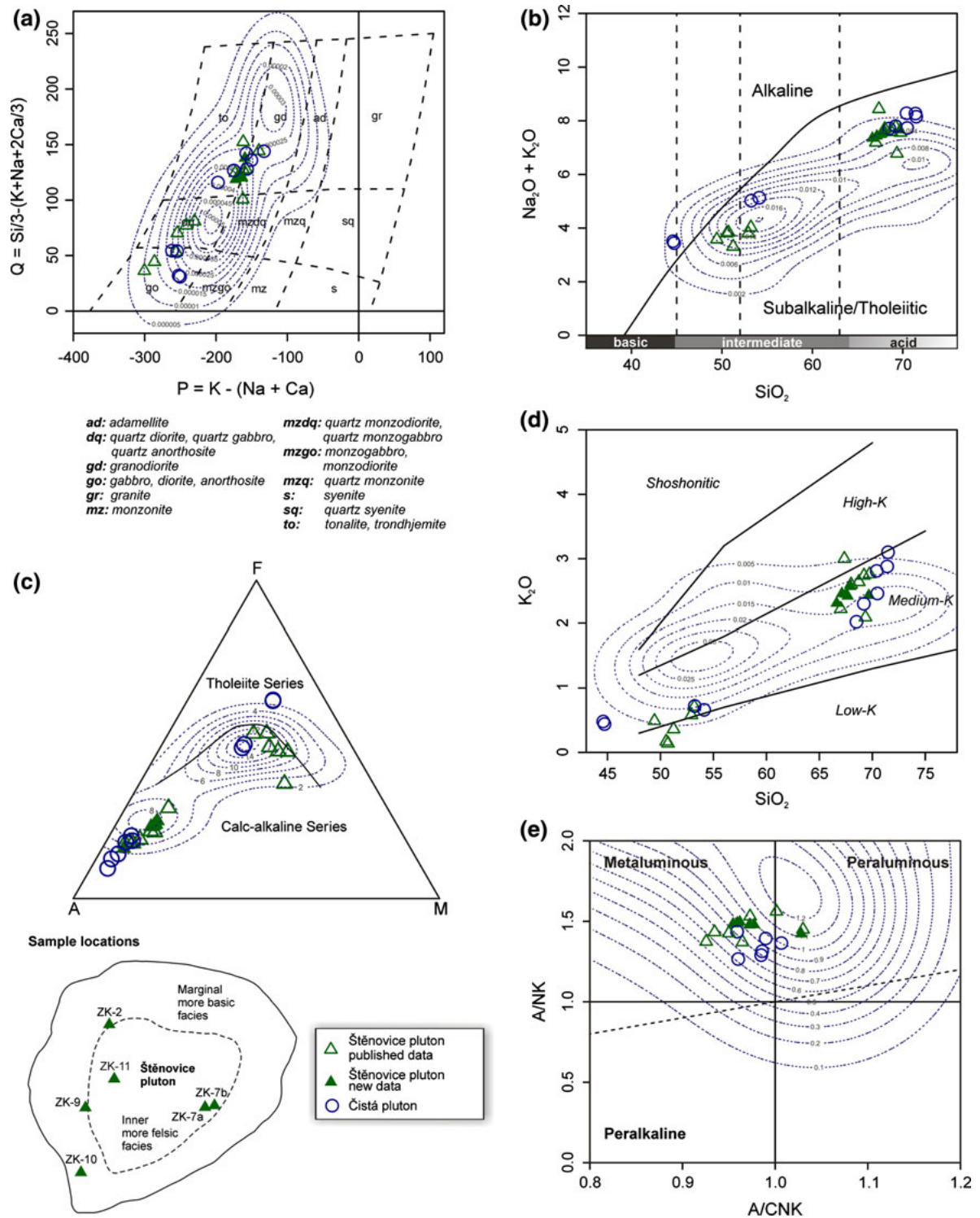


Fig. 4 Major-element-based classification of the Štěnovice and Čistá granitoids. The isolines as plotted by GCDkit (Janoušek et al. 2006a) portray the statistical distribution of the medium-K calc-alkaline Sázava suite, Central Bohemian Plutonic Complex (Janoušek et al. 2000, 2004a and unpublished data). (a) Multi-cationic P–Q plot (Debon and Le Fort 1983); *P* represents the proportion of K-feldspar to plagioclase and *Q* the quartz content. (b) SiO_2 – $\text{Na}_2\text{O} + \text{K}_2\text{O}$ (TAS) diagram with the discrimination boundary between the

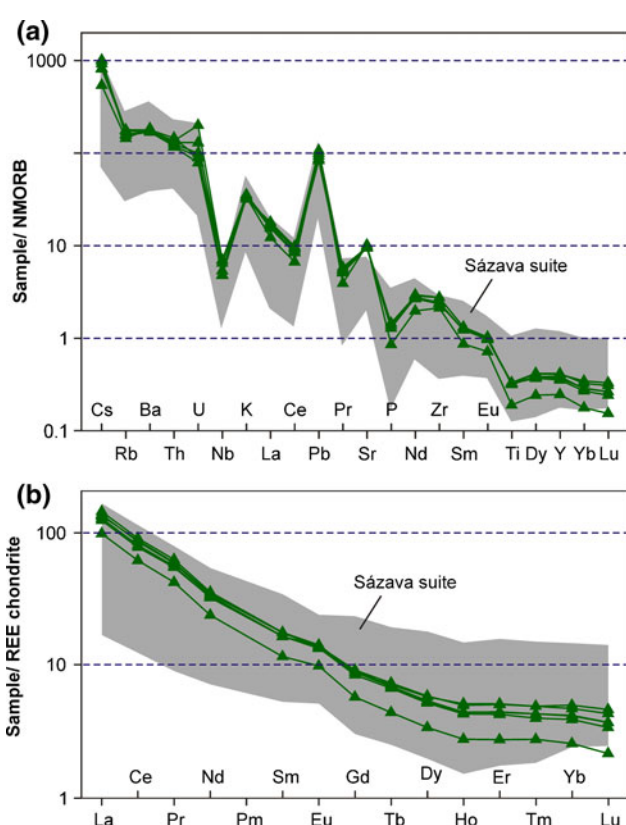
subalkaline and alkaline domains after Irvine and Baragar (1971). (c) AFM diagram ($A = \text{Na}_2\text{O} + \text{K}_2\text{O}$, $F = \text{FeO}_t$, $M = \text{MgO}$, all in wt. %: Irvine and Baragar 1971). (d) SiO_2 – K_2O plot with the discrimination boundaries between the low-K, medium-K, high-K calc-alkaline, and shoshonitic rocks of Peccerillo and Taylor (1976). The more basic types correspond to low-K, whereas the acid rocks belong mostly to a medium-K association. (e) Molar $\text{Al}_2\text{O}_3 / (\text{CaO} + \text{Na}_2\text{O} + \text{K}_2\text{O})$ vs $\text{Al}_2\text{O}_3 / (\text{Na}_2\text{O} + \text{K}_2\text{O})$ (A/CNK vs A/NK, Shand 1943) plot of Maniar and Piccoli (1989) discriminating between metaluminous, peraluminous and peralkaline compositions. The plotted data points are metaluminous–subaluminous. Inset sketch map shows locations of geochemical sample

The mg number ($\text{mg}\# = \text{molar Mg}/(\text{Mg} + \text{Fe}_t)$) of the newly collected samples varies only a little between 40 and 45, and sodium prevails significantly over potassium ($\text{K}_2\text{O}/\text{Na}_2\text{O} = 0.46$ – 0.51 ; ESM, Part 4).

TRACE ELEMENTS

The compositions of the newly collected samples were normalized by average normal mid-ocean ridge basalt (NMORB; Sun and McDonough 1989; Fig. 5a). The patterns are all enriched in LILE (Rb, Ba, Th, U, and K), starting at $>140 \times \text{NMORB}$ (Rb, Ba) and falling to less than $0.3 \times \text{NMORB}$ (Lu). All show superimposed peaks in Cs, Pb, and Sr; however, the most typical is a strong depletion in HFSE (troughs in Nb, P, and Ti).

The REE contents in the Štěnovice pluton do not vary significantly ($\Sigma\text{REE} = 107.6$ – 159.1 ; ESM, Part



4). The chondrite-normalized patterns have a slightly curved (convex down) shape with a fair degree of LREE/HREE enrichment ($\text{La}_N / \text{Yb}_N = 27.4$ – 38.2).

Fig. 5 Trace-element distribution in the studied granitoids of the Štěnovice pluton. a Normal Mid-Ocean Ridge Basalt (NMORB) normalized spider plots (Sun and McDonough 1989). b Chondrite-normalized (Boynton 1984) REE patterns. The shaded field denotes the range of compositions known from the medium-K calc-alkaline Sázava suite, Central Bohemian Plutonic Complex (Janoušek *et al.* 2000, 2004a and unpublished data)

They start at approximately $100\text{--}145 \times$ chondrite (La) and drop to $2.2\text{--}4.7 \times$ chondrite (Lu); typical is a weak positive Eu anomaly ($\text{Eu}/\text{Eu}^* = 1.1\text{--}1.2$; Fig. 5b).

The Zr concentrations broadly decreasing with silica indicate that saturation in zircon was reached, the occurrence of inheritance unlikely, and the zircon thermometry is applicable (Watson and Harrison 1983; Hoskin *et al.* 2000; Miller *et al.* 2003; Janoušek 2006). The calculated mean zircon saturation temperature is $783 \pm 14 \text{ }^\circ\text{C}$ (2σ , excluding the calibration and analytical errors).

INFERENCES ON GEOTECTONIC SETTING OF THE ŠTĚNOVICE PLUTON

In the NMORB-normalized spiderplots, the LILE/HFSE enrichments and deep troughs in HFSE of the analyzed samples resemble those observed in K-rich basalts in the continental margin arc settings (e.g., Saunders *et al.* 1991; Pearce and Parkinson 1993; Tatsumi and Eggins 1995). The new data including those compiled from the literature (Čadková *et al.* 1985; Breiter and Sokol 1997) confirm such a notion (see selected diagrams in Fig. 6). For instance, in the Y vs. Nb and Ta + Yb vs. Rb plots after Pearce *et al.* (1984), all the samples fall into the Volcanic Arc Granites domain (VAG in Fig. 6a–b). Similarly, in the Ta/Yb vs. Th/Ta as well as Yb vs. Th/Ta diagrams (Schandl and Gorton 2002) the Štěnovice analyses occupy the Active Continental Margins field (ACM in Fig. 6c–d).

NEW ZIRCON GEOCHRONOLOGY OF THE ŠTĚNOVICE PLUTON

The sample for zircon dating (ZK-7) was taken in an active quarry near Štěnovický Borek ~1 km ESE of the pluton center (Fig. 2; WGS84 coordinates are N49.64991032°, E13.43986331°). The zircon grains were separated from the sample using the Wilfley shaking table and heavy liquids and were then mounted in epoxy-filled block and polished. Isotopic analysis of zircon by laser ablation ICP-MS followed the technique described in Košler *et al.* (2002) and in Košler and Sylvester (2003). A Thermo-Finnigan Element 2 sector field ICP-MS coupled to a 213 NdYAG laser (New Wave Research UP-213) at Bergen University, Norway, was used to measure Pb/U and Pb isotopic ratios in zircons. The sample introduction system was modified to enable simultaneous nebulization of a tracer solution and laser ablation of the solid sample (Horn *et al.* 2000). Natural TI ($^{205}\text{Tl}/^{203}\text{Tl} = 2.3871$; Dunstan *et al.* 1980), ^{209}Bi and enriched ^{233}U and ^{237}Np (> 99%) were used in the tracer solution, which was aspirated to the plasma in an argon–helium carrier gas mixture through an Apex desolvation nebulizer (Elemental Scientific) and a T-piece tube attached to the back end of the plasma torch. A helium gas line carrying the sample from the laser cell to the plasma was also attached to the T-piece tube.

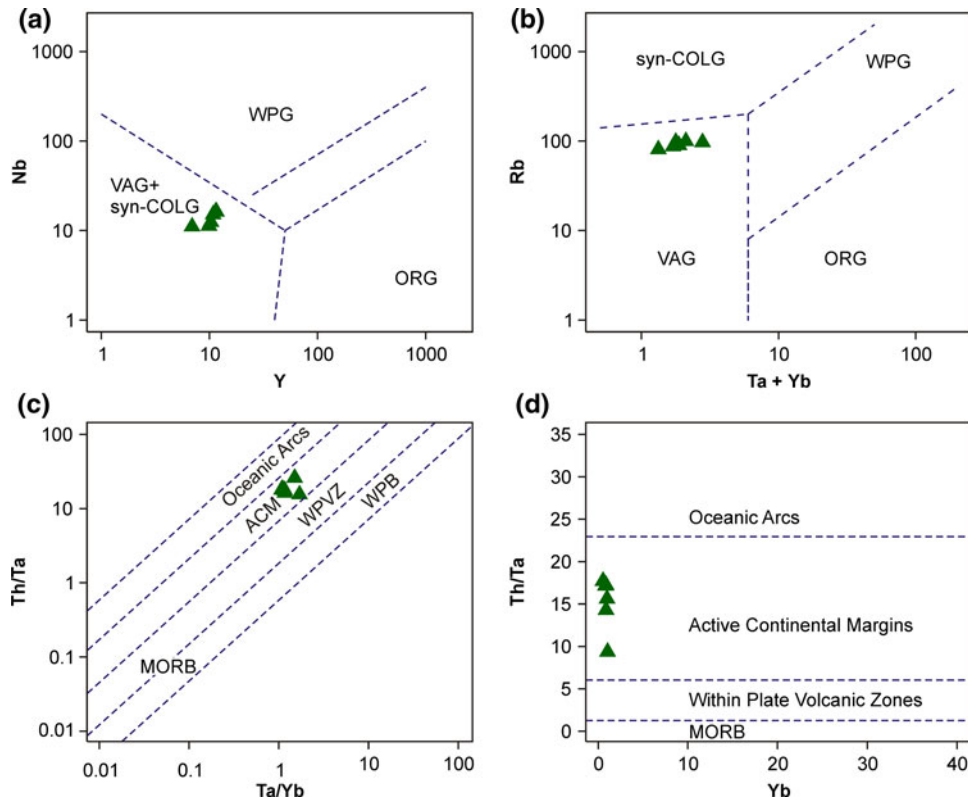


Fig. 6 Geotectonic diagrams of Pearce *et al.* (1984): a Y vs. Nb plot, b Ta + Yb vs. Rb plot. The labeled fields are Volcanic Arc Granites (VAG), Within- Plate Granites (WPG), Syn-Collisional Granites (syn-COLG) and Ocean Ridge Granites (ORG). Geotectonic diagrams of Schandl and Gorton (2002) originally designed to decipher the geotectonic setting of felsic volcanic suites: c Ta/Yb vs. Th/Ta plot, d Yb vs. Th/Ta plot. The diagrams discriminate between rocks intruding in Oceanic Arcs, Active Continental Margins (ACM), and Within-Plate Volcanic Zones (WPVZ). Field of Mid-Oceanic Ridge Basalts (MORB) and Within-Plate Basalts (WPZ) is delineated for comparison

The laser was fired at a repetition rate of 10 Hz and energy of ca. 0.5 J/cm². Linear laser rasters (100 microns) were produced by repeated scanning of the laser beam at a speed of 10 microns/second across the zircon sample surface. Typical acquisitions consisted of 35 s measurement of blank with Tl–Bi–U–Np solution followed by measurement of U and Pb signals from the ablated zircon for another 110 s. The data were acquired in time resolved—peak jumping—pulse counting mode with 1 point measured per peak for masses 202 (flyback), 203 and 205 (Tl), 206 and 207 (Pb), 209 (Bi), 233 (U), 237 (Np), 238 (U), 249 (²³³U oxide), 253 (²³⁷Np oxide) and 254 (²³⁸U oxide). Raw data were corrected for dead time of the electron multiplier and processed offline in a spreadsheet-based program (Lamdate; Košler *et al.* 2002). Data reduction included correction for gas blank, laser-induced elemental fractionation of Pb and U and instrument mass bias. Minor formation of

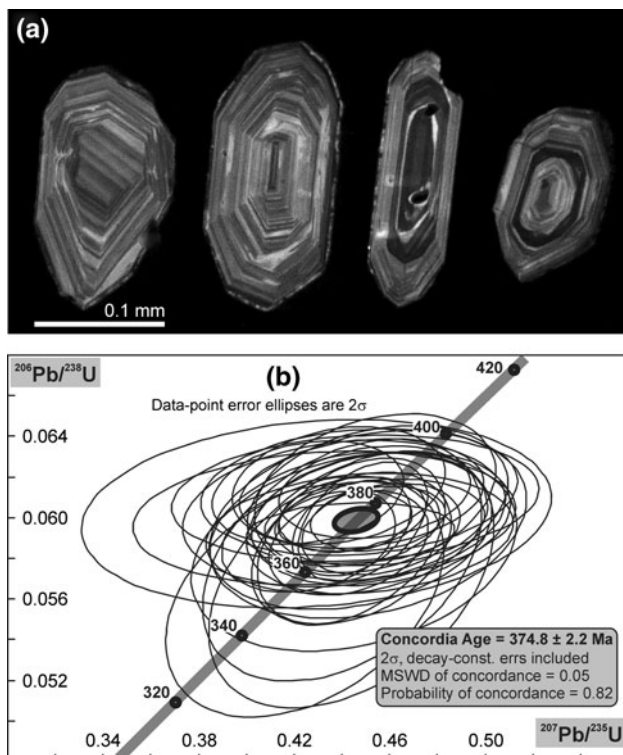


Fig. 7 (a) Representative cathodoluminescence images of analyzed magmatic zircon grains from the sample of Štěnovice granodiorite (ZK-7). (b) U–Pb Concordia diagram for zircons from the Štěnovice granodiorite (33 analyses in total). All data are plotted with 2σ uncertainties.

oxides of U and Np was corrected for by adding signal intensities at masses 249, 253, and 254 to the intensities at masses 233, 237, and 238, respectively. No common Pb correction was applied to the data. Zircon reference material 91500 (1065 Ma; Wiedenbeck *et al.* 1995) was periodically analyzed during the measurement

for quality control purposes. From the sample of the Štěnovice granodiorite, 33 zircon grains with clear magmatic oscillatory zoning (Fig. 7a) yielded concordant U–Pb isotopic ages with the mean age of 375 ± 2 Ma (2σ ; Fig. 7b; ESM, Part 5); this is interpreted as the age of the crystallization of the Štěnovice pluton.

STRUCTURE AND MAGNETIC FABRIC OF THE ŠTĚNOVICE PLUTON

Magmatic foliations and lineations

Magmatic (hypersolidus) foliations and lineations are macroscopically discernible planar and linear shape-preferred orientations of mineral grains (also referred to as the mineral fabric), respectively, acquired during the presence of a melt and showing no evidence of subsolidus deformation (Pater-son *et al.* 1989, 1998; Vernon 2000). In the Štěnovice pluton, the magmatic lineation is defined by the alignment of euhedral hornblende crystals, and the magmatic (mineral) foliation is defined by biotite flakes, plagioclase, and K-feldspar grains (ESM, Part 2a). The intensity of the mineral fabric decreases from the pluton/ wall-rock contact inward, and the fabric ellipsoid is typically oblate throughout the pluton, i.e., the mineral foliation is more intensely developed than the lineation. Near the pluton margins where the mineral foliation is stronger, the flattened microgranular enclaves are oriented subparallel to this foliation (ESM, Part 2b). The lineation is subvertical (plunge is $80\text{--}90^\circ$), the foliation also dips steeply ($70\text{--}90^\circ$) and strikes subparallel to the outer pluton margin

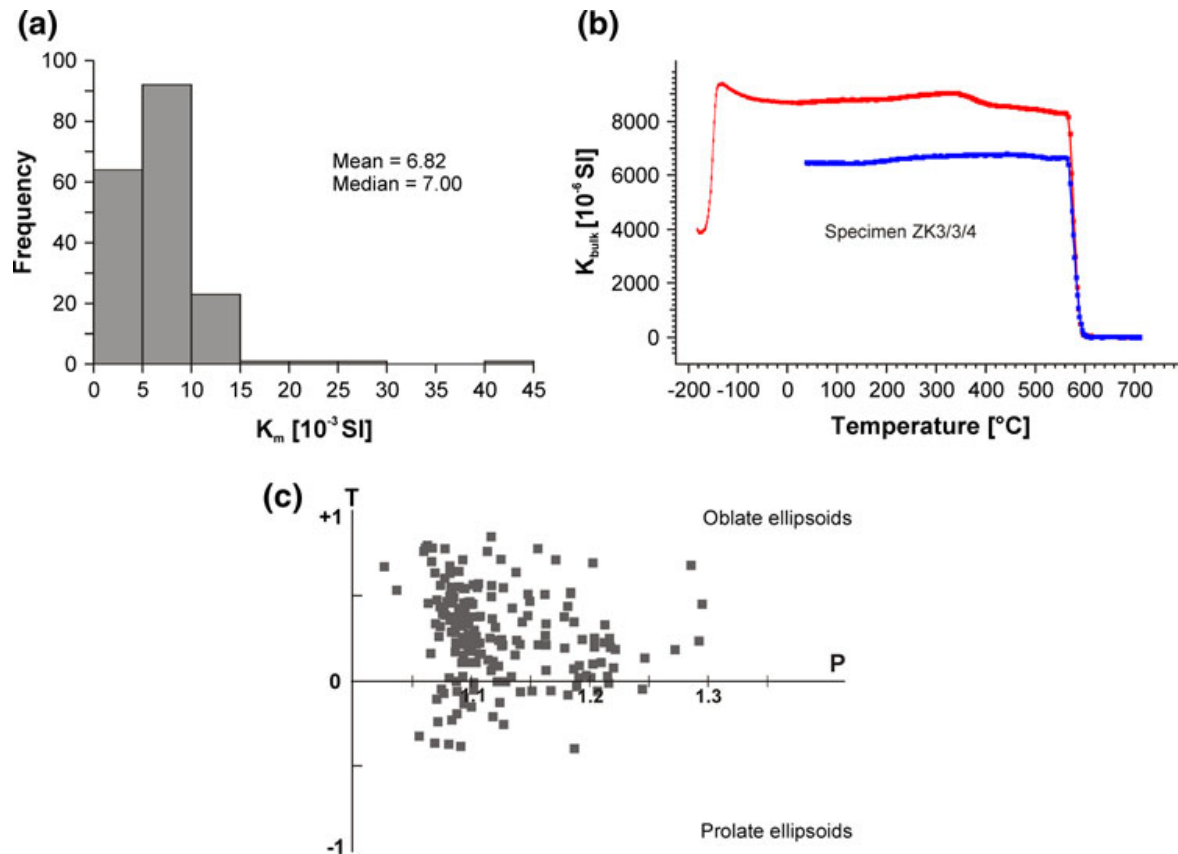


Fig. 8 (a) Histogram of the bulk susceptibility distribution for all specimens from the Štěnovice pluton. (b) Heating magnetic susceptibility vs. temperature curve for one representative specimen of the granodiorite (ZK3/3/4), the shape of the curve and Curie temperature of about 580 °C (drop in bulk susceptibility to zero) proves magnetite as the main carrier of the AMS. (c) Magnetic anisotropy P–T plot summarizing all data from the Štěnovice pluton. The AMS ellipsoid is mostly oblate ($T > 0$) and the degree of anisotropy (P) is low to moderate, clustering between 1.06 and 1.22

(Fig. 2). Magmatic foliation in the pluton thus defines a concentric, “onion-skin” pattern decoupled from the regional host-rock structures.

Anisotropy of magnetic susceptibility (ams)

The anisotropy of magnetic susceptibility (AMS) was used to quantitatively characterize the magnetic fabric and its gradients in the pluton. A total of 183 oriented specimens were taken using a portable drill at 13 stations throughout the pluton. The AMS was measured with a KLY-4S Kappabridge apparatus at the Institute of Geophysics, Academy of Sciences of the Czech Republic. A statistical analysis of the AMS data was carried out using the ANI-SOFT package of programs (written by M. Chadima and V. Jelínek; www.agico.com). The measured AMS data and parameters are listed in the Electronic Supplementary Material (Part 6).

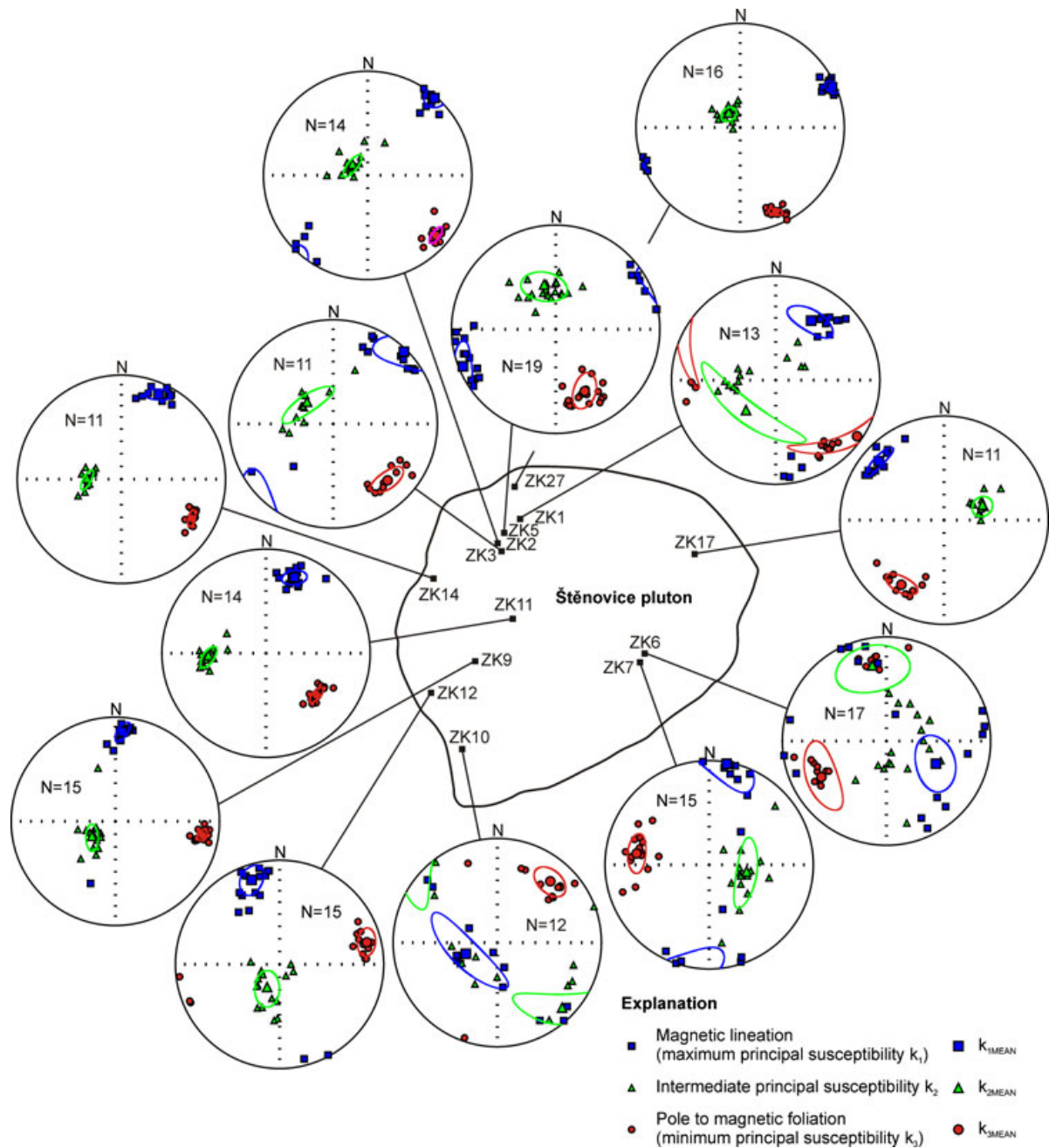


Fig. 9 Simplified map of the Štěnovice pluton (bold outline) showing stereographic projections (equal area, lower hemisphere) of principal susceptibilities at each station, including their mean orientations and confidence ellipses.

The AMS data are represented by the k_m , P , and T parameters defined as follows: (1) $k_m = (k_1 + k_2 + k_3)/3$; (2) $P = k_1/k_3$; and (3) $T = 2\ln(k_2/k_3)/\ln(k_1/k_3) - 1$; where $k_1 \geq k_2 \geq k_3$ are the principal susceptibilities. The parameter k_m represents the mean magnetic susceptibility, which reflects the qualitative and quantitative content of magnetic minerals in the rock. The parameter P (Nagata 1961), called the degree of AMS, reflects the eccentricity of the AMS ellipsoid and thus indicates the intensity of the preferred orientation of the magnetic minerals in the rock.

The parameter T (Jelínek 1981) characterizes the symmetry of the AMS ellipsoid; it varies from -1 (perfectly linear magnetic fabric) through 0 (transition between linear and planar magnetic fabric) to +1 (perfectly planar magnetic fabric). In fabric studies, the maximum principal susceptibility (k_1) is referred to as the magnetic lineation, and the minimum principal susceptibility (k_3) defines a pole to the magnetic foliation; their orientations are presented in stereograms in the geographic (in situ) coordinate system and as locality mean values on the map.

Magnetic mineralogy

The mean magnetic susceptibility of the analyzed samples is in the order of 10^{-3} – 10^{-2} [SI]; the frequency distribution of the bulk susceptibility of the samples is shown in Fig. 8a. Such a high susceptibility is typical of ferromagnetic granites (e.g., Bouchez 1997) and indicates the presence of a ferromagnetic fraction that controls the rock susceptibility.

In order to specify the ferromagnetic carriers, the temperature variation of susceptibility was investigated on one specimen (ZK3/3/4) using the KLY-4S Kappabridge, CS-3 Furnace and CS-L Cryostat apparatus at the Institute of Geophysics, Academy of Sciences of the Czech Republic. The measured data were processed using the computer code Cureval (AGICO, Inc.). The susceptibility variations with temperature were measured in the temperature range of -196 °C to 5 °C where no changes in mineralogy appear and then in the interval from room temperature to 700 °C. The measurements of the magnetic susceptibility variation with temperature are presented in Fig. 8b. A clear Verwey transition exists in the low-temperature part of the curve (between -165 °C and -150 °C) as well as an abrupt decrease in susceptibility around 580 °C (T_c ; the Curie temperature of magnetite), both proving that magnetite, which is a common accessory phase, is the main carrier of the AMS in the Štěnovice pluton.

Magnetic fabric parameters and orientation

The degree of magnetic anisotropy (P) varies from 1.027 to 1.295 with the majority of specimens between $P = 1.060$ and $P = 1.150$ (Fig. 8c). The shape parameter (T) ranges from -0.396 to 0.844, indicating both prolate (16% specimens) but predominantly oblate (84% specimens) shapes of the AMS ellipsoid (Fig. 8c). On the map, the average values of P and T (calculated as arithmetic mean at each locality) exhibit no significant spatial variations within the pluton except for P being higher at some stations near the pluton margin (mean value is $P = 1.3$) compared to the center (mean value is $P = 1.08$; ESM, Part 7).

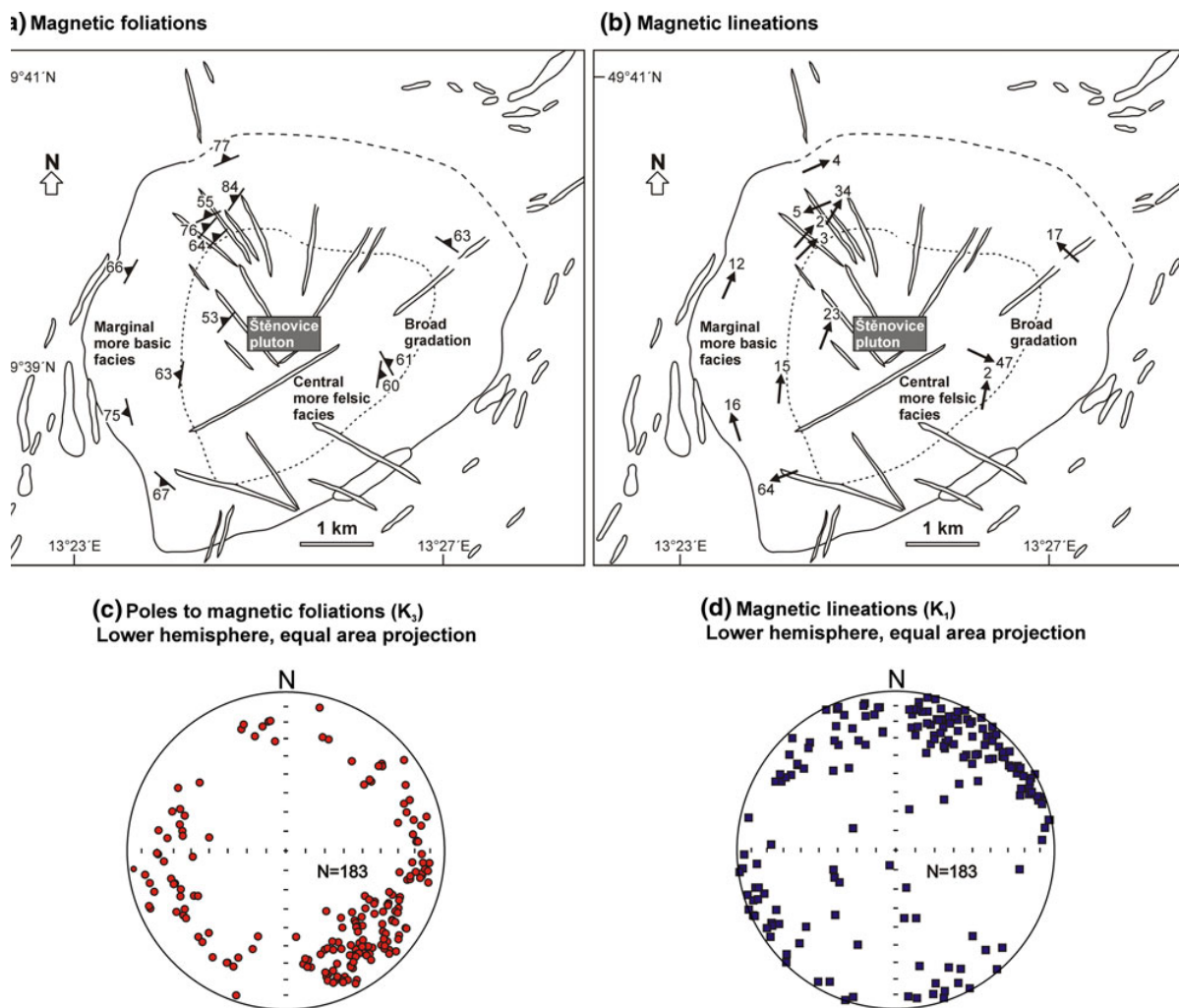


Fig. 10 a, b Maps of magnetic foliations and lineations (mean values at each station) in the Štěnovice pluton. Foliations are steep and margin-parallel, lineations plunge shallowly to moderately at variable trends but in many cases are subparallel to the pluton margin. c, d Synoptic stereographic projections (equal area, lower hemisphere) of all magnetic foliations and lineations in the pluton

Magnetic foliations are generally steep (dip ranges from 48° to 89°) and margin-parallel throughout the pluton (Figs. 9, 10), corresponding to the mesoscopic (magmatic) foliations (compare Figs. 2 and 10a, c). Both mesoscopic and magnetic foliations define an “onion-skin” pattern. The plunge of magnetic lineations is highly variable ranging from 0° to 82° but most of the lineations plunge shallowly (0–40°; 93% specimens) and trend parallel to the pluton margin (Figs. 9, 10b, d).

GEOLOGIC SETTING, STRUCTURE, AND MAGNETIC FABRIC OF THE ČISTÁ PLUTON

The Čistá pluton, dated at 373.1 ± 1.1 Ma using the Pb–Pb single zircon evaporation method (Venera *et al.* 2000), has an elliptical shape in plan view (8.5×6 km, ~ 38 km²) with its long axis oriented \sim NE–SW (Fig. 11a; see Klomínský 1963; Chlupáčová *et al.* 1975; Kopecký *et al.* 1997 for other details on regional geology). On the basis of a gravimetric survey verified by several boreholes, the three-dimensional pluton shape at depth is a steeply dipping cylinder (stock) plunging northeast (Fig. 11b; Kopecký *et al.* 1997). The pluton intruded across the poorly exposed low-grade Neoproterozoic (Ediacaran) phyllites and metabasalts to the northwest and a Cambrian tabular pluton to the southeast (the ~ 505 Ma Tis granite; Venera *et al.* 2000). The contact of the Čistá pluton against its wall-rock is generally steep and dips inward or outward in different parts of the pluton. The southwestern end of the pluton is concealed beneath the Carboniferous cover, while its northwestern margin is poorly exposed and is parallel to the \sim NE–SW-trending lithologic contacts in the Neoproterozoic host (Fig. 11a). The granodiorite/Tis granite contact is delineated by a cataclastic–mylonite and associated alkaline-metasomatic (fenite) zone (Fig. 11a).

An up to 3-km wide thermal aureole, characterized by hornfels and spotted schists, is developed in the Neoproterozoic wall/rock southeast of the Tis granite and along the northwestern margin of the Čistá granodiorite (Fig. 11a). As the Čistá granodiorite intruded across the large tabular body of the Tis granite (Kopecký *et al.* 1997; Fig. 11b), the northwestern segment of the aureole likely reflects superimposed thermal effects on wall-rock from both intrusions.

The Čistá pluton is normally zoned; an outer rim composed of strongly foliated (a complete transition from magmatic to subsolidus foliation was described by Venera *et al.* 2000) and more mafic amphibole–biotite granodiorite (plagioclase prevails over K-feldspar) with abundant mafic microgranular enclaves grades inward into more felsic, medium- to fine-grained biotite granodiorite with a weak or macroscopically not discernible magmatic fabric. The overall internal structure of the pluton is concentric, defined by steep margin-parallel foliation associated with variably oriented hornblende lineation (see structural map in Fig. 6 in Venera *et al.* 2000). Late \sim NW–SE-trending dikes of granodiorite, diorite porphyry, and aplite cut across the pluton (Fig. 11a), implying that the granodiorite body underwent a post-emplacement brittle extension parallel to the long axis of the pluton (in plan view).

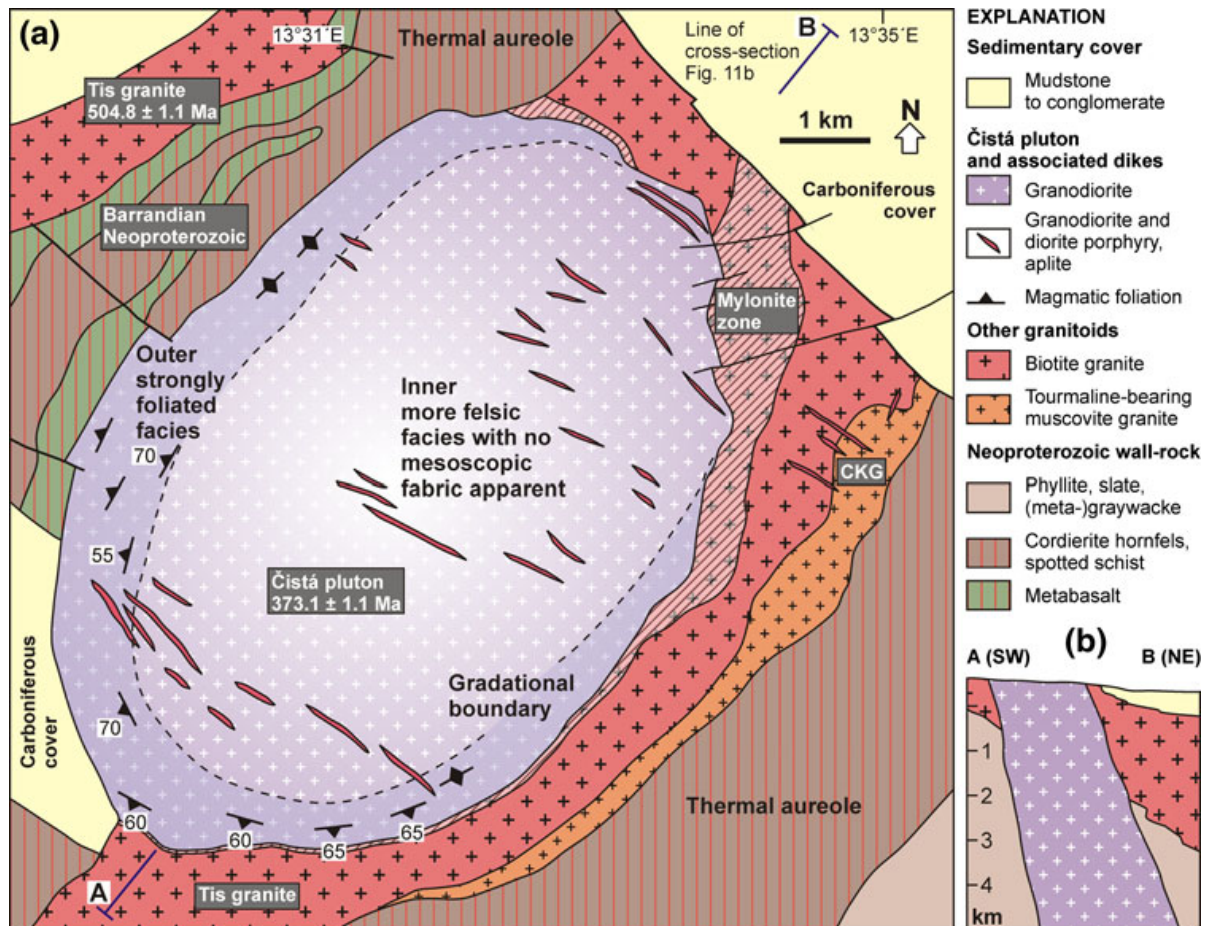


Fig. 11 (a) Simplified geologic map of the Čistá pluton. The pluton intrudes the Neoproterozoic metasedimentary rocks to the northwest and the Late Cambrian Tis granite to the southeast. Geologic background compiled from the Czech Geological Survey 1:50,000 map (sheets 12–13 Jesenice and 12–31 Plasy), Klomínský (1963), and Kopecký *et al.* (1997); structural data taken from Klomínský (1963) and Kopecký *et al.* (1997). Evaporation Pb–Pb zircon ages of Venera *et al.* (2000) for the Čistá granodiorite and the Tis granite are also shown. (b) Simplified NE–SW cross-section across the pluton and its host rock. Based on geophysical and borehole data the pluton has steeply inclined cylindrical shape; modified from Kopecký *et al.* (1997)

The most in-depth investigation into the internal structure and magnetic (AMS) fabric of the Čistá pluton was presented by Chlupáčová *et al.* (1975). Their AMS data corroborate the overall concentric structure of the pluton (Fig. 12) and also indicate a generally oblate shape of the AMS ellipsoids and increasing degree of magnetic anisotropy toward the pluton margin. Similarly to the Štěňovice pluton, the main AMS carrier in the Čistá pluton is magnetite, which particularly near the pluton margin, also grew mimetically enhancing the shape-preferred orientation of biotite flakes (Hrouda *et al.* 1971, 1972; Chlupáčová *et al.* 1975). Except for one station (No. 7 in Fig. 12), magnetic foliations are steep and margin-parallel and magnetic lineations plunge steeply to moderately

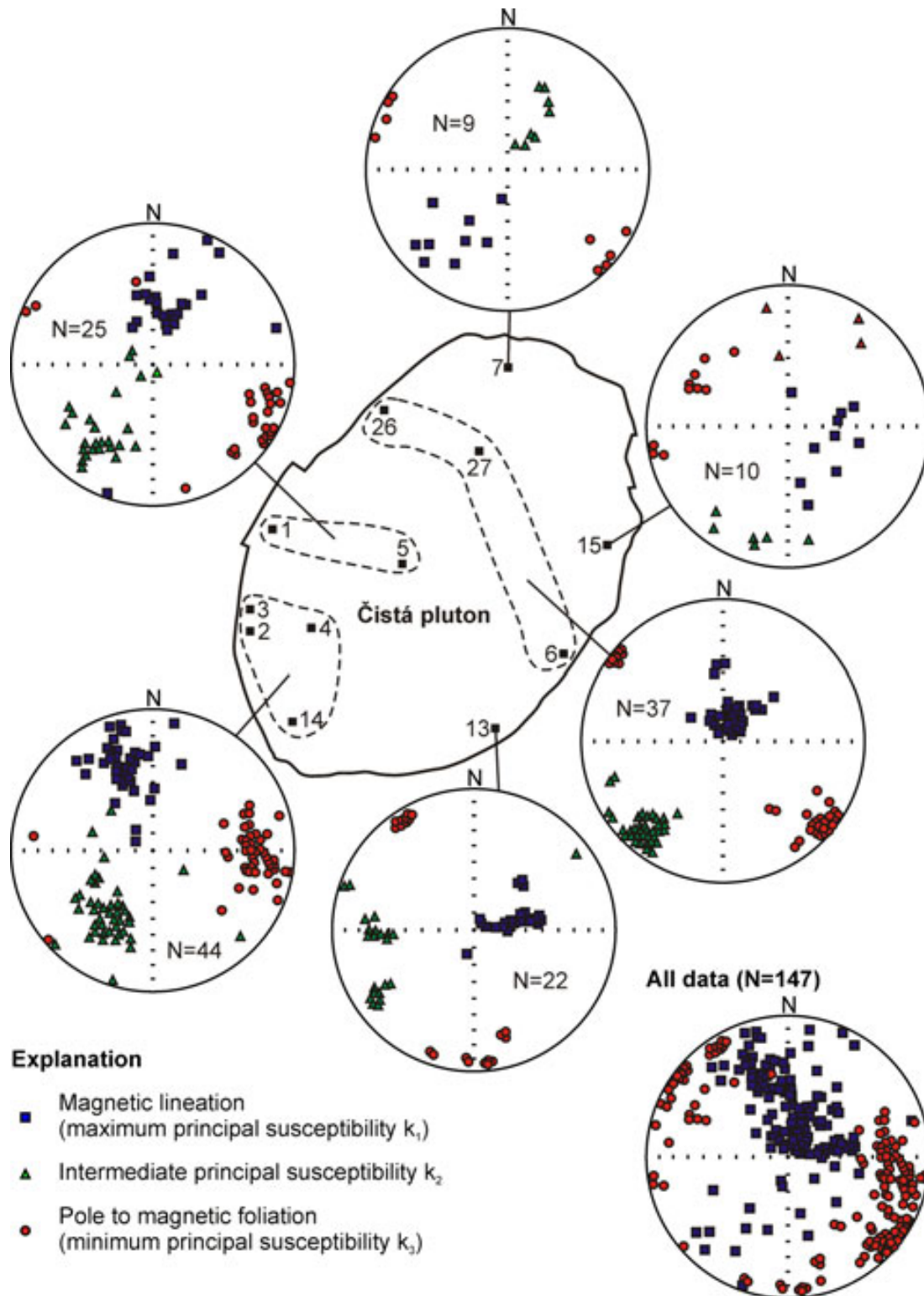


Fig. 12 Simplified map showing orientation of principal susceptibilities at 13 stations in the Čistá pluton (bold outline). All the AMS data from the pluton are also summarized in the synoptic stereonet (stereographic projections are equal area, lower hemisphere). Note the steep, margin-parallel magnetic foliations and steep to NNE-plunging magnetic lineations. The AMS data were taken from Chlupáčová *et al.* (1975)

(Fig. 12). In a synoptic stereonet, magnetic foliation poles thus concentrate near the periphery of the diagram while magnetic lineations define a prominent cluster close to its center passing into a cluster of data points corresponding to lineations plunging moderately to the ~NNE (Fig. 12). The apparent pre-ponderance of the ~NE–SW magnetic foliations is a sampling bias caused by the lack of stations at the NE and SW ends of the pluton.

INTERPRETATION OF STRUCTURE AND EMPLACEMENT OF THE ŠTĚNOVICE AND ČISTÁ PLUTONS

The following lines of evidence suggest that the Štěnovice and Čistá plutons have characteristics typical of concentrically expanded plutons (CEPs) emplaced via diapirism and/or in situ lateral expansion (Paterson and Vernon 1995; Dietl and Koyi 2002).

1. Both plutons have steep margins and elliptical shapes in plan view. As inferred from gravimetric and borehole data, the Čistá pluton continues downward for at least 5 km as an inclined, steep-sided cylinder (Fig. 11b; Kopecký *et al.* 1997). Similarly, the Štěnovice pluton has an outward-dipping steep margin near the present-day erosion surface and, on the basis of our gravimetric interpretation, extends down for at least 6–8 km as a downward-narrowing cone with a weakly elliptical cross-section (Fig. 3c).
2. Both plutons are surrounded by distinct thermal and structural aureoles. Lithologic contacts and the host rock structures are notably deflected in a wide zone around the Štěnovice pluton. The width of this aureole corresponds to 1/3 of the pluton radius, which is well comparable to other examples of CEPs (e.g., Paterson *et al.* 1991; Paterson and Fowler 1993; Paterson and Vernon 1995; Miller and Paterson 1999). The interpretation of the aureole in the Neoproterozoic host rocks northwest of the Čistá pluton is not so straightforward, as the aureoles of both the Tis and Čistá plutons overlap. Large portions of this margin are poorly exposed and parallel to the trend of regional structures, thus provide no or ambiguous information on the emplacement of the pluton. The contact of the Čistá pluton against the Tis granite is a tens to hundreds meters wide high-temperature mylonite zone (Fig. 11a), which may represent a narrow ductile aureole wherein the host, thermally softened Tis granite (Venera *et al.* 2000) accommodated strain related to the emplacement of the Čistá pluton. It has been shown by He *et al.* (2009) that examining wall-rock structures within aureoles of CEPs is crucial in distinguishing between ballooning (in situ lateral expansion of a pluton producing large flattening strains in the wall-rock) from purely diapiric magma

emplacement accommodated by downward return flow of the wall-rock. In the case of both plutons examined here, however, the lack of exposure and scarcity of structural data from the aureoles (particularly in segments at a high angle to regional host-rock structures) preclude rigorous distinction between these two end-member, but commonly closely interlinked, modes of emplacement.

3. In both plutons, no internal contacts were found that could be used to define smaller within-pluton intrusive units representing individual magma batches or sheets. Instead, the plutons are normally zoned with the outer more mafic facies passing gradually into a more felsic interior (Klomínský 1963, 1965; Kopecký *et al.* 1997; Figs. 2, 11a). The gravimetric survey indicates no significant change in rock densities in the deeper sections of the plutons that could possibly reflect the presence of denser bodies of gabbros or diorites or large screens of the Neoproterozoic host rock down to depth of at least ~8 km (Fig. 3c). This, in turn, suggests that even at such depth the plutons are compositionally rather homogeneous like near the present-day surface. We thus interpret that both the Štěnovice and Čistá plutons intruded either as single, coherent magma blobs with sidewall fractional crystallization producing the normal zoning, or as two or just a few coeval, thus not well recognizable, nested somewhat more felsic into less felsic batches (e.g., Chlupáčová *et al.* 1975).
4. In both plutons, the steeply dipping mineral (mesoscopic) foliations define margin-parallel, concentric (“onion-skin”) patterns (Figs. 2, 11a) that are also typical of CEPs (e.g., Ramsay 1989; Paterson and Fowler 1993; Miller and Paterson 1999; Molyneux and Hutton 2000; Siegesmund and Becker 2000; Galadí-Enríquez *et al.* 2003; Tahiri *et al.* 2007; He *et al.* 2009). This notion is supported by the AMS reflecting the shape anisotropy or mimetic growth of magnetite (Hrouda *et al.* 1971), as the magnetic foliations in both plutons are margin-parallel and generally mimic the mesoscopic foliations.

In the Čistá pluton, both mineral (hornblende) and magnetic (magnetite) lineations plunge steeply to moderately (Fig. 12), which was interpreted by Chlupáčová *et al.* (1975) as a result of bulk stretching during diapiric magma ascent through a steep-sided conduit. By contrast, magnetic lineations are margin-parallel (circumferential) and plunge $< 40^\circ$ in the Štěnovice pluton (this study, Figs. 9, 10b, d) suggesting that the finite principal stretching in the magma was oriented at a high angle to the presumed steep magma ascent path. With the aid of gravimetric data indicating that the Štěnovice pluton has a downward-narrowing shape at depth (Fig. 3c), we suggest that, upon arrival to the present-day exposure level, the bulk steep magma ascent converted to lateral stretching

along walls as the conduit broadened. Perhaps, continuing divergent magma flow or arrival of a new magma surge into the hotter pluton center then caused fairly minor margin-perpendicular flattening and lateral along-wall stretching of the outer, highly crystallized magma carapace. The strain recorded by the magnetite fabric was weak, however, as indicated by the lack of subsolidus deformation in the outer granodiorite and generally low fabric intensity in the pluton. Such a mechanism would explain the concentric magmatic (mineral) foliation intensifying toward the pluton margin, shallowly plunging margin-parallel magnetite lineation, and oblate shape of the AMS ellipsoid.

In short, the inferences developed above suggest that the Štěnovice and Čistá plutons intruded as steep-sided and vertically extensive magma batches (stocks) that pierced and, at least in the case of the Štěnovice pluton, expanded laterally into the upper crustal host rocks. Hence, both plutons are largely discordant and post-kinematic with respect to the regional ductile structures (cleavage, large-scale folds) in their adjacent host rocks - a point that will become particularly important in the following section.

DISCUSSION

Over the past decade, a vigorous discussion has centered on the location and polarity of possible subduction zones in the Bohemian Massif during the Variscan orogeny (e.g., Konopásek and Schulmann 2005; Medaris *et al.* 2005; Franke 2000, 2006; Finger *et al.* 2007; Schulmann *et al.* 2009; Edel and Schulmann 2009; Dörr and Zulauf 2010). The unresolved issues include the exact number of lithospheric microplates involved (separated by oceanic domains), the deformation styles, kinematics, timing, and duration of subductions and subsequent collisions, as well as the link between subduction and magmatism. We envisage that the Štěnovice and Čistá plutons may help to unravel these questions and provide additional information on the yet poorly understood and in many points controversial early (Mid- to Late-Devonian) stages of the Variscan orogeny in the central Bohemian Massif.

The Late Devonian calc-alkaline plutonism in the Teplá–Barrandian unit

The major- and trace-element whole-rock geochemical characteristics, such as normal calc-alkaline chemistry, prevalence of Na over K, deep troughs in HFSE on NMORB-normalized diagrams accompanied by a strong enrichment of hydrous-fluid mobile LILE (Figs. 4, 5, 6), resemble igneous suites from active continental margin arc settings (e.g. Wilson 1989; Tatsumi and Eggins 1995). However,

no analyses of basic rocks are available, and it is a well-known fact that the igneous-arc-like signature in granites can be equivocal. Their chemistry may both reflect the true setting as well as signature inherited from a source through either remelting of metaigneous arc-related rocks (Arculus 1987), or anatexis of immature psammitic sediments containing arc-derived detritus (Roberts and Clemens 1993; Janoušek *et al.* 2010a, b). This holds true especially for the syn-collisional and post-collisional uplift settings, when a range of crustal sources is available for melting (Pitcher 1982; Pearce *et al.* 1984; Bonin 1990; Barbarin 1990; Pearce 1996).

Strikingly geochemically similar but significantly younger are Na-rich granodiorites, tonalites, and quartz diorites of the Sázava suite of the Central Bohemian Plutonic Complex (Fig. 1b; 354 ± 4 Ma, Janoušek *et al.* 2004a). These plutonic rocks are intimately associated with abundant (olivine, clinopyroxene-) amphibole-bearing gabbros and gabbrodiorites, which had to come from a slightly depleted mantle source modified by slab-derived fluids (Janoušek *et al.* 2004a, 2010a). Comparison of the whole-rock geochemistry of the Štěnovice and Čistá granitoids with that of the Sázava suite shows that all these plutons belong to one family of calc-alkaline and metaluminous–subaluminous plutonic rocks, having an overlapping range of major- and trace-element compositions as well as the overall shape of the trace-element patterns (Figs. 4, 5). This concerns also the REE patterns, characterized by the presence of a slight positive Eu anomaly. This phenomenon is by no means rare in the Sázava suite and was interpreted as a result of fractionation of amphibole-dominated assemblage or partial melting of amphibole-bearing sources (Janoušek *et al.* 2000). Slight differences are observed only in Cs, Pb, Zr, and Sr that seem to be somewhat enriched in the Štěnovice pluton compared to the Sázava suite. On the basis of the above, we conclude that the Štěnovice and Čistá plutons have been generated in an initial continental magmatic arc setting. The Pb–Pb single zircon age of 373 ± 1 Ma for the Čistá granodiorite (Venera *et al.* 2000) and the newly determined U–Pb age of 375 ± 2 Ma for the Štěnovice granodiorite also rank these plutons to the oldest vestiges of Variscan arc-related plutonic activity in the Bohemian Massif. The only comparable Late Devonian ages were obtained from the Staré Sedlo and Mirovice orthogneisses in the roof pendants of the Central Bohemian Plutonic Complex (Fig. 1b; 375 ± 5 Ma, 373 ± 5 Ma, 369 ± 4 Ma; Košler *et al.* 1993) and somewhat younger age from the Teufelsberg diorite at the southernmost tip of the TBU (Fig. 1b; 359 ± 2 Ma; Bues *et al.* 2002).

Tectonic implications

In the following interpretations, we consider only the Late Devonian to early Carboniferous calc-alkaline plutons, which have intrusive contacts against the TBU and thus are indisputably fixed in their original emplacement position in the upper crust. We exclude other comparable granitoid or meta-granitoid complexes that are allochthonous or have been sheared, displaced, or even buried to and exhumed from greater depths (e.g., Janoušek *et al.* 2006b; Verner *et al.* 2009).

The supracrustal TBU is specific in that it hosts the arc-related calc-alkaline plutons while it occupies the hanging-wall position with respect to the neighboring Saxothuringian and Moldanubian units in the center of the Bohemian Massif (Fig. 1a, b). Thus, the TBU is the overriding plate for all the hypothetical subduction zones (Fig. 1a). The question arises whether the Late Devonian to early Carboniferous arc-related magmas were generated by the SE-directed subduction of the narrow Saxothuringian Ocean along the present-day Saxothuringian/Teplá–Barrandian boundary (Fig. 1a; e.g., Zulauf 1997b; O'Brien 2000; Janoušek *et al.* 2004b; Konopásek and Schulmann 2005; Janoušek and Holub 2007; Machek *et al.* 2009; Schulmann *et al.* 2009; Žák *et al.* 2009), or by the opposite NW-directed subduction of the Gföhl Ocean between the Moldanubian unit and southeastern margin of the TBU now occupied by the Central Bohemian Plutonic Complex (Fig. 1a, b; e.g., Medaris *et al.* 2005; Franke 2000, 2006), or even by subduction of the Raabs Ocean beneath the Moldanubian unit along the eastern margin of the Bohemian Massif (Finger *et al.* 2007). We argue that the Štěnovice and Čistá plutons may help to resolve this conundrum and also complement the existing information to examine the spatial and temporal pattern of Variscan plutonism and regional deformation in the TBU.

The earliest Variscan ~NW–SE shortening related to the subduction and subsequent Saxothuringian/Teplá–Barrandian collision is recorded along the NW margin of the TBU at around 380 Ma (Schäfer *et al.* 1997; Zulauf 1997a; Timmermann *et al.* 2006; Dörr and Zulauf 2010). This Givetian/Frasnian shortening led here to the top-to-the-NW thrusting and crustal stacking (Zulauf 1997a, 2001; Dörr *et al.* 1998), causing syn-collisional exhumation of crustal rocks and surface uplift in the NW segment of the TBU. The uplift and exhumation is also reflected in the mica cooling ages (Fig. 1b) and in the deposition of Givetian flysch in the Barrandian basin with the source area in the western TBU (Strnad and Mihaljevič 2005). The overall shortening of the TBU due to the Saxothuringian ocean subduction and subsequent Saxothuringian/Teplá–Barrandian collision lasted from at least ~380 Ma to ~346 Ma, the upper age limit being now precisely bracketed by the

syn-tectonic plutons of the Central Bohemian Plutonic Complex (Žák *et al.* 2005a, b, 2009; Janoušek *et al.* 2010a).

The geochronologic data indicate that the Variscan calc-alkaline plutonism in the TBU started at around ~375–373 Ma with the emplacement of the small-volume Štěnovice and Čistá plutons (Fig. 1b). As detailed earlier,

these two plutons are largely discordant to the regional ductile structures in their nearby host rocks, in contrast to the ductilely deformed calc-alkaline granitoids emplaced at approximately the same time near the present-day TBU/ Moldanubian boundary (the ~380–365 Ma Staré Sedlo and Mirotice complexes in Fig. 1b; the significance of this tectonomagmatic event remains enigmatic). This suggests that while the central part of the TBU was little affected by the pervasive Variscan overprint largely preserving Cadomian structures (Hajná *et al.* 2010), the TBU margins were deforming during the Late Devonian to early Carboniferous (Fig. 1b; e.g., Zulauf 1997a).

The initial calc-alkaline plutonic activity at ~375–373 Ma in the central TBU was followed by a magmatic “flare-up” from ~354 to ~346 Ma to form the bulk of the Central Bohemian Plutonic Complex, leading to significant localization of the background compressive/transpressional deformation into this thermally softened domain along the entire SE flank of the TBU (Fig. 1b; Holub *et al.* 1997a; Scheuvens and Zulauf 2000; Janoušek *et al.* 2004a, 2010a; Žák *et al.* 2005a, b, 2009). The > 20 M.y. gap between the closure of the Saxothuringian Ocean by continental collision (~380 Ma) and the ~375 Ma minor and ~354 to ~346 Ma voluminous and increasingly potassic plutons (Janoušek *et al.* 1995, 2000; Holub *et al.* 1997b) may represent a time lag needed for the generation of large-volume magmas above a subducting slab and their ascent to the upper-crustal levels. Such a timing of deformation and plutonism in the TBU thus fits well the general time scales of production of calc-alkaline magmas, which may post-date the termination of subduction by as much as 30–50 My depending on the availability of water (e.g., Bonin 1990).

In any case, the cessation of the arc-related plutonic activity in the TBU seems to coincide with subduction of the Saxothuringian felsic meta-igneous crust, the HP–HT metamorphism of which resulted in the formation of felsic garnet–kyanite granulites at ~340 Ma (Janoušek *et al.* 2004b; Janoušek and Holub 2007). At ~343–335 Ma, the southeastern edge of the Central Bohemian Plutonic Complex (including the TBU roof pendants; Fig. 1b) and the Moldanubian middle crust were also intruded by (ultra-)potassic melasyenitoids and melagranitoids (Klötzli and Parrish 1996; Holub 1997; Gerdes *et al.* 2000b; Janoušek and Gerdes 2003; Janoušek and Holub 2007; Verner *et al.* 2006, 2008; Kusiak *et al.* 2010; Kotková *et al.* 2010).

In summary, the older ~375–354 Ma calc-alkaline plutons intruded only the upper-crustal TBU to the ~NW whereas the younger (~346–335 Ma), progressively more potassium-rich plutons to the ~SE are in intrusive contact with both the TBU and mid-crustal rocks of the Moldanubian Unit (Fig. 1b; Holub *et al.* 1997a, b; Žák *et al.* 2005a). Such a spatial–temporal–compositional shift of plutonism is consistent with a northwesterly subduction/ collision zone located along the Teplá–Barrandian/Saxothuringian boundary as a principal geodynamic cause of the Late Devonian/early Carboniferous arc-related magmatism in the TBU.

CONCLUSIONS

The Štěnovice and Čistá granodiorite–tonalite plutons are interpreted as representing the initial Late Devonian stage of subsequent early Carboniferous voluminous plutonism in the upper crust of the central Bohemian Massif. The whole-rock and trace-element geochemical characteristics of the granodiorites–tonalites are consistent with the calc-alkaline magma having been generated in a continental margin arc setting. These two plutons are largely discordant to the regional ductile structures in their nearby host rocks and have characteristics of concentrically expanded plutons (CEPs): elliptical cross-section in plan view, steep contacts, inferred downward-narrowing conical shape, faint normal zoning, and margin-parallel magmatic fabric decoupled from the regional host-rock structures. Combined with the existing geochronologic, geochemical, and tectonic data, the Štěnovice and Čistá plutons indicate an overall shift of plutonic activity from the ~NW to the ~SE in the upper-crustal TBU during Late Devonian

to early Carboniferous, accompanied by a general compositional trend of the magmas from medium-K calc-alkaline to shoshonitic/ultrapotassic. Such a pattern in the plutonic activity is compatible with the SE-directed (in the present-day coordinates) subduction of the Saxothuringian Ocean beneath the Teplá–Barrandian upper plate as a principal cause of the arc-related plutonism.

ACKNOWLEDGMENTS

We gratefully acknowledge Fritz Finger and Philippe Olivier for their detailed and critical reviews and Associate Editor Marlina Elburg for helpful comments and careful editorial handling of the manuscript. This work also benefited greatly from discussions with František Hrouda, Marta Chlupáčová, František Holub, Kryštof Verner, Václav Kachlík, Gernold Zulauf, and Josef Klomínský on various aspects of Variscan magmatism in the Bohemian Massif. František Veselovský of the Czech Geological Survey is thanked for zircon separations. This research was supported by the Czech Academy

of Sciences (Grant No. KJB30012702 to Z. Kratinová), by the Grant Agency of the Czech Republic (Grant No. 205/07/ 0992 to V. Janoušek), and by the Ministry of Education, Youth and Sports of the Czech Republic Research Plan No. MSM0021620855. This study is part of the Ph.D. research of Jakub Trubač.

REFERENCES

- Arculus RJ (1987) The significance of source versus process in the tectonic controls of magma genesis. *J Volcanol Geotherm Res* 32:1–12
- Barbarin B (1990) Granitoids: main petrogenetic classifications in relation to origin and tectonic setting. *Geol J* 25:227–238
- Bartošek J, Chlupáčová M, Šťovíčková N (1969) Petrogenesis and structural position of small granitoid intrusions in the aspect of geophysical data. *J Geol Sci Appl Geophys* 8:37–65
- Bonin B (1990) From orogenic to anorogenic settings: evolution of granitoid suites after a major orogenesis. *Geol J* 25:261–270
- Bouchez JL (1997) Granite is never isotropic: an introduction to AMS studies of granitic rocks. In: Bouchez JL, Hutton DHW, Stephens WE (eds) *Granite: from segregation of melt to emplacement fabrics*. Kluwer, Amsterdam, pp 95–112
- Boynton WV (1984) Cosmochemistry of the rare earth elements: meteorite studies. In: Henderson P (ed) *Rare earth element geochemistry*. Elsevier, Amsterdam, pp 63–114
- Breiter K, Sokol A (1997) Chemistry of the Bohemian granitoids: geotectonic and metallogenetic implications. *J Geol Sci Econ Geol Mineral* 31:75–96
- Bues C, Dörr W, Fiala J, Vejnar Z, Zulauf G (2002) Emplacement depths and radiometric ages of Paleozoic plutons of the Neukirchen–Kdyně massif: differential uplift and exhumation of Cadomian basement due to Carboniferous orogenic collapse (Bohemian Massif). *Tectonophysics* 352:225–243
- Čadková Z, Jakeš P, Haková M, Mrázek P (1985) Geochemical catalogue of the basic network. In: *Lithogeochemical Database of the Czech Geological Survey, Prague* (unpublished manuscript)
- Chlupáčová M, Hrouda F, Rejl L (1975) The fabric, genesis, and relative age of the granitic rocks of the Čistá–Jesenice massif (Czechoslovakia), as studied by magnetic anisotropy. *Gerlands Beitr Geophys* 84:487–500
- Dallmeyer RD, Urban M (1998) Variscan vs Cadomian tectonothermal activity in northwestern sectors of the Teplá–Barrandian zone, Czech Republic: constraints from $^{40}\text{Ar}/^{39}\text{Ar}$ ages. *Geol Rundsch* 87:94–106
- Debon F, Le Fort P (1983) A chemical–mineralogical classification of common plutonic rocks and associations. *Trans Roy Soc Edinb Earth Sci* 73:135–149

- Didier J, Barbarin B (eds) (1991) *Enclaves and granite petrology*. Elsevier, Amsterdam
- Dietl C, Koyi HA (2002) Emplacement of nested diapirs: results of centrifuge modelling. *J Virtual Explor* 6:81–88
- Dörr W, Zulauf G (2010) Elevator tectonics and orogenic collapse of a Tibetan-style plateau in the European Variscides: the role of the Bohemian shear zone. *Int J Earth Sci* 99:299–325
- Dörr W, Fiala J, Vejnar Z, Zulauf G (1998) U–Pb zircon ages and structural development of metagranitoids of the Teplá crystalline complex: evidence for pervasive Cambrian plutonism within the Bohemian Massif (Czech Republic). *Geol Rundsch* 87:135–149
- Dunstan LP, Gramlich JW, Barnes IL, Purdy WC (1980) Absolute isotopic abundance and the atomic weight of a reference sample of thallium. *J Res Natl Bureau Stand* 85:1–10
- Edel JB, Schulmann K (2009) Geophysical constraints and model of the “Saxothuringian and Rhenohercynian subductions–magmatic arc system” in NE France and SW Germany. *Bull Soc Geol Fr* 180:545–558
- Finger F, Roberts MP, Haunschmid B, Schermaier A, Steyrer HP (1997) Variscan granitoids of central Europe: their typology, potential sources and tectonothermal relations. *Mineral Petrol* 61:67–96
- Finger F, Gerdes A, Janoušek V, René M, Riegler G (2007) Resolving the Variscan evolution of the Moldanubian sector of the Bohemian Massif: the significance of the Bavarian and the Moravo–Moldanubian tectonometamorphic phases. *J Geosci* 52:9–28
- Finger F, René M, Gerdes A, Riegler G (2009) The Saxo–Danubian granite belt: magmatic response to postcollisional delamination of mantle lithosphere below the southwestern sector of the Bohemian Massif (Variscan orogen). *Geol Carpath* 60:205–212
- Franke W (2000) The mid-European segment of the Variscides: tectonostratigraphic units, terrane boundaries and plate tectonic evolution. In: Franke W, Haak V, Oncken O, Tanner D (eds) *Orogenic processes: quantification and modelling in the Variscan belt*, vol 179. *Geol Soc London Spec Publ*, London, pp 35–61
- Franke W (2006) The Variscan orogen in Central Europe: construction and collapse. In: Gee DG, Stephenson RA (eds) *European lithosphere dynamics*, vol 34. *Geol Soc London Memoirs*, London, pp 333–343
- Galadí-Enríquez E, Galindo-Zaldívar J, Simancas F, Exposito I (2003) Diapiric emplacement in the upper crust of a granitic body: the La Bazana granite (SW Spain). *Tectonophysics* 361:83–96

- Gerdes A (2001) Magma homogenization during anatexis, ascent and/or emplacement? Constraints from the Variscan Weinsberg Granites. *Terra Nova* 13:305–312
- Gerdes A, Wörner G, Henk A (2000a) Post-collisional granite generation and HT–LP metamorphism by radiogenic heating: the Variscan South Bohemian Batholith. *J Geol Soc London* 157:577–587
- Gerdes A, Wörner G, Finger F (2000b) Hybrids, magma mixing and enriched mantle melts in post-collisional Variscan granitoids: the Rastenberg Pluton, Austria. In: Franke W, Haak V, Oncken O, Tanner D (eds) *Orogenic processes: quantification and modelling in the Variscan belt*, vol 179. *Geol Soc London Spec Publ*, London, pp 415–431
- Gerdes A, Friedl G, Parrish RR, Finger F (2003) High-resolution geochronology of Variscan granite emplacement—the South Bohemian Batholith. *J Czech Geol Soc* 48:53–54
- Glodny J, Grauert B, Fiala J, Vejnar Z, Krohe A (1998) Metapegmatites in the western Bohemian massif: ages of crystallisation and metamorphic overprint, as constrained by U–Pb zircon, monazite, garnet, columbite and Rb–Sr muscovite data. *Geol Rundsch* 87:124–134
- Hajná J, Žák J, Kachlík V, Chadima M (2010) Subduction-driven shortening and differential exhumation in a Cadomian accretionary wedge: the Teplá–Barrandian unit, Bohemian Massif. *Precambrian Res* 176:27–45
- He B, Xu YB, Paterson SR (2009) Magmatic diapirism of the Fangshan pluton, southwest of Beijing, China. *J Struct Geol* 31:615–626
- Hibbard MJ (1991) Textural anatomy of twelve magma-mixed granitoid systems. In: Didier J, Barbarin B (eds) *Enclaves and granite petrology*. Elsevier, Amsterdam, pp 431–444
- Hibbard MJ (1995) *Petrography to petrogenesis*. Prentice Hall, New Jersey
- Holub FV (1997) Ultrapotassic plutonic rocks of the durbachite series in the Bohemian Massif: petrology, geochemistry, and petrogenetic interpretation. *J Geol Sci Econ Geol Mineral* 31:5–26
- Holub FV, Cocherie A, Rossi P (1997a) Radiometric dating of granitic rocks from the Central Bohemian Plutonic Complex: constraints on the chronology of thermal and tectonic events along the Barrandian-Moldanubian boundary. *CR Geosci* 325:19–26
- Holub FV, Machart J, Manová M (1997b) The Central Bohemian Plutonic Complex: geology, chemical composition and genetic interpretation. *J Geol Sci Econ Geol Mineral* 31:27–50
- Horn I, Rudnick RL, McDonough WF (2000) Precise elemental and isotope ratio determination by simultaneous solution nebulization and laser ablation-ICP-MS: application to U–Pb geochronology. *Chem Geol* 164:281–301

- Hoskin PWO, Kinny PD, Wyborn D, Chappell BW (2000) Identifying accessory mineral saturation during differentiation in granitoid magmas: an integral approach. *J Petrol* 41:1365–1396
- Hrouda F, Chlupáčová M, Rejl L (1971) The mimetic fabric of magnetite in some foliated granodiorites, as indicated by magnetic anisotropy. *Earth Planet Sci Lett* 11:381–384
- Hrouda F, Chlupáčová M, Rejl L (1972) Changes in the magnetite content and magnetite fabric during fenitization, as investigated by petromagnetic methods. *N Jb Miner Abh* 177:61–72
- Irvine TM, Baragar WR (1971) A guide to the chemical classification of common volcanic rocks. *Canad J Earth Sci* 8:523–548
- Janoušek V (2006) Saturnin, R language script for application of accessory-mineral saturation models in igneous geochemistry. *Geol Carpath* 57:131–142
- Janoušek V, Gerdes A (2003) Timing the magmatic activity within the Central Bohemian Pluton, Czech Republic: conventional U–Pb ages for the Sázava and Tábora intrusions and their geotectonic significance. *J Czech Geol Soc* 48:70–71
- Janoušek V, Holub F (2007) The causal link between HP–HT metamorphism and ultrapotassic magmatism in collisional orogens: case study from the Moldanubian Zone of the Bohemian Massif. *Proc Geol Assoc* 118:75–86
- Janoušek V, Rogers G, Bowes DR (1995) Sr–Nd isotopic constraints on the petrogenesis of the Central Bohemian Pluton, Czech Republic. *Geol Rundsch* 84:520–534
- Janoušek V, Bowes DR, Rogers G, Farrow CM, Jelínek E (2000) Modelling diverse processes in the petrogenesis of a composite batholith: the Central Bohemian Pluton, Central European Hercynides. *J Petrol* 41:511–543
- Janoušek V, Braithwaite CJR, Bowes DR, Gerdes A (2004a) Magma-mixing in the genesis of Hercynian calc-alkaline granitoids: an integrated petrographic and geochemical study of the Sázava intrusion, Central Bohemian Pluton, Czech Republic. *Lithos* 78:67–99
- Janoušek V, Finger F, Roberts MP, Frýda J, Pin C, Dolejš D (2004b) Deciphering petrogenesis of deeply buried granites: whole-rock geochemical constraints on the origin of largely undepleted felsic granulites from the Moldanubian Zone of the Bohemian Massif. *Trans Roy Soc Edinb Earth Sci* 95:141–159
- Janoušek V, Farrow CM, Erban V (2006a) Interpretation of whole-rock geochemical data in igneous geochemistry: introducing Geochemical Data Toolkit (GCDkit). *J Petrol* 47:1255–1259

- Janoušek V, Gerdes A, Vrána S, Finger F, Erban V, Friedl G, Braithwaite CJR (2006b) Low-pressure granulites of the Lišov Massif, southern Bohemia: Viséan metamorphism of Late Devonian plutonic arc rocks. *J Petrol* 47:705–744
- Janoušek V, Wiegand B, Žák J (2010a) Dating the onset of Variscan crustal exhumation in the core of the Bohemian Massif: new U–Pb single zircon ages from the high-K calc-alkaline granodiorites of the Blatná suite, Central Bohemian Plutonic Complex. *J Geol Soc London* 167:347–360
- Janoušek V, Konopásek J, Ulrich S, Erban V, Tajčmanová L, Jeřábek P (2010b) Geochemical character and petrogenesis of Pan-African Amspoort suite of the Boundary Igneous Complex in the Kaoko Belt (NW Namibia). *Gondwana Res.* 18: 688–707.
- Jelínek V (1981) Characterization of the magnetic fabric of rocks. *Tectonophysics* 79:T63–T67
- Klomínský J (1963) Geology of the Čistá massif. *J Geol Sci Geol* 3:7–27
- Klomínský J (1965) The Štěnovice granodiorite massif. *J Geol Sci Geol* 8:75–98
- Klötzli US, Parrish RR (1996) Zircon U/Pb and Pb/Pb geochronology of the Rastenberg granodiorite, South Bohemian Massif, Austria. *Mineral Petrol* 58:197–214
- Konopásek J, Schulmann K (2005) Contrasting early Carboniferous field geotherms: evidence for accretion of a thickened orogenic root and subducted Saxothuringian crust (Central European Variscides). *J Geol Soc London* 162:463–470
- Kopecký L, Chlupáčová M, Klomínský J, Sokol A (1997) The Čistá–Jesenice pluton in western Bohemia: geochemistry, geology and ore potential. *J Geol Sci Econ Geol Mineral* 31:97–127
- Košler J, Sylvester PJ (2003) Present trends and the future of zircon in geochronology: laser ablation ICP-MS. In: Hanchar JM, Hoskin PWO (eds) *Zircon*. *Rev Mineral Geoch* 53:243–275
- Košler J, Aftalion M, Bowers DR (1993) Mid-late Devonian plutonic activity in the Bohemian Massif: U–Pb zircon isotopic evidence from the Staré Sedlo and Mirovice gneiss complexes, Czech Republic. *N Jb Miner Mh* 9:417–431
- Košler J, Rogers G, Roddick JC, Bowers DR (1995) Temporal association of ductile deformation and granitic plutonism: Rb–Sr and ⁴⁰Ar–³⁹Ar evidence from roof pendants above the Central Bohemian Pluton, Czech Republic. *J Geol* 103:711–717
- Košler J, Bowers DR, Farrow CM, Hopgood AM, Rieder M, Rogers G (1997) Constraints on the timing of events in the multi-episodic history of the Teplá–Barrandian complex, western Bohemia, from integration of deformational sequence and Rb–Sr isotopic data. *N Jb Miner Mh* 5:203–220

- Košler J, Fonneland H, Sylvester P, Tubrett M, Pedersen RB (2002) U–Pb dating of detrital zircons for sediment provenance studies– a comparison of laser ablation ICP-MS and SIMS techniques. *Chem Geol* 182:605–618
- Kotková J, Schaltegger U, Leichmann J (2010) Two types of ultrapotassic plutonic rocks in the Bohemian Massif–coeval intrusions at different crustal levels. *Lithos* 115:163–176
- Kovaříková P, Siebel W, Jelínek E, Štemprok M, Kachlík V, Holub F, Blecha V (2007) Petrology, geochemistry and zircon age for redwitzite at Abertamy, NW Bohemian Massif (Czech Republic): tracing the mantle component in Late Variscan intrusions. *Chem Erde* 67:151–174
- Kovaříková P, Siebel W, Jelínek E, Štemprok M, Kachlík V, Holub FV, Blecha V (2010) Dioritic intrusions of the Slavkovský les (Kaiserwald), Western Bohemia: their origin and significance in late Variscan granitoid magmatism. *Int J Earth Sci* 99:545–565
- Kusiak MA, Dunkley DJ, Suzuki K, Kachlík V, Kedzior A, Lekki J, Opluštil S (2010) Chemical (non-isotopic) and isotopic dating of Phanerozoic zircon—a case study of durbachite from the Třebíč Pluton, Bohemian Massif. *Gondwana Res* 17:153–161
- Machek M, Ulrich S, Janoušek V (2009) Strain coupling between upper mantle and lower crust: natural example from the Běstvina granulite body, Bohemian Massif. *J Met Geol* 27:721–737
- Maniar PD, Piccoli PM (1989) Tectonic discriminations of granitoids. *Geol Soc Am Bull* 101:635–643
- Medaris G, Wang H, Jelínek E, Mihaljevič M, Jakeš P (2005) Characteristics and origins of diverse Variscan peridotites in the Gföhl Nappe, Bohemian Massif, Czech Republic. *Lithos* 82:1–23
- Miller RB, Paterson SR (1999) In defense of magmatic diapirs. *J Struct Geol* 21:1161–1173
- Miller CF, McDowell SM, Mapes RW (2003) Hot and cold granites? Implications of zircon saturation temperatures and preservation of inheritance. *Geology* 31:529–532
- Molyneux SJ, Hutton DHW (2000) Evidence for significant granite space creation by the ballooning mechanism: the example of the Ardara pluton, Ireland. *Geol Soc Am Bull* 112:1543–1558
- Mrlina J (1993) Gravity field of the West Bohemian Proterozoic formation. *Geol Pružk* 35:326–333 (in Czech)
- Nagata T (1961) *Rock magnetism*. Maruzen, Tokyo
- O'Brien PJ (2000) The fundamental Variscan problem: high-temperature metamorphism at different depths and high-pressure metamorphism at different temperatures. In: Franke W, Haak V, Oncken O, Tanner D (eds) *Orogenic processes: quantification and modelling in the Variscan belt*, vol 179. *Geol Soc London Spec Publ*, London, pp 369–386

- Paterson SR, Fowler TK (1993) Re-examining pluton emplacement processes. *J Struct Geol* 15:191–206
- Paterson SR, Vernon RH (1995) Bursting the bubble of ballooning plutons: a return to nested diapirs emplaced by multiple processes. *Geol Soc Am Bull* 107:1356–1380
- Paterson SR, Vernon RH, Tobisch OT (1989) A review of criteria for identification of magmatic and tectonic foliations in granitoids. *J Struct Geol* 11:349–363
- Paterson SR, Vernon RH, Fowler TK (1991) Aureole tectonics. In: Kerrick DM (ed) *Contact metamorphism*. *Rev Mineral* 26:673–722
- Paterson SR, Fowler TK, Schmidt KL, Yoshinobu AS, Yuan ES, Miller RB (1998) Interpreting magmatic fabric patterns in plutons. *Lithos* 44:53–82
- Pearce JA (1996) Sources and settings of granitic rocks. *Episodes* 19:120–125
- Pearce JA, Parkinson IJ (1993) Trace element models of mantle melting: application to volcanic arc petrogenesis. In: Prichard HM, Alabaster T, Harris NBW, Neary CR (eds) *Magmatic processes and plate tectonics*, vol 76. *Geol Soc London Spec Publ*, London, pp 373–403
- Pearce JA, Harris NW, Tindle AG (1984) Trace element discrimination diagrams for the tectonic interpretation of granitic rocks. *J Petrol* 25:956–983
- Peccerillo A, Taylor SR (1976) Geochemistry of the Eocene calc-alkaline volcanic rocks from the Kastamonu area, northern Turkey. *Contrib Mineral Petrol* 58:63–81
- Pitcher WS (1982) Granite type and tectonic environment. In: Hsü KJ (ed) *Mountain building processes*. Academic Press, London, pp 19–40
- Ramsay JG (1989) Emplacement kinematics of a granite diapir: the Chindamora batholith, Zimbabwe. *J Struct Geol* 11:191–209
- Roberts MP, Clemens JD (1993) Origin of high-potassium, calc-alkaline, I-type granitoids. *Geology* 21:825–828
- Saunders AD, Norry MJ, Tarney J (1991) Fluid influence on the trace element compositions of subduction zone magmas. In: Tarney J, Pickering KT, Knipe RJ, Dewey JF (eds) *The behaviour and influence of fluids in subduction zones*. The Royal Society, London, pp 151–166
- Schäfer J, Neuroth H, Ahrendt H, Dörr W, Franke W (1997) Accretion and exhumation at a Variscan active margin, recorded in the Saxothuringian flysch. *Geol Rundsch* 86:599–611
- Schandl ES, Gorton MP (2002) Application of high field strength elements to discriminate tectonic settings in VMS environments. *Econ Geol* 97:629–642

- Scheuvens D, Zulauf G (2000) Exhumation, strain localization, and emplacement of granitoids along the western part of the Central Bohemian shear zone (Bohemian Massif). *Int J Earth Sci* 89:617–630
- Schulmann K, Konopásek J, Janoušek V, Lexa O, Lardeaux JM, Edel JB, Štípská P, Ulrich S (2009) An Andean type Palaeozoic convergence in the Bohemian Massif. *CR Geosci* 341:266–286
- Shand SJ (1943) Eruptive rocks. Their genesis, composition, classification, and their relation to ore-deposits with a chapter on meteorite. Wiley, New York
- Siebel W, Trzebski R, Stettner G, Hecht L, Casten U, Höndorf A, Müller P (1997) Granitoid magmatism of the NW Bohemian massif revealed: gravity data, composition, age relations and phase concept. *Geol Rundsch* 86:S45–S63
- Siebel W, Breiter K, Wendt I, Höndorf A, Henjes-Kunst F, René M (1999) Petrogenesis of contrasting granitoid plutons in western Bohemia (Czech Republic). *Mineral Petrol* 65:207–235
- Siebel W, Chen F, Satir M (2003) Late-Variscan magmatism revisited: new implications from Pb-evaporation zircon ages on the emplacement of redwitzites and granites in NE Bavaria. *Int J Earth Sci* 92:36–53
- Siebel W, Shang CK, Reitter E, Rohrmüller J, Breiter K (2008) Two distinctive granite suites in the SW Bohemian Massif and their record of emplacement: constraints from geochemistry and zircon $^{207}\text{Pb}/^{206}\text{Pb}$ chronology. *J Petrol* 49:1853–1872
- Siegesmund S, Becker JK (2000) Emplacement of the Ardara pluton (Ireland): new constraints from magnetic fabrics, rock fabrics and age dating. *Int J Earth Sci* 89:307–327
- Slaby E, Martin H (2008) Mafic and felsic magma interaction in granites: the Hercynian Karkonosze pluton (Sudetes, Bohemian Massif). *J Petrol* 49:353–391
- Štemprok M, Holub FV, Novák J (2003) Multiple magmatic pulses of the eastern volcano-plutonic complex, Krušné hory/Erzgebirge batholith, and their phosphorus contents. *Bull Geosci* 78:277–296
- Strnad L, Mihaljevič M (2005) Sedimentary provenance of Mid-Devonian clastic sediments in the Teplá-Barrandian Unit (Bohemian Massif): U–Pb and Pb–Pb geochronology of detrital zircons by laser ablation ICP-MS. *Mineral Petrol* 84:47–68
- Sun SS, McDonough WF (1989) Chemical and isotopic systematics of oceanic basalts: implications for mantle composition and processes. In: Saunders AD, Norry M (eds) *Magmatism in ocean basins*, vol 42. Geol Soc London Spec Publ, London, pp 313–345

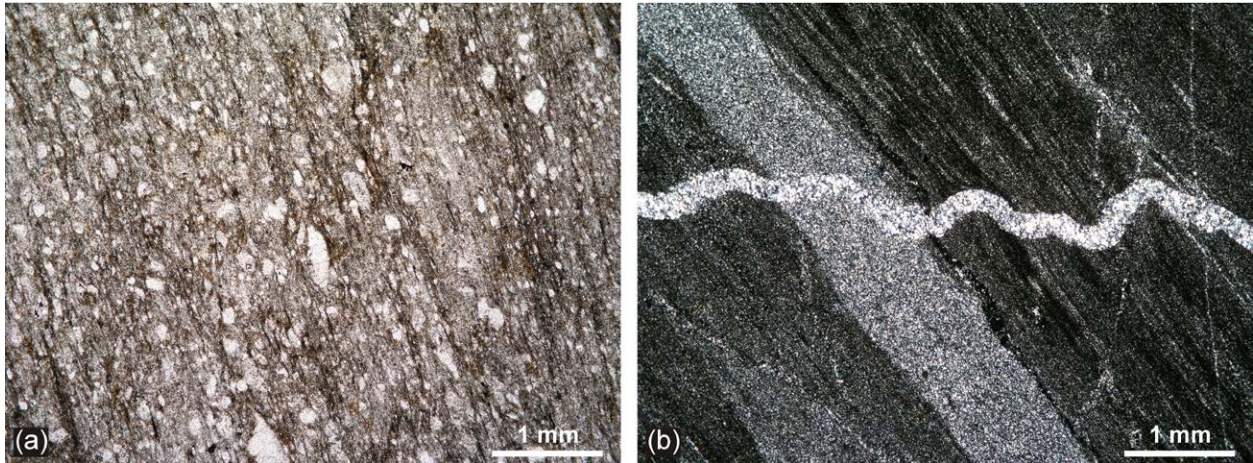
- Tahiri A, Simancas JF, Azor A, Galindo-Zaldívar J, Lodeiro FG, El Hadi H, Poyatos DM, Ruiz-Constán A (2007) Emplacement of ellipsoid-shaped (diapiric ?) granite: structural and gravimetric analysis of the Oulmes granite (Variscan Meseta, Morocco). *J Afr Earth Sci* 48:301–313
- Tatsumi Y, Eggins S (1995) Subduction zone magmatism. *Frontiers in Earth Sciences*. Blackwell, Cambridge, Massachusetts
- Timmerman MJ (2008) Palaeozoic magmatism. In: McCann T (ed) *The geology of Central Europe*. Volume 1: Precambrian and Palaeozoic. Geological Society, London, pp 665–748
- Timmermann H, Dörr W, Krenn E, Finger F, Zulauf G (2006) Conventional and in situ geochronology of the Teplá Crystalline unit, Bohemian Massif: implications for the processes involving monazite formation. *Int J Earth Sci* 95:629–647
- Venera Z, Schulmann K, Kröner A (2000) Intrusion within a transtensional tectonic domain: the Čistá granodiorite (Bohemian Massif)–structure and rheological modelling. *J Struct Geol* 22:1437–1454
- Verner K, Žák J, Hrouda F, Holub F (2006) Magma emplacement during exhumation of the lower- to mid-crustal orogenic root: the Jihlava syenitoid pluton, Moldanubian Unit, Bohemian Massif. *J Struct Geol* 28:1553–1567
- Verner K, Žák J, Nahodilová R, Holub F (2008) Magmatic fabrics and emplacement of the cone-sheet-bearing Knížecí Stolec durbachitic pluton (Moldanubian Unit, Bohemian Massif): implications for mid-crustal reworking of granulitic lower crust in the Central European Variscides. *Int J Earth Sci* 97:19–33
- Verner K, Buriánek D, Vrána S, Vondrovic L, Pertoldová J, Hanžl P, Nahodilová R (2009) Tectonometamorphic features of geological units along the northern periphery of the Moldanubian Zone (Bohemian Massif). *J Geosci* 54:87–100
- Vernon RH (1984) Microgranitoid enclaves in granites–globules of hybrid magma quenched in a plutonic environment. *Nature* 309:438–439
- Vernon RH (2000) Review of microstructural evidence of magmatic and solid-state flow. *El Geosci* 5:1–23
- Watson EB, Harrison TM (1983) Zircon saturation revisited: temperature and composition effects in a variety of crustal magma types. *Earth Planet Sci Lett* 64:95–304
- Wiedenbeck M, Alle P, Corfu F, Griffin WL, Meier M, Oberli F, von Quadt A, Roddick JC, Spiegel W (1995) Three natural zircon standards for U–Th–Pb, Lu–Hf, trace element and REE analyses. *Geostand Newslett* 19:1–23

- Wilson M (1989) *Igneous petrogenesis*. Unwin Hyman, London
- Winchester JA (2002) Palaeozoic amalgamation of Central Europe: new results from recent geological and geophysical investigations. *Tectonophysics* 360:5–21
- Žák J, Holub FV, Verner K (2005a) Tectonic evolution of a continental magmatic arc from transpression in the upper crust to exhumation of mid-crustal orogenic root recorded by episodically emplaced plutons: the Central Bohemian Plutonic Complex (Bohemian Massif). *Int J Earth Sci* 94:385–400
- Žák J, Schulmann K, Hrouda F (2005b) Multiple magmatic fabrics in the Sázava pluton (Bohemian Massif, Czech Republic): a result of superposition of wrench-dominated regional transpression on final emplacement. *J Struct Geol* 27:805–822
- Žák J, Dragoun F, Verner K, Chlupáčová M, Holub FV, Kachlík V (2009) Forearc deformation and strain partitioning during growth of a continental magmatic arc: the northwestern margin of the Central Bohemian Plutonic Complex, Bohemian Massif. *Tectonophysics* 469:93–111
- Zulauf G (1997a) From very low-grade to eclogite-facies metamorphism: tilted crustal sections as a consequence of Cadomian and Variscan orogeny in the Teplá–Barrandian unit (Bohemian Massif). *Geotekt Forsch* 89:1–302
- Zulauf G (1997b) Constriction due to subduction: evidence for slab pull in the Mariánské Lázně Complex (central European Variscides). *Terra Nova* 9:232–236
- Zulauf G (2001) Structural style, deformational mechanisms and paleodifferential stress along an exposed crustal section: constraints on the rheology of quartzofeldspathic rocks at supra- and infrastructural levels (Bohemian Massif). *Tectonophysics* 332:211–237

ELECTRONIC APPENDICES

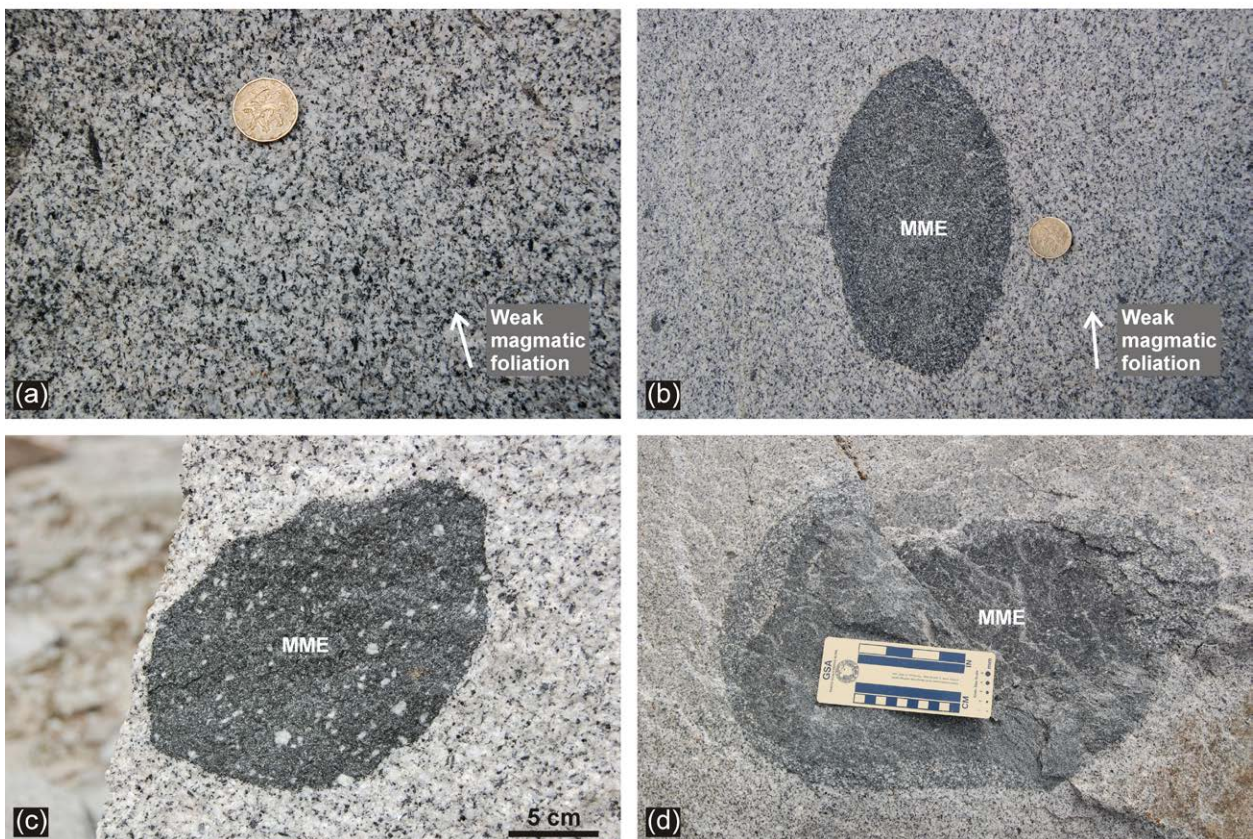
Electronic Supplementary Material (Part 1)

Examples of microstructures in the Neoproterozoic host rock to the Štěnovice pluton. (a) Meta-graywacke from the aureole exhibits rough to continuous spaced cleavage with mimetic biotite growing along cleavage domains. (b) Foliated and finely banded chert.



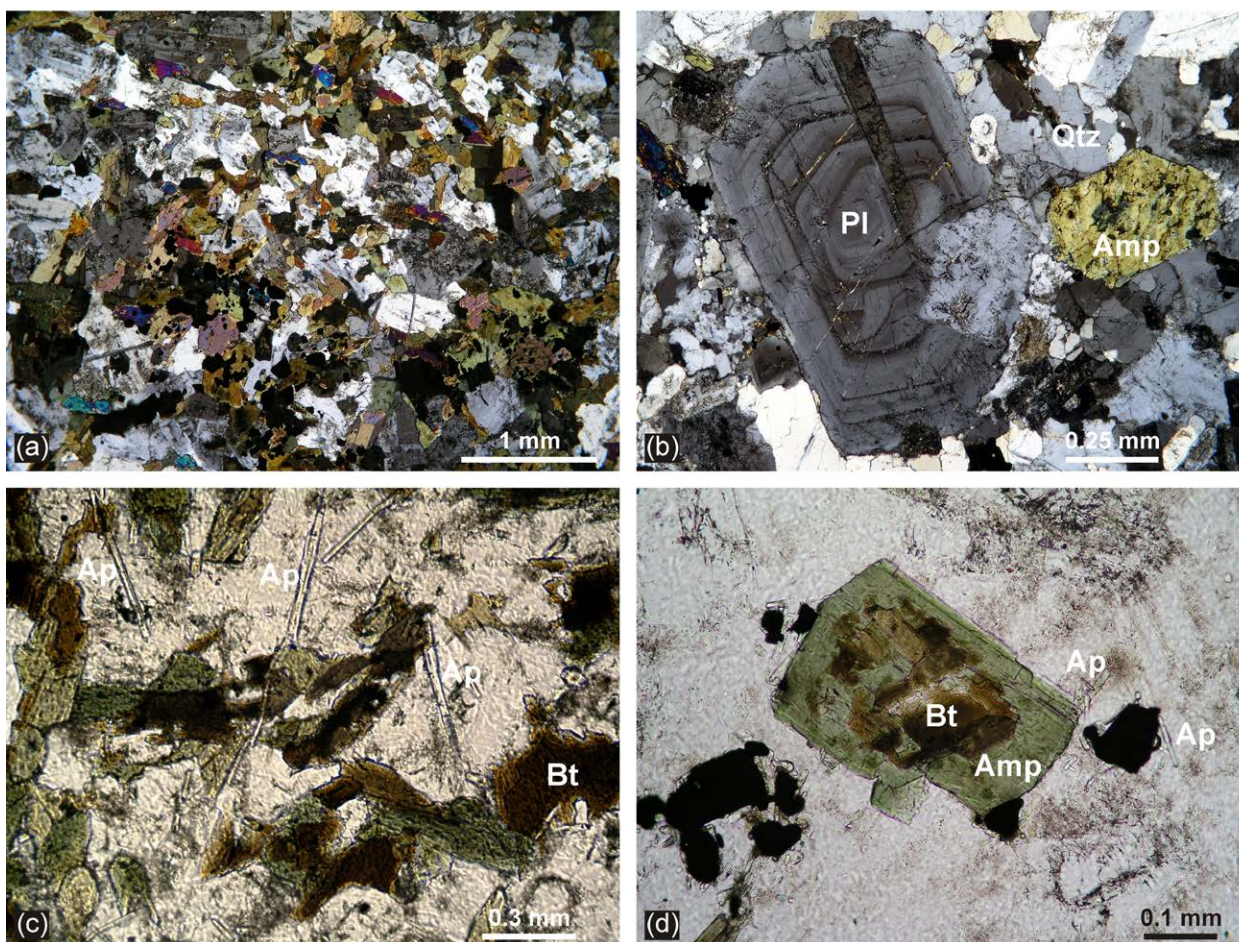
Electronic Supplementary Material (Part 2)

(a) Steep, margin-parallel magmatic foliation in the Štěnovice granodiorite. The foliation is macroscopically defined by the shape-preferred orientation of biotite and amphibole; Nebílovský Borek quarry. (b, c) Quartz diorite enclaves in the central facies of the Štěnovice granodiorite. The enclaves are aligned parallel to magmatic foliation in the host granodiorite; Nebílovský Borek quarry. (d) Double enclave in the central facies of the Štěnovice granodiorite; Nebílovský Borek quarry.



Electronic Supplementary Material (Part 3)

(a) Photomicrograph of magmatic texture of the Štěnovice granodiorite exhibiting no solid-state deformation. Station ZK 10, crossed polars. (b) Close-up of a plagioclase crystal with concentric zoning and a prominent resorption surface. Station ZK 9, crossed polars. (c) Acicular apatite crystals (indicative of a strong undercooling of the magma, Hibbard 1995) enclosed in a matrix of feldspars and quartz. Small irregular crystals of amphibole and biotite. Station ZK 10, plane-polarized light. (d) Subhedral amphibole crystal enclosing resorbed biotite remnants, a disequilibrium texture potentially resulting from a sudden basification of a magma chamber (Hibbard 1995). The hornblende crystal is surrounded mostly by plagioclase; opaque grains of an ore mineral and short prismatic apatite crystals are also abundant. Station ZK 7, plane-polarized light.



Zoned plutons as markers of regional tectonic and geodynamic setting

Electronic Supplementary Material (Part 4)

Geochemical data from the Štěnovice pluton

Sample	ZK-2	ZK-7a	ZK-7b	ZK-10	ZK-9	ZK-11
Locality	Štěnovický vrch	Nebilovský Borek	Nebilovský Borek	Nový Mlýn	Čížice	Na Zbytkách
Latitude [WGS 84]	49.66628311	49.64991032	49.64991032	49.63676264	49.64999196	49.65653454
Longitude [WGS 84]	13.40692981	13.43986331	13.43986331	13.40069887	13.40337102	13.41069371
SiO ₂	66.63	67.13	67.54	67.67	67.94	69.67
TiO ₂	0.40	0.41	0.41	0.41	0.42	0.24
Al ₂ O ₃	16.17	16.11	16.34	16.29	16.45	16.00
FeOt	2.56	2.82	2.68	2.53	2.66	1.55
MnO	0.06	0.05	0.06	0.06	0.06	0.04
MgO	1.18	1.24	1.25	1.12	1.22	0.59
CaO	3.31	3.32	3.35	3.16	3.15	2.38
Na ₂ O	5.04	4.97	5.04	5.10	5.06	5.23
K ₂ O	2.31	2.46	2.45	2.42	2.57	2.43
P ₂ O ₅	0.15	0.16	0.17	0.15	0.17	0.10
LOI	0.69	0.67	0.62	0.49	0.65	0.56
Total	98.51	99.35	99.91	99.38	100.30	98.77
K ₂ O/Na ₂ O	0.46	0.49	0.49	0.47	0.51	0.46
A/CNK	0.96	0.95	0.96	0.97	0.98	1.03
mg#	45.11	43.94	45.40	44.11	44.98	40.42
Rb	98	90	87	97	100	81
Cs	6.5	7.1	7.0	5.8	5.7	3.8
Ba	1062	1067	1070	1097	1123	1164
Sr	867	857	875	850	874	916
Be	3	3	3	4	3	3
Th	15.7	14.3	15.1	16.3	17.5	14.0
U	6.1	4.3	4.7	9.4	4.2	3.7
Zr	204	176	174	180	204	157
Hf	4.9	4.5	4.4	4.7	5.1	4.0
Nb	15.1	12.5	11.3	16.2	16.3	11.1
Ta	0.91	1.00	0.88	1.74	1.12	0.79
Ga	26	23	22	23	24	21
Sn	1	2	1	2	2	1
Mo	0.4	0.2	0.3	2.9	0.2	0.2
W	0.2	0.3	0.3	11.0	0.3	1.1
Cr	23	17	27	17	23	15
Ni	11	12	12	9	11	4
Co	6	7	6	5	6	3
V	36	40	43	38	40	18
Sc	4	4	4	4	4	2
Cu	0.8	0.6	0.6	1.5	0.9	0.5
Pb	26	25	26	32	28	30
Zn	60	50	50	40	60	40
As	1.2	0.6	0.5	1.3	1.2	1.2
La	44.9	38.5	40.0	42.7	41.7	30.6
Ce	73.7	63.0	65.4	69.4	71.1	50.1
Pr	7.69	6.72	6.87	7.21	7.32	5.18
Nd	21.5	19.7	19.5	20.2	20.8	14.4
Sm	3.47	3.23	3.24	3.25	3.45	2.28
Eu	1.05	1.03	1.00	0.99	1.01	0.73
Gd	2.32	2.36	2.24	2.25	2.35	1.50
Tb	0.33	0.33	0.32	0.34	0.35	0.21
Dy	1.75	1.71	1.68	1.87	1.90	1.10
Ho	0.32	0.32	0.31	0.37	0.36	0.20
Er	0.94	0.93	0.90	1.08	1.07	0.58
Tm	0.14	0.14	0.13	0.16	0.16	0.09
Yb	0.87	0.88	0.82	1.05	0.99	0.54
Lu	0.12	0.12	0.11	0.15	0.14	0.07
ΣREE	159.1	139.0	142.5	151.0	152.7	107.6

Zoned plutons as markers of regional tectonic and geodynamic setting

Electronic Supplementary Material (Part 5)

Laser ablation ICP-MS U–Pb data for zircons from the Štĕnovice granodiorite (sample ZK-7)

Analysis	Atomic ratios				Apparent ages (Ma)			
	^{207}Pb		^{206}Pb		^{207}Pb		^{206}Pb	
	^{235}U	1 σ (abs)	^{238}U	1 σ (abs)	^{235}U	1 σ (abs)	^{238}U	1 σ (abs)
11	0.4440	0.0203	0.0595	0.0019	373.1	14.3	372.5	11.7
12	0.4408	0.0554	0.0602	0.0029	370.8	39.0	376.9	17.9
13	0.4564	0.0443	0.0599	0.0027	381.8	30.9	375.3	16.3
15	0.4537	0.0329	0.0612	0.0019	379.8	23.0	383.2	11.3
16	0.4294	0.0805	0.0602	0.0038	362.7	57.2	376.9	23.0
18	0.4258	0.0327	0.0612	0.0021	360.2	23.3	383.1	12.6
20	0.4413	0.0230	0.0598	0.0012	371.2	16.2	374.6	7.4
21	0.4564	0.0271	0.0594	0.0018	381.7	18.9	372.2	11.2
23	0.4439	0.0321	0.0589	0.0033	373.0	22.6	368.7	20.3
24	0.4402	0.0478	0.0579	0.0049	370.4	33.7	362.9	29.7
25	0.4440	0.0488	0.0570	0.0052	373.1	34.3	357.1	31.5
26	0.4245	0.0476	0.0561	0.0048	359.2	33.9	352.0	29.6
33	0.4451	0.0557	0.0583	0.0040	373.9	39.2	365.4	24.3
39	0.4444	0.0252	0.0602	0.0015	373.3	17.7	376.6	9.1
40	0.4505	0.0412	0.0597	0.0028	377.6	28.8	374.0	17.2
41	0.4435	0.0356	0.0593	0.0012	372.7	25.1	371.1	7.4
43	0.4385	0.0364	0.0616	0.0024	369.2	25.7	385.2	14.3
44	0.4483	0.0418	0.0612	0.0022	376.1	29.3	382.8	13.3
45	0.4327	0.0656	0.0600	0.0027	365.1	46.5	375.5	16.3
46	0.4559	0.0359	0.0598	0.0017	381.4	25.0	374.2	10.6
47	0.4443	0.0301	0.0597	0.0017	373.3	21.1	373.7	10.3
51	0.4550	0.0230	0.0600	0.0013	380.8	16.0	375.4	7.9
53	0.4473	0.0542	0.0613	0.0025	375.4	38.0	383.3	15.5
54	0.4428	0.0273	0.0588	0.0021	372.2	19.2	368.1	12.9
56	0.4439	0.0341	0.0585	0.0031	373.0	24.0	366.4	18.7
57	0.4509	0.0543	0.0597	0.0038	377.9	38.0	373.6	23.0
58	0.4437	0.0482	0.0594	0.0032	372.9	33.9	371.8	19.3
59	0.4489	0.0221	0.0598	0.0024	376.5	15.5	374.4	14.6
61	0.4456	0.0629	0.0610	0.0025	374.2	44.1	381.4	15.4
63	0.4538	0.0413	0.0612	0.0032	380.0	28.8	382.9	19.3
64	0.4551	0.0446	0.0607	0.0031	380.8	31.1	380.0	18.9
65	0.4475	0.0526	0.0592	0.0024	375.5	36.9	370.9	14.8
70	0.4261	0.0298	0.0590	0.0022	360.4	21.2	369.4	13.1

Electronic Supplementary Material (Part 6)

List of AMS data from the Štĕnovice pluton

Station	Latitude	Longitude	Sample	Km	K ₁	K ₂	K ₃	L	F	P	P'	T	U	dk _{1,geo}	ik _{1,geo}	dk _{2,geo}	ik _{2,geo}	dk _{3,geo}	ik _{3,geo}
ZK1	49.67035060	13.41223581	1/1/1	5.86E-03	6.05E-03	5.93E-03	5.59E-03	1.020	1.061	1.082	1.085	0.498	0.483	47	17	285	59	145	25
			1/1/2	6.12E-03	6.32E-03	6.19E-03	5.85E-03	1.021	1.058	1.080	1.083	0.466	0.451	50	33	262	53	151	16
			1/1/3	7.37E-03	7.61E-03	7.41E-03	7.09E-03	1.026	1.045	1.073	1.074	0.264	0.247	42	28	259	56	141	17
			1/1/4	6.08E-03	6.28E-03	6.15E-03	5.82E-03	1.021	1.058	1.080	1.083	0.469	0.454	46	19	276	62	143	20
			1/1/5	7.81E-03	8.07E-03	7.88E-03	7.48E-03	1.024	1.054	1.079	1.081	0.386	0.370	49	12	287	69	143	18
			1/2/1	5.72E-03	5.94E-03	5.72E-03	5.50E-03	1.039	1.041	1.081	1.081	0.021	0.001	44	42	258	43	151	18
			1/2/2	5.49E-03	5.66E-03	5.54E-03	5.26E-03	1.022	1.053	1.076	1.078	0.399	0.383	41	22	266	61	138	19
			1/2/3	5.18E-03	5.33E-03	5.24E-03	4.96E-03	1.016	1.057	1.074	1.078	0.562	0.550	37	26	253	58	135	16
			1/2/4	5.53E-03	5.70E-03	5.50E-03	5.40E-03	1.036	1.019	1.056	1.057	-0.320	-0.332	36	28	267	50	142	26
			1/3/1	2.51E-02	2.60E-02	2.54E-02	2.38E-02	1.025	1.068	1.094	1.097	0.459	0.441	175	8	64	68	268	21
			1/3/2	6.12E-03	6.35E-03	6.17E-03	5.85E-03	1.029	1.053	1.084	1.085	0.290	0.271	172	7	68	65	265	24
			1/3/3	6.50E-03	6.74E-03	6.60E-03	6.16E-03	1.021	1.071	1.093	1.098	0.544	0.528	168	26	31	56	269	20
			1/3/4	6.14E-03	6.43E-03	6.11E-03	5.88E-03	1.052	1.040	1.094	1.094	-0.129	-0.151	163	14	28	71	256	13
ZK2	49.66628311	13.40692981	2/1/1	1.23E-02	1.30E-02	1.22E-02	1.17E-02	1.070	1.045	1.118	1.119	-0.209	-0.235	33	1	299	79	123	11
			2/1/2	1.01E-02	1.06E-02	1.01E-02	9.55E-03	1.043	1.061	1.107	1.107	0.164	0.139	36	7	277	77	127	12
			2/1/3	9.16E-03	9.60E-03	9.14E-03	8.72E-03	1.050	1.049	1.102	1.102	-0.012	-0.036	226	6	338	75	135	13
			2/1/4	1.04E-02	1.10E-02	1.05E-02	9.84E-03	1.048	1.063	1.114	1.115	0.128	0.101	40	14	268	69	134	15
			2/1/5	1.08E-02	1.12E-02	1.07E-02	1.03E-02	1.052	1.035	1.088	1.089	-0.192	-0.213	226	17	354	64	130	19
			2/1/6	1.05E-02	1.09E-02	1.03E-02	1.01E-02	1.055	1.025	1.081	1.083	-0.368	-0.384	41	4	299	72	132	18
			2/1/7	1.02E-02	1.06E-02	1.02E-02	9.86E-03	1.039	1.035	1.075	1.075	-0.049	-0.067	38	2	300	79	128	11
			2/2/1	1.36E-02	1.41E-02	1.36E-02	1.30E-02	1.043	1.043	1.087	1.087	-0.001	-0.022	50	11	282	73	142	14
			2/2/2	1.03E-02	1.07E-02	1.03E-02	9.97E-03	1.038	1.031	1.071	1.071	-0.103	-0.120	40	23	268	58	140	21
			2/2/3	8.31E-03	8.62E-03	8.24E-03	8.06E-03	1.047	1.022	1.069	1.071	-0.362	-0.376	224	1	322	80	134	10
			2/2/4	1.14E-02	1.20E-02	1.13E-02	1.10E-02	1.062	1.027	1.091	1.093	-0.382	-0.400	211	4	308	61	118	28
			2/2/5	9.61E-03	9.91E-03	9.77E-03	9.16E-03	1.014	1.066	1.082	1.087	0.637	0.626	40	6	290	74	132	15
			2/2/6	1.17E-02	1.21E-02	1.16E-02	1.13E-02	1.044	1.027	1.072	1.073	-0.236	-0.252	42	9	258	79	133	7
			2/2/7	1.09E-02	1.12E-02	1.10E-02	1.05E-02	1.018	1.052	1.071	1.073	0.474	0.460	230	27	29	62	135	9
ZK3	49.66541391	13.40734874	3/1/1	8.14E-03	8.53E-03	8.18E-03	7.70E-03	1.044	1.061	1.108	1.108	0.161	0.136	26	10	271	67	119	20
			3/1/2	8.25E-03	8.63E-03	8.30E-03	7.84E-03	1.040	1.058	1.100	1.101	0.178	0.155	24	9	278	61	118	28
			3/1/3	9.10E-03	9.42E-03	9.19E-03	8.69E-03	1.026	1.057	1.085	1.087	0.375	0.358	21	22	263	50	126	32
			3/2/1	1.20E-02	1.29E-02	1.19E-02	1.11E-02	1.085	1.076	1.167	1.168	-0.052	-0.090	240	10	363	66	146	22
			3/2/2	7.96E-03	8.28E-03	8.04E-03	7.54E-03	1.030	1.067	1.099	1.101	0.380	0.360	45	9	298	62	139	26
			3/2/3	1.00E-02	1.05E-02	1.00E-02	9.49E-03	1.045	1.057	1.104	1.104	0.115	0.090	48	9	297	64	142	24
			3/2/4	8.78E-03	9.15E-03	8.80E-03	8.38E-03	1.040	1.050	1.092	1.092	0.112	0.090	55	8	315	55	150	34
			3/3/1	8.53E-03	8.96E-03	8.48E-03	8.14E-03	1.056	1.041	1.100	1.100	-0.152	-0.176	223	44	23	45	123	10
			3/3/2	8.16E-03	8.42E-03	8.21E-03	7.83E-03	1.025	1.049	1.074	1.076	0.322	0.306	26	24	257	54	128	25
			3/3/3	1.59E-02	1.65E-02	1.60E-02	1.51E-02	1.034	1.057	1.093	1.094	0.254	0.233	53	12	298	63	149	24
			3/3/4	8.68E-03	9.07E-03	8.79E-03	8.20E-03	1.032	1.072	1.106	1.108	0.380	0.359	57	7	315	60	151	29
ZK5	49.66679290	13.40881758	5/1/1	7.70E-03	7.96E-03	7.84E-03	7.30E-03	1.015	1.073	1.090	1.096	0.644	0.631	239	10	351	66	145	22
			5/1/2	8.31E-03	8.64E-03	8.46E-03	7.84E-03	1.021	1.079	1.102	1.107	0.564	0.547	244	17	9	63	147	21
			5/1/3	1.02E-02	1.07E-02	1.03E-02	9.73E-03	1.039	1.053	1.094	1.095	0.154	0.132	238	14	348	54	139	32
			5/1/4	8.52E-03	8.86E-03	8.64E-03	8.08E-03	1.025	1.069	1.096	1.100	0.455	0.437	252	14	11	63	156	23
			5/1/5	7.73E-03	7.97E-03	7.87E-03	7.36E-03	1.013	1.068	1.082	1.088	0.677	0.666	57	7	308	70	149	19
			5/1/6	7.84E-03	8.11E-03	7.96E-03	7.44E-03	1.019	1.069	1.090	1.094	0.557	0.542	239	6	339	61	146	28
			5/2/1	7.12E-03	7.43E-03	7.20E-03	6.72E-03	1.032	1.072	1.105	1.108	0.378	0.356	67	8	325	57	162	32
			5/2/2	8.45E-03	8.83E-03	8.47E-03													

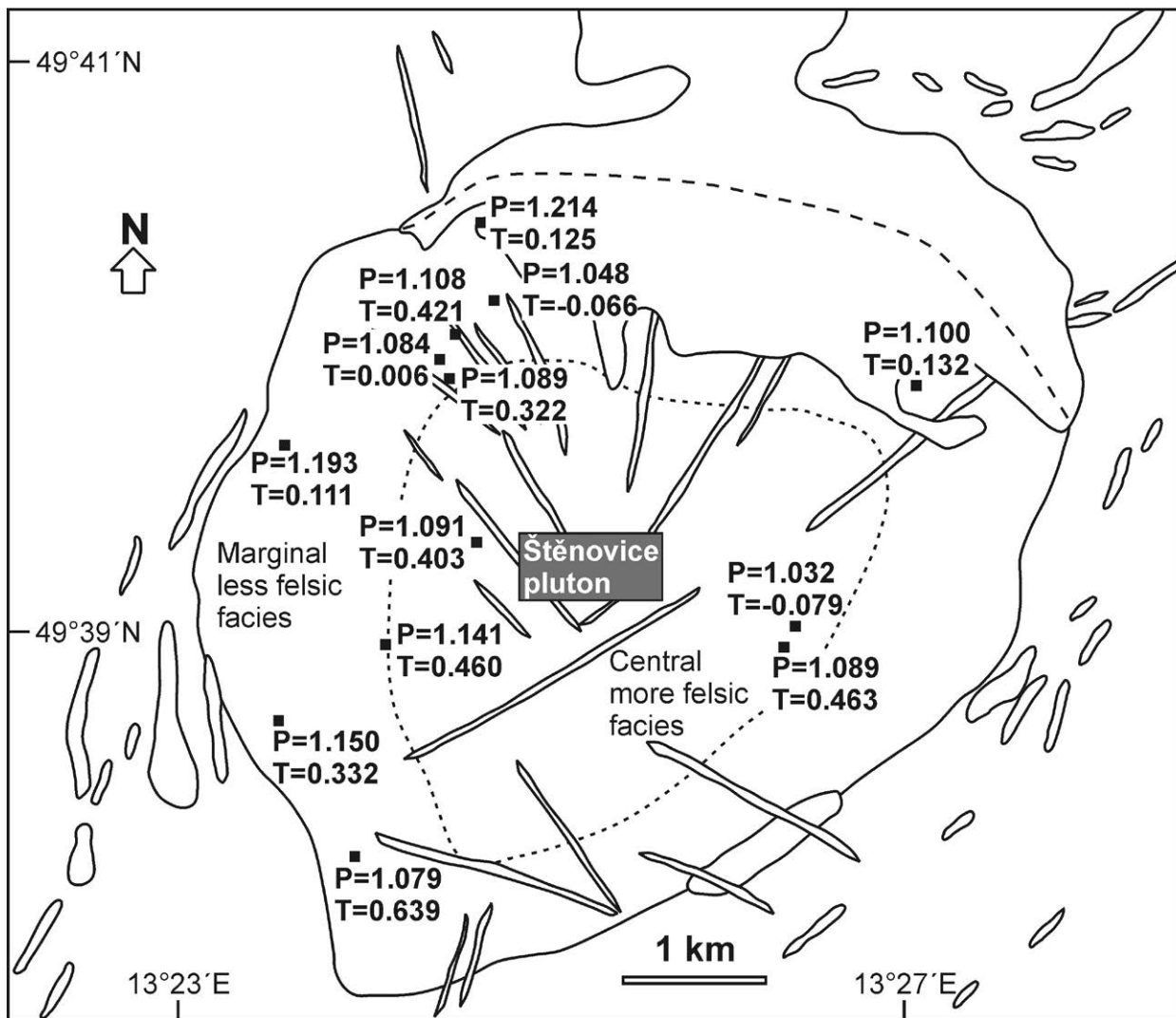
Zoned plutons as markers of regional tectonic and geodynamic setting

Station	Latitude	Longitude	Sample	Km	K ₁	K ₂	K ₃	L	F	P	P'	T	U	dK ₁ geo	iK ₁ geo	dK ₂ geo	iK ₂ geo	dK ₃ geo	iK ₃ geo	...
			5/3/3	7.23E-03	7.52E-03	7.29E-03	6.87E-03	1.031	1.061	1.094	1.096	0.323	0.303	263	3	359	62	171	28	
			5/3/4	8.30E-03	8.66E-03	8.37E-03	7.88E-03	1.034	1.062	1.099	1.100	0.282	0.260	264	13	19	61	168	26	
			5/3/5	7.70E-03	8.05E-03	7.76E-03	7.29E-03	1.037	1.065	1.105	1.106	0.265	0.242	79	1	346	64	170	26	
			5/3/6	8.31E-03	8.69E-03	8.36E-03	7.88E-03	1.039	1.062	1.103	1.104	0.214	0.191	255	9	359	55	159	33	
			5/3/7	8.45E-03	8.79E-03	8.56E-03	7.99E-03	1.027	1.072	1.100	1.104	0.453	0.434	79	2	346	59	170	31	
ZK6	49.65163163	13.43980481	6/1/1	4.19E-03	4.29E-03	4.26E-03	4.02E-03	1.007	1.060	1.067	1.074	0.780	0.774	73	4	174	72	341	18	
			6/1/2	3.68E-03	3.80E-03	3.72E-03	3.54E-03	1.020	1.052	1.073	1.076	0.438	0.423	262	1	170	71	352	19	
			6/1/3	4.29E-03	4.33E-03	4.31E-03	4.22E-03	1.004	1.023	1.027	1.029	0.673	0.669	282	6	159	80	13	9	
			6/1/4	3.70E-03	3.80E-03	3.74E-03	3.57E-03	1.017	1.046	1.064	1.066	0.458	0.445	82	6	185	67	349	22	
			6/1/5	5.23E-03	5.40E-03	5.29E-03	4.98E-03	1.020	1.062	1.084	1.087	0.496	0.481	86	8	198	69	353	19	
			6/1/6	3.84E-03	3.94E-03	3.89E-03	3.68E-03	1.012	1.056	1.069	1.074	0.637	0.627	99	22	218	50	354	32	
			6/1/7	4.56E-03	4.71E-03	4.61E-03	4.38E-03	1.022	1.053	1.077	1.079	0.406	0.390	250	9	144	62	345	27	
			6/2/1	3.13E-03	3.20E-03	3.18E-03	3.01E-03	1.006	1.055	1.062	1.068	0.789	0.783	347	8	91	61	253	28	
			6/2/2	4.32E-03	4.47E-03	4.36E-03	4.12E-03	1.026	1.056	1.083	1.085	0.361	0.344	18	68	166	19	260	11	
			6/2/3	4.34E-03	4.47E-03	4.35E-03	4.19E-03	1.027	1.038	1.066	1.067	0.164	0.148	354	26	111	43	244	36	
			6/2/4	3.91E-03	4.00E-03	3.97E-03	3.76E-03	1.006	1.056	1.063	1.069	0.798	0.792	155	8	51	59	250	30	
			6/2/5	5.02E-03	5.19E-03	5.08E-03	4.79E-03	1.022	1.060	1.084	1.087	0.460	0.444	334	2	66	52	243	38	
			6/2/6	3.26E-03	3.33E-03	3.31E-03	3.15E-03	1.007	1.052	1.060	1.065	0.764	0.758	156	20	33	56	256	26	
			6/3/1	5.35E-03	5.50E-03	5.46E-03	5.11E-03	1.008	1.069	1.078	1.085	0.778	0.771	138	16	18	60	236	25	
			6/3/2	4.23E-03	4.35E-03	4.29E-03	4.04E-03	1.015	1.062	1.078	1.083	0.606	0.595	138	28	3	53	241	22	
			6/3/3	3.87E-03	3.96E-03	3.93E-03	3.72E-03	1.009	1.056	1.066	1.071	0.706	0.698	340	20	102	55	240	27	
			6/3/4	3.95E-03	4.10E-03	3.99E-03	3.75E-03	1.028	1.065	1.095	1.097	0.389	0.370	338	3	74	62	246	28	
ZK7	49.64991032	13.43986331	7/1/11	3.32E-03	3.46E-03	3.35E-03	3.14E-03	1.034	1.066	1.102	1.104	0.312	0.290	9	6	112	63	276	26	
			7/1/2	1.47E-03	1.56E-03	1.48E-03	1.39E-03	1.054	1.065	1.123	1.123	0.092	0.063	12	2	104	41	279	49	
			7/1/3	3.14E-03	3.34E-03	3.13E-03	2.97E-03	1.068	1.052	1.124	1.124	-0.123	-0.151	163	53	49	17	308	32	
			7/1/4	3.50E-03	3.62E-03	3.54E-03	3.33E-03	1.025	1.062	1.089	1.091	0.423	0.405	196	4	100	57	289	33	
			7/2/1	2.10E-03	2.18E-03	2.10E-03	2.03E-03	1.040	1.035	1.077	1.077	-0.070	-0.088	44	54	171	24	273	26	
			7/2/2	1.15E-03	1.22E-03	1.15E-03	1.09E-03	1.063	1.062	1.129	1.129	-0.002	-0.033	13	11	131	67	279	20	
			7/2/3	2.87E-03	2.98E-03	2.92E-03	2.70E-03	1.022	1.083	1.106	1.112	0.570	0.552	24	5	123	60	291	32	
			7/2/4	1.39E-03	1.45E-03	1.41E-03	1.32E-03	1.025	1.071	1.098	1.102	0.468	0.450	15	2	108	58	284	29	
			7/2/5	3.58E-03	3.76E-03	3.62E-03	3.36E-03	1.039	1.077	1.120	1.122	0.315	0.290	199	0	108	65	289	25	
			7/2/6	3.40E-03	3.53E-03	3.43E-03	3.24E-03	1.030	1.059	1.090	1.092	0.325	0.305	207	8	98	66	300	23	
			7/2/7	7.79E-04	8.07E-04	7.86E-04	7.43E-04	1.027	1.058	1.087	1.089	0.363	0.344	18	15	128	51	278	35	
			7/3/1	3.40E-03	3.61E-03	3.39E-03	3.18E-03	1.063	1.067	1.134	1.134	0.028	-0.003	357	1	88	49	266	41	
			7/3/2	3.10E-03	3.29E-03	3.12E-03	2.89E-03	1.056	1.077	1.137	1.137	0.154	0.123	162	2	67	63	253	27	
			7/3/3	3.96E-03	4.13E-03	3.99E-03	3.76E-03	1.036	1.059	1.097	1.098	0.232	0.210	29	25	147	46	281	34	
			7/3/4	4.43E-03	4.58E-03	4.52E-03	4.19E-03	1.013	1.079	1.093	1.101	0.714	0.703	161	7	46	74	253	14	
ZK9	49.64999196	13.40337102	9/1/1	8.68E-03	9.18E-03	8.88E-03	8.00E-03	1.034	1.110	1.148	1.155	0.513	0.487	3	14	220	73	95	10	
			9/1/2	8.28E-03	8.76E-03	8.44E-03	7.62E-03	1.038	1.108	1.150	1.156	0.469	0.441	359	33	222	49	104	22	
			9/1/3	7.61E-03	8.03E-03	7.62E-03	7.19E-03	1.053	1.061	1.117	1.117	0.064	0.036	5	11	256	60	101	28	
			9/1/4	6.68E-03	7.01E-03	6.82E-03	6.22E-03	1.027	1.097	1.127	1.134	0.549	0.528	9	12	251	66	103	21	
			9/1/5	6.62E-03	6.91E-03	6.75E-03	6.19E-03	1.024	1.090	1.117	1.123	0.565	0.546	7	12	251	66	102	21	
			9/1/6	8.23E-03	8.74E-03	8.42E-03	7.52E-03	1.038	1.120	1.162	1.170	0.510	0.481	6	12	244	68	100	18	
			9/1/7	6.92E-03	7.29E-03	6.97E-03	6.48E-03	1.046	1.076	1.125	1.126	0.239	0.211	4	7	249	74	95	14	
			9/2/1	8.59E-03	9.20E-03	8.67E-03	7.91E-03	1.061	1.096	1.163	1.164	0.212	0.176	7	15	232	69	101	14	
			9/2/2	6.89E-03	7.30E-03	7.00E-03	6.36E-03	1.044	1.100	1.148	1.152	0.382	0.352	3	24	218	62	100	14	
			9/2/3	6.90E-03	7.29E-03	6.95E-03	6.47E-03	1.048	1.074	1.126	1.127	0.211	0.183	11	12	228	75	103	9	
			9/2/4	5.88E-03	6.15E-03	5.98E-03	5.51E-03	1.028	1.086	1.117	1.122	0.498	0.477	9	10	247	72	102	15	
			9/2/5	9.49E-03	1.02E-02	9.74E-03	8.57E-03	1.042	1.136	1.184	1.192	0.517	0.486	354	26	209	59	92	16	
			9/2/6	1.07E-02	1.15E-02	1.12E-02	9.55E-03	1.029	1.170	1.203	1.221	0.696	0.671	202	36	342	46	96	21	
			9/2/7	8.40E-03	8.90E-03	8.47E-03	7.82E-03	1.051	1.084	1.139	1.140	0.238	0.207	4	17	222	69	98	13	
			9/2/8	6.65E-03	7.04E-03	6.79E-03	6.12E-03	1.036	1.110	1.150	1.157	0.493	0.466	4	23	211	64	98	11	
ZK10	49.63676264	13.40069887	10/1/1	6.65E-04	6.91E-04	6.85E-04	6.18E-04	1.009	1.107	1.117	1.131	0.844	0.836	173	54	306	26	48	22	
			10/1/2	2.67E-04	2.75E-04	2.69E-04	2.57E-04	1.023	1.046	1.070	1.071	0.338	0.321	312	11	208	52	50	36	
			10/1/3	7.21E-04	7.49E-04	7.40E-04	6.73E-04	1.013	1.100	1.114	1.125	0.762	0.751	133	10	238	57	37	31	
			10/1/4	1.63E-03	1.74E-03	1.68E-03	1.50E-03	1.051	1.106	1.163	1.166	0.338	0.305	253	56	147	11	50	32	
			10/1/5	5.19E-04	5.38E-04	5.20E-04	4.95E-04	1.035	1.050	1.087	1.087	0.172	0.152	297	65	107	24	199	4	
			10/2/1	8.64E-04	9.15E-04	8.76E-04	8.01E-04	1.045	1.094	1.143	1.146	0.345	0.315	311	19	180	62	48	20	
			10/2/2	7.45E-04	7.82E-04	7.51E-04	7.01E-04	1.041	1.072	1.116	1.117	0.260	0.235	246	55	122	21	21	7	
			10/2/3	4.06E-04	4.25E-04	4.09E-04	3.84E-04	1.040	1.063	1.105	1.106	0.219	0.195	202	82	322	4	53	7	
			10/2/4	2.19E-04	2.22E-04	2.20E-04	2.14E-04	1.008	1.028	1.037	1.038	0.537	0.530	151	16	264	54	51	32	
			10/2/5	3.51E-04	3.62E-04	3.54E-04	3.36E-04	1.021	1.054	1.076	1.078	0.436	0.421	140	2	234	69	49	21	
			10/2/6	3.05E-04	3.19E-04	3.05E-04	2.92E-04	1.044	1.047	1.093	1.093	0.030	0.008	240	56	118	20	18	26	
			10/2/7	3.76E-04	3.93E-04	3.74E-04	3.62E-04	1.050	1.032	1.084	1.084	-0.225	-0.244	164	7					

Station	Latitude	Longitude	Sample	Km	K ₁	K ₂	K ₃	L	F	P	P'	T	U	dK ₁ geo	iK ₁ geo	dK ₂ geo	iK ₂ geo	dK ₃ geo	iK ₃ geo
			17/2/3	9.11E-03	9.60E-03	9.18E-03	8.55E-03	1.045	1.075	1.123	1.124	0.242	0.215	320	17	82	61	222	23
			17/2/4	9.21E-03	9.72E-03	9.27E-03	8.63E-03	1.048	1.074	1.126	1.127	0.204	0.176	334	15	92	61	238	24
ZK27	49.67561737	13.41308875	27/1/1	7.03E-03	7.72E-03	7.05E-03	6.33E-03	1.096	1.113	1.220	1.220	0.080	0.031	67	9	304	74	159	13
			27/1/2	7.99E-03	8.76E-03	7.93E-03	7.26E-03	1.104	1.093	1.207	1.207	-0.056	-0.102	70	3	331	71	161	19
			27/1/3	8.06E-03	8.91E-03	8.10E-03	7.15E-03	1.099	1.133	1.246	1.247	0.139	0.085	245	1	342	77	155	13
			27/1/4	8.60E-03	9.57E-03	8.54E-03	7.70E-03	1.121	1.109	1.244	1.244	-0.048	-0.102	253	3	352	72	162	17
			27/1/5	7.53E-03	8.18E-03	7.55E-03	6.87E-03	1.083	1.100	1.191	1.191	0.090	0.046	66	16	301	64	162	20
			27/1/6	8.66E-03	9.42E-03	8.65E-03	7.91E-03	1.089	1.093	1.191	1.191	0.020	-0.023	251	6	356	70	159	20
			27/1/7	7.00E-03	7.63E-03	7.03E-03	6.35E-03	1.086	1.107	1.203	1.203	0.102	0.057	58	11	297	70	151	17
			27/1/8	7.68E-03	8.37E-03	7.77E-03	6.90E-03	1.077	1.126	1.213	1.215	0.227	0.181	61	0	330	82	151	8
			27/2/1	9.28E-03	1.00E-02	9.39E-03	8.41E-03	1.069	1.117	1.194	1.196	0.244	0.202	62	4	299	83	152	6
			27/2/2	8.45E-03	9.42E-03	8.54E-03	7.40E-03	1.103	1.153	1.272	1.274	0.184	0.126	245	2	347	80	155	10
			27/2/3	8.18E-03	8.94E-03	8.21E-03	7.39E-03	1.089	1.112	1.210	1.211	0.109	0.062	64	13	287	72	157	12
			27/2/4	7.41E-03	8.08E-03	7.51E-03	6.64E-03	1.076	1.131	1.217	1.220	0.252	0.205	71	5	321	74	162	15
			27/2/5	1.09E-02	1.19E-02	1.09E-02	9.91E-03	1.090	1.098	1.197	1.197	0.037	-0.008	63	6	250	84	153	1
			27/2/6	8.66E-03	9.39E-03	8.67E-03	7.91E-03	1.083	1.097	1.187	1.188	0.073	0.030	65	8	298	77	157	10
			27/2/7	8.13E-03	9.10E-03	8.25E-03	7.04E-03	1.103	1.172	1.292	1.295	0.237	0.176	69	5	318	77	160	12
			27/2/8	1.02E-02	1.11E-02	1.03E-02	9.14E-03	1.082	1.125	1.217	1.219	0.200	0.153	248	0	338	75	158	15

Electronic Supplementary Material (Part 7)

Map showing spatial distribution of P and T parameters within the Štěnovice pluton. The degree of anisotropy (P) is slightly elevated at some stations near the pluton margin.



Chapter III:

Zoned plutons as markers of regional tectonic and geodynamic setting

Article III.-2:

Intrusive and deformation history of the Ševětín Pluton, Moldanubian Batholith: record of poly-phase tectonic evolution of the Blanice Graben, Bohemian Massif (2014)

Zachariáš J., **Trubač J.**:

Journal of Geosciences **59**: 441–456

Status: Published

Intrusive and deformation history of the Ševětín Pluton, Moldanubian Batholith: record of polyphase tectonic evolution of the Blanice Graben, Bohemian Massif

Jiří Zachariáš^{1*}, Jakub Trubač²

¹Institute of Geochemistry, Mineralogy and Mineral Resources, Faculty of Science, Charles University in Prague, Albertov 6, 128 43 Prague 2, Czech Republic; jiri.zacharias@natur.cuni.cz

²Czech Geological Survey, Klárov 3, 118 21 Prague 1, Czech Republic

*Corresponding author

Keywords: Moldanubian Zone, Moldanubian Batholith, Blanice Graben, paleostress analysis, AMS study, Pb–Zn veins

Received: 20 February 2014; accepted: 3 October 2014 September 2014; handling editor: J. Žák

The online version of this article (doi: 10.3190/jgeosci.175) contains supplementary electronic material.

Running title: Intrusive and structural evolution of the Ševětín Pluton, Moldanubian Batholith

ABSTRACT

The Ševětín Pluton, located c. 15 km NNE of České Budějovice, is a small, isolated, petrologically and structurally complex intrusive body that is genetically related to the youngest intrusions of the Moldanubian Batholith. As documented in this study, its overall shape, internal magmatic fabric as well as brittle structures (dikes, veins, joints, faults) are, however, related to the formation and polyphase tectonic evolution of the Blanice Graben, an about 200 km long and 5–15 km wide NNE–SSW-trending, deep-seated fault zone that cuts across the Moldanubian Unit.

In total, one pre-intrusive and three syn- to post-intrusive tectonic phases have been distinguished. The oblique, NW–SE oriented compression controlled both the intrusion of the Ševětín biotite–muscovite granite and the early stage of its brittle deformation. Sigmoidal pattern of magnetic foliations in this pluton documents its mostly solid-state deformation during oblique sinistral movements on the main faults of the Blanice Graben. The subsequent strike-slip phase was characterized by E–W oriented subhorizontal extension and can be correlated with the intrusion of c. 270 Ma old microgranodiorite dikes. The last extensional phase was associated with the formation of subeconomic Pb–Zn–(Ag?) quartz–calcite veins at c. 265 Ma.

INTRODUCTION

Extensional tectonics associated with late-orogenic evolution of collisional orogens is often coupled with extensive crustal melting and subsequent granitic magma emplacement into the middle to upper crustal levels. Simultaneously, large-scale shear zones are formed in the continental crust to accommodate its stretching (e.g. Malavieille 1993; Faure 1995). At late stages of this scenario, shallow crustal levels are dominated by brittle tectonics and by formation tectonically-controlled sedimentary basins.

Granitic bodies emplaced in tectonically active zones can be used both as passive and active markers of crustal deformation, but also have the potential of dating these processes. Anisotropy of magnetic susceptibility (AMS) is a widely used method for analysis of cryptic magmatic to solid-state deformational fabrics in such granitoid rocks. Moreover, the paleostress orientation and stress ratio can be inferred from examining mode-I fractures (dikes, veins, joints), as well as from interpretation of striations (slickenlines) along fault planes.

This study focuses on the identification of tectonic regimes that controlled the evolution of central and southern parts of the c. 200 km long and NNE–SSW-trending Blanice Graben in the core of the Bohemian Massif. Its formation documents the final stages of orogenic collapse associated with the formation of linear Permo–Carboniferous sedimentary basins, as well as with repeated magmatic and hydrothermal activity. In all these aspects, the Blanice Graben resembles similar tectonic zones of Variscan Europe. Our goal was achieved through a detailed study of the magmatic and solid-state deformational fabrics of the Ševětín Pluton, a small intrusion genetically related to the Moldanubian Batholith.

REGIONAL SETTING

Moldanubian Zone (Fig. 1a) represents a heterogeneous assemblage of medium- to high-grade metamorphic rocks, mainly paragneisses and migmatites, locally with calcareous, graphitic and metabasic intercalations as well as bodies of granulite, eclogite and serpentinite (e.g. Fiala et al. 1995). It is usually subdivided into the lower crustal/upper mantle Gföhl Unit with numerous occurrences of HP–HT granulite (e.g. Racek et al. 2006; Janoušek and Holub 2007; Franěk et al. 2011) and eclogite (e.g. Medaris et al. 2005) massifs and into the medium-pressure mid-crustal Drosendorf and Ostrong units (Dallmeyer et al. 1995; Franke 2000). Recent structural studies documented that many of the high-pressure lithologies within the Gföhl Unit represent vertical extrusions of lower crustal rocks (e.g. Finger et al. 2007; Franěk et al. 2011; Schulmann et al. 2014). The granulite-facies

metamorphism occurred at about 340 Ma (e.g. Friedl et al. 2011), followed by rapid exhumation to mid-crustal levels (c. 338–335 Ma) and subsequent nearly isobaric cooling through ~300 °C between c. 320–310 Ma (e.g. Matte et al. 1985).

The Moldanubian Batholith (or South Bohemian; c. 6 000 km²) is the largest Variscan magmatic complex in the Bohemian Massif. It has a horseshoe shape with western (Bavarian) and eastern (Moravo–Moldanubian) branches joining in the Waldviertel area (Austria). The eastern branch forms a NNE–SSW trending domal structure formed by gravity-driven diapiric upwelling of the metapelitic middle crust (Žák et al. 2011; Verner et al. 2014). The Moldanubian Batholith consists of three to four principal intrusive groups (mostly S and S/I types, rarely I-type; e.g. Holub et al. 1995; Klečka and Matějka 1996; Matějka and Janoušek 1998; Gerdes et al. 2000, 2003; Gerdes 2001; Finger et al. 2009; Breiter 2010), ranging in age from c. 330–323 Ma to c. 305–302 Ma (see, e.g., the review of Bankwitz et al. 2004).

The Blanice Graben (also called the Kouřim–Blanice–Kaplice–Rödl fault zone; Fig. 1a) extends from Český Brod E of Prague to Linz in Austria. On a regional scale, it belongs to a set of conjugate sinistral (NE–SW; e.g. Vitis, Rödl, Diendorf) and dextral (NW–SE; e.g. Pfahl, Danube) shear zones in the southern part of the Bohemian Massif, which resulted from late Variscan N–S oriented compression (Brandmayr et al. 1995).

The southernmost (Austrian) part of the Blanice Graben (also referred to as the Rödl shear zone) is a sinistral ductile shear zone with NE–SW-trending, steeply dipping foliation and subhorizontal stretching lineation. Synkinematic mylonitization was dated at around 288–281 Ma (Brandmayr et al. 1995; Ar–Ar method); however, these ages most probably only represent cooling below the muscovite blocking temperature. Paleostress analysis of brittle faults and fractures from the same zone documented their formation in the strike-slip regime under NW–SE and NE–SW oriented subhorizontal maximum principal stress direction (s_1) and minimum principal stress direction (s_3), respectively. The authors, however, suggested that the brittle deformation phase and related movements corresponded to Alpine tectonic reactivation of the Rödl shear zone at c. 170–180 Ma. In the northern (Czech) part of the Rödl fault zone, Vrána and Bártek (2005) found indicators of sinistral displacement ~17 km south of Kaplice. The early ductile phase of this deformation is constrained to 303 ± 5 Ma by Ar–Ar dating of hornblende from a dike of quartz diorite porphyry dike (Vrána et al. 2005) that intruded syn-kinematically during the development of the mylonitic fabric in the fault/shear zone.

A late stage of tectonomagmatic activity in the Blanice Graben is indicated by the 270 ± 2 Ma Ar–Ar

age of hornblende from a pyroxene microgranodiorite dike near Dehetník (Fig. 1a; Košler et al. 2001). The parental magma of this dike originated from mixing between remelted lower crustal (Moldanubian) rocks and primary magmas derived from an upper mantle source (Košler et al. 2001; Vrána and Janoušek 2006).

The tectonic activity along the faults of the Blanice Graben can also be inferred from the presence of several discontinuous occurrences (erosional relics) of Permo–Carboniferous (Gzhelian to Cisurlian; c. 300–275 Ma) sedimentary successions (Holub 2001). It is not clear whether these originally formed a continuous sedimentary basin. If so, then it was about 12 km wide and at least 130 km long. The main and late stages of sedimentation were accompanied by movements along the eastern faults of the Blanice Graben. This is indicated by: (i) the location of the axis of maximum subsidence close to the eastern margin of the Blanice Graben, (ii) the presence of proluvial conglomerates exclusively along the eastern marginal fault and (iii) the general dip of the strata to the E (10–40°). The maximum thickness of the Permo–Carboniferous strata is at least ~700–800 m in the northern (near Český Brod) and central relics (near Tábor), but attains only ~380 m in the southern relic (near České Budějovice). The most intense subsidence in the Blanice Graben occurred at c. 280–270 Ma. The tectonic history of the Blanice Graben was also reflected in several episodes of hydrothermal activity: Au–Ag (oldest, c. 300 Ma), Ag–Pb–Zn (most widespread) and U (youngest, c. 260 Ma, subeconomic). The geology, mineralogy and tectonic evolution of the Au–Ag deposits were summarized by Zachariáš et al. (2004, 2009) and Zachariáš and Hübst (2012). The Ag–Pb–Zn, mostly vein-type deposits are characterized by quartz–carbonate gangue, by abundance of galena accompanied by sphalerite and Ag-phases (miargyrite, pyrargyrite, argentite and native silver) and by the scarcity of Fe-sulfides (pyrite, arsenopyrite and pyrrhotite). The most important mining districts from the north to the south are Stříbrná Skalice, Ratibořské Hory–Stará Vožice, and Rudolfovo. Similar Pb–Zn bearing mineralization, however without known Ag-phases, was also identified in the studied Ševětín Pluton (see below).

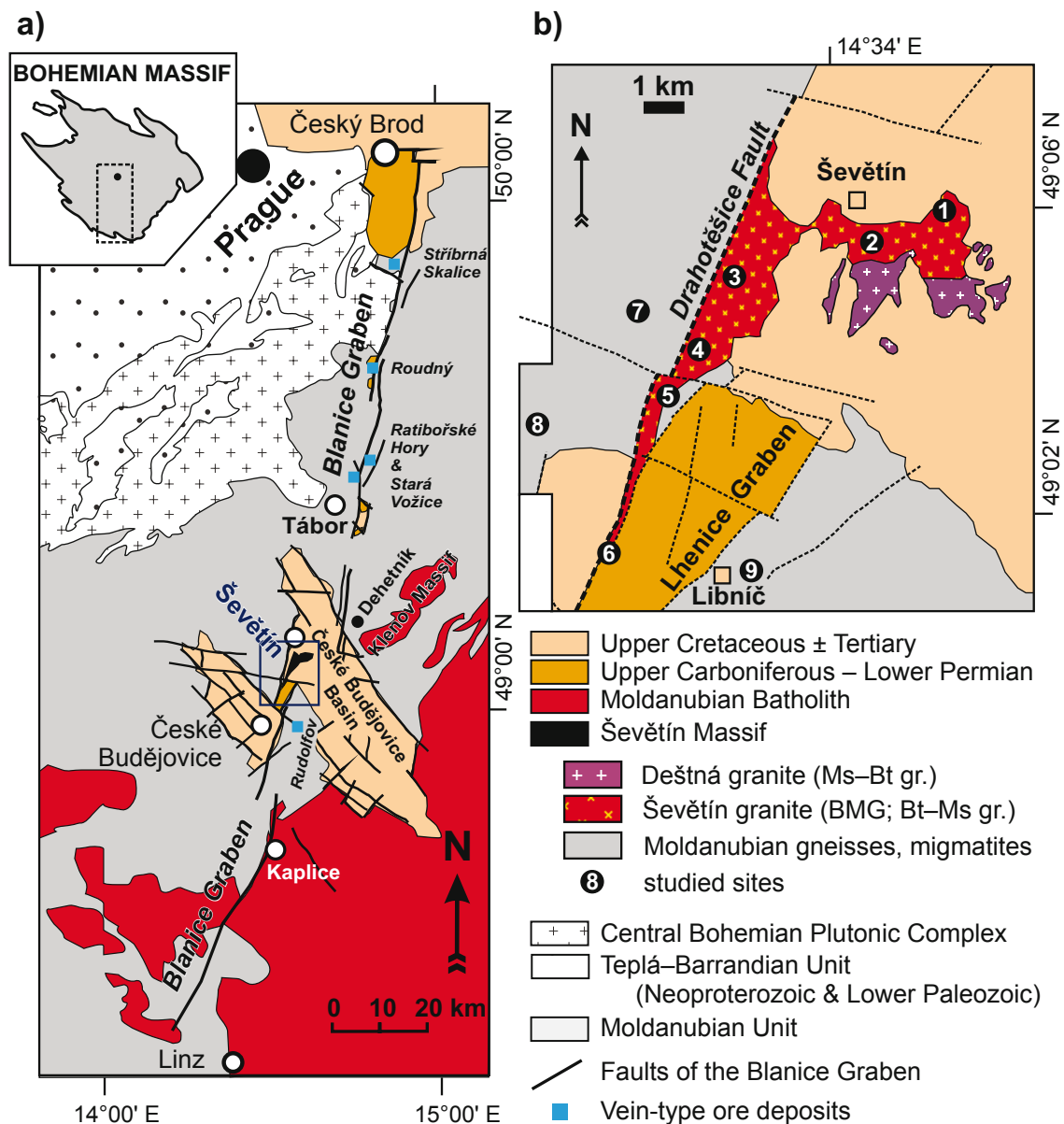


Fig. 1 Simplified geological map of the Blanice Graben (a) and of the Ševětín Pluton (b).

ŠEVĚTÍN PLUTON

The Ševětín Pluton (SP) forms a small composite body that intruded the southern part of the Moldanubian Zone c. 15 km NNE of České Budějovice (Fig. 1a). To the N and NE, it is overlain by the Upper Cretaceous and Tertiary sedimentary rocks of the České Budějovice Basin. The SP shows a triangular shape, apparently stretched along the NNW–SSE trending Drahotěšice Fault (Fig. 1b; a western-peripheral fault of the Blanice Graben system). It is not clear whether this contact is tectonic or intrusive. To the south, the SP narrows down to < 300–500 m and is partly overlain in its southern parts by Permian sediments of the Lhenice Graben.

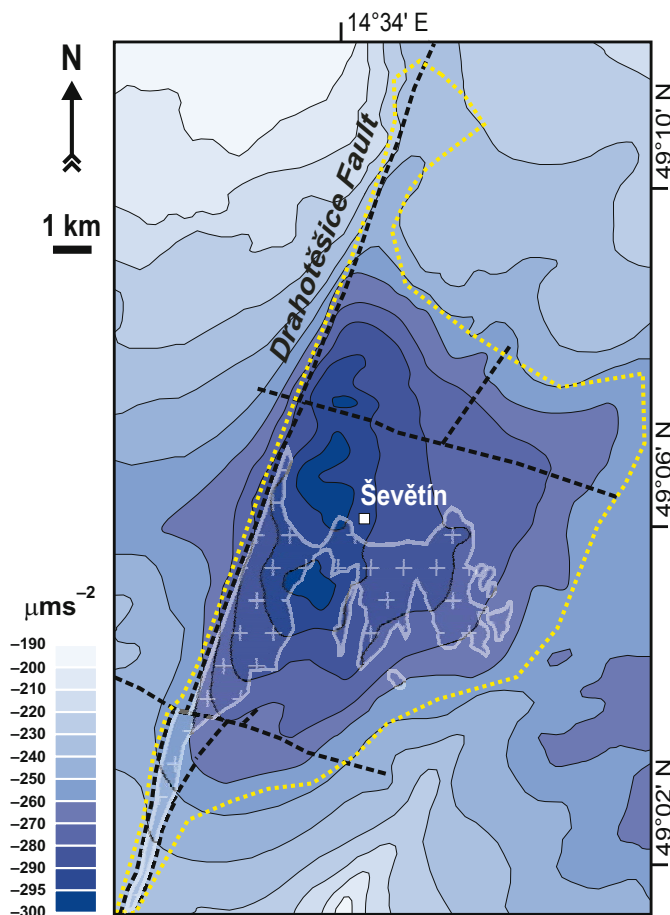


Fig. 2 Bouguer anomaly map of the Ševětín area (after Čuta et al. 1975 and Šalanský 1981). The negative Δg anomaly in the center corresponds to the presence of the Ševětín granite (average density 2620 kg/m^3). The dotted line highlights approximate extent of the Ševětín Pluton, based on interpretation of gravity data and sparse drilling (modified after Kadlec et al. 1978).

Based on gravimetric survey (Čuta et al. 1975; Kadlec et al. 1978; Šalanský 1981) the SP extends to the N, NE and E beneath the sedimentary cover (Fig. 2). The actual size of the Pluton is therefore likely larger than its exposed parts (c. 23 km^2). Its western contact is steeply dipping and parallel with the Drahotěšice Fault, while the eastern is shallowly dipping. The NNE–SSW trending array of local gravity minima, located about 1.0–1.5 km to the E of the Drahotěšice Fault, may indicate a root zone of the SP.

The SP consists of three principal granite units: (i) two-mica cordierite or cordierite–andalusite-bearing Deštná granite (Klečka et al. 1991; René et al. 1999; Matějka et al. 2003); (ii) biotite–muscovite granite (Suk et al. 1978; Matějka 1991; Janoušek et al. 2002) and (iii) fine-grained biotite granite (Janoušek et al. 2002).

The Deštná granite (DG) represents the oldest intrusive phase and crops out only in the central and southeastern parts of the Pluton, being largely covered by Cretaceous and Tertiary sedimentary rocks. It is medium-grained, locally porphyritic (K-feldspar) and rich in muscovite (muscovite > biotite). Cordierite and andalusite form grains up to 1 mm in size (Matějka et al., 2003). Its absolute age is not known but it is believed to belong to the group of “Eisgarn-type” granites (c. 327–328 Ma; Friedl et al. 1996; Gerdes et al. 2003).

The biotite–muscovite granite (BMG) occupies most of the northern and western parts of the Pluton. It is medium- to fine-grained, locally with biotite clots that resulted from replacement of cordierite by muscovite \pm biotite (Janoušek et al. 2002). Biotite granite (BtG) was recently identified only in the Ševětín quarry and its areal extent is small (c. 200 \times 100 m; Janoušek et al. 2002). Both BMG and BtG granites were probably coeval and are also collectively referred to as the Ševětín granite. Their absolute age is not known. The parental magmas of the BMG and BtG are thought to have represented a mixture of a relatively primitive source (mantle-derived melts or metabasic rocks) and more evolved material geochemically corresponding to mature Moldanubian metasedimentary rocks or to their melts (Janoušek et al. 2002).

The SP was intruded by various dikes: lamprophyre (Ambrož 1935), pyroxene microgranodiorite (Vrána et al. 1993; Košler et al. 2001) and by aplite or leucogranite (this study; Zachariáš and Štrba 2014). The age of the microgranodiorite dike swarm (270 ± 3 Ma ^{39}Ar – ^{40}Ar ; Košler et al. 2001) thus represents the lower age limit for the Ševětín granite intrusion.

Brittle–ductile and brittle deformation of the granites is a conspicuous feature of the SP. Both the DG and BMG are strongly deformed, while the BtG is only weakly deformed or even undeformed (Janoušek et al. 2002). The presence of specific deformation features in quartz grains from Ševětín (Vrána 1987), together with some geochemistry indications (Vrána et al. 1993), led these authors to suppose an impact-related origin of the Ševětín structure. This idea was, however, later abandoned (Cordier et al. 1994; Košler et al. 2001).

Various types of hydrothermal mineralization are known from the SP, associated with the individual stages of brittle deformation of the Pluton. These include quartz–feldspar veins, quartz veins and quartz–carbonate veins (e.g. Čtvrtník and Pavlíček 2002; Welser and Zikeš 2009 and references therein). The latter are associated with uneconomic Pb–Zn ores, a probable analogue of the Ag–Pb–Zn ores of the Blanice Graben (e.g. Rudolfovo and Ratibořské Hory–Stará Vožice ore districts).

METHODS

This paper is based on three methodological approaches: (i) orientation and kinematic analysis of mesoscopic structures on outcrop scale; (ii) paleostress analysis of fault-slip data and (iii) AMS study of preferred mineral orientation, focused on the identification of relic magmatic fabric and of its solid-state modification.

The study area is relatively flat and outcrops for application of the above methods are scarce. We identified only six suitable localities within, and three, outside the Pluton, referred to as SEV1 to

SEV9 sites/samples. The most important and also the largest and best exposed site was an active quarry (with dimensions of c. 600 × 350 × 50 m) in the northern part of the Pluton (SEV2), close to the southeastern margin of the Ševětín village. The number of measured data (mostly joints) at the other sites usually varied from 20 to 45 and was thus significantly less than at the Ševětín quarry (over 300). Therefore, some joint systems discernible in the Ševětín quarry may have been missed elsewhere.

Orientation analysis of structural data was performed in the Stereo32 software. All stereoplots represent lower hemisphere equal area projections, except stated otherwise. Paleostress analysis of fault-slip data was done using the numerical Gauss method (Žalohar and Vrabec 2007); the data were processed in the T-Tecto software (version 3.0; author J. Žalohar; http://www2.arnes.si/~jzaloh/t-tecto_homepage.htm).

A total of 16 oriented cores were sampled using a hand-held drill at 7 stations throughout the Pluton. After cutting, these samples yielded 78 standard specimens with a volume of 10 cm³. The AMS was measured at low field (450 Am⁻¹) with a MFK1-A Kappabridge instrument in the Laboratory of Rock Magnetism, Institute of Geology and Paleontology, Charles University in Prague. Statistical treatment and analysis of the AMS data were carried out using the ANISOFT 4.2 program package (<http://www.agico.com>). All the measured data and parameters are presented in the Electronic Supplement to this article.

The AMS data are represented by the k_m , P , and T parameters defined as follows: (1) $k_m = (k_1 + k_2 + k_3)/3$; (2) $P = k_1/k_3$; and (3) $T = 2\ln(k_2/k_3)/\ln(k_1/k_3) - 1$; where $k_1 \geq k_2 \geq k_3$ are the principal susceptibilities. Parameter k_m represents the mean bulk magnetic susceptibility, which reflects the proportion and type of magnetic minerals in the analyzed rock. Parameter P (Nagata 1961), the degree of AMS, reflects the eccentricity of the AMS ellipsoid and may thus be related to the intensity of preferred orientation of the magnetic minerals. Parameter T (Jelínek 1981) characterizes the symmetry of the AMS ellipsoid; it varies from -1 (perfectly prolate ellipsoid) through 0 (triaxial ellipsoid) to $+1$ (perfectly oblate ellipsoid). In magnetic fabric studies, the maximum principal susceptibility (k_1) is referred to as the magnetic lineation and the minimum principal susceptibility (k_3) defines a pole to the magnetic foliation; their orientations are presented in stereograms in the geographic (in situ) coordinate system. GPS coordinates of drill-cores used in the AMS study as well as of other studied sites are given in the Electronic Supplement. All the data were collected in 2012 and 2013.

RESULTS

Orientation analysis of brittle structures in the Ševětín quarry

Joints

Joints of several generations represent the most ubiquitous mesoscopic phenomena in the Ševětín Pluton. In total, we distinguished six types of joints (referred to as P_1 through P_6) in the quarry with respect to their orientation (Fig. 3).

P_1 joints represent the most prominent structures in the quarry (Fig. 4a). They strike NE–SW and dip moderately to SE. They are regularly spaced (about 5–20 cm) and represent typical extension joints as indicated by the frequent presence of plumose hackles and rib marks (Fig. 4b). The longitudinal axis of rib marks is roughly identical with the dip line and their shape implies step-ward

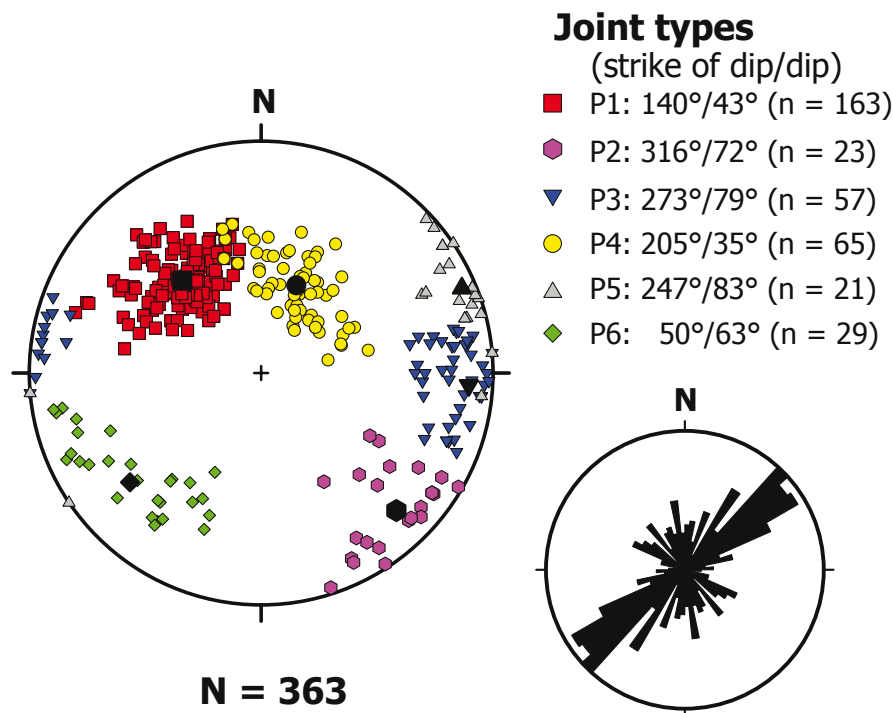


Fig. 3 Summary plot of poles of joints from the active Ševětín quarry and rose diagram of joint strikes. The maxima of the individual joint types given in the legend were converted from the respective eigenvectors.

propagation of P_1 joints upward along the dip line. The visibility of ribs and hackles is highlighted by greenish coatings of epidote–chlorite and by even younger scarce coatings of calcite.

P_2 joints are much less frequent than P_1 . Strictly geometrically, they resemble a conjugate system to P_1 joints. However, we found no unambiguous evidence for the presence of a conjugate P_1 – P_2 system.

P_3 joints are steep, N–S trending and locally filled in by veins of greyish quartz. Some of P_3 joints contain hackles and rib marks; however, they are less visible than those at the P_1 joints. Locally, the

joints may display systematic down-slip of northern segments (Fig. 4c). Therefore, they represent most probably mixed Mode I–II fractures.

P_4 joints strike mostly NW–SE and dip moderately to the SW. They frequently show evidence for shear movements and usually do not crosscut P_1 joints. Some are rimmed by feldspathic masses (up

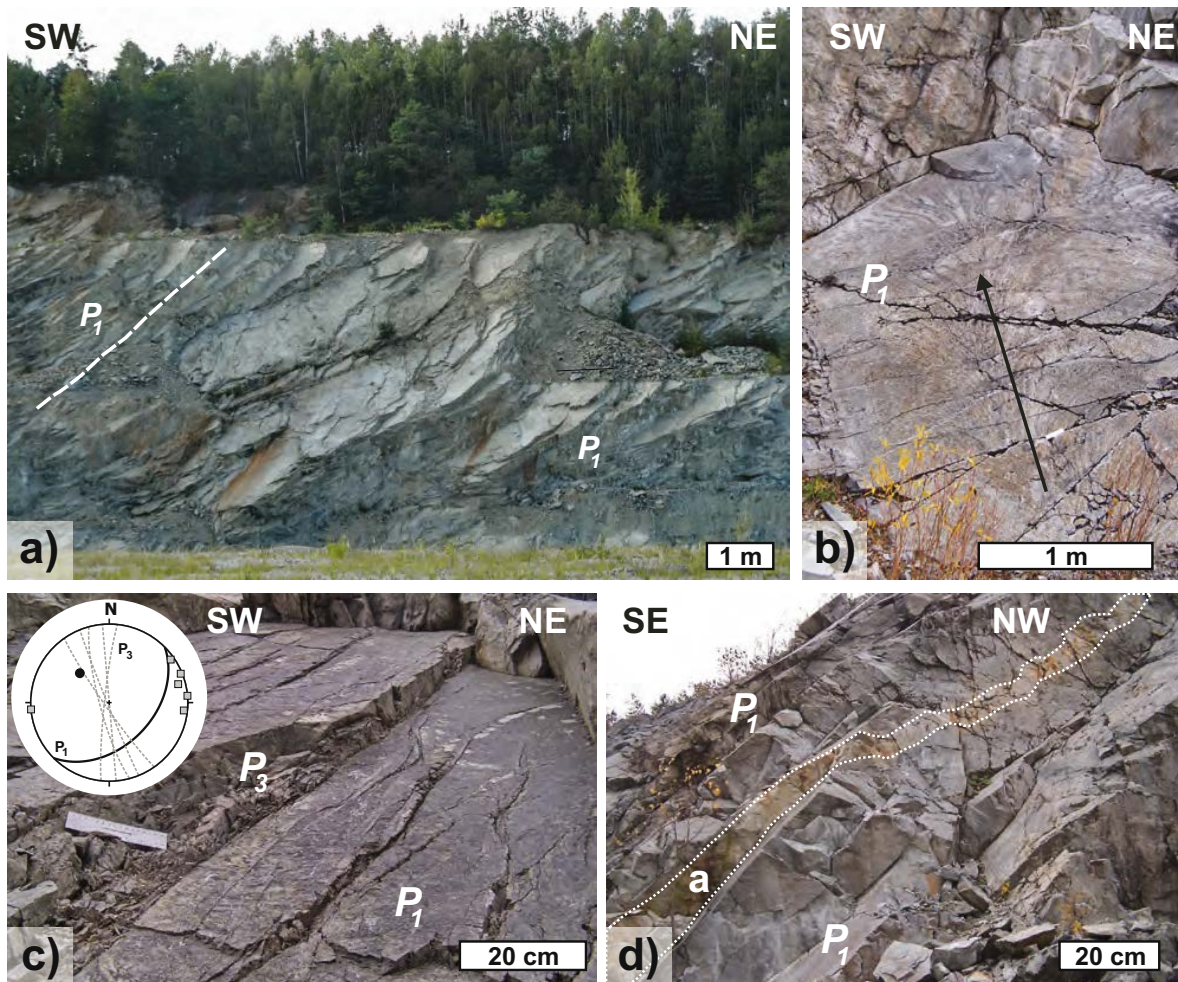


Fig. 4 Photos of P_1 joints at the new Ševětín quarry: **a** – Moderately inclined P_1 joints in the southwestern wall of the quarry. **b** – Detail of plumose hackles and rib marks on the surface of a P_1 joint. The arrow indicates the axis of the plume and upward direction of the fracture opening. **c** – P_1 joint crosscut by steep P_3 joints, accompanied by systematic down-throw of the northeastern segments. **d** – Dike of aplite intruding the BMG between two P_1 joints.

to 1.5 cm thick), while the others host veins of greyish quartz.

P_5 and P_6 joints are oriented WNW–ESE and dip steeply to the NE to ENE (P_5) or to SE (P_6). Some P_5 joints were filled in by late calcite veins (CC3). Both calcite veins and P_5 joints represent extension fractures (Mode I).

Dikes

We identified several aplite and pegmatitic dikes in the quarry. The largest is a pinkish aplite ~20 cm thick, at least 70–60 m long along its strike, and c. 10 m along the dip. It is parallel or subparallel to P_1 joints (Fig. 4d). Other observed aplite dikes are much smaller, mostly less than 5 cm thick, and of a more variable orientation. Most of them, however, are still subparallel with P_1 joints (Fig. 5a). In addition to aplite, several dikes of leucocratic granite (10 to 50 cm thick) can be found in the southwestern wall of the quarry, but these were not accessible for direct structural measurements. It can be seen in Fig. 6 that these dikes are first parallel to P_1 joints, but later steepen and finally one

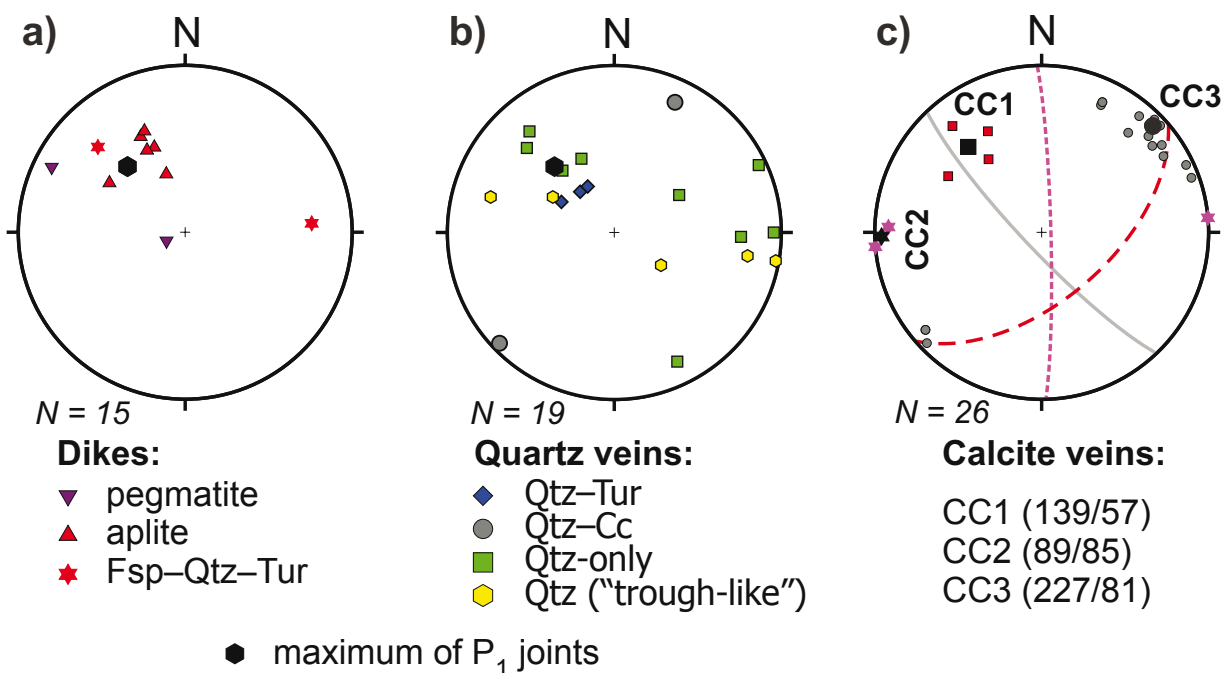


Fig. 5 Summary diagrams for intrusive dikes (a), quartz veins (b) and calcite veins (c) observed in the BMG granite in the Ševětín quarry.

of them approaches almost vertical orientation at the bottom of the quarry wall. Another felsic but much thicker zone (dike?) is located above these dikes and is also parallel to P_1 joints.

Hydrothermal veins

Several types/generations of hydrothermal veins and of transitional late-magmatic to early hydrothermal products can be identified in the Ševětín quarry. The latter are represented by fractures/veins with feldspathic rims, which may contain quartz, hornblende and/or tourmaline in the core. They are usually less than 2 cm thick and mostly parallel to P_1 joints.



Fig. 6 Parallel dikes of leucogranite (highlighted by shading) in the southern wall of the active Ševětín quarry. Note they are initially parallel with P_1 joints, but later become much steeper.

Probably three generations of hydrothermal quartz veins exist in the quarry (Fig. 5b): (i) The undoubtedly oldest, less than 5 mm thick quartz veinlets with tourmaline, slightly oblique to P_1 joints and locally crosscutting them; (ii) Up to several cm thick veins of greyish quartz (with finely disseminated chlorite and/or pyrite), more or less subparallel to P_4 joints and (iii) Older growth zones in the veins of late calcite (CC3).

With respect to their orientation, three clusters of calcite veins and veinlets were identified (Fig. 5c) and referred to as CC1, CC2, CC3. Veins of the late calcite (CC3) are the most frequent. They are extensional in nature, as indicated by bilaterally symmetrical growth zones and less frequently by crustiform or breccia textures. We found them associated with P_3 joints, but they may also accompany the main fault (being parallel with it). Čtvrtník and Pavlíček (2002) described about 20 cm thick calcite vein (CC3?) with abundant sphalerite and/or galena spatially associated with the main fault. However, we found only one calcite vein with sparse sphalerite grains. The other two groups (CC2, CC1) may represent two separate and older but volumetrically minor calcite generations. Alternatively, they may have been coeval with the CC3 group as the fluids just reached structures of different orientation.

Faults and fault-slip data

Two major more or less parallel faults (striking NE–SW and inclined 70 to 85° to the SE) crop out in the Ševětín quarry (for details, see Zachariáš and Štrba 2014). They are oblique to the Drahotěšice Fault and are associated with numerous second-order small-scale faults. The fault plane of the western fault is flanked by c. 0.5 m wide zone of friable gouge of dark appearance. Rocks in an about 50–80 m wide zone between these two faults are highly fractured. Although both faults

probably accumulated most of the brittle deformation, the fault planes themselves are almost free of identifiable striation. Striations are, however, rather frequent within the highly fractured zone. We identified a total of 65 fault planes with slickenlines in the Ševětín quarry that were included in the paleostress analysis. Fault-slip data from other sites were sparse (less than three per locality) and thus excluded.

Paleostress analysis of fault-slip data

Our calculations started with a larger maximum misfit value (50–60°) between the theoretical and real slip vectors and were repeated until lower misfit values (15–20°) and numerically stable solutions were obtained. The analysis resulted in the separation of fault-slip data into three populations representing separate tectonic phases (Fig. 7). They differ in the orientation of the paleostress axes and in the stress ratio (represented by the D parameter, where $D = (\sigma_2 - \sigma_3) / (\sigma_1 - \sigma_3)$).

Phase 1 represented an oblique compression regime, with the maximum principal stress in the NW–SE direction. The minimum principal stress (σ_3) was moderately inclined to the W.

Phase 2 reflected a strike-slip regime, as indicated by subvertical orientation of the intermediate stress axis (σ_2). The maximum principal stress (σ_1) was oriented N–S and the least principal stress (σ_3) E–W.

Phase 3 corresponded to an extensional regime with maximum subhorizontal σ_3 in the NNE–SSW direction.

Orientation analysis of brittle structures on a regional scale

Three to four dominant joint systems are identified on a regional scale: the P_1 system is best recognizable in the northern part of the SP (Fig. 8; sites 1–3), but is still identifiable across the whole Pluton. At a single locality (site 4), the P_1 system grades into steep joints, similar in orientation to P_3 joints at the Ševětín quarry (site 2). Most localities, and notably the abandoned quarry south of the village of Vitín (site 3; the second largest outcrop after the Ševětín quarry), lack P_4 joints.

Ductile structures in the surrounding Moldanubian unit

Localities outside the Ševětín Pluton are represented by sillimanite–biotite paragneisses (site 7), migmatites (site 8) and migmatitic biotite gneisses (site 9). They all show subhorizontal metamorphic foliation (S_i ; Figs 8 and 9a). Stretching lineation (L_i) is, however, visible only in the paragneiss (site 7), where it is subhorizontal and trends NW–SE (Fig. 9b). At the same locality we also identified open folds with moderately inclined axial planes and with well-developed

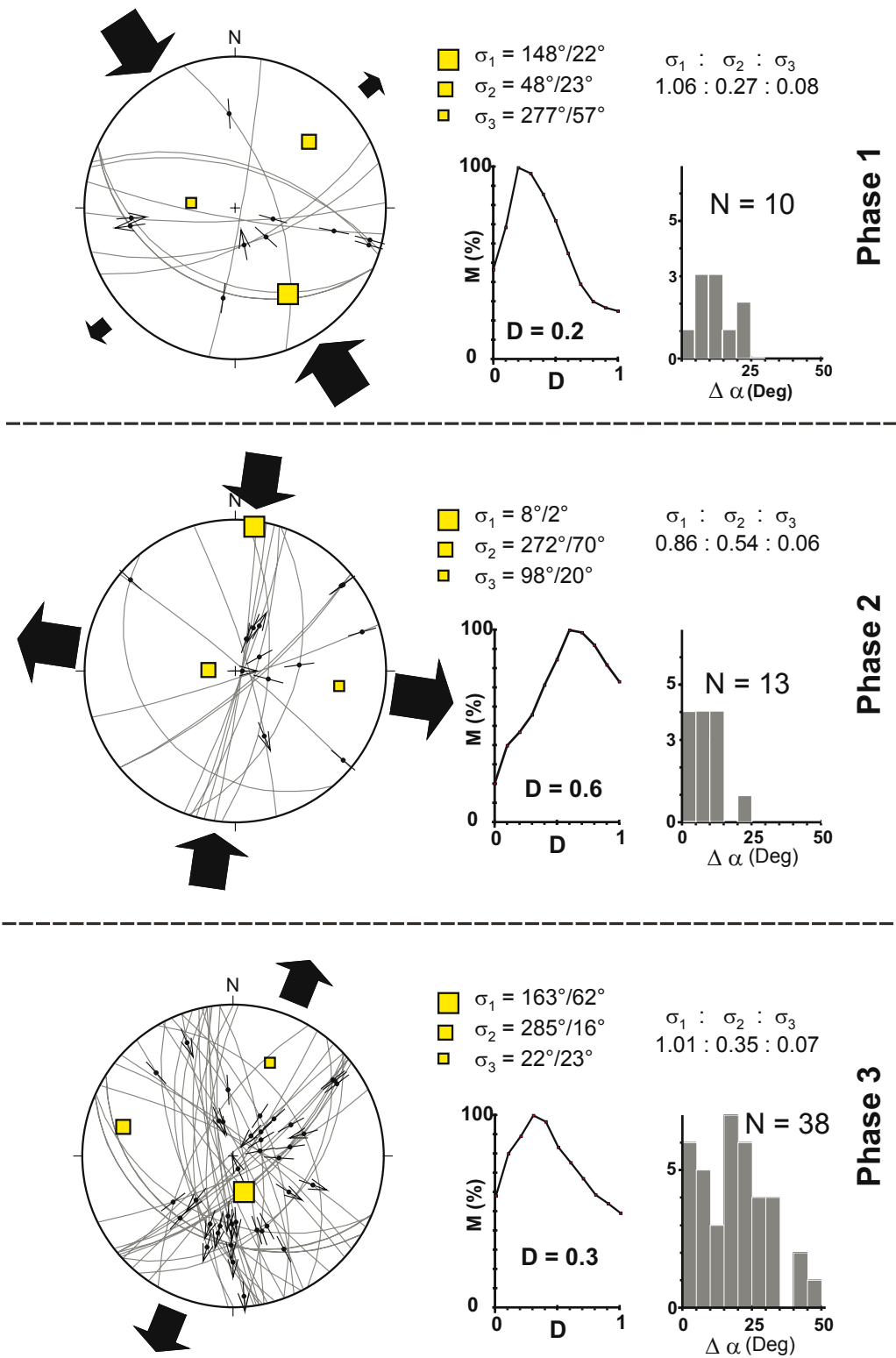


Fig. 7 Separation of fault-slip data, based on paleostress inversion analysis using the Gauss method (Žalohar and Vrabec 2007), into three stress phases. All stereoplots represent lower hemisphere equal angle projections. Solid arrows indicate orientations of maximum horizontal compression and/or extension. The other diagrams show the confidence of the parameter D estimate and histograms of deviation between the calculated and measured slip vectors.

second-order chevron-like folds in the hinge zones (Fig. 9b). All the folds exhibit the same axis orientation, identical with the strike and dip of the stretching lineation.

Magnetic fabric parameters and orientation of the Ševětín Pluton

Bulk susceptibility

The bulk magnetic susceptibility of the measured specimens is of the order of 10^{-5} (Fig. 10a; SI units are used throughout this paper), characteristic of paramagnetic granites (e.g., Hrouda and Kahan 1991; Bouchez 1997). A slight increase in the bulk susceptibility can be seen from the SEV2b (32×10^{-6} to 39×10^{-6}) through the SEV2c, SEV3, SEV4 (60×10^{-6} to 73×10^{-6}) to the SEV2a, SEV6 and SEV1 granites (74×10^{-6} to 104×10^{-6}).

P and T parameters

The Ševětín granite is characterized by a low degree of anisotropy not exceeding 1.2 (corresponding to 12% magnetic anisotropy) for most of the analyzed specimens (Fig. 10b).

Sample SEV1 ($P = 1.013$ – 1.054) is the least anisotropic, SEV2b ($P = 1.040$ – 1.058), SEV2c ($P = 1.033$ – 1.069 ; one outlier with $P = 1.263$) and SEV3 ($P = 1.024$ – 1.084) are slightly more so. The degree of anisotropy of samples SEV2a and SEV4 is more widely scattered from 1.044 to 1.085 (Fig. 10b). The highest degree of anisotropy was measured in the SEV6 specimens ($P = 1.072$ – 1.119).

In contrast to the slight differences in the P parameter, the granites exhibit a mutually comparable range of shape parameter from highly prolate (T as low as -0.826) to highly oblate ($T = 0.879$ at most), as well as a distinct trend of concomitantly increasing oblateness and degree of anisotropy (Fig. 10b).

Orientations

In terms of orientation, all the granite samples except SEV3 and SEV6 exhibit N–S to NE–SW trending, steep to moderately dipping magnetic foliation, indicated by clusters of the k_3 axes in the stereonet (Fig. 11a). In sample SEV3, the magnetic foliation is also steep; however, it trends NW–SE. Notably, individual k_3 axes in this sample are broadly scattered along a girdle with a pole located at the maximum magnetic lineation (maximum of the k_1 axes). Magnetic foliation in the sample SEV6 trends E–W.

Magnetic lineations (k_1 axes) are usually well defined and of subhorizontal plunge. They trend N–S to NE–SW, except samples SEV6 (E–W) and SEV3 (NW–SE) and form clusters in the stereonet.

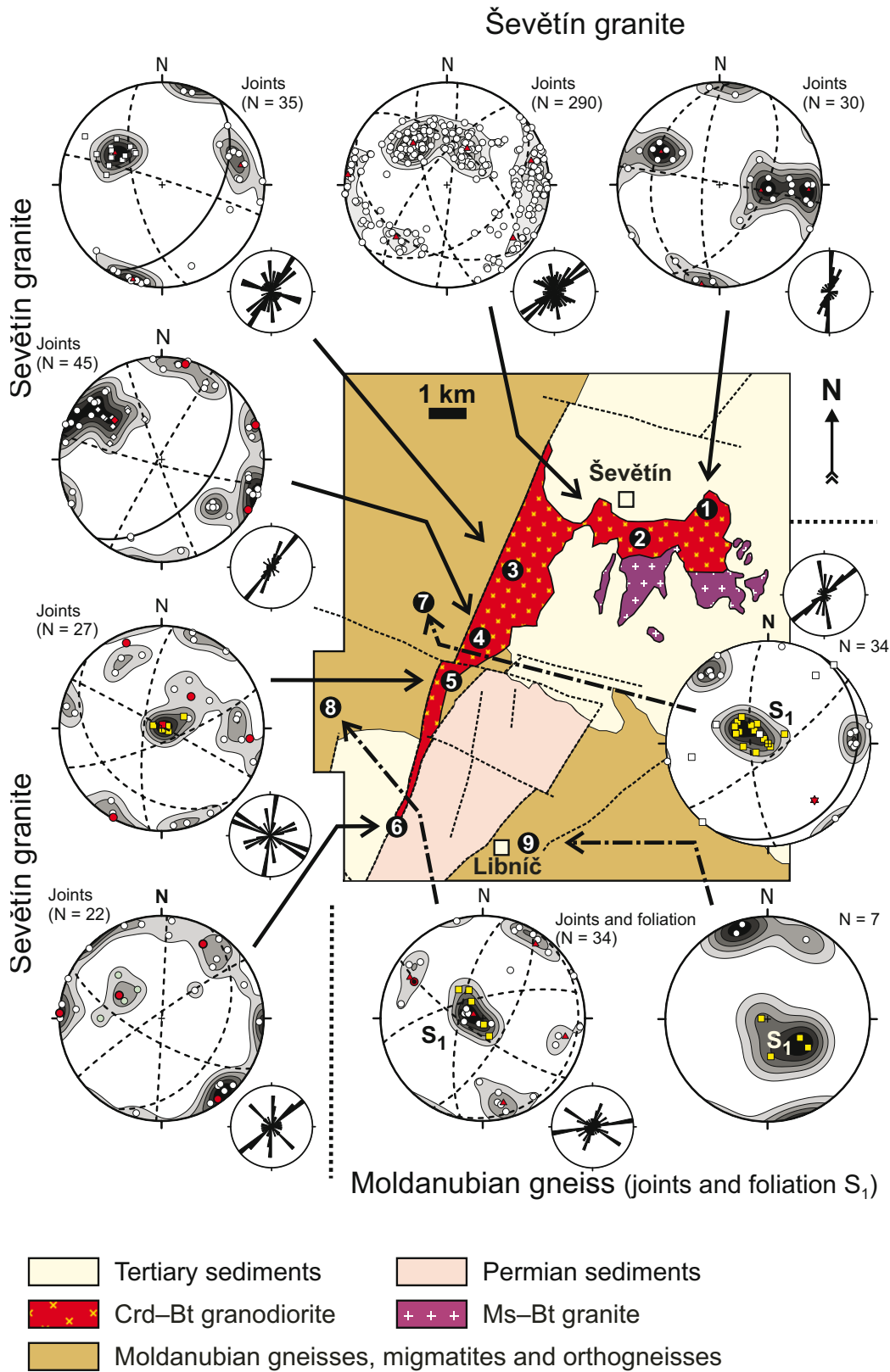


Fig. 8 Orientation of joints and of metamorphic foliation (S_1) in the Ševětín Pluton and its neighborhood.

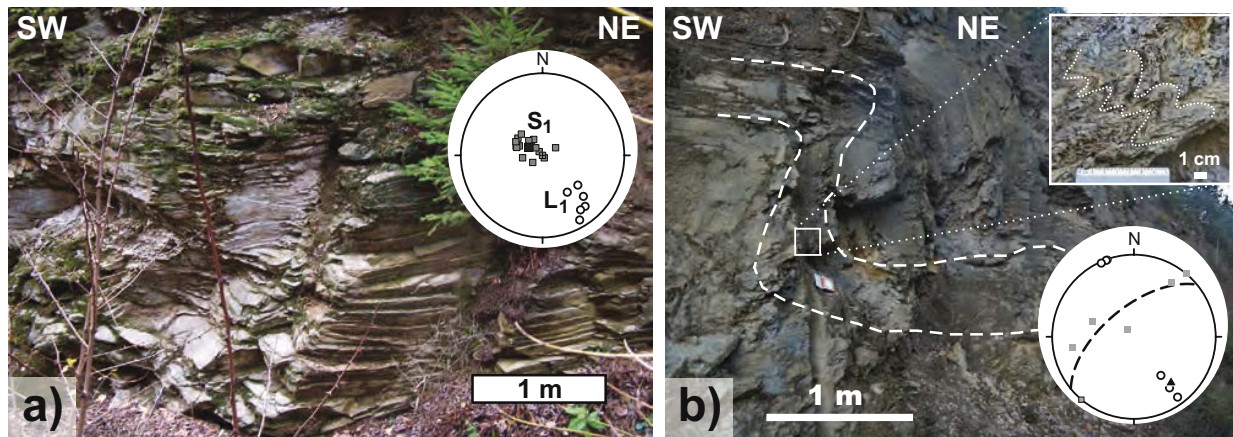


Fig. 9a – Subhorizontal metamorphic foliation (S_1) of biotite paragneiss in the railway cut near Chotýčany (Stop 5). The stereogram shows the orientation of the poles of metamorphic foliation (S_1 ; full squares) and of metamorphic stretching lineation (L_1 ; open circles). **b** – Local development of a small-scale flexure/fold in paragneiss from the same outcrop as the previous photo. The inserted photograph documents second-order chevron-like folds in the hinge zone of the main fold. The stereogram shows the orientation of fold limbs (full squares), of measured fold axes of chevron-like folds (open circles) and of the constructed π -pole (full triangle) and circle (dashed). Note the identical trend and plunge of metamorphic stretching lineation and of fold axes.

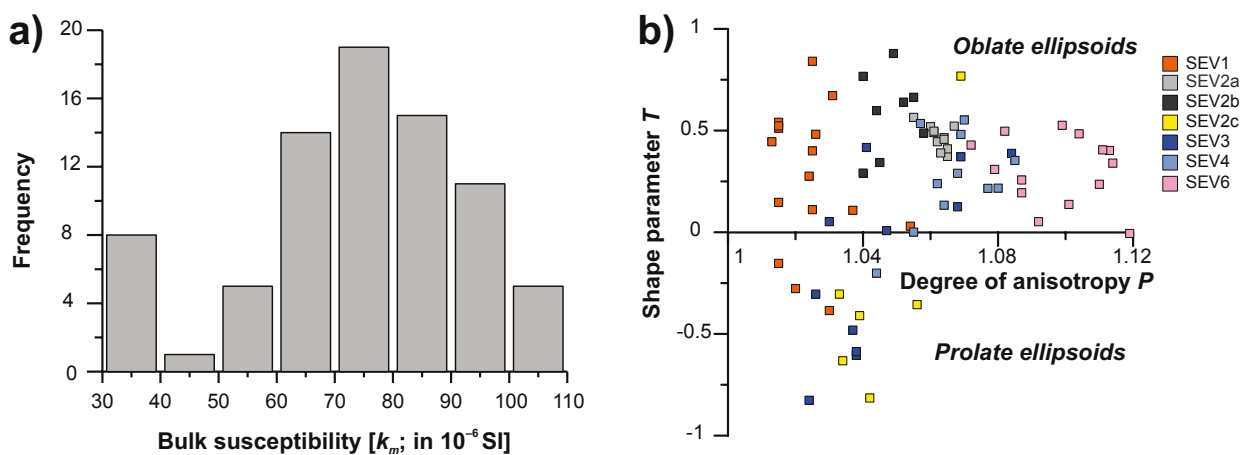


Fig. 10 Magnetic properties for all the studied samples from the Ševětín Pluton. **a** – Summary histogram of the mean magnetic susceptibility; **b** – Magnetic anisotropy P–T plot.

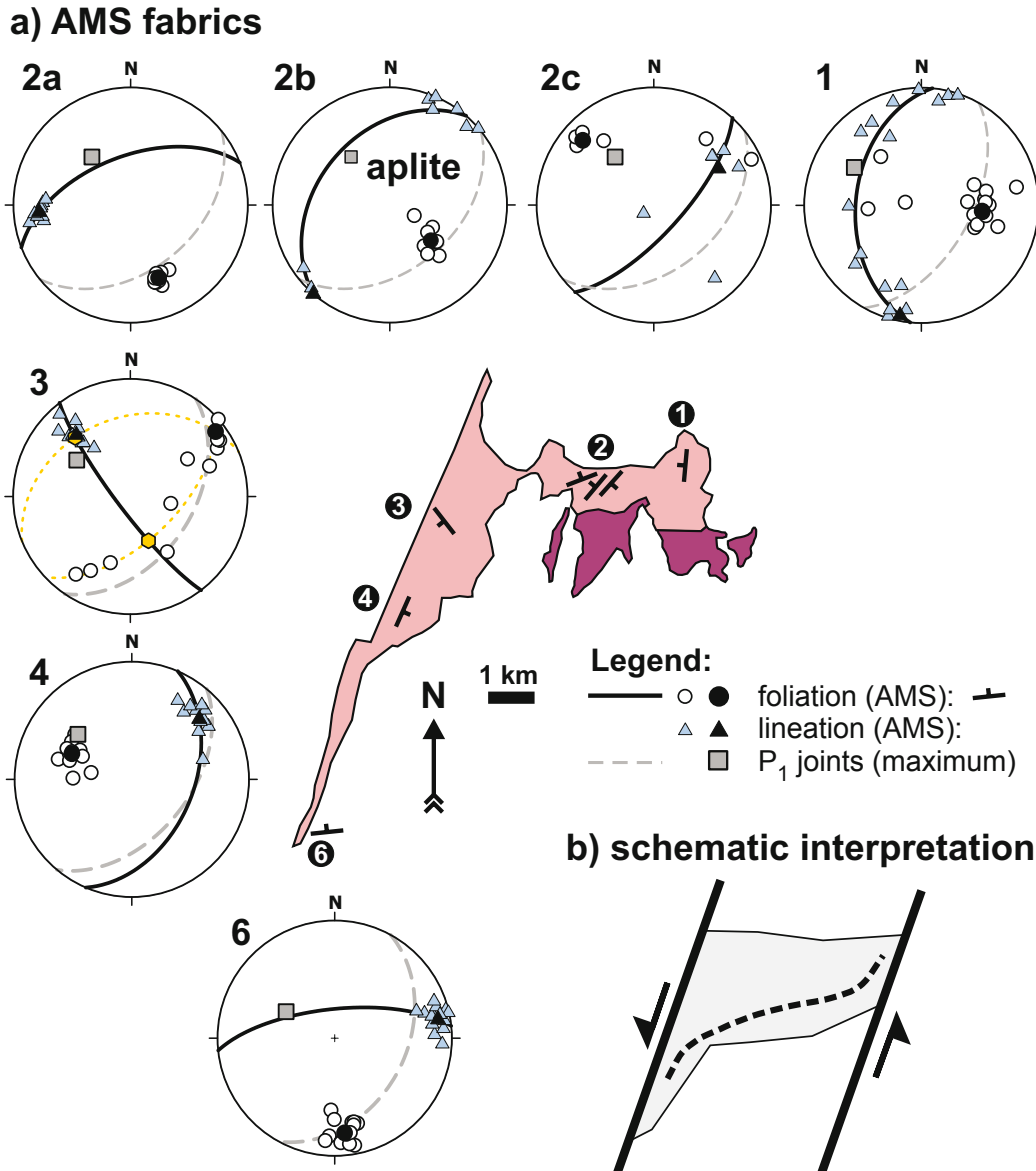


Fig. 11a – Orientation of magnetic foliation (poles represented by the k3 axes and by the mean plane) and lineations (represented by k1 axes) at the Ševětín Pluton. The orientation of P1 joints (mean pole and plane) is also plotted, for comparison with Fig. 8. The apparent inverse orientation of k1 and k3 axes at the site 3 (SEV3), compared to other sites, may be due to the presence of cordierite, while the magnetic susceptibility of the other samples is controlled by biotite and muscovite. b – Schematic summary of magnetic foliation trends across the Ševětín Pluton. The overall sigmoidal shape of this trend points to mostly solid-state deformation of the Ševětín granite during oblique sinistral movements on the main faults of the Blanice Graben.

The only exception is sample SEV1, where the individual k_1 axes are scattered along a girdle with a pole at the maximum of the k_3 axes.

DISCUSSION

Relative age relationships between joints, dikes and veins

The P_1 joints represent the oldest population of joints because: (i) late magmatic dikes of aplite and leucogranite show similar orientation as P_1 joints (Fig. 4a); (ii) neither the aplite dikes are crosscut by P_1 joints, nor are the P_1 joints cut by the dikes (Fig. 4d) and (iii) P_1 joints are displaced by other types of joints (P_3 , P_4 , P_5 ; see Fig. 4c).

Displacement relationships indicate that P_4 joints are older than P_5 . Late formation of P_5 and P_6 joints can be deduced indirectly from spatial association of extension veins of late calcite (CC3) with these joints. Relative age of P_2 joints remains questionable. Similar orientation of P_2 joints and of CC2 calcite points to post- P_1 and pre- P_5 nature of P_2 joints.

Summary of the intrusive and deformational evolution of the Ševětín Pluton

Late metamorphic phase

The metamorphic foliation (S_1 ; this study) in Moldanubian rocks to the W and SE of the SP can be, on regional scale, correlated with the subhorizontal foliation S_4 of Franěk et al. (2011). Its formation was related to the LP–MT stage of deformation of the Moldanubian Unit at c. 340 Ma (Franěk et al. 2011). Further to the E of the SP; the metamorphic foliation becomes gradually steeper due to diapiric formation of the Pelhřimov granite–dome complex (Verner et al. 2014) at c. 328–327 Ma. In contrast to the Pelhřimov Complex (Klenov Pluton) the relations between the metamorphic fabrics in the Moldanubian rocks, and the magmatic and solid-state deformation fabrics in the SP are more obscure: (i) the BMG lacks mesoscopically visible magmatic fabrics as well as clear S_1 overprint; (ii) there is no change in the dip of S_1 foliation in the Moldanubian rocks towards the SP; (iii) the magnetic foliation of the SP is much steeper than the metamorphic foliation; (iv) sparse folds in the Moldanubian paragneisses with axial planes trending NW–SE and dipping moderately to SW (Fig. 9b) must have postdated the S_1 foliation and indicate NE–SW oriented local shortening.

Intrusion of the Ševětín Pluton

The SP is volumetrically dominated by two intrusive units: the Deštná granite (DG) and the biotite–muscovite granite (BMG). Their absolute intrusive ages are not known, however, the DG is petrologically and geochemically similar to the Klenov granite that has been recently dated at 328.4 ± 0.2 Ma and 327.1 ± 0.2 Ma (U–Pb monazite; Verner et al. 2014), while the BMG might be similar in age to the Freistadt granodiorite (302 ± 2 Ma; Friedl et al. 1992), or slightly older. An age of c. 305 Ma (BMG) is compatible with the onset of sedimentation in the Blanice Graben, as well as with the oldest dated tectonic and intrusive activity at the Rödl fault zone (Vrána et al. 2005). The two intrusive units also differ in shape: the DG is only slightly elongated in the E–W to ENE–SWS direction, while the BMG is markedly elongated in NNE–SSW direction (Figs 1 and 2), i.e. parallel with the strike of the Blanice Graben. Temporal separation of the BMG and DG intrusions is therefore possible.

The mean magnetic susceptibility of all the studied samples (Fig. 10a) indicates that micas are the main carrier of the susceptibility. This is also reflected in the dominant planar fabric. The BMG almost lacks evidence for ductile deformation; therefore, we consider the planar magnetic fabric to reflect magmatic foliation. The AMS fabric pattern reveals a transition from NNE–SSW trending foliation at the eastern margin of the SP, through NE–SW trending foliations in the center, back to NNE–SSW trends at the western margin. The overall sigmoidal pattern (Fig. 11b) of magnetic foliation across the SP points either to synkinematic intrusion of the BMG during sinistral strike-slip activity on the Blanice Graben fault system or to subsolidus modification of magmatic foliation (trending E–W to NE–SW) during sinistral strike-slip motion. The latter option is supported by moderate gradual increase in the anisotropy of AMS data from the E (site 1) towards the W (sites 4 and 6) that points to higher strain and higher solid-state deformation in the vicinity of the western margin of the Blanice Graben, than along the eastern margin. Importantly, asymmetry of the gravimetric anomaly (Fig. 2) and alignment of gravity minima (NNE–SSW) suggest that the BMG was rooted/intruded along the western margin of the Blanice Graben.

Sample SEV3 is the only exception to the above-described regional trends. Apparent inversion of the k_1 and k_3 maxima might be due to the presence (relics?) of cordierite in the studied sample. The cordierite is known to define an inverse magnetic fabric (Rochette et al. 1992), where k_1 and k_3 represent the pole of magnetic foliation and lineation, respectively. If this is true in our case, then SEV3 defines the same trend of magmatic foliation and lineation as the other samples. Cordierite forms sparse phenocrysts in the DG. Its original presence in the BMG is indicated only by clusters of

micas rimming rare cordierite relics (Janoušek et al. 2002). The SEV3 sample may thus represent less altered BMG granite.

The only mesoscopic indication of magmatic foliation we found in the BMG (site SEV2a), where biotite defines weak planar fabric (dip direction/dip: 170°/85°). This resembles the dip direction of magnetic foliation from site SEV6 (354°/70°) and SEV2a (339°/60°). There is, however, not enough data to discuss the extent of solid-state modification of the magmatic fabric.

Early brittle deformation phase (oblique compression regime)

Fault-slip data from the BMG at the Ševětín quarry indicate NW–SE oriented subhorizontal compression. The orientation of the minimum principal stress axis (σ_3 : 277°/57°) is more or less similar to the maximum of the poles of P_1 joints (320°/47°), which are extensional in nature. Similarly, most of the late magmatic dikes (aplite, leucogranite or pegmatite) also exhibit poles clustered tightly around the P_1 maximum (Fig. 5a). The same holds for early hydrothermal quartz veins with minor tourmaline. All these data thus unambiguously indicate the long persistency of a minimum stress axis moderately inclined to the NW to W. The orientation of the maximum principal stress axis (slightly inclined to the SE) was favorable for oblique sinistral movements along the main faults of the Blanice Graben (Fig. 12b). Overall persistence of orientation of P_1 joints across the whole studied area, compared to curved trends of magnetic foliations, may indicate that major oblique strike-slip movements along the faults of Blanice Graben occurred before formation of P_1 joints.

Mid-stage brittle deformation phase (strike-slip regime)

This phase, which is mostly indicated by numerical analysis of the fault-slip data, points to subhorizontal N–S oriented compression and subhorizontal E–W oriented extension (Fig. 12c). This is compatible with the orientation of P_3 joints, as well as with the formation some the thin aplite dikes or the monomineral quartz veins (free of tourmaline/feldspar). Overall scarcity of hydrothermal veins coupled with this tectonic phase, however, indicates only a short-lived and relatively insignificant hydrothermal activity.

The magmatic activity (270 ± 2 Ma; Košler et al. 2001) ascribed to this phase produced NNE–SSW to N–S trending and steeply dipping dikes of pyroxene-bearing microgranodiorite (Vrána et al. 1993) and quartz monzodiorite (Vrána and Janoušek 2006).

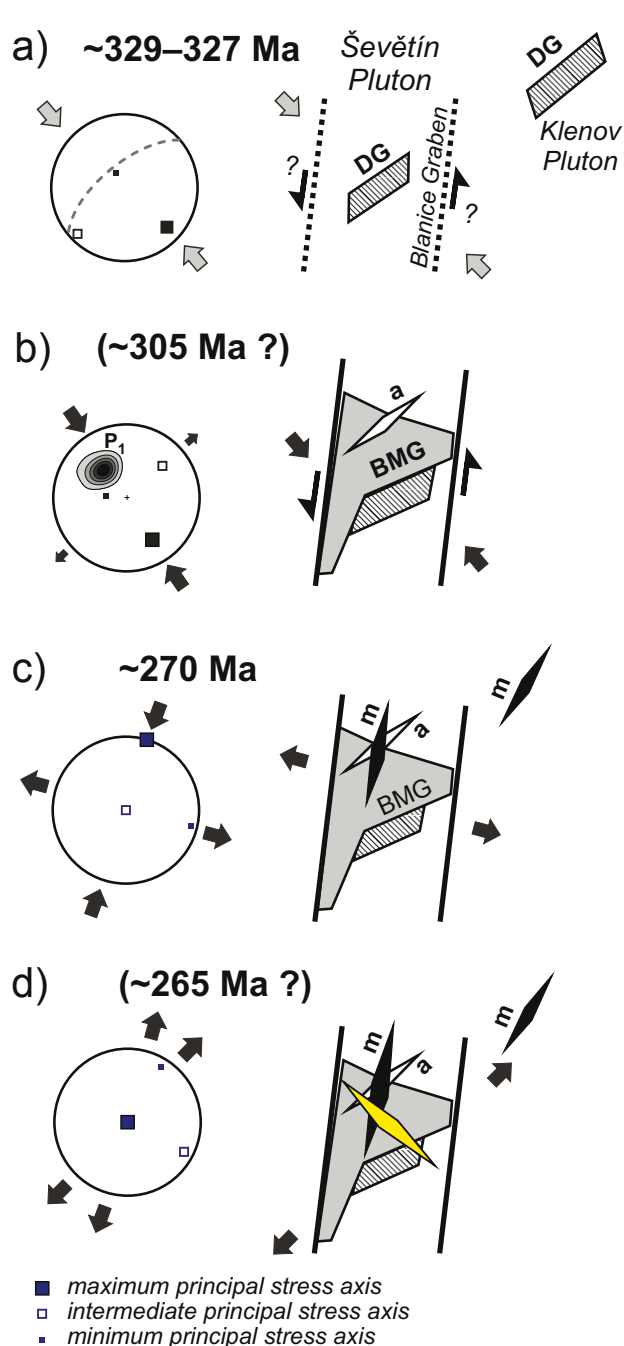


Fig. 12 Schematic model of emplacement of the Ševětín Pluton in the context of evolution of the Blanice Graben: **a** – intrusion of the two-mica Deštná type granite under NW–SE oriented compression; **b** – intrusion of biotite–muscovite granite (BMG), followed by more or less coeval formation of extensional P_1 joints and of aplitic dikes under oblique compression; **c** – strike-slip phase and late intrusion of the 270 Ma old pyroxene microgranodiorite dike into the relatively cool Ševětín Pluton; **d** – late extensional phase coupled with the formation NW–SE trending hydrothermal (quartz)–calcite veins with uneconomic Pb–Zn ores.

Late brittle deformation phase (extension regime)

Numerous fault-slip data indicate NNE–SSW oriented subhorizontal extension (Fig. 12d). The maximum of poles of late (quartz)–calcite (CC3) tension veins is shifted clockwise by c. 20–30°; however, it is still compatible with the stress axes calculated from the fault-slip data. The minor change in the strike of the P_6 relative to the P_5 joints most probably also reflects the clockwise rotation of the σ_1 and σ_3 stress axes. During this phase, the main stage of late hydrothermal activity occurred within the Blanice Graben, as indicated by the uneconomic Pb–Zn ores (hydrothermal veins).

CONCLUSIONS

A structural study of the Ševětín Pluton (SP) enabled detailed reconstruction of the Blanice Graben tectonic evolution and of associated magmatic activity:

- The AMS study revealed steeply to moderately dipping planar magnetic fabrics that we interpreted mostly as solid-state in origin, especially in the vicinity of the Drahotěšice Fault (western margin of the Blanice Graben). Local preservation of original magmatic foliation is possible in the central to eastern parts of the SP. The overall sigmoidal trend of the magnetic fabrics indicates sinistral movements along the Blanice Graben fault systems postdating the intrusion of the biotite–muscovite granite (BTG) of the SP. This is further supported by well-defined subhorizontal magnetic lineation. The magnetic fabric of the SP is thus in sharp contrast to the subhorizontal metamorphic foliation and subhorizontal NW–SE trending stretching lineation in the surrounding Moldanubian host rocks.
- Paleostress and kinematic analysis of brittle structures allowed differentiation of three tectonic phases (oblique compression, strike-slip and extension), which postdated the intrusion of the BMG.
- The oblique compression phase comprised both the emplacement of the BMG and early stages of its brittle deformation. It was accompanied by the formation of NE–SW trending joints (P_1) and dikes (aplite), both dipping moderately to the SE.
- The strike-slip phase indicates more or less E–W trending extension and can be correlated with the intrusion of c. 270 Ma microgranodiorite dikes. The orientation of the stress axis was, however, unfavorable for the main movements on the major faults of the Blanice Graben.
- The extension phase was accompanied by the formation of hydrothermal Pb–Zn–(Ag) quartz–carbonate veins and scarce P_5 and P_6 tension joints.

Acknowledgements. This paper was supported by the Grant Agency of Charles University (project No. 151810). We also greatly acknowledge the constructive reviews of P. Pitra and R. Grygar and the editorial comments of J. Žák and V. Janoušek. This study is a part of Ph.D. research of Jakub Trubač.

Electronic supplementary material. List of the AMS data and of GPS coordinates of all studied sites is available online at the Journal web site (<http://dx.doi.org/10.3190/jgeosci.175>). This study is a part of Ph.D. research of Jakub Trubač.

REFERENCES

- Ambrož V (1935) Study on the metamorphic rocks between Hluboká and Týn nad Vltavou. *Spisy přírodověd Fak Univ Karl* 138: 1–44 (in Czech)
- Bankwitz P, Bankwitz E, Thomas R, Wemmer K, Kämpf H (2004) Age and depth evidence for pre-exhumation joints in granite plutons: fracturing during the early cooling stage of felsic rock. In: Cosgrove JW, Engelder T (eds) *The Initiation, Propagation and Arrest of Joints and Other Fractures*. Geological Society of London Special Publications 231: 25–47
- Bouchez JL (1997) Granite is never isotropic: an introduction to AMS studies of granitic rocks. In: Bouchez JL, Hutton DHW, Stephens W (eds) *Granite: From Segregation of Melt to Emplacement Fabrics*. Kluwer Academic Publishers, Dordrecht, pp 95–112
- Brandmayr M, Dallmeyer RD, Handler R, Wallbrecher E (1995) Conjugate shear zones in the Southern Bohemian Massif (Austria): implications for Variscan and Alpine tectonothermal activity. *Tectonophysics* 248: 97–116
- Breiter K (2010) Geochemical classification of Variscan granitoids in the Moldanubicum (Czech Republic, Austria). *Abh Geol B-A* 65: 19–25
- Cordier P, Vrána S, Doukhan JC (1994) Shock metamorphism in quartz at Ševětín and Sušice (Bohemia)? A T.E.M. investigation. *Meteoritics* 29: 98–99
- Čtvrtník J, Pavlíček V (2002) Occurrence of colored sphalerite at Ševětín. *Minerál* 10: 9–12 (in Czech)
- Čuta J, Manová M, Šalanský K (1975) Explanations to geophysical map 1:25 000, sheet 22-444 Ševětín. Unpublished report, Geofyzika Brno, Prague, pp 1–22 (in Czech)
- Dallmayer RD, Franke W, Weber K (eds) (1995) *Pre-Permian Geology of Central and Eastern Europe*. Springer-Verlag, Berlin, pp 1–604
- Faure M. (1995) Late orogenic Carboniferous extensions in the Variscan French Massif Central. *Tectonics* 14: 132–153
- Fiala J, Fuchs G., Wendt J.I. (1995) VII.C.1 Stratigraphy. In: Dallmayer RD, Franke W, Weber K (eds) *Pre-Permian Geology of Central and Eastern Europe*. Springer-Verlag, Berlin, pp 417–428
- Finger F, Gerdes A, Janoušek V, René M, Riegler G (2007) Resolving the Variscan evolution of the Moldanubian sector of the Bohemian Massif: the significance of the Bavarian and the Moravo–Moldanubian tectonometamorphic phases. *J Geosci* 52: 9–28

- Finger F, René M, Gerdes A, Riegler G (2009) The Saxo-Danubian Granite Belt: magmatic response to postcollisional delamination of mantle lithosphere below the southwestern sector of the Bohemian Massif (Variscan Orogen). *Geol Carpathica* 60: 205–212
- Franěk J, Schulmann K, Lexa O, Tomek C, Edel JB (2011) Model of syn-convergent extrusion of orogenic lower crust in the core of the Variscan belt: implications for exhumation of high-pressure rocks in large hot orogens. *J Metamorph Geol* 29: 53–78
- Franke W (2000) The mid-European segment of the Variscides: tectonostratigraphic units, terrane boundaries and plate tectonic evolution. In: Franke W, Haak V, Oncken O, Tanner D (eds) *Orogenic Processes, Quantification and Modelling in the Variscan Belt*. Geological Society of London Special Publications 179: 35–61
- Friedl G, von Quadt A, Frasl G, Finger F (1992) Neue U/Pb Altersdaten aus der südlichen Böhmisches Masse. *Frankfurter Geowiss Arb A11*: 217–218 (in German)
- Friedl G, von Quadt A, Frasl G, Finger F (1996) Timing der Intrusionstätigkeit im Südböhmischen Batholith: 6. Symposium Tektonik-Strukturgeologie-Kristallingeologie, Salzburg, 10–15 April 1996. Fakultas Universitätsverlag, Vienna, pp 127–130 (in German)
- Friedl G, Cooke RA, Finger F, McNaughton NJ, Fletcher IR (2011) Timing of Variscan HP–HT metamorphism in the Moldanubian Zone of the Bohemian Massif: U–Pb SHRIMP dating on multiply zoned zircons from a granulite from the Dunkelsteiner Wald Massif, Lower Austria. *Mineral Petrol* 102: 63–75
- Gerdes A (2001) Magma homogenization during anatexis, ascent and/or emplacement? Constraints from the Variscan Weinsberg Granites. *Terra Nova* 13: 305–312
- Gerdes A, Wörner G, Henk A (2000) Post-collisional granite generation and HT–LP metamorphism by radiogenic heating: the Variscan South Bohemian Batholith. *J Geol Soc, London* 157: 577–587
- Gerdes A, Friedl G, Parrish RR, Finger F (2003) High-resolution geochronology of Variscan granite emplacement – the South Bohemian Batholith. *J Czech Geol Soc* 48: 53–54
- Holub V (2001) The occurrences of the Permo–Carboniferous sequences in the Blanice Graben. In: Pešek J, Holub V, Jaroš J, Malý L, Martínek K, Prouza V, Spudil J, Tásler R *Geology and Deposits of Upper Paleozoic Limnic Basins of the Czech Republic*. Czech Geological Survey, Prague, pp 197–207 (in Czech)
- Holub FV, Klečka M, Matějka D (1995) Igneous activity. In: Dallmeyer RD, Franke W, Weber K (eds) *Pre-Permian Geology of Central and Eastern Europe*. Springer-Verlag, Berlin, pp 444–452

- Hrouda F, Kahan Š (1991) The magnetic fabric relationship between sedimentary and basement nappes in the High Tatra Mountains, N. Slovakia. *J Struct Geol* 13: 431–442
- Janoušek V, Holub FV (2007) The causal link between HP–HT metamorphism and ultrapotassic magmatism in collisional orogens: case study from the Moldanubian Zone of the Bohemian Massif. *Proc Geol Assoc* 118: 75–86
- Janoušek V, Vrána S, Erban V (2002) Petrology, geochemical character and petrogenesis of a Variscan post-orogenic granite: case study from the Ševětín Massif, Moldanubian Batholith, Southern Bohemia. *J Czech Geol Soc* 7: 1–22
- Jelínek V (1981) Characterization of the magnetic fabric of rocks. *Tectonophysics* 79: T63–T67
- Kadlec E, Odstrčil J, Šalanský K (1978) Summary Processing of Geophysical Data from the South-Bohemian Basins Area. Unpublished report, Geofyzika Brno, Prague, 1–175 (in Czech)
- Klečka M, Matějka D (1996) Moldanubian Batholith – an example of the evolution of the Late Paleozoic granitoid magmatism in the Moldanubian Zone, Bohemian Massif (Central Europe). In: Srivastava RK, Chandra R (eds) *Magmatism in Relation to Diverse Tectonic Settings*. Oxford and IBH Publishing Co., New Delhi, pp 353–373
- Klečka M, Matějka D, Jalovec J, Vaňková V (1991) Geochemical research of a granitoid group of the Eisgarn type in the S part of the Central massif of the Moldanubian Pluton. *Zpr geol výzk v roce 1989*, 109–111 (in Czech)
- Košler J, Kelley SP, Vrána S (2001) $^{40}\text{Ar}/^{39}\text{Ar}$ hornblende dating of a microgranodiorite dyke: implications for early Permian extension in the Moldanubian Zone of the Bohemian Massif. *Int J Earth Sci (Geol Rundsch)* 90: 379–385
- Malavieille J (1993) Late orogenic extension in mountain belts: insights from the Basin and Ranges and the Late Paleozoic Variscan Belt. *Tectonics* 12: 1115–1130
- Matějka D (1991) Geochemical and Petrological Characteristics of Rocks of the Moldanubian Zone South of Veselí nad Lužnicí: A Relationship Between the Ševětín Granodiorite and Rocks of The Eisgarn Type. Unpublished Ph.D. thesis, Charles University, Prague, pp 1–148 (in Czech)
- Matějka D, Janoušek V (1998) Whole-rock geochemistry and petrogenesis of granites from the northern part of the Moldanubian Batholith (Czech Republic). *Acta Univ Carol, Geol* 42: 73–79
- Matějka D, Nosek T, René M (2003) Petrogenesis of two-mica granites of the Ševětín Massif. *Mitt Österr Miner Ges* 148: 359–371

- Matte P, Maluski H, Echtler H (1985) Variscan eastward ductile shearing in the Waldviertel nappes (South eastern Bohemian Massif, Austria) – $^{39}\text{Ar}/^{40}\text{Ar}$ data. *Compt Rend Acad Sci serie II* 301: 721–726
- Medaris LG, Wang H, Jelínek E, Mihaljevič M, Jakeš P (2005) Characteristics and origins of diverse Variscan peridotites in the Gföhl Nappe, Bohemian Massif, Czech Republic. *Lithos* 82: 1–23
- Nagata T (1961) *Rock Magnetism*. Maruzen, Tokyo, pp 1–350
- Racek M, Štípská P, Pitra P; Schulmann K, Lexa O (2006) Metamorphic record of burial and exhumation of orogenic lower and middle crust: a new tectonothermal model for the Drosendorf Window (Bohemian Massif, Austria). *Mineral Petrol* 86: 221–251
- René M, Matějka D, Klečka M (1999) Petrogenesis of granites of the Klenov Massif. *Acta Montana* 113: 107–134
- Rochette P, Jackson MJ, Aubourg C (1992) Rock magnetism and the interpretation of anisotropy of magnetic susceptibility. *Rev Geophys* 30: 209–226
- Schulmann K, Lexa O, Janoušek V, Lardeaux JM, Edel JB (2014) Anatomy of a diffuse cryptic suture zone: an example from the Bohemian Massif, European Variscides. *Geology* 42: 275–278
- Suk M, Dornič J, Hokr Z, Holásek O, Holub V, Líbalová J, Odehnal L, Sattran V, Šalanský K, Zima K, Žebera K (1978) Explanations to the general geological map of the ČSSR 1:25000, sheet 22-444 Ševětín. Czech Geological Survey, Prague, pp 1–65 (in Czech)
- Šalanský K (1981) Explanations to geophysical map 1:25 000, sheet 22-442 Dolní Bukovsko. Unpublished report, Geofyzika Brno, Prague, pp 1–16 (in Czech)
- Verner K, Žák J, Šrámek J, Paclíková J, Zavřelová A, Machek M, Finger F, Johnson K (2014) Formation of elongated granite–migmatite domes as isostatic accommodation structures in collisional orogens. *J Geodyn* 73: 100–117
- Vrána S (1987) The Ševětín astrobleme, southern Bohemia, Czechoslovakia. *Geol Rdsch*, 76: 505–528
- Vrána S, Bártek J (2005) Retrograde metamorphism in a regional shear zone and related chemical changes: the Kaplice Unit of muscovite–biotite gneisses in the Moldanubian Zone of southern Bohemia, Czech Republic. *J Czech Geol Soc* 50: 43–57
- Vrána S, Janoušek V (2006) Late-orogenic Variscan magmatism: the case of quartz monzodiorite dykes from the Blanice Graben, southern Bohemia. *J Czech Geol Soc* 51: 231–248
- Vrána S, Bendl J, Buzek F (1993) Pyroxene microgranodiorite dykes from the Ševětín structure, Czech Republic: mineralogical, chemical and isotopic indication of a possible impact melt origin. *J Czech Geol Soc* 38: 129–148

- Vrána S, Slabý J, Bendl J (2005) The Kaplice dyke swarm of biotite granodiorite porphyry and its relationship to the Freistadt granodiorite, Moldanubian Batholith. *J Czech Geol Soc* 50: 9–17
- Welser P, Zikeš J (2009) Minerals from the Ševětín quarry. *Minerál* 17: 326–334 (in Czech)
- Zachariáš J, Hübst Z (2012) Structural evolution of the Roudný gold deposit, Bohemian Massif: a combination of paleostress analysis and review of historical documents. *J Geosci* 57: 87–103
- Zachariáš J, Štrba M (2014) Evolution of brittle deformations in the granite from the quarry at Ševětín near České Budějovice and their relationship to formation of Pb–Zn ores. *Sbor Jihočes Muz (Čes Budějovice), přír Vědy* 54: 70–85 (in Czech)
- Zachariáš J, Frýda J, Paterová B, Mihaljevič M (2004) Arsenopyrite and As-bearing pyrite from the Roudný deposit, Bohemian Massif. *Mineral Mag* 68: 31–46
- Zachariáš J, Paterová B, Pudilová M (2009) Mineralogy, fluid inclusion, and stable isotope constraints on the genesis of the Roudný Au–Ag deposit, Bohemian Massif. *Econ Geol* 104: 53–72
- Žák J, Verner K, Finger F, Faryad SW, Chlupáčová M, Veselovský F (2011) The generation of voluminous S-type granites in the Moldanubian unit, Bohemian Massif, by rapid isothermal exhumation of the metapelitic middle crust. *Lithos* 121: 25–40
- Žalohar J, Vrabec M (2007) Paleostress analysis of heterogeneous fault-slip data: the Gauss method. *J Struct Geol* 29: 1798–1810

ELECTRONIC APPENDIX

Electronic Supplementary Material, Part 1
List of the AMS data

Site	Sample	Latitude - WGS84, North (°)	Longitude - WGS84, East (°)	Lithologic unit	Specimen	Km	L	F	P	Pj	T	U	K1 trend	K1 plunge	K2 trend	K2 plunge	K3 trend	K3 plunge					
1	SEV1	N49° 5' 33.037" 49.09251	E14° 34' 38.990" 14.577415	Ševětín granite	S7/1/1	69.883770	1.01	1.01	1.02	1.02	-0.28	-0.28	359	2	90	38	266	52					
					S7/1/2	78.120210	1.01	1.01	1.02	1.02	0.15	0.14	194	30	85	30	320	45					
					S7/1/3	80.466370	1.01	1.02	1.03	1.03	0.48	0.48	345	10	245	43	85	45					
					S7/1/4	77.908780	1.00	1.01	1.02	1.02	0.54	0.54	320	20	221	24	86	58					
					S7/1/5	81.977370	1.00	1.02	1.03	1.03	0.84	0.84	329	19	222	41	78	43					
					S7/2/1	82.333080	1.02	1.01	1.03	1.03	-0.39	-0.39	335	36	191	48	79	19					
					S7/2/2	77.734470	1.00	1.01	1.02	1.02	0.51	0.51	204	25	315	38	90	42					
					S7/2/3	67.127090	1.01	1.01	1.03	1.03	0.11	0.11	9	11	270	39	113	49					
					S7/2/4	80.141700	1.03	1.03	1.05	1.05	0.03	0.02	229	26	332	26	100	53					
					S7/3/1	69.585820	1.01	1.02	1.03	1.03	0.40	0.40	14	4	280	41	109	48					
					S7/3/2	86.963100	1.01	1.01	1.02	1.02	-0.15	-0.16	18	2	109	11	281	79					
					S7/3/3	104.239100	1.01	1.03	1.03	1.03	0.67	0.67	197	2	290	57	106	33					
					S7/4/1	74.160870	1.02	1.02	1.04	1.04	0.11	0.10	197	8	295	45	99	44					
					S7/4/2	81.432370	1.01	1.02	1.02	1.02	0.28	0.27	188	11	289	43	87	44					
					S7/4/3	79.125430	1.00	1.01	1.02	1.02	0.52	0.52	231	34	339	24	97	46					
					S7/4/4	77.381040	1.00	1.01	1.01	1.01	0.45	0.44	269	38	171	10	69	50					
2	SEV2a	N49° 5' 31.263" 49.092018	E14° 34' 38.990" 14.577415	Ševětín granite	S1/1/1	81.118750	1.02	1.05	1.07	1.07	0.52	0.51	265	21	18	46	158	36					
					S1/1/2	87.171100	1.02	1.05	1.06	1.07	0.47	0.45	260	26	16	43	149	36					
					S1/1/3	88.598450	1.02	1.05	1.06	1.06	0.49	0.48	264	22	17	45	156	37					
					S1/1/4	93.449300	1.02	1.04	1.06	1.06	0.45	0.43	272	26	27	41	159	38					
					S1/1/5	93.819060	1.01	1.05	1.06	1.06	0.52	0.51	270	25	27	45	161	35					
					S1/1/6	74.498090	1.01	1.04	1.06	1.06	0.57	0.56	268	24	25	45	160	35					
					S1/2/1	93.500100	1.02	1.05	1.06	1.06	0.50	0.49	263	25	29	51	159	27					
					S1/2/2	93.886630	1.02	1.04	1.07	1.07	0.37	0.36	260	14	11	55	162	31					
					S1/2/3	90.982490	1.02	1.05	1.07	1.07	0.41	0.40	263	21	21	50	159	32					
					S1/2/4	94.197130	1.02	1.04	1.06	1.07	0.39	0.38	265	19	20	52	163	32					
					S1/2/5	92.481540	1.02	1.05	1.06	1.07	0.46	0.45	274	28	33	42	162	35					
					2	SEV2b	N49° 5' 33.037" 49.09251	E14° 34' 38.693" 14.577415	Aplite dike	S2/1/1	32.370880	1.01	1.04	1.05	1.06	0.64	0.63	234	10	335	49	136	40
										S2/1/2	32.845930	1.01	1.04	1.04	1.04	0.77	0.76	20	5	287	33	117	56
										S2/1/3	35.697150	1.01	1.03	1.05	1.05	0.34	0.33	23	0	293	19	113	72
										S2/1/4	33.768480	1.01	1.03	1.04	1.04	0.29	0.28	35	0	305	33	126	57
										S2/1/5	35.531300	1.01	1.05	1.06	1.06	0.66	0.66	224	3	316	41	130	49
2	SEV2c	N49° 5' 27.813" 49.091059	E14° 34' 51.025" 14.58084	Ševětín granite	S3/1/1	68.482400	1.02	1.23	1.26	1.29	0.80	0.78	140	20	260	54	38	29					
					S3/1/3	54.556130	1.01	1.06	1.07	1.08	0.77	0.76	231	81	335	2	65	9					
					S3/2/1	62.143970	1.04	1.02	1.06	1.06	-0.36	-0.37	51	35	195	49	308	18					
					S3/2/2	59.318300	1.04	1.00	1.04	1.05	-0.82	-0.82	50	35	204	52	311	13					
					S3/2/3	65.936100	1.03	1.01	1.03	1.04	-0.63	-0.64	52	25	199	60	315	14					
S3/2/4	46.424070	1.02	1.01	1.03	1.03	-0.30	-0.31	66	22	185	51	322	31										

Electronic Supplementary Material, Part 1
List of the AMS data

Site	Sample	Latitude - WGS84, North (°)	Longitude - WGS84, East (°)	Lithologic unit	Specimen	Km	L	F	P	Pj	T	U	K1 trend	K1 plunge	K2 trend	K2 plunge	K3 trend	K3 plunge																						
3	SEV3	N49° 4' 51.312"	E14° 32' 11.450"	Ševětín granite	S4/1/1	67.784620	1.02	1.02	1.05	1.05	0.01	0.00	319	33	139	57	49	0																						
							14.536514	S4/1/2	71.483090	1.02	1.05	1.07	1.07	0.37	0.36	318	38	169	47	61	16																			
							S4/1/3	73.911280	1.03	1.06	1.08	1.09	0.39	0.37	319	39	161	49	58	11																				
							S4/1/4	70.726580	1.03	1.04	1.07	1.07	0.13	0.11	319	33	164	54	57	12																				
							S4/2/1	75.875940	1.01	1.03	1.04	1.04	0.42	0.41	323	47	55	1	146	43																				
							S4/2/2	70.865510	1.03	1.01	1.04	1.04	-0.61	-0.61	314	28	67	37	197	41																				
							S4/2/3	70.786350	1.02	1.01	1.03	1.03	-0.30	-0.31	323	28	197	48	69	28																				
							S4/2/4	72.695910	1.02	1.00	1.02	1.03	-0.83	-0.83	324	21	227	18	100	61																				
							S4/2/5	68.648540	1.01	1.02	1.03	1.03	0.05	0.05	319	8	220	47	57	41																				
							S4/2/7	73.379870	1.03	1.01	1.04	1.04	-0.48	-0.49	312	18	81	62	215	20																				
							S4/2/8	73.115140	1.03	1.01	1.04	1.04	-0.59	-0.59	316	29	82	47	208	29																				
							4	SEV4	N49° 3' 52.401"	E14° 31' 40.699"	Ševětín granite	S8/1/1	53.647440	1.03	1.02	1.04	1.05	-0.20	-0.21	56	22	153	18	279	61															
														14.527972	S8/1/2	74.487800	1.03	1.06	1.09	1.09	0.35	0.34	75	37	191	30	308	38												
S8/1/3	90.014930	1.02	1.05	1.07	1.07	0.55								0.54	51	22	163	43	302	39																				
S8/1/4	81.548560	1.02	1.05	1.07	1.07	0.48								0.47	38	29	157	42	285	35																				
S8/1/5	68.823710	1.02	1.04	1.07	1.07	0.29								0.28	30	23	136	32	271	48																				
S8/1/6	65.752560	1.03	1.03	1.06	1.06	0.00								-0.01	55	31	167	32	292	42																				
S8/1/7	60.074210	1.02	1.04	1.06	1.06	0.24								0.22	43	21	155	44	295	39																				
S8/1/8	54.434660	1.01	1.04	1.06	1.06	0.54								0.53	47	15	149	38	299	48																				
S8/2/1	69.504130	1.03	1.04	1.06	1.06	0.13								0.12	39	21	147	39	287	44																				
S8/2/2	65.054680	1.03	1.05	1.08	1.08	0.22								0.20	50	25	160	37	295	43																				
S8/2/3	78.084800	1.03	1.05	1.08	1.08	0.22								0.20	43	14	143	35	295	52																				
5	-	N49° 3' 21.138"	E14° 31' 17.818"	Ševětín granite	no AMS data	no AMS data								no AMS data	no AMS data	no AMS data	no AMS data	no AMS data	no AMS data	no AMS data	no AMS data	no AMS data	no AMS data	no AMS data	no AMS data															
																										49.055872	14.521616													
							6	SEV6	N49° 1' 37.219"	E14° 30' 43.419"	Ševětín granite	S6/1/1	76.212880													1.03	1.05	1.08	1.08	0.31	0.29	75	22	322	43	183	39			
																										14.512061	S6/1/2	89.278180	1.02	1.05	1.07	1.07	0.43	0.42	72	27	309	46	180	32
																										S6/1/3	93.783970	1.03	1.08	1.11	1.12	0.40	0.38	88	16	319	66	183	18	
																										S6/1/4	87.250260	1.04	1.08	1.11	1.12	0.34	0.32	82	17	303	68	176	14	
																										S6/1/5	87.061920	1.04	1.07	1.11	1.11	0.24	0.21	85	8	324	76	177	12	
																										S6/1/6	87.630360	1.04	1.06	1.10	1.10	0.14	0.11	93	9	331	74	185	14	
																										S6/1/7	69.256930	1.03	1.08	1.11	1.12	0.41	0.38	77	15	288	73	169	8	
																										S6/2/1	103.937700	1.06	1.06	1.12	1.12	-0.01	-0.03	81	6	322	78	172	10	
																										S6/2/2	100.178000	1.04	1.05	1.09	1.09	0.05	0.03	77	16	309	65	173	19	
																										S6/2/3	102.359900	1.03	1.05	1.09	1.09	0.26	0.24	73	10	325	60	168	28	
																										S6/2/4	89.940220	1.03	1.05	1.09	1.09	0.19	0.17	70	11	320	62	165	26	
S6/2/6	98.732250	1.02	1.06	1.08	1.09	0.50	0.48	76	3	341	62	167	28																											
S6/2/7	97.138000	1.03	1.08	1.10	1.11	0.48	0.47	77	1	346	65	168	25																											
S6/2/8	102.880900	1.02	1.08	1.10	1.10	0.53	0.51	77	9	325	68	171	20																											
7	-	N49° 4' 29.548"	E14° 30' 29.420"	sillimanite–biotite	no AMS data	no AMS data	no AMS data	no AMS data	no AMS data	no AMS data	no AMS data	no AMS data	no AMS data	no AMS data	no AMS data	no AMS data	no AMS data	no AMS data																						
																			49.074874	14.508172																				
																			8	-	N49° 2' 43.470"	E14° 29' 1.764"	migmatitic gneiss	no AMS data	no AMS data	no AMS data	no AMS data	no AMS data	no AMS data	no AMS data	no AMS data	no AMS data	no AMS data	no AMS data	no AMS data	no AMS data				
49.045408	14.483823																																							
9	-	N49° 1' 18.012"	E14° 33' 19.008"	migmatitic biotite	no AMS data	no AMS data	no AMS data	no AMS data	no AMS data	no AMS data	no AMS data	no AMS data	no AMS data	no AMS data	no AMS data	no AMS data	no AMS data	no AMS data	no AMS data																					
		49.02167	14.55528																																					

Chapter III:

Zoned plutons as markers of regional tectonic and geodynamic setting

Article III.-3:

A plate-kinematic model for the assembly of the Bohemian Massif constrained by structural relations around granitoid plutons (2014)

Žák J., Verner K., Janoušek V., Holub F.V., Kachlík V., Finger F., Hajná J., Tomek F., Vondrovic L., **Trubač J.**

In: Schulmann K., Oggiano G., Lardeaux J.M., Janoušek V., Martínez Catalán J.R. (Eds), The Variscan orogeny: extent, timescale and the formation of the European crust.

Geological Society London – Special Publications **405**: 169–196

Status: Published

A plate-kinematic model for the assembly of the Bohemian Massif constrained by structural relationships around granitoid plutons

Jiří Žák¹, Kryštof Verner^{2,3}, Vojtěch Janoušek^{2,3}, František V. Holub³, Václav Kachlík¹, Fritz Finger⁴, Jaroslava Hajná¹, Filip Tomek¹, Lukáš Vondrovič^{2,3}, Jakub Trubač^{1,2,3}

¹ Institute of Geology and Palaeontology, Faculty of Science, Charles University, Albertov 6, Prague, 12843, Czech Republic

² Czech Geological Survey, Klárov 3, Prague, 11821, Czech Republic

³ Institute of Petrology and Structural Geology, Faculty of Science, Charles University, Albertov 6, Prague, 12843, Czech Republic

⁴ Division of Mineralogy, University of Salzburg, Hellbrunnerstraße 34, A-5020 Salzburg, Austria

ABSTRACT

This paper summarizes the current knowledge on the nature, kinematics, and timing of movement along major tectonic boundaries in the Bohemian Massif and demonstrates how the Variscan plutonism and deformation evolved in space and time. Four main episodes are recognized. (1) Late Devonian to early Carboniferous subduction and continental underthrusting of the Saxothuringian Unit beneath the Teplá–Barrandian Unit resulted in the orogen-perpendicular shortening and growth of an inboard magmatic arc during ~354–346 Ma. (2) The subduction-driven shortening was replaced by collapse of the Teplá–Barrandian upper crust, exhumation of the high-grade (Moldanubian) core of the orogen at ~346–337 Ma, and by dextral strike-slip along orogen-perpendicular ~NW–SE shear zones. (3) Following closure of a Rhenohercynian Ocean basin, the Brunia microplate was underthrust beneath the eastern flank of the Saxothuringian/Teplá–Barrandian/Moldanubian ‘assemblage’. This process commenced at c. 346 Ma in the northeast and ceased at c. 335 in the southwest. (4) Late readjustments within the amalgamated Bohemian Massif included crustal exhumation and ~330–327 Ma, mainly S-type granite plutonism along the edge of the Brunia indenter, and peripheral tectonothermal activity driven by strike-slip faulting and possibly mantle delamination around the consolidated Bohemian Massif’s interior until late Carboniferous/earliest Permian times.

The Bohemian Massif of central Europe is the largest inlier of once continuous but now largely dismembered Ouachita–Appalachian–Variscan orogenic belt (Fig. 1) that formed during the Devonian to Carboniferous closure of the Rheic Ocean and other small oceanic domains by convergence of the Gondwana and Laurussia supercontinents (e.g. Franke 1989; Pin 1990; Matte 2001; Winchester 2002; Winchester *et al.* 2006; Ballèvre *et al.* 2009; Faure *et al.* 2009; Faryad & Kachlík 2013; Edel *et al.*

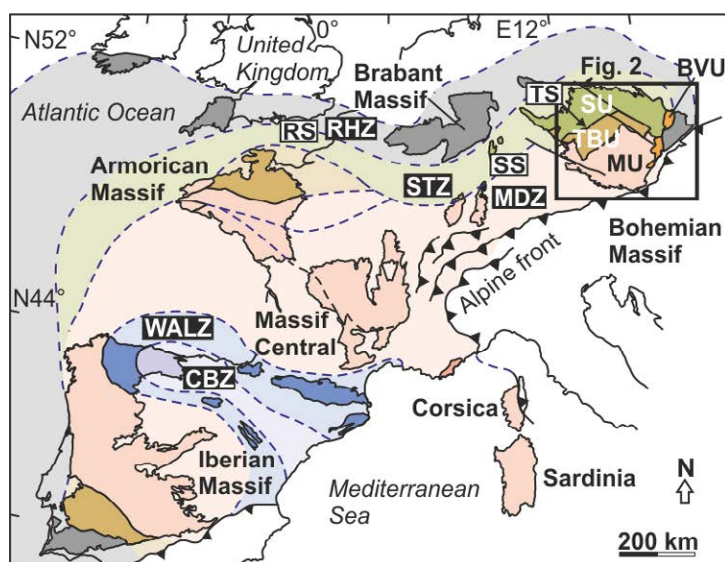


Fig. 1. Overview geological map showing basement outcrop areas and principal lithotectonic zones and sutures of the Variscan orogenic belt in Europe. Bohemian Massif is the easternmost inlier of the orogen. Compiled from Winchester (2002), Asch (2003), and Martínez-Catalán (2011, 2012).

EUROPEAN VARISCIDES

Tectonic zones

RHZ Rhenohercynian Zone
 STZ Saxothuringian Zone
 MDZ Moldanubian Zone
 WALZ West Asturian–Leonese Zone
 CBZ Cantabrian Zone

Principal sutures

RS Rheic suture
 SS Saxothuringian suture
 TS Teplá suture (continuation of Saxothuringian suture)

Lithotectonic units in the Bohemian Massif

SU Saxothuringian Unit
 TBU Teplá–Barrandian Unit
 MU Moldanubian Unit
 BVU Brunovistulian Unit and other Neoproterozoic terranes of Avalonian affinity in tectonic windows

2013; Kroner & Romer 2013). A characteristic feature of the Variscan Orogeny was involvement of multiple microplates of the Cadomian or Avalonian affinity that were partially extended or entirely detached from the northern margin of Gondwana during the late Cambrian to Early Ordovician times (e.g. Pin & Marini 1993; Franke 2000; Matte 2001; Murphy & Nance 2002; Nance & Linnemann 2008; von Raumer & Stampfli 2008; Nance *et al.* 2010, 2012). These microplates were then stuck in a broad collision zone between Gondwana and Laurussia as the two supercontinents converged, resulting in multiple subduction, accretion, and collision events along margins of the neighbouring microplates.

This style of orogeny is greatly exemplified in the Bohemian Massif, which is a mosaic consisting of several lithotectonic units (Figs 1 & 2). The timing and kinematics of their amalgamation and further development during the Variscan Orogeny have been vigorously debated and summarized in several plate-tectonic reconstructions (e.g. Matte 1986, 1991, 2001; Franke 1989; Pharaoh 1999; Pitra *et al.* 1999; Franke & Żelazniewicz 2002; Winchester 2002; Edel *et al.* 2003; Franke 2006; Finger *et al.* 2007; Schulmann *et al.* 2009; Kroner & Romer 2013). This short contribution is not meant as a comprehensive review, but rather focuses on granitoid and syenitoid plutons as temporal and

strain markers of regional deformation, utilizing modern structural data in combination with geochronology, mainly U–Pb dating on zircon. Below, we first briefly describe the principal lithotectonic units in the interior of the Bohemian Massif and then comment on the nature, kinematics, and timing of movements along their boundaries. Based on these data sets, we propose a plate-tectonic model and outline some relevant open questions and possible directions for future research.

MAJOR LITHOTECTONIC UNITS IN THE INTERIOR OF THE BOHEMIAN MASSIF

Saxothuringian Unit

The northerly and north-westerly Saxothuringian Unit (Fig. 2) consists of late Neoproterozoic volcano-sedimentary successions, interpreted as a back-arc and retro-arc system of the Cadomian orogen, intruded by a voluminous late Neoproterozoic to early Cambrian granitoid plutonic complex (the Lusatian Massif, LM in Fig. 2; Kröner *et al.* 1994, 1995; Linnemann & Romer 2002; Linnemann *et al.* 2000, 2004, 2008; Tichomirowa *et al.* 2012). The Cadomian basement is overlain unconformably by Lower Palaeozoic volcano-sedimentary passive-margin successions (Buschmann *et al.* 2006) and both units host orthogneisses and bimodal metavolcanic rocks of chiefly Cambro–Ordovician and late Devonian to early Carboniferous protolith ages (Patočka & Smulikowski 2000; Kröner *et al.* 2001; Oberc-Dziedzic *et al.* 2005a, b; Nowak *et al.* 2011). This Neoproterozoic–Early Paleozoic package was affected by Variscan subduction-related HP–LT greenschist/blueschist to (U)HP–HT metamorphism and was then strongly reworked during nappe stacking and extensional unroofing under MP–MT to greenschist-facies conditions. The latter process was associated with, and followed by, strike-slip movements along major ~NW–SE-trending faults (Aleksandrowski *et al.* 1997; Marheine *et al.* 2002; Mazur *et al.* 2006). Importantly, relics of blueschist-facies rocks with cooling ages constrained at around 360 Ma (Cháb & Vrána 1979; Smulikowski 1995; Maluski & Patočka 1997; Marheine *et al.* 2002; Faryad & Kachlík 2013; cf. Žáčková *et al.* 2010), together with diamond-bearing metasedimentary rocks and granulites, delineate the margins of the Saxothuringian Unit (Behr *et al.* 1982; Schmädicke 1991; Schäfer *et al.* 1997; Willner *et al.* 1997; Kröner & Willner 1998; Kröner *et al.* 1998; Massonne 2001; Mueller & Massonne 2001; Rötzler & Romer 2001; Willner *et al.* 2002; O’Brien & Rötzler 2003; Konopásek & Schulmann 2005; Schmädicke *et al.* 2010; Kotková *et al.* 2011). Indeed, the Saxothuringian Unit has been regarded as a separate collage of microplates in the framework of the Bohemian Massif (e.g. Cymerman *et al.* 1997; Żelaźniewicz 1997; Mazur *et al.* 2006), though

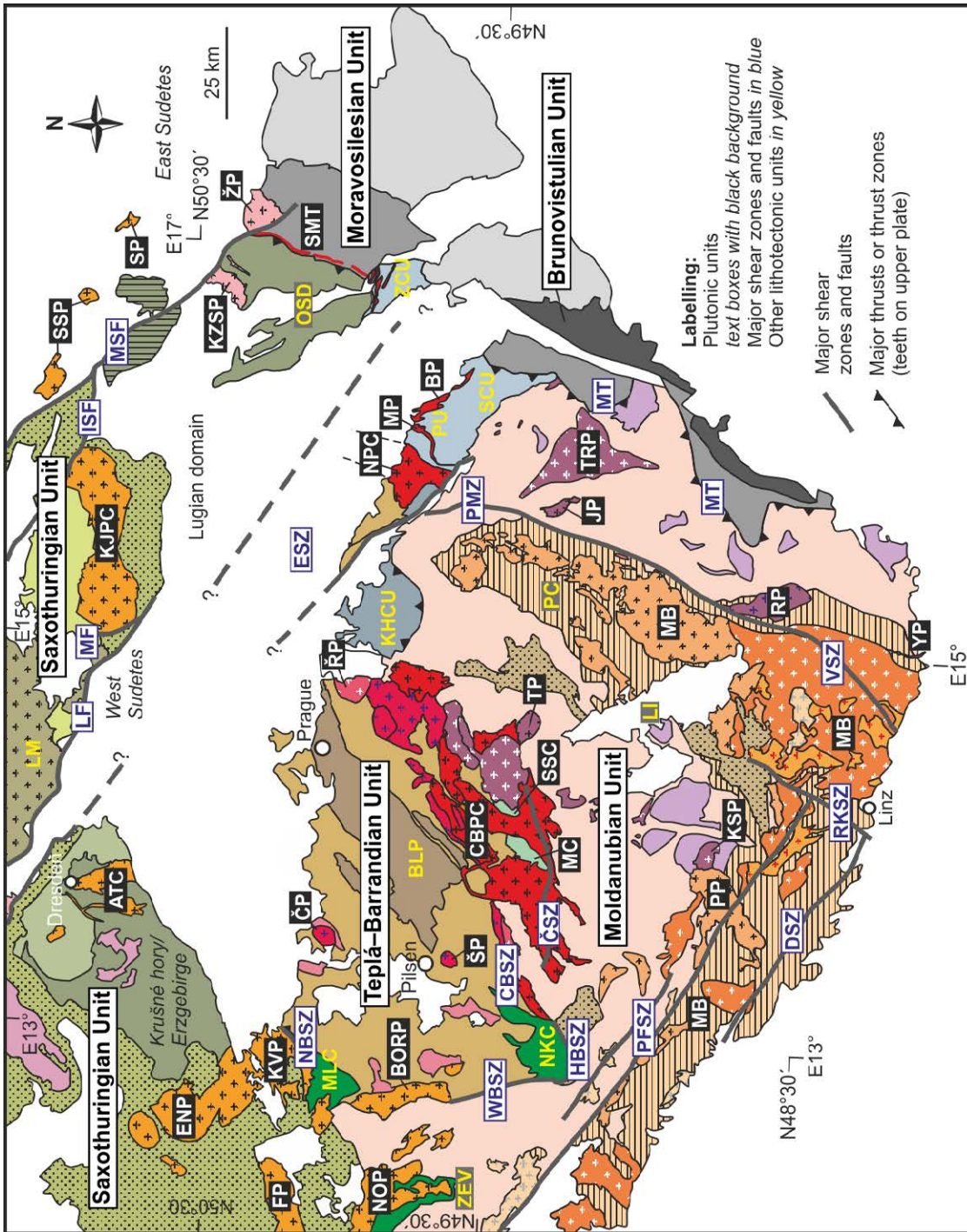









Fig. 2. Greatly simplified geological map of the interior Bohemian Massif emphasizing geologic units and tectonic features discussed in the text. Compiled from Fusán *et al.* (1967) and Cháb *et al.* (2007). Plutonic units: ATC, Altenberg–Teplice caldera; BORP, Bor Pluton; BP, Budislav Pluton; CBPC, Central Bohemian Plutonic Complex; ČP, Čistá Pluton; ENP, Eibenstock–Nejdek Pluton; FP, Fichtelgebirge(Smrčiny) Pluton; JP, Jihlava Pluton; KJPC, Krkonoše–Jizera Plutonic Complex; KSP, Knížecí Stolec Pluton; KVP, Karlovy Vary Pluton; KZSP, Kłodzko–Złoty Stok Pluton; MB, Moldanubian Batholith; MC, Mirovice Complex; MP, Miřetín Pluton; NOP, Northern Oberpfalz Pluton; NPC, Nasavrky Plutonic Complex; PP, Plechý Pluton; RP, Rastenberg Pluton; ŘP, Říčany Pluton; SMT, Staré Město tonalite sill; SP, Strzelin Pluton; ŠP, Štěnovice Pluton; SSC, Staré Sedlo Complex; SSP, Strzegom–Sobótka Pluton; TP, Tábor Pluton; TRP, Třebíč Pluton; YP, Ybbs

Zoned plutons as markers of regional tectonic and geodynamic setting


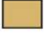




Pluton; ŽP, Žulová Pluton. Shear zones and faults: CBSZ, Central Bohemian shear zone; ČSZ, Červená shear zone; DSZ, Danube shear zone; ESZ, Elbe shear zone; HBSZ, Hoher Bogen shear zone; ISF, Intra-Sudetic Fault; LF, Lusatian Fault; MF, Machnín Fault; MSF, Marginal-Sudetic Fault; MT, Moldanubian thrust; NBSZ, North Bohemian shear zone; PFSZ, Pfahl shear zone; PMZ, Příbyslav mylonite zone; RKSZ, Rodl–Kaplice shear zone; VSZ, Vitis shear zone; WBSZ, West Bohemian shear zone. Other geologic units: BLP, Barrandian Lower Palaeozoic successions; KHCU, Kutná Hora Crystalline Unit; LI, Lišov granulite; LM, Lusatian Massif; MLC, Mariánské Lázně Complex; NKC, Neukirchen–Kdyně Complex; OSD, Orlica–Sněžník Dome; PC, Pelhřimov Complex; PU, Polička Crystalline Unit; SCU, Svratka Crystalline Unit; ZEV, Erbendorf–Vohenstrauss Zone; ZCU, Zábřeh Crystalline Unit.

KEY

Saxothuringian Unit




-  Neoproterozoic to Lower Paleozoic metasedimentary and metaigneous rocks with Variscan greenschist facies overprint and relics of HP–LT blueschist facies rocks
-  Neoproterozoic basement with MP–MT Variscan overprint
-  Neoproterozoic to lower Cambrian granitoids
-  Upper Cambrian to Lower Ordovician (meta-)granitoids and orthogneisses
-  High-grade units with (U)HP rocks with tectonically intercalated relics of HP–LT rocks re-equilibrated under greenschist to amphibolite facies conditions
-  High-grade rocks in Góry Sówie (migmatite, minor granulite and garnet peridotite inclusions)
-  Granulites and associated (U)HP rocks

Teplá–Barrandian Unit


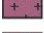
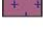
-  Neoproterozoic to lower Cambrian volcano-sedimentary successions,
-  Neoproterozoic and Lower Paleozoic rocks in roof pendants of Variscan plutons, and comparable rocks along the northeastern margin of the Moldanubian Unit (undivided)
-  Neoproterozoic to Cambro–Ordovician basic to ultrabasic (meta-)igneous rocks
-  Cambrian granitoids and orthogneisses
-  Lower Paleozoic volcano-sedimentary overlap successions
-  Upper Devonian orthogneisses in roof pendants

VARISCAN PLUTONIC ROCKS





Early-orogenic (syn-collisional) arc-related granitoids

-  Medium-K calc-alkaline Sázava suite and related rocks
-  High-K calc-alkaline Blatná suite and related rocks
-  Other suites (undifferentiated)



(Ultra-)potassic melasyenitoids and melagranitoids

-  Melasyenites to melagranites (durbachite suite)
-  Two-pyroxene melasyenites
-  Granodiorites, melagranites, quartz monzonites, quartz diorites




Moldanubian Unit

-  Heterogeneous assemblages dominated by paragneisses and migmatites with minor bodies of orthogneisses, marble, amphibolite, quartzite, and eclogite (Monotonous and Variegated "Series", Gföhl assemblage, undivided)
-  Mica schists and retrogressed rocks
-  Major bodies of granulites and associated (U)HP rocks including mantle peridotites and eclogites
-  Migmatites in association with granite plutons

Metamorphic complexes along the northeastern margin of the Moldanubian Unit



-  Orthogneisses and mica schists with (U)HP rocks
-  Low-grade to medium-grade metamorphic rocks

Moravosilesian and Brunovistulian units

-  Neoproterozoic basement (Brunia)
-  Moravian Zone (strongly reworked and imbricated Neoproterozoic basement with inverted Variscan metamorphic zonation)
-  Devonian pre-flysch succession and Upper Devonian to Lower Carboniferous siliciclastic sedimentary rocks (Variscan flysch)

Late-orogenic (post-collisional) "peripheral" granitoids

Saxothuringian granitoids and plutons in the East Sudetes

-  Various biotite and two-mica granites, commonly porphyritic, minor diorites to granodiorites (redwitzites)
-  Compositionally diverse intrusions including granodiorite (dominant), tonalite, syenite, and diorite

Moldanubian Batholith


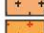
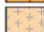

-  "Weinsberg" granite
-  "Eisgarn" granite
-  Freistadt granodiorite
-  Other granitoids (undivided)

Fig. 2. Continued

uncertainty exists as to how far it travelled from, or whether it remained attached to, the northern margin of Gondwana in the early Paleozoic Era (Linnemann *et al.* 2004).

During the waning stages of Variscan Orogeny (c. 330–305 Ma; Fig. 3), the Saxothuringian Unit was intruded by several granite plutons of diverse geochemical composition ranging from I-types (e.g. main portion of the Krkonoše–Jizera Plutonic Complex, KJPC in Fig. 2; Słaby & Martin 2008) to strongly peraluminous S- and A-types bearing Sn–W mineralization (most granite units in the Krušné hory/Erzgebirge; Fig. 2; see Förster *et al.* 1999, Štemprok *et al.* 2003, Förster & Romer 2010, and Breiter 2012 for reviews). The plutons continue to the southwest and cross-cut boundaries between lithotectonic units with no apparent change in composition or age (e.g. Northern Oberpfalz, NOP; Figs 2 & 3).

Teplá–Barrandian Unit

The upper-crustal Teplá–Barrandian Unit in the centre of the Bohemian Massif (Fig. 2) occupies the hanging-wall position with respect to the neighbouring Saxothuringian and Moldanubian units and is thus the overriding plate for all the hypothetical subduction zones. Moreover, a large central portion of this unit has never been buried to great depths and thus has escaped the Variscan pervasive metamorphism and ductile deformation (Suchý *et al.* 1996, 2007; Hajná *et al.* 2010, 2011, 2012). The Teplá–Barrandian Unit consists of generally low-grade Neoproterozoic basement intruded by Cambro–Ordovician plutons and overlain unconformably by the early Paleozoic (early Cambrian to middle Givetian) passive margin volcano-sedimentary successions (Fig. 2; Zulauf 1997b; Chlupáč *et al.* 1998; Dörr *et al.* 1998, 2002; Hajná *et al.* 2010, 2011). The largest part of the Teplá–Barrandian Neoproterozoic basement to the south, west, and northwest of the Lower Paleozoic overlap successions was interpreted as a Cadomian accretionary wedge with a related volcanic arc preserved along the southeastern flank of the unit, albeit severely reworked by Variscan deformation (Waldhausrová 1984; Sláma *et al.* 2008a; Hajná *et al.* 2010, 2011). Small remnants of Cadomian intra- and back-arc basins also occur close to the Teplá–Barrandian/Moldanubian boundary (Sláma *et al.* 2008a; Hajná *et al.* 2010, 2011).

There are three important features associated with the Teplá–Barrandian Unit. First, as inferred from seismic anisotropy by Babuška & Plomerová (1992, 2001, 2013), Plomerová *et al.* (2005), and Babuška *et al.* (2008, 2010), the Teplá–Barrandian mantle lithosphere exhibits olivine fabric different from that of in the neighbouring Saxothuringian and Moldanubian units, perhaps being inherited from the Cadomian accretion and subduction.

Zoned plutons as markers of regional tectonic and geodynamic setting

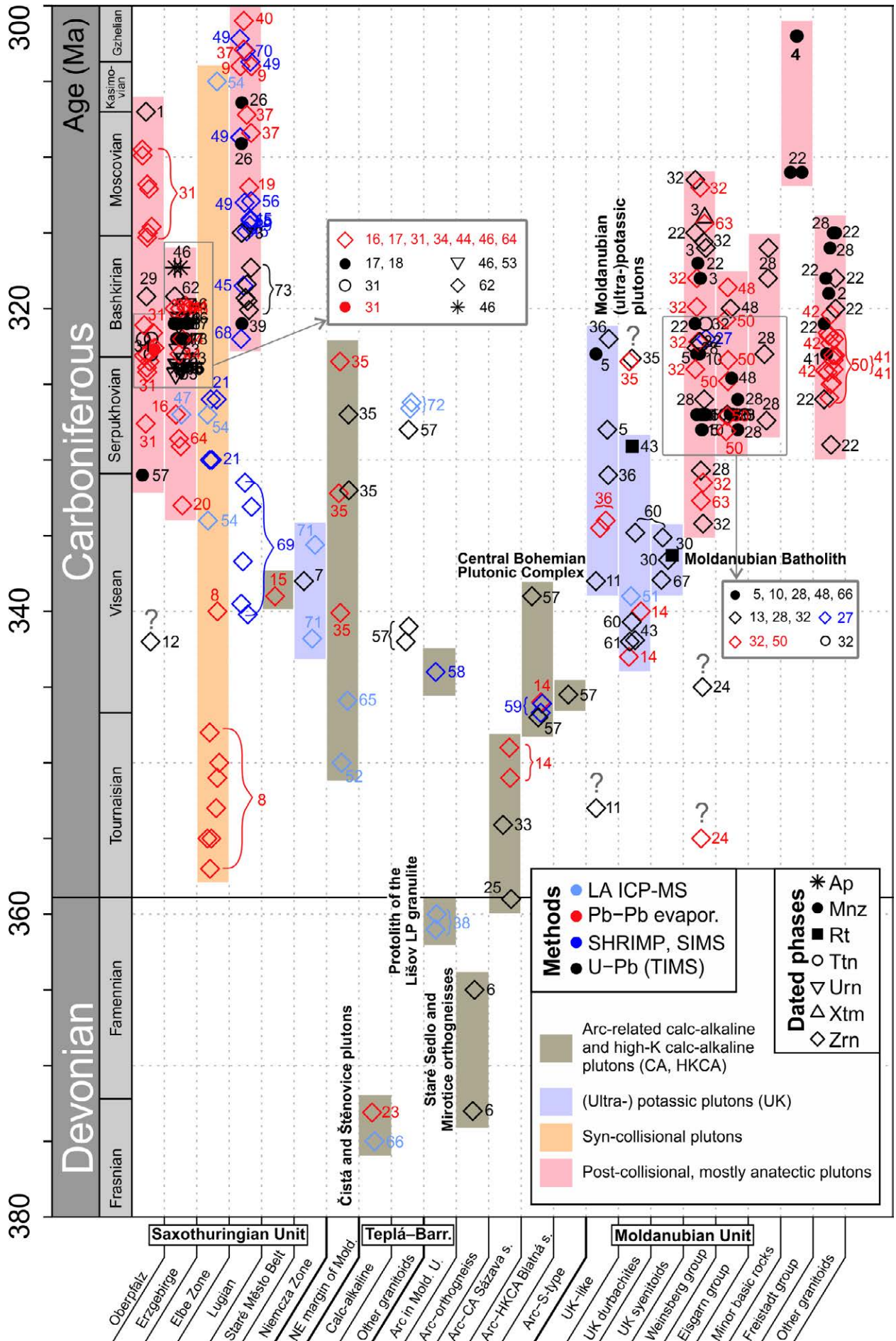


Fig. 3. Overview of the U–Pb and Pb–Pb ages from Late Devonian to late Carboniferous plutonic rocks of the Bohemian Massif. The stratigraphic table is based on International Stratigraphic Chart, version 2013/1 (<http://www.stratigraphy.org/ICSchart/ChronostratChart2013-01.pdf>). Mineral abbreviations after Kretz (1983). References: 1 –Wendt *et al.* (1986); 2 – Frasl & Finger (1991); 3 –von Quadt & Finger (1991); 4 –Friedl *et al.* (1992); 5 – Friedl *et al.* (1993); 6 – Košler *et al.* (1993); 7 – Oliver *et al.* (1993); 8 – Wenzel *et al.* (1993); 9 – Kröner *et al.* (1994); 10 – Friedl *et al.* (1996); 11 – Klötzli & Parrish (1996); 12 –Köhler & Hölzl (1996); 13 –Finger *et al.* (1997); 14 – Holub *et al.* (1997a); 15 – Parry *et al.* (1997); 16 –Tichomirowa (1997); 17 –Förster (1998); 18 –Förster *et al.* (2009); 19 –Hammer *et al.* (1999); 20 –Kempe *et al.* (1999); 21 – Nasdala *et al.* (1999); 22 – Propach *et al.* (2000); 23 – Venera *et al.* (2000); 24 – Klötzli *et al.* (2001); 25 – Bues *et al.* (2002); 26 –Turniak & Bröcker (2002); 27 – Finger *et al.* (2003); 28 – Gerdes *et al.* (2003); 29 – Chen *et al.* (2003); 30 – Janoušek & Gerdes (2003); 31 – Siebel *et al.* (2003); 32 – Chen & Siebel (2004); 33 – Janoušek *et al.* (2004); 34 – Kempe *et al.* (2004); 35 – Schulmann *et al.* (2005); 36 – Siebel *et al.* (2005); 37 –Turniak *et al.* (2005); 38 – Janoušek *et al.* (2006); 39 –Klomínský *et al.* (2007); 40 –Turniak *et al.* (2006); 41 – Siebel *et al.* (2006a); 42 – Siebel *et al.* (2006b); 43 – Kotková *et al.* (2007); 44 – Kovaříková *et al.* (2007); 45 – Machowiak & Armstrong (2007); 46 – Romer *et al.* (2007); 47 –Hofmann *et al.* (2008); 48 – Klein *et al.* (2008); 49 – Kusiak *et al.* (2008); 50 – Siebel *et al.* (2008); 51 – unpublished data cited in Verner *et al.* (2008); 52 –Vondrovic & Verner (2008); 53 – Förster *et al.* (2009); 54 – Hofmann *et al.* (2009); 55 – Kusiak *et al.* (2009); 56 – Awdankiewicz *et al.* (2010); 57 – Dörr & Zulauf (2010); 58 – Finger *et al.* (2010); 59 – Janoušek *et al.* (2010); 60 – Kotková *et al.* (2010); 61 – Kusiak *et al.* (2010); 62 –Romer *et al.* (2010); 63 – Siebel *et al.* (2010); 64 – Tichomirowa & Leonhardt (2010); 65 – Vondrovic *et al.* (2011); 66 – Žák *et al.* (2011a); 67 – Holub *et al.* (2012); 68 – Kryza *et al.* (2012); 69 – Mikulski *et al.* (2013); 70 – Oberc-Dziedzic *et al.* (2013); 71 –Pietranik *et al.* (2013); 72 –Trubač *et al.* (2013); 73 –Žák *et al.* (in print).

Second, its northwestern tip structurally overlies the Mariánské Lázně meta-ophiolite complex (MLC in Fig. 2) which exhibits the earliest Cambrian (c. 540 Ma) and early Ordovician (c. 480 Ma) protolith ages (Bowes & Aftalion 1991; Timmermann *et al.* 2004), interpreted as recording attachment of oceanic lithosphere and rifting of the 'proto-Teplá–Barrandian' margin, respectively (Timmermann *et al.* 2004; Sláma *et al.* 2008a). The late Devonian ages (c. 380 Ma) in the complex then constrain its Variscan subduction-related eclogite-facies metamorphism (Beard *et al.* 1995; Zulauf 1997b). Taken together, the present-day northwestern margin of the Teplá–Barrandian Unit must have acted repeatedly as an active plate margin with subduction of oceanic crust during both the Cadomian and Variscan orogenies (e.g. Zulauf 1997b; Dörr *et al.* 2002; Dörr & Zulauf 2010).

Third, the Teplá–Barrandian upper crust was intruded by a number of Late Devonian to early Carboniferous calc-alkaline granitoid plutons (Figs 2 & 3) that bear a distinctive geochemical imprint of subduction (Palivcová 1984; Janoušek *et al.* 1995; Holub *et al.* 1997b; Janoušek *et al.* 2000, 2004a,

2006; Verner *et al.* 2009a; Vondrovic *et al.* 2011) and reveal a consistent spatial–temporal–compositional trend (Žák *et al.* 2011a). The earliest, late Devonian (~375–373 Ma) Čistá and Štěnovice plutons occupy the centre (ČP and SP in Fig. 2; Klomínský 1963, 1965; Kopecký *et al.* 1997; Venera *et al.* 2000; Žák *et al.* 2011a), whereas the early Carboniferous (~354–337 Ma) plutons form a large continental magmatic arc along the southeastern flank of the Teplá–Barrandian Unit (the Central Bohemian Plutonic Complex, CBPC in Fig. 2; Holub *et al.* 1997a, b; Dörr *et al.* 1998; Janoušek *et al.* 2004a, 2010; Dörr & Zulauf 2010). The arc itself shows internal compositional zoning from the older ~354 Ma calc-alkaline intrusions to the north and northwest through ~346 Ma high-K calc-alkaline in the centre to ~343–337 Ma ultrapotassic plutons along its southeastern margin (Fig. 2; Janoušek *et al.* 1995; Holub *et al.* 1997a, b; Žák *et al.* 2005a). The exception are the Late Devonian Mirovice and Staré Sedlo orthogneisses (MC and SSC in Fig. 2; ~380–365 Ma; Košler *et al.* 1993) which also exhibit calc-alkaline arc-related geochemical signature (Košler & Farrow 1994) but occur in the roof of the central part of the plutonic complex (Fig. 2). They were deformed prior to emplacement of at least 20 M.y. younger high-K calc-alkaline and still younger ultrapotassic plutons. Interestingly, dismembered and reworked parts of comparable arc-related rocks can also be found in the Moldanubian Unit (the Lišov granulite, LI in Fig. 2; Janoušek *et al.* 2006).

The Moldanubian Unit

In contrast to the above, the Moldanubian Unit s.s. (Fig. 2; considered here without metamorphic complexes along its northeastern margin; Pertoldová *et al.* 2010 and references therein) is deeply eroded middle to lower crust characterized by a complex Variscan tectonometamorphic history (e.g. Vrána *et al.* 1995; Finger *et al.* 2007; Faryad *et al.* 2010; Franěk *et al.* 2011). It has been recently interpreted as representing an orogenic root (Schulmann *et al.* 2005, 2008, 2009). Except for rare Paleoproterozoic (~2.1 Ga) meta-igneous rocks (Wendt *et al.* 1993), large portions of the Moldanubian Unit have Neoproterozoic to early Paleozoic igneous and siliciclastic protoliths, the latter now represented by the LP–HT, commonly sillimanite- and cordierite-bearing and migmatitic biotite paragneisses ('the Monotonous Series'). On the other hand, other meta-sedimentary complexes contain abundant lenses of marble, amphibolite, and quartzite ('the Variegated Series'; Fuchs & Matura 1976; Kröner *et al.* 1988; Fiala *et al.* 1995; Linner 1996) and are, at least partly, Early Palaeozoic in age (Janoušek *et al.* 2008). The Moldanubian Unit also contains intercalations and relics of Neoproterozoic and Cambro–Ordovician orthogneisses (e.g. Friedl *et al.* 2004) as well as (U)HP eclogite- to granulite-facies and mantle rocks (Becker & Altherr 1992; Becker 1997; Kotková *et al.*

1997; Vrána & Frýda 2003; Nakamura *et al.* 2004; Medaris *et al.* 2005, 2006; Naemura *et al.* 2009, 2011). Together with various types of migmatites and migmatized granite gneisses, these rocks have been collectively termed 'the Gföhl assemblage' (see Petrakakis 1997; Franke 2000; Finger *et al.* 2007 and Faryad 2011 for detailed reviews and terminology) and interpreted in previous studies as parts of a single nappe ('the Gföhl nappe'; e.g. Tollmann 1982, 1995; Franke 1999, 2006). This view has been challenged in favour of vertical 'forceful' exhumation along separate channel-like domains in response to buoyancy forces and crustal shortening (Franěk *et al.* 2006, 2011; Maierová *et al.* 2012). Although exceptions do occur, the inferred ages of the granulite-facies metamorphism concentrate around 340 Ma throughout the Moldanubian Unit (van Breemen *et al.* 1982; Aftalion *et al.* 1989; Wendt *et al.* 1994; Kröner *et al.* 2000; Janoušek *et al.* 2006; Kotková 2007; Sláma *et al.* 2008b; Tajčmanová *et al.* 2010; Friedl *et al.* 2011).

Latest findings, however, point to a more complex pre-340 Ma burial and exhumation history of the (U)HP rocks within the Moldanubian Unit (Prince *et al.* 2000; Faryad *et al.* 2009, 2010, 2013; Friedl *et al.* 2011).

The Moldanubian Unit hosts several plutonic suites (Figs 2 & 3). An older, rather specific one is represented by ultrapotassic melagranitoids to melasyenitoids ('durbachites' and related rocks) with U–Pb zircon ages ranging from ~343 to ~335 Ma (Holub 1997; Holub *et al.* 1997a; Janoušek & Gerdes 2003; Janoušek & Holub 2007; Verner *et al.* 2008; Kotková *et al.* 2010; Kusiak *et al.* 2010; Holub *et al.* 2012). The 'durbachites' also intruded the upper-crustal rocks along the southeastern flank of the Teplá–Barrandian Unit and the high-K calc-alkaline granitoids of the Central Bohemian Plutonic Complex (Fig. 2). Recent petrogenetic interpretations suggest that the primary (ultra-) potassic magmas, to be subsequently mixed with anatectic melts, were derived from anomalous lithospheric mantle strongly enriched in Large Ion Lithophile Elements (LILE) and Light Rare Earth Elements (LREE) (Janoušek *et al.* 1995; Holub 1997; Wenzel *et al.* 1997; Becker *et al.* 1999; Janoušek *et al.* 2000; Gerdes *et al.* 2000a; von Raumer *et al.* in print). Furthermore, Janoušek & Holub (2007) and Lexa *et al.* (2011) explained the temporal and spatial link between the ultrapotassic plutons and HP granulites (Fig. 2) as a result of contamination of the local mantle by subducted/relaminated Ordovician felsic metaigneous rocks of Saxothuringian provenance, the presumed protolith to the Moldanubian granulites (Janoušek *et al.* 2004b).

The other suites of crustally-derived granitoids include coarse-grained I- to S-type K-feldspar-phyr-ic biotite granites dated at c. 331–323 Ma ('the Weinsberg granite'; Figs 2 & 3) and peraluminous S-type two-mica granites dated at c. 330 to 328–327 Ma ('the Eisgarn granite'; Fig. 2; U–Pb zircon

ages according to Gerdes *et al.* 2003). Together with intrusions of the Freistadt biotite granodiorite (Figs 2 & 3), late highly fractionated granites, and minor basic bodies these two suites compose the Moldanubian Batholith (MB in Fig. 2), the largest plutonic body in the entire Variscan belt (Liew *et al.* 1989; Vellmer & Wedepohl 1994; Holub *et al.* 1995; Klötzli & Parrish 1996; Klečka & Matějka 1996; Finger *et al.* 1997; Gerdes *et al.* 2000a, b, 2003; Gerdes 2001; Klötzli *et al.* 2001; Finger *et al.* 2009; Breiter 2010; Žák *et al.* 2011b). In the map view, the individual intrusive units of the batholith are clustered in two nearly perpendicular segments oriented ~WNW–ESE and ~NNE–SSW (Fig. 2). The former is defined by a number of separate smaller plutons that involve both 'Eisgarn' and 'Weinsberg' granites whereas the latter, hosted by a complex of cordierite-bearing migmatites and migmatized paragneisses, is chiefly made up of the 'Eisgarn granite' (Žák *et al.* 2011b).

Brunovistulian Unit

In contrast to the above units that share the Cadomian or 'West African' affinity (e.g. Drost *et al.* 2004; Linnemann *et al.* 2004; Drost *et al.* 2011), the Brunovistulian Unit (Fig. 2; 'Brunia') underlying the eastern margin of the Bohemian Massif is an exotic terrane of problematic provenance more akin to Avalonia (Friedl *et al.* 2000; Kalvoda *et al.* 2008). Its pre-Variscan evolution was thus rather different from that of the remainder of the Bohemian Massif and involved late Neoproterozoic terrane accretion followed by extensive post-collisional plutonism at around 595–585 Ma and deposition of Neoproterozoic to early Paleozoic successions onto the welded terranes (van Breemen *et al.* 1982; Dudek 1980; Finger *et al.* 1989; Jelínek & Dudek 1993; Finger & Steyrer 1995; Fritz *et al.* 1996; Schulmann & Gayer 2000; Finger *et al.* 2000a, b; Leichmann & Höck 2008).

KEY OBSERVATIONS ON THE NATURE, TIMING, AND KINEMATICS ALONG MAJOR TECTONIC BOUNDARIES IN THE BOHEMIAN MASSIF AND THEIR RELATION TO GRANITOID PLUTONISM

Orogen-parallel ~NE–SW-trending boundaries

The Teplá suture

The Saxothuringian/Teplá–Barrandian boundary, referred to as the Teplá suture (TS in Fig. 1), is in fact a broad zone consisting of an imbricated stack of NW-directed nappes, involving portions of both subducted oceanic lithosphere and overriding margin of the Teplá–Barrandian Unit, that were exhumed from the suture and thrust over the Saxothuringian foreland (Fig. 2; Behr *et al.* 1982;

Franke 1989; Kachlík 1993; Schäfer *et al.* 1997; Mazur & Alexandrowski 2001). Relics of these nappes also extend as a series of klippen further to the west and northwest (Erbendorf–Vohenstraus Zone, ZEV in Fig. 2, Münchberg, Frankenberg, and Wildenfels nappes). The suture formed initially by the SE-directed subduction and closure of the Saxothuringian Ocean, welding the Saxothuringian and Teplá–Barrandian units at around 380 Ma (Franke 1989; Beard *et al.* 1995; Schäfer *et al.* 1997; Zulauf 1997b). As proposed by O'Brien (2000), Janoušek *et al.* (2004b), Konopásek & Schulmann (2005), Janoušek & Holub (2007), and Lexa *et al.* (2011), the Saxothuringian subduction continued in continental underthrusting until c. 340 Ma and its waning stages thus broadly overlapped with the onset of normal movements and collapse of the Teplá–Barrandian Unit at around 346 Ma (Zulauf 1994; Scheuvens & Zulauf 2000; Zulauf *et al.* 2002; Žák *et al.* 2005a; Dörr & Zulauf 2010; Janoušek *et al.* 2010).

In detail, recent structural work suggests that the deformation resulting from the Saxothuringian/Teplá–Barrandian convergence was rather complex in the overriding Teplá–Barrandian plate (Fig. 4). The deformation was strongly partitioned into pure shear-dominated domains that accommodated orogen-perpendicular ~WNW–ESE shortening alternating with narrow, orogen-parallel, high-strain zones that recorded dextral transpression or lateral extrusion (Fig. 4a; Hajná *et al.* 2012). The orogen-parallel zones were localized along pre-existing lithologic boundaries or in the softened thermal aureoles of the arc plutons (Fig. 4b; Žák *et al.* 2005b; Machek *et al.* 2009; Hajná *et al.* 2012). As with the arc-related plutonism, these zones indicate younging of deformation in the overriding Teplá–Barrandian plate from ~370–380 in the northwest to c. 346 Ma in the southeast (Hajná *et al.* 2011; Žák *et al.* 2011a).

The Teplá–Barrandian/Moldanubian boundary

This boundary (variously referred to as 'the Central Bohemian suture', 'Central Bohemian shear zone', or 'Gföhl suture') is one of the most intriguing tectonic features of the Bohemian Massif, unique in that every possible sense of movement was invoked to explain its kinematic evolution (Tollmann 1982; Rajlich 1987, 1988; Matte *et al.* 1990; Košler *et al.* 1995; Pitra *et al.* 1999; Scheuvens & Zulauf 2000; Franke 2000; Franke & Żelaźniewicz 2002; Medaris *et al.* 2005; Žák *et al.* 2005a, b, 2009a, 2012; Dörr & Zulauf 2010).

The earliest record of the Variscan Orogeny along the Teplá–Barrandian/Moldanubian boundary is preserved in the lower to middle Devonian siliciclastic successions (Chlupáč 1989) and in the late Devonian (~380–365 Ma) Mirovice and Staré Sedlo orthogneisses (Figs 2 & 3). The latter meta-granitoids are sheeted, exhibit subhorizontal intrusive contacts, flat-lying solid-state foliation, and

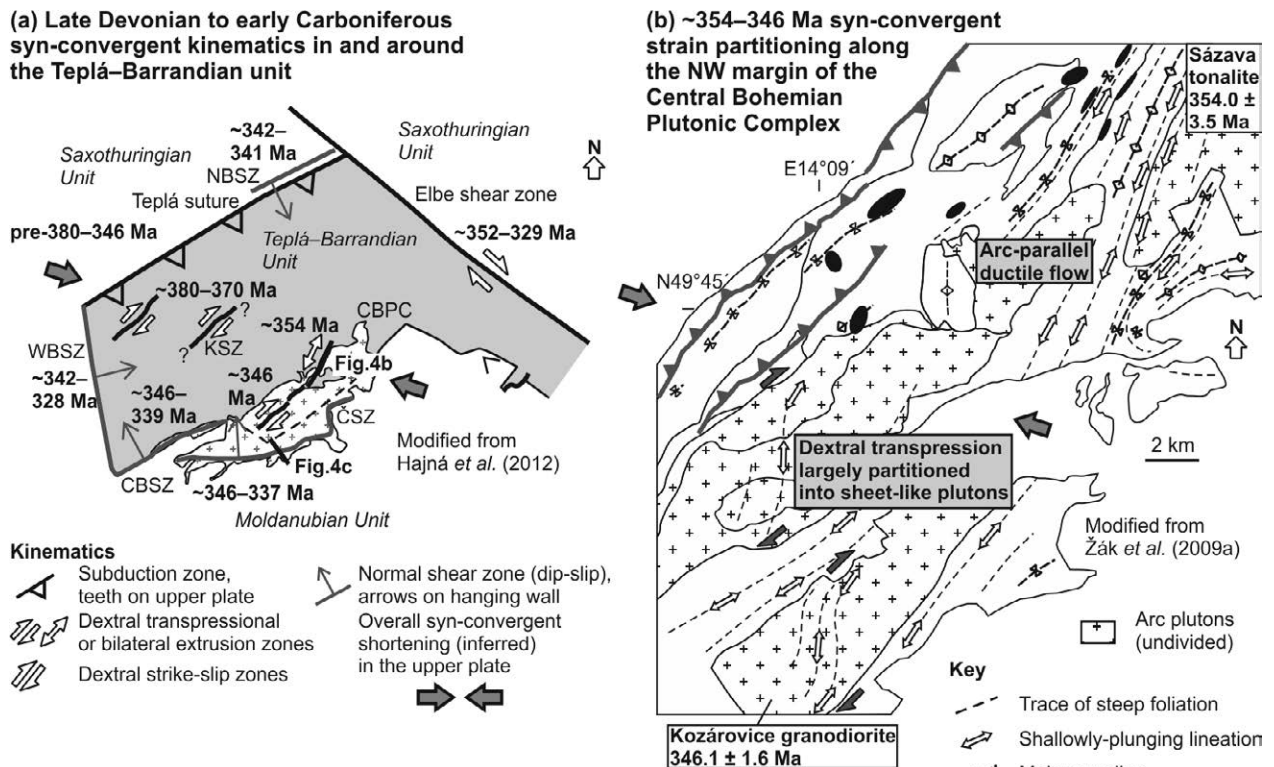


Fig. 4. Structural sketches summarizing deformation, kinematics, and plutonism during prolonged Late Devonian to early Carboniferous convergence of the Saxothuringian and Teplá–Barrandian units. **(a)** Map of major shear zones inside and around the Teplá–Barrandian Unit showing overall ~WNW–ESE shortening in the upper crust replaced by normal movements and onset of exhumation of the Moldanubian Unit from c. 346 Ma onwards. See Hajná *et al.* (2012) for details. CBPC, Central Bohemian Plutonic Complex; CBSZ, Central Bohemian shear zone; ČSZ, Červená shear zone; KSZ, Krakovec shear zone; NBSZ, North Bohemian shear zone; WBSZ, West Bohemian shear zone. **(b)** Close-up of the northwestern margin of the Central Bohemian Plutonic Complex. The background ~WNW–ESE shortening was partitioned into arc-parallel ductile flow or dextral transpression depending on the orientation of syn-tectonic plutons. See Žák *et al.* (2009a) for details. **(c)** A kinematic switch from transpression to ductile normal shearing is recorded in the ~346 Ma Blatná and Červená granodiorites of the Central Bohemian Plutonic Complex. This change marks on the onset of exhumation of the southeasterly high-grade Moldanubian Unit. See Žák *et al.* (2005a, 2012) and Janoušek *et al.* (2010) for details.

~NE–SW subhorizontal stretching lineation, and are commonly characterized by a prolate fabric ellipsoid (Tomek 2011; Tomek & Žák 2011). A different structural pattern is observed in the earliest, c. 354 Ma calc-alkaline intrusions (Sázava suite) of the Central Bohemian Plutonic Complex which were syntectonic with partitioned regional dextral transpression characterized by the ~WNW–ESE arc-perpendicular shortening and arc-parallel horizontal stretching (Fig. 4b; Žák *et al.* 2005a, b, 2009a; Hajná *et al.* 2012). This transpressive deformation lasted till c. 346 Ma when it was replaced by ductile normal shearing along the Červená shear zone (ČSZ in Fig. 2) associated with exhumation of the high-grade core of the orogen, the Moldanubian Unit (Fig. 4c; Holub *et al.* 1997b; Žák *et al.* 2005a, 2012; Janoušek *et al.* 2010). The cessation of ductile deformation along the Teplá–Barrandian/Moldanubian boundary is bracketed by the c. 336 Ma post-tectonic Říčany Pluton in the northeast (ŘP in Fig. 2; Janoušek *et al.* 1997; Trubač *et al.* 2009) and by undeformed melasyenites including c. 338 Ma dykes (Holub *et al.* 2012) and c. 337 Ma Tábor Pluton (TP in Fig. 2) that intruded discordantly the Moldanubian gneisses to the southeast of the shear zone (Janoušek & Gerdes 2003; Žák *et al.* 2005a).

The Moldanubian thrust system

Along the eastern margin of the Bohemian Massif, the Moldanubian Unit has been thrust over the Brunia microplate (MT in Fig. 2; e.g. Suess 1912; Dudek 1980; Schulmann *et al.* 1991, 2005, 2008; Fritz & Neubauer 1993; Štípská & Schulmann 1995; Fritz *et al.* 1996; Racek *et al.* 2006; Finger *et al.* 2007; Kalvoda *et al.* 2008). The highly oblique, top-to-the-NNE Saxothuringian–Moldanubian/Brunia collision presumably commenced prior to 346 Ma in the northeast (Schulmann & Gayer 2000; Jastrzębski 2009; Chopin *et al.* 2012), also constrained by the syntectonic Staré Město tonalite sill (SMT in Fig. 2 and 5a; Parry *et al.* 1997, dated at 344.5 ± 1.1 Ma and 339.4 ± 1.1 Ma by Štípská *et al.* 2004). The Brunia underthrusting resulted in a ~NNE–SSW-trending belt of imbricated nappe stacks along the whole eastern margin of the Bohemian Massif (the Moravosilesian Unit; Fig. 2). Geophysical data indicate that the Brunia microplate, exposed in tectonic windows of the Moravian nappes, continues ~70 km westward beneath the Moldanubian rocks (Mísař 1994; Schulmann *et al.* 2008; Guy *et al.* 2011; Verner *et al.* in print). The inferred westernmost front edge of the Brunia microplate at depth coincides with the Přebyslav mylonite zone at the present-day erosional level (PMZ in Fig. 2). This zone was recognized as an important, crustal-scale geophysical and tectonic boundary that cuts across the entire Moldanubian Unit along the ~NNE–SSW direction and was associated with oblique-slip (dextral, W-side-up) movements initiated at around 335 Ma (Fig. 5b; Verner *et al.* 2006; Kotková *et al.* 2010) and renewed at ~330–327 Ma (Fig. 5c; Žák *et al.* 2011b; Verner *et al.* in print).

Orogen-perpendicular ~NW–SE-trending boundaries

The Sudetic fault system

The northeasternmost margin of the Bohemian Massif ('the Sudetes') is cut by a series of major faults (Fig. 2; Lusatian, Machnín, Intra-Sudetic, Marginal-Sudetic; e.g. Aleksandrowski *et al.* 1997; Danišík *et al.* 2012), referred to as the Sudetic fault system here. The fault-bounded blocks host several granitoid plutons (Fig. 2; e.g. Strzegom–Sobótka, Strzelin, Kłodzko–Złoty Stok, Žulová; see Mazur *et al.* 2007, Mikulski *et al.* 2013, and Oberc-Dziedzic *et al.* 2013 for reviews) that are largely concealed and their internal fabrics and structural relations are yet to be examined in detail. The exception is the shallow-level Krkonoše–Jizera Plutonic Complex (KJPC in Fig. 2; e.g. Klomínský 1969; Mierzejewski 2002; Słaby & Martin 2008; Žák *et al.* 2009b), a classic area of granite geology that has become world-famous through the pioneering work of Cloos (1925). Existing radiometric ages of granites in this plutonic complex scatter widely from 329 ± 17 Ma (Rb–Sr; Pin *et al.* 1987) to 304 ± 14 Ma (U–Pb; Kröner *et al.* 2001; see Awdankiewicz *et al.* 2010 for review), however, recent U–Pb zircon ages point to a more restricted time span from 322 ± 3 Ma (porphyritic biotite granite; Kryza *et al.* 2012) to 313 ± 3 Ma (dykes cutting the granite; Awdankiewicz *et al.* 2010). The plutonic complex intruded into already cold crust and postdated both the blueschist (>360 Ma) and greenschist (c. 340 Ma) facies tectonometamorphic events in its host rocks (Maluski & Patočka 1997; Marheine *et al.* 2002; Mazur *et al.* 2006). The granite generation and emplacement was thus presumably controlled by extensional unroofing and dextral displacement along the Sudetic fault system (Fig. 6; Aleksandrowski *et al.* 1997; Žák *et al.* in print). The early ductile shearing commenced at around 337–335 Ma and was also associated with the opening of a mid-Viséan molasse basin (Turnau *et al.* 2002). Magnetic fabric analysis by Diot *et al.* (1995) and Žák *et al.* (in print) indicates that the plutonic complex recorded ~WNW–ESE horizontal stretching and was also syn-tectonic with dextral movements along the Intra-Sudetic Fault (Fig. 6).

The Elbe shear zone

The more southerly Elbe shear zone (ESZ in Fig. 2), which runs across the northern portion of the Bohemian Massif, is a broad zone of dextral shearing with prolonged kinematic history and causing significant dextral offset of the amalgamated Saxothuringian/Teplá–Barrandian units. The earliest ductile movements were recorded within a ~50–100 km wide belt of the mid- to upper-crustal rocks between the south-westerly Moldanubian and north-easterly Saxothuringian units (Fig. 2). The dominant ductile deformation is characterized here by the ~NW–SE metamorphic foliation,

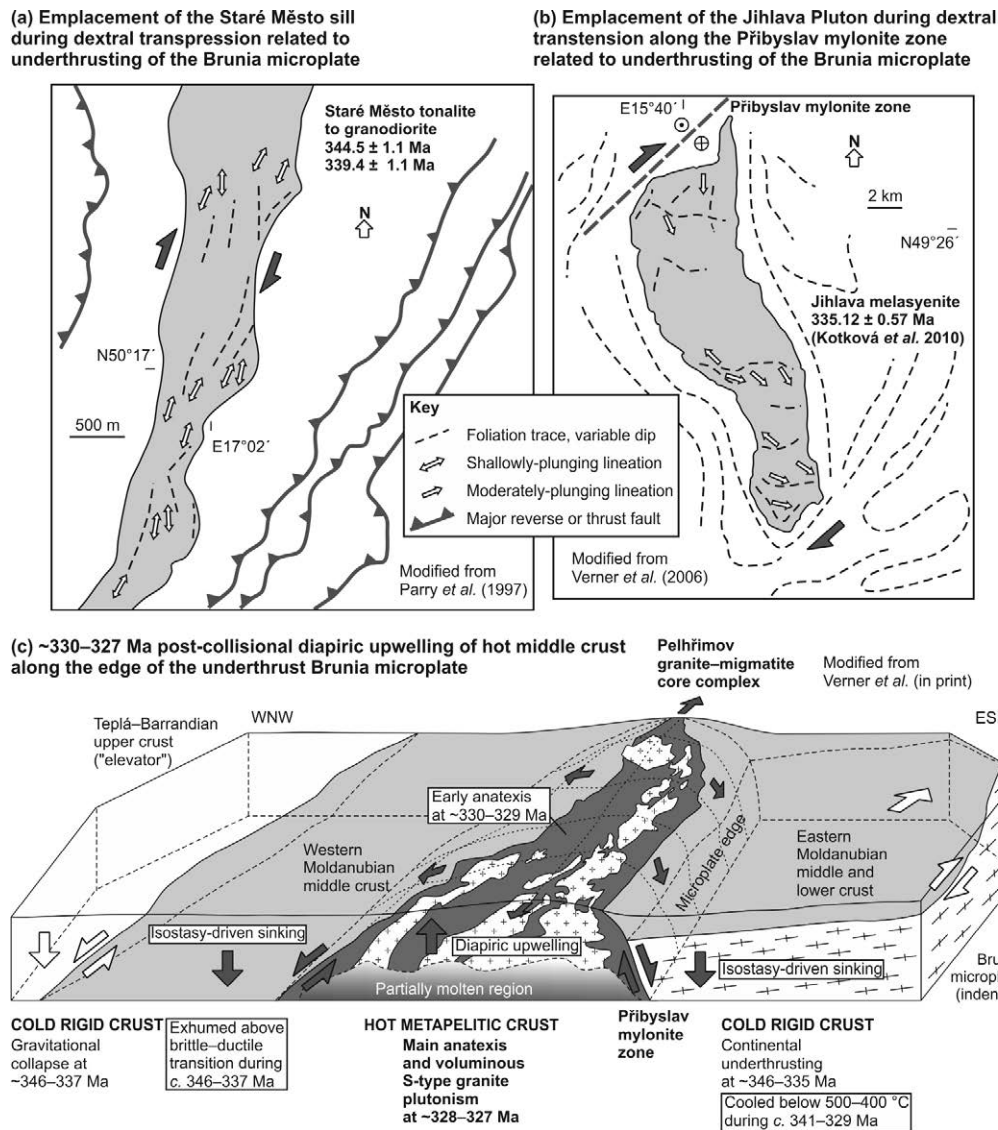


Fig. 5. Examples of syn-tectonic plutons emplaced during and after underthrusting of the Brunia microplate along the eastern margin of the Bohemian Massif. (a) The Staré Město sill records syn-magmatic dextral transpression resulting from early stages of the continental underthrusting in the northeast. See Parry *et al.* (1997) for details. (b) Sigmoidal-shaped Jihlava melasyenite was emplaced later (c. 335 Ma) during the same process as the Brunia microplate proceeded farther to the south-southwest. See Verner *et al.* (2006) for details. (c) Subsequently, the microplate edge acted as a rigid backstop that localized large-scale diapiric upwelling of a granite–migmatite dome, referred to as the Pelhřimov Complex, at around 330–327 Ma. See Žák *et al.* (2011b) and Verner *et al.* (in print) for details.

subhorizontal ~NW–SE stretching lineation, and dextral strike-slip kinematics (Fig. 7; Synek & Oliveriová 1993; Kachlík 1999; Scheck *et al.* 2002; Verner *et al.* 2009a; Vondrovic *et al.* 2011). The broad Elbe shear zone hosts several syn-tectonic calc-alkaline, granodiorite-dominated intrusions emplaced at various stages of deformation. These include the Nasavrky Plutonic Complex (NPC in Fig. 2; Hrouda *et al.* 1999), Budislav and Miřetín plutons (BP and MP in Fig. 2; Verner *et al.* 2009; Verner & Vondrovic

2010; Vondrovic *et al.* 2011). The latter two intrusions were dated at 350 ± 5 Ma (Vondrovic & Verner 2010) and 346 ± 5 Ma (Vondrovic *et al.* 2011), respectively, and are comparable to the arc-related granitoids of the Central Bohemian Plutonic Complex (Vondrovic *et al.* 2011). The Budislav Pluton was coeval with ductile dextral shearing along the Elbe shear zone whereas the Miřetín Pluton records ~WNW–ESE transpression that post-dates the dextral movements (Fig. 7; Pertoldová *et al.* 2010; Vondrovic *et al.* 2011; cf. Pitra *et al.* 1994; Pitra 2012). Subsequently, the Elbe shear zone was multiply reactivated in the brittle–ductile and brittle regime during the early Carboniferous times (e.g. Wenzel *et al.* 1997; Hofmann *et al.* 2009; Verner *et al.* 2009a).

The Pfahl shear zone

The Pfahl shear zone (PSZ in Fig. 2) extends for more than 150 km along strike and together with the sub-parallel south-westerly Danube shear zone (DSZ in Fig. 2) is a major tectonic feature of the southwestern Bohemian Massif (e.g. Peucker-Ehrenbrink & Behr 1993; Brandmayr *et al.* 1995; Büttner & Kruhl 1997; Büttner 2007). The existing U–Pb and Pb–Pb ages and structural relations of granitoid rocks associated with the shear zone indicate the initial stages of dextral shearing at ~342–327 Ma and mylonitic deformation coeval with granite emplacement from ~331–321 Ma (Fig. 8; Chen & Siebel 2004; Siebel *et al.* 2005, 2006b; Verner *et al.* 2009b). Slip along the Pfahl shear zone continued after emplacement of the ~322–323 Ma Patersdorf granite which is truncated by the shear zone (Siebel *et al.* 2006b). Conflicting views exist on whether the shear zone separates two different basement terranes or just intersects the otherwise continuous southwestern Moldanubian Unit (Finger *et al.* 2007, 2010; Siebel *et al.* 2008, 2009; Finger *et al.* 2010; Finger & René, 2009).

Strike-slip-related emplacement and syn-magmatic deformation of the Krkonoše–Jizera Plutonic Complex, Saxothuringian Unit

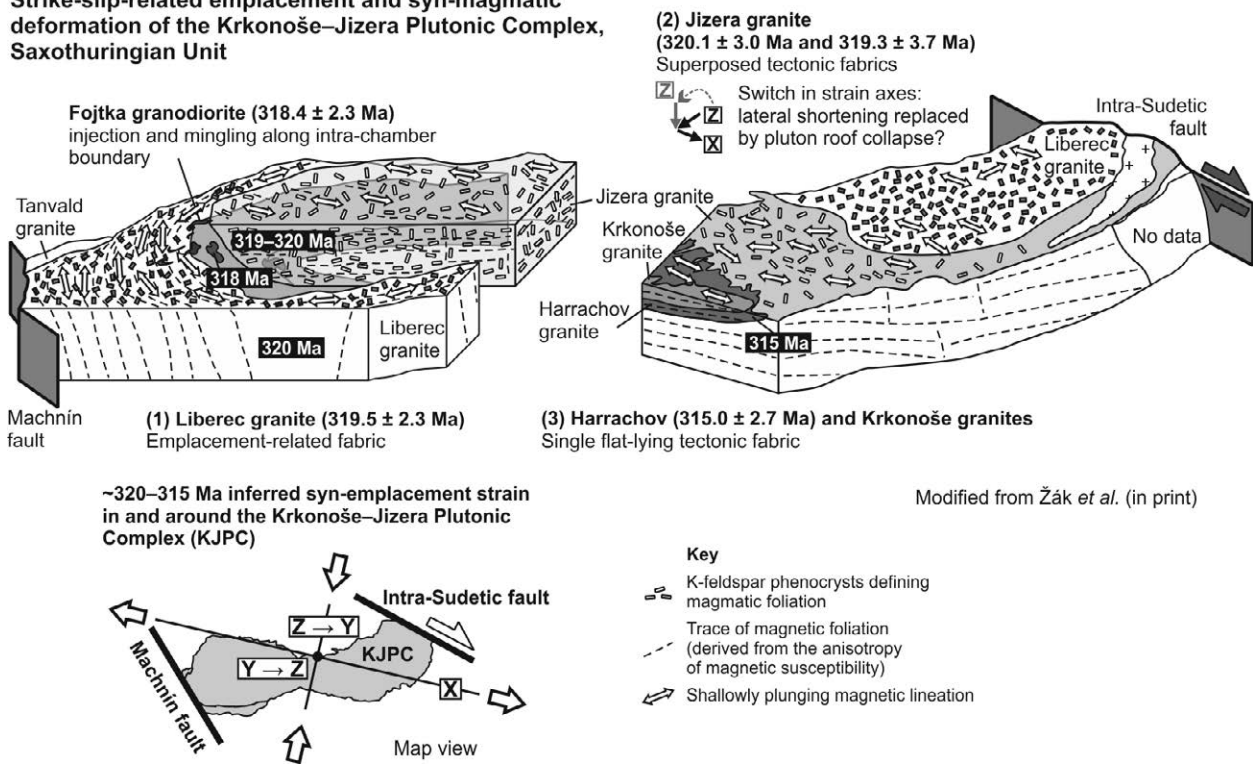


Fig. 6. Schematic block-diagram showing the inferred inward- and upward- younging emplacement sequence and fabric evolution recorded in the c. 320–315 Ma Krkonoše–Jizera Plutonic Complex. Magmatic fabrics evolve from outer margin-parallel to those recording strain related to strike-slip movements along the major pluton-bounding faults. See Žák *et al.* (in print) for details.

Successive syn-tectonic emplacement of calc-alkaline plutons into the broad ductile Elbe shear zone

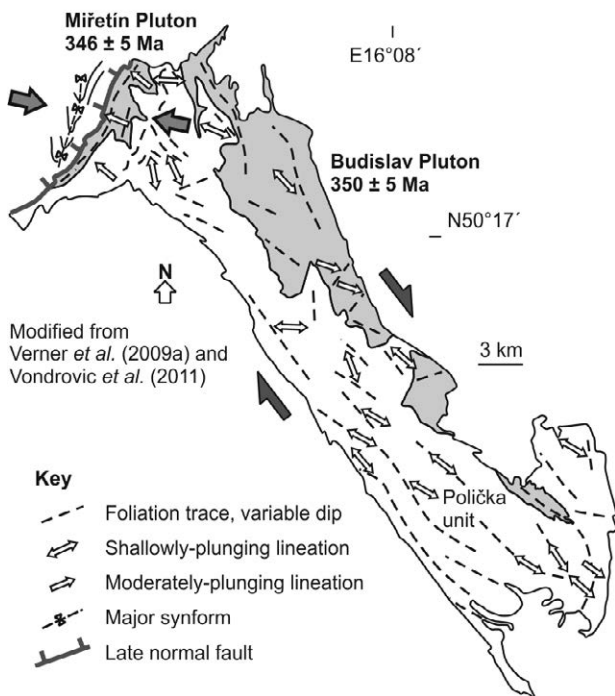


Fig. 7. Fabric patterns of syn-tectonic calc-alkaline plutons emplaced during early stages of ductile movements along the Elbe shear zone at around 350–345 Ma. See Verner *et al.* (2009a) and Vondrovič *et al.* (2011) for details.

A TENTATIVE MODEL LINKING THE VARISCAN OROGENIC DEFORMATION WITH PLUTONISM IN THE BOHEMIAN MASSIF

The Variscan Orogeny in the Bohemian Massif was accompanied by episodic granitoid plutonism with several peaks of the plutonic activity that are now well constrained by geochronologic data. As opposed to an outdated view of granites in the Bohemian Massif as post-tectonic (e.g. Franke 2000, 2006), it has been shown that most of the plutons are in fact syn-tectonic and play a key role in constraining the timing, regime, and kinematics of Variscan orogenic deformations (Figs 4–8; e.g. Diot *et al.* 1995; Büttner & Kruhl 1997; Parry *et al.* 1997; Scheuven & Zulauf 2000; Venera *et al.* 2000; Žák *et al.* 2005a, b, 2009a, 2011a, b; Verner *et al.* 2006, 2008, 2009a, b; Vondrovic *et al.* 2011; Hajná *et al.* 2012; this study).

The earliest Variscan orogenic deformation in the interior of the Bohemian Massif is recorded by a dramatic change in sedimentation from carbonates to Givetian siliciclastic flysch successions (~388–383 Ma; e.g. Chlupáč 1989; Chlupáč *et al.* 1998; Strnad & Mihaljevič 2005 and references therein). This event may be linked to the onset of the SE-directed frontal subduction of the Saxothuringian Ocean (Fig. 9a) leading to exhumation of (U)HP rocks, uplift and cooling along the western margin of the Teplá–Barrandian Unit (~387–365 Ma; Kachlík 1993; Kotková *et al.* 1995; Zulauf 1997a; Dallmeyer & Urban 1998; Strnad & Mihaljevič 2005; Konopásek & Schulmann 2005; Hajná *et al.* 2012). At approximately the same time, the opposite, southeastern flank of the Teplá–Barrandian Unit was intruded by the ~380–365 Ma protolith to Mirovice and Staré Sedlo orthogneisses (Fig. 9a; Košler *et al.* 1993), interpreted as a sill complex emplaced during previously unrecognized but still enigmatic transtensional event (Tomek 2011). All in all, the Late Devonian oceanic subduction resulted in suturing the Saxothuringian and Teplá–Barrandian units at c. 380 Ma (Schäfer *et al.* 1997; Zulauf 1997a) and presumably continued in underthrusting of the Saxothuringian passive margin until the high-grade metamorphism at c. 340 Ma (O'Brien 2000; Konopásek & Schulmann 2005; Schulmann *et al.* 2009).

In one view, the Saxothuringian oceanic subduction produced the minor ~373–375 Ma Štěnovice and Čistá granodiorite plutons in the central Teplá–Barrandian Unit (Fig. 9a; Žák *et al.* 2011a) and culminated in the development of a large magmatic arc along its southeastern flank at around 354–346 Ma (Figs 3, 4, 9a; Konopásek & Schulmann 2005; Žák *et al.*, 2005a, 2009a, 2011a, 2012; Janoušek & Holub 2007; Schulmann *et al.* 2009). The associated, southeast-migrating transpressional deformation (from the Teplá suture towards the orogen's interior) is well recorded in the

Strike-slip-related emplacement and syn-magmatic deformation of the Eisgarn-type granites along the Pfahl shear zone

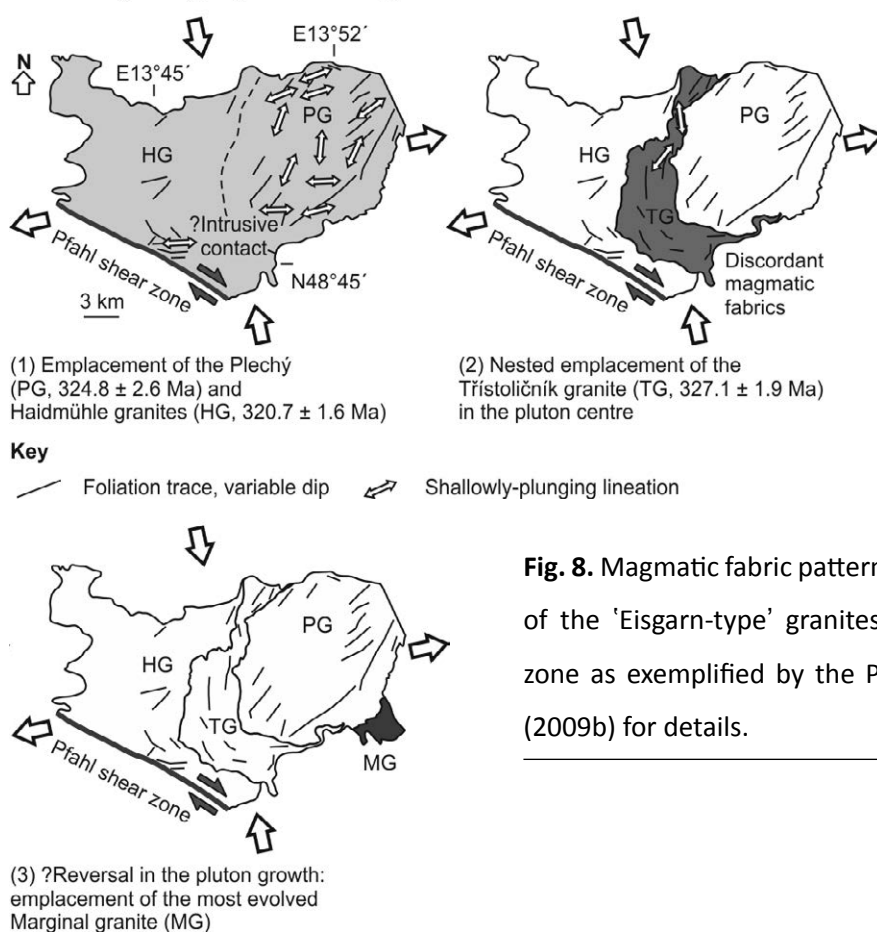


Fig. 8. Magmatic fabric pattern and syn-tectonic emplacement of the 'Eisgarn-type' granites along the dextral Pfahl shear zone as exemplified by the Plechý Pluton. See Verner *et al.* (2009b) for details.

Modified from Verner *et al.* (2009b)

arc granitoids and is characterized by orogen-perpendicular WNW–ESE to NW–SE shortening and orogen-parallel stretching (Figs 4a, 4b, 9a; Zulauf 1997a; Žák *et al.* 2009a; Hajná *et al.* 2012). In alternative hypotheses, the Staré Sedlo and Mirovice orthogneisses and the Central Bohemian Plutonic Complex are linked to opposite, westward subduction of either Gföhl or Raabs ocean (Franke 1999, 2006; Kachlík 1999; Finger *et al.* 2007; Babuška & Plomerová 2013).

The convergent stage was terminated by a rapid gravity-driven collapse of the thickened Teplá–Barrandian upper crust (Fig. 9b). The main phase of ductile normal shearing lasted from c. 346 to c. 337 Ma (Fig. 4c; Scheuven & Zulauf 2000; Žák *et al.* 2005a; Dörr & Zulauf 2010; Janoušek *et al.* 2010; Franěk *et al.* 2011; Holub *et al.* 2012; Žák *et al.* 2012) and was associated with exhumation of the adjacent high-grade core of the orogen, the Moldanubian Unit, including the granulite-facies rocks (Franěk *et al.* 2006, 2011), and with emplacement of (ultra-)potassic 'durbachite' plutons (Fig. 9a; Wenzel *et al.* 1997; Janoušek & Holub 2007; Verner *et al.* 2008).

It is interesting to note that the upper crustal collapse broadly overlapped with the inferred timing

of the earliest ductile movements along the orogen-perpendicular ~NW–SE-trending dextral strike-slip shear zones. The northeastern portion of the amalgamated Saxothuringian/Teplá–Barrandian/Moldanubian block has been truncated and dextrally displaced along the Sudetic and Elbe fault zones that parallel the southeastern margin of Baltica (Franke & Żelaźniewicz 2002), with movements starting from ~355–346 Ma (Fig. 7; Verner *et al.* 2009a) and lasting till at least ~315 Ma (Wenzel *et al.* 1997; Hofmann *et al.* 2009; Pertoldová *et al.* 2010; Vondrovic *et al.* 2011). In turn, this suggests that the orogenic processes governed by the prolonged frontal Saxothuringian subduction/underthrusting, including the internal deformation of the Teplá–Barrandian overriding plate, were abruptly replaced by gravity-driven collapse (Figs 4c & 9b; e.g. Zulauf 1994; Zulauf *et al.* 2002; Dörr & Zulauf 2010; Franěk *et al.* 2011; Žák *et al.* 2012) and by dextral strike-slip movements (Fig. 9c), which could have been caused by the overall westward motion of Gondwana with respect to Laurussia since c. 345 Ma (e.g. Martínez Catalán 2011 and references therein).

Subsequently, while most of the orogenic ductile deformation and exhumation was completed in the central Bohemian Massif in the vicinity of the Teplá–Barrandian Unit by ~339–337 Ma (Žák *et al.* 2012), the eastern part of the Moldanubian Unit was still involved in an underthrusting/collision with the Brunia microplate, closing oceanic domains correlative with the Rhenohercynian Ocean as witnessed by several fragments of oceanic crust (Höck *et al.* 1997; Soejono *et al.* 2010). Brunia continental underthrusting lead to extrusion of the Moldanubian rocks over the top of Brunia, nappe emplacement at ~341–339 Ma (Štípská & Schulmann 1995), and propagation of the microplate edge as far west as the Přebyslav mylonite zone (Fig. 9b). Our structural data around the Jihlava Pluton suggest that this process overlapped with, and was followed by, dextral, W-side-up shearing along the Přebyslav mylonite zone at ~338–335 Ma (Figs 5b & 3b; Verner *et al.* 2006) and most likely terminated prior to c. 330 Ma when the Moldanubian rocks were unroofed and exposed to erosion (Štípská & Schulmann 1995; Scharbert *et al.* 1997; Vrána & Novák 2000; Hartley & Otava 2001; Kotková *et al.* 2007). Later on, Brunia acted as a 'passive' rigid backstop localizing extensive migmatization and rapid exhumation of the Moldanubian metasedimentary rocks along its edge to produce vast volumes of S-type granitoids at ~330–327 Ma (Figs 5c & 9c; the Pelhřimov Complex; Bell *et al.* 2011; Žák *et al.* 2011b; Verner *et al.* in print).

The waning stages of the Variscan Orogeny were characterized by tectonothermal activity in the periphery around the 'stable' core of the Bohemian Massif (Fig. 9c) and included emplacement of huge volumes of the northerly and westerly granitoids in the Saxothuringian Zone and Northern Oberpfalz (e.g. Hecht *et al.* 1997; Siebel *et al.* 1997; Förster *et al.* 1999; Förster & Romer 2010; Breiter

Zoned plutons as markers of regional tectonic and geodynamic setting

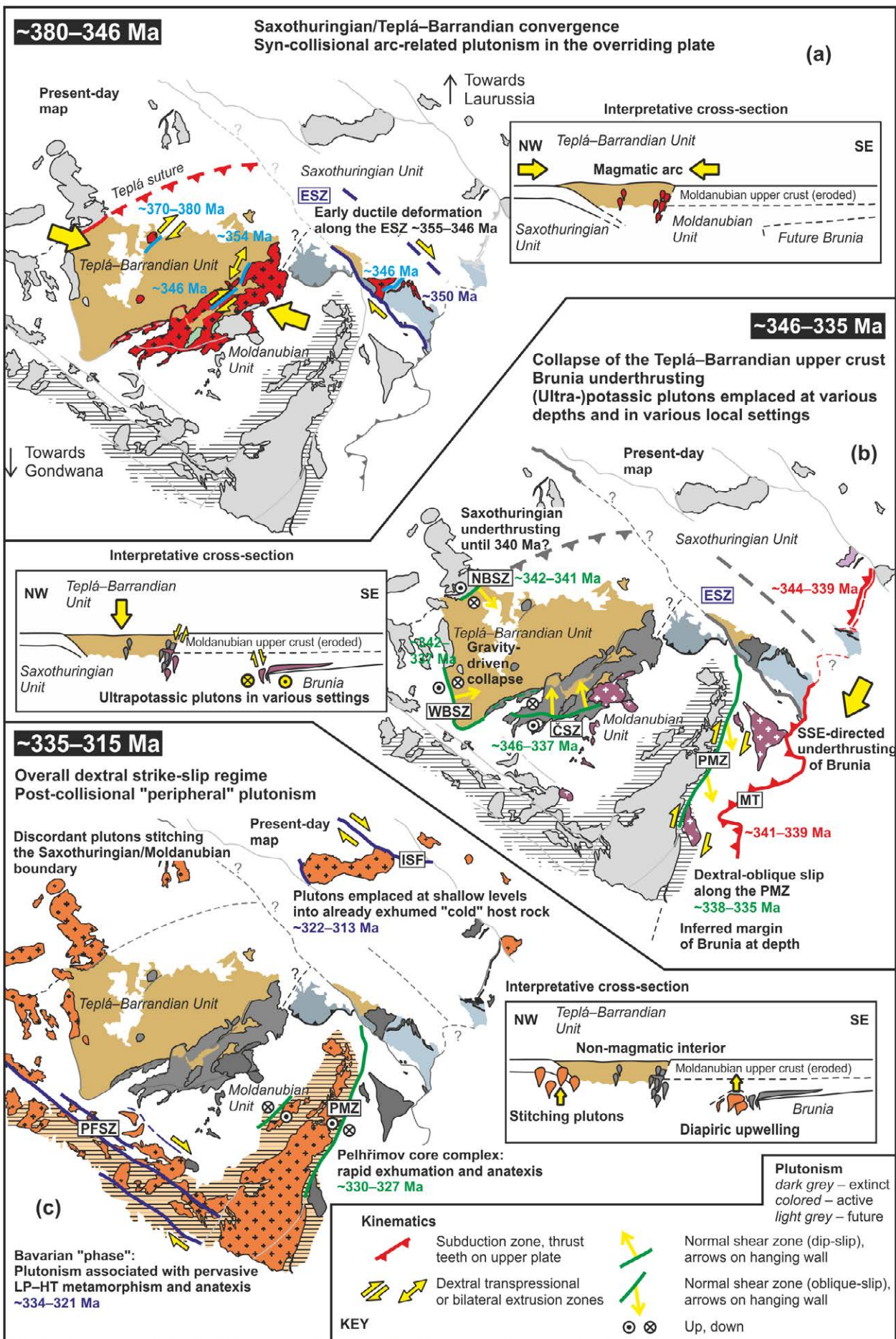


Fig. 9. Greatly idealized sketch emphasizing spatial, temporal, and compositional pattern of Variscan plutonism in the Bohemian Massif. The plutonism is also linked to kinematics and timing of movement along principal tectonic boundaries as inferred from geochronologic and structural data. See text for details and references. Note that the scheme portrays kinematics on the present-day geological background; the exact amount of shortening and of displacement along each shear zone or fault is difficult to reconstruct during relevant time intervals. Also note that Variscan deformations were typically three-dimensional and complex along each boundary. Shear zones and faults: CBSZ, Central Bohemian shear zone; ČSZ, Červená shear zone; ESZ, Elbe shear zone; ISF, Intra-Sudetic Fault; MT, Moldanubian thrust; NBSZ, North Bohemian shear zone; PFSZ, Pfahl shear zone; PMZ, Přebyslav mylonite zone; WBSZ, West Bohemian shear zone.

et al. 2012) and ~334–321 Ma LP–HT metamorphism, crustal anatexis, and associated plutonism in the southwestern Moldanubian Unit (Fig. 9c; e.g. Kalt *et al.* 1999, 2000; Klein *et al.* 2008; Tropper *et al.* 2006; Finger *et al.* 2009). These late-stage events affected already exhumed crust at shallow levels and were linked to continuing movements along the ~NW–SE strike-slip faults (e.g. the Krkonoše–Jizera Plutonic Complex, Aleksandrowski *et al.* 1997; Plechý Pluton, Verner *et al.* 2009b; Figs 6 & 8) or reflected high heat flux caused by mantle delamination as proposed by Henk *et al.* (2000) and Finger *et al.* (2009). Alternatively, Verner *et al.* (in print) proposed that at least some of these granites, commonly in association with migmatites, may represent large-scale diapir-type instabilities accommodating vertical isostatic re-equilibration of the orogen after the microplate convergence. Later destruction of the orogenic belt, post-orogenic igneous activity, intracontinental basin development, and multiple reactivations along the inherited basement fault zones are another part of the story and are not dealt with in detail here.

CONCLUDING REMARKS AND OPEN QUESTIONS

The above overview is, of course, far from being conclusive and complete. However, it at least clearly demonstrates how the orogenic processes and related deformation and plutonism evolved in space and time. As a consequence of overall convergence of Gondwana and Laurussia, four main episodes can be recognized in the interior Bohemian Massif:

- 1) Microplate attachment by prolonged, nearly frontal oceanic subduction and continental underthrusting of the Saxothuringian Unit beneath the Teplá–Barrandian Unit resulted in the orogen-perpendicular shortening and orogen-parallel extension in the overriding plate (Fig. 9a). The plate convergence was crowned by the emplacement of huge volumes of calc-alkaline, magmatic-arc granitoids at ~354–346 Ma (the Central Bohemian Plutonic Complex).

- 2) The subduction-driven shortening was replaced by dextral strike-slip along the orogen-perpendicular shear zones as the convergence of intervening microplates became increasingly overridden by overall westward motion of Gondwana and Laurussia during the early Carboniferous times. This was broadly contemporaneous with collapse of the Teplá–Barrandian upper crust, (ultra-)potassic plutonism, and exhumation of the high-grade (Moldanubian) core of the orogen at ~346–337 Ma (Fig. 9b).
- 3) Following the subduction and closure of the easterly Rhenohercynian Ocean basins, an Avalonian-type Brunia microplate was underthrust to the south-southwest beneath the eastern flank of the Saxothuringian/Teplá–Barrandian/Moldanubian ‘assemblage’ (~346–335 Ma). This was a dominant process that shaped the eastern margin of the Bohemian Massif and its waning stages were also accompanied by emplacement of the (ultra-)potassic plutons (Fig. 9b).
- 4) Late readjustments within the amalgamated Bohemian Massif included rapid exhumation and voluminous ~327–330 Ma S-type-dominated granite plutonism, tectonothermal activity at the periphery around the consolidated orogen’s core (Fig. 9c), followed by destruction of the orogenic belt, post-orogenic igneous activity, continental basin development, and multiple reactivations along the inherited basement fault zones.

Finally, we close our overview by pointing out some of the open issues that we find most controversial or least understood and that could be potential goals for future research, namely: (1) the existence of the ‘Gföhl suture’ between the Teplá–Barrandian and Moldanubian units, i.e. whether they represent once separate microplates surrounded by oceanic lithosphere or are just variously reworked segments of a single microplate; (2) the role of easterly, west-directed subduction zones in generating arc-magmatism in the central Bohemian Massif; (3) amounts of both vertical and horizontal displacements and crustal shortening within the orogen during any of the above four episodes; (4) exact age(s) of the (U)HP metamorphic peak in eclogite–granulite-facies rocks, mechanisms and timing of their exhumation; (5) sense, timing, and amounts of relative microplate rotations in course of the Variscan Orogeny; (6) the evolution of Variscan palaeotopography and possible orogenic plateaux in space and time; (7) the role of mantle delamination in driving granitoid plutonism and related tectonothermal activity, and (8) the nature of forces leading to destruction of the orogenic belt.

We gratefully acknowledge two anonymous reviewers for their constructive comments to the original manuscript and Karel Schulmann for careful editorial handling. Our research into granites

was supported from the Grant Agency of the Czech Republic through grants No. P210/11/1168 (to Jiří Žák) and 205/09/0630 (to František Holub) as well as from the Ministry of Education, Youth and Sports of the Czech Republic (Grant No. LK11202, Research Plans No. MSM0021620855 and SVV261203), and Charles University in Prague Research Program PRVOUK P44. This study incorporates parts of Ph.D. research by Jakub Trubač, Lukáš Vondrovic, and Filip Tomek.

REFERENCES

- Aftalion, M., Bowes, D. R. & Vrána, S. 1989. Early Carboniferous U–Pb zircon age of garnetiferous, perpotassic granulites, Blanský les massif, Czechoslovakia. *Neues Jahrbuch für Mineralogie, Monatshefte*, 4, 145–152.
- Aleksandrowski, P., Kryza, R., Mazur, S. & Žaba, J. 1997. Kinematic data on major Variscan strike-slip faults and shear zones in the Polish Sudetes, northeast Bohemian Massif. *Geological Magazine*, 134, 727–739.
- Asch, K. 2003. The 1:5 million international geological map of Europe and adjacent areas: development and implementation of a GIS-enabled concept. *Geologisches Jahrbuch, Sonderhefte*, A3. E. Schweizerbart Publishers, Stuttgart
- Awdankiewicz, M., Awdankiewicz, H., Kryza, R. & Rodionov, N. 2010. SHRIMP zircon study of a micromonzodiorite dyke in the Karkonosze Granite, Sudetes (SW Poland): age constraints for late Variscan magmatism in Central Europe. *Geological Magazine*, 147, 77–85.
- Babuška, V. & Plomerová, J. 1992. The lithosphere in central Europe – seismological and petrological aspects. *Tectonophysics*, 207, 141–163.
- Babuška, V. & Plomerová, J. 2001. Subcrustal lithosphere around the Saxothuringian–Moldanubian Suture Zone – a model derived from anisotropy of seismic wave velocities. *Tectonophysics*, 332, 185–199.
- Babuška, V. & Plomerová, J. 2013. Boundaries of mantle-lithosphere domains in the Bohemian Massif as extinct exhumation channels for high-pressure rocks. *Gondwana Research*, 23, 973–987.
- Babuška, V., Plomerová, J. & Vecsey, L. 2008. Mantle fabric of western Bohemian Massif (central Europe) constrained by 3D seismic P and S anisotropy. *Tectonophysics*, 462, 149–163.
- Babuška, V., Fiala, J. & Plomerová, J. 2010. Bottom to top lithosphere structure and evolution of western Eger Rift (Central Europe). *International Journal of Earth Sciences*, 99, 891–907.
- Ballèvre, M., Bosse, V., Ducassou, C. & Pitra, P. 2009. Palaeozoic history of the Armorican Massif: models for the tectonic evolution of the suture zones. *Comptes Rendus Geoscience*, 341, 174–201.
- Beard, B. L., Medaris, L. G., Johnson, C. M., Jelínek, E., Tonika, J. & Riciputi, L. R. 1995. Geochronology and geochemistry of eclogites from the Mariánské Lázně Complex, Czech Republic: implications for Variscan orogenesis. *Geologische Rundschau*, 84, 552–567.
- Becker, H. 1997. Petrological constraints on the cooling history of high-temperature garnet peridotite massifs in lower Austria. *Contributions to Mineralogy and Petrology*, 128, 272–286.

- Becker, H. & Altherr, R. 1992. Evidence from ultra-high-pressure marbles for recycling of sediments into the mantle. *Nature*, 358, 745–748.
- Becker, H., Wenzel, T. & Volker, F. 1999. Geochemistry of glimmerite veins in peridotites from Lower Austria – implications for the origin of K-rich magmas in collision zones. *Journal of Petrology*, 40, 315–338.
- Behr, H. J., Engel, W. & Franke, W. 1982. Variscan wildflysch and nappe tectonics in the Saxothuringian Zone (Northeast Bavaria, West Germany). *American Journal of Science*, 282, 1438–1470.
- Bell, B., Johnson, K., Žák, J., Verner, K. & Schwartz, J. J. 2011. Migmatization and melt generation in the Monotonous Unit, Moldanubian Batholith, Czech Republic: implications of zircon Pb/U (SHRIMP-RG) ages and Hf isotope compositions. *Geological Society of America Abstracts with Programs*, 43, 66.
- Bowes, D. R. & Aftalion, M. 1991. U–Pb zircon isotopic evidence for early Ordovician and late Proterozoic units in the Mariánské Lázně Complex, Central European Hercynides. *Neues Jahrbuch für Mineralogie, Monatshefte*, 7, 315–326.
- Brandmayr, M., Dallmeyer, R. D., Handler, R. & Wallbrecher, E. 1995. Conjugate shear zones in the Southern Bohemian Massif (Austria): implications for Variscan and Alpine tectonothermal activity. *Tectonophysics*, 248, 97–116.
- Breiter, K. 2010. Geochemical classification of Variscan granitoids in the Moldanubicum (Czech Republic, Austria). *Abhandlungen der Geologischen Bundesanstalt*, 65, 19–25.
- Breiter, K. 2012. Nearly contemporaneous evolution of the A- and S-type fractionated granites in the Krušné hory/Erzgebirge Mts., Central Europe. *Lithos*, 151, 105–121.
- Bues, C., Dörr, W., Fiala, J., Vejnar, Z. & Zulauf, G. 2002. Emplacement depths and radiometric ages of Paleozoic plutons of the Neukirchen–Kdyně Massif: differential uplift and exhumation of Cadomian basement due to Carboniferous orogenic collapse (Bohemian Massif). *Tectonophysics*, 352, 225–243.
- Buschmann, B., Elicki, O. & Jonas, P. 2006. The Cadomian unconformity in the Saxo-Thuringian Zone, Germany: palaeogeographic affinities of Ediacaran (terminal Neoproterozoic) and Cambrian strata. *Precambrian Research*, 147, 387–403.
- Büttner, S. H. 2007. Late Variscan stress-field rotation initiating escape tectonics in the south-western Bohemian Massif: a far field response to late-orogenic extension. *Journal of Geosciences*, 52, 29–43.

- Büttner, S. H. & Kruhl, J. H. 1997. The evolution of a late-Variscan high-T/low-P region: the southeastern margin of the Bohemian Massif. *Geologische Rundschau*, 86, 21–38.
- Cháb, J., Stráník, Z. & Eliáš, M. 2007. Geological map of the Czech Republic 1:500,000. Czech Geological Survey, Prague.
- Cháb, J. & Vrána, S. 1979. Crossite–actinolite amphiboles of the Krkonoše–Jizera Crystalline Complex and their geological significance. *Bulletin of the Central Geological Survey*, 56, 143–150.
- Chen, F. K. & Siebel, W. 2004. Zircon and titanite geochronology of the Fürstenstein granite massif, Bavarian Forest, NW Bohemian Massif: pulses of the late Variscan magmatic activity. *European Journal of Mineralogy*, 16, 777–788.
- Chen, F., Siebel, W. & Satir, M. 2003. Geochemical and isotopic composition and inherited zircon ages as evidence for lower crustal origin of two Variscan S-type granites in the NW Bohemian Massif. *International Journal of Earth Sciences*, 92, 173–184.
- Chlupáč, I. 1989. Stratigraphy of the Sedlčany–Krásná Hora metamorphic 'Islet' in Bohemia (Proterozoic? to Devonian). *Journal for Mineralogy and Geology*, 34, 1–16.
- Chlupáč, I., Havlíček, V., Kříž, J., Kukul, Z. & Štorch, P. 1998. Paleozoic of the Barrandian (Cambrian to Devonian). Czech Geological Survey, Prague.
- Chopin, F., Schulmann, K., Skrzypek, E., Lehmann, J., Dujardin, J. R., Martelat, J. E., Lexa, O., Corsini, M., Edel, J. B., Štípská, P. & Pitra, P. 2012. Crustal influx, indentation, ductile thinning and gravity redistribution in a continental wedge: building a Moldanubian mantled gneiss dome with underthrust Saxothuringian material (European Variscan belt). *Tectonics*, 31, doi:10.1029/2011TC002951
- Cloos, H. 1925. Einführung in die tektonische Behandlung magmatischer Erscheinungen (Granittektonik). 1. Das Riesengebirge in Schlesien. Gebrüder Bornträger, Berlin.
- Cymerman, Z., Piasecki, M. A. J. & Seston, R. 1997. Terranes and terrane boundaries in the Sudetes, northeast Bohemian Massif. *Geological Magazine*, 134, 717–725.
- Dallmeyer, R. D. & Urban, M. 1998. Variscan vs Cadomian tectonothermal activity in northwestern sectors of the Teplá–Barrandian Zone, Czech Republic: constraints from $^{40}\text{Ar}/^{39}\text{Ar}$ ages. *Geologische Rundschau*, 87, 94–106.
- Danišík, M., Štěpančíková, P. & Evans, N. J. 2012. Constraining long-term denudation and faulting history in intraplate regions by multisystem thermochronology: an example of the Sudetic Marginal Fault (Bohemian Massif, central Europe). *Tectonics*, 31, doi:10.1029/2011TC003012

- Diot, H., Mazur, S. & Pin, C. 1995. Karkonosze Batholith (NE Bohemian Massif): the evidence for pluton emplacement during transtensional–extensional collapse. *Journal of the Czech Geological Society*, 43, 62.
- Dörr, W. & Zulauf, G. 2010. Elevator tectonics and orogenic collapse of a Tibetan-style plateau in the European Variscides: the role of the Bohemian shear zone. *International Journal of Earth Sciences*, 99, 299–325.
- Dörr, W., Fiala, J., Vejnar, Z. & Zulauf, G. 1998. U–Pb zircon ages and structural development of metagranitoids of the Teplá Crystalline Complex: evidence for pervasive Cambrian plutonism within the Bohemian Massif (Czech Republic). *Geologische Rundschau*, 87, 135–149.
- Dörr, W., Zulauf, G., Fiala, J., Franke, W. & Vejnar, Z. 2002. Neoproterozoic to Early Cambrian history of an active plate margin in the Teplá–Barrandian Unit: a correlation of U–Pb isotopic-dilution-TIMS ages (Bohemia, Czech Republic). *Tectonophysics*, 352, 65–85.
- Drost, K., Linnemann, U., McNaughton, N., Fatka, O., Kraft, P., Gehmlich, M., Tonk, C. & Marek, J. 2004. New data on the Neoproterozoic–Cambrian geotectonic setting of the Teplá–Barrandian volcano-sedimentary successions: geochemistry, U–Pb zircon ages, and provenance (Bohemian Massif, Czech Republic). *International Journal of Earth Sciences*, 93, 742–757.
- Drost, K., Gerdes, A., Jeffries, T., Linnemann, U. & Storey, C. 2011. Provenance of Neoproterozoic and early Paleozoic siliciclastic rocks of the Teplá–Barrandian unit (Bohemian Massif): evidence from U–Pb detrital zircon ages. *Gondwana Research*, 19, 213–231.
- Dudek, A. 1980. The crystalline basement block of the Outer Carpathians in Moravia: Brunovistulicum. *Transactions of the Czechoslovak Academy of Sciences, Mathematical and Natural Science Series*, 90, 3–85.
- Edel, J. B., Schulmann, K. & Holub, F. V. 2003. Anticlockwise and clockwise rotations of the Eastern Variscides accommodated by dextral lithospheric wrenching: palaeomagnetic and structural evidence. *Journal of the Geological Society, London*, 160, 209–218.
- Edel, J. B., Schulmann, K., Skrzypek, E. & Chopin, F. 2013. Tectonic evolution of the European Variscan belt constrained by palaeomagnetic, structural and anisotropy of magnetic susceptibility data from the Northern Vosges magmatic arc (eastern France). *Journal of the Geological Society, London*, 170, 785–804.

- Faryad, S. W. 2011. Distribution and geological position of high-/ultrahigh-pressure units within the European Variscan belt: a review. In: Dobrzhinetskaya, L. F., Faryad, S. W., Wallis, S. & Cuthbert, S. (eds) Ultrahigh-pressure metamorphism: 25 years after the discovery of coesite and diamond. Elsevier, Amsterdam, 361–397.
- Faryad, S. W. & Kachlík, V. 2013. New evidence of blueschist facies rocks and their geotectonic implication for Variscan suture(s) in the Bohemian Massif. *Journal of Metamorphic Geology*, 31, 63–82.
- Faryad, S. W., Dolejš, D. & Machek, M. 2009. Garnet exsolution in pyroxene from clinopyroxenites in the Moldanubian zone: constraining the early pre-convergence history of ultramafic rocks in the Variscan orogen. *Journal of Metamorphic Geology*, 27, 655–671.
- Faryad, S. W., Nahodilová, R. & Dolejš, D. 2010. Incipient eclogite facies metamorphism in the Moldanubian granulites revealed by mineral inclusions in garnet. *Lithos*, 114, 54–69.
- Faryad, S. W., Jedlička, R. & Ettinger, K. 2013. Subduction of lithospheric upper mantle recorded by solid phase inclusions and compositional zoning in garnet: example from the Bohemian Massif. *Gondwana Research*, 23, 944–955.
- Faure, M., Lardeaux, J. M. & Ledru, P. 2009. A review of the pre-Permian geology of the Variscan French Massif Central. *Comptes Rendus Geoscience*, 341, 202–213.
- Fiala, J., Fuchs, G. & Wendt, J. I. 1995. Moldanubian Zone – stratigraphy. In: Dallmeyer, R. D., Franke, W. & Weber, K. (eds) Pre-Permian geology of Central and Eastern Europe. Springer, Berlin, 417–428.
- Finger, F. & René, M. 2009. A comment on 'Two distinctive granite suites in the SW Bohemian Massif and their record of emplacement: constraints from geochemistry and zircon $^{207}\text{Pb}/^{206}\text{Pb}$ chronology' by Siebel *et al.* *Journal of Petrology* 49, 1853–1872. *Journal of Petrology*, 50, 591–593.
- Finger, F. & Steyrer, H. P. 1995. A tectonic model for the eastern Variscides: indications from a chemical study of amphibolites in the south-eastern Bohemian Massif. *Geologica Carpathica*, 46, 137–150.
- Finger, F., Frasl, G., Höck, V. & Steyrer, H. P. 1989. The granitoids of the Moravian Zone of northeastern Austria: products of Cadomian active continental margin? *Precambrian Research*, 45, 235–245.
- Finger, F., Roberts, M. P., Haunschmid, B., Schermaier, A. & Steyrer, H. P. 1997. Variscan granitoids of central Europe: their typology, potential sources and tectonothermal relations. *Mineralogy and Petrology*, 61, 67–96.

- Finger, F., Hanžl, P., Pin, C., von Quadt, A. & Steyrer, H. P. 2000a. The Brunovistulian: Avalonian Precambrian sequence at the eastern end of the Central European Variscides? In: Franke, W., Haak, V., Oncken, O. & Tanner, D. (eds) *Orogenic processes: quantification and modelling in the Variscan belt*. Geological Society, London, Special Publications, 179, 103–112.
- Finger, F., Tichomirowa, M., Pin, C. & Hanžl, P. 2000b. Relics of early-Panafrican metabasite-metarhyolite formation in the Brno Massif, Moravia, Czech Republic. *International Journal of Earth Sciences*, 89, 328–335.
- Finger, F., Doblmayr, P., Friedl, G., Gerdes, A., Krenn, E. & von Quadt, A. 2003. Petrology of the Weinsberg granite in the South Bohemian Batholith: new data from the mafic end members. *Journal of the Czech Geological Society*, 48, 46–47.
- Finger, F., Gerdes, A., Janoušek, V., René, M. & Riegler, G. 2007. Resolving the Variscan evolution of the Moldanubian sector of the Bohemian Massif: the significance of the Bavarian and the Moravo–Moldanubian tectonometamorphic phases. *Journal of Geosciences*, 52, 9–28.
- Finger, F., Gerdes, A., René, M. & Riegler, G. 2009. The Saxo-Danubian Granite Belt: magmatic response to post-collisional delamination of mantle lithosphere below the south-western sector of the Bohemian Massif (Variscan orogen). *Geologica Carpathica*, 60, 205–212.
- Finger, F., Dunkley, D. J. & René, M. 2010. Remnants of Early Carboniferous I-type granodiorite plutons in the Bavarian Forest and their bearing on the tectonic interpretation of the south-western sector of the Bohemian Massif (Bavarian Zone). *Journal of Geosciences*, 55, 321–332.
- Förster, H. J. 1998. The chemical composition of REE–Y–Th–U-rich accessory minerals in peraluminous granites of the Erzgebirge–Fichtelgebirge region, Germany: Part I, the monazite-(Ce)–brabantite solid solution series. *American Mineralogist*, 83, 259–272.
- Förster, H. J. & Romer, R. L. 2010. Carboniferous magmatism. In: Linnemann, U. & Romer, R. L. (eds) *Pre-Mesozoic geology of Saxo-Thuringia – from the Cadomian active margin to the Variscan orogen*. Schweizerbart Publishers, Stuttgart, 287–308.
- Förster, H. J., Tischendorf, G., Trumbull, R. B. & Gottesmann, B. 1999. Late-collisional granites in the Variscan Erzgebirge, Germany. *Journal of Petrology*, 40, 1613–1645.
- Förster, H. J., Romer, R. L., Gottesmann, B., Tischendorf, G. & Rhede, D. 2009. Are the granites of the Aue–Schwarzenberg Zone (Erzgebirge, Germany) a major source for metalliferous ore deposits? A geochemical, Sr–Nd–Pb isotopic, and geochronological study. *Neues Jahrbuch für Mineralogie, Abhandlungen*, 186, 163–184.

- Franěk, J., Schulmann, K. & Lexa, O. 2006. Kinematic and rheological model of exhumation of high pressure granulites in the Variscan orogenic root: example of the Blanský les granulite, Bohemian Massif, Czech Republic. *Mineralogy and Petrology*, 86, 253–276.
- Franěk, J., Schulmann, K., Lexa, O., Tomek, Č. & Edel, J. B. 2011. Model of syn-convergent extrusion of orogenic lower crust in the core of the Variscan belt: implications for exhumation of high-pressure rocks in large hot orogens. *Journal of Metamorphic Geology*, 29, 53–78.
- Franke, W. 1989. Variscan plate tectonics in Central Europe – current ideas and open questions. *Tectonophysics*, 169, 221–228.
- Franke, W. 1999. Tectonic and plate tectonic units at the north Gondwana margin: evidence from the central European Variscides. *Abhandlungen der Geologischen Bundesanstalt*, 54, 7–14.
- Franke, W. 2000. The mid-European segment of the Variscides: tectonostratigraphic units, terrane boundaries and plate tectonic evolution. In: Franke, W., Haak, V., Oncken, O. & Tanner, D. (eds) *Orogenic processes: quantification and modelling in the Variscan belt*. Geological Society, London, Special Publications, 179, 35–61.
- Franke, W. 2006. The Variscan orogen in Central Europe: construction and collapse. In: Gee, D. G. & Stephenson, R. A. (eds) *European Lithosphere Dynamics*. Geological Society, London, Memoirs, 32, 333–343.
- Franke, W. & Żelaźniewicz, A. 2002. Structure and evolution of the Bohemian Arc. In: Winchester, J. A., Pharaoh, T. C. & Verniers, J. (eds) *Palaeozoic amalgamation of Central Europe*. Geological Society, London, Special Publications, 201, 279–293.
- Frasl, G. & Finger, F. 1991. Geologisch-petrographische Exkursion in den österreichischen Teil des Südböhmischen Batholiths. *Beihefte European Journal of Mineralogy*, 3, 23–40.
- Friedl, G., von Quadt, A., Frasl, G. & Finger, F. 1992. Neue U/Pb Altersdaten aus der südlichen Böhmischen Masse. *Frankfurter Geowissenschaftliche Arbeiten Serie A. Geologie-Paläontologie*, A11, 217–218.
- Friedl, G., von Quadt, A., Ochsner, A. & Finger, F. 1993. Timing of the Variscan Orogeny in the southern Bohemian Massif (NE-Austria) deduced from new U–Pb zircon and monazite dating. *Terra Abstracts*, 5, 235–236.
- Friedl, G., von Quadt, A. & Finger, F. 1996. Timing der Intrusionstätigkeit im Südböhmischen Batholith. In: *Symposium Tektonik–Strukturgeologie–Kristallingeologie*, Salzburg, 10–15 April 1996, Book of Abstracts. Fakultas Universitätsverlag, Vienna, 127–130.

- Friedl, G., Finger, F., McNaughton, N. J. & Fletcher, I. R. 2000. Deducing the ancestry of terranes: SHRIMP evidence for South America-derived Gondwana fragments in central Europe. *Geology*, 28, 1035–1038.
- Friedl, G., Finger, F., Paquette, J. L., von Quadt, A., McNaughton, N. J. & Fletcher, I. R. 2004. Pre-Variscan geological events in the Austrian part of the Bohemian Massif deduced from U/Pb zircon ages. *International Journal of Earth Sciences*, 93, 802–823.
- Friedl, G., Cooke, R., Finger, F., McNaughton, N. & Fletcher, I. 2011. Timing of Variscan HP–HT metamorphism in the Moldanubian Zone of the Bohemian Massif: U–Pb SHRIMP dating on multiply zoned zircons from a granulite from the Dunkelsteiner Wald Massif, Lower Austria. *Mineralogy and Petrology*, 102, 63–75.
- Fritz, H. & Neubauer, F. 1993. Kinematics of crustal stacking and dispersion in the south-eastern Bohemian Massif. *International Journal of Earth Sciences*, 82, 556–565.
- Fritz, H., Dallmeyer, R. D. & Neubauer, F. 1996. Thick-skinned versus thin-skinned thrusting: rheology controlled thrust propagation in the Variscan collisional belt (the southeastern Bohemian Massif, Czech Republic–Austria). *Tectonics*, 15, 1389–1413.
- Fuchs, G. & Matura, A. 1976. Zur Geologie des Kristallins der südlichen Böhmisches Masse. *Jahrbuch der Geologischen Bundesanstalt*, 119, 1–43.
- Fusán, O., Kodým, O., Matějka, A. & Urbánek, L. 1967. Geological map of Czechoslovakia 1:500,000. Central Geological Survey, Prague.
- Gerdes, A. 2001. Magma homogenization during anatexis, ascent and/or emplacement? Constraints from the Variscan Weinsberg granites. *Terra Nova*, 13, 305–312.
- Gerdes, A., Wörner, G. & Finger, F. 2000a. Hybrids, magma mixing and enriched mantle melts in post-collisional Variscan granitoids: the Rastenberg Pluton, Austria. In: Franke, W., Haak, V., Oncken, O. & Tanner, D. (eds) *Orogenic processes: quantification and modelling in the Variscan belt*. Geological Society, London, Special Publications, 179, 415–431.
- Gerdes, A., Wörner, G. & Henk, A. 2000b. Post-collisional granite generation and HT–LP metamorphism by radiogenic heating: the Variscan South Bohemian Batholith. *Journal of the Geological Society, London*, 157, 577–587.
- Gerdes, A., Friedl, G., Parrish, R. R. & Finger, F. 2003. High-resolution geochronology of Variscan granite emplacement – the South Bohemian Batholith. *Journal of the Czech Geological Society*, 48, 53–54.

- Guy, A., Edel, J. B., Schulmann, K., Tomek, Č. & Lexa, O. 2011. A geophysical model of the Variscan orogenic root (Bohemian Massif): implications for modern collisional orogens. *Lithos*, 124, 144–157.
- Hajná, J., Žák, J., Kachlík, V. & Chadima, M. 2010. Subduction-driven shortening and differential exhumation in a Cadomian accretionary wedge: the Teplá–Barrandian Unit, Bohemian Massif. *Precambrian Research*, 176, 27–45.
- Hajná, J., Žák, J. & Kachlík, V. 2011. Structure and stratigraphy of the Teplá–Barrandian Neoproterozoic, Bohemian Massif: a new plate-tectonic reinterpretation. *Gondwana Research*, 19, 495–508.
- Hajná, J., Žák, J., Kachlík, V. & Chadima, M. 2012. Deciphering the Variscan tectonothermal overprint and deformation partitioning in the Cadomian basement of the Teplá–Barrandian Unit, Bohemian Massif. *International Journal of Earth Sciences*, 101, 1855–1873.
- Hammer, J., Eidam, J., Röber, B. & Ehling, C. 1999. Prävariszischer und variszischer granitoider Magmatismus am NE-Rand des Böhmisches Massivs – Geochemie und Petrogenese. *Zeitschrift für Geologische Wissenschaften*, 27, 401–415.
- Hartley, A. J. & Otava, J. 2001. Sediment provenance and dispersal in a deep marine foreland basin: the Lower Carboniferous Culm Basin, Czech Republic. *Journal of the Geological Society, London*, 158, 137–150.
- Hecht, L., Vignerresse, J. L. & Morteani, G. 1997. Constraints on the origin of zonation of the granite complexes in the Fichtelgebirge (Germany and Czech Republic): evidence from a gravity and geochemical study. *Geologische Rundschau*, 86, S93–S109.
- Henk, A., von Blanckenburg, F., Finger, F., Schaltegger, U. & Zulauf, G. 2000. Syn-convergent high-temperature metamorphism and magmatism in the Variscides: a discussion of potential heat sources. In: Franke, W., Haak, V., Oncken, O. & Tanner, D. (eds) *Orogenic processes: quantification and modelling in the Variscan belt*. Geological Society, London, Special Publications, 179, 387–399.
- Höck, V., Montag, O. & Leichmann, J. 1997. Ophiolite remnants at the eastern margin of the Bohemian Massif and their bearing on the tectonic evolution. *Mineralogy and Petrology*, 60, 267–287.

- Hofmann, M., Linnemann, U., Gerdes, A. & Ullrich, B. 2008. Closure of the Rheic Ocean and the final pulse of the Variscan Orogeny in the Bohemian Massif – timing of large-scale strike-slip processes and basement exhumation by LA-ICP-MS U–Pb zircon dating from the Elbe Zone (Saxo-Thuringian Zone, Germany). In: Königshof, P. & Linnemann, U. (eds) From Gondwana and Laurussia to Pangaea: dynamics of oceans and supercontinents. Final Meeting of IGCP 497 and IGCP 499, 20th International Senckenberg-Conference & 2nd Geinitz-Conference, Abstracts and Programme, 53.
- Hofmann, M., Linnemann, U., Gerdes, A., Ullrich, B. & Schauer, M. 2009. Timing of dextral strike-slip processes and basement exhumation in the Elbe Zone (Saxo-Thuringian Zone): the final pulse of the Variscan Orogeny in the Bohemian Massif constrained by LA-SF-ICP-MS U-Pb zircon data. In: Murphy, J. B., Keppie, J. D. & Hynes, A. J. (eds) Ancient orogens and modern analogues. Geological Society, London, Special Publications, 327, 197–214.
- Holub, F. V. 1997. Ultrapotassic plutonic rocks of the durbachite series in the Bohemian Massif: petrology, geochemistry and petrogenetic interpretation. *Journal of Geological Sciences, Economic Geology, Mineralogy*, 31, 5–26.
- Holub, F. V., Cocherie, A. & Rossi, P. 1997a. Radiometric dating of granitic rocks from the Central Bohemian Plutonic Complex (Czech Republic): constraints on the chronology of thermal and tectonic events along the Moldanubian-Barrandian boundary. *Comptes Rendus de l'Academie de Sciences – Serie Ila: Sciences de la Terre et des Planetes*, 325, 19–26.
- Holub, F. V., Machart, J. & Manová, M. 1997b. The Central Bohemian Plutonic Complex: geology, chemical composition and genetic interpretation. *Journal of Geological Sciences, Economic Geology, Mineralogy*, 31, 27–50.
- Holub, F. V., Klečka, M. & Matějka, D. 1995. Igneous activity. In: Dallmeyer, R. D., Franke, W. & Weber, K. (eds) Pre-Permian geology of Central and Eastern Europe. Springer Verlag, Berlin, 444–452.
- Holub, F. V., Schmitz, M. D., Verner, K., Janoušek, V. & Veselovský, F. 2010. Geochemical and temporal relations of ultrapotassic plutons and dyke swarms in South Bohemia . In: Kohút, M. (ed.) Dating 2010. Conference proceedings. State Geological Institute of Dionýz Štúr, Bratislava, 13–14.
- Holub, F.V., Verner, K. & Schmitz, M.D. 2012. Temporal relations of melagranite porphyry dikes and durbachitic plutons in South Bohemia. *Geoscience Research Reports for 2011*, 23–25.

- Hrouda, F., Táborská, Š., Schulmann, K., Ježek, J. & Dolejš, D. 1999. Magnetic fabric and rheology of co-mingled magmas in the Nasavrky Plutonic Complex (E Bohemia): implications for intrusive strain and emplacement mechanism. *Tectonophysics*, 307, 98–111.
- Janoušek, V. & Gerdes, A. 2003. Timing the magmatic activity within the Central Bohemian Pluton, Czech Republic: conventional U–Pb ages for the Sázava and Tábor intrusions and their geotectonic significance. *Journal of the Czech Geological Society*, 48, 70–71.
- Janoušek, V. & Holub, F. V. 2007. The causal link between HP–HT metamorphism and ultrapotassic magmatism in collisional orogens: case study from the Moldanubian Zone of the Bohemian Massif. *Proceedings of the Geologists' Association*, 118, 75–86.
- Janoušek, V., Rogers, G. & Bowes, D. R. 1995. Sr–Nd isotopic constraints on the petrogenesis of the Central Bohemian Pluton, Czech Republic. *Geologische Rundschau*, 84, 520–534.
- Janoušek, V., Rogers, G., Bowes, D.R. & Vaňková, V. 1997. Cryptic trace-element variation as an indicator of reverse zoning in a granitic pluton: the Říčany granite, Czech Republic. *Journal of the Geological Society, London*, 154, 807–815.
- Janoušek, V., Bowes, D. R., Rogers, G., Farrow, C. M. & Jelínek, E. 2000. Modelling diverse processes in the petrogenesis of a composite batholith: the Central Bohemian Pluton, Central European Hercynides. *Journal of Petrology*, 41, 511–543.
- Janoušek, V., Braithwaite, C. J. R., Bowes, D. R. & Gerdes, A. 2004a. Magma-mixing in the genesis of Hercynian calc-alkaline granitoids: an integrated petrographic and geochemical study of the Sázava intrusion, Central Bohemian Pluton, Czech Republic. *Lithos*, 78, 67–99.
- Janoušek, V., Finger, F., Roberts, M. P., Frýda, J., Pin, C. & Dolejš, D. 2004b. Deciphering the petrogenesis of deeply buried granites: whole-rock geochemical constraints on the origin of largely undepleted felsic granulites from the Moldanubian Zone of the Bohemian Massif. *Transactions of the Royal Society of Edinburgh, Earth Sciences*, 95, 141–159.
- Janoušek, V., Gerdes, A., Vrána, S., Finger, F., Erban, V., Friedl, G. & Braithwaite, C. J. R. 2006. Low-pressure granulites of the Lišov Massif, Southern Bohemia: Viséan metamorphism of Late Devonian plutonic arc rocks. *Journal of Petrology*, 47, 705–744.
- Janoušek, V., Vrána, S., Erban, V., Vokurka, K. & Drábek, M. 2008. Metabasic rocks in the Varied Group of the Moldanubian Zone, southern Bohemia – their petrology, geochemical character and possible petrogenesis. *Journal of Geosciences*, 53, 31–64.

- Janoušek, V., Wiegand, B. & Žák, J. 2010. Dating the onset of Variscan crustal exhumation in the core of the Bohemian Massif: new U–Pb single zircon ages from the high-K calc-alkaline granodiorites of the Blatná suite, Central Bohemian Plutonic Complex. *Journal of the Geological Society, London*, 167, 347–360.
- Jastrzębski, M. 2009. A Variscan continental collision of the West Sudetes and the Brunovistulian Terrane: a contribution from structural and metamorphic record of the Stronie Formation, the Orlica–Śnieżnik Dome, SW Poland. *International Journal of Earth Sciences*, 98, 1901–1923.
- Jelínek, E. & Dudek, A. 1993. Geochemistry of the subsurface Precambrian plutonic rocks from the Brunovistulian Complex in the Bohemian Massif, Czechoslovakia. *Precambrian Research*, 62, 103–125.
- Kachlík, V. 1993. The evidence for late Variscan nappe thrusting of the Mariánské Lázně Complex over the Saxothuringian Terrane (west Bohemia). *Journal of the Czech Geological Society*, 38, 43–58.
- Kachlík, V. 1999. Relationship between Moldanubicum, the Kutná Hora Crystalline Unit and Bohemicum (Central Bohemia, Czech Republic): a result of polyphase Variscan nappe tectonics. *Journal of the Czech Geological Society*, 44, 201–291.
- Kalt, A., Berger, A. & Blümel, P. 1999. Metamorphic evolution of cordierite-bearing migmatites from the Bayerische Wald (Variscan Belt, Germany). *Journal of Petrology*, 40, 601–627.
- Kalt, A., Corfu, F. & Wijbrans, J. R. 2000. Time calibration of a P–T path from a Variscan high-temperature low-pressure metamorphic complex (Bayerischer Wald, Germany), and the detection of inherited monazite. *Contributions to Mineralogy and Petrology*, 138, 143–163.
- Kalvoda, J., Bábek, O., Fatka, O., Leichmann, J., Melichar, R., Nehyba, S. & Špaček, P. 2008. Brunovistulian Terrane (Bohemian Massif, Central Europe) from late Proterozoic to late Paleozoic: a review. *International Journal of Earth Sciences*, 97, 497–518.
- Kempe, U., Wolf, D., Ebermann, U. & Bombach, K. (1999). 330 Ma Pb/Pb single zircon evaporation ages for the Altenberg Granite Porphyry, Eastern Erzgebirge (Germany): implications for Hercynian granite magmatism and tin mineralisation. *Zeitschrift für Geologische Wissenschaften*, 27, 385–400.
- Kempe, U., Bombach, K., Schlothauer, T., Hutschenreuter, J., Wolf, D., Matukov, D. & Sergeev, S. 2004. Pb/Pb and U/Pb zircon dating of subvolcanic rhyolite as a time marker for Hercynian granite magmatism and Sn mineralisation in the Eibenstock granite, Erzgebirge, Germany: considering effects of zircon alteration. *Mineralium Deposita*, 39, 646–669.

- Klečka, M. & Matějka, D. 1996. Moldanubian Batholith – an example of the evolution of the Late Palaeozoic granitoid magmatism in the Moldanubian Zone, Bohemian Massif (Central Europe). In: Srivastava, R. K. & Chandra, R. (eds) *Magmatism in relation to diverse tectonic settings*. Oxford & IBH Publishing Co., New Delhi, 353–373.
- Klein, T., Kiehm, S., Siebel, W., Shang, C.K., Rohrmüller, J., Dörr, W. & Zulauf, G. 2008. Age and emplacement of late-Variscan granites of the western Bohemian Massif with main focus on the Hauzenberg granitoids (European Variscides, Germany). *Lithos*, 102, 478–507.
- Klomínský, J. 1963. Geology of the Čistá Massif. *Journal of Geological Sciences, Geology*, 3, 7–27.
- Klomínský, J. 1965. The Štěnovice granodiorite Massif. *Journal of Geological Sciences, Geology*, 8, 75–98.
- Klomínský, J. 1969. The Krkonoše–Jizera granitoid Massif. *Journal of Geological Sciences, Geology*, 15, 1–134.
- Klomínský, J., Schovánek, P., Jarchovský, T., Sulovský, P. & Toužimský, M. 2007. Contact of the Tanvald and Liberec granites near Jablonec nad Nisou. *Geoscience Research Reports for 2006*, 24–29.
- Klötzli, U. S. & Parrish, R. R. 1996. Zircon U/Pb and Pb/Pb geochronology of the Rastenberg granodiorite, South Bohemian Massif, Austria. *Mineralogy and Petrology*, 58, 197–214.
- Klötzli, U. S., Koller, F., Scharbert, H. G. & Höck, V. 2001. Cadomian lower-crustal contributions to Variscan granite petrogenesis (South Bohemian Pluton, Austria): constraints from zircon typology and geochronology, whole-rock, and feldspar Pb–Sr isotope systematics. *Journal of Petrology*, 42, 1621–1642.
- Konopásek, J. & Schulmann, K. 2005. Contrasting Early Carboniferous field geotherms: evidence for accretion of a thickened orogenic root and subducted Saxothuringian crust (Central European Variscides). *Journal of the Geological Society, London*, 162, 463–470.
- Kopecký, L., Chlupáčová, M., Klomínský, J. & Sokol, A. 1997. The Čistá–Jesenice pluton in western Bohemia: geochemistry, geology and ore potential. *Journal of Geological Sciences, Economic Geology, Mineralogy*, 31, 97–127.
- Košler, J. & Farrow, C. M. 1994. Mid-late Devonian arc-type magmatism in the Bohemian Massif: Sr and Nd isotope and trace element evidence from the Staré Sedlo and Mirovice gneiss complexes, Czech Republic. *Journal of the Czech Geological Society*, 39, 56–58.
- Košler, J., Aftalion, M. & Bowes, D. R. 1993. Mid-late Devonian plutonic activity in the Bohemian Massif: U–Pb zircon isotopic evidence from the Staré Sedlo and Mirovice gneiss complexes, Czech Republic. *Neues Jahrbuch für Mineralogie, Monatshefte*, 1993, 417–431.

- Košler, J., Rogers, G., Roddick, J. C. & Bowes, D. R. 1995. Temporal association of ductile deformation and granitic plutonism: Rb–Sr and ⁴⁰Ar–³⁹Ar evidence from roof pendants above the Central Bohemian Pluton, Czech Republic. *Journal of Geology*, 103, 711–717.
- Kotková, J., Kröner, A., Todt, W. & Fiala, J. 1995. Zircon dating of north Bohemian granulites, Czech Republic: further evidence for the Lower Carboniferous high-pressure event in the Bohemian Massif. *Geologische Rundschau*, 85, 154–161.
- Kotková, J., Harley, S. L. & Fišera, M. 1997. A vestige of very high-pressure (c. 28 kbar) metamorphism in the Variscan Bohemian Massif, Czech Republic. *European Journal of Mineralogy*, 9, 1017–1033.
- Kotková, J., Gerdes, A., Parrish, R. R. & Novák, M. 2007. Clasts of Variscan high-grade rocks within Upper Visean conglomerates – constraints on exhumation history from petrology and U–Pb chronology. *Journal of Metamorphic Geology*, 25, 781–801.
- Kotková, J., Schaltegger, U. & Leichmann, J. 2010. Two types of ultrapotassic plutonic rocks in the Bohemian Massif – coeval intrusions at different crustal levels. *Lithos*, 115, 163–176.
- Kotková, J., O'Brien, P. J. & Ziemann, M. A. 2011. Diamond and coesite discovered in Saxony-type granulite: solution to the Variscan garnet peridotite enigma. *Geology*, 39, 667–670.
- Kovaříková, P., Siebel, W., Jelínek, E., Štemprok, M., Kachlík, V., Holub, F. V. & Blecha, V. 2007. Petrology, geochemistry and zircon age for redwitzite at Abertamy, NW Bohemian Massif (Czech Republic): tracing the mantle component in Late Variscan intrusions. *Chemie der Erde – Geochemistry*, 67, 151–174.
- Köhler, H. & Hölzl, S. 1996. The age of the Leuchtenberg granite (NE Bavaria, Germany). A revision on account of new U–Pb zircon ages. *Neues Jahrbuch für Mineralogie, Monatshefte*, 5, 212–222.
- Kretz, R. 1983. Symbols for rock-forming minerals. *American Mineralogist*, 68, 277–279.
- Kröner, A. & Willner, A. P. 1998. Time of formation and peak of Variscan HP–HT metamorphism of quartz-feldspar rocks in the Central Erzgebirge, Saxony, Germany. *Contributions to Mineralogy and Petrology*, 132, 1–20.
- Kröner, A., Wendt, I., Liew, T. C., Compston, W., Todt, W., Fiala, J., Vaňková, V. & Vaněk, J. 1988. U–Pb zircon and Sm–Nd model ages of high-grade Moldanubian metasediments, Bohemian Massif, Czechoslovakia. *Contributions to Mineralogy and Petrology*, 99, 257–266.
- Kröner, A., Hegner, E., Hammer, J., Haase, G., Bielicki, K. H., Krauss, M. & Eidam, J. 1994. Geochronology and Nd–Sr systematics of Lusatian granitoids – significance for the evolution of the Variscan orogen in East-Central-Europe. *Geologische Rundschau*, 83, 357–376.

- Kröner, A., Willner, A. P., Hegner, E., Frischbutter, A., Hofmann, J. & Bergner, R. 1995. Latest Precambrian (Cadomian) zircon ages, Nd isotopic systematics and P–T evolution of granitoid orthogneisses of the Erzgebirge, Saxony and Czech Republic. *Geologische Rundschau*, 84, 437–456.
- Kröner, A., Jaeckel, P., Reischmann, T. & Kroner, U. 1998. Further evidence for an early Carboniferous (c. 340 Ma) age of high-grade metamorphism in the Saxonian granulite complex. *Geologische Rundschau*, 86, 751–766.
- Kröner, A., O'Brien, P. J., Nemchin, A. A. & Pidgeon, R. T. 2000. Zircon ages for high pressure granulites from South Bohemia, Czech Republic, and their connection to Carboniferous high temperature processes. *Contributions to Mineralogy and Petrology*, 138, 127–142.
- Kröner, A., Jaeckel, P., Hegner, E. & Opletal, M. 2001. Single zircon ages and whole rock Nd isotopic systematics of early Palaeozoic granitoid gneisses from the Czech and Polish Sudetes (Jizerské hory, Krkonoše Mountains and Orlice–Sněžník Complex). *International Journal of Earth Sciences*, 90, 304–324.
- Kroner, U. & Romer, R. L. 2013. Two plates – many subduction zones: the Variscan orogeny reconsidered. *Gondwana Research*, 24, 298–329.
- Kryza, R., Crowley, Q. G., Larionov, A. Pin, C., Oberc-Dziedzic, T., & Mochnacka K. 2012. Chemical abrasion applied to SHRIMP zircon geochronology: an example from the Variscan Karkonosze Granite (Sudetes, SW Poland). *Gondwana Research*, 21, 757–767.
- Kusiak, M. A., Dunkley, D. J., Suzuki, K., Kachlík, V., Kedzior, A., Lekki, J. & Opluštil, S. 2010. Chemical (non-isotopic) and isotopic dating of Phanerozoic zircon – a case study of durbachite from the Třebíč Pluton, Bohemian Massif. *Gondwana Research*, 17, 153–161.
- Kusiak, M. A., Dunkley, D. J., Słaby, E., Martin, H. & Budzyń, B. 2009. Sensitive high-resolution ion microprobe analysis of zircon reequilibrated by late magmatic fluids in a hybridized pluton. *Geology*, 37, 1063–1066.
- Kusiak, M. A., Suzuki, K., Dunkley, D. J., Lekki, J., Bakun-Czubarow, N., Paszkowski, M. & Budzyń, B. 2008. EPMA and PIXE dating of monazite in granulites from Stary Gieraltów, NE Bohemian Massif, Poland. *Gondwana Research*, 14, 675–685.
- Leichmann, J. & Höck, V. 2008. The Brno Batholith: an insight into the magmatic and metamorphic evolution of the Cadomian Brunovistulian Unit, eastern margin of the Bohemian Massif. *Journal of Geosciences*, 53, 281–305.

- Lexa, O., Schulmann, K., Janoušek, V., Štípská, P., Guy, A. & Racek, M. 2011. Heat sources and trigger mechanisms of exhumation of HP granulites in Variscan orogenic root. *Journal of Metamorphic Geology*, 29, 79–102.
- Liew, T. C., Finger, F. & Höck, V. 1989. The Moldanubian granitoid plutons in Austria: chemical and isotopic studies bearing on their environmental setting. *Chemical Geology*, 76, 41–55.
- Linnemann, U. & Romer, R. L. 2002. The Cadomian Orogeny in Saxo-Thuringia, Germany: geochemical and Nd–Sr–Pb isotopic characterization of marginal basins with constraints to geotectonic setting and provenance. *Tectonophysics*, 352, 33–64.
- Linnemann, U., Gehmlich, M., Tichomirowa, M., Buschmann, B., Nasdala, L., Jonas, P., Lützner, H. & Bombach, K. 2000. From Cadomian subduction to Early Palaeozoic rifting: the evolution of Saxo-Thuringia at the margin of Gondwana in the light of single zircon geochronology and basin development (Central European Variscides, Germany). In: Franke, W., Haak, V., Oncken, O. & Tanner, D. (eds) *Orogenic processes: quantification and modelling in the Variscan Belt*. Geological Society, London, Special Publications, 179, 131–153.
- Linnemann, U., McNaughton, N. J., Romer, R. L., Gehmlich, M., Drost, K. & Tonk, C. 2004. West African provenance for Saxo-Thuringia (Bohemian Massif): did Armorica ever leave pre-Pangean Gondwana? U/Pb-SHRIMP zircon evidence and the Nd-isotopic record. *International Journal of Earth Sciences*, 93, 683–705.
- Linnemann, U., Pereira, F., Jeffries, T. E., Drost, K. & Gerdes, A. 2008. The Cadomian orogeny and the opening of the Rheic Ocean: the diachrony of geotectonic processes constrained by LA-ICP-MS U-Pb zircon dating (Ossa-Morena and Saxo-Thuringian Zones, Iberian and Bohemian massifs). *Tectonophysics*, 461, 21–43.
- Linner, M. 1996. Metamorphism and partial melting of paragneisses of the Monotonous Group, SE Moldanubicum (Austria). *Mineralogy and Petrology*, 58, 215–234.
- Machek, M., Ulrich, S. & Janoušek, V. 2009. Strain coupling between upper mantle and lower crust: natural example from the Běstvína granulite body, Bohemian Massif. *Journal of Metamorphic Geology*, 27, 721–737.
- Machowiak, K. & Armstrong, R. 2007. SHRIMP U–Pb zircon age from the Karkonosze granite. *Mineralogia Polonica Special Papers*, 31, 193–196.
- Maierová, P., Čadek, O., Lexa, O. & Schulmann, K. 2012. A numerical model of exhumation of the orogenic lower crust in the Bohemian Massif during the Variscan orogeny. *Studia Geophysica et Geodaetica*, 56, 595–619.

- Maluski, H. & Patočka, F. 1997. Geochemistry and $^{40}\text{Ar}/^{39}\text{Ar}$ geochronology of the mafic metavolcanic rocks from the Rýchory Mountains complex (west Sudetes, Bohemian Massif): palaeotectonic significance. *Geological Magazine*, 134, 703–716.
- Marheine, D., Maluski, H., Kachlík, V., Patočka, F. & Żelaźniewicz, A. 2002. The $^{40}\text{Ar}/^{39}\text{Ar}$ ages from the West Sudetes (NE Bohemian Massif): constraints on the Variscan polyphase tectonothermal development. In: Winchester, J. A., Pharaoh, T. C. & Verniers, J. (eds) *Palaeozoic amalgamation of Central Europe*. Geological Society, London, Special Publications, 201, 133–155.
- Martínez Catalán, J. R. 2011. Are the oroclines of the Variscan belt related to late Variscan strike-slip tectonics? *Terra Nova*, 23, 241–247.
- Martínez Catalán, J. R. 2012. The Central Iberian arc, an orocline centered in the Iberian Massif and some implications for the Variscan belt. *International Journal of Earth Sciences*, 101, 1299–1314.
- Massonne, H. J. 2001. First find of coesite in the ultrahigh-pressure metamorphic area of the central Erzgebirge, Germany. *European Journal of Mineralogy*, 13, 565–570.
- Matte, P. 1986. Tectonics and plate-tectonics model for the Variscan belt of Europe. *Tectonophysics*, 126, 329–374.
- Matte, P. 1991. Accretionary history and crustal evolution of the Variscan belt in western Europe. *Tectonophysics*, 196, 309–337.
- Matte, P. 2001. The Variscan collage and orogeny (480–290 Ma) and the tectonic definition of the Armorica microplate: a review. *Terra Nova*, 13, 122–128.
- Matte, P., Maluski, H., Rajlich, P. & Franke, W. 1990. Terrane boundaries in the Bohemian Massif: result of large-scale Variscan shearing. *Tectonophysics*, 177, 151–170.
- Mazur, S. & Alexandrowski, P. 2001. The Tepla(?)/Saxothuringian suture in the Karkonosze–Izera Massif, western Sudetes, central European Variscides. *International Journal of Earth Sciences*, 90, 341–360.
- Mazur, S., Aleksandrowski, P., Kryza, R. & Oberc-Dziedzic, T. 2006. The Variscan Orogen in Poland. *Geological Quarterly*, 50, 89–118.
- Mazur, S., Aleksandrowski, P., Turniak, k., Awdankiewicz, M. 2007. Geology, tectonic evolution and Late Palaeozoic magmatism of Sudetes – an overview. In: Kozłowski, A., Wiszniewska, J. (eds) *Granitoids in Poland*. *Archivum Mineralogiae Monograph*, 1, 59–87.
- Medaris, L. G., Wang, H., Jelínek, E., Mihaljevič, M. & Jakeš, P. 2005. Characteristics and origins of diverse Variscan peridotites in the Gföhl Nappe, Bohemian Massif, Czech Republic. *Lithos*, 82,

1–23.

- Medaris, L. G., Beard, B. L. & Jelínek, E. 2006. Mantle-derived, UHP garnet pyroxenite and eclogite in the Moldanubian Gföhl nappe, Bohemian Massif: a geochemical review, new P–T determinations, and tectonic interpretation. *International Geology Review*, 48, 765–777.
- Mierzejewski, M. P. 2002. Additional data and remarks to Hans Cloos' work in the Karkonosze Mts (Riesengebirge). *Zeitschrift der geologischen Wissenschaften*, 30, 37–48.
- Mikulski, S. Z., Williams, I. S., Bagiński, B. 2013. Early Carboniferous (Viséan) emplacement of the collisional Kłodzko–Złoty Stok granitoids (Sudetes, SW Poland): constraints from geochemical data and zircon U–Pb ages. *International Journal of Earth Sciences*, 102, 1007–1027.
- Mísař, Z. 1994. Terranes of eastern Bohemian Massif: tectonostratigraphic and lithological units of the Moravicum and Moldanubicum. *Journal of the Czech Geological Society*, 39, 71–73.
- Mueller, H. J. & Massonne, H. J. 2001. Experimental high pressure investigation of partial melting in natural rocks and their influence on V–P and V–S. *Physics and Chemistry of the Earth, Part A: Solid Earth and Geodesy*, 26, 325–332.
- Murphy, J. B. & Nance, R. D. 2002. Sm–Nd isotopic systematics as tectonic tracers: an example from West Avalonia in the Canadian Appalachians. *Earth-Science Reviews*, 59, 77–100.
- Naemura, K., Hirajima, T. & Svojtka, M. 2009. The pressure–temperature path and the origin of phlogopite in spinel–garnet peridotites from the Blanský les Massif of the Moldanubian Zone, Czech Republic. *Journal of Petrology*, 50, 1795–1827.
- Naemura, K., Ikuta, D., Kagi, H., Otake, S., Ueda, T., Ohi, S., Kobayashi, T., Svojtka, M. & Hirajima, T. 2011. Diamond and other possible ultradeep evidence discovered in the orogenic spinel–garnet peridotite from the Moldanubian Zone of the Bohemian Massif, Czech Republic. In: Dobrzhinetskaya, L. F., Faryad, S. W., Wallis, S. & Cuthbert, S. (eds) *Ultrahigh-pressure metamorphism: 25 years after the discovery of coesite and diamond*. Elsevier, Amsterdam, 78–111.
- Nakamura, D., Svojtka, M., Naemura, K. & Hirajima, T. 2004. Very high-pressure (>4 GPa) eclogite associated with the Moldanubian Zone garnet peridotite (Nové Dvory, Czech Republic). *Journal of Metamorphic Geology*, 22, 593–603.
- Nance, R. D. & Linnemann, U. 2008. The Rheic Ocean: origin, evolution, and significance. *GSA Today*, 18, 4–12.
- Nance, R. D., Gutiérrez-Alonso, G., Keppie, J. D., Linnemann, U., Murphy, J. B., Quesada, C., Strachan, R. A. & Woodcock, N. H. 2010. Evolution of the Rheic Ocean. *Gondwana Research*, 17, 194–222.

- Nance, R.D., Gutiérrez-Alonso, G., Keppie, J.D., Linnemann, U., Murphy, J.B., Quesada, C., Strachan, R.A. & Woodcock, N.H. 2012. A brief history of the Rheic Ocean. *Geoscience Frontiers*, 3, 125–135.
- Nowak, I., Żelaźniewicz, A., Dörr, W., Franke, W. & Larionov, A. N. 2011. The Iżera metabasites, West Sudetes, Poland: geologic and isotopic U–Pb zircon evidence of Devonian extension in the Saxothuringian Terrane. *Lithos*, 126, 435–454.
- Nasdala, L., Wenzel, T., Pidgeon, R. T. & Kronz, A. 1999. Internal structures and dating of complex zircons from Meissen Massif monzonites, Saxony. *Chemical Geology*, 156, 331–341.
- O'Brien, P. J. 2000. The fundamental Variscan problem: high-temperature metamorphism at different depths and high-pressure metamorphism at different temperatures. In: Franke, W., Haak, V., Oncken, O. & Tanner, D. (eds) *Orogenic processes: quantification and modelling in the Variscan Belt*. Geological Society, London, Special Publications, 179, 369–386.
- O'Brien, P. J. & Rötzler, J. 2003. High-pressure granulites: formation, recovery of peak conditions and implications for tectonics. *Journal of Metamorphic Geology*, 21, 3–20.
- Oberc-Dziedzic, T., Kryza, R., Klimas, K., Fanning, M. C. & Madej, S. 2005a. Gneiss protolith ages and tectonic boundaries in the NE part of the Bohemian Massif (Fore-Sudetic Block, SW Poland). *Geological Quarterly*, 49, 363–378.
- Oberc-Dziedzic, T., Pin, C. & Kryza, R. 2005b. Early Palaeozoic crustal melting in an extensional setting: petrological and Sm–Nd evidence from the Iżera granite-gneisses, Polish Sudetes. *International Journal of Earth Sciences*, 94, 354–368.
- Oberc-Dziedzic, T., Kryza, R., Pin, C. & Madej, S. 2013. Sequential granite emplacement: a structural study of the late Variscan Strzelin intrusion, SW Poland. *International Journal of Earth Sciences*, 102, 1289–1304.
- Oliver, G. J. H., Corfu, F. & Krogh, T. E. 1993. U–Pb ages from SW Poland: evidence for a Caledonian suture zone between Baltica and Gondwana. *Journal of the Geological Society, London*, 150, 355–369.
- Palivcová, M. 1984. Basic series of an 'Andinotype' batholithic association in the Variscan Central Bohemian Pluton. *Geologica Carpathica*, 35, 39–60.
- Parry, M., Štípská, P., Schulmann, K., Hroudá, F., Ježek, J. & Kröner, A. 1997. Tonalite sill emplacement at an oblique plate boundary: northeastern margin of the Bohemian Massif. *Tectonophysics*, 280, 61–81.

- Patočka, F. & Smulikowski, W. 2000. Early Palaeozoic intracontinental rifting and incipient oceanic spreading in the Czech/Polish East Krkonoše/Karkonosze Complex, West Sudetes (NE Bohemian Massif). *Geologia Sudetica*, 33, 1–15.
- Pertoldová, J., Verner, K., Vrána, S., Buriánek, D., Štědrá, V. & Vondrovic, L. 2010. Comparison of lithology and tectonometamorphic evolution of units at the northern margin of the Moldanubian Zone: implications for geodynamic evolution in the northeastern part of the Bohemian Massif. *Journal of Geosciences*, 55, 299–319.
- Petrakakis, K. 1997. Evolution of Moldanubian rocks in Austria: review and synthesis. *Journal of Metamorphic Geology*, 15, 203–222.
- Peucker-Ehrenbrink, B. & Behr, H. J. 1993. Chemistry of hydrothermal quartz in the post-Variscan 'Bavarian Pfahl' system, F.R. Germany. *Chemical Geology*, 103, 85–102.
- Pharaoh, T. C. (1999). Palaeozoic terranes and their lithospheric boundaries within the Trans-European Suture Zone (TESZ): a review. *Tectonophysics*, 314, 17–41.
- Pietranik, A., Storey, C. & Kierczak, J. 2013. The Niemcza diorites and monzodiorites (Sudetes, SW Poland): a record of changing geotectonic setting at ca. 340 Ma. *Geological Quarterly*, 57, 325–334.
- Pin, C. 1990. Variscan oceans: ages, origins and geodynamic implications inferred from geochemical and radiometric data. *Tectonophysics*, 177, 215–227.
- Pin, C. & Marini, F. 1993. Early Ordovician continental break-up in Variscan Europe: Nd–Sr isotope and trace element evidence from bimodal igneous associations of the Southern Massif Central, France. *Lithos*, 29, 177–196.
- Pin, C., Mierzejewski, M. & Duthou, J. L. 1987. Rb–Sr isochron age of the Karkonosze granite from the Sklarska Poreba Huta quarry and the determination of initial $87\text{Sr}/86\text{Sr}$ ratio in this granite. *Przegląd Geologiczny*, 10, 512–517.
- Pitra, P. 2012. Emplacement, structural and P–T evolution of the ~346 Ma Miřetín Pluton (eastern Teplá–Barrandian Zone, Bohemian Massif): implications for regional transpressional tectonics – Discussion. *Journal of Geosciences*, 57, 189–191.
- Pitra, P., Burg, J. P., Schulmann, K. & Ledru, P. 1994. Late orogenic extension in the Bohemian Massif: petrostructural evidence in the Hlinsko region. *Geodinamica Acta*, 7, 15–30.
- Pitra, P., Burg, J. P. & Guiraud, M. 1999. Late Variscan strike-slip tectonics between the Teplá–Barrandian and Moldanubian terranes (Czech Bohemian Massif). *Journal of the Geological Society, London*, 156, 1003–1020.

- Plomerová, J., Vecsey, L., Babuška, V., Granet, M. & Achauer, U. 2005. Passive seismic experiment mosaic – a pilot study of mantle lithosphere anisotropy of the Bohemian Massif. *Studia Geophysica et Geodaetica*, 49, 541–560.
- Prince, C. I., Košler, J., Vance, D. & Günther, D. 2000. Comparison of laser ablation ICP-MS and isotope dilution REE analyses – implications for Sm–Nd garnet geochronology. *Chemical Geology*, 168, 255–274.
- Propach, G., Baumann, A., Schulz-Schmalschlager, M. & Grauert, B. (2000). Zircon and monazite U–Pb ages of Variscan granitoid rocks and gneisses in the Moldanubian Zone of eastern Bavaria, Germany. *Neues Jahrbuch für Geologie und Paläontologie, Monatshefte*, 6, 345–377.
- Racek, M., Štípská, P., Pitra, P., Schulmann, K. & Lexa, O. 2006. Metamorphic record of burial and exhumation of orogenic lower and middle crust: a new tectonothermal model for the Drosendorf Window (Bohemian Massif, Austria). *Mineralogy and Petrology*, 86, 221–251.
- Rajlich, P. 1987. Variszische duktile Tektonik im Böhmischem Massiv. *Geologische Rundschau*, 76, 755–786.
- Rajlich, P. 1988. Variscan shearing kinematics in the Bohemian Massif: Moldanubian and Moravo–Silesian junction. *Acta Universitatis Carolinae, Geologica*, 1988, 387–400.
- Romer, R. L., Thomas, R., Stein, H. J. & Rhede, D. 2007. Dating multiply overprinted Sn-mineralized granites – examples from the Erzgebirge, Germany. *Mineralium Deposita*, 42, 337–359.
- Romer, R. L., Förster, H. J. & Štemprok, M. 2010. Age constraints for the late-Variscan magmatism in the Altenberg–Teplice Caldera (Eastern Erzgebirge/Krušné hory). *Neues Jahrbuch für Mineralogie, Abhandlungen*, 187, 289–305.
- Rötzler, J. & Romer, R. L. 2001. P–T–t evolution of ultrahigh-temperature granulites from the Saxon Granulite Massif, Germany. Part I: petrology. *Journal of Petrology*, 42, 1995–2013.
- Schäfer, J., Neuroth, H., Ahrendt, H., Dorr, W. & Franke, W. 1997. Accretion and exhumation at a Variscan active margin, recorded in the Saxothuringian flysch. *Geologische Rundschau*, 86, 599–611.
- Scharbert, S., Breiter, K. & Frank, W. 1997. The cooling history of the southern Bohemian Massif. *Journal of the Czech Geological Society*, 42, 24.
- Scheck, M., Bayer, U., Otto, V., Lamarche, J., Banka, D. & Pharaoh, T. 2002. The Elbe Fault System in North Central Europe – a basement controlled zone of crustal weakness. *Tectonophysics*, 360, 281–299.

- Scheuven, D. & Zulauf, G. 2000. Exhumation, strain localization, and emplacement of granitoids along the western part of the Central Bohemian shear zone (Bohemian Massif). *International Journal of Earth Sciences*, 89, 617–630.
- Schmädicke, E. 1991. Quartz pseudomorphs after coesite in eclogites from the Saxonian Erzgebirge. *European Journal of Mineralogy*, 3, 231–238.
- Schmädicke, E., Gose, J. & Will, T. M. 2010. The P–T evolution of ultra high temperature garnet-bearing ultramafic rocks from the Saxonian Granulitgebirge Core Complex, Bohemian Massif. *Journal of Metamorphic Geology*, 28, 489–508.
- Schulmann, K. & Gayer, R. 2000. A model for continental accretionary wedge developed by oblique collision: the NE Bohemian Massif. *Journal of the Geological Society, London*, 157, 401–416.
- Schulmann, K., Ledru, P., Autran, A., Melka, R., Lardeaux, J. M., Urban, M. & Lobkowicz, M. 1991. Evolution of nappes in the eastern margin of the Bohemian Massif: a kinematic interpretation. *Geologische Rundschau*, 80, 73–92.
- Schulmann, K., Kröner, A., Hegner, E., Wendt, I., Konopásek, J., Lexa, O. & Štípská, P. 2005. Chronological constraints on the pre-orogenic history, burial and exhumation of deep-seated rocks along the eastern margin of the Variscan orogen, Bohemian Massif, Czech Republic. *American Journal of Science*, 305, 407–448.
- Schulmann, K., Lexa, O., Štípská, P., Racek, M., Tajčmanová, L., Konopásek, J., Edel, J. B., Peschler, A. & Lehmann, J. 2008. Vertical extrusion and horizontal channel flow of orogenic lower crust: key exhumation mechanisms in large hot orogens? *Journal of Metamorphic Geology*, 26, 273–297.
- Schulmann, K., Konopásek, J., Janoušek, V., Lexa, O., Lardeaux, J. M., Edel, J. B., Štípská, P. & Ulrich, S. 2009. An Andean type Palaeozoic convergence in the Bohemian Massif. *Comptes Rendus Geoscience*, 341, 266–286.
- Siebel, W., Trzebski, R., Stettner, G., Hecht, L., Casten, U., Höhndorf, A. & Müller, P. 1997. Granitoid magmatism of the NW Bohemian Massif revealed: gravity data, composition, age relations and phase concept. *Geologische Rundschau*, 86, S45–S63.
- Siebel, W., Chen, F. & Satir, M. 2003. Late-Variscan magmatism revisited: new implications from Pb- evaporation zircon ages on the emplacement of redwitzites and granites in NE Bavaria. *International Journal of Earth Sciences*, 92, 36–53.

- Siebel, W., Blaha, U., Chen, F. & Rohrmüller, J. 2005. Geochronology and geochemistry of a dyke-host rock association and implications for the formation of the Bavarian Pfahl shear zone, Bohemian Massif. *International Journal of Earth Sciences*, 94, 8–23.
- Siebel, W., Hann, H. P., Shang, C. K., Rohrmüller, J. & Chen, F. 2006a. Coeval late-Variscan emplacement of granitic rocks: an example from the Regensburg Forest, NE Bavaria. *Neues Jahrbuch für Mineralogie, Abhandlungen*, 183, 13–26.
- Siebel, W., Thiel, M. & Chen, F. 2006b. Zircon geochronology and compositional record of late- to post-kinematic granitoids associated with the Bavarian Pfahl zone (Bavarian Forest). *Mineralogy and Petrology*, 8, 45–62.
- Siebel, W., Shang, C. K., Reitter, E., Rohrmüller, J. & Breiter, K. 2008. Two distinctive granite suites in the SW Bohemian Massif and their record of emplacement: constraints from geochemistry and zircon $^{207}\text{Pb}/^{206}\text{Pb}$ chronology. *Journal of Petrology*, 49, 1853–1872.
- Siebel, W., Shang, C.K., Reitter, E., Rohrmüller, J. & Breiter, K. 2009. Two distinctive granite suites in the southwestern Bohemian Massif: reply to F. Finger and M. René. *Journal of Petrology*, 50, 595–599.
- Siebel, W., Hann, H., Danišík, M., Shang, C., Berthold, C., Rohrmüller, J., Wemmer, K. & Evans, N. 2010. Age constraints on faulting and fault reactivation: a multi-chronological approach. *International Journal of Earth Sciences*, 99, 1187–1197.
- Słaby, E. & Martin, H. 2008. Mafic and felsic magma interaction in granites: the Hercynian Karkonosze Pluton (Sudetes, Bohemian Massif). *Journal of Petrology*, 49, 353–391.
- Sláma, J., Dunkley, D. J., Kachlík, V. & Kusiak, M. A. 2008a. Transition from island-arc to passive setting on the continental margin of Gondwana: U–Pb zircon dating of Neoproterozoic metaconglomerates from the SE margin of the Teplá–Barrandian Unit, Bohemian Massif. *Tectonophysics*, 461, 44–59.
- Sláma, J., Košler, J., Condon, D. J., Crowley, J. L., Gerdes, A., Hanchar, J. M., Horstwood, M. S. A., Morris, G. A., Nasdala, L., Norberg, N., Schaltegger, U., Schoene, B., Tubrett, M. N. & Whitehouse, M. J. 2008b. Plešovice zircon – a new natural reference material for U–Pb and Hf isotopic microanalysis. *Chemical Geology*, 249, 1–35.
- Smulikowski, W. 1995. Evidence of glaucophane-schist facies metamorphism in the East Karkonosze Complex, West Sudetes, Poland. *Geologische Rundschau*, 84, 720–737.

- Soejono, I., Žáčková, E., Janoušek, V., Machek, M. & Košler, J. 2010. Vestige of an Early Cambrian incipient oceanic crust incorporated in the Variscan orogen: Letovice Complex, Bohemian Massif. *Journal of the Geological Society, London*, 167, 1113–1130.
- Štemprok, M., Holub, F. V. & Novák, J. 2003. Multiple magmatic pulses of the Eastern Volcano-Plutonic Complex, Krušné hory/Erzgebirge batholith, and their phosphorus contents. *Bulletin of Geosciences*, 78, 277–296.
- Štípská, P. & Schulmann, K. 1995. Inverted metamorphic zonation in a basement-derived nappe sequence, eastern margin of the Bohemian Massif. *Geological Journal*, 30, 385–413.
- Štípská, P., Schulmann, K. & Kröner, A. 2004. Vertical extrusion and middle crustal spreading of omphacite granulite: a model of syn-convergent exhumation (Bohemian Massif, Czech Republic). *Journal of Metamorphic Geology*, 22, 179–198.
- Strnad, L. & Mihaljevič, M. 2005. Sedimentary provenance of Mid-Devonian clastic sediments in the Teplá–Barrandian Unit (Bohemian Massif): U–Pb and Pb–Pb geochronology of detrital zircons by laser ablation ICP-MS. *Mineralogy and Petrology*, 84, 47–68.
- Suchý, V., Rozkošný, I., Žák, K. & Franců, J. 1996. Epigenetic dolomitization of the Přídolí formation (Upper Silurian), the Barrandian basin, Czech Republic: implications for burial history of the Lower Paleozoic strata. *Geologische Rundschau*, 85, 264–277.
- Suchý, V., Sýkorová, I., Melka, K., Filip, J. & Machovič, V. 2007. Illite ‘crystallinity’, maturation of organic matter and microstructural development associated with lowest-grade metamorphism of Neoproterozoic sediments in the Teplá–Barrandian unit, Czech Republic. *Clay Minerals*, 42, 503–526.
- Suess, F. E. 1912. Die moravische Fenster und ihre Beziehung zum Grundgebirge des Hohen Gesenkes. *Denkschriften Österreichische Akademie der Wissenschaften, Mathematisch-naturwissenschaftliche Klasse*, 88, 541–631.
- Synek, J. & Oliveriová, D. 1993. Terrane character of the north-east margin of the Moldanubian Zone: the Kutná Hora Crystalline Complex, Bohemian Massif. *Geologische Rundschau*, 82, 566–582.
- Tajčmanová, L., Soejono, I., Konopásek, J., Košler, J. & Klötzli, U. 2010. Structural position of high-pressure felsic to intermediate granulites from NE Moldanubian domain (Bohemian Massif). *Journal of the Geological Society, London*, 167, 329–345.
- Tichomirowa, M. 1997. 207Pb/206Pb-Einzelzirkondatierungen zur Bestimmung des Intrusionsalters des Niederbobritzscher Granites. *Terra Nostra*, 8, 183–184.

- Tichomirowa, M. & Leonhardt, D. 2010. New age determinations (Pb/Pb zircon evaporation, Rb/Sr) on the granites from Aue-Schwarzenberg and Eibenstock, Western Erzgebirge, Germany. *Zeitschrift für Geologische Wissenschaften*, 38, 99–123.
- Tichomirowa, M., Sergeev, S. A., Berger, H. J. & Leonhardt, D. 2012. Inferring protoliths of high-grade metamorphic gneisses of the Erzgebirge using zirconology, geochemistry and comparison with lower-grade rocks from Lusatia (Saxothuringia, Germany). *Contributions to Mineralogy and Petrology*, 164, 375–396.
- Timmermann, H., Štědrá, V., Gerdes, A., Noble, S. R., Parrish, R. R. & Dörr, W. 2004. The problem of dating high-pressure metamorphism: a U–Pb isotope and geochemical study on eclogites and related rocks of the Mariánské Lázně Complex, Czech Republic. *Journal of Petrology*, 45, 1311–1338.
- Tollmann, A. 1982. Großräumiger variszischer Deckenbau im Moldanubikum und neue Gedanken zum Variszikum Europas. *Geotektonische Forschungen*, 64, 1–91.
- Tollmann, A. 1995. Das Ausmass des variszischer Deckbaues im Moldanubikum. *Krystalinikum*, 18, 117–132.
- Tomek, F. 2011. The Late Devonian to Early Carboniferous kinematic evolution of the Teplá–Barrandian/Moldanubian boundary. Diploma thesis, Charles University in Prague.
- Tomek, F. & Žák, J. 2011. The Late Devonian to early Carboniferous kinematic evolution of the Teplá–Barrandian/Moldanubian boundary. *Proceedings of the 2nd Congress of the Czech and Slovak geological societies*, 94.
- Tropper, P., Deibl, I., Finger, F. & Kaindl, R. 2006. P–T–t evolution of spinel–cordierite–garnet gneisses from the Sauwald Zone (Southern Bohemian Massif, Upper Austria): is there evidence for two independent late-Variscan low-P/high-T events in the Moldanubian Unit? *International Journal of Earth Sciences*, 95, 1019–1037.
- Trubač, J., Žák, J., Chlupáčová, M. & Janoušek, V. 2009. Magnetic fabric of the Říčany granite, Bohemian Massif: a record of helical magma flow? *Journal of Volcanology and Geothermal Research*, 181, 25–34.
- Trubač, J., Janoušek, V., Žák, J. & Gerdes, A. 2013. Geochemistry and petrogenesis of a nested granite intrusion – the Sedmihoří composite Stock (Bohemian Massif). *Mineralogical Magazine*, 77, 2360.

- Turnau, E., Żelaźniewicz, A. & Franke W. 2002. Middle to early late Viséan onset of late orogenic sedimentation in the Intra-Sudetic Basin, West Sudetes: miospore evidence and tectonic implication. *Geologia Sudetica*, 34, 9–16.
- Turniak, K. & Bröcker, M. 2002. Age of the two-mica granite from the Strzegom–Sobótka Massif: new data from U/Pb monazite and xenotime study. *Mineralogical Society of Poland – Special Papers*, 20, 211–213.
- Turniak, K., Tichomirowa, M. & Bombach, K. 2005. Zircon Pb-evaporation ages of granitoids from the Strzegom–Sobótka Massif (SW Poland). *Mineralogical Society of Poland – Special Papers*, 25, 241–245.
- Turniak, K., Tichomirowa, M. & Bombach, K. 2006. Pb-evaporation zircon ages of post-tectonic granitoids from the Strzelin Massif (SW Poland). *Mineralogia Polonica – Special Papers*, 29, 212–215.
- van Breemen, O., Aftalion, M., Bowes, D. R., Dudek, A., Mísař, Z., Povondra, P. & Vrána, S. 1982. Geochronological studies of the Bohemian Massif, Czechoslovakia, and their significance in the evolution of Central Europe. *Transactions of the Royal Society of Edinburgh, Earth Sciences*, 73, 89–108.
- Vellmer, C. & Wedepohl, K. H. 1994. Geochemical characterization and origin of granitoids from the South Bohemian Batholith in Lower Austria. *Contributions to Mineralogy and Petrology*, 118, 13–32.
- Venera, Z., Schulmann, K. & Kröner, A. 2000. Intrusion within a transtensional tectonic domain: the Čistá granodiorite (Bohemian Massif) – structure and rheological modelling. *Journal of Structural Geology*, 22, 1437–1454.
- Verner, K., Žák, J., Hroudá, F. & Holub, F. V. 2006. Magma emplacement during exhumation of the lower- to mid-crustal orogenic root: the Jihlava syenitoid pluton, Moldanubian Unit, Bohemian Massif. *Journal of Structural Geology*, 28, 1553–1567.
- Verner, K., Žák, J., Nahodilová, R. & Holub, F. 2008. Magmatic fabrics and emplacement of the cone-sheet-bearing Knížecí Stolec durbachitic pluton (Moldanubian Unit, Bohemian Massif): implications for mid-crustal reworking of granulitic lower crust in the Central European Variscides. *International Journal of Earth Sciences*, 97, 19–33.
- Verner, K., Buriánek, D., Vrána, S., Vondrovic, L., Pertoldová, J., Hanžl, P. & Nahodilová, R. 2009a. Tectonometamorphic features of geological units along the northern periphery of the Moldanubian Zone. *Journal of Geosciences*, 54, 87–100.

- Verner, K., Žák, J., Pertoldová, J., Šrámek, J., Sedlák, J., Trubač, J. & Týcová, P. 2009b. Magmatic history and geophysical signature of a post-collisional intrusive center emplaced near a crustal-scale shear zone: the Plechý granite pluton (Moldanubian batholith, Bohemian Massif). *International Journal of Earth Sciences*, 98, 517–532.
- Verner, K., Žák, J., Šrámek, J., Paclíková, J., Zavřelová, A., Machek, M., Finger, F. & Johnson, K. in print. Formation of elongated granite–migmatite domes as isostatic accommodation structures in collisional orogens. *Journal of Geodynamics*, doi:10.1016/j.jog.2013.10.002
- Vondrovic, L. & Verner, K. 2008. The record of structural evolution and U–Pb zircon dating of the tonalite intrusions (Polička Crystalline Unit, Bohemian Massif). In: Poblet, J., Medina, M.G., Pedreira, D. & Fernández, C.L. (eds) *International meeting of young researchers in structural geology and tectonics – programme and extended abstracts*. University of Oviedo, Spain, 369–373.
- Vondrovic, L. & Verner, K. 2010. The record of structural evolution and U–Pb zircon dating of the tonalite intrusions (Polička Crystalline Unit, Bohemian Massif). *Trabajos de Geología*, 30, 316–321.
- Vondrovic, L., Verner, K., Buriánek, D., Halodová, P., Kachlík, V. & Míková, J. 2011. Emplacement, structural and P–T evolution of the ~346 Ma Miřetín Pluton (eastern Teplá–Barrandian Zone, Bohemian Massif): implications for regional transpressional tectonics. *Journal of Geosciences*, 56, 343–357.
- von Quadt, A. & Finger, F. 1991. Geochronologische Untersuchungen im österreichischen Teil des Südböhmischen Batholiths: U–Pb Datierungen an Zirkonen, Monaziten und Xenotimen des Weinsberger Granits. *Beihefte European Journal of Mineralogy*, 1, 281.
- von Raumer, J. F. & Stampfli, G. M. 2008. The birth of the Rheic Ocean – Early Palaeozoic subsidence patterns and subsequent tectonic plate scenarios. *Tectonophysics*, 461, 9–20.
- von Raumer, J. F., Finger, F., Veselá, P. & Stampfli, G. M. in print. Durbachites–vaugnerites – a geodynamic marker in the central European Variscan orogen. *Terra Nova*, doi:10.1111/ter.12071
- Vrána, S. & Frýda, J. 2003. Ultrahigh-pressure grossular-rich garnetite from the Moldanubian Zone, Czech Republic. *European Journal of Mineralogy*, 15, 43–54.
- Vrána, S. & Novák, M. 2000. Petrology and geochemistry of granulite clasts in the Visean Luleč conglomerate, Kulm in central Moravia, Czech Republic. *Bulletin of the Czech Geological Survey*, 75, 405–413.

- Vrána, S., Blümel, P. & Petrakakis, K. 1995. Moldanubian Zone – metamorphic evolution. In: Dallmeyer, R. D., Franke, W. & Weber, K. (eds) *Pre-Permian geology of Central and Eastern Europe*. Springer, Berlin, 453–468.
- Waldhausrová, J., 1984. Proterozoic volcanics and intrusive rocks of the Jílové Zone (Central Bohemia). *Krystalinikum*, 17, 77–97.
- Wendt, I., Lenz, H. & Delisle, G. 1986. Gesamtgesteins- und Mineraldatierungen des Falkenberger Granits. *Geologisches Jahrbuch*, E34, 1–85.
- Wendt, J. I., Kröner, A., Fiala, J. & Todt, W. 1993. Evidence from zircon dating for existence of approximately 2.1 Ga old crystalline basement in southern Bohemia, Czech Republic. *Geologische Rundschau*, 82, 42–50.
- Wendt, J. I., Kröner, A., Fiala, J. & Todt, W. 1994. U–Pb zircon and Sm–Nd dating of Moldanubian HP/HT granulites from south Bohemia, Czech Republic. *Journal of the Geological Society*, London, 151, 83–90.
- Wenzel, T., Hengst, M. & Pilot, J. 1993. The plutonic rocks of the Elbe Valley-Zone (Germany): evidence for the magmatic development from single-zircon evaporation and K–Ar age determinations. *Chemical Geology*, 104, 75–92.
- Wenzel, T., Mertz, D. F., Oberhänsli, R., Becker, T. & Renne, P. R. 1997. Age, geodynamic setting, and mantle enrichment processes of a K-rich intrusion from the Meissen Massif (northern Bohemian Massif) and implications for related occurrences from the mid-European Hercynian. *Geologische Rundschau*, 86, 556–570.
- Willner, A. P., Rötzler, K. & Maresch, W. V. 1997. Pressure–temperature and fluid evolution of quartzofeldspathic metamorphic rocks with a relic high-pressure, granulite-facies history from the central Erzgebirge (Saxony, Germany). *Journal of Petrology*, 38, 307–336.
- Willner, A. P., Sebazungu, E., Gerya, T. V., Maresch, W. V. & Krohe, A. 2002. Numerical modelling of PT-paths related to rapid exhumation of high-pressure rocks from the crustal root in the Variscan Erzgebirge Dome (Saxony/Germany). *Journal of Geodynamics*, 33, 281–314.
- Winchester, J. A. 2002. Palaeozoic amalgamation of Central Europe: new results from recent geological and geophysical investigations. *Tectonophysics*, 360, 5–21.
- Winchester, J. A., Pharaoh, T. C., Verniers, J., Ioane, D. & Seghedi, A. 2006. Palaeozoic accretion of Gondwana-derived terranes to the East European Craton: recognition of detached terrane fragments dispersed after collision with promontories. In: Gee, D. G. & Stephenson, R. A. (eds) *European lithosphere dynamics*. Geological Society, London, *Memoirs*, 32, 232–332.

- Žáčková, E., Konopásek, J., Jeřábek, P., Finger, F. & Košler, J. 2010. Early Carboniferous blueschist facies metamorphism in metapelites of the West Sudetes (Northern Saxothuringian Domain, Bohemian Massif). *Journal of Metamorphic Geology*, 28, 361–379.
- Žák, J., Holub, F. V. & Verner, K. 2005a. Tectonic evolution of a continental magmatic arc from transpression in the upper crust to exhumation of mid-crustal orogenic root recorded by episodically emplaced plutons: the Central Bohemian Plutonic Complex (Bohemian Massif). *International Journal of Earth Sciences*, 94, 385–400.
- Žák, J., Schulmann, K. & Hrouda, F. 2005b. Multiple magmatic fabrics in the Sázava pluton (Bohemian Massif, Czech Republic): a result of superposition of wrench-dominated regional transpression on final emplacement. *Journal of Structural Geology*, 27, 805–822.
- Žák, J., Dragoun, F., Verner, K., Chlupáčová, M., Holub, F. V. & Kachlík, V. 2009a. Forearc deformation and strain partitioning during growth of a continental magmatic arc: the northwestern margin of the Central Bohemian Plutonic Complex, Bohemian Massif. *Tectonophysics*, 469, 93–111.
- Žák, J., Verner, K., Klomínský, J. & Chlupáčová, M. 2009b. 'Granite tectonics' revisited: insights from comparison of K-feldspar shape-fabric, anisotropy of magnetic susceptibility (AMS), and brittle fractures in the Jizera granite, Bohemian Massif. *International Journal of Earth Sciences*, 98, 949–967.
- Žák, J., Kratinová, Z., Trubač, J., Janoušek, V., Sláma, J. & Mrlina, J. 2011a. Structure, emplacement, and tectonic setting of Late Devonian granitoid plutons in the Teplá–Barrandian unit, Bohemian Massif. *International Journal of Earth Sciences*, 100, 1477–1495.
- Žák, J., Verner, K., Finger, F., Faryad, S. W., Chlupáčová, M. & Veselovský, F. 2011b. The generation of voluminous S-type granites in the Moldanubian Unit, Bohemian Massif, by rapid isothermal exhumation of the metapelitic middle crust. *Lithos*, 121, 25–40.
- Žák, J., Verner, K., Holub, F.V., Kabele, P., Chlupáčová, M. & Halodová, P. 2012. Magmatic to solid state fabrics in syntectonic granitoids recording early Carboniferous orogenic collapse in the Bohemian Massif. *Journal of Structural Geology*, 36, 27–42.
- Žák, J., Verner, K., Sláma, J., Kachlík, V. & Chlupáčová, M. in print. Multistage magma emplacement and progressive strain accumulation in the shallow-level Krkonoše–Jizera plutonic complex, Bohemian Massif. *Tectonics*, doi:10.1002/tect.20088
- Żelaźniewicz, A. 1997. The Sudetes as a Palaeozoic orogen in central Europe. *Geological Magazine*, 134, 691–702.
- Zulauf, G. 1994. Ductile normal faulting along the West Bohemian Shear Zone (Moldanubian/

Teplá–Barrandian boundary): evidence for late Variscan extensional collapse in the Variscan Internides. *Geologische Rundschau*, 83, 276–292.

Zulauf, G. 1997a. Constriction due to subduction: evidence for slab pull in the Mariánské Lázně Complex (central European Variscides). *Terra Nova*, 9, 232–236.

Zulauf, G. 1997b. From very low-grade to eclogite-facies metamorphism: tilted crustal sections as a consequence of Cadomian and Variscan orogeny in the Teplá–Barrandian unit (Bohemian Massif). *Geotektonische Forschungen*, 89, 1–302.

Zulauf, G., Bues, C., Dörr, W. & Vejnar, Z. 2002. 10 km minimum throw along the West Bohemian shear zone: evidence for dramatic crustal thickening and high topography in the Bohemian Massif (European Variscides). *International Journal of Earth Sciences*, 91, 850–864.

SUMMARY OF THE MAIN CONCLUSIONS



The ambition of this **Ph.D. Thesis** has been to modestly contribute to the research on formation of compositional and textural zoning in shallow-level granitic plutons. The aim was to assess the processes responsible for emplacement of individual plutons/pulses and the origin of compositional zoning in a great detail, from the pluton down to the micro-scale.

This **Ph.D. Thesis** benefits from a multidisciplinary quantitative approach to the study of magmatic systems. Extensive sets of structural, magnetic, gravimetric, geochemical (major- and trace-element, isotopic), and U–Pb geochronologic data were acquired from several composite granite plutons of Devonian to Carboniferous age in the Bohemian Massif. I believe that only such comprehensive studies on well-selected case examples have a potential to provide a generally applicable, in-depth understanding of zoning origin, mechanisms of pluton construction, and magma sources/evolution in the composite magmatic systems.

In terms of methodology, specific techniques were developed for sample preparation. Mathematical approaches have been designed and applied to the interpretation of geochemical data, with potential applications to other studies in igneous systems. The integration of field and quantitative data sets obtained by range of methods has provided new insights into emplacement mechanisms of magma in the upper crust and the origin of modal/compositional zoning in granitic plutons.

The **Chapter I** with **Articles I.-1** and **I.-2** integrating the data with numerical simulations allowed us to formulate generally applicable petrogenetic models for multi-stage thermal–chemical–mechanical evolution of magmatic systems in the Earth's crust.

In these case studies, a comprehensive petrogenetic model was developed on the basis of a detailed study of the Říčany Pluton. It is tracking the magma evolution from partial melting of a metapelitic source, through the formation of a stratified magma chamber and rejuvenation of the crystal mush by invading mafic melts, to the emplacement of the remobilized granitic magmas in the shallow crust, likely accompanied by magma withdrawal during volcanic eruptions.

In particular, **the Article I.-1** brings a detailed study of a nested reversely zoned, granitic Říčany Pluton where was proposed a comprehensive model for formation of reversely zoned plutons. First, a stratified magma chamber develops in which K-feldspar-rich cumulates settle to the bottom, or are attached to the sidewalls, leaving behind a crystal-poor more silicic magma in the upper layer. This K-feldspar cumulate along with interstitial melt is re-mobilized by the basaltic intrusions and underplating. This setup leads to a density inversion that eventually

causes a major gravity-driven overturn. The remobilized granitic magma carries fragments of these cumulates and mafic enclaves towards the surface.

The **Article I.-2** describes petrography and mineral chemistry of a sample of coarse-grained, weakly porphyritic biotite granite of the Říčany Pluton with the following conclusions:

- Accessory phases control the behaviour of many trace elements in differentiation of felsic granitic systems.
- A great proportion of essential structural components (e.g., P, Zr, LREE) used in apatite, zircon and monazite saturation thermometry is incorporated into other minerals. This may lead to significant overestimation of the liquidus temperatures. In this case the zircon saturation temperatures would be overestimated by c. 40 °C due to significant contents of Zr in the early crystallized rutile.
- In the studied sample, over 80 % of the whole-rock Zr and Hf and c. 10–30 % of HREE, U, Th, Nb, Ta, Ti, Cd, Co and Ni are contained in resistant accessory phases Zrn and Rt. Thus the pressure vessel or sample fusion, and not merely a combined acid attack, are absolutely essential in sample decomposition were these elements to be determined quantitatively. Moreover, these elements will be kept in residue left after granite weathering, and thus will be rather hard to release into the environment.

The **Chapter II** with **Articles II.-1 and II.-2** allowed discussing formation of magmatic strain patterns in composite granite diapirs in a considerable detail; in particular a comparison is made between the theoretical model and real observations in granite plutons. Next, the new emplacement mechanism invoking “helical flow” is invoked because the structural and AMS data do not comply with existing models proposed for the emplacement of elliptical, onion-skin plutons (e.g. single-pulse vs. nested diapirism, ballooning, laccolith-like emplacement).

In detail, the **Article II.-1** is focused on the Melechov Pluton which is a unique composite granitic body in the northern part of the Moldanubian Batholith. The intrusive fabrics record incremental strain gradient in a granite diapir during final emplacement to the middle crust. The main conclusions are as follows:

- The Melechov Pluton is interpreted as a mid-crustal, vertically extensive granitic diapir with an apical part (diapir head) exposed at the present-day erosion level. The diapir head exhibits an overall concentric structure defined both by compositional zoning and magnetic fabric, and especially the latter is consistent with an idealized picture of igneous diapirs

known from the literature.

- Margin-parallel, outward-dipping magnetic foliations are associated with oblate shapes of the susceptibility ellipsoids and higher degree of anisotropy, passing inward into weaker triaxial to prolate fabric. Magnetic fabric of the inner Melechov granite, in places oriented at a high angle to the internal contacts and ductile host-rock structures, is interpreted as recording the internal diapir circulation as predicted by theoretical models..
- In terms of intensity and symmetry, the intrusive strain estimations from the AMS data using the Ježek–Hrouda method (SUSIE) are in agreement with strain gradients in the heads of model Newtonian diapirs travelling a distance of two body radii. Still, magnitudes of the calculated strains are lower near the outer margin of the Melechov diapir. The low degree of anisotropy and calculated strain intensities across the diapir are consistent with granitic magma ascent as a dilute, crystal-poor suspension followed by crystallization of fabric markers and their response to strain near the final emplacement level. This mechanism explains why the generally weak intrusive fabrics may still be capable of recording the within-diapir strain gradient.
- The SUSIE method has been proven to be particularly useful for strain estimations from the AMS in granite plutons, which otherwise typically lack reliable strain markers.

Article II.-2 brings new emplacement model based on structural and AMS data for the Říčany Pluton. The observed mesoscopic and magnetic fabrics are interpreted as a result of helical flow. The main conclusions are:

- The difference in K-feldspar phenocrysts contents caused significant difference in viscosities: the outer granite rich in K-feldspar phenocrysts (SPm) presumably had viscosity an order of magnitude higher than the central, relatively phenocrysts-poor granite (WPC).
- This assumption is in agreement with an exponential increase in viscosity with crystal content as predicted by the Einstein-Roscoe equation for solid–liquid mixtures.
- Considering the Říčany Pluton as a steep-sided cylindrical body, the Hagen-Poiseuille equation for fluid flow through a pipe can be applied to infer the flow mechanism within the pluton. Contrasting viscosities of the two magmas with dissimilar phenocrysts contents then would cause their different velocities during ascent. Consequently, faster subvertical flow of low-viscosity (phenocryst-poor) magma in the pluton center may have generated helical (subhorizontal) flow in the outer, high-viscosity and phenocrysts-rich layer.
- This two-layer model explains well the finite fabric pattern, with concentric, steep foliations

and magnetic lineations being subhorizontal along the pluton margin and subvertical in the centre. Taking into account the shallow emplacement level, the Říčany Pluton may be viewed as a conduit linking a deeper magma chamber with a volcanic system at the surface..

The **Chapter III** with **Articles III.-1, III.-2 and III.-3** brought new insights into the role of regional tectonics, including subduction, collision, continental indentation and late-orogenic strike-slip faulting, in granite emplacement and syn-magmatic deformation.

The **Article III.-1** describes the Štěnovice and Čistá granodiorite-tonalite plutons which are interpreted as representing the initial Late Devonian stage of subsequent early Carboniferous voluminous plutonism in the upper crust of the central Bohemian Massif.

The main conclusions are:

- The whole-rock and trace-element geochemical characteristics of the granodiorites-tonalites are consistent with the calcalkaline magma having been generated in a continental margin arc setting.
- These two plutons are largely discordant to the regional ductile structures in their nearby host rocks and have characteristics of concentrically expanded plutons (CEPs): elliptical cross-section in plan view, steep contacts, inferred downward-narrowing conical shape, faint normal zoning, and margin-parallel magmatic fabric decoupled from the regional host-rock structures.
- Combined with the existing geochronologic, geochemical, and tectonic data, the Čistá and Štěnovice plutons indicate an overall shift of plutonic activity from the ~NW to the ~SE in the upper-crustal Teplá–Barrandian Unit during Late Devonian to Early Carboniferous times. This temporal trend was accompanied by a general compositional shift from normal-K calc-alkaline to shoshonitic/ultrapotassic magmas.
- Such a pattern in the plutonic activity is compatible with the SE-directed subduction of the Saxothuringian Ocean beneath the Teplá–Barrandian plate as a principal cause of the Variscan arc-related plutonism in the core of the Bohemian Massif.

The **Article III.-2** is a structural study of the Ševětín Pluton that enabled detailed reconstruction of the Blanice Graben tectonic evolution and of the associated magmatic activity:

- The AMS study discovered steeply to moderately dipping planar magnetic fabrics that are interpreted mostly as solid-state in origin. Original magmatic foliation was preserved locally, in the central to eastern parts of the Ševětín Pluton.
- The overall sigmoidal trend of the magnetic fabrics indicates sinistral movements along the Blanice Graben fault systems postdating the intrusion of the biotite–muscovite granites of the Ševětín Pluton. This is further supported by well-defined subhorizontal magnetic lineation. The magnetic fabric of the Ševětín Pluton is thus in sharp contrast to the subhorizontal metamorphic foliation and subhorizontal NW–SE trending stretching lineation in the Moldanubian host rocks.
- Paleostress and kinematic analysis of brittle structures allowed us to distinguish three tectonic phases (oblique compression, strike-slip and extension), which post-dated the intrusion of the biotite–muscovite granite.
- The oblique compression phase comprised both the emplacement of the granite and early stages of its brittle deformation. It was accompanied by the formation of NE–SW trending joints (P_1) and dykes (aplite), both dipping moderately to the SE.
- The strike-slip phase indicates more or less E–W trending extension and can be correlated with the intrusion of c. 270 Ma microgranodiorite dikes. The orientation of the stress axis was, however, unfavourable for any further significant movements on the major faults of the Blanice Graben.
- The extension phase was accompanied by the formation of hydrothermal Pb–Zn–(Ag) quartz–carbonate veins and scarce P_5 and P_6 tension joints.

The **Article III.-3** summarizes tectonic evolution in the Bohemian Massif and clearly demonstrates how the orogenic processes and related deformation and plutonism evolved in space and time. As a consequence of overall convergence of Gondwana and Laurussia, four main episodes are recognized in the interior Bohemian Massif. For this thesis the most relevant are the final stages that corresponded to late readjustments within the amalgamated Bohemian Massif and that included rapid exhumation and voluminous ~327–330 Ma S-type-dominated granite plutonism.

The tectonothermal activity at the periphery around the consolidated orogen's core was followed by destruction of the orogenic belt, post-orogenic igneous activity, continental basin development, and multiple reactivations along the inherited basement fault zones.

On a global scale, this research has contributed to the discussion of processes that play main role in origin of igneous zoning in granitic plutons, especially at shallow crustal levels. Moreover it yielded general conclusions regarding the overall geodynamic context, sources of granitic magma in subduction and collisional settings, and its evolution right till emplacement. The study brings broader implications for timing, sources and development of Variscan plutonism in Bohemian Massif and as such to the magmatic and tectonic evolution of the Variscan orogen as a whole.

APPENDICES



Published Articles

I.-2; II.-1; II.-2; III.-1; III.-2; III.-3